On the accuracy of seismic fragilities for actual linear/nonlinear structural systems: the modified intensity measure method

Dissertation

submitted to and approved by the

Faculty of Architecture, Civil Engineering and Environmental Sciences
Technische Universität Braunschweig

and the

Department of Civil and Environmental Engineering
University of Florence

in candidacy for the degree of a
Doktor-Ingenieur (Dr.-Ing.) /
Dottore di Ricerca in Civil and Environmental Engineering[*)]

by
Matteo Ciano
born 03/05/1988
from Formia, Italy

Submitted on	16 April 2021
Oral examination on	17 June 2021
Professorial advisors	Prof. Dr.-Ing. Klaus Thiele Prof. Dr.-Ing. Massimiliano Gioffrè

2022

*) Either the German or the Italian form of the title may be used.

Universities of Florence, Perugia, Pisa and Braunschweig

International Doctorate in Civil and Environmental Engineering - XXXIII cycle

Curriculum: design, verification and control

On the accuracy of seismic fragilities for actual linear/nonlinear structural systems: the modified intensity measure method

---

PhD candidate: **Matteo Ciano**

Italian supervisor: **Prof. M. Gioffré**
German supervisor: **Prof. K. Thiele**

October 2020

Abstract

On the accuracy of seismic fragilities for actual linear/nonlinear structural systems: the modified intensity measure method

by

Matteo Ciano

In Performance-Based Earthquake Engineering (PBEE) the evaluation of structural efficiency by fragility analysis is formalized through a methodology with a probabilistic basis. Probabilistic treatment is required since there are the uncertainties of the seismic event properties (e.g. earthquake intensity), ground motion features and of the complex structural system response (e.g. nonlinear dynamic behaviour). A multidisciplinary knowledge, such as geology, seismology, civil engineering, etc., aims to apply this methodology based on the performance. The greatest interest for structural civil engineering is focused to two parameters in PBEE, that are the seismic intensity measure IM and the system demand parameter D, which reflect the seismic hazard and the structural response, respectively.

Several definitions can be provided for the demand parameter and the intensity measure in order to investigate the different quantities that characterize the structural response and the seismic input. In general, for both of these definitions, the formalization is provided in terms of acceleration, displacement, energy, etc. The fragility analysis for a structural system is based on these parameters, i.e. D and IM, to develop the fragility curves. Seismic fragilities quantify the probability that the structural response of a system overcomes specified limit states for given seismic intensity measure (IM). The intensity measure is an intermediate variable that connects the seismic fragility analysis with the structural analysis, and the demand parameter depends intensely on the chosen IM. Specific features are required of an ideal IM, it should be efficient and sufficient. The efficiency is inherent to the low dispersion that should be characterize the demand parameters and IM, while the sufficiency imples that D evaluated by a seismic ground motion acceleretion with an IM value should be only dependent on the value of this IM, and not on other seismic groud motion features (i.e. fault mechanims, magnitude, etc.).

The common method used in PBEE to estimate the seismic fragility curve is based on scaling the seismic accelerograms with a reference intensity measure IM. This method is widely applied because it is simple and, together with Monte Carlo simulation, it overcomes the problem of the limited number of natural recorded ground motions available for fragility analysis. This method describe a helpful tool for the structural engineering, but on the contrary it gives limited if any information on the structural seismic performance when the dependence between the IM and D is weak. In the probabilist field, the IM and D take a meaning of stochastic variables. When the two variables are not dependent it is a clear violation of the efficiency condition that the IM must possess. The dependence between these variables plays a fundamental role on the accuracy in fragility analysis. In particular, this dependence depedes on the seismic direction, the intensity measure and the demand parameter considered. For

the same IM the dependence can vary significantly with different seismic directions, with which the fragility analysis is developed. The method based on scaled seismic ground motion acceleration is very useful, this is not questioned, but it needs the use of efficient IM for give accurate results.

This thesis presents a general approach to improve the accuracy in fragilities estimation when the dependence between the intensity measure IM and the demand parameter D is weak and the widely used method in Performance-Based Earthquake Engineering does not give accurate results. This general approach is based on a modified version of the current intensity measure method. In particular, once an IM is chosen it is mapped in a suitable space where D and the IM are correlated (i.e. are dependent). The proposed algorithm is based on a linear transformation of samples of a given IM, which improves the correlation with a set of demand parameters. Fragility curves are obtained using the transformed IM samples and compared with those estimated with the standard approach. In general, this methodology can be apply for any classical IM definitions. Numerical results for single/multi-degree of freedom systems case are provided. In particular, for the category of the complex real multi-degree of freedom system, a numerical model of a structural system of a school in Norcia (Italy), that was affected by the 2016 earthquake sequence, is also considered. Finally, the effectiveness of this general approach is demonstrated for all the case studies considering linear/nonlinear behaviour by comparing the fragility estimates obtained with a chosen seismic intensity measure and the its modified version.

Acknowledgment

I want to sincerely thank my academic mentors Prof. Massimiliano Gioffré and Prof. Klaus Thiele for guiding me during this PhD program, passing on their experience in the world of research and for their precious advice.

I would like to thank all professors of the doctoral board on the Italian and German side.

During this experience I met many colleagues not only from my cycle, it was a real pleasure to share this experience with them, I thank them.

Finally, my biggest thanks go to my family, girlfriend and friends for the moral support that was crucial to achieving this important goal.

"A reasonable probability is the only certainty."

Edgar Watson Howe

Contents

List of Figures

List of Tables

Abbreviations

ATC	Applied Technology Council
BRAD	Buckling-Restrained Axial Damper
CDF	Cumulative Distribution Function
D	Demand Parameter
$\mathfrak{D}$	Damage State
DOF	Degree Of Freedom
DV	Decision Variable
FE	Finite Element
FEMA	Federal Emergency Management Agency
FNA	Fast Nonlinear Analysis
IM	Intensity Measure
LS	Limit State
MC	Monte Carlo
MDOF	Multi-Degree Of Freedom
mIM	Modified Intensity Measure
PBEE	Performance-Based Earthquake Engineering
PEER	Pacific Earthquake Engineering Research Center
PDF	Probability Density Function
PGA	Peak Ground Acceleration

PSD	Power Spectral Density
RCF	Reinforced Concrete Frame
SDOF	Single Degree Of Freedom

Chapter 1

Introduction

1.1 General overview of the topic

Earthquakes are natural phenomena that are caused by the movement of tectonic plates deep below the earth's crust. The energy released during these phenomena spreads through seismic waves and produces ground movement and accelerations at earth's surface. The nature of earthquake induces on the civil structures an inertia forces and dynamic oscillations. For this reason, in seismic regions these natural phenomena produce many collapses for several class of structures.

The traditional aim of seismic engineering design has been to prevent structural collapse. After the 1994 Northridge and 1995 Kobe earthquakes [1, 2], the damage level, economic loss due to downtime and repair cost of the structures were unacceptably high even if those structures were complied with available seismic design protocol at that era. This has produced, a shift on the main focus for the seismic engineering towards building performance. For this regard, the awareness gained of the scientific community therefore has introduced the concept of Performance-Based Earthquake Engineering (PBEE). First-generation PBEE [3] is defined as a design framework for considering the desired system performance at various intensity levels of seismic haz-

ard. The combination of desired performance and hazard levels are used as design criteria. Subsequently, other documents [4–7] were introduced that are part of this first-generation family, where the element deformation and force acceptability criteria corresponding to the performance are specified for different structural and non-structural elements for linear, nonlinear, static, and dynamic analysis. For both, the demand and capability of a structural system there is not a probabilistic description with these criteria. Moreover, the element performance evaluation does not take into account the global performance. The shortcomings of the first-generation procedures incapable to a probabilistic evaluation of system performance measures, such as monetary losses, downtime, and causalities, brought to the development of the second-generation PBEE by Pacific Earthquake Engineering Research Center (PEER), USA. The base of this last generation methodology regards to the rigorous estimation in probabilistic field for the different uncertainties in seismic engineering, such as the earthquake intensity, ground motion characterization, structural response, physical damage, and economic and human losses.

The PEER methodology is formalized in a probabilist assessment framework in terms of hazard analysis, structural/nonstructural analysis, damage analysis and loss analysis. In particular, referring in [8], the outcome of each step is mathematically characterized by one of four generalized variables: intensity measure IM, structural demand parameter D (commonly called engineering demand parameter), damage state $\mathfrak{D}$, and decision variable DV. For an example of these variables consider to the peak ground acceleration (PGA), inter-story drift, structural component damage, and repair cost, respectively. In general, these variables are expressed in a probabilistic sense as conditional probabilities of exceedance.

Fragility analysis is formalized to developing the structural/nonstructural and damage analysis for produce the fragility curve. This curve is the conditional failure probability of a structural system given the seismic event with level intensity $\xi = IM$.

Several procedures were proposed in literature to estimate the fragilities. A definition, that it is easy to interpret, is based on the concept of the relative frequency [9]. The failure probability is the number of the structural performances that exceed the prefixed threshold on the total observed number of the seismic events with ξ. The previously definition of failure probability can be applied increasing the ξ value that multiplies a numbers of scaled ground motion acceleration time series in reference to own IM to evaluate the structural response observations. In [10] the Federal Emergency Management Agency (FEMA), proposes a fragility analysis methodology based on the scaling phase of the accelerograms with a selected IM. This method is all the more accurate as the total number of observations increases, and for its easy understanding, it is more used in the structural civil engineers society being a very practical tool. The use of Monte Carlo (MC) simulation together the FEMA's method allows to properly propagate uncertainty on structural models and earthquake features. In this context, it is common practice to distinguish epistemic and aleatory uncertainties [11, 12]. Other definitions are taken into account in PBEE, where a lognormal fragility curve is generally assumed [13]. This considerably reduces the computational burden since only the median and log-standard deviation of the fragility curve have to be estimated.

The choice of the intensity measure is another key issue in the implementation of the PBEE methodologies, as well as for the fragility curves development. First contribution in [14] introduces the notion of "efficiency" and "sufficiency" of an IM. In this context, an intensity measure can be efficient if it produces low dispersion on the structural parameter investigated. While the sufficiency property has meaning in reference to the D evaluated by a seismic ground motion acceleration with $\xi = IM$ value, it should be only dependent of this selected IM, and not on other seismic ground motion features (e.g. magnitude, source distance, ect.). These criteria describe a guide to choose an intensity measure for structural fragility assessment.

1.2 Main contributions

Considering the widespread use of the practical methodology in PBEE, as propose by FEMA [10], where the fragility analysis is developed scaling the ground motion acceleration time series with a reference intensity measure, in this research thesis work the study of the accuracy in fragility estimation based on this kind of method is developed. The uncertainties related to the use of intensity measures (IMs) in fragility analysis is considered. The reason for this, comes from the recent contribution reported in [15]. It is demonstrated that if the dependence between D and IM is weak, the fragility estimate provides any if limited informations on structural seismic performance. The weak dependence relating to the used parameters in fragility analysis, i.e. D and IM, is a strict consequence of the violation of the efficiency property required for IM.

Along this line, in this thesis a general approach is proposed to improve the accuracy in fragility analysis when the dependence between D and IM is weak and the widely used method in PBEE [10] does not give accurate results. Therefore the purpose is achieved according to identifying several specific objectives, which can be summarized in the following key points:

1. in-depth study of the theoretical problem of determining accurate results in fragility analysis;

2. investigation of the dependence between D and several IMs for simple or complex linear/nonlinear structural systems;

3. development of the general methodology based on a modified version of the current intensity measure method;

4. demonstrate the validity and efficiency of the proposed method compared to that commonly used in fragility analysis.

1.3 Thesis structure

The thesis is organized with the following structure of the contents.

Chapter 1 presents the general overview of the addressed topic in this work, the research objectives and main contributions.

Chapter 2 introduces the necessary tools normally used to modeling and quantify in earthquake engineering. In particular, elements of the probability theory and statistics, the stochastic structural dynamic problem, seismic acceleration ground motion stochastic process and the Monte Carlo simulation are described.

Chapter 3 focuses attention on the fundamental concepts regard to the fragility analysis. A complete literature overview on the different approaches for the derivation of fragility functions and the formulations to approximate/estimate these curves are provided together the algorithm of the most widespread methodology in PBEE. The main demand parameters and intensity measures used in earthquake engineering are reported.

Chapter 4 addresses the accuracy in fragility analysis provided by the intensity measures and the related issue with the problem definition of the fragilities. The proposed algorithm to define the modified version of an intensity measure is presented. To introduce this methodology, an application example based on simple linear elementary oscillator is shown.

Chapter 5 reports the fragility analysis improvement for analytical systems with a single or multiple degree of freedom and linear/nonlinear behaviour. For each of these dynamic system typologies, first the dependence between the selected demand param-

eter and an intensity measure is studied, second this dependence is improved by the modified intensity measure approach, and finally the obtained fragilities by an original intensity measure and the relative modified version are compared.

Chapter 6 faces the accuracy improvement for real complex multi-degree of freedom structural system. The Norcia school building is the selected case study. First of all, the seismic hazard for the Norcia school site is characterized, second, the dependence between several demand parameters and an intensity measures is investigated for linear/nonlinear behaviour of the school building model, third, the modified versions of some selected intensity measures are defined by the proposed methodology in order to improve the dependence with the structural demand parameters, and finally, a comparison is carried out for the fragility functions resulting by the original intensity measures and their modified versions.

Chapter 7 makes a summary of the research activity, the major conclusions drawn from this study.

Chapter 2

Tools in earthquake engineering

2.1 Introduction

For second-generation approaches in PBEE and, particularly, in the seismic fragility analysis, an aleatory treatment is necessary. This achievement is obtained by considering the classical models used in earthquake engineering with a probabilistic view. To model the physical behaviour of structural systems, i.e. continuous bodies, in classical mechanics the equations of dynamic equilibrium as a function of precise weights are used. The behavioral hypothesis of a particular system provides simpler or more complicated formulations. In this context and for this present research work, the uncertainties are considered only in reference to the seismic hazard, while the quantities related to properties of the structural system (the weights) are deterministic, i.e. the epistemic uncertainties are not considered.

This chapter introduces the main mathematical and physical concepts used in this thesis for modelling the structural systems behaviour evolution and simulation the seismic ground motion actions in order to quantify and represent, as a stochastic variables, the structural capacity and seismic request to a system (the demand parameter and intensity measure).

2.2 Probability theory and statistics

In wide and modern view related to the stochastic structural dynamic and the randomness of the earthquake events is required. In this section, the probability and statistical concepts bases are introduced.

The objective is to provide a strong definition and/or a contextualization for main quantities that will be used in the following chapters of this thesis.

2.2.1 Stochastic variables

The outcomes for most physical problems are numerical values. In a completely general affirmation, an aleatory phenomenon can be represented by a random number X (e.g. demand parameter D or intensity measure IM). Since the value of X depends on the trial outcome which is represented by a sample point ω belonging to space sample Ω, X is clearly a function defined on Ω. It is possible to write [16]:

$$X = X(\omega)\,, \quad \text{with} \quad \omega \in \Omega \tag{2.1}$$

where $X(\omega)$ is called a random variable, aleatory variable or stochastic variable. Typically, the argument ω is omitted and it is praxis in science literature to consider for simplicity X. There are two types of random variables:

- the discrete stochastic variables are capable of taking on only a finite or countably infinite number of distinct values;
- the continuous stochastic variables are capable of taking on any values within one or several given intervals.

A continuous random variable is necessarily associated with an uncountable sample space. In general, a stochastic variable may be vectorially valued and it will called random vector.

A function of X, i.e. $Y = g(X)$, is also a random variable. The $g(\cdot)$, for a easy concept, is a function with at most a finite number of discontinuities, namely Borel function [16]. A general case of m functions of n random variables can be considered; let $X_1, X_2, \ldots, X_n$ be stochastic variables, then

$$Y_k = g_k(X_1, X_2, \ldots, X_n) \quad \text{with} \quad k = 1, 2, \ldots, m\,;\, m \leq n \tag{2.2}$$

are also aleatory variables if the g_k's are Borel functions.

2.2.2 The probability characterization

If a random variable is discrete, the direct mode to define the probabilities for X to take discrete values is

$$P_X(x) = P_r(X = x) \quad \text{with} \quad x = a_1, a_2, \ldots, a_n \tag{2.3}$$

where n may be finite or infinite. The (2.3) is also called probability function of the random variable X and x is the state variable or the range variable of X. It is possible to define the probability distribution function or cumulative distribution function (CDF) of X as

$$F_X(x) = P_X(x) = P_r(X \leqslant x) = \sum_{x_i \leqslant x} P_X(x_i)\,. \tag{2.4}$$

The (2.4) must satisfy the following

$$F_X(-\infty) = 0 \quad \text{and} \quad F_X(+\infty) = 1\,. \tag{2.5}$$

However, the probability function cannot be used to describe a continuous aleatory variable unlike for the CDF which is suitable. By the derivative of $F_X(x)$ is defined

the probability density function (PDF)

$$f_X(x) = \frac{dF_X(x)}{dx} = \lim_{\Delta x \to 0} \frac{F_X(x + \Delta x) - F_X(x)}{\Delta x} \tag{2.6}$$

assuming the existence of this derivative. From the inversion of Eq. (2.5) it is provided

$$F_X(x) = \int_{-\infty}^{x} f_X(x')\, dx' \tag{2.7}$$

using the condition $F_X(-\infty) = 0$, and for upper limit of the integral that goes to $+\infty$, or simply ∞, provides

$$\int_{-\infty}^{\infty} f_X(x)\, dx = F_X(\infty) = 1 \tag{2.8}$$

which is often referred as the normalization condition of a PDF.

The expected value of X is defined as

$$E[X] = \int_{-\infty}^{\infty} x f_X(x)\, dx \tag{2.9}$$

and it is well defined only when $\int_{-\infty}^{\infty} |x| f_X(x)\, dx < \infty$. The expected value is also called as ensemble average, statistical average, the mean and mathematical expectation.

Let X and Y be a two discrete stochastic variables. A physical contextualization can be provided considering X and Y as D and IM, respectively. The probability for $X = x$ on the condition that $Y = y$ is given by

$$P_{X|Y}(x|y) = \frac{P_{XY}(x, y)}{P_Y(y)} \tag{2.10}$$

that is valid only when $P_Y(y) > 0$. The random variable X is said to be independent

to that Y if $P_{X|Y}(x|y) = P_X(x)$ [16]. In the case of continuous random variables

$$\frac{f_{XY}(x,y)\,dx\,dy}{f_Y(y)\,dy} = \frac{f_{XY}(x,y)\,dx}{f_Y(y)}\,. \tag{2.11}$$

The limiting form is the probability for X to be the infinitesimal interval $[x, x+dx]$ conditional on $Y = y$. Therefore, the conditional probability density function is

$$f_{X|Y}(x|y) = \frac{f_{XY}(x,y)}{f_Y(y)} = \frac{f_{XY}(x,y)}{\int_{-\infty}^{\infty} f_{XY}(x,y)\,dx} \tag{2.12}$$

that is again meaningful for $f_Y(y) > 0$. The definition of independence for two continuous aleatory variables is

$$f_{X|Y}(x|y) = f_X(x) \tag{2.13}$$

which implies

$$f_{XY}(x,y) = f_X(x) f_Y(y)\,. \tag{2.14}$$

The first part of (2.12) can be rewritten to define the joint probability density as

$$f_{XY}(x,y) = f_Y(y) f_{X|Y}(x|y) \tag{2.15}$$

and its integration gives

$$f_X(x) = \int_{-\infty}^{\infty} f_{XY}(x,y)\,dy = \int_{-\infty}^{\infty} f_{X|Y}(x|y) f_Y(y)\,dy \tag{2.16}$$

which shows as the unconditional probability function may be computed from the conditional probability density.

The validity of (2.13) through (2.16) is extended to the discrete or mixed continuous-discrete stochastic variable by admitting the Dirac delta function in the representation of the various probability densities. The conditional CDF can be obtained from the

integration of (2.12):

$$F_{X|Y}(x|y) = \frac{\int_{-\infty}^{x} f_{XY}(x', y)\, dx'}{f_Y(y)} \tag{2.17}$$

manipulation and integration provides

$$F_X(x) = \int_{-\infty}^{\infty} F_{X|Y}(x|y) f_Y(y)\, dy\,. \tag{2.18}$$

The expected value of X on the condition that Y takes on a value y is given by

$$E[X|Y = y] = \int_{-\infty}^{\infty} x f_{X|Y}(x|y)\, dx \tag{2.19}$$

and it is well defined if $\int_{-\infty}^{\infty} x f_{X|Y}(x|y)\, dx < \infty$. The expectation of $E[X|Y]$ is given as

$$E\{E[X|Y = y]\} = \int_{-\infty}^{\infty} \left[\int_{-\infty}^{\infty} x f_{X|Y}(x|y)\, dx \right] f_Y(y)\, dy = E[X] \tag{2.20}$$

i.e. the expected value of X.

2.2.3 Moments

A class of expected values is that of the various powers of one or several random variables. These expected values are the moments. For a single stochastic variable the $E[X]$ is known as the first moment, $E[X^2]$ the second moment and $E[X^n]$ the n-th moment. For two or more random variables the quantity $E[X^m Y^n]$ is called the joint moment of X and Y of the $(m+n)$-th order, and $E[X_1^{n_1} X_2^{n_2} \dots X_k^{n_k}]$ the joint moment of $X_1, X_2, \dots, X_k$ of the $(n_1 + n_2 + \dots + n_k)$-th order.

Let $\mu_X = E[X]$ be the first moment of X, i.e. the mean value; the quantity $E[(X - \mu_X)^n]$ is called the n-th central moment of X, $E[(X - \mu_X)^m (Y - \mu_Y)^n]$ the $(m+n)$-th joint central moment of X and Y. For the following expression is attributed

specific name

$$E[(X-\mu_X)^2] = E[X^2] - \mu_X^2 = \sigma_X^2 \tag{2.21}$$

it is the variance of X. The square root of the variance, namely σ_X, is called the standard deviation of X. For two random variables, it is defined as

$$E[(X-\mu_X)(Y-\mu_Y)] = E[XY] - \mu_X\mu_Y = C_{XY} \tag{2.22}$$

i.e. the covariance of X and Y. The two random variables, X and Y, are said to be uncorrelated or linear independent if their covariance is zero, i.e. $C_{XY} = 0$. The covariance clearly describes when two aleatory variables are uncorrelated, however the uncorrelated is not sufficient condition for the independence definition.

More convenient is to normalize the covariance to define the correlation coefficient

$$\rho_{XY} = \frac{C_{XY}}{\sigma_X\sigma_Y}\,. \tag{2.23}$$

The correlation coefficient has always values between -1 and 1; the random variables X and Y, for $\rho_{XY} = 0$ are independent, while for $\rho_{XY} = -1$ or $\rho_{XY} = 1$ are dependent or correlated.

It is a consolidated praxis in the stochastic field to work with standardized variables. The standardization or auto-scaling of the aleatory variable X as

$$Z(X) = \frac{X-\mu_X}{\sigma_X} \tag{2.24}$$

namely the standardized random variable which has the following properties

$$E[Z] = \frac{E[X-\mu_X]}{\sigma_X} = 0 \quad \text{and} \quad \sigma_Z^2 = \frac{E[(X-\mu_X)^2]}{\sigma_X^2} = 1 \tag{2.25}$$

i.e. Z has zero-mean and unit variance.

2.2.4 Stochastic processes

A stochastic process is a parameterized family of random variables with the parameter (or parameters) which is belonging to an indexing set (or sets) [17]. An interpretation of this definition can be done considering the random displacement of an arbitrary system. In this context, the interest for the random displacement focus not only one time but also at other times, i.e. a family of aleatory variables $X(t_1), X(t_2), \ldots$. The entire family is $\{X(t) : t \in T\}$, or simply $X(t)$, where t takes values in the set T. Adding another dependency parameter, $\{X(t) : t \in T, s \in S\}$ or simply $X(t, s)$. In general, t and s have meaning of time and space coordinates.

A stochastic process is also called time series, typically for time-parametered random processes. If the indexing set is finite, a random process is a random vector; if the indexing set is countably infinite, it is a random sequence. Moreover, a stochastic process can be defined discrete or continuous depending upon whether it is a family of discrete or continuous random variables. In particular, the adjective continuous does not refer to the continuity of random function with respect to its parameter. Since the parameter may belong to a countable or an uncountable indexing set, a stochastic process can be defined in one of four broad categories [17]:

- continuously parametered continuous stochastic processes;
- continuously parametered discrete stochastic processes;
- discretely parametered continuous stochastic processes;
- discretely parametered discrete stochastic processes.

2.3 Bases of stochastic structural dynamic

Concepts regard the dynamic behaviour of civil structures to earthquake excitation are introduced in this section. The structural dynamics problem is formulated through an idealization of the real systems with a linear/nonlinear single or multi-degree of freedom model. For these models, the equilibrium equation of motion under seismic excitation in stochastic form are introduced. Most of the these notions are extracted from [18].

2.3.1 Linear single degree of freedom system

The simple structures can be idealized as a concentrated or lumped mass supported by a massless structure with stiffness in the lateral direction. The number of independent displacements required to define the positions of all the masses relative to their original position is called the number of degrees of freedom (DOFs) for dynamic analysis. An idealized one-story structure can be described thought a single degree of freedom (SDOF) system as shown in Figure 2.1a.

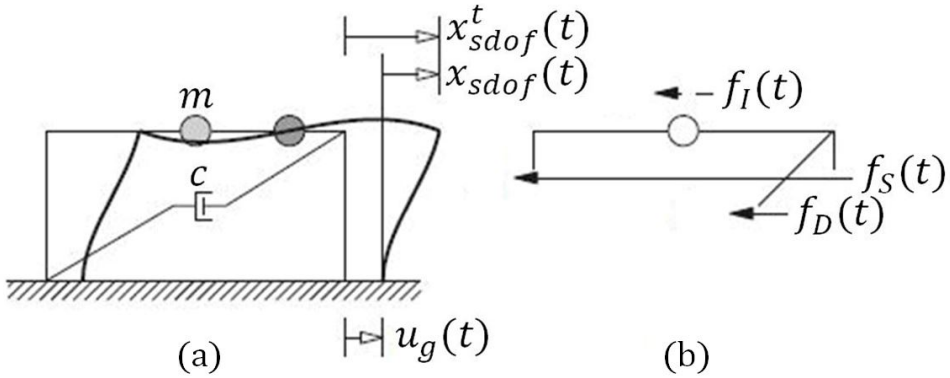

Figure 2.1: Single degree of freedom system to a sample of ground motion $u_g(t)$: (a) idealization scheme; (b) dynamic equilibrium (sample of (2.26)).

The dynamic equilibrium for ground acceleration stochastic process $A(t)$ is generalized as

$$F_I(t) + F_D(t) + F_S(t) = 0 \tag{2.26}$$

i.e. the sum of inertia force $F_I(t)$, damping force $F_D(t)$ and stiffness force $F_S(t)$ in the time. In general context, $F_S(t)$ is a function of the displacement or deformation response process $X_{sdof}(t)$ of SDOF system

$$F_S(t) = F_S(t, X_{sdof}(t)) \tag{2.27}$$

and this relation can be specified depending on the system behaviour (e.g. linear). Figure 2.1b shows the concept of dynamic equilibrium for a sample of inertia force $f_I(t)$, of damping force $f_D(t)$ and stiffness force $f_S(t)$.

The damping force is attributable to the phenomenon by which free viration steadily diminishes in amplitude. The energy of the vibrating system is dissipated by various mechanisms, and often more than one mechanism may be present at the same time (i.e. thermal effect, internal friction, etc...). Usually, the damping is represented in a highly idealized manner. The equivalent viscous damping concept is used to describe the damping forces in classical dynamic

$$F_D(t) = c\dot{X}_{sdof}(t) \tag{2.28}$$

where the constant c is the viscous damping coefficient (force x time/length) and $\dot{X}_{sdof}(t)$ is the velocity response process of SDOF system. The displacement ground process $U_g(t)$, imposed to the base of an system during an earthquake events, determines the total displacement process on mass m of SDOF system

$$X^t_{sdof}(t) = U_g(t) + X_{sdof}(t) \tag{2.29}$$

both $X^t_{sdof}(t)$ and $U_g(t)$ refer to the same inertial frame of reference and their positive directions coincide. One sample of quantities in (2.29) are schematized in Figure 2.1a. Only the relative motion $X_{sdof}(t)$ between the mass and the base due to structural deformation produces stiffness and damping forces. The $F_I(t)$ is related to the total

acceleration process $\ddot{X}^t_{sdof}(t)$ and mass by

$$F_I(t) = m\ddot{X}^t_{sdof}(t)\,. \tag{2.30}$$

Substituting Eqs. (2.27), (2.28) and (2.30) in (2.26) provides

$$m\ddot{X}_{sdof}(t) + c\dot{X}_{sdof}(t) + Fs(t, X_{sdof}(t)) = -mA(t) \tag{2.31}$$

the equation of motion for SDOF system, where the quantity $-mA(t)$ is the external force process that is evaluated from each samples of ground acceleration $a(t)$ of $A(t)$ and $\ddot{X}_{sdof}(t)$ is the acceleration response process of SDOF system. The demand parameter D_{sdof} for general SDOF system to $A(t)$ can be provide as

$$D_{sdof} = \max_{0 \leqslant t \leqslant \tau} |X_{sdof}(t)| \tag{2.32}$$

where τ is the time length of $A(t)$.

If the (2.27) is contextualized for linear SDOF system, i.e. the relation that describes $F_S(t)$ is linear

$$F_S(t) = kX_{lsdof}(t) \tag{2.33}$$

where k is the lateral stiffness (force/length), the equation of motion governing the displacement response process $X_{lsdof}(t)$ of linear SDOF system to $A(t)$ is written as

$$m\ddot{X}_{lsdof}(t) + c\dot{X}_{lsdof}(t) + kX_{lsdof}(t) = -mA(t) \tag{2.34}$$

dividing by m gives

$$\ddot{X}_{lsdof}(t) + 2\zeta\omega_0\dot{X}_{lsdof}(t) + \omega_0^2 X_{lsdof}(t) = -A(t) \tag{2.35}$$

where $\omega_0 = \sqrt{k/m}$ is the natural pulsation and $\zeta = c/2m\omega_0$ is the damping ratio.

Considering a linear SDOF system, Equation (2.32) becomes the response spectra

$$S_d(T,\zeta) = D_{lsdof} = \max_{0 \leqslant t \leqslant \tau} |X_{lsdof}(t)| \tag{2.36}$$

where $T = 2\pi/\sqrt{k/m}$ and D_{lsdof} are the period and demand parameter of linear SDOF system to $A(t)$ for linear elementary oscillator by Eq. (2.35) with changing T value, respectively. The pseudo-velocity and pseudo-acceleration response spectra are

$$S_v(T,\zeta) = (2\pi/T) S_d(T,\zeta) \tag{2.37}$$

$$S_a(T,\zeta) = (2\pi/T)^2 S_d(T,\zeta)\,. \tag{2.38}$$

As an example, a sample of the response spectrum, pseudo-velocity and pseudo-acceleration response spectrum for the El Centro 1940 earthquake are shown in Figure 2.2, assuming $\zeta = 2\%$.

The (2.34) and (2.35) are a second order differential equations, and their classical resolution is obtained with the sum of complementary solution $X^c_{lsdof}(t)$ and particular solution $X^p_{lsdof}(t)$, that is, $X_{lsdof}(t) = X^c_{lsdof}(t) + X^p_{lsdof}(t)$. The solution can be provide by numerical time-stepping methods for integration of differential equations, e.g. the Newmark's method [19].

2.3.2 Nonlinear single degree of freedom system

In earthquake engineering, there is the interest to studying the dynamic response of inelastic systems because many structures are designed with the expectation that they will undergo some cracking, yielding, and damage during intense ground shaking caused

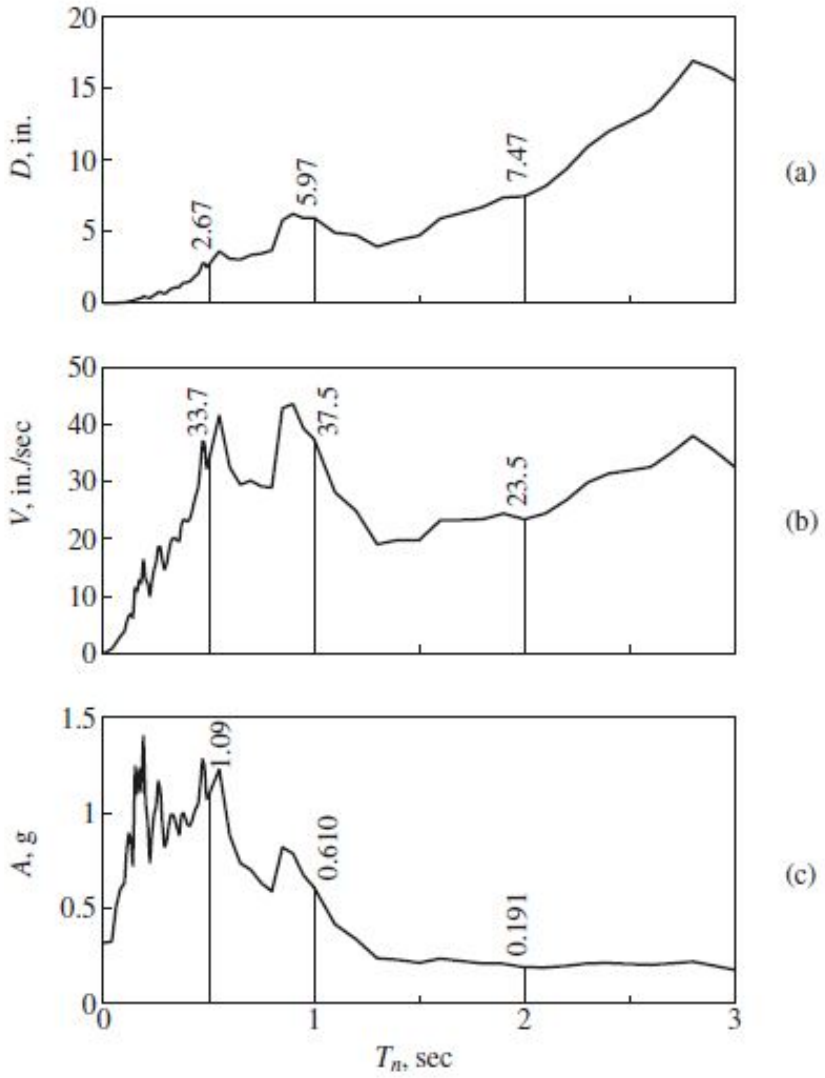

Figure 2.2: Response spectra sample with $\zeta = 2\%$ for El Centro 1940 ground motion: (a) response spectrum; (b) pseudo-velocity response spectrum; (c) pseudo-acceleration response spectrum [18].

by earthquake events.

For example, let consider a structural steel component. When this element undergoes the cyclic deformations expected during earthquakes, the typical force-deformation relation is inelastic [20], i.e. nonlinear. This implies that the force–deformation relation is path dependent, i.e., it depends on whether the deformation is increasing or decreasing. The stiffness force is an implicit function of deformation as in Eq. (2.27).

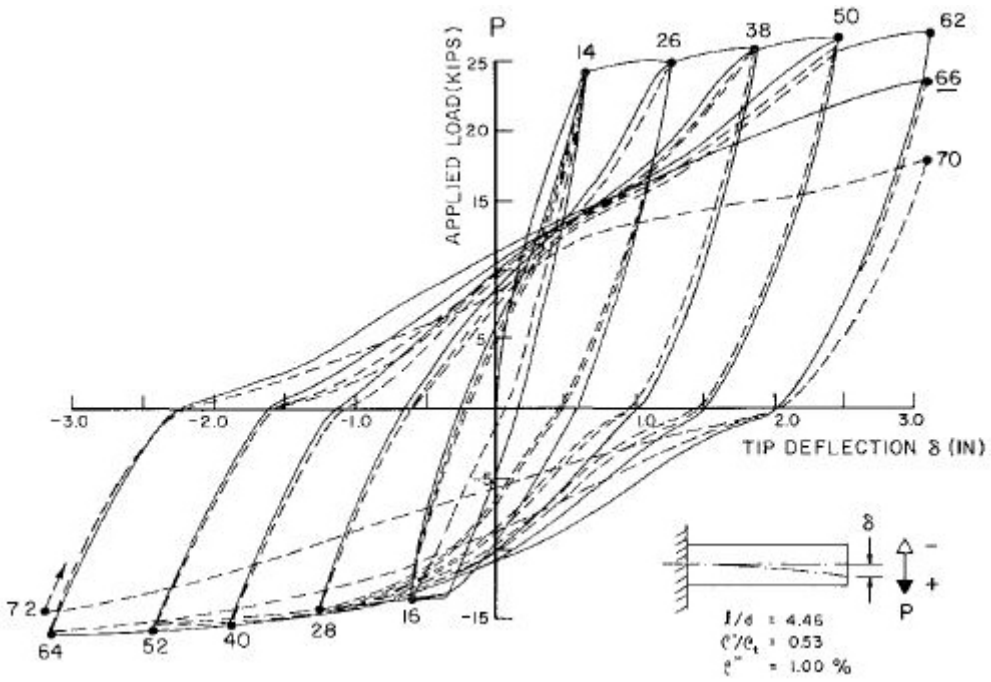

Figure 2.3: Force-deformation relation for a reinforced concrete element to a cyclic load [21].

This behaviour is also manifested for the reinforced concrete elements to cyclic load, as it shows in Figure 2.3 extracted form the experimental campaign in [21]. A relation as in Figure 2.3 is described with a hysteretic model, in which the system behaviour is characterized with a late reactivity to the applied stresses and depending on the previous deformation state.

Duffing single degree of freedom system

Duffing in [22] has introduced a nonlinear equation describing an oscillator with a cubic nonlinearity. Many physical systems can be approximate with the Duffing's model since it has apparent and enigmatic simplicity or because it is a convenient mathematical model to investigate new solution methods.

The source of the nonlinearity in a mechanical system that results in its dynamic behaviour being modelled by the Duffing equation is the stiffness. Stiffness is generally a function of position or deformation (2.27), this means that the $F_s(t)$, and the resulting

displacement process $X_{dsdof}(t)$ of Duffing's oscillator have a nonlinear relationship. If the system is symmetric, i.e., the stiffness characteristic is the same when there is a compression or tension, then the restoring force can be approximated as a series in $X_{dsdof}(t)$ in which the exponents of $X_{dsdof}(t)$ are odd integers. If this series is truncated after the first two terms, then the force–deformation relationship is given by

$$F_S(t) = kX_{dsdof}(t) \pm k\gamma X^3_{dsdof}(t) \tag{2.39}$$

where γ is an constant that describe the nonlinear behaviour. For $\gamma = 0$ the (2.39) becomes (2.33), i.e. linear. If the cubic term in (2.39) is positive (negative), the stiffness undergoes a hardening (softening) because it becomes stiffer (softer) as the displacement increases. For a numerical treatment, considering the positive or negative cubic term is equivalent. By considering positive cubic term (hardening) and substituting the Eqs. (2.39), (2.28) and (2.30) in (2.26) provides

$$m\ddot{X}_{dsdof}(t) + c\dot{X}_{dsdof}(t) + k\left(X_{dsdof}(t) + \gamma X^3_{dsdof}(t)\right) = -mA(t) \tag{2.40}$$

dividing by m gives

$$\ddot{X}_{dsdof}(t) + 2\zeta\omega_0\dot{X}_{dsdof}(t) + \omega_0^2\left(X_{dsdof}(t) + \gamma X^3_{dsdof}(t)\right) = -A(t) \tag{2.41}$$

i.e. the equation of motion for Duffing SDOF system to $A(t)$. The (2.40) or (2.41) differential ordinary equation can be solved with the iterative Runge-Kutta method [23].

Bouc-Wen single degree of freedom system

Commonly model used in seismic structural analysis to describe the hysteretic behaviour of systems was introduced by Bouc [24]. Bouc's model has been modified and improved further to include the time dependent degradation and pinching effects

commonly observed in structures subjected to earthquake induced ground motions. Because of the analytical simplicity, Bouc's model has been of special interest later and it was extensively used by Wen [25].

In reference to (2.27), the restoring or stiffness force in the Bouc-Wen model is influenced also by the velocity response process of SDOF system

$$F_S(t) = F_S(t, X_{sdof}(t), \dot{X}_{sdof}(t)) \tag{2.42}$$

i.e. the impulses of external force influence the system response. To include the hysteretic behaviour along with that linear, Wen in [26] has proposed the following expression to model the restoring force in (2.42)

$$F_S(t) = k\left[\eta X_{bwsdof}(t) + (1-\eta)W(t)\right] \tag{2.43}$$

where $W(t)$ is auxiliary process which has hysteretic characteristics. Thus the second part in the (2.43) represents a nonlinear element in parallel with that linear represented by the first part. The quantity η is a weighting constant, it represents the relative participations of the linear and nonlinear terms. When $\eta = 1$ the (2.43) becomes (2.33), i.e. only a linear behaviour is provided.

To model the hysteretic behaviour through $W(t)$ in(2.43), it was proposed an endochronic law [25]

$$\dot{W}(t) = \gamma \dot{X}_{bwsdof}(t) - \alpha|\dot{X}_{bwsdof}(t)|\,|W(t)|^{n-1}W(t) - \beta\dot{X}_{bwsdof}(t)|W(t)|^n \tag{2.44}$$

where the four constants γ, α, β and n are a parameters that modify the shape of hysteretic curve [27].

Substituting the Eqs. (2.43), (2.28) and (2.30) in (2.26) provides

$$m\ddot{X}_{bwsdof}(t) + c\dot{X}_{bwsdof}(t) + k\left[\eta X_{bwsdof}(t) + (1-\eta)W(t)\right] = -mA(t) \quad \text{with} \quad \text{Eq. (2.44)} \tag{2.45}$$

dividing by m

$$\ddot{X}_{bwsdof}(t) + 2\zeta\omega_0\dot{X}_{bwsdof}(t) + \omega_0^2\left[\eta X_{bwsdof}(t) + (1-\eta)W(t)\right] = -A(t) \quad \text{with} \quad \text{Eq. (2.44)} \tag{2.46}$$

i.e. the equation of motion that governs the response process of Bouc-Wen SDOF system subjected to $A(t)$. The (2.45) or (2.46) differential ordinary equation can be always solved with the iterative Runge-Kutta method [23].

2.3.3 Linear multi-degree of freedom system

As base to the finite element (FE) method, which is one of the most important developments in applied mechanics [28], the concept of equations of motion for multi-degree of freedom (MDOF) system subject to earthquake excitation are formulated here. Main aim of this, is to predicting how structures respond to earthquake-induced motion at the base of the structure. To introduce these notions, a idealized multi-storey frame with n number of floors is considered (Figure 2.4). For each floor, a lumped mass is taken into account and the whole massless structure provides the stiffness in the lateral direction. Follows, a simple treatment where a single DOF of system, in horizontal direction, is considered applied at each storey.

By analogy to dynamic equilibrium for SDOF system in (2.26), for the MDOF is provided as

$$\boldsymbol{F}_I(t) + \boldsymbol{F}_D(t) + \boldsymbol{F}_S(t) = 0 \tag{2.47}$$

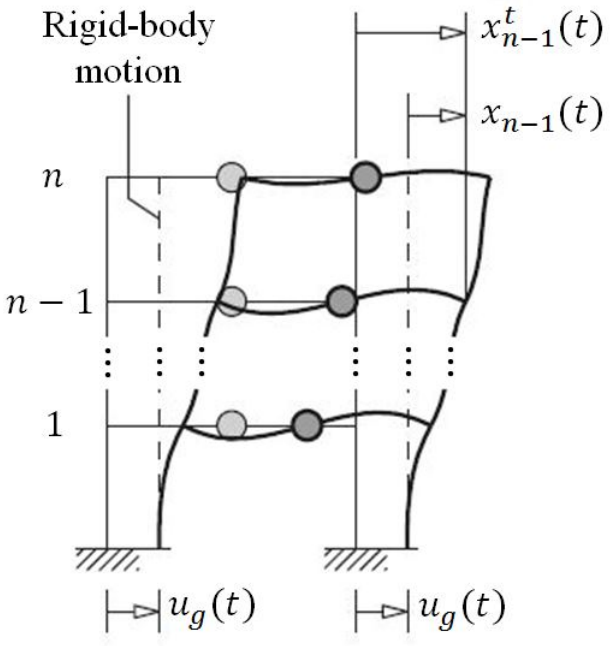

Figure 2.4: Multi-degree of freedom system idealization to a sample of ground motion $u_g(t)$.

where $\boldsymbol{F}_I(t)$, $\boldsymbol{F}_D(t)$, $\boldsymbol{F}_S(t)$ are the inertia, damping and stiffness (or restoring) vector force process, respectively.

Let consider a sample of ground motion $u_g(t)$ of $U_g(t)$, the total (or absolute) displacement sample on j-th DOF is

$$x_j^t(t) = u_g(t) + x_j(t)\,, \quad j = 1, \ldots, n \tag{2.48}$$

where $x_j(t)$ is a sample of relative motion on j-th DOF. Considering the all n-DOF, the (2.48) can be rewritten as vector relation

$$\boldsymbol{x}^t(t) = u_g(t)\mathbf{1} + \boldsymbol{x}(t) \tag{2.49}$$

where $\mathbf{1}$ is a unitary vector with order n, i.e. each of its elements is equal to one. The

(2.49) is a sample of the following

$$\boldsymbol{X}^t(t) = U_g(t)\mathbf{1} + \boldsymbol{X}(t) \tag{2.50}$$

i.e. the total vector displacement process of the n-DOF system to the ground motion process $U_g(t)$ that determines the vector deformation process $\boldsymbol{X}(t)$ of system. The $\boldsymbol{F}_I(t)$ is related to the total vector accelerations process $\ddot{\boldsymbol{X}}^t(t)$ as

$$\boldsymbol{F}_I(t) = \boldsymbol{M}\,\ddot{\boldsymbol{X}}^t(t) \tag{2.51}$$

where $\boldsymbol{M}$ is the n x n mass matrix of the system.

For equivalent viscous damping and linear behaviour of system, in reference to the example of linear SDOF system (Eqs. (2.28) and (2.33)), the $\boldsymbol{F}_D(t)$ and $\boldsymbol{F}_S(t)$ are formulated as

$$\boldsymbol{F}_D(t) = \boldsymbol{C}\,\dot{\boldsymbol{X}}(t) \tag{2.52}$$

and

$$\boldsymbol{F}_S(t) = \boldsymbol{K}\,\boldsymbol{X}(t)\,. \tag{2.53}$$

In Eq. (2.52), $\boldsymbol{C}$ is the n x n damping matrix and $\dot{\boldsymbol{X}}(t)$ is the vector velocity response process of the system, while in Eq. (2.53), $\boldsymbol{K}$ is the n x n stiffness matrix of the system.

Substituting Eqs. (2.51), (2.52) and (2.53) in Eq. (2.47) and using Eq. (2.50) gives

$$\boldsymbol{M}\,\ddot{\boldsymbol{X}}(t) + \boldsymbol{C}\,\dot{\boldsymbol{X}}(t) + \boldsymbol{K}\,\boldsymbol{X}(t) = -\boldsymbol{M}\mathbf{1}\,A(t) \tag{2.54}$$

the equations of motion for linear MDOF system, with linear viscous damping, to the ground acceleration process $A(t)$. The (2.54) describes a coupled system of n partial differential equations that provide the vector displacement response process $\boldsymbol{X}(t)$ of the system.

To generalize the result in (2.54), that is contextualized in Figure 2.4, considering a

linear MDOF system with diffused mass, linear viscous damping and d discrete DOFs, the equations of motion become

$$\boldsymbol{M}\,\ddot{\boldsymbol{X}}(t) + \boldsymbol{C}\,\dot{\boldsymbol{X}}(t) + \boldsymbol{K}\,\boldsymbol{X}(t) = -\boldsymbol{M}\,\boldsymbol{i}\,A(t) \tag{2.55}$$

where $\boldsymbol{i}$ is the influence vector that has unitary (zero) components for the DOFs activated (unactivated) by the earthquake excitation. In general, the Eqs. (2.54) and (2.55) can be solved with the direct integration method (time-stepping methods) that provides the solution of coupled equations system. This type of resolution, even if it involves very high computational burdens, allows solving very complex systems with nonlinear behavior and with nonclassical damping [18].

Modal Analysis

A simpler and computationally advantageous treatment can be faced in the case of linear MDOF system with classical dumping, such as equivalent viscous dumping (Eq. (2.52)), and subjected to generic inputs (not just seismic excitement).

Let be $\boldsymbol{Q}(t)$ the vector generalized force process that perturbs the linear MDOF system with d discrete DOFs and linear viscous damping, the equations of motion as

$$\boldsymbol{M}\,\ddot{\boldsymbol{X}}(t) + \boldsymbol{C}\,\dot{\boldsymbol{X}}(t) + \boldsymbol{K}\,\boldsymbol{X}(t) = \boldsymbol{Q}(t) \tag{2.56}$$

i.e. a coupled system of partial differential equations that describes the $\boldsymbol{X}(t)$ of the system to generic input $\boldsymbol{Q}(t)$. The (2.56) can be decoupled so as to have the d linearly independent equations by making a change of coordinates from generalized to modal or normal. This is therefore possible through the modal analysis, which thus allows easy resolution of the dynamic equilibrium problem for a MDOF system. Starting from the

(2.56) in free oscillations and without damping

$$\boldsymbol{M}\,\ddot{\boldsymbol{x}}\,(t) + \boldsymbol{K}\,\boldsymbol{x}(t) = \boldsymbol{0} \tag{2.57}$$

where $\boldsymbol{0}$ is null vector. It is worth noting that the solution of (2.57) (i.e $\boldsymbol{x}(t)$) is not a process since it only depends on the system features which are invariant in a linear system in free oscillations. Let imagine that this solution is given by a d x 1 vector $\boldsymbol{u}$ multiplied by a scalar time dependent sinusoidal function

$$\boldsymbol{x}(t) = \boldsymbol{u}\,\sin(\omega t) \tag{2.58}$$

Substituting Eq. (2.58) and its second derivative in Eq. (2.57) gives the following homogeneous system

$$\left(-\omega^2\,\boldsymbol{M} + \boldsymbol{K}\right)\,\boldsymbol{u} = \boldsymbol{0}\,. \tag{2.59}$$

The trivial solution is not taken into consideration as it has no engineering significance. Therefore by imposing the determinant of coefficient matrix associated with (2.59) equal to zero, it is provided the classic eigenvalues and eigenvectors problem [29]. Resolution of this problem provides

$$\omega_r^2 \in \mathbb{R}^+ \quad \text{and} \quad \boldsymbol{u}_r, \quad \text{with} \quad r = 1, \ldots, d\,, \tag{2.60}$$

the natural pulsations and the respective modal shapes of d-DOF system. Let be $\boldsymbol{U}$ the modal matrix as

$$\boldsymbol{U} = [\boldsymbol{u}_1\ \boldsymbol{u}_2\ \ldots\ \boldsymbol{u}_d] \tag{2.61}$$

in which r-th column is the r-th eigenvector, i.e. the r-th modal shape $\boldsymbol{u}_r$ in (2.60). The Eq. (2.61) describes a system of linearly independent vectors, therefore it is such as to have non-zero determinant.

According to [29], the solution in generalized coordinates of (2.56) can be described through the modal matrix as

$$\boldsymbol{X}(t) = \boldsymbol{U}\boldsymbol{\Phi}(t) \tag{2.62}$$

where $\boldsymbol{\Phi}(t)$ is vector process of the normalized coordinates. Substituting Eq. (2.62), its first and second derivatives in Eq. (2.56) provides

$$\boldsymbol{M}\,\boldsymbol{U}\ddot{\boldsymbol{\Phi}}(t) + \boldsymbol{C}\,\boldsymbol{U}\dot{\boldsymbol{\Phi}}(t) + \boldsymbol{K}\,\boldsymbol{U}\boldsymbol{\Phi}(t) = \boldsymbol{Q}(t) \tag{2.63}$$

which it is premultiplied for both members by the transposed modal matrix so as to obtain

$$\boldsymbol{I}\ddot{\boldsymbol{\Phi}}(t) + \boldsymbol{N}\dot{\boldsymbol{\Phi}}(t) + \boldsymbol{\Lambda}\,\boldsymbol{\Phi}(t) = \boldsymbol{U}^T\boldsymbol{Q}(t) \tag{2.64}$$

where $\boldsymbol{I} = \boldsymbol{U}^T\boldsymbol{M}\,\boldsymbol{U}$, $\boldsymbol{N} = \boldsymbol{U}^T\boldsymbol{C}\,\boldsymbol{U}$ and $\boldsymbol{\Lambda} = \boldsymbol{U}^T\boldsymbol{K}\,\boldsymbol{U}$ are the identity matrix, spectral matrix and modal damping matrix. The identity matrix is provided if the modal shapes are normalized in reference to mass matrix.

Necessary condition for it to be possible to decouple the system in (2.56) is that the $\boldsymbol{I}$, $\boldsymbol{N}$ and $\boldsymbol{\Lambda}$ are diagonal matrices. By definition the identity and spectral matrices have the following representation

$$\boldsymbol{I} = \begin{bmatrix} 1 & \dots & 0 \\ \vdots & \ddots & \vdots \\ 0 & \dots & 1 \end{bmatrix} \quad \text{and} \quad \boldsymbol{\Lambda} = \begin{bmatrix} \omega_1^2 & \dots & 0 \\ \vdots & \ddots & \vdots \\ 0 & \dots & \omega_d^2 \end{bmatrix} \tag{2.65}$$

i.e. have positive elements along the main diagonal. The diagonal definition is not immediate for $\boldsymbol{N}$, but it depends as the viscous damping is expressed. Typically, the problem is solved with a definition of modal damping according to Rayleigh [29] or by choosing a constant damping for each modal form, ζ_r with $r = 1, \dots, d$, in order to

make $\boldsymbol{N}$ diagonal

$$\boldsymbol{N} = \begin{bmatrix} 2\zeta_1\omega_1 & \dots & 0 \\ \vdots & \ddots & \vdots \\ 0 & \dots & 2\zeta_d\omega_d \end{bmatrix}. \tag{2.66}$$

The system in (2.64), with the matrices in (2.65) and (2.66), therefore consists in d linearly independent differential equations in the modal space as

$$\ddot{\Phi}_r(t) + 2\zeta_r\omega_r\dot{\Phi}_r(t) + \omega_r^2\Phi_r(t) = \boldsymbol{u}_r^T\boldsymbol{Q}(t) = q(t), \quad \text{for} \quad r = 1, \dots, d\,. \tag{2.67}$$

Dynamic problem in (2.56) can be seen as the sum of the response of individual elementary oscillators

$$\boldsymbol{X}(t) = \sum_{r=1}^{d} \boldsymbol{u}_r\Phi_r(t) \tag{2.68}$$

i.e. the superposition of d modal contributions (2.67).

This treatment through the modal analysis is still valid by considering $\boldsymbol{Q}(t) = -\boldsymbol{M}\boldsymbol{i}A(t)$ in (2.56), modal superposition (Eq. (2.68)) provides the vector response process $\boldsymbol{X}(t)$ of linear MDOF system excited by the ground motion acceleration process.

2.3.4 Nonlinear multi-degree of freedom system

The response of real structural MDOF systems subjected to a large dynamic inputs, a clear example of this is the seismic action, is necessarily manifested in a field of nonlinear behaviour. Usually, this nonlinearity considers the large displacements effects and/or the nonlinear material properties. The nonlinear behaviour related to the materials is manifested when the stress-strain or force-deformation relationship is nonlinear. This suggests that on the base of the material properties and design assumptions for a structural system, a specific nonlinear analysis typology can be conducted.

For civil structures realized by steel and concrete materials, the design philosophy is

to determine a limited number of members which require ductility with a clear failure mechanism. The localized demand for ductility, rather than being received by selected structural members, can be satisfied with the introduction into the structural system of local dissipative elements (rubber base isolators, viscous dampers etc...). In this view, a real structural MDOF system is considered to have a linear behavior with a widespread localization of nonlinearity with a predetermined law. The latter, is the case treated in this thesis work for the development of nonlinear analysis.

Fast Nonlinear Analysis

The Fast Nonlinear Analysis (FNA) [30] describes an computationally advantageous solution for the development of nonlinear analysis where the localized nonlinearities are present in the system. The FNA can be developed for both static and dynamic analysis. Since very structures have a limited number of points or members in which nonlinear behaviour takes place, in the case of dynamic loads, it is becoming common practice to consider concentrated damping, base isolation and other energy dissipation elements.

Extracted from [30], the Figure 2.5 shows idealizations of systems with concentrated nonlinearity, which if are subjected to a dynamic load such as an earthquake, the dynamic problem can be solved with the FNA.

Considering a linear discrete d-DOF system with viscous damping and l number of concentrated nonlinearities, subjected to the vector generalized force process $\boldsymbol{Q}(t)$ (e.g. seismic action $\boldsymbol{Q}(t) = -\boldsymbol{M}\,\boldsymbol{i}\,A(t)$), the equations of motion through the FNA is

$$\boldsymbol{M}\,\ddot{\boldsymbol{X}}\,(t) + \boldsymbol{C}\,\dot{\boldsymbol{X}}\,(t) + \boldsymbol{K}\,\boldsymbol{X}(t) + \boldsymbol{F}_{nl}(t) = \boldsymbol{Q}(t) \tag{2.69}$$

where $\boldsymbol{F}_{nl}(t)$ is the global vector nonlinear force process that encloses the nonlinear force process for each node where the nonlinearity is located in the system. The $\boldsymbol{F}_{nl}(t)$

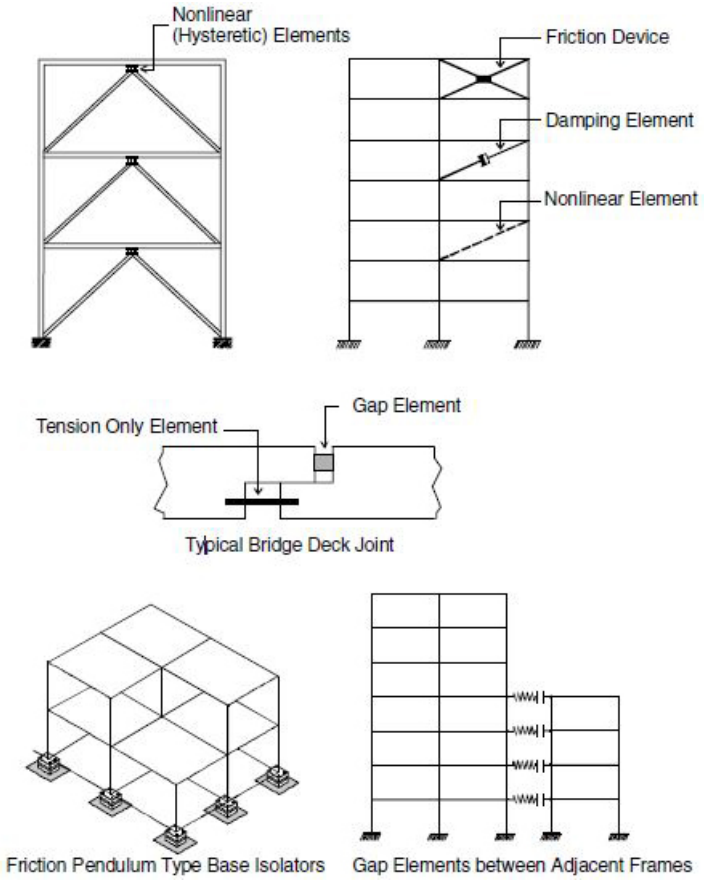

Figure 2.5: Idealizations of MDOF systems with concentrated nonlinearity [30].

is computed by iteration at each time instant as

$$\boldsymbol{F}_{nl}(t) = \boldsymbol{B}^T \boldsymbol{F}(t) \tag{2.70}$$

where $\boldsymbol{B}$ is l x d nonlinear deformation matrix, that is not time dependent, and $\boldsymbol{F}(t)$ is the l order vector nonlinear force process in which the l-th nonlinear force process can be described by Bouc-Wen hysteretic model in Eqs. (2.43) and (2.44). Actually, the presence of concentrated nonlinearities is achieved by means of elements which in any case possess effective elasticity, therefore the (2.69) becomes

$$\boldsymbol{M}\,\ddot{\boldsymbol{X}}(t) + \boldsymbol{C}\,\dot{\boldsymbol{X}}(t) + (\boldsymbol{K} + \boldsymbol{K}_e)\;\boldsymbol{X}(t) + \boldsymbol{F}_{nl}(t) = \boldsymbol{Q}(t) + \boldsymbol{K}_e\,\boldsymbol{X}(t) \tag{2.71}$$

where $\boldsymbol{K}_e$ is the d x d effective stiffness matrix that has non null elements in reference to the nonlinear DOFs. If the vector effective external force process and elastic stiffness matrix are defined as

$$\bar{\boldsymbol{F}}\,(t) = \boldsymbol{Q}(t) - \boldsymbol{F}_{nl}(t) + \boldsymbol{K}_e\,\boldsymbol{X}(t) \tag{2.72}$$

and

$$\bar{\boldsymbol{K}} = \boldsymbol{K} + \boldsymbol{K}_e\,, \tag{2.73}$$

respectively, the (2.71) can be written as:

$$\boldsymbol{M}\,\ddot{\boldsymbol{X}}\,(t) + \boldsymbol{C}\,\dot{\boldsymbol{X}}\,(t) + \bar{\boldsymbol{K}}\;\boldsymbol{X}(t) = \bar{\boldsymbol{F}}\,(t)\,. \tag{2.74}$$

Solution of the (2.74) is provided by the modal analysis in Subsection 2.3.3, taking care to replace in (2.63) the stiffness matrix of the system $\boldsymbol{K}$ and the vector generalized force process $\boldsymbol{Q}(t)$ with the Eqs. (2.73) and (2.72), respectively. The result is decoupling of the equations system, i.e. a d linear independent differential equations in the modal space as following are provided

$$\ddot{\Phi}_r(t) + 2\zeta_r\omega_r\dot{\Phi}_r(t) + \omega_r^2\Phi_r(t) = \boldsymbol{u}_r^T\,\bar{\boldsymbol{F}}\,(t) = \bar{f}(t), \quad \text{for} \quad r = 1,\ldots,d \tag{2.75}$$

and the response process is given by the modal superposition in (2.68).

2.4 Seismic acceleration ground motion stochastic processes

In this section, a two methodologies for generating samples of acceleration ground motion stochastic processes are shown. The substantial differences for them are related to the time modulation typology and the calibration procedure. These methods, together

the Monte Carlo simulation, are used for represent the seismic hazard for a structural dynamic system.

2.4.1 Spectra-compatible stochastic process

Samples of the spectra-compatible stochastic process are generated with the methodology proposed in [31]. The basic hypothesis of this generating method is that a zero-mean stationary Gaussian random process is fully defined by power spectral density (PSD) function. The algorithm generates quasi-stationary acceleration time histories $a(t)$, whose response spectrum is consistent with the one proposed by seismic codes (e.g. Eurocode).

Let $a_i(t)$ be the i-th sample of spectra-compatible acceleration process $A(t)$ with one sided power spectral density function $G_a(\omega)$, $\omega = 2\pi/T$, defined by the superposition of N_a harmonics [32]

$$a_i(t) = \varphi(t) \sum_{k=1}^{N_a} \sqrt{2G_a(\omega_k)\Delta\omega}\cos(\omega_k t + \phi_{k,i}) \tag{2.76}$$

where $\phi_{k,i}$ are independent random phases uniformly distributed in the interval $[0, 2\pi)$. The modulating function $\varphi(t)$ is described as

$$\varphi(t) = \begin{cases} \left(\frac{t}{t_1}\right)^2 & t < t_1 \\ 1 & t_1 \leq t \leq t_2 \quad \text{with} \quad t_2 = t_1 + T_s \\ \exp[-\beta\,(t - t_2)] & t > t_2 \end{cases} \tag{2.77}$$

where $\beta = 0.3$ and T_s is time-observing window (i.e. duration segment).

Assuming a target pseudo-acceleration response spectrum $S_a(\omega, \zeta)$, iterative algo-

rithm starts considering the initial PSD $G_a^{(0)}(\omega)$ described as

$$\begin{cases} G_a^{(0)}(\omega_k) = 0\,, & 0 \leqslant \omega_k \leqslant \omega_l \cong 1 rad/s \\ G_a^{(0)}(\omega_k) = \frac{4\zeta}{\omega_k \pi - 4\zeta\omega_{k-1}} \left(\frac{S_a(\omega_k,\zeta)^2}{\eta_U(\omega_k,\zeta)^2} - \Delta\omega \sum_{h=1}^{k-1} G_a(\omega_h) \right)\,, & \omega_k > \omega_l \end{cases} \tag{2.78}$$

where η_U is the peak factor given by the equation

$$\eta_U = \sqrt{2 \ln \left[2N_U \left[1 - \exp\left(-{\delta_U}^{1.2} \sqrt{\pi \ln(2N_U)} \right) \right] \right]} \tag{2.79}$$

with the following approximate parameters

$$N_U = \frac{T_s}{2\pi} \omega_k \left(-\ln P \right)^{-1}\,, \quad \text{with} \quad P = 0.5 \tag{2.80}$$

P is the not-exceeding probability, and

$$\delta_U = \left[1 - \frac{1}{1-\zeta^2} \left(1 - \frac{2}{\pi} \arctan \frac{\zeta}{\sqrt{1-\zeta^2}} \right)^2 \right]^{1/2} \tag{2.81}$$

which determined the input PSD process has a smooth shape and $\zeta << 1$. Then a sample $a_i(t)$ is generated using (2.76) and the associated response spectrum is estimated. If this response spectrum is not consistent with the target $S_a(\omega,\zeta)$ given by the seismic code, e.g. it is at least equal to ninety percent of the target spectrum in the period range of $0 - 2\,s$, then the PSD at the current iteration step j is corrected using [33]

$${G_a}^{(j+1)}(\omega) = {G_a}^{(j)}(\omega) \left[\frac{S_a(\omega,\zeta)^2}{{\tilde{S}_a}^{(j)}(\omega,\zeta)^2} \right] \tag{2.82}$$

where ${\tilde{S}_a}^{(j)}(\omega,\zeta)$ is the approximate response spectrum at the j-th iteration step. A representation of ${\tilde{S}_a}^{(j)}(\omega,\zeta)$ is given by crossing problem in [33]

$${\tilde{S}_a}^{(j)}(\omega,\zeta) = {\omega_0}^2 \eta_U \sqrt{\lambda_{0,U}(\omega_0,\zeta)} \tag{2.83}$$

in which, the peak factor in Eq. (2.79) is evaluated by the parameters:

$$N_U = \frac{T_s}{2\pi}\sqrt{\frac{\lambda_{2,U}(\omega_0,\zeta)}{\lambda_{0,U}(\omega_0,\zeta)}}\,(-\ln P)^{-1}\,, \quad \text{with} \quad P = 0.5 \tag{2.84}$$

and

$$\delta_U = \sqrt{1 - \frac{\lambda_{1,U}(\omega_0,\zeta)^2}{\lambda_{0,U}(\omega_0,\zeta)\lambda_{2,U}(\omega_0,\zeta)}}\,. \tag{2.85}$$

Moreover, $\lambda_{h,U}(\omega_0,\zeta)$ with $h = 0, 1, 2$ are the response spectral moments defined as

$$\lambda_{h,U}(\omega_0,\zeta) = \int_0^\infty \omega^h |H(\omega,\omega_0,\zeta)|^2 G_a(\omega)\,d\omega \tag{2.86}$$

where $|H(\omega,\omega_0,\zeta)|^2 = \left[\left({\omega_0}^2 - \omega^2\right)^2 + 4\zeta^2{\omega_0}^2\omega^2\right]^{-1}$ is th energy transfer function.

The iterative procedure stops when the sample response spectrum $\tilde{S_a}^{(j)}(\omega,\zeta)$ satisfy the criteria to be consistent with the target, then the associated ${G_a}^{(j)}(\omega)$ is used in Eq. (2.76) for generate samples of quasi-stationary spectra-compatible stochastic process.

2.4.2 Non-stationary stochastic process

Features related to seismic events can be fully described by a non-stationary process by modulating the amplitude and frequency of a stationary process as proposed in [34]. This class of non-stationary processes lends very easily to calibration through seismic acceleration recordings data.

Let $a(t)$ be a samples of ground motion acceleration time series of the non-stationary process

$$A(t) = c(t)Y(\phi(t)) \tag{2.87}$$

where $Y(t)$ is a real-valued zero-mean wide sense stationary process with variance σ_Y^2 and one sided spectral density $G_Y(f)$, $c(t)$ and $\phi(t)$ are amplitude and frequency

modulating deterministic functions, respectively. In particular, $c(t)$ is a slowly varying real-valued deterministic function modulating the variance of $A(t)$, while $\phi(t)$ is a positive, real valued function that satisfy the conditions $\phi(0) = 0$ and $\dot{\phi}(0) > 0$ for $t \geq 0$. In this way the process $A(t)$ is derived from $Y(t)$ by modulating its amplitude and frequency.

It can be demonstrated that the variance of $A(t)$ at time t has the expression [34]

$$\sigma^2(t) = c^2(t)\sigma_Y^2 \tag{2.88}$$

while the time-dependent one-sided spectral density of $A(t)$ can be defined as

$$G_A(t, f) = c^2(t) G_Y\left(f \frac{t}{\phi(t)}\right) . \tag{2.89}$$

The modulating function $\phi(t)$ determines the rate at which the spectral density of $A(t)$ changes with time. If $\phi(t) = t$ one obtains

$$G_A(t, f) = c^2(t) G_Y(f) \tag{2.90}$$

and the process $A(t)$ in (2.87) is a uniformly modulated process.

For the time-dependent one-sided spectral density in Eq. (2.90), it can be assumed to have a m time intervals where the PSD is constant in the time. According to this, the one sided spectral $G_A^{(j)}(f)$ in each of these m intervals can be modeled using the k-modal function

$$G_A^{(j)}(f) = \sum_{i=1}^{k^{(j)}} d_i^{(j)} \exp\left[-b_i^{(j)}\left(2\pi f - \Omega_i^{(j)}\right)^2\right] \tag{2.91}$$

with $j = 1, \ldots, m$, where $k^{(j)}$ can be chosen in each interval in order to describe the numbers of dominant modes in the spectral density function. The parameters $d_i^{(j)}$, $b_i^{(j)}$, $\Omega_i^{(j)}$, $j = 1, \ldots, m$, $i = 1, \ldots, k$ can be calibrated using the average spectral density

estimated in each of the m intervals.

Virtual time histories acceleration samples $a(t)$ of the non-stationary process in (2.87) can be generated using the approximation

$$A(t) = c(t) \sum_{q=1}^{Q} \sigma_q \left[V_q \cos \omega_q(t) t + W_q \sin \omega_q(t) t \right] \tag{2.92}$$

where $\omega_q(t) = \omega_q \phi(t)/t$, while V_q and W_q are uncorrelated random variables with zero mean and unit variance. It can be demonstrated that the process $A(t)$ in (2.92) has energy of magnitude $c^2(t)\sigma_q^2$ at the time dependent frequencies $\omega_k(t) = 2\pi f_q(t)$, $q = 1, \ldots, Q$. It is worth noting that the time variation is discrete and is limited to the m time intervals which define Equation (2.91) where it was assumed $\phi(t) = t$. Furthermore, V_q and W_q are assumed to be Gaussian.

2.5 Monte Carlo simulation

To solve a several stochastic problems, in applied science and engineering is praxis to use the Monte Carlo simulation method. In order to provide a generalized mathematical definition for the MC method considering an generation algorithm based on an random variable X for define a stochastic problem. Let $(\Omega, \mathfrak{F}, P)$ be a probability space defined by space sample Ω, a subset of space sample $\mathfrak{F}$ and a probability measure P. The X is a $\mathbb{R}^d$-valued, $d > 1$, stochastic variable with a known PDF that is defined on $(\Omega, \mathfrak{F}, P)$. Independent samples by the generation algorithm provide the properties estimation for the stochastic problem.

A solution based on the MC method needs the development of the following steps [35]:

1. generate independent samples of the random parameters and functions for definition of the stochastic problem;

2. solve the resulting deterministic problems from the correspondent generated samples in previous step;

3. estimate the solution properties of the stochastic problem through a statistical analysis of the collection of deterministic solutions.

In general, most algorithms for generating samples of random variables, stochastic processes and random fields use the transformation with and without memory of aleatory variables with uniformly distributed PDF and Gaussian variables with zero-mean and unit variance.

Chapter 3

Seismic fragility analysis concept

3.1 Introduction

Main motivation of this work is the improvement of the more widespread method in PBEE for estimate a structural/nonstructural system performance by developing the fragilities. In this chapter, the fundamental concepts for the seismic fragility assessment is collected.

The literature overview focuses the attention on the current methodologies for evaluate the fragility curve, in this context, the variables and quantities are examined, and the correlated issues are discussed.

3.2 Fundamentals

The fragility concept in earthquake engineering filed was introduced in [11, 36–38]. The authors have defined the fragility function as a failure frequency for structural and components on the PGA (IM), where the frequency of occurrence of various levels of ground motion is defined precisely in terms of this intensity measure. The modern challenge in earthquake engineering is to quantify the seismic risk at specified site and understand as this influences the performance for a structural/nonstructural system.

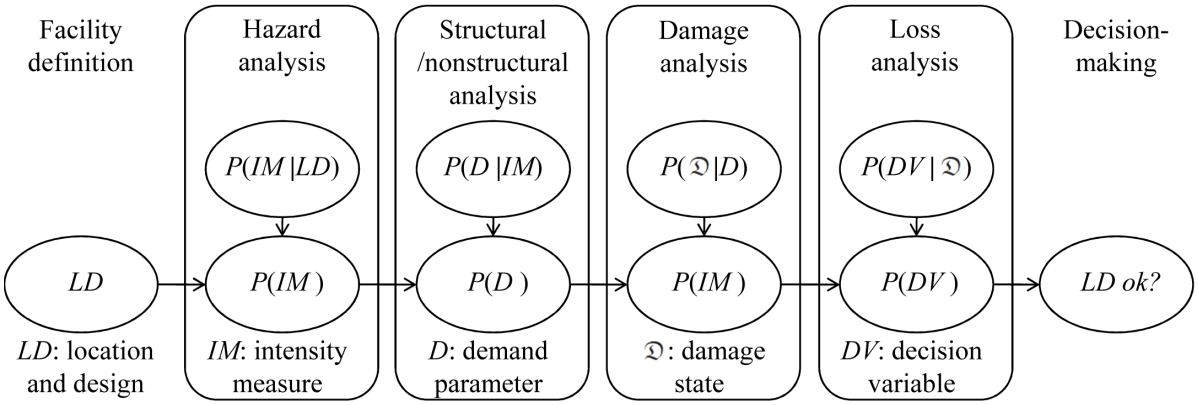

Figure 3.1: PEER probabilistic framework [8, 39].

Given the non-deterministic nature for the earthquake, this quantification makes sense only if it is undertaken in the aleatory field. In this context, the PEER produces the second-generation PBEE probabilistic framework [8, 39], which is divided into four rigorous, consistent and independent stages linked with four intermediate output variables. These stages include hazard analysis, structural/nonstructural analysis, damage analysis and loss analysis where the output variables are intensity measure IM, structural demand parameter D, damage state $\mathfrak{D}$ and decision variable DV, respectively. In general, these variables are expressed in a probabilistic sense as conditional probabilities of exceedance, e.g. $P(\mathfrak{D}|IM)$. The main assumption in PEER's methodology is that it can be considerate as a discrete Markov process [40] in which the conditional probabilities between parameters are independent. The conceptual methodology of the PEER is illustrated in Figure 3.1. The fragility analysis is based on two stages of the PEER's methodology, i.e. the structural/nonstructural and damage analysis, and its results are formalized in the fragility function. For the structural seismic engineering, the fragility curve is described by the mathematical relation which expresses the failure probability of a structural system given the seismic event with level intensity $\xi = IM$ [37, 41–43]. Failure is not necessarily the collapse of the structure, and it can be defined on the structural performance for prefixed threshold on the damage state $\mathfrak{D}$. According to this definition, failure occurs when the demand exceeds a defined limit capacity.

Once a threshold on $\mathfrak{D}$ is defined as limit state (LS) of the structural performance, the failure probability is

$$P_{LS}(\xi) = P(LS|IM = \xi) \tag{3.1}$$

i.e. the conditional probability that the structural performance enters in the set of LS given the event with level IM. Other formulation can be described by defining the system demand parameter D and the structural capacity associated with a LS

$$P_{\bar{D}}(\xi) = P(D \geqslant \bar{D}|IM = \xi) \tag{3.2}$$

where $\bar{D}$ is the prefixed particular value of D. More general definition of the failure probability can be formulated by considering the event $\{D \in I \subset \mathbb{R}\}$ that defines the damage state $\mathfrak{D}$ for the structural system

$$P_f(\xi) = P(\mathfrak{D}|IM = \xi) = P(D \in I \subset \mathbb{R}|IM = \xi) \tag{3.3}$$

i.e. the probability that a structural system enters a damage state given the ground motion with intensity measure ξ.

The fragilities can be derived form the following approaches [44–46]:

- **Empirical**: fragility is created by fitting a function to the observation recorded during experimental tests or real evidences [47, 48]. Usually, this kind of fragility curves are built starting from the observations acquired during post-earthquake survey, obviously this fragility has lack of generality [49];
- **Analytical**: fragility is based on the results of numerical models [50, 51]. In this case particular attention must be placed on the choice of the analysis typology and how uncertainties are considered in the model;
- **Heuristic**: fragility is based on expert judgments, a pool of experts guess or judge

failure probability as a function of environmental excitation. This approach is useful when empirical observations are very limited [52];

- **Hybrid**: the above approaches can be combined to build fragility [53, 54], reducing the computational effort but controlling the bias.

The post-earthquake survey-based procedures need the most possible reliable damage-earthquake data set. A number of such procedures, e.g. [55, 56], focus attention for collected damage data through a post-earthquake survey. The involved quantities regard to material properties, apparent structural deficiencies and building site location. These informations can be utilized to arrive at a rating score or index in which the numerical value usually determines whether the building is safe or unsafe, with respect to the traditional goal of assuring life safety. An other use of the collected information is to develop seismic assessment tools in the form of fragility curves [42, 57]. These empirical-based approaches are specific for a particular seismic-tectonic region. Unsatisfactory damage estimates are provide when the empirical approaches are applied to regions other than those for which they were developed. For this reason, they found limited use for the seismic vulnerability assessment with reference to a different specific seismic area. In general, the seismic vulnerability and risk assessment procedures need a multiple performance evaluations within consequence-based framework, which may only be feasible with simulation-based procedures, i.e. analytical approaches.

Before computational resources were available for the development of analytic fragility curves by means of heavy simulations, heuristic approaches were found very useful and used. The Applied Technology Council (ATC) had relied on expert opinion with limited observed data from the 1971 San Fernando earthquake [52], it is one of the first applications of fragility modeling to civil infrastructure subjected to earthquake demand. The reliability of the fragilities in [52] which were identified in terms of damage state probability matrices, anyway it is questionable in that the fragilities are subjective and

the associated degree of structures conservation is unknown. Based on a loss estimation methodology [58], the building capacity is represented by a nonlinear static pushover curve, roof displacement against base shear, and building response to an input scenario earthquake (considering the local site conditions) is determined with the capacity spectrum method [59]. The building response is then entered into the associated built-in fragility curves defined at the thresholds of four discrete damage states (slight, moderate, extensive, and complete), defined separately for the structural system and for drift and acceleration sensitive non-structural components, to perform the loss estimation given the occupancy class of the building [60]. However, the more significant issue for these fragilities development way is that does not provide uncertainty propagation.

Recent trends in the fragility estimations are related to use analytical simulations. The relation between structural response and earthquake ground motion intensity (i.e. D and IM), which is the base for deriving the fragility curves, is established through analytical simulations. It is also taken into account the earthquake characterization, structural damage, performance limits, etc. Singhal and Kiremidjian [61] had developed fragility curves for low-, mid-, and high-rise reinforced concrete frames (RCFs) that were designed using seismic provisions. The uncertainty in structural capacity and demand was taken into account through Monte Carlo simulations. Stochastically generated frame models randomly were paired with simulated ground motion records in the nonlinear time history analysis. Comparing these fragilities with those in [52], it was revealed that the heuristic fragility functions were rather unrealistic in that they neglect probabilities of severe damage or collapse under a large earthquake such as the 1994 Northridge earthquake. Later, Singhal and Kiremidjian [62] had presented a Bayesian method for updating the fragility curves that they had earlier developed for low-rise RCFs to estimating confidence bounds on those fragilities, by using the observed building damage data from the 1994 Northridge earthquake. This had shown differences between the curves estimated before and after the update.

Shinozuka et al. [42] had developed both empirical and analytical fragility curves for bridges. The empirical fragility curves utilize the observed bridge damage data from the 1995 Kobe earthquake. In contrast, the analytical fragility curves utilize such data that were simulated from the nonlinear time history analysis of stochastically generated models of two typical bridges in Memphis, TN, taking into account the uncertainty in structural material properties.

Porter et al. [63] had proposed an assembly-based vulnerability framework to assessing the seismic vulnerability of buildings on a building-specific basis. The proposed approach differs from the above analytical procedures in that "a vulnerability function" that relates the seismic losses to the seismic intensity was developed for a particular building and the damage to individual assemblies was determined for this purpose. The seismic losses were assessed using stripe analyses. The structural response to each scaled ground motion was entered into assembly fragility curves, and the associated damage to each structural and non-structural element in the building and to its contents was determined as outlined in the study. The total damage was then expressed in terms of the sum of repair and loss-of-use costs as a fraction of replacement cost. After performing a regression analysis on the generated data, the seismic vulnerability function was obtained for a particular building. The application of the proposed framework to a steel moment frame building had revealed that substantial uncertainty exists in the vulnerability function derived for the building.

A probabilistic framework for seismic design and assessment of structures in a demand and capacity format, addressing the uncertainties in hazard, structural, damage, and loss analyses was developed by Cornell et al. [64]. The structural demand was assessed using a suite of ground motions and the median structural demand was represented by a log-linear function of seismic intensity. The structural demand was

assumed to be distributed lognormally about the median with constant logarithmic standard deviation. In the same year the concept of the vector-valued Probabilistic Seismic Hazard Analysis was introduced in [65]. This methodology aims a site-specific joint hazard evaluation of two or more ground motion IMs.

Kafali and Grigoriu in [66] had introduced the concepts of the fragility surface which in the seismic ground motion intensity is characterized by site seismic activity matrix, i.e. the relative frequency of the earthquakes with various moment magnitude and source to site distance. Analytical fragility surfaces were shown for structural/nonstructural system considering different limit states. In later the authors in [67] had compared this methodology with those classically used.

Nielson et al. [50] had obtained an analytical fragilities for different class of typical bridges in USA. It was adopted a 3-dimensional analytical models and a suite of synthetic ground motions to developing the nonlinear time history analysis. Multiple bridge components were considered in the fragility analyses, namely the columns, fixed bearings, expansion bearings, and abutments. The contributions of these components were accounted for by developing joint probability models of their seismic demands. Within this contribution, the authors had shown that these fragility curves can be used in determining the potential losses resulting from earthquakes, retrofitting prioritizations, and post-earthquake inspection decisions.

A new analytical approach for the derivation of fragility curves for masonry buildings was proposed in [51]. The authors in this contribution had shown a methodology based on nonlinear stochastic analyses of building prototypes. The MC simulation were used to generate mechanical parameters and nonlinear analyses were performed. In particular, nonlinear static (pushover) analyses were used to define the probability distributions of each damage state while a nonlinear dynamic analyses allow to deter-

mine the probability density function of the displacement demand corresponding to different levels of ground motion.

In the last decade, the issue related to the accuracy in fragility analysis begun to interest in the earthquake engineering community [68]. In last paper the authors had proposed a two-stage approach to generate improved fragility functions using field measurement and experimental data, i.e. a hybrid method. The Bayesian updating approach was employed to further update the derived fragilities using hybrid simulation results.

The influence of the number of analysis on the accuracy of the analytical fragility curves obtained by linear regression and maximum likelihood estimates have been studied in [69]. Different statistical measures were used to estimate the quality of fragility functions derived by considering varying numbers of ground motions. Within this contribution the authors had demonstrated that the least-squares method for deriving fragility functions converges much faster than the maximum likelihood and sum-of-squares approaches.

Grigoriu [15] has opened a very interested discussion in the scientific community related to the accuracy in fragility functions. Simple systems subjected to a synthetic ground motion acceleration process were considered to demonstrate that the dependence between the demand parameter and intensity measure plays a fundamental role in fragility estimation. The author with this contribution has greatly influenced this thesis work.

Currently, several authors try to find the best IM for build fragility functions. The optimal intensity measure for a concrete dams is selected over a set of seventy IM definitions [70]. The selection procedure is based in terms of efficiency, practicality, proficiency, sufficiency, and hazard compatibility. This work is the first to apply the PBEE concepts for buildings in the particular case of dams.

Bojórquez et al. [71] introduce a new definition of intensity measure. According to the authors, this new IM is able to increase the efficiency in the prediction of nonlinear behaviour and higher modes effects of structures subjected to earthquake ground motions with different characteristics. This IM definition is based on multiple ordinates of pseudo-acceleration response spectrum.

The use of more promising IMs for analytical fragilities developed in the 3-d reinforced concrete bridge models case is discussed in [72]. Main goal it is statically compare fragility curves for multiple configurations of a typical class of Italian bridges, when using different IMs. Belief of the authors is that the adequacy of a certain IM is assessed in terms of direct correlation with measures of structural response (i.e. demand parameters).

Nguyen et al. [73] investigate the correlation between seismic responses of nuclear power plants components and different IM definitions to identify the best IMs for correlate the damage of nuclear power plant structures. A series of Pearson's correlation coefficients are calculated to recognize the correlation for develop analytical fragility curves. It is demonstrated that the classical IMs reported in literature are not the best choices to archive the structural performance with the fragilities.

Sevieri et al. [74] focus particular attention on the issue concerning the uncertainties for the empirical fragilities development referring to the dams. The record-to-record variability of ground motions is considered with a set of selected events. Main focus of the authors is the quantification of the effect of the epistemic uncertainties related to the variability of the material mechanical parameters on the seismic fragility analysis of dams.

However at the present, in PBEE for each of these different approaches (i.e. empirical, analytical, etc...) the problem concerning the dependence between the structural demand and the seismic input characterizations, represented by D and IM, respectively, has not been completely resolved and, in many scientific works, it is not even

considered.

Particular attention in this thesis falls on the analytical fragility curves development. Anyway, all the previous approaches (e.g. analytical) can be used to develop the PEER's methodology (Figure 3.1) allowing the consideration of the inherent uncertainties. In reference to Kennedy et al. ([11, 12]), the uncertainties are distinct into epistemic and aleatory. The epistemic uncertainties are related to parameters that characterize the model (e.g. parameters of constitutive model), these uncertainties reflect incomplete knowledge regarding the distributions and parameters used in the fragility assessment. While those in second group, the aleatory uncertainties, regard to the random nature of the considered seismic event, i.e. independent ground motion acceleration history time series with same statistical features. Epistemic uncertainties are of particular attention [75, 76], however this work only focuses on those aleatory. The reason of this, is to concerted the research on fragility analysis accuracy related to IM.

3.3 Fragility function evaluations

The failure probability can be approximated as a lognormal distribution function [42, 77, 78]. The structural capacity is assumed to be lognormally distributed with median A_m and lognormal standard deviation β. It follows that, the (3.3) can be approximate as the Cumulative Distribution Function (CDF)

$$\tilde{P}_f(\xi) = \Phi\left(\frac{\ln \xi - \ln A_m}{\beta}\right) \tag{3.4}$$

where $\Phi(\cdot)$ is the standard normal CDF. This fragility model assumption is used to the define the likelihood function

$$L(A_m, \beta) = \prod_{k=1}^{N} [\tilde{P}_f(\xi_k)]^{x_k} [1 - \tilde{P}_f(\xi_k)]^{1-x_k} \tag{3.5}$$

in which a set of N samples input-output (ξ_k, x_k), $k = 1, \ldots, N$, are considered, $x_k = 1$ or 0 depending whether or not there is failure to a seismic event with level ξ_k. The parameters in the lognormal fragility approximation $\tilde{P}_f(\xi)$ (3.4), i.e. A_m and β, are estimated by maximizing the (3.5) [42]

$$(\hat{A}_m, \hat{\beta}) = \arg\max_{A_m, \beta} [L(A_m, \beta)] \,, \tag{3.6}$$

or equivalently, by minimizing the negative log-likelihood [79]

$$(\hat{A}_m, \hat{\beta}) = \arg\min_{A_m, \beta} [-\ln \min L(A_m, \beta)] \,. \tag{3.7}$$

The formulation in (3.7) is generally preferred since it is computationally advantageous. The failure probability in (3.4) does not require the scaling of the accelerograms until failure and, agreeing with maximum likelihood estimation [80], the measure of $\mathfrak{D}$ is assumed binary (i.e. 1 if failure, 0 otherwise).

In general context, an other way to describe the fragilities is to use the relative frequency definition [9]. This definition, in the PBEE is contextualized to define the failure probability as the number of the system structural performances that exceed the prefixed threshold on the damage state (i.e. specified LS) on the total number of the seismic events with ξ that occur. According to last definition, the (3.3) can be estimate as

$$\hat{P}_f(\xi_k) = \sum_{i=1}^{n_s} 1(d_{k,i} \in I)/n_s \tag{3.8}$$

where $1(\cdot)$ is the indicator function, n_s the number of seismic events with intensity

measure ξ_k and $d_{k,i}$, $i = 1, \ldots, n_s$, are samples of the system demand parameter at the level ξ_k. For $n_s \to \infty$, the fragility curve estimate by (3.8) converges to (3.3). The pragmatic formulation of $\hat{P}_f(\xi_k)$ is common diffused [67, 81–83], and it is actual proposed in the FEMA's methodology framework [10]. In this methodology, the fragility function is built by scaling samples of ground motion acceleration time series in reference to a IM, in order to have the intensity level $IM = \xi_k$. Samples of the demand parameters are computed and for each level ξ_k the fragility is estimated by (3.8). This method is widely applied because it is simple and, together with Monte Carlo simulation, it overcomes the problem of the limited number of natural recorded ground motions available for fragility analysis.

In order to improve the structural performance estimates (e.g. fragilities) several methods were proposed in the literature to consider two parameters IMs, also known as vector-valued IMs [84–86]. This method is used for develop empirical fragility functions [87, 88], and it is based on the logistic regression [89]. However, Baker in [90] has also used this methodology for estimate analytical fragility. Once a collapse class $C \in [0, 1]$ is defined, which it has the same binary concept in (3.5) (i.e. $C = 1$ if structural performance exceeds the LS or otherwise $C = 0$), the fragility can be estimated performing regression analysis [91]

$$\hat{P}_f(\xi_k, x_2) = P(C|\{IM = \xi = x_1, x_2\}) = \frac{\exp(\hat{\beta}_0 + \hat{\beta}_1 x_2)}{1 + \exp(\hat{\beta}_0 + \hat{\beta}_1 x_2)} \tag{3.9}$$

where $\hat{\beta}_0$ and $\hat{\beta}_1$ are coefficients, which are estimated by logistic regression on C, and the predictor variable x_2, on a data set of n_s seismic record with different level ξ_k, $k = 1, \ldots, N$. The (3.9) describes conditional probability to have collapse given the vector-valued $\{IM = \xi = x_1, x_2\}$, where the predictor x_2 is assumed as a different intensity measure to that x_1 or it is as a other helpful parameter to improve information on the structural performance. In particular, $\hat{\beta}_0$ and $\hat{\beta}_1$ need to be evaluated for each

ξ_k, and the expected value of (3.9) for each of this level ξ_k

$$E[P(C|\{\xi_k, x_2\})] = P(C|\xi_k) = \hat{P}_f(\xi_k) \tag{3.10}$$

gives the fragility estimated with (3.8).

It is worth noting that, considering the (3.10), $\hat{P}_f(\xi_k, x_2)$ improves the information on structural performance, and if it is compared to the probability evaluated by single IM (3.8), it provides accurate results, otherwise the logistic regression on $\hat{P}_f(\xi_k)$, with x_2, does not improve the information.

3.4 Demand parameters

Seismic demands represent the requirements imposed by ground motions on relevant structural performance parameters. The localized demands depend on many local and global response characteristics of structures. Typically, the structural damage is related to the maximum deformations or accelerations, but also by the amount of dissipated energy due to cyclic loading can be an damage indicator [92, 93]. However, in this work only the displacement or acceleration-based demand parameters are considered. The demand parameters Ds are evaluated for each degree of freedom of structural system model. In particular, the single degree of freedom system and complex multi-degree of freedom system are used as structural models. For both of them, the linear and nonlinear behaviour are considered.

Let $\boldsymbol{X}(t)$ be the response vector-valued process of an arbitrary MDOF structural system and $X_{sdof}(t)$ be the response process of a SDOF arbitrary oscillator to the same

ground acceleration $A(t)$. The demand parameter for MDOF and SDOF system are

$$D = \max_{0 \leqslant t \leqslant \tau} |h(\boldsymbol{X}(t))| \tag{3.11}$$

and Equation (2.32), respectively, where τ is the time length of $A(t)$, while $h(\cdot)$ is a function mapping the response $\boldsymbol{X}(t)$ into the demand parameter of interest, such as:

- the maximum absolute displacement D_d;
- the maximum absolute acceleration D_a;
- the maximum absolute inter-story displacement (i.e. drift) D_{dr}.

In particular, considering a linear behaviour for the SDOF system (see Subsection 2.3.1), the Equation (2.36) provides the demand parameter definition of linear simple system.

3.5 Intensity measures

The seismic intensity measures (IMs) depict the seismic hazard for an earthquake, and as a consequence, the structural response analysis is conditioned on the chosen IM in a seismic risk assessment framework. As previously instructed [14], the desired IM should be sufficient and efficient, and have a hazard curve that is relatively easy to compute, "hazard computability" [94]. In search of these optimum features, the authors have proposed several IMs.

Two groups of IMs are usually used to define the seismic fragilities:

1. functional of samples of seismic ground acceleration process $A(t)$, such as PGA;

2. functional of filtered version of samples of $A(t)$, e.g. single/multiple ordinates of pseudo-acceleration response spectrum $S_a(T)$ for different structural system periods T [95, 96].

In particular, the IMs in the second group, that are widely used to define the fragilities, depend on the D on which the analysis is based [97–100].

The more general categorization that can be done for IMs, is to distinguish the those scalar from vector-value intensity measures [98]. The scalar IMs are divided into two definitions: non-structure specific IMs calculated directly from the ground-motion time histories; structure-specific IMs calculated directly from the response spectra, where the spectral ordinates can be at the first or other structural system period, at a period range and multiple periods. The major definitions of these kind of intensity measures reported in literature are shown in Table 3.1 and Table 3.2, where notions and references are indicated. The trend in the past was to use the PGA as an IM, such as in [37], while recently the use of the IM computed on the system response (Table 3.2) is widely diffused [98] for the fragilities development (e.g. using (3.4) or (3.8)). Different versions of the scalar intensity measures in Table 3.1 and Table 3.2 are used in this work:

$$IM_1 = PGA \tag{3.12}$$

$$IM_2 = S_a(T_1, \zeta_1) \tag{3.13}$$

$$IM_3 = S_a(T_3, \zeta_3) \tag{3.14}$$

$$IM_4 = I_h \tag{3.15}$$

$$IM_5 = S^*(T_1, \zeta_1, c, \gamma) \tag{3.16}$$

Table 3.1: Non-structure specific intensity measures.

	Notion	Name and reference	Relation
Acceleration related	PGA	Peak ground acceleration	$PGA = \max_{0 \leqslant t \leqslant \tau} \lvert A(t) \rvert$ $A(t)$ =ground motion acceleration process τ =time lenght of $A(t)$
	I_A	Arias intensity [101]	$I_A = \frac{\pi}{2g} \int_0^\tau A^2(t)\, dt$
	CAV	Cumulative absolute velocity [102]	$CAV = \int_0^\tau \lvert A(t) \rvert\, dt$
	I_a	Compound acc. related IM [103]	$I_a = PGA\, t_d^{1/3}$ $t_d = t_2 - t_1$ $t_1 = t(5\%\, I_A)$ $t_2 = t(95\%\, I_A)$
	I_c	Characteristic intensity [104]	$I_c = (a_{rms})^{3/2} \sqrt{t_d}$ $a_{rms} = \sqrt{\frac{1}{t_d} \int_{t_1}^{t_2} A^2(t)\, dt}$
Velocity related	PGV	Peak ground velocity	$PGV = \max_{0 \leqslant t \leqslant \tau} \lvert V_g(t) \rvert$ $V_g(t)$ =ground motion velocity process
	I_F	Fajfar intensity [105]	$I_F = PGV\, t_d^{1/4}$
	CAD	Cumulative absolute displacement [106]	$CAD = \int_0^\tau \lvert V_g(t) \rvert\, dt$
	I_v	Compound vel. related IM [103]	$I_v = PGV^{2/3}\, t_d^{1/3}$
	IV	Incremental velocity [107]	
	SED	Specific energy density	$SED = \int_0^\tau V_g^2(t)\, dt$
Displacement related	PGD	Peak ground displacement	$PGD = \max_{0 \leqslant t \leqslant \tau} \lvert U_g(t) \rvert$ $U_g(t)$ =ground motion process
	I_d	Compound disp. related IM [103]	$I_d = PGD\, t_d^{1/3}$
	ID	Incremental displacement [107]	

Table 3.2: Structure specific intensity measures.

	Notion	Name and reference	Relation
Spectral	$S_a(T_i, \zeta_i)$	Pseudo-acceleration response spectrum ordinate	Equation (2.38) for selected i-th structural period T_i and associated damping ratio ζ_i, $i = 1, \ldots, MDOF$
	E_{Ir}	Relative input energy [108]	$E_{Ir} = -\int_0^\tau A(t)\,\dot{X}_r(t)\,dt$ $\dot{X}_r(t)$ = relative velocity series process of linear SDOF
	E_{Ia}	Absolute input energy [108]	$E_{Ia} = \int_0^\tau V_g(t)\,\ddot{X}_a(t)\,dt$ $\ddot{X}_a(t)$ = absolute acceleration series process of linear SDOF
Integral	ASI	Acceleration spectrum intensity	$ASI = \int_{0.1}^{0.5} S_a(T, \zeta)\,dT$ see Eq. (2.38)
	I_h	Housner intensity [109]	$I_h = \int_{0.1}^{2.5} S_v(T, \zeta)\,dT$ see Eq. (2.37)
	$V_{E_{Ir}}S$	Relative input equivalent velocity spectrum	$V_{E_{Ir}}S = \int_{0.1}^{3.0} \sqrt{2E_{Ir}}\,dT$
	$V_{E_{Ia}}S$	Absolute input equivalent velocity spectrum	$V_{E_{Ia}}S = \int_{0.1}^{3.0} \sqrt{2E_{Ia}}\,dT$
	$MASI$	Modified ASI	$MASI = \int_{0.2T_i}^{1.5T_i} S_a(T, \zeta)\,dT$
	MI_h	Modified I_h	$MI_h = \int_{0.2T_i}^{1.5T_i} S_v(T, \zeta)\,dT$
	$MV_{E_{Ir}}S$	Modified $V_{E_{Ir}}S$	$MV_{E_{Ir}}S = \int_{0.2T_i}^{1.5T_i} \sqrt{2E_{Ir}}\,dT$
	$MV_{E_{Ia}}S$	Modified $V_{E_{Ia}}S$	$MV_{E_{Ia}}S = \int_{0.2T_i}^{1.5T_i} \sqrt{2E_{Ia}}\,dT$
Multi-parameters	S^*	Cordova IM [110]	$S^*(T_1, \zeta_1, c, \gamma) =$ $S_a(T_1, \zeta_1)\left(\frac{S_a(cT_1, \zeta_1)}{S_a(T_1, \zeta_1)}\right)^\gamma$ $c = 2$, $\gamma = 0.5$
	$\bar{S}_a(\boldsymbol{T}^*)$	Geometric mean of $S_a(T)$ ordinates [111]	$\bar{S}_a(\boldsymbol{T}^*) =$ $(\prod_{i=1}^n S_a(T_i, \zeta_i))^{1/n}$ n =modal shapes of interest
	S_{N1}	Period elongation related IM [112]	$S_{N1} = S_a(T_1, \zeta_1)^\gamma\, S_a(cT_1, \zeta_1)^{1-\gamma}$ $c = 1.5$, $\gamma = 0.5$
	S_{N2}	Second period elongation related IM [112]	$S_{N2} = S_a(T_1, \zeta_1)^\gamma\, S_a(T_2, \zeta_2)^{1-\gamma}$ $\gamma = 0.75$

Table 3.3: Vector-valued intensity measures.

Notion	Reference	Relation
$\{S_a(T_1,\zeta_1), R_{T_1,T_n}\}$	[84]	see Eq. (2.38) $R_{T_1,T_n} = \frac{S_a(T_n,\zeta_n)}{S_a(T_1,\zeta_1)}$ for n-th period T_n and associated ζ_n
$\{S_a(T_1,\zeta_1), \varepsilon\}$	[113]	$\varepsilon = \frac{\ln S_a(T_1,\zeta_1) - [\ln S_a(T_1,\zeta_1)]_\mu}{[\ln S_a(T_1,\zeta_1)]_\sigma}$ $[\ln S_a(T_1,\zeta_1)]_\mu$ = mean of $\ln S_a(T_1,\zeta_1)$ $[\ln S_a(T_1,\zeta_1)]_\sigma$ = standard deviation of $\ln S_a(T_1,\zeta_1)$
$\{S_a(T_1,\zeta_1), m\}$	[113]	m = moment magnitude
$\{S_a(T_1,\zeta_1), R_{T_1,T_n}, \varepsilon\}$	[87]	
$\{PGA, m\}$	[86]	

where T_1 and T_3 are the MDOF system first and third structural natural periods, respectively, with associated damping ratios ζ_1 and ζ_3; I_h is the Housner intensity, defined as the integral of the pseudo-velocity spectrum with damping ratio ζ in the range $T = 0.1 - 2.5\,s$ [109]; $S^*(T_1,\zeta_1,c,\gamma)$ is the multi-parameter scalar intensity measure reported in [110] with $c = 2$ and $\gamma = 0.5$.

The use of vector-valued IMs in PBEE is also widespread. Several authors has proposed a second variable x_2, that it is used together a first scalar IM, (i.e. $\{IM = \xi = x_1, x_2\}$) to estimate the fragility function as in Equation (3.9). Baker and Cornell [87] have developed fragilities performing the regression analysis with a third predictor variable x_3, which has the same meaning of x_2 in (3.9), in order to consider a three vector-valued IM (i.e. $\{IM = \xi = x_1, x_2, x_3\}$). Table 3.3 reports the vector-valued IMs definitions with notions and literature references.

The scalar intensity measure definitions in Table 3.1 and Table 3.2 were introduced in literature by focusing attention on the efficiency and sufficiency conditions. For example, it was demonstrated that the Eq. (3.13) is an IM more efficient that in Eq.

(3.12) [114]. Nevertheless, though the (3.13) for tall and long-period structural systems as well as buildings subjected to near-source seismic events is a valid IM, it is shown in [14, 115] that $S_a(T_1)$ can be inefficient and insufficient. This is due because $S_a(T_1)$ does not take into account the higher mode shape contributions and period lengthening owing to structural nonlinearity. For this reason, it was proposed several IMs as an adjustments of $S_a(T_1)$ (e.g. Eq. (3.16)) [14, 110–112, 116]. These proposals are not only describe an efficient IMs for all damage levels of a prefixed structure, but also taken into account the IM computability through a ground motion hazard analysis without the need of any new attenuation relationships. In literature many spectrum-based IMs (Table 3.2) were investigated and, generally, the velocity related IMs in Table 3.1 show a better correlation with the deformation demands [117–120].

As opposed to a scalar IM, a vector-valued one is a vector of more than one IM (see Table 3.3), which commonly comprises of two or three parameters. A good predictor for ordinary ground motions was shown by the vector-valued IM based on $S_a(T_1)$ and spectral values at other structural periods [87, 121, 122].

3.6 Monte Carlo algorithm for fragilities

A contextualization of the MC method in earthquake engineering field can be formalized, as also recommended by FEMA [10], through an algorithm which include the previously declared steps in Section 2.5. Considering an arbitrary structural system, the fragility analysis is developed as:

1. selection of a finite set of intensity measure $\{\xi_k\}$, $k = 1, \ldots, N$;

2. generation of n_s independent samples $a_i(t)$, $i = 1, \ldots, n_s$, of acceleration ground motion process $A(t)$ using a specific method (e.g. one in Section 2.4);

3. for each of the values $\{\xi_k\}$ scale the n_s acceleration records, $a_i(t)$, in order to

have the intensity level $IM = \xi_k$, $\xi_k > 0$;

4. given a prefixed limit state value, samples of the demand parameter $d_{k,i}$, $k = 1, \ldots, N$ and $i = 1, \ldots, n_s$, are computed through the formalization of dynamic problem;

5. for each of the values $\{\xi_k\}$ estimate fragility as in Equation (3.8).

The five-steps algorithm based on scaling seismic accelorograms by a reference IM provide the uncertainty propagation related to the earthquake randomness. Use of MC provides the overcome the limited number of natural recorded ground motion available for fragility analysis.

Chapter 4

The role of intensity measures on the accuracy of seismic fragilities

4.1 Introduction

Seismic fragilities are the probability that structural response of a system overcomes specified limit values for given seismic intensity measures. In this chapter, issue related to the accuracy of the fragility curves is addressed. Representation of the problem with a mathematical formulation is discussed, and main quantities, in reference to the aleatory treatment, that influence the accuracy in fragility analysis is shown.

Novel contribution in this work which is a general approach for the improvement of fragilities accuracy is presented.

4.2 Overview on issue

Consider a unitary mass elementary linear oscillator to spectra-compatible stochastic process (see Subsection 2.4.1), the dynamic equilibrium is provided by Equation (2.35) and the system demand parameter D_{lsdof} can be considered by Equation (2.36).

Figure 4.1 shows scatter plots of $n_s = 500$ samples of D_{lsdof}, for $\omega_0 = 2\pi$ and

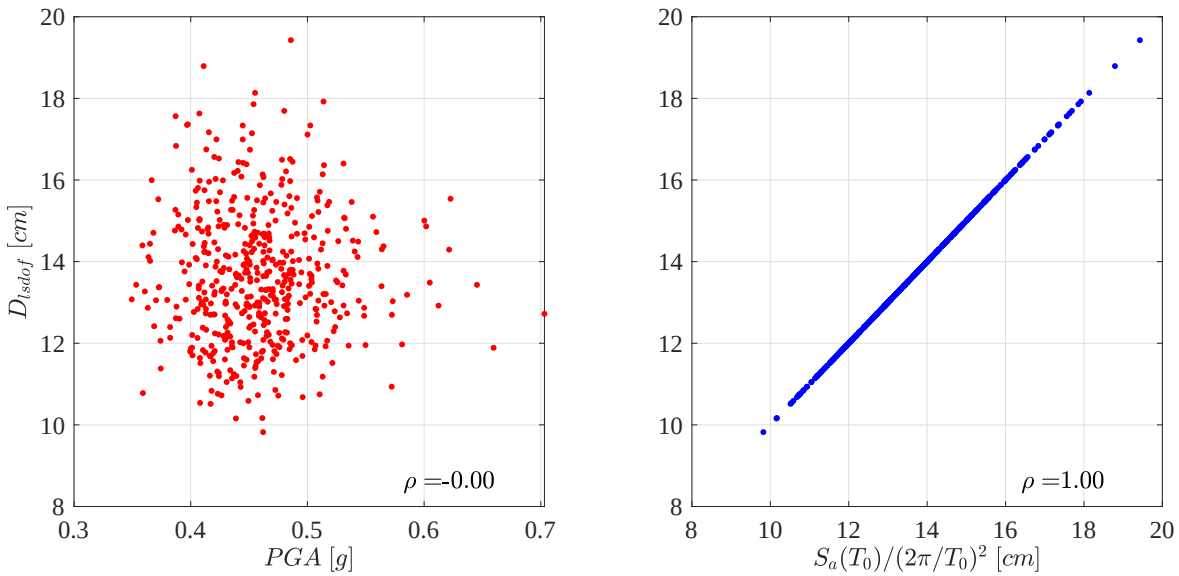

Figure 4.1: Scatter plots of $n_s = 500$ samples for linear SDOF system with $\omega_0 = 2\pi$ and $\zeta = 5\%$: (PGA, D_{lsdof}) (left panel); $(S_a(T_0)/(2\pi/T_1)^2, D_{lsdof})$ (right panel).

$\zeta = 5\%$ as system properties, versus selected IMs. In each panels, on right bottom, the correlation coefficient ρ (Eq. (2.23)) between the random variables which are on the considered panel plot axes is reported. The most used intensity measure definitions in PBEE are taken into account, i.e. PGA and a single ordinate of $S_a(T)$ (Eqs (3.12) and (3.13)) on the left and right panel of Figure 4.1, respectively. In particular, for the contextualization of (3.13) in reference to the linear SDOF case, the first period T_1 in (3.13) coincides with the natural period $T_0 = 2\pi/\omega_0$ of the system. The conceptual example for linear SDOF that is illustrated in Figure 4.1 demonstrates as the PGA and the ordinate of $S_a(T)$ at T_0 are independent and strong dependent with D_{lsdof} since the correlation coefficient is zero and one, respectively, and this, as shown below, will determines no accuracy or accuracy in fragility analysis, respectively. Definitively, this very simple example gives the achievement in which the PGA produces high dispersion on the demand parameter, i.e. (3.12) is not a efficient IM.

It is widely known in literature that the PGA and single ordinate of $S_a(T)$ provide poor and best information on the seismic performance for linear SDOF system [67].

Nevertheless, in reference to the fragilities defined as functions of single/multiple ordinates of the pseudo-acceleration response spectrum $S_a(T)$ in PBEE, it is a critical assumption to think that $S_a(T)$ captures sufficient information on the seismic ground acceleration process such that the demand parameters of nonlinear, complex, real, MDOF structures correlate satisfactory with single/multiple ordinates of $S_a(T)$. The author in [15] has investigated the validity of this assumption for simple linear/nonlinear structures. In particular, it has been declared that:

- first, the demand parameter D for Bouc-Wen single degree of freedom (Subsection 2.3.2), i.e. hysteretic model widely used to describe the nonlinear characteristics for structural systems, and ordinates of $S_a(T)$ are weakly dependent.

  This is of significant concern since the Bouc–Wen SDOF system is a simplistic model for realistic structures, large values of the D and the intensity measure IM as a single ordinate of $S_a(T)$ are nearly independent, and large values of D are associated with excessive damage or even structural collapse;

- second, demand parameter D for linear $MDOF$ system with two or more modes and multiple ordinates of $S_a(T)$ are weakly dependent.

  Since vector-valued IMs constitute an improvement over their scalar-valued versions, they do not address the fundamental weakness of this class of IMs, i.e., the fact that responses of complex, nonlinear structures and responses of selected SDOF linear oscillators to seismic ground accelerations can differ significantly and, generally, are weakly dependent. This suggests that the uncertainty in the responses of realistic structures cannot be reduced to an acceptable level by conditioning on multiple ordinates of $S_a(T)$.

In summary, the contribution in [15] suggests that the fragility functions based on the definitions of single/multiple ordinates of $S_a(T)$ have a large uncertainties which limit their usefulness. Despite this aspect, this IM in scalar/vector-valued version is still

widely used for the fragility analysis of real structures with nonlinear behaviour.

In all cases, in general, the substantial and unstated assumption is that it is possible to accurately predict the response of complex nonlinear structural systems using the results of linear SDOF systems (e.g. $S_a(T)$) or the specific characteristic of the input ground motion acceleration (e.g. PGA). This aspect questions the goodness with which all the procedures reported in the literature for develop the fragility analysis based on the definition of an IM, such as the one in Section 3.6, can have reliable results for the study of real and complex systems seismic performance.

Scientific debate on the current use of common IMs (Section 3.5) in PBEE is still open. Then it is legitimate to think how to try to improve the accuracy in fragility estimates using these IMs, given that despite the limits they have, they are still used. For this reason, if it wants to evaluate useful information on seismic structural performance of a system, to focus attention on the accuracy in fragility analysis with the use of current IMs, it is very crucial to consider these issues.

The main questions in this topic concerning:

- *Is the fragility curve accurate or not?*
- *How is possible to quantify the accuracy level?*
- *Can this curve be improved?*

The author in [15] has answered the first two questions. In particular, the dependence between the demand parameter D and intensity measure IM provides the understanding on the accuracy, and different statistical tools was proposed to measure this dependence, which includes correlation coefficients, copula models and multivariate extreme value theory. The Grigoriu's scientific contribution is based on the Bouc-Wen SDOF and a linear two-DOF system.

One of main focus of this thesis is precisely to provide an answer to the third question in all cases. Since the findings in [15] concern to simplified cases, in this present research work the answers for first two questions are also given into the case of linear/nonlinear real complex MDOF systems.

4.3 Problem definition

On the finding in [15], a discussion on the issue related to the accuracy in the fragility analysis is open into the scientific seismic engineering community. Starting from the concept of the failure probability expressed by Equation (3.3), the fragility can be also defined as

$$P_f(\xi) = E[1(D \in I \subset \mathbb{R}|IM = \xi)] = \int_I f_{D|IM}\,(x|\xi)\,dx \tag{4.1}$$

i.e. the probability that a structural system enters a damage state given a ground motion with scalar/vector-valued intensity measure ξ. The quantities $1(\cdot)$ and $f_{D|IM}(\cdot|\xi)$ indicate the indicator function and the probability density function of the conditional variable $D|(IM = \xi)$ (demand parameter given the intensity measure), respectively. The fragility in (4.1) is usually estimated from the structural response to scaled seismic time histories, $a(t)$ of the stochastic process $A(t)$ [123], and its accuracy depends on the scaling procedure, the sample size and the IMs properties.

To be useful, IMs need to be efficient, i.e., structural demand parameters D on IM have small variances, and sufficient, i.e., the $f_{D|IM}(\cdot|\xi)$ is completely defined for given IM [14, 100]. For efficient IMs, the distribution of the conditional variables $D|IM$ can be estimated from relatively small sets of structural responses. For sufficient IMs, the conditional random variables $D|$(seismic hazard) and $D|IM$ have similar distributions so that probability plots of structural damage versus IMs, i.e., fragilities, are meaningful.

When D and IM are strongly dependent, the random variable $D|IM$ has small variance, i.e. $f_{D|IM}(\cdot|\xi)$ is concentrated about its mean value. On the contrary, when D and IM are weakly dependent the random variable $D|IM$ has large variance. In the limit, $f_{D|IM}(\cdot|\xi)$ becomes a δ-function or D and $D|IM$ have the same PDF (see Subsection 2.2.2) when D and $D|IM$ are perfectly correlated or independent, respectively. In the latter case, the fragility in (4.1) does not depend on ξ i.e.

$$P_f(\xi) = E[1(D \in I \subset \mathbb{R})] = \int_I f_D(x)\, dx \tag{4.2}$$

which gives no information on the structural performance for an earthquake with given intensity measure $IM = \xi$.

As a clear example for the dependence between D and IM influences the results in fragility analysis, and consequently its accuracy for giving informations on the seismic performance, is shown in Figure 4.2. The fragility curves in this figure refer to the simplified case of linear SDOF system with $\omega_0 = 2\pi$ and $\zeta = 5\%$ to spectra-compatible stochastic process $A(t)$. These results are obtained using the MC algorithm in Section 3.6 for the $n_s = 500$ samples of $A(t)$ and limit state $\bar{D}_{lsdof} = 35\,cm$. In particular, the dotted red line are developed considering as IM the (3.12), while the continuous blue curve for the ordinate of $S_a(T)$ at T_0.

The considered variables dependence are the same shown at the scatter plots in Figure 4.1. Concerning the Figure 4.2, when the D_{lsdof} and PGA are independent (left panel of Figure 4.1), the fragility ($IM_1 = PGA$) for defintion does not depend on the IM as in Equation (4.2), so no any performance information for linear SDOF is provided; since D_{lsdof} and $S_a(T_0)$ are strongly dependent (right panel of Figure 4.1), perfectly correlated ($\rho = 1$), the fragility curve for $IM_2 = S_a(T_0)$ is the δ-function, and it gives the best performance information for linear SDOF.

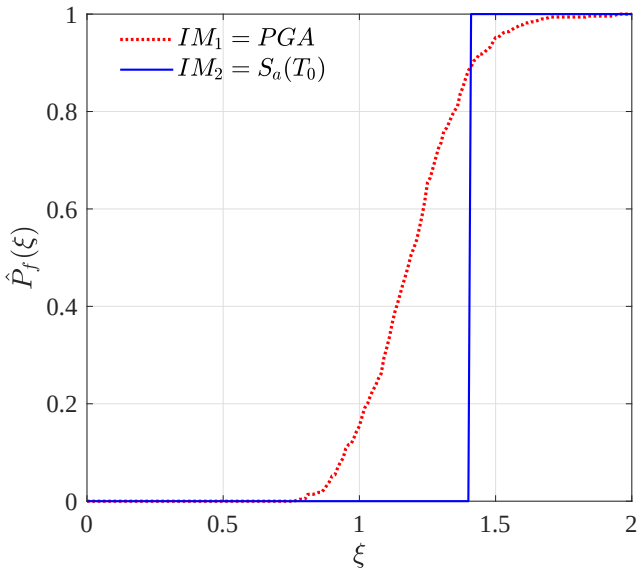

Figure 4.2: Fragilities against intensity level ξ considering different definitions of IMs for linear SDOF system with $\omega_0 = 2\pi$ and $\zeta = 5\%$, limit state $\bar{D}_{lsdof} = 35\,cm$.

The very simple example in Figure 4.1 demonstrates the role of the IM on the accuracy in fragility analysis. A chosen IM definition influences the accuracy of the fragility analysis result, i.e. the ability that the fragility curve based on this IM provides valid information of seimic performance for a structual system. Within this context, especially if Eq. (3.3) is estimated by Eq. (3.8), as it is in the commonly used method [10], it is crucial to quantify the dependence between the demand parameter D and various IM definitions to implicitly determine whether or not fragilities, defined as function of the commonly used IMs, can provide useful information for PBEE of actual complex MDOF linear and nonlinear structural systems. The commonly used method assumption that can accurately predict the seismic performance of complex nonlinear structural systems using IMs based on the features of the seismic input or the response results of linear SDOF systems, it loses credibility after the reasons previously introduced.

Nevertheless, in PBEE the most widespread intensity measure, i.e. PGA and ordi-

nates of $S_a(T)$, are still used [124–126] considering the limits they determine in fragility analysis.

4.4 The modified intensity measure

The improvement of the dependence for the stochastic variables demand parameter D and intensity measure IM, which determines a variance reduction on conditional variable $D|IM$, it is the set objective which translates into a refinement of the information provided by the fragility function.

In the current section, general and advantageous approach to improve the accuracy in fragilities estimation when the dependence between IM and D is weak and the widely used method in PBEE [10] does not give accurate results is introduced. The proposed approach is based on a linear transformation of samples of a given intensity measure, which improves the correlation with a set of demand parameters. This transformation provides the definition of the modified version of the current intensity measure approach. In particular, once classical IM (Section 3.5) is chosen it is mapped in a suitable space where D and the IM are correlated. The novel proposed methodology is formulated to be can apply for linear/nonlinear structural system.

The general method can be applied to all IMs used in PBEE in order to construct fragilities that promise more accurate information than those obtained from unmodified IMs.

Let $D^{(j,l)}$ be the j-th system demand parameter (e.g. maximum displacement) with $j = 1, \ldots, m$, $l = 1, \ldots, k$, where m is the number of demand parameters of interest for arbitrary linear/nonlinear structural system at l number of intensity level. For each l corresponds a level coefficient ξ_l. Since the dependence between $D^{(j,l)}$, $j = 1, \ldots, m$ and $l = 1, \ldots, k$, and IM is a measure to quantify the accuracy in the estimation

of the (4.1), when this dependence is weak a not accurate results are provided by fragility analysis. To overcome this issue it is proposed to replace samples of a chosen standard intensity measure IM with a suitable linear transformation that modifies the dependence with the selected demand parameters samples.

In particular, the following steps are developed:

1. for each n_s samples, $a_i^{(l)}(t)$, $i = 1, \dots, n_s$, of the random process $A^{(l)}(t)$ the corresponding IM and $D^{(j,l)}$ are evaluated, i.e. im_i and $d_i^{(j,l)}$, $i = 1, \dots, n_s$;

2. for each of these samples, the z-scores $z(d_i^{(j,l)})$ and $z(im_i)$, $i = 1, \dots, n_s$, of the standardized random variables

$$Z(D^{(j,l)}) = \frac{D^{(j,l)} - E[D^{(j,l)}]}{\sigma_{D^{(j,l)}}}, \quad j = 1, \dots, m, \quad l = 1, \dots, k \tag{4.3}$$

$$Z(IM) = \frac{IM - E[IM]}{\sigma_{IM}} \tag{4.4}$$

   are computed as in (2.24), respectively;

3. for each pair of samples $z(d_i^{(j,l)})$ and $z(im_i)$, it is possible to evaluate the distance from perfect correlation

$$e_i^{(j,l)} = z(d_i^{(j,l)}) - z(im_i), \quad i = 1, \dots, n_s, \quad j = 1, \dots, m, \quad l = 1, \dots, k; \tag{4.5}$$

4. the average distance of the j demand parameters on l is estimated

$$\bar{e}_i = \frac{1}{k\,m} \sum_{l=1}^{k} \sum_{j=1}^{m} e_i^{(j,l)}, \quad i = 1, \dots, n_s; \tag{4.6}$$

5. the linear transformation

$$mim_i = [z(im_i) + \bar{e}_i]\sigma_{IM} + E[IM], \quad i = 1, \dots, n_s \tag{4.7}$$

gives samples that can be considered the realizations of a new intensity measure, called, modified intensity measure mIM.

In particular, it is noted that, there has never been any discussion of a dependence on l for the intensity measure, i.e. $IM^{(l)}$. Regardless of system behaviour for any l used to scale $A^{(l)}(t)$, the dependence between $D^{(j,l)}$ and $IM^{(l)}$ is the same that of $D^{(j,l)}$ and IM.

Depending on the behaviour of the structural system, in the previous five-steps methodology, the following aspects can be taken into account

- **linear behaviour**: the dependence between D and IM is the same at each intensity level which is scaled the input as in Section 3.6. For this reason, the linear behaviour allows a simplified treatment in which the unscaled stochastic process input $A^{(l)}(t)$ is considered, i.e. $l = 1$, which is equivalent to consider an unitary level coefficient ($\xi_l = 1$) that corresponds to unscaled $A(t)$. In this case, refer to $A^{(l)}(t)$ or $A(t)$ is the same. Consequently, the same consideration is also valid for the corresponding values of D;

- **nonlinear behaviour**: the dependence between D and IM changes for different intensity level considered. Since the nonlinearity is manifested directly on the demand parameters, the quantity in Equation (4.3) is defined for different level of interest, i.e. $l > 1$, in which the process input $A^{(l)}(t)$ is scaled ($\xi_l A(t)$). The procedure to determine the modified intensity measure mIM, for a nonlinear system, needs to be defined on different intensity levels.

For greater clarity, it is worth noting that, first, if the random variables defined in Equations (4.3) and (4.4) are linearly dependent, the correlation coefficient is equal to one and the scatter plots of pairs of samples $z(d_i^{(j,l)})$ and $z(im_i)$ describe straight line.

Second, the samples obtained with Equation (4.6) can be considered as realizations of a vector $\bar{E}$.

Third, for a structural system with linear (nonlinear) behaviour, it needs to consider $l = 1$ ($l > 1$).

Fourth, the $m = 1$ can be considered for SDOF system case, or if for a MDOF system the interest falls on one demand parameter.

Fifth, for $m = 1$ and $l = 1$ (i.e. one demand parameter and one intensity level), the correlation estimated from the n_s samples of D and mIM is exactly one. When $m > 1$ and $l > 1$, $m = 1$ and $l > 1$ or $m > 1$ and $l = 1$, it is not possible to have perfect correlation, but anyway the correlation between $D^{(j,l)}$ and mIM is significantly higher than the one estimated from samples of $D^{(j,l)}$ and IM.

It follows that, for linear/nonlinear structural system, the mIM samples obtained with Equation (4.7), considering the five-steps procedure above, can be used to scale the ground acceleration records to build fragility curves by the MC algorithm in Section 3.6 that give more accurate information on the structural system performance when compared with the standard intensity measures.

Effectiveness of the mIM definition can be preliminary demonstrated by taking up the simpler case previously introduced in Section 4.2, i.e. the linear SDOF system with $\omega_0 = 2\pi$ and $\zeta = 5\%$ to $n_s = 500$ samples of the spectra-compatible stochastic process. In particular, unsatisfactory results are provided through the fragility analysis with the use of PGA (Eq. (3.12)). Then the modified version of the $IM_1 = PGA$ is provided by the five-steps novel approach, i.e. $mIM_1 = mPGA$, in order to: first, improve the dependence between D_{lsdof} and PGA; second, determine the accuracy increment for the estimation of (4.1) considering the $mPGA$. Since the system has one DOF and is linear, the five-steps approach is developed by setting $m = 1$ and $l = 1$.

The initial correlation between D_{lsdof} and PGA is zero (see left panel of Figure 4.1). Then, samples of D_{lsdof} and PGA are first transformed into their standardized versions using Equations (4.3) and (4.4), respectively, and the distance from perfect correlation is evaluated by Equation (4.5). In this particular case, since $m = 1$ and $l = 1$, the n_s samples provided by (4.5) coincide with those provided with (4.6), and then they can be directly collected in the variable $\bar{E}$ that is used to correct the samples of $Z(PGA)$. The last step is to evaluate samples of the modified intensity measure $mPGA$ using Equation (4.7).

Left panel of Figure 4.3 reports the scatter plots and the correlation coefficients ρ before and after the correction in the standardized space, i.e. $(Z(IM_1), Z(D_{lsdof}))$, and $(Z(IM_1) + \bar{E}, Z(D_{lsdof}))$, respectively. The right panel shows the scatter plots of the same samples (before and after the correction) linearly transformed back into their original space by Eq. (4.7), i.e. (IM_1, D_{lsdof}), and (mIM_1, D_{lsdof}), respectively. In general, this figure refer to the scatter plots in red dots (green circles) for before (after)

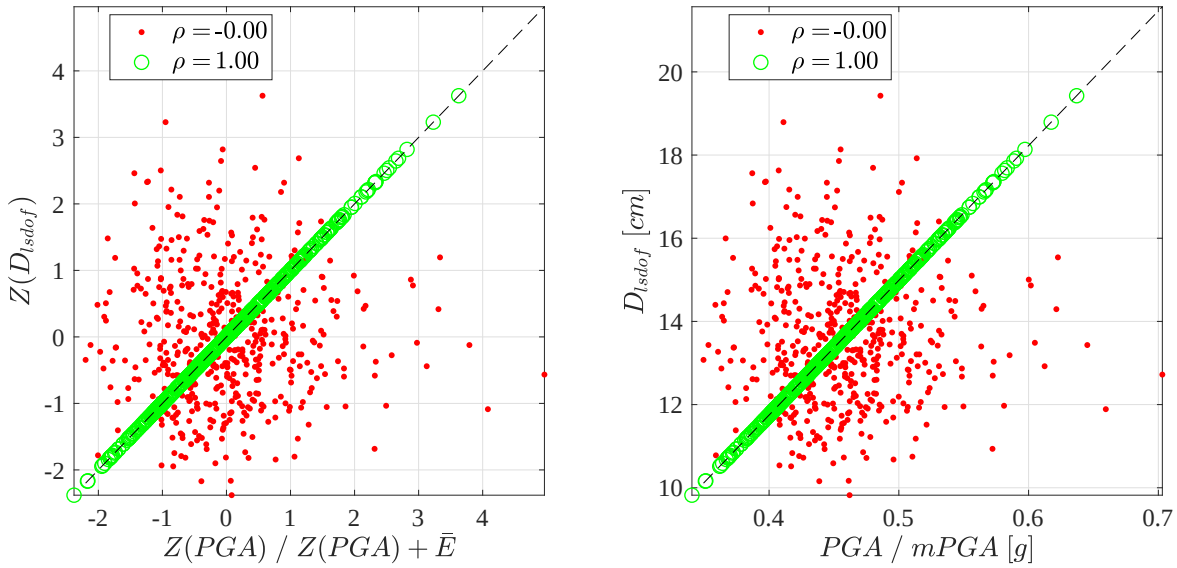

Figure 4.3: Scatter plots of $n_s = 500$ samples for linear SDOF system with $\omega_0 = 2\pi$ and $\zeta = 5\%$: $(Z(PGA), Z(D_{lsdof}))$ red dots, $(Z(PGA) + \bar{E}, Z(D_{lsdof}))$ green circles (left panel); (PGA, D_{lsdof}) red dots, $(mPGA, D_{lsdof})$ green circles (right panel).

the correction. The dashed black line is the geometric place that describes the best correlation and it is completely matched with the green circles, i.e. scatter plots after the correction.

The development of the fragility curve using the MC algorithm (Section 3.6) by considering as intensity measure the $mIM_1 = mPGA$ for the linear SDOF system, with $\omega_0 = 2\pi$ and $\zeta = 5\%$, to $n_s = 500$ samples of spectra-compatible stochastic process $A(t)$ and assuming $\bar{D}_{lsdof} = 35\,cm$ is reported in Figure 4.4. In particular, this figure describes a comparison between the fragility function before the correction of the correlation in dotted red line for IM_1 (same results in Figure 4.2) and after the correction in dash-dotted green line by using mIM_1. It is worth noting that the fragility curve obtained with the modified intensity measures (dash-dotted green line) is steeper than that estimated using the original intensity measure (dotted red line). This is consistent with that discussed in Section 4.3 about a random variable $D|IM$. It follows that, the matched unitary correlation coefficient (Figure 4.3) provided by mIM determines that the curve for IM_1 becomes as δ-function with the use of mIM_1 in Figure 4.4.

The Figures 4.3 and 4.4 demonstrate for a simplified linear SDOF system case the ability of the proposed procedure to improve the correlation between the selected demand parameter and intensity measure. This will result into an improved accuracy in the fragility curve.

Another aspect that should not be overlooked is that the modified intensity measure methodology does not substantially change the probability density function of the original intensity measure. About this concept, Figure 4.5 shows the PDF estimation of $IM_1 = PGA$ and $mIM_1 = mPGA$ in the left and right panel, respectively. In each panels, on the right top, the first four statistical moments estimated of the probability distribution is provided. The first two statistical moments are the same.

In the following chapters, usefulness of the modified intensity measure approach for

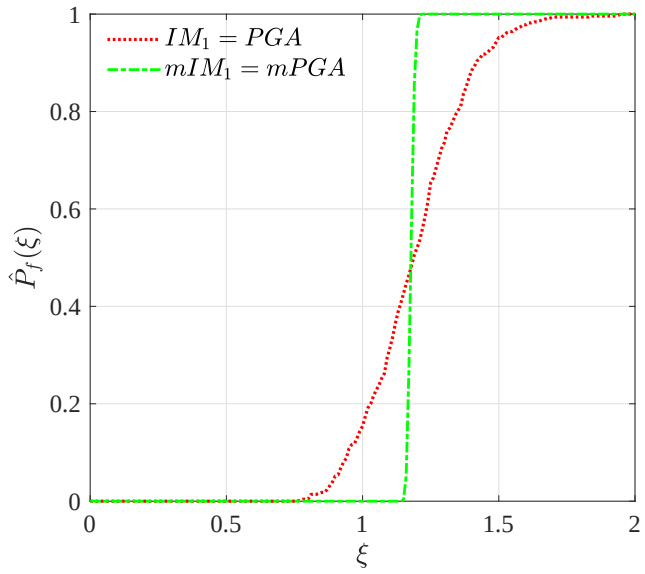

Figure 4.4: Fragilities against intensity level ξ considering the intensity measure PGA and its modified version $mPGA$ for linear SDOF system with $\omega_0 = 2\pi$ and $\zeta = 5\%$, limit state $\bar{D}_{lsdof} = 35\,cm$.

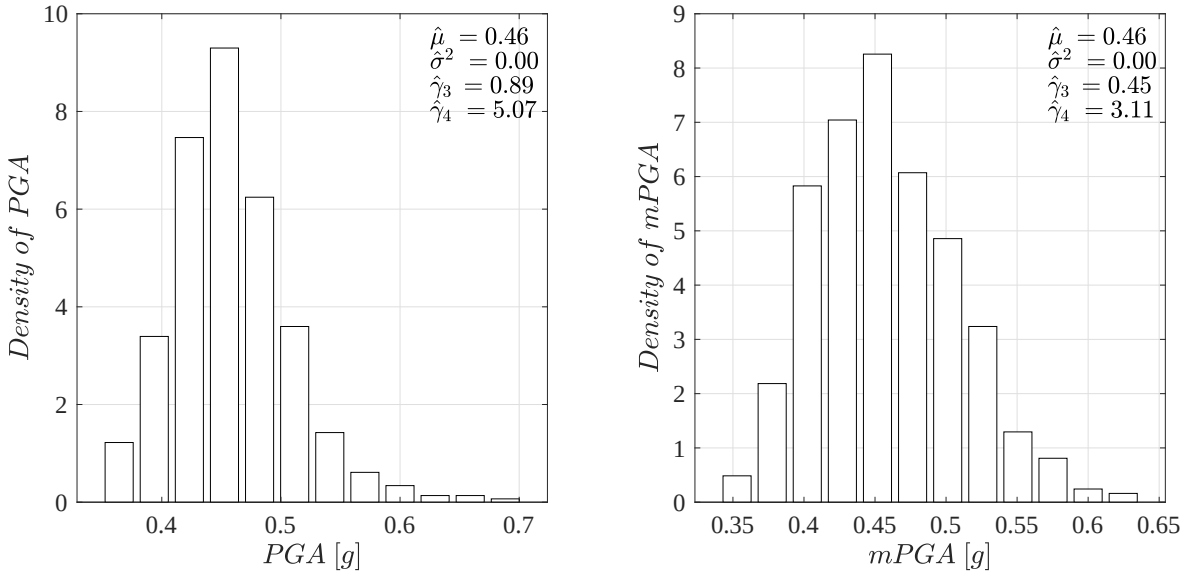

Figure 4.5: Estimated PDF for $n_s = 500$ samples of PGA (left panel) and $mPGA$ (right panel) computed with $m = k = 1$.

other cases regarding the nonlinearity behaviour and complexity for MDOF systems will be shown.

Chapter 5

Fragility analysis accuracy improvement for analytical systems

5.1 Introduction

Aim of this chapter is to demonstrate the validity and effectiveness of the modified intensity measure approach in Section 4.4 to improve the results accuracy provided by fragility analysis. To introducing this general methodology, preliminary results were provided for the linear single degree of freedom system to spectra-compatible stochastic process in Subsection 2.4.1 .

The formulation of the novel approach is applied herein to some analytical systems, which are again subjected to samples of spectra-compatible stochastic process. In particular, nonlinear elementary oscillators and linear/nonlinear multi-degree of freedom systems are considered. The use of this artificial acceleration ground motion typology is common used in PBBE for the structural design, e.g. [127–129]. For this reason, in the absence of natural records to describe the seismic hazard, the spectra-compatible accelerations can be a valid alternative. Most widespread intensity measure definitions usually used in PBEE are taken into account for making a comparison on fragility analysis results obtained with the them classical and modified version.

5.2 Duffing oscillator

Consider a unitary mass elementary Duffing oscillator to spectra-compatible stochastic process, the dynamic equilibrium is provided by Equation (2.41) and the system demand parameter D_{dsdof} can be provided by

$$D_{dsdof} = \max_{0 \leqslant t \leqslant \tau} |X_{dsdof}(t)| \tag{5.1}$$

where τ is the time length of spectra-compatible stochastic process $A(t)$.

Figure 5.1 and 5.2 show scatter plots of $n_s = 500$ samples of $D^{(l)}_{dsdof}$, for $\omega_0 = 2\pi$, $\zeta = 5\%$ and $\gamma = 3$ as system properties (in Eq. (2.41)), and the widespread IMs in PBEE, i.e. PGA and $S_a(T_0)$ (single ordinate of $S_a(T)$), respectively. In these figures, for each panels, the correlation coefficient ρ is reported on the right bottom, while on the top, the number of level intensity l and corresponding level coefficient ξ_l are shown. From left to right panels, the random variable demand parameter in Equation (5.1) is computed with increasing level intensity of the stochastic process input, i.e. $A^{(l)}(t) = \xi_l A(t)$. Since the system has nonlinear behaviour, in particular, the kind of cubic (Eq. (2.41)), the samples values of demand parameter at prefixed intensity level $D^{(l)}_{dsdof}$ change for different l. To consider the IM rather $\xi_l IM$ does not change the dependence versus $D^{(l)}_{dsdof}$. The first panels from left correspond to unscaled process $A(t)$ ($\xi_l = 1$).

Results in Figure 5.1 confirm that the Equation (3.12) is inadequate intensity measure also for a nonlinear simple SDOF system, and it seems that the dependence between $D^{(l)}_{dsdof}$ and PGA is invariant with the considered level intensity.

Scatter plots in Figure 5.2 refer to the contextualization of (3.13) for the SDOF case, the first period T_1 in (3.13) coincides with the natural period $T_0 = 2\pi/\omega_0$ of the system. These results shown that the $S_a(T_0)$ is weak dependent with the demand parameter of

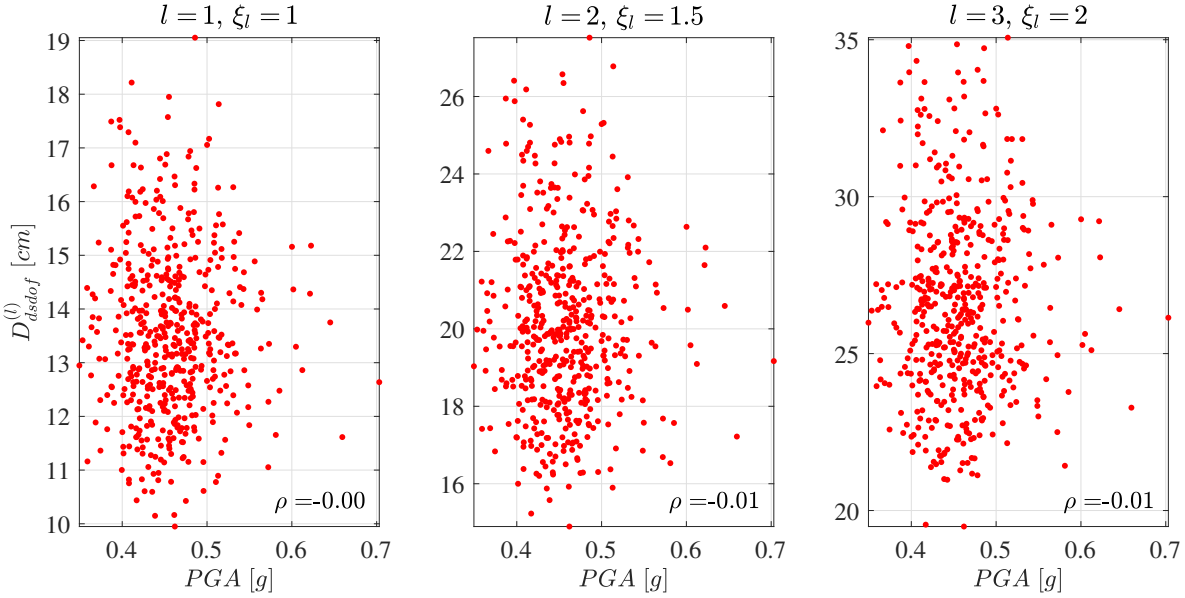

Figure 5.1: Scatter plots of $n_s = 500$ samples of $(PGA, D^{(l)}_{dsdof})$ for Duffing SDOF system with $\omega_0 = 2\pi$, $\zeta = 5\%$ and $\gamma = 3$: $l = 1$ with $\xi_l = 1$ (left panel); $l = 2$ with $\xi_l = 1.5$ (center panel); $l = 3$ with $\xi_l = 2$ (right panel).

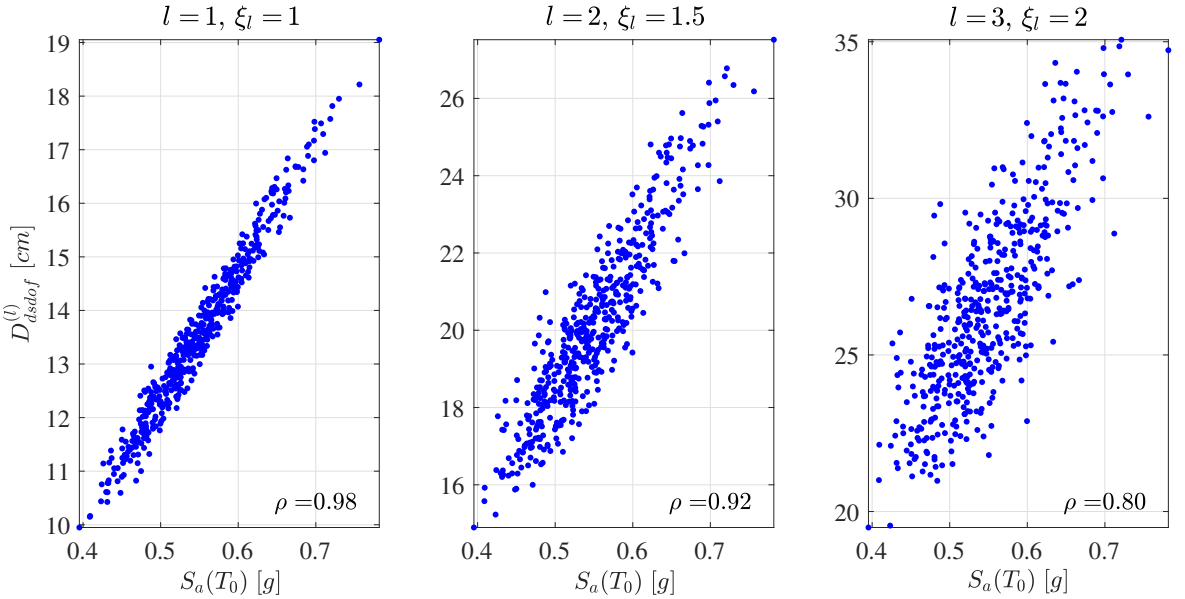

Figure 5.2: Scatter plots of $n_s = 500$ samples of $(S_a(T_0), D^{(l)}_{dsdof})$ for Duffing SDOF system with $\omega_0 = 2\pi$, $\zeta = 5\%$ and $\gamma = 3$: $l = 1$ with $\xi_l = 1$ (left panel); $l = 2$ with $\xi_l = 1.5$ (center panel); $l = 3$ with $\xi_l = 2$ (right panel).

Duffing system. Increasing ξ_l, the dispersion of $S_a(T_0)$ on $D^{(l)}_{dsdof}$ is also increasing, and these demonstrate as $S_a(T_0)$ is not efficient IM for Duffing oscillator. Similar results were obtained in [15] considering stationary Gaussian band limited white noise as input process for Duffing system.

5.2.1 Dependence improvement

The procedure described in Section 4.4 is applied to improving dependence for Duffing oscillator. In particular, for this case the methodology is adopted with $j = m = 1$ and $k = 3$, $l = 1, 2, 3$. Since the system has one DOF, subscript j is omitted.

Initial correlation between $D^{(l)}_{dsdof}$ and PGA or $S_a(T_0)$ (Figure 5.1 or 5.2) can be improved using the modified intensity measure approach. Samples of the demand parameters and the two IMs are first transformed into their standardized versions using Equations (4.3) and (4.4) and the distance from perfect correlation is evaluated by Equation (4.5). The next step is to evaluate the n_s average distances using Eq. (4.6) and collecting them in the vector $\bar{E}$ which is used to correct the standardized samples of PGA or $S_a(T_0)$, i.e. $Z(PGA)$ or $Z(S_a(T_0))$. Then, samples of the modified intensity measure mIM are computed by Equation (4.7).

Figure 5.3 and 5.4 show the obtained results for the intensity measure $IM_1 = PGA$ and $IM_2 = S_a(T_0)$, respectively. In these figures, the scatter plots and the correlation coefficients before and after the correction in standardized space, i.e. $(Z(IM_q), Z(D^{(l)}_{dsdof}))$ and $(Z(IM_q) + \bar{E}, Z(D^{(l)}_{dsdof}))$, $q = 1, 2$, respectively, are reported. From left to right panels, ξ_l increases.

For the same samples, Figure 5.5 and 5.6 report the scatter plots before and after the correction linearly transformed back into the original space representation by Eq. (4.7), i.e. $(IM_q, D^{(l)}_{dsdof})$ and $(mIM_q, D^{(l)}_{dsdof})$, $q = 1, 2$, respectively. Once again the intensity level increases from the left to right panels.

In general, the results regard PGA (see Figure 5.3 and 5.5) are marked with red

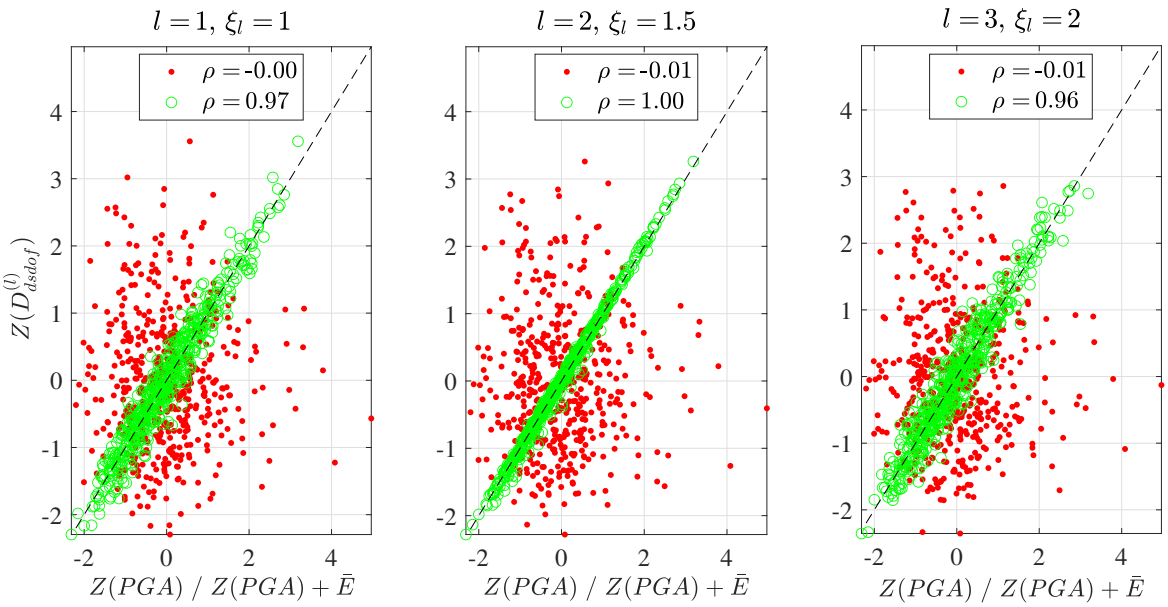

Figure 5.3: Scatter plots of $n_s = 500$ samples of $(Z(PGA), Z(D^{(l)}_{dsdof}))$ red dots, $(Z(PGA)+\bar{E}, Z(D^{(l)}_{dsdof}))$ green circles for Duffing SDOF system with $\omega_0 = 2\pi$, $\zeta = 5\%$ and $\gamma = 3$: $l = 1$ with $\xi_l = 1$ (left panel); $l = 2$ with $\xi_l = 1.5$ (center panel); $l = 3$ with $\xi_l = 2$ (right panel).

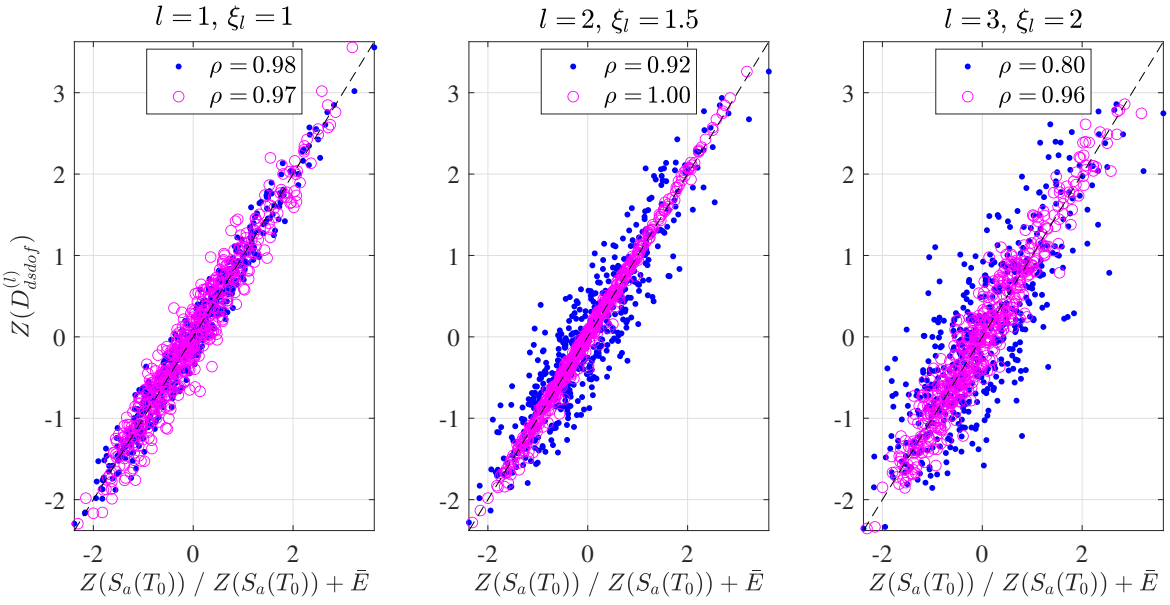

Figure 5.4: Scatter plots of $n_s = 500$ samples of $(Z(S_a(T_0)), Z(D^{(l)}_{dsdof}))$ blue dots, $(Z(S_a(T_0)) + \bar{E}, Z(D^{(l)}_{dsdof}))$ magenta circles for Duffing SDOF system with $\omega_0 = 2\pi$, $\zeta = 5\%$ and $\gamma = 3$: $l = 1$ with $\xi_l = 1$ (left panel); $l = 2$ with $\xi_l = 1.5$ (center panel); $l = 3$ with $\xi_l = 2$ (right panel).

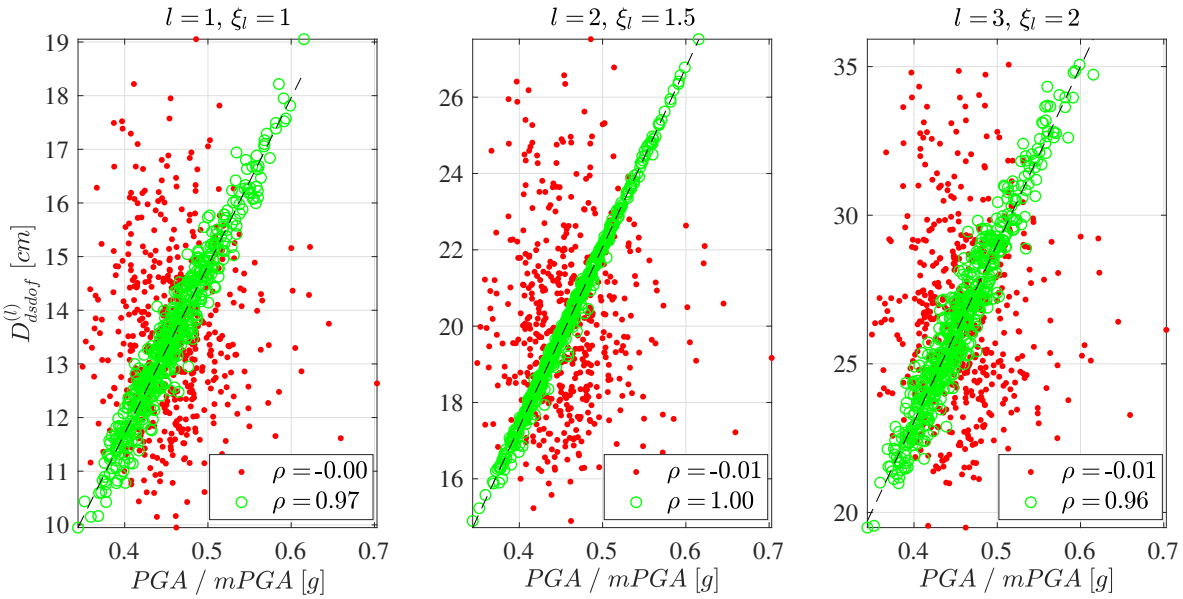

Figure 5.5: Scatter plots of $n_s = 500$ samples of $(PGA, D^{(l)}_{dsdof})$ red dots, $(mPGA, D^{(l)}_{dsdof})$ green circles for Duffing SDOF system with $\omega_0 = 2\pi$, $\zeta = 5\%$ and $\gamma = 3$: $l = 1$ with $\xi_l = 1$ (left panel); $l = 2$ with $\xi_l = 1.5$ (center panel); $l = 3$ with $\xi_l = 2$ (right panel).

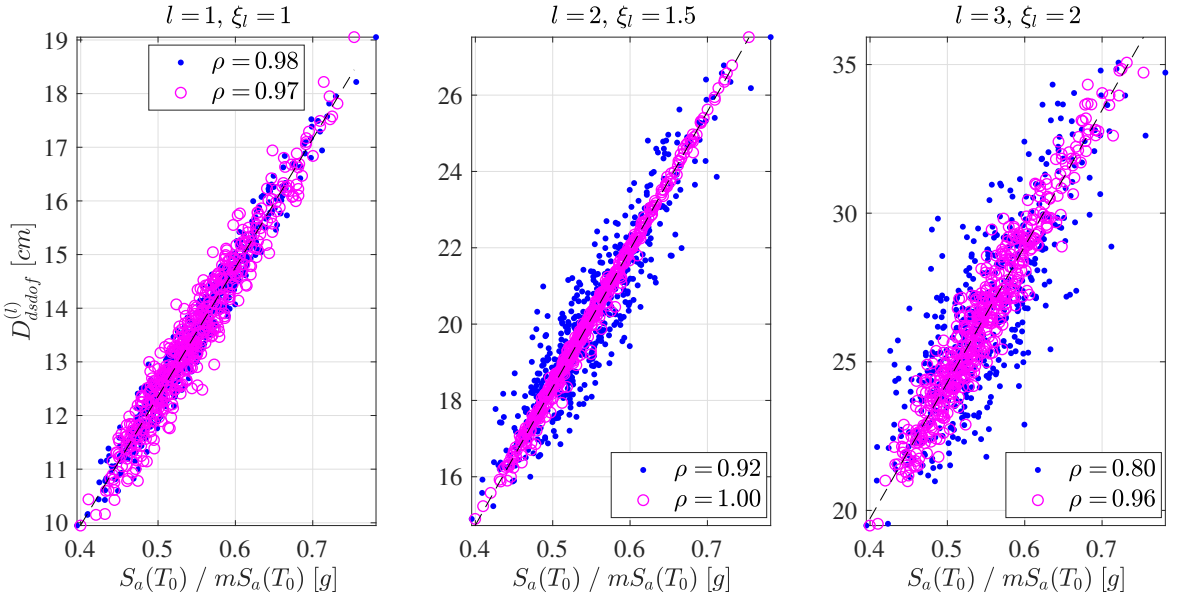

Figure 5.6: Scatter plots of $n_s = 500$ samples of $(S_a(T_0), D^{(l)}_{dsdof})$ blue dots, $(mS_a(T_0), D^{(l)}_{dsdof})$ magenta circles for Duffing SDOF system with $\omega_0 = 2\pi$, $\zeta = 5\%$ and $\gamma = 3$: $l = 1$ with $\xi_l = 1$ (left panel); $l = 2$ with $\xi_l = 1.5$ (center panel); $l = 3$ with $\xi_l = 2$ (right panel).

dots and green circle, before and after the correlation improvement, while the those for $S_a(T_0)$ are blue dots and magenta circles (before and after, Figure 5.4 and 5.6).

The results obtained for PGA and $S_a(T_0)$ demonstrate the ability of mIM algorithm to improve the correlation between Duffing demand parameter and intensity measures for different values of l. Satisfactory dependence are provided, in all cases after the definition of mIM_q, $q = 1, 2$, the correlation coefficient tends to be unitary for each l, in particular, $\rho \geq 0.96$.

The slight decrease in correlation between $Z(D^{(l)}_{dsdof})$ and $Z(S_a(T_0)) + \bar{E}$ or $D^{(l)}_{dsdof}$ and $mS_a(T_0)$, left panel of Figure 5.4 or 5.6, represents an acceptable compromise in that this correlation for $l = 1$ is sold to improve the one at higher intensity levels, i.e. $l = 2, 3$ (center and right panels of Figure 5.4 and 5.6). This aspect is attributable to the definition of $\bar{E}$ (Eq. (4.6)). However a reasonable sacrifice, ρ changes from 0.98 to 0.97, considering the benefits that are produced in terms of dependence for the higher intensity levels.

Figure 5.7 and 5.8 show the PDFs, an estimation by normalized histogram, and the first four statical moments form samples of the original intensity measures IM_q, $q = 1, 2$ (left panels) and their modified versions mIM_q (right panels). In particular, Figure 5.7 shows the results for $IM_1 = PGA$, while Figure 5.8 refers to $IM_2 = S_a(T_0)$. It is interesting to note that the linear transformation of the obtained intensity measure samples for Duffing oscillator case does not significantly change the intensity measures first four statistical moments (see Figure 5.8). In Figure 5.7, the mean and variance of the probability density function of PGA and $mPGA$ are the same.

5.2.2 Fragility analysis

The algorithm in Section 3.6 is used to develop fragility analysis for the Duffing system. In particular, fragilities obtained considering standard IMs are compared with those

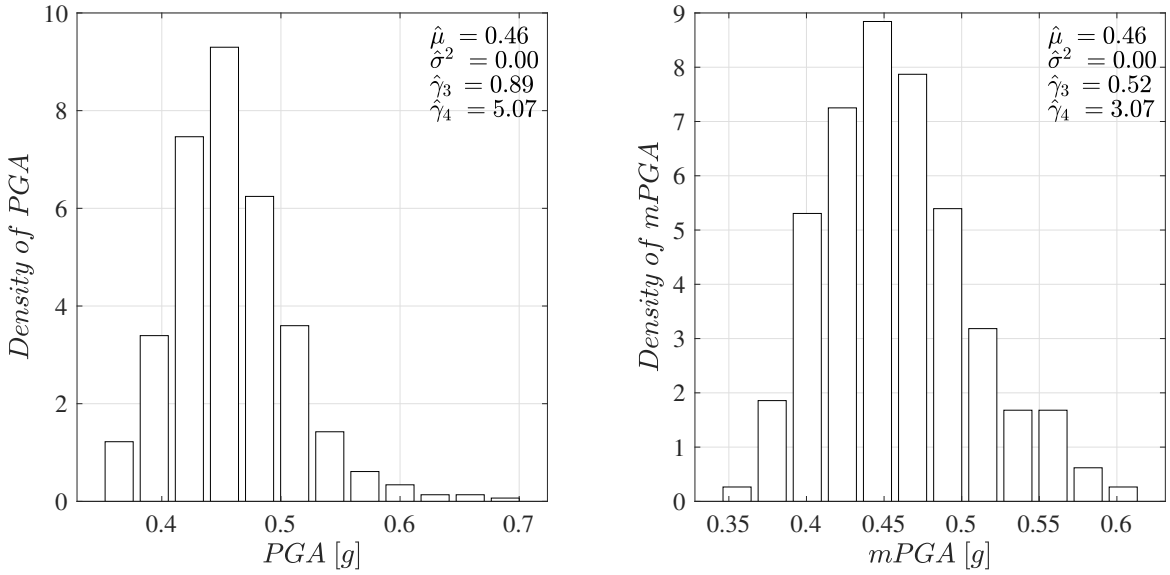

Figure 5.7: Estimated PDF for $n_s = 500$ samples of PGA (left panel) and $mPGA$ (right panel) computed with $m = 1$ and $k = 3$.

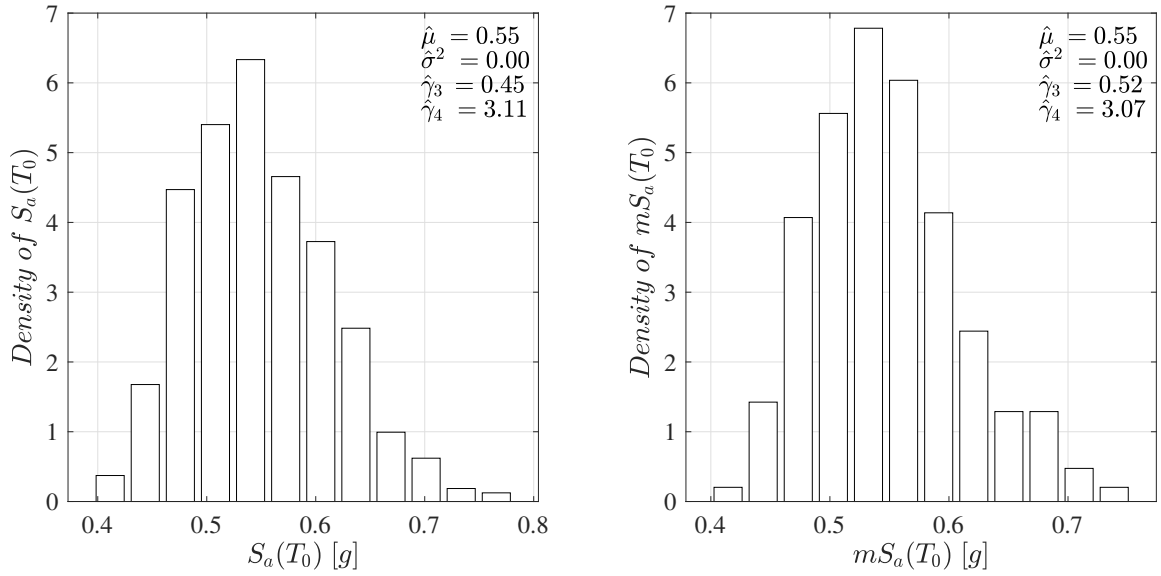

Figure 5.8: Estimated PDF for $n_s = 500$ samples of $S_a(T_0)$ (left panel) and $mS_a(T_0)$ (right panel) computed with $m = 1$ and $k = 3$.

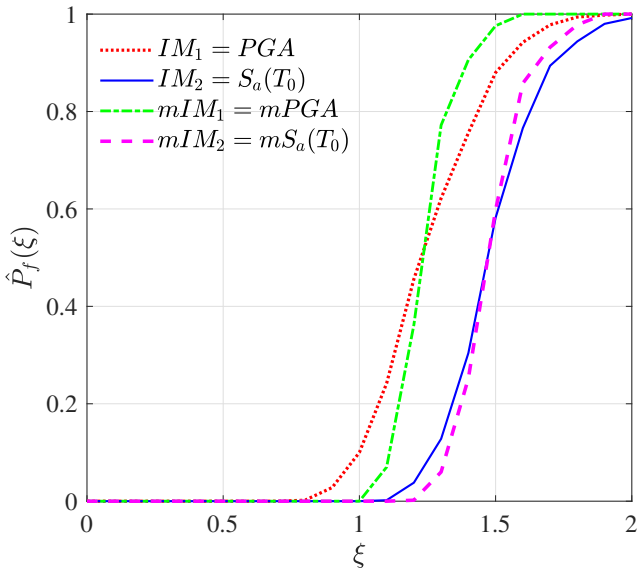

Figure 5.9: Fragilities against intensity level ξ for different definitions of IMs and its modified version $mIMs$ for Duffing SDOF system with $\omega_0 = 2\pi$, $\zeta = 5\%$, $\gamma = 3$ and limit state $\bar{D}_{dsdof} = 35\,cm$.

evaluate by its $mIMs$. It is shown that, the dependence improvement for Duffing oscillator by the modified intensity measure definition, i.e. previous Subsection 5.2.1 , determines a better estimation of the fragility function.

In Figure 5.9 the fragility curves for Duffing oscillator, with $\omega_0 = 2\pi$, $\zeta = 5\%$ and $\gamma = 3$, to $n_s = 500$ samples of spectra-compatible stochastic process and prefixed LS value $\bar{D}_{dsdof} = 35\,cm$ are shown. The dotted red line regards to PGA and that in dash-dotted green to $mPGA$, while continuous blue line refers to $S_a(T_0)$ and the that dashed magenta to its modified version $mS_a(T_0)$. For both cases, the transition from IM_q, $q = 1, 2$, to mIM_q produce an improvement on accuracy in fragility analysis. The conditional variables $D^{(l)}_{dsdof}|mIM_q$, $l = 1, 2, 3$ and $q = 1, 2$, have less variance if compared those of $D^{(l)}_{dsdof}|IM_q$. Graphically it can be seen that the curves referring to mIM_q have a greater slope than IM_q.

5.3 Bouc-Wen oscillator

The dynamic equilibrium for unitary mass Bouc-Wen SDOF system to spectra-compatible stochastic process $A(t)$ is described in Equation (2.46), and the demand parameter can be given as

$$D_{bwsdof} = \max_{0 \leqslant t \leqslant \tau} |X_{bwsdof}(t)| \tag{5.2}$$

i.e. the maximum absolute of displacement vector, where τ is the time length of $A(t)$.

Scatter plots of $n_s = 500$ samples of $D^{(l)}_{bwsdof}$, using $\omega_0 = 2\pi$, $\zeta = 5\%$ and $\eta = 0.9$ in Eq. (2.46) and $\gamma = 3$, $\alpha = 0.5$, $\beta = 5$ and $n = 1$ in Eq. (2.44), and different IMs (Eqs. (3.12)-(3.13)) are reported in Figures 5.10 - 5.11. In each panels of these figures, the information about the dependence between $D^{(l)}_{bwsdof}$ and IM, i.e. ρ on right bottom, is reported, and in the top, it is shown the number of level intensity l and corresponding level coefficient ξ_l. From left to right panels, the random variable demand parameter in Equation (5.2) is computed with increasing level intensity of the stochastic process input, i.e. $A^{(l)}(t) = \xi_l A(t)$. Samples values of demand parameter at prefixed intensity level, i.e. $D^{(l)}_{bwsdof}$, change for different l. The first panels from left correspond to unscaled process $A(t)$ ($\xi_l = 1$).

Figure 5.10 and 5.11 refer to Eq. (3.12) and Eq. (3.13), with T_1 that coincides with the natural period $T_0 = 2\pi/\omega_0$, respectively.

Even if it is considered a low contribution of the hysteretic process $W(t)$ in the dynamic equilibrium, i.e. $\eta = 0.9$ in Eq. (2.46) (for $\eta = 1$ the system in fully linear), both PGA and $S_a(T_0)$ determine high dispersion on $D^{(l)}_{bwsdof}$, $l = 1, 2, 3$.

Also for Bouc-Wen oscillator to spectra-compatible stochastic process, it is shown that (3.12) is an inappropriate IM (Figure 5.10); results which are also not encouraging are provided considering $IM_2 = S_a(T_0)$ (Figure 5.11).

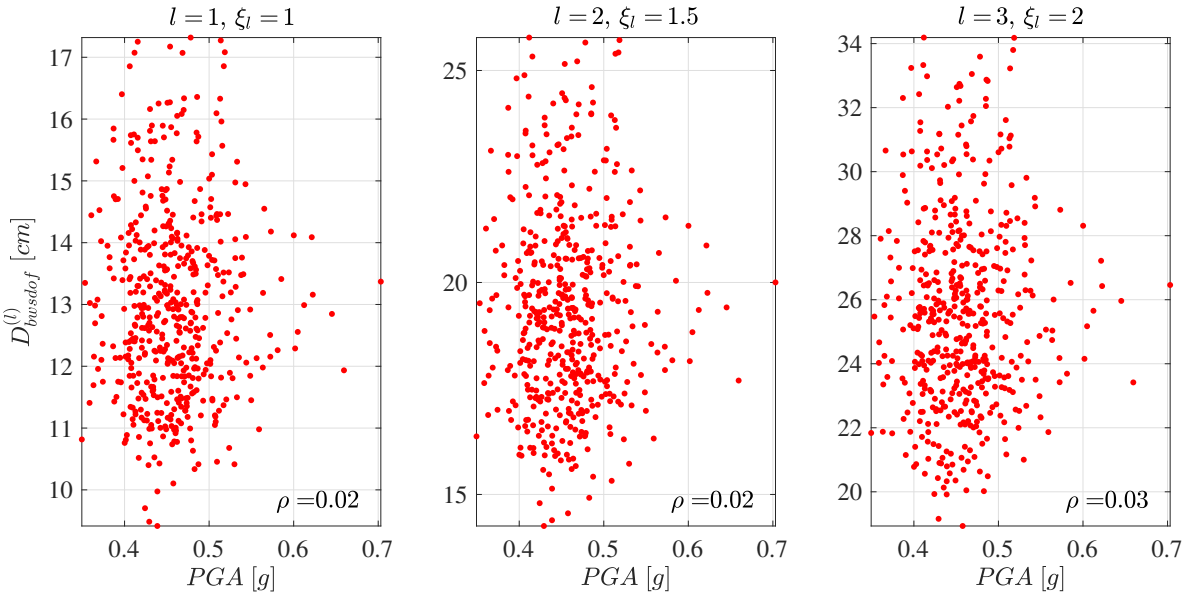

Figure 5.10: Scatter plots of $n_s = 500$ samples of $(PGA, D^{(l)}_{bwsdof})$ for Bouc-Wen SDOF system with $\omega_0 = 2\pi$, $\zeta = 5\%$, $\eta = 0.9$, $\gamma = 3$, $\alpha = 0.5$, $\beta = 5$ and $n = 1$: $l = 1$ with $\xi_l = 1$ (left panel); $l = 2$ with $\xi_l = 1.5$ (center panel); $l = 3$ with $\xi_l = 2$ (right panel).

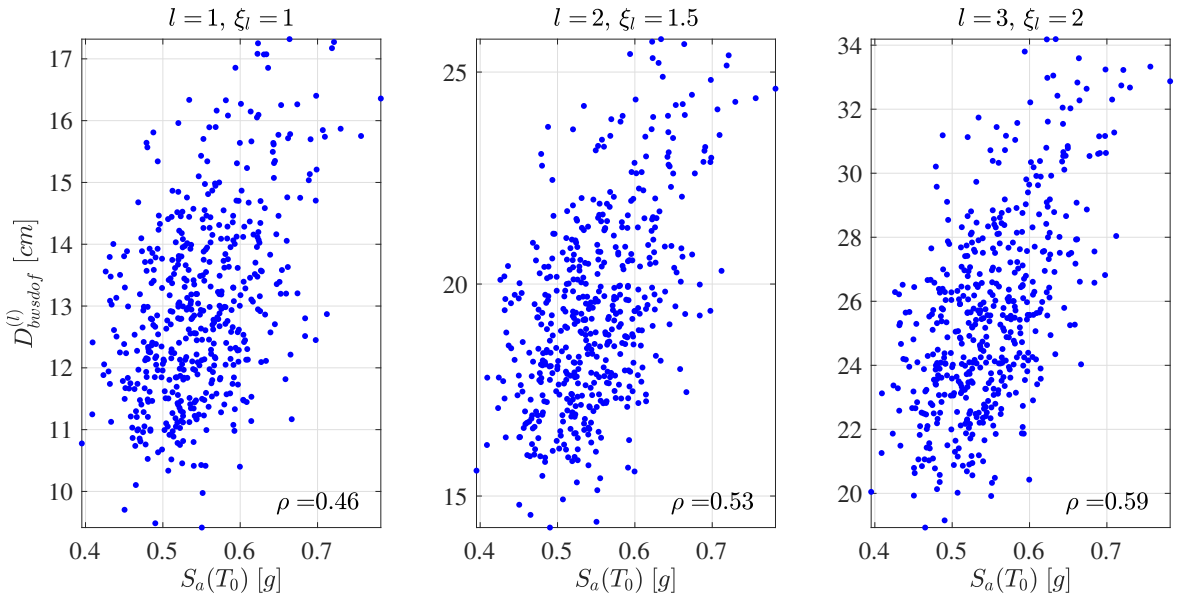

Figure 5.11: Scatter plots of $n_s = 500$ samples of $(S_a(T_0), D^{(l)}_{bwsdof})$ for Bouc-Wen SDOF system with $\omega_0 = 2\pi$, $\zeta = 5\%$, $\eta = 0.9$, $\gamma = 3$, $\alpha = 0.5$, $\beta = 5$ and $n = 1$: $l = 1$ with $\xi_l = 1$ (left panel); $l = 2$ with $\xi_l = 1.5$ (center panel); $l = 3$ with $\xi_l = 2$ (right panel).

5.3.1 Dependence improvement

To improve dependence between the demand parameter for Bouc-Wen oscillator and IM_q, $q = 1, 2$, the algorithm to define the modified intensity measure (Section 4.4) is used considering $j = m = 1$ (one DOF). The subscript j is omitted, and $k = 3$, i.e. $l = 1, 2, 3$.

The initial correlation (dependence) between $D^{(l)}_{bwsdof}$ and PGA or $S_a(T_0)$ (Figure 5.10 or 5.11) can be improved using the modified intensity measure approach. Samples of the demand parameters and the two IMs are first transformed into their standardized versions using Equations (4.3) and (4.4) and the distance from perfect correlation is evaluated by Equation (4.5). The n_s average distances using Eq. (4.6) are collected in the vector $\bar{E}$ which is used to correct the standardized samples of PGA or $S_a(T_0)$, i.e. $z(PGA)$ or $z(S_a(T_0))$. Then, samples of the modified intensity measure mIM are computed by Equation (4.7).

Figure 5.12 and 5.13 regard to $IM_1 = PGA$ and $IM_2 = S_a(T_0)$, respectively. In these figures, the scatter plots and ρ before and after the correction in standardized space, i.e. $(Z(IM_q), Z(D^{(l)}_{bwsdof}))$ and $(Z(IM_q) + \bar{E}, Z(D^{(l)}_{bwsdof}))$, $q = 1, 2$, respectively, are shown. From left to right panels, ξ_l increases.

In Figure 5.14 and 5.15 are reported, for the same samples in Figures 5.12 and 5.13, the scatter plots before and after the correction in the original space representation, i.e. $(IM_q, D^{(l)}_{bwsdof})$ and $(mIM_q, D^{(l)}_{bwsdof})$, $q = 1, 2$, respectively.

The results obtained by PGA (see Figure 5.3 and 5.5) are marked with red dots and green circle, before and after the correlation improvement. For $S_a(T_0)$, the blue dots and magenta circles indicate results before and after the correction (Figure 5.13 and 5.15).

The results regard to $mPGA$ and $mS_a(T_0)$, for different l, show the effectiveness of

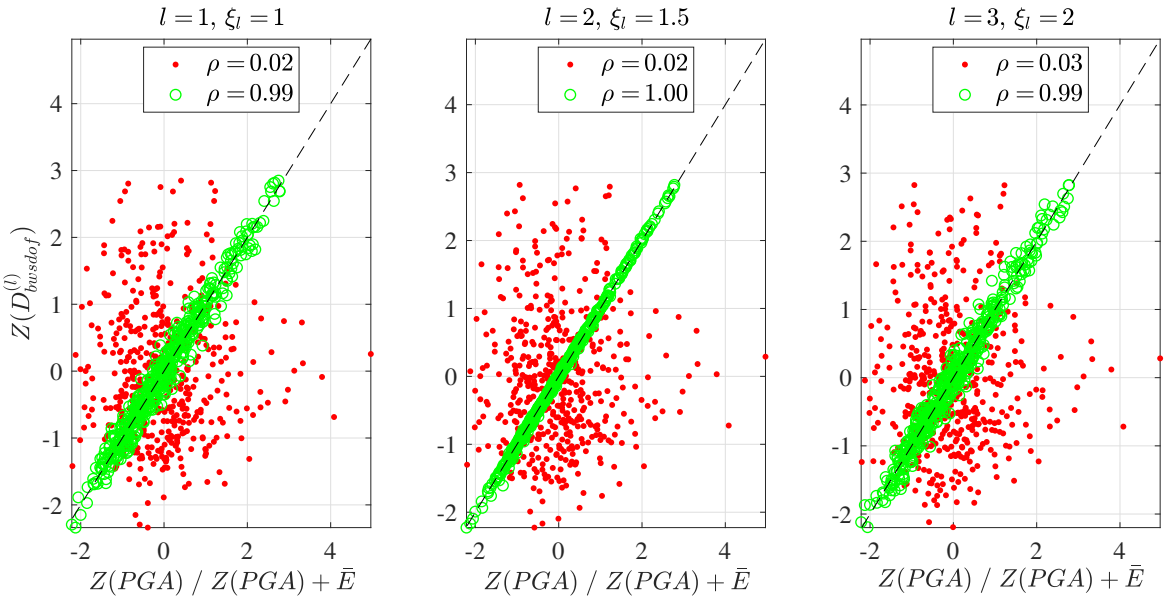

Figure 5.12: Scatter plots of $n_s = 500$ samples of $(Z(PGA), Z(D^{(l)}_{bwsdof}))$ red dots, $(Z(PGA)+\bar{E}, Z(D^{(l)}_{bwsdof}))$ green circles for Bouc-Wen SDOF system with $\omega_0 = 2\pi$, $\zeta = 5\%$, $\eta = 0.9$, $\gamma = 3$, $\alpha = 0.5$, $\beta = 5$ and $n = 1$: $l = 1$ with $\xi_l = 1$ (left panel); $l = 2$ with $\xi_l = 1.5$ (center panel); $l = 3$ with $\xi_l = 2$ (right panel).

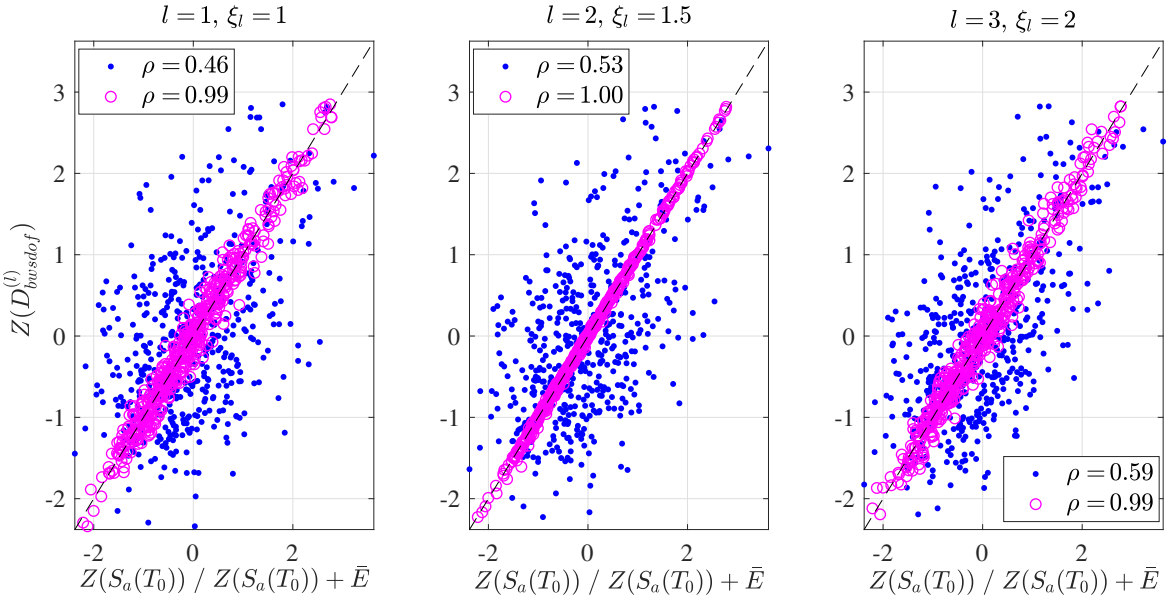

Figure 5.13: Scatter plots of $n_s = 500$ samples of $(Z(S_a(T_0)), Z(D^{(l)}_{bwsdof}))$ blue dots, $(Z(S_a(T_0))+\bar{E}, Z(D^{(l)}_{bwsdof}))$ magenta circles for Bouc-Wen SDOF system with $\omega_0 = 2\pi$, $\zeta = 5\%$, $\eta = 0.9$, $\gamma = 3$, $\alpha = 0.5$, $\beta = 5$ and $n = 1$: $l = 1$ with $\xi_l = 1$ (left panel); $l = 2$ with $\xi_l = 1.5$ (center panel); $l = 3$ with $\xi_l = 2$ (right panel).

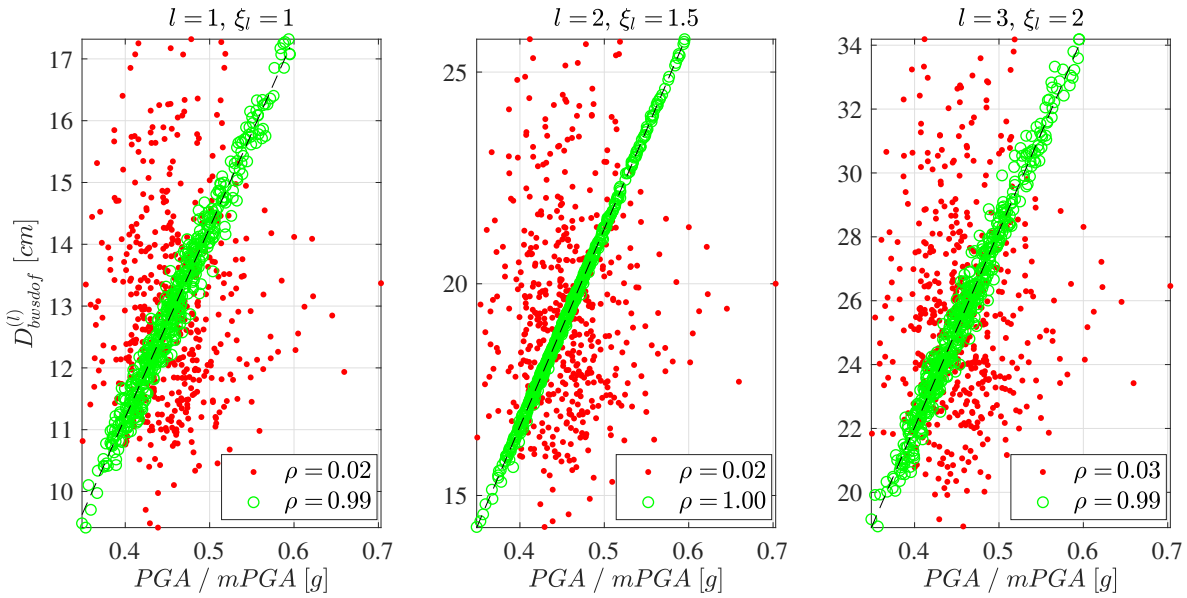

Figure 5.14: Scatter plots of $n_s = 500$ samples of $(PGA, D^{(l)}_{bwsdof})$ red dots, $(mPGA, D^{(l)}_{bwsdof})$ green circles for Bouc-Wen SDOF system with $\omega_0 = 2\pi$, $\zeta = 5\%$, $\eta = 0.9$, $\gamma = 3$, $\alpha = 0.5$, $\beta = 5$ and $n = 1$: $l = 1$ with $\xi_l = 1$ (left panel); $l = 2$ with $\xi_l = 1.5$ (center panel); $l = 3$ with $\xi_l = 2$ (right panel).

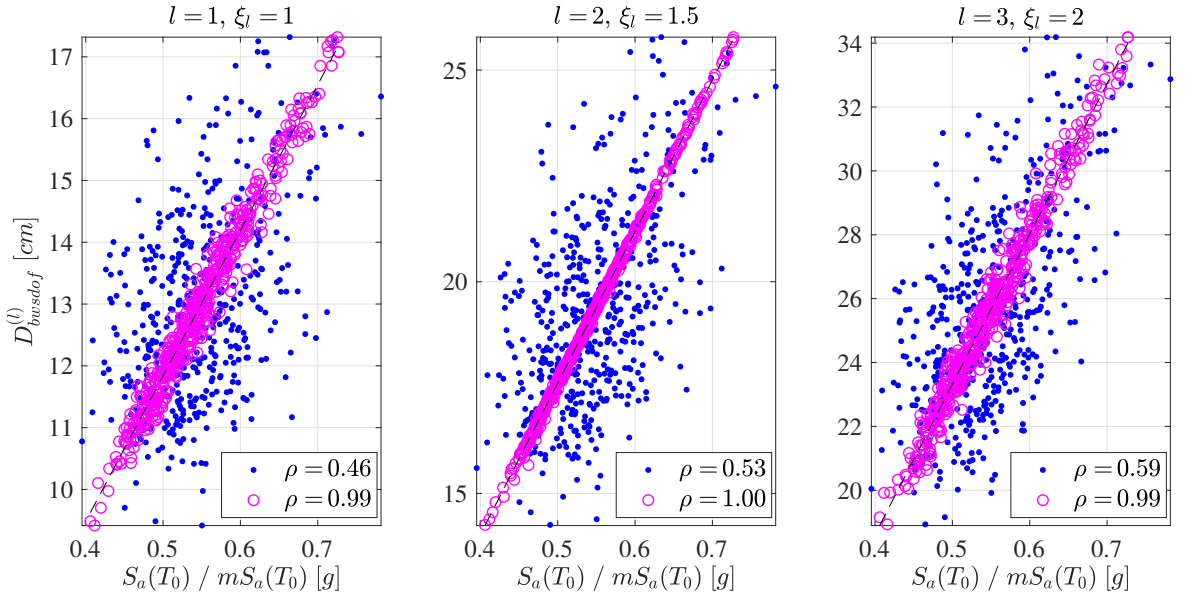

Figure 5.15: Scatter plots of $n_s = 500$ samples of $(S_a(T_0), D^{(l)}_{bwsdof})$ blue dots, $(mS_a(T_0), D^{(l)}_{bwsdof})$ magenta circles for Bouc-Wen SDOF system with $\omega_0 = 2\pi$, $\zeta = 5\%$, $\eta = 0.9$, $\gamma = 3$, $\alpha = 0.5$, $\beta = 5$ and $n = 1$: $l = 1$ with $\xi_l = 1$ (left panel); $l = 2$ with $\xi_l = 1.5$ (center panel); $l = 3$ with $\xi_l = 2$ (right panel).

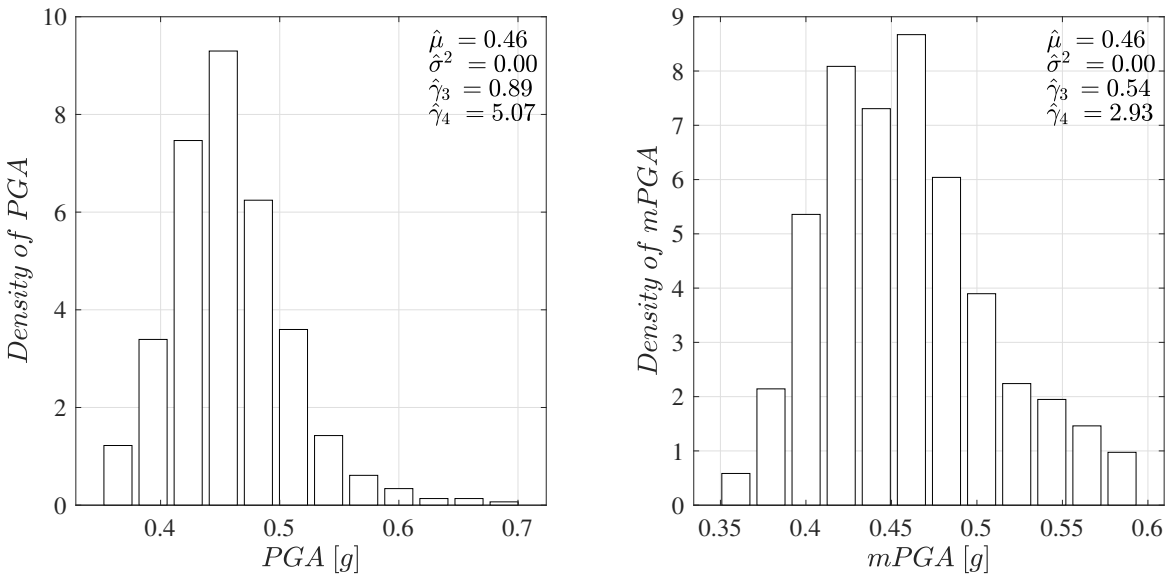

Figure 5.16: Estimated PDF for $n_s = 500$ samples of PGA (left panel) and $mPGA$ (right panel) computed with $m = 1$ and $k = 3$.

the modified intensity measure approach to improve the correlation between Bouc-Wen demand parameter and intensity measures. After the definition of mIM_q, $q = 1, 2$, the correlation coefficient is practically unitary for each considered l.

For Bouc-Wen SDOF system, again, the linear transformation which are based the samples of mIM (Eq. (4.7)) does not change substantially the probability density function estimation of intensity measure. Figure 5.16 and 5.17 report the comparison for PDFs and the first four statical moments estimations between before, IM_q, $q = 1, 2$ (left panels), and after the dependence improvement, mIM_q (right panels). Figure 5.16 refers to PGA and $mPGA$, while Figure 5.17 to $S_a(T_0)$ and $mS_a(T_0)$. In particular, both the mean and variance of the PDF of IM_q and mIM_q, $q = 1, 2$, are the same.

5.3.2 Fragility analysis

Results of the fragility analysis, i.e. fragilities obtained from procedure in Section 3.6 considering original IMs and its $mIMs$, about the Bouc-Wen oscillator are shown

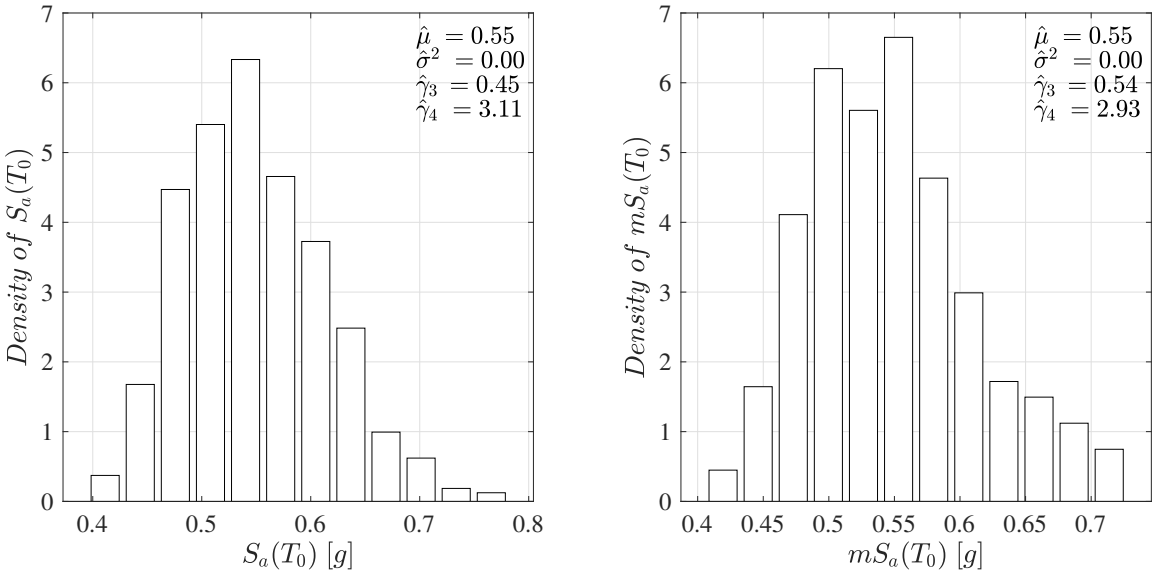

Figure 5.17: Estimated PDF for $n_s = 500$ samples of $S_a(T_0)$ (left panel) and $mS_a(T_0)$ (right panel) computed with $m = 1$ and $k = 3$.

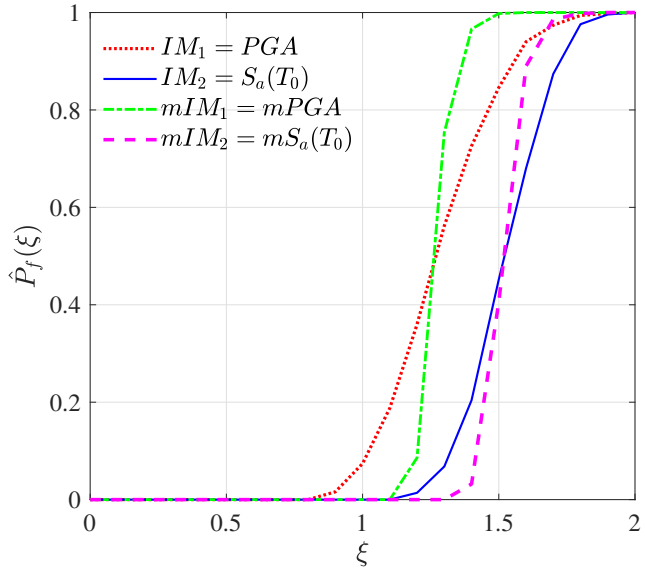

Figure 5.18: Fragilities against intensity level ξ for different definitions of IMs and its modified version $mIMs$ for Bouc-Wen SDOF system with $\omega_0 = 2\pi$, $\zeta = 5\%$, $\eta = 0.9$, $\gamma = 3$, $\alpha = 0.5$, $\beta = 5$, $n = 1$ and limit state $\bar{D}_{bwsdof} = 35\,cm$.

in this subsection. The dependence improvement for $D^{(l)}_{bwsdof}$, $l = 1, 2, 3$, and mIM_q, $q = 1, 2$, (Subsection 5.3.1) will be determine an accuracy improvement in fragility estimates too.

Figure 5.18 shows fragility functions for Bouc-Wen SDOF system to $n_s = 500$ samples of spectra-compatible stochastic process for $\omega_0 = 2\pi$, $\zeta = 5\%$, $\eta = 0.9$, $\gamma = 3$, $\alpha = 0.5$, $\beta = 5$, $n = 1$ and limit state $\bar{D}_{bwsdof} = 35\,cm$. In this figure, the dotted red, dash-dotted green, continuous blue and dashed magenta curve refer to PGA, $mPGA$, $S_a(T_0)$ and $mS_a(T_0)$, respectively. From IM_q, $q = 1, 2$, to mIM_q, the produced fragility functions describe a more accurate results for the fragility analysis.

5.4 Three-storey plane frame

As example of a MDOF structural system, consider a three-storey plane frame with transverse elements. The numerical model is developed with standard beam elements to obtain the reinforced concrete frame. Constraints are applied on numerical model in order to have only a DOF at each storey in horizontal direction, i.e. three degree of freedom.

Both, linear and nonlinear dynamic analysis are performed to obtain the structural response process $\boldsymbol{X}(t)$ to spectra-compatible stochastic process $A(t)$. Standard transverse elements are used for the bracing system in the linear analyses, while nonlinear link elements are used to model the dissipative transverses by using the model in [25]. In this last case, the FNA (see in Subsection 2.3.4) is used to evaluate efficiently the response since the model has a limited number of nonlinear elements, only given by the bracing system at each storey.

Table 5.1 and Figure 5.19 report the three mode shapes and modal parameters

Table 5.1: FE model modal parameters of three-storey plane frame.

Modal shape #	**Period** $[s]$	**Frequency** $[Hz]$	**Pulsation** $[rad/s]$
1	0.352	2.844	17.871
2	0.126	7.953	49.971
3	0.087	11.462	72.017

of the FE model. Samples of $\boldsymbol{X}(t)$ are computed by linear/nonlinear time domain

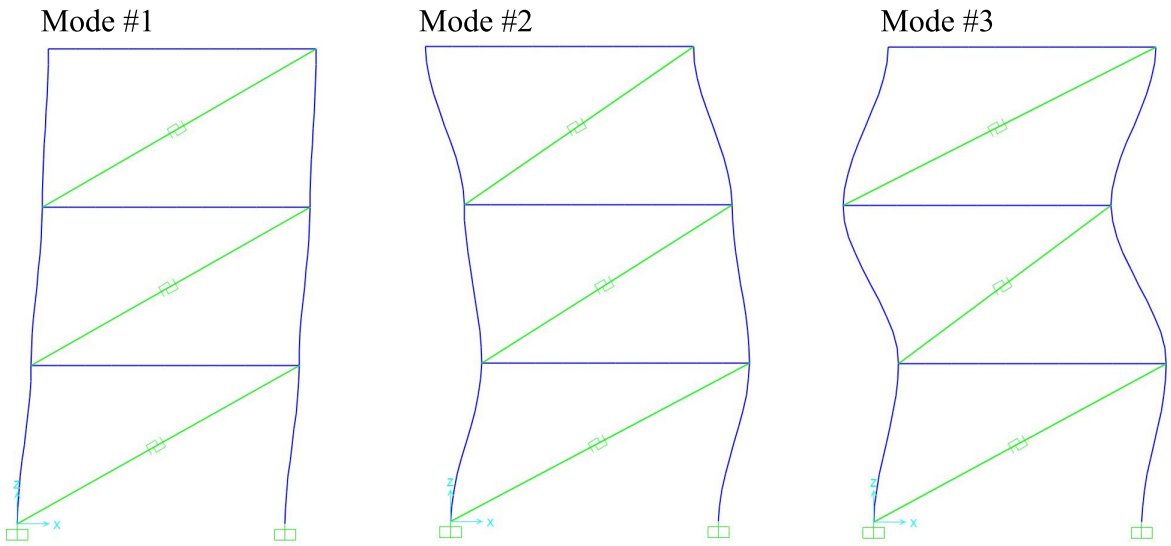

Figure 5.19: FE model mode shapes of three-storey plane frame.

numerical dynamic structural analysis assuming proportional damping ratio $\zeta = 5\%$ in order to define

$$D_d^{(j)} = \max_{0 \leqslant t \leqslant \tau} |h^{(j)}(\boldsymbol{X}(t))|, \quad j = 1, \ldots, m \tag{5.3}$$

i.e. the maximum absolute displacement at the j-th storey. Where τ is the time length of $A(t)$ and $h^{(j)}(\cdot)$ is a function that mapping the response $\boldsymbol{X}(t)$ to the j-th demand parameter of interest. Since the system has three DOFs, the Equation (5.3) is applied for $m = 3$. For nonlinear dynamic analysis, the (5.3) is used to define, considering different input level intensity number l and corresponding level coefficient ξ_l, i.e. $A^{(l)}(t) = \xi_l A(t)$, the demand parameter at each storey $D_d^{(j,l)}$ to investigate the dependence with IMs at prefixed l. Dependence between system demand parameters

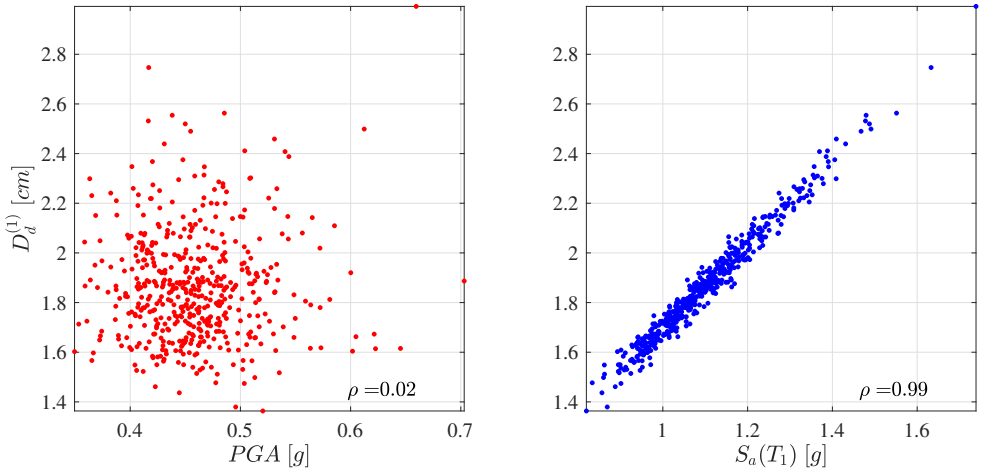

Figure 5.20: Scatter plots of $n_s = 500$ samples for three-storey plane frame: $(PGA, D_d^{(1)})$ (left panel); $(S_a(T_1), D_d^{(1)})$ (right panel) - linear analysis.

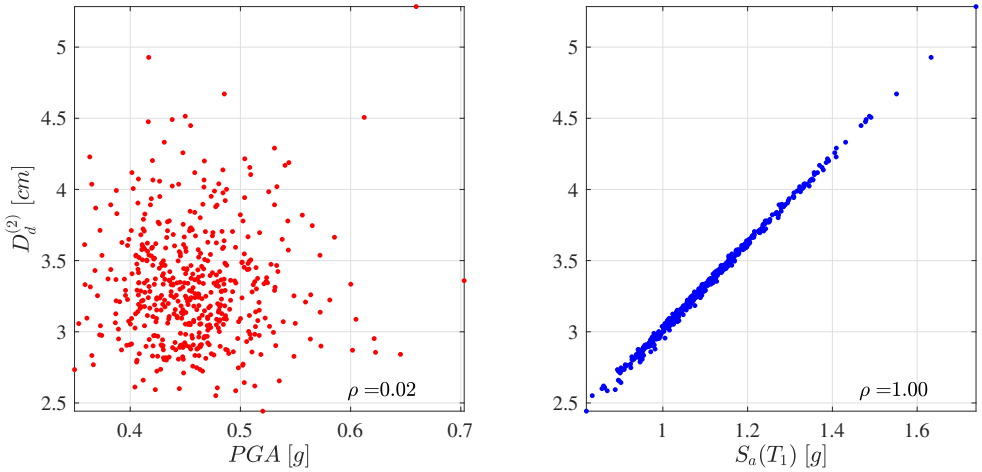

Figure 5.21: Scatter plots of $n_s = 500$ samples for three-storey plane frame: $(PGA, D_d^{(2)})$ (left panel); $(S_a(T_1), D_d^{(2)})$ (right panel) - linear analysis.

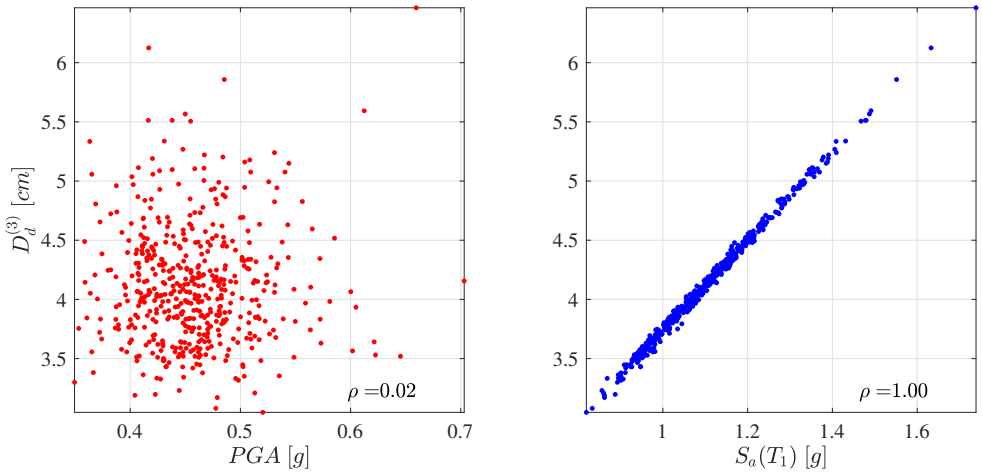

Figure 5.22: Scatter plots of $n_s = 500$ samples for three-storey plane frame: $(PGA, D_d^{(3)})$ (left panel); $(S_a(T_1), D_d^{(3)})$ (right panel) - linear analysis.

and IMs for linear analysis and different l does not change. Then, in the last case the $D_d^{(j)}$ is only computed for unmultiplied input, i.e. $A(t) = A^{(l=1)}(t)$, the apex l is omitted.

For each samples of $A(t)$, the PGA and the pseudo-acceleration response spectra $S_a(T, \zeta)$, with $\zeta = 5\%$, are computed to study the dispersion on $D_d^{(j)}$ or $D_d^{(j,l)}$, $j, l = 1, 2, 3$. Then, the intensity measures in Equation (3.12) and (3.13) are considered to investigate the dependence.

Figures 5.20 - 5.22 show scatter plots of $n_s = 500$ samples of the demand parameters $D_d^{(j)}$, $j = 1, 2, 3$, and the selected IMs for linear dynamic analysis. The left panels regard to IM_1, while the those on right to IM_2. Concerning these results, the PGA produces high dispersion on $D_d^{(j)}$, $j = 1, 2, 3$, i.e. for linear simple MDOF system the Eq. (3.12) is not efficient intensity measure. Contrarily, the dependence between $S_a(T_1)$ and $D_d^{(j)}$, $j = 1, 2, 3$, is strong since the correlation coefficient ρ is practically one (right panel of Figures 5.20 - 5.22).

For nonlinear analysis, scatter plots of $n_s = 500$ samples of the demand parameters $D_d^{(j,l)}$, $j, l = 1, 2, 3$, and IM_q, $q = 1, 2$, are developed and shown in Figures 5.23 - 5.28 . In each panel of these figures, on the top l and corresponding ξ_l value are reported, while on right bottom, it is shown ρ. From left to right panels, the level intensity of input, $A^{(l)}(t)$, increasing. Figures 5.23 - 5.25 and Figures 5.26 - 5.28 refer to PGA and $S_a(T_1)$, respectively. In general, the nonlinear behaviour assumption for MDOF system, i.e. presence of concentrated nonlinearities, changes completely the obtained correlation between the demand parameters and IMs in the linear case. Correlation decreases for the increasing value of l and ξ_l.

Although it would seem that $IM_1 = PGA$ decreases dispersion on $D_d^{(j,l)}$, $j, l = 1, 2, 3$, if it is compared with the results by linear dynamic analysis, anyway the pro-

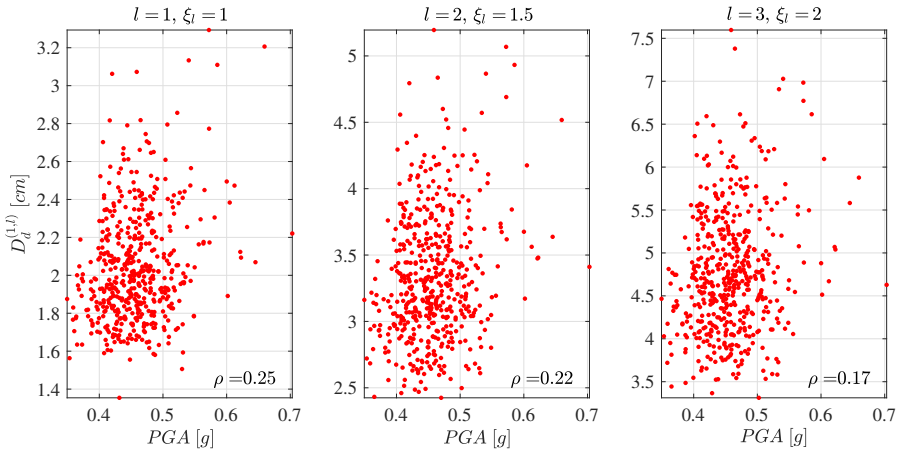

Figure 5.23: Scatter plots of $n_s = 500$ samples for three-storey plane frame $(PGA, D_d^{(1,l)})$: $l = 1$ with $\xi_l = 1$ (left panel); $l = 2$ with $\xi_l = 1.5$ (center panel); $l = 3$ with $\xi_l = 2$ (right panel) - nonlinear analysis.

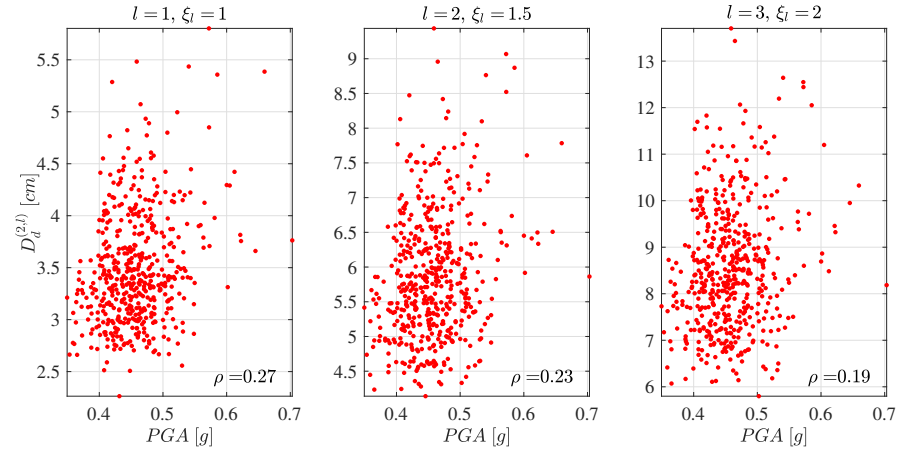

Figure 5.24: Scatter plots of $n_s = 500$ samples for three-storey plane frame $(PGA, D_d^{(2,l)})$: $l = 1$ with $\xi_l = 1$ (left panel); $l = 2$ with $\xi_l = 1.5$ (center panel); $l = 3$ with $\xi_l = 2$ (right panel) - nonlinear analysis.

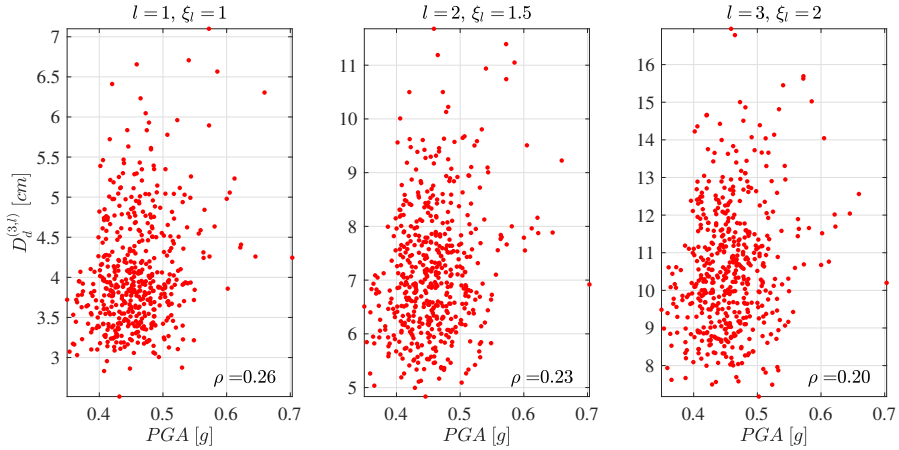

Figure 5.25: Scatter plots of $n_s = 500$ samples for three-storey plane frame $(PGA, D_d^{(3,l)})$: $l = 1$ with $\xi_l = 1$ (left panel); $l = 2$ with $\xi_l = 1.5$ (center panel); $l = 3$ with $\xi_l = 2$ (right panel) - nonlinear analysis.

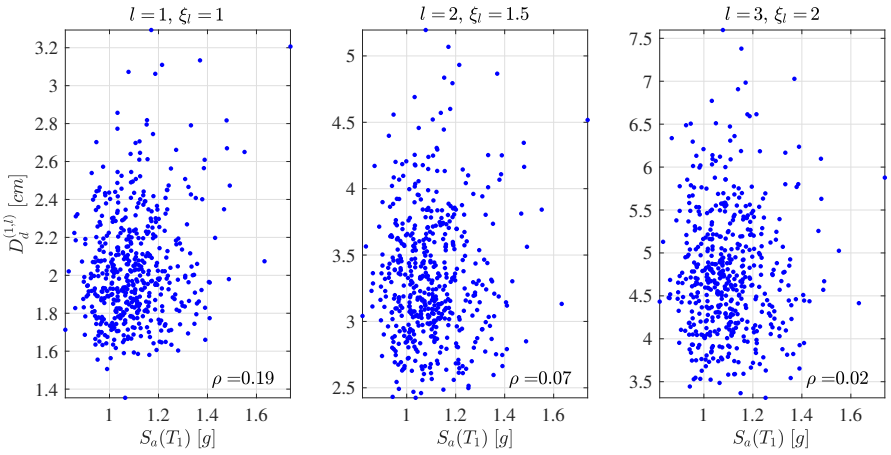

Figure 5.26: Scatter plots of $n_s = 500$ samples for three-storey plane frame $(S_a(T_1), D_d^{(1,l)})$: $l = 1$ with $\xi_l = 1$ (left panel); $l = 2$ with $\xi_l = 1.5$ (center panel); $l = 3$ with $\xi_l = 2$ (right panel) - nonlinear analysis.

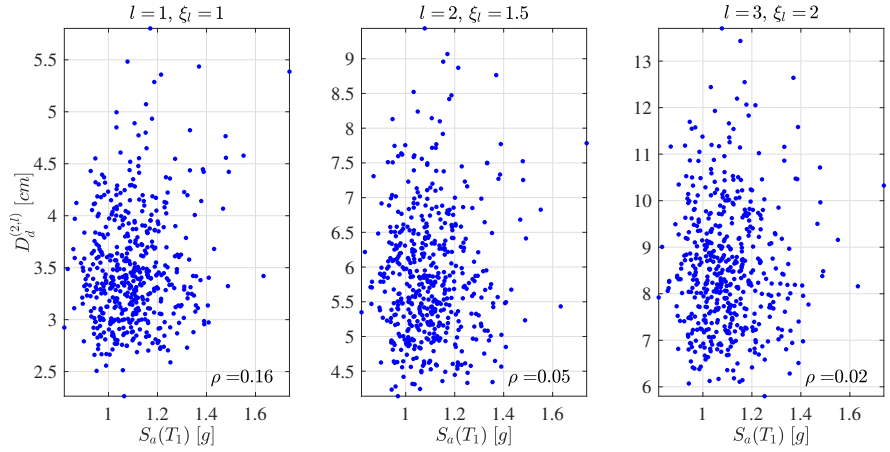

Figure 5.27: Scatter plots of $n_s = 500$ samples for three-storey plane frame $(S_a(T_1), D_d^{(2,l)})$: $l = 1$ with $\xi_l = 1$ (left panel); $l = 2$ with $\xi_l = 1.5$ (center panel); $l = 3$ with $\xi_l = 2$ (right panel) - nonlinear analysis.

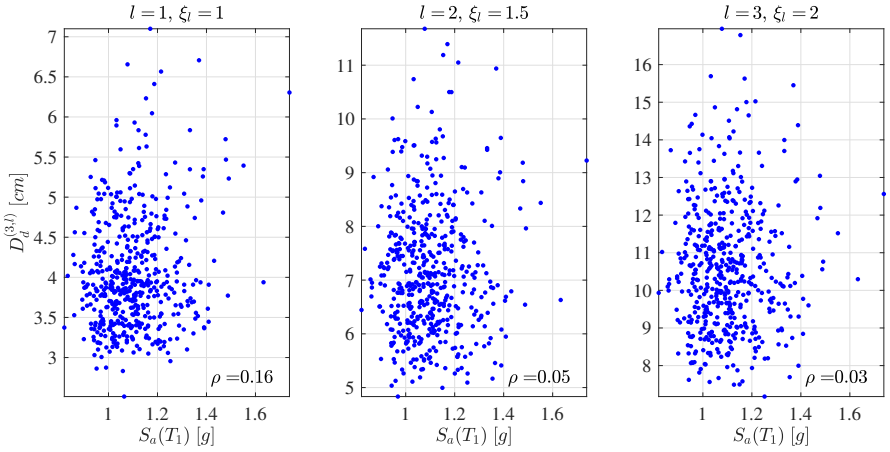

Figure 5.28: Scatter plots of $n_s = 500$ samples for three-storey plane frame $(S_a(T_1), D_d^{(3,l)})$: $l = 1$ with $\xi_l = 1$ (left panel); $l = 2$ with $\xi_l = 1.5$ (center panel); $l = 3$ with $\xi_l = 2$ (right panel) - nonlinear analysis.

vided dependence is weak (Figures 5.23 - 5.25). In any case, the stochastic variables $D_d^{(j,l)}|S_a(T_1)$, $j,l = 1,2,3$, have large variance (see Figures 5.26 - 5.28), and this aspect suggests that $IM_2 = S_a(T_1)$ is not a efficient intensity measure for simple nonlinear MDOF structural system.

5.4.1 Dependence improvement

The modified intensity measure strategy is applied to decrease the dispersion of the selected IMs on the demand parameters of the linear/nonlinear MDOF structural system. Two different behaviours for the three-storey plane frame and the selected intensity measures are taken into account for the application of five-steps algorithm, described in Section 4.4, considering the following:

- linear behaviour, the methodology is applied considering as demand parameter $D_d^{(j)}$, for $j = 1,\ldots,m$ with $m = 3$, and the intensity measure in Equation (3.12);
- nonlinear behaviour, the methodology is applied considering as demand parameter $D_d^{(j,l)}$, for $j = 1,\ldots,m$ and $l = 1,\ldots,k$ with $m,k = 3$, and the intensity measures in Equations (3.12) and (3.13).

In both cases, the dependence between the demand parameters and the selected IMs are improved using the modified intensity measure approach.

Since the (3.13) is an efficient intensity measure for linear analysis (right panel of Figures 5.20 - 5.22), the dependence (correlation) improvement is not necessary.

Samples of the demand parameters and the considered IMs are first transformed into their standardized versions using Equations (4.3) and (4.4) and the distance from perfect correlation is evaluated by Equation (4.5). The n_s average distances using Eq. (4.6) are collected in the vector $\bar{E}$ which is used to correct the standardized samples of PGA or $S_a(T_1)$, i.e. $z(PGA)$ or $z(S_a(T_1))$, in order to compute samples of the modified intensity measure $mPGA$ or $mS_a(T_1)$, respectively, by Equation (4.7).

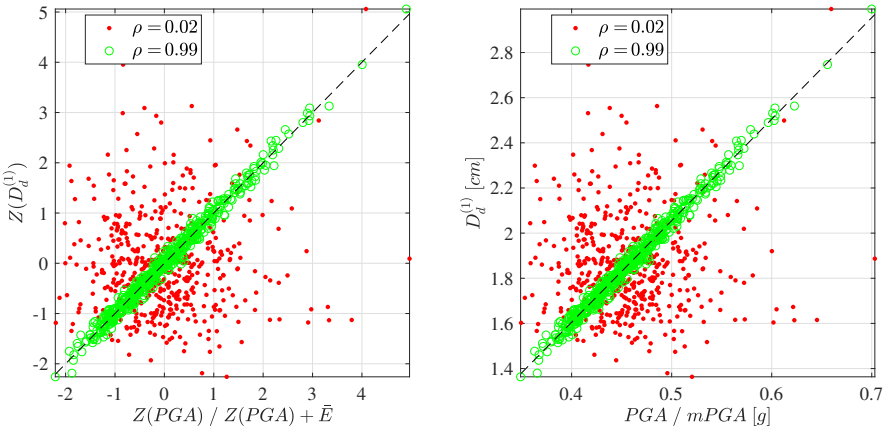

Figure 5.29: Scatter plots of $n_s = 500$ samples for three-storey plane frame: $(Z(PGA), Z(D_d^{(1)}))$ red dots, $(Z(PGA) + \bar{E}, Z(D_d^{(1)}))$ green circles (left panel); $(PGA, D_d^{(1)})$ red dots, $(mPGA, D_d^{(1)})$ green circles (right panel) - linear analysis.

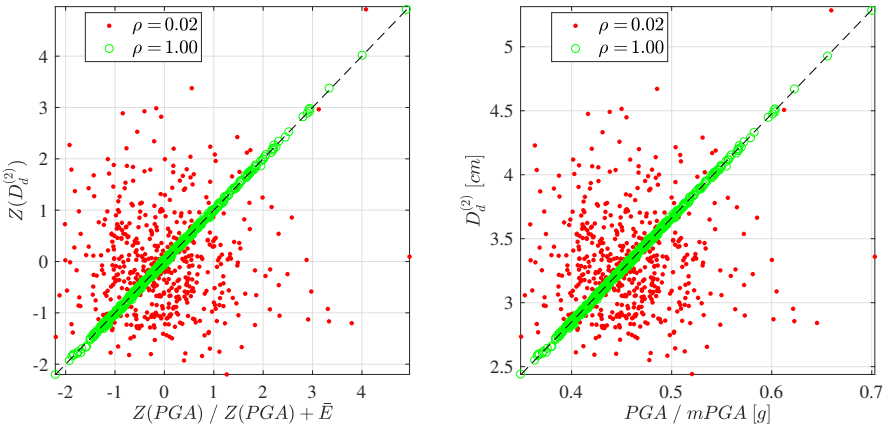

Figure 5.30: Scatter plots of $n_s = 500$ samples for three-storey plane frame: $(Z(PGA), Z(D_d^{(2)}))$ red dots, $(Z(PGA) + \bar{E}, Z(D_d^{(2)}))$ green circles (left panel); $(PGA, D_d^{(2)})$ red dots, $(mPGA, D_d^{(2)})$ green circles (right panel) - linear analysis.

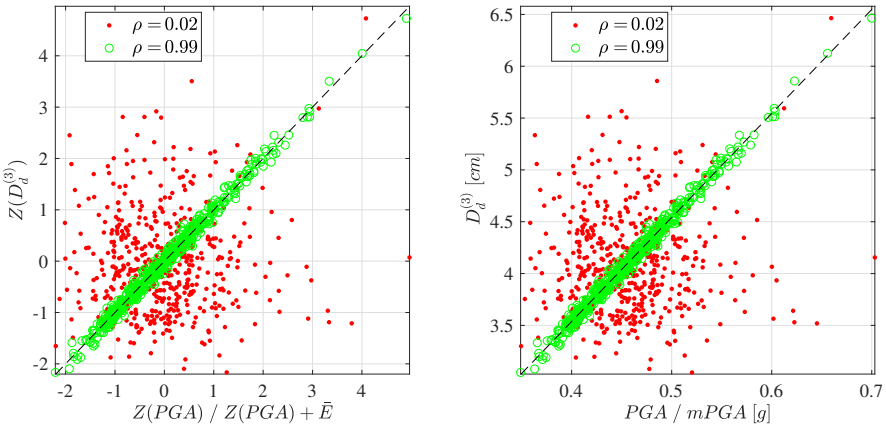

Figure 5.31: Scatter plots of $n_s = 500$ samples for three-storey plane frame: $(Z(PGA), Z(D_d^{(3)}))$ red dots, $(Z(PGA) + \bar{E}, Z(D_d^{(3)}))$ green circles (left panel); $(PGA, D_d^{(3)})$ red dots, $(mPGA, D_d^{(3)})$ green circles (right panel) - linear analysis.

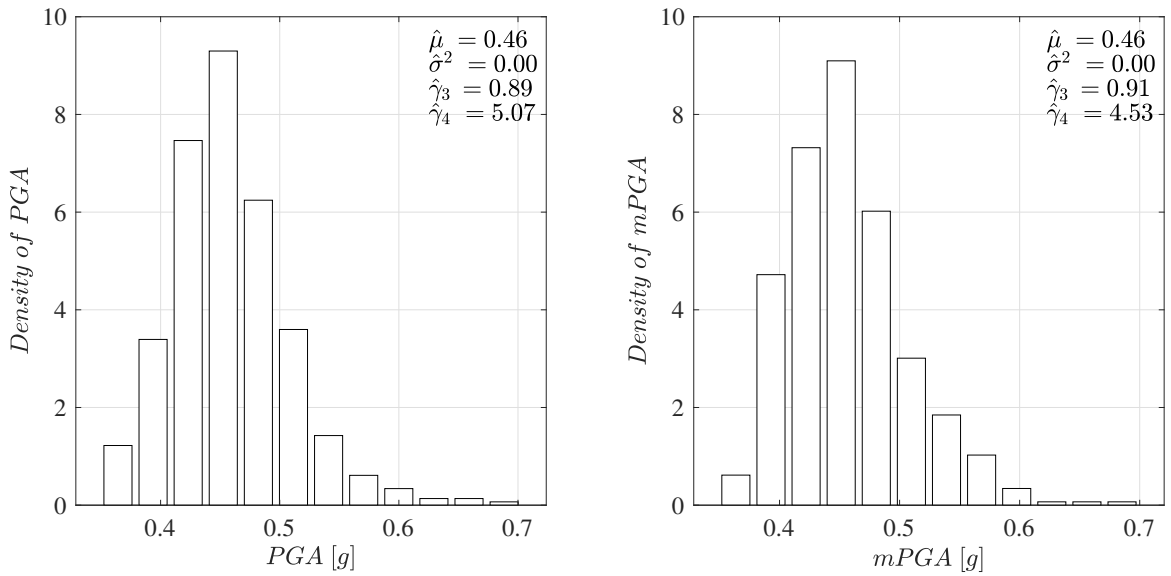

Figure 5.32: Estimated PDF for $n_s = 500$ samples of PGA (left panel) and $mPGA$ (right panel) computed with $m = 3$ and $k = 1$.

Firstly, the obtained results for the linear behaviour are shown. Figures 5.29 - 5.31 report scatter plots of $n_s = 500$ samples resulting from the demand parameters $D_d^{(j)}$, $j = 1, 2, 3$, and PGA for linear dynamic analysis. Left panels refer to the standardized space in which the random variables dispersion are represented, while the those on the right regard to normal space. In general, for each panel the changes in color from red $((Z(PGA), Z(D_d^{(j)}))$ or $(PGA, D_d^{(j)}))$ to green $((Z(PGA) + \bar{E}, Z(D_d^{(j)}))$ or $(mPGA, D_d^{(j)}))$ describe the correlation improvement in order to produce low variance for the conditional stochastic variables.

Figure 5.32 shows the normalized histogram (estimated PDF) and the first four statical moments from samples of the original intensity measures $IM_1 = PGA$ (left panel) and its modified version $mIM_1 = mPGA$ (right panel). Comparing the two probability distribution estimates, it is not shown significantly change.

The results are now shown by considering the system response process assuming

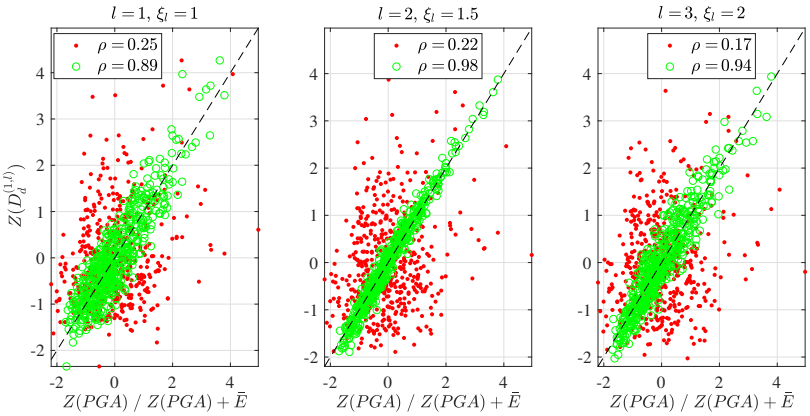

Figure 5.33: Scatter plots of $n_s = 500$ samples for three-storey plane frame, $(Z(PGA), Z(D_d^{(1,l)}))$ red dots, $(Z(PGA)+\bar{E}, Z(D_d^{(1,l)}))$ green circles: $l=1$ with $\xi_l = 1$ (left); $l=2$ with $\xi_l = 1.5$ (center); $l=3$ with $\xi_l = 2$ (right) - nonlinear analysis.

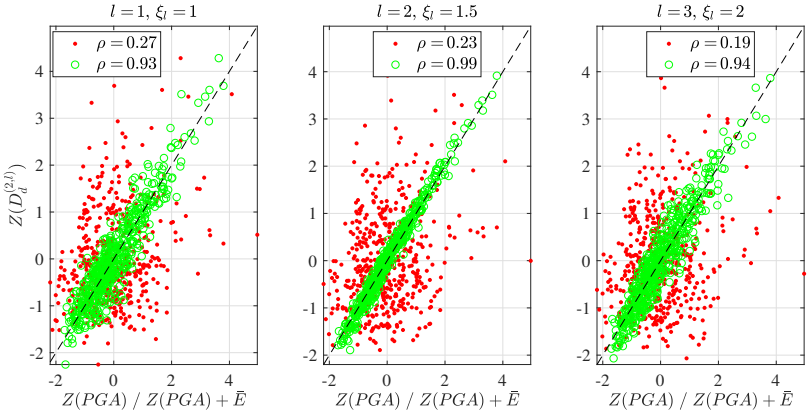

Figure 5.34: Scatter plots of $n_s = 500$ samples for three-storey plane frame, $(Z(PGA), Z(D_d^{(2,l)}))$ red dots, $(Z(PGA)+\bar{E}, Z(D_d^{(2,l)}))$ green circles: $l=1$ with $\xi_l = 1$ (left); $l=2$ with $\xi_l = 1.5$ (center); $l=3$ with $\xi_l = 2$ (right) - nonlinear analysis.

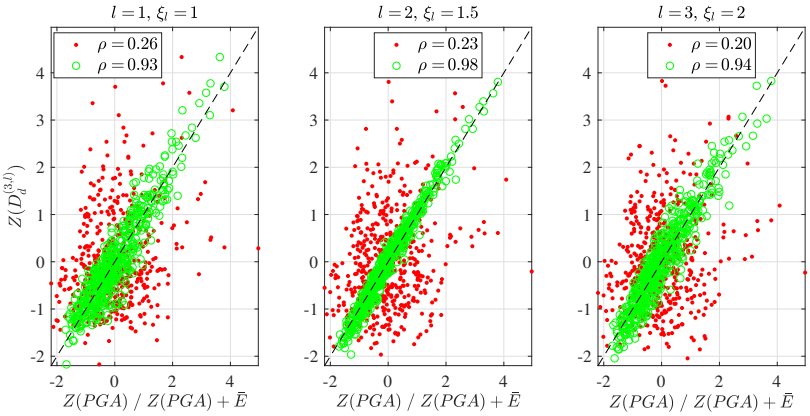

Figure 5.35: Scatter plots of $n_s = 500$ samples for three-storey plane frame, $(Z(PGA), Z(D_d^{(3,l)}))$ red dots, $(Z(PGA)+\bar{E}, Z(D_d^{(3,l)}))$ green circles: $l=1$ with $\xi_l = 1$ (left); $l=2$ with $\xi_l = 1.5$ (center); $l=3$ with $\xi_l = 2$ (right) - nonlinear analysis.

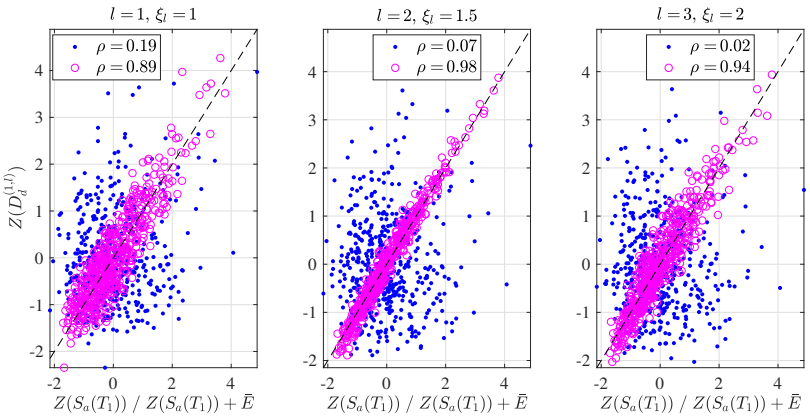

Figure 5.36: Scatter plots of $n_s = 500$ samples for three-storey plane frame, $(Z(S_a(T_1)), Z(D_d^{(1,l)}))$ blue dots, $(Z(S_a(T_1)) + \bar{E}, Z(D_d^{(1,l)}))$ magenta circles: $l = 1$ with $\xi_l = 1$ (left); $l = 2$ with $\xi_l = 1.5$ (center); $l = 3$ with $\xi_l = 2$ (right) - nonlinear analysis.

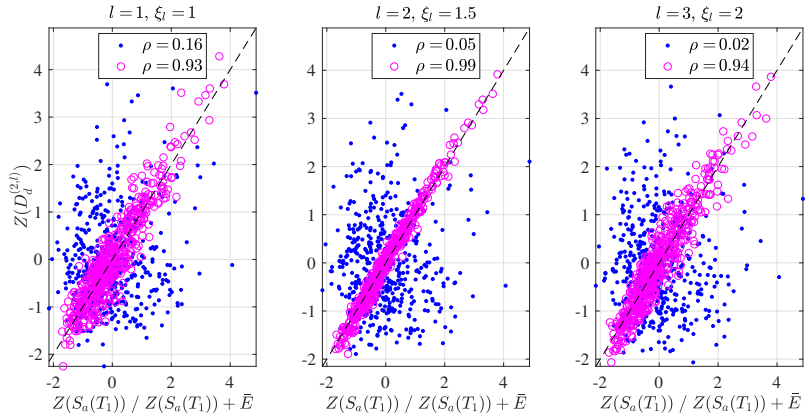

Figure 5.37: Scatter plots of $n_s = 500$ samples for three-storey plane frame, $(Z(S_a(T_1)), Z(D_d^{(2,l)}))$ blue dots, $(Z(S_a(T_1)) + \bar{E}, Z(D_d^{(2,l)}))$ magenta circles: $l = 1$ with $\xi_l = 1$ (left); $l = 2$ with $\xi_l = 1.5$ (center); $l = 3$ with $\xi_l = 2$ (right) - nonlinear analysis.

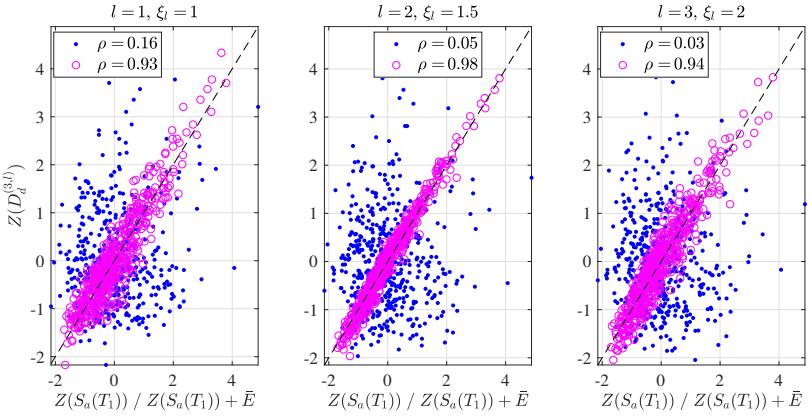

Figure 5.38: Scatter plots of $n_s = 500$ samples for three-storey plane frame, $(Z(S_a(T_1)), Z(D_d^{(3,l)}))$ blue dots, $(Z(S_a(T_1)) + \bar{E}, Z(D_d^{(3,l)}))$ magenta circles: $l = 1$ with $\xi_l = 1$ (left); $l = 2$ with $\xi_l = 1.5$ (center); $l = 3$ with $\xi_l = 2$ (right) - nonlinear analysis.

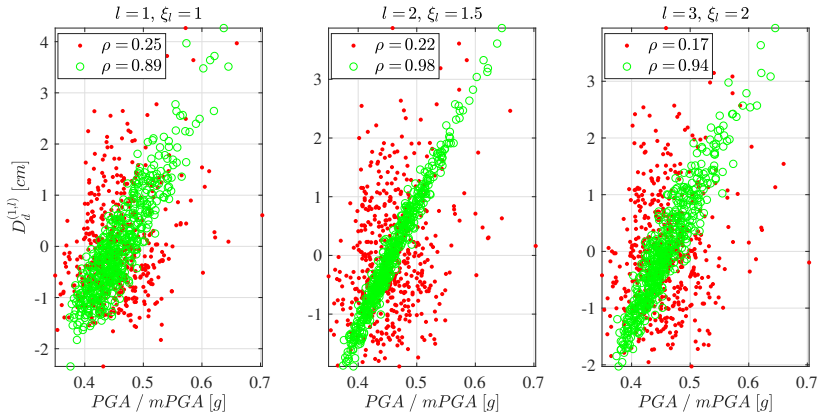

Figure 5.39: Scatter plots of $n_s = 500$ samples for three-storey plane frame, $(PGA, D_d^{(1,l)})$ red dots, $(mPGA, D_d^{(1,l)})$ green circles: $l = 1$ with $\xi_l = 1$ (left); $l = 2$ with $\xi_l = 1.5$ (center); $l = 3$ with $\xi_l = 2$ (right) - nonlinear analysis.

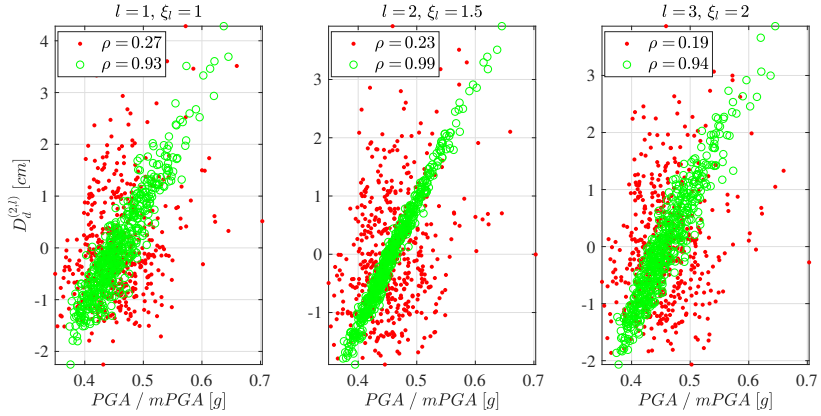

Figure 5.40: Scatter plots of $n_s = 500$ samples for three-storey plane frame, $(PGA, D_d^{(2,l)})$ red dots, $(mPGA, D_d^{(2,l)})$ green circles: $l = 1$ with $\xi_l = 1$ (left); $l = 2$ with $\xi_l = 1.5$ (center); $l = 3$ with $\xi_l = 2$ (right) - nonlinear analysis.

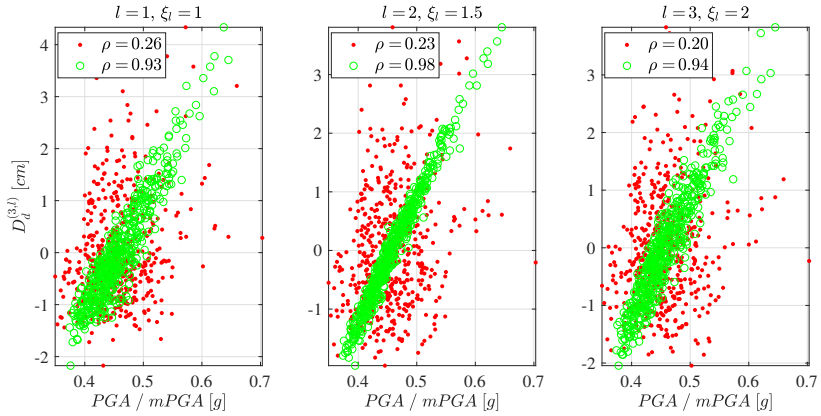

Figure 5.41: Scatter plots of $n_s = 500$ samples for three-storey plane frame, $(PGA, D_d^{(3,l)})$ red dots, $(mPGA, D_d^{(3,l)})$ green circles: $l = 1$ with $\xi_l = 1$ (left); $l = 2$ with $\xi_l = 1.5$ (center); $l = 3$ with $\xi_l = 2$ (right) - nonlinear analysis.

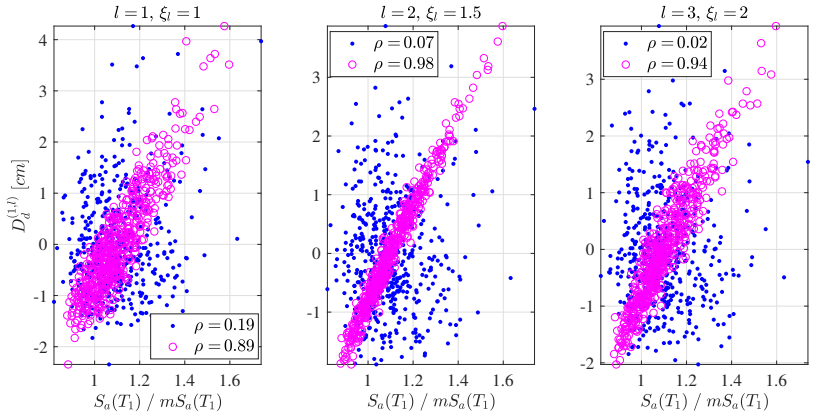

Figure 5.42: Scatter plots of $n_s = 500$ samples for three-storey plane frame, $(S_a(T_1), D_d^{(1,l)})$ blue dots, $(mS_a(T_1), D_d^{(1,l)})$ magenta circles: $l = 1$ with $\xi_l = 1$ (left); $l = 2$ with $\xi_l = 1.5$ (center); $l = 3$ with $\xi_l = 2$ (right) - nonlinear analysis.

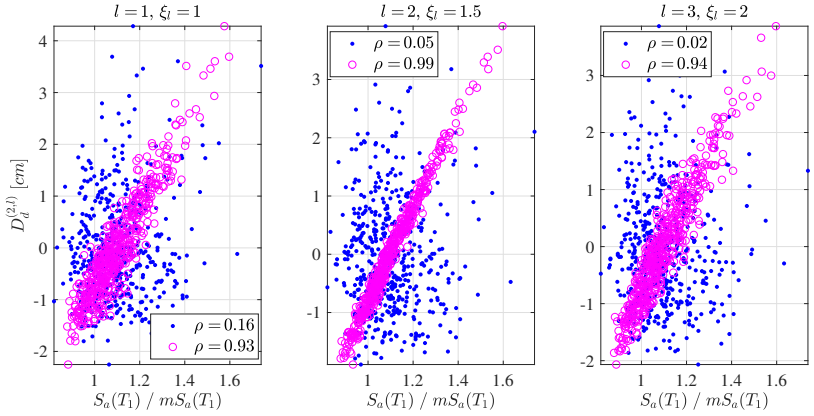

Figure 5.43: Scatter plots of $n_s = 500$ samples for three-storey plane frame, $(S_a(T_1), D_d^{(2,l)})$ blue dots, $(mS_a(T_1), D_d^{(2,l)})$ magenta circles: $l = 1$ with $\xi_l = 1$ (left); $l = 2$ with $\xi_l = 1.5$ (center); $l = 3$ with $\xi_l = 2$ (right) - nonlinear analysis.

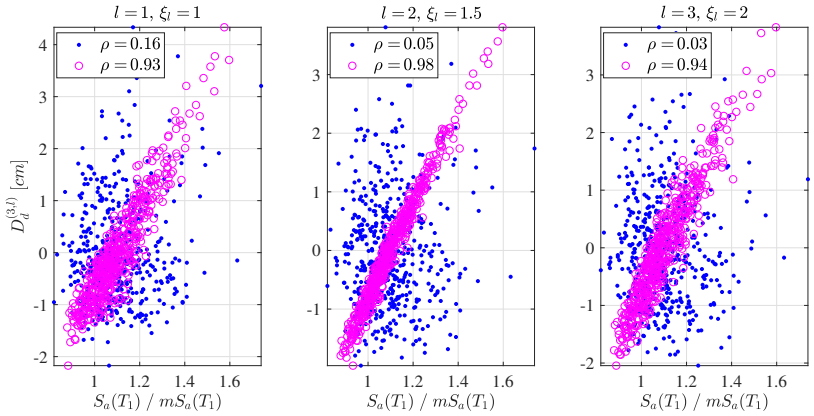

Figure 5.44: Scatter plots of $n_s = 500$ samples for three-storey plane frame, $(S_a(T_1), D_d^{(3,l)})$ blue dots, $(mS_a(T_1), D_d^{(3,l)})$ magenta circles: $l = 1$ with $\xi_l = 1$ (left); $l = 2$ with $\xi_l = 1.5$ (center); $l = 3$ with $\xi_l = 2$ (right) - nonlinear analysis.

nonlinear behaviour. Scatter plots of $n_s = 500$ samples in standardized representation regard to $IM_1 = PGA$ and $IM_2 = S_a(T_1)$ are reported in Figures 5.33 - 5.35 and Figures 5.36 - 5.38 , respectively. The dispersion of $(Z(IM_q), Z(D_d^{(j,l)}))$ and $(Z(IM_q) + \bar{E}, Z(D_d^{(j,l)}))$, $q = 1, 2$ and $j, l = 1, \ldots, 3$, are shown. While, the results back into the normal space representation, i.e. $(IM_q, D_d^{(j,l)})$ and $(mIM_q, D_d^{(j,l)})$, $q = 1, 2$ and $j, l = 1, \ldots, 3$, are shown in Figures 5.39 - 5.44 . In particular, Figures 5.39 - 5.41 and Figures 5.42 - 5.44 regard to PGA and $S_a(T_1)$, respectively.

Generalizing, for each of these figures (Figures 5.33 - 5.44), from left to right panels the level intensity of input process, i.e. l and associated ξ_l, increases.

For this case, the modified intensity measure approach is used for IM_q, $q = 1, 2$, and $m, k = 3$ and, it shows good results since ρ tends to be unitary in standardized and normal space after the correction in correlation, see green and magenta circles in Figures 5.33 - 5.44 .

Figure 5.45 and 5.46 report the probability density function estimates and the associated first four statical moments before (left panels), i.e IM_q, $q = 1, 2$, and after the correlation improvement (right panels), mIM_q, $q = 1, 2$. In particular, Figure 5.33 refers to PGA and its modified version $mPGA$, instead Figure 5.46 to $S_a(T_1)$ and $mS_a(T_1)$. It is possible to see how the modified intensity measure PDFs not change substantially in reference to the those of original IMs.

5.4.2 Fragility analysis

In this present subsection, the fragility analysis results obtained using the procedure in Section 3.6 with original and modified intensity measures for the case of the three-storey plane frame with both linear and nonlinear behaviour are presented.

Previous definitions of mIM_q, $q = 1, 2$, (Subsection 5.4.1) allow to decrease the dispersion on the system demand parameters (efficient IMs), and consequently the

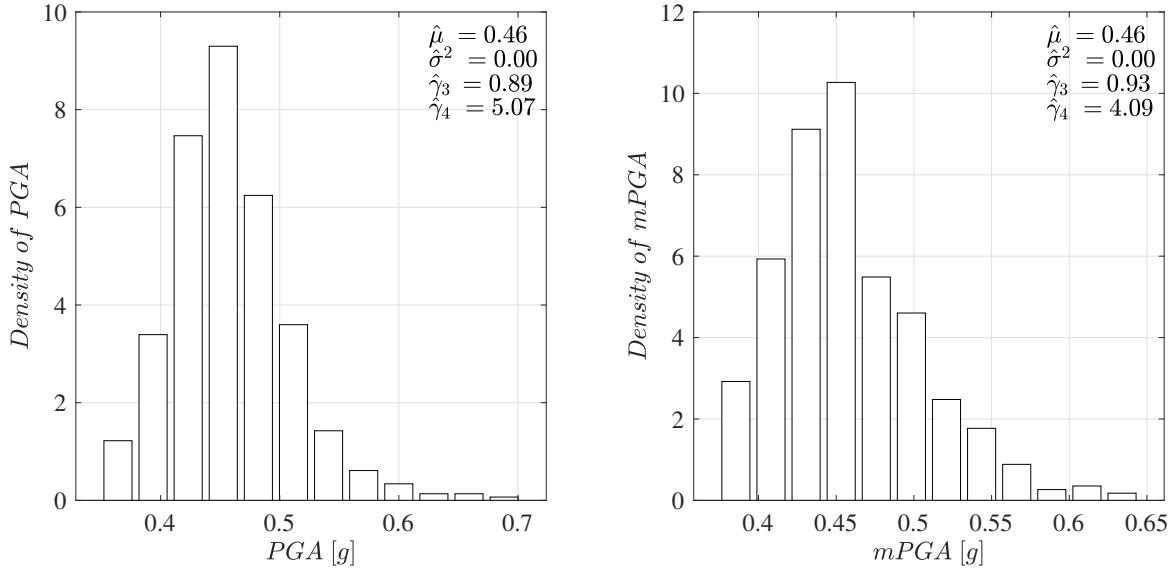

Figure 5.45: Estimated PDF for $n_s = 500$ samples of PGA (left panel) and $mPGA$ (right panel) computed with $m = 3$ and $k = 3$.

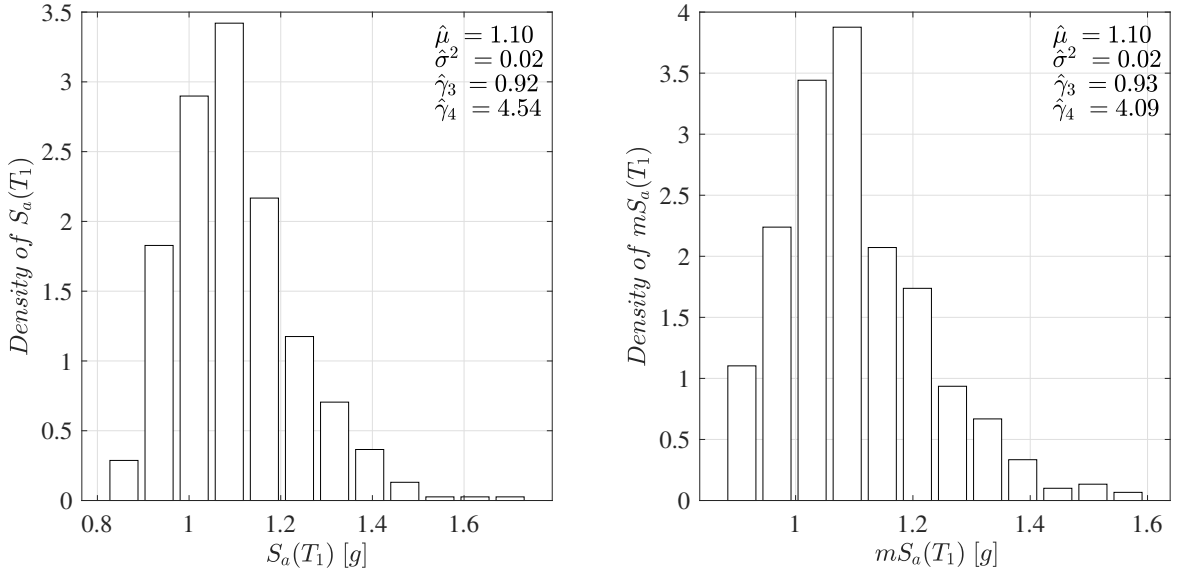

Figure 5.46: Estimated PDF for $n_s = 500$ samples of $S_a(T_1)$ (left panel) and $mS_a(T_1)$ (right panel) computed with $m = 3$ and $k = 3$.

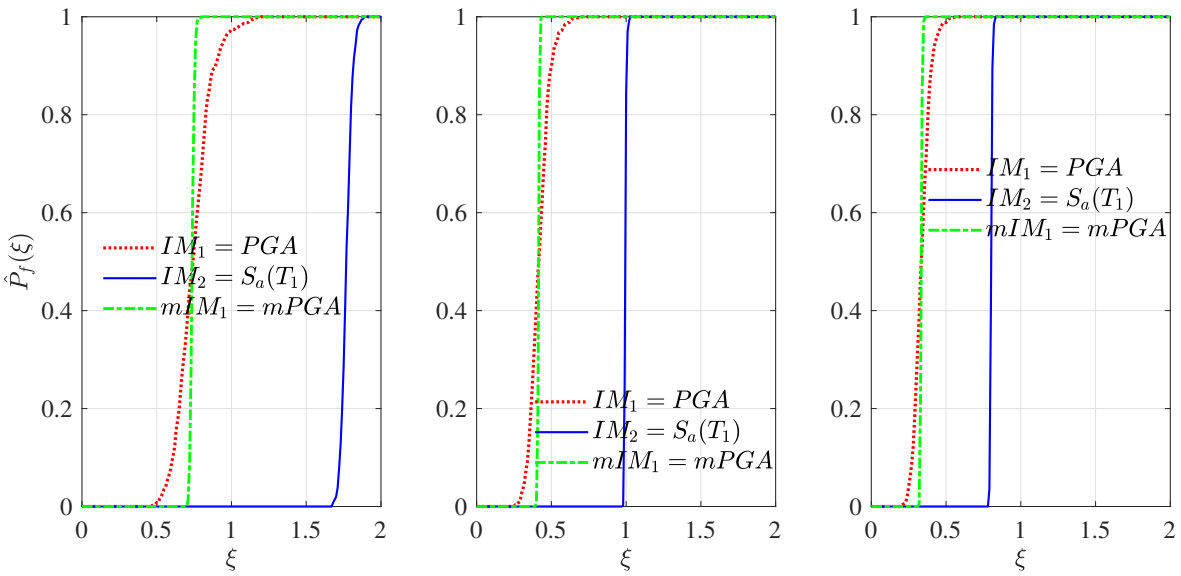

Figure 5.47: Fragilities against intensity level ξ for different definitions of IMs and its modified version $mIMs$ for three-storey plane frame assuming limit state $\bar{D}_d^{(j)} = 3\,cm$, $j = 1, \ldots, 3$, and considering: #1 storey (left); #2 storey (center); #3 storey (right) - linear analysis.

development of more accurate fragilities respect to those obtained by original intensity measures are evaluated. This aspect is clear considering the less variance which have the conditional random variables demand parameter given $mIMs$ for linear/nonlinear system behaviour. Figure 5.47 reports fragility curves by $n_s = 500$ samples of spectra-compatible stochastic process $A(t)$ considering the demand parameter at #1 storey $D_d^{(1)}$ (left panel), at #2 storey $D_d^{(2)}$ (center) and at #3 storey $D_d^{(3)}$ (right), for linear analysis. Limit states for each storey $\bar{D}_d^{(j)} = 3\,cm$, $j = 1, \ldots, 3$, are considered. Dotted red, dash-dotted green and continuous blue curve regards to PGA, $mPGA$ and $S_a(T_1)$, respectively.

Fragility function for modified version of $S_a(T_1)$ is not developed since the original one, i.e. Eq. (3.13), does not require the dependence improvement. Instead this aspect it is necessary for the fragility analysis for nonlinear behaviour of system.

Figures 5.48 - 5.50 show results for the fragility analysis obtained by considering

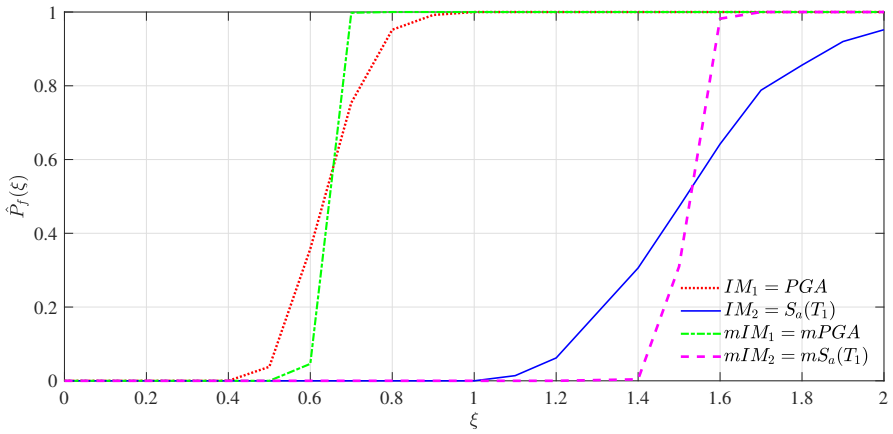

Figure 5.48: Fragilities against intensity level ξ for different definitions of IMs and its modified version $mIMs$ for three-storey plane frame at #1 storey assuming limit state $\bar{D}_d^{(1)} = 3\,cm$ - nonlinear analysis.

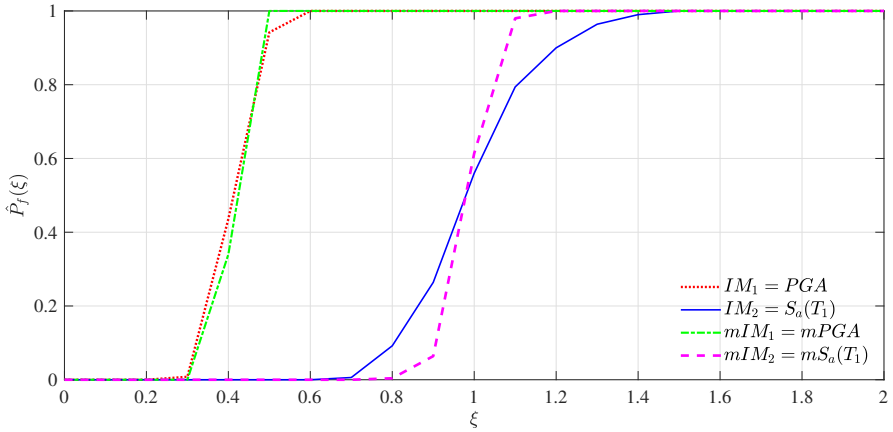

Figure 5.49: Fragilities against intensity level ξ for different definitions of IMs and its modified version $mIMs$ for three-storey plane frame at #2 storey assuming limit state $\bar{D}_d^{(2)} = 3\,cm$ - nonlinear analysis.

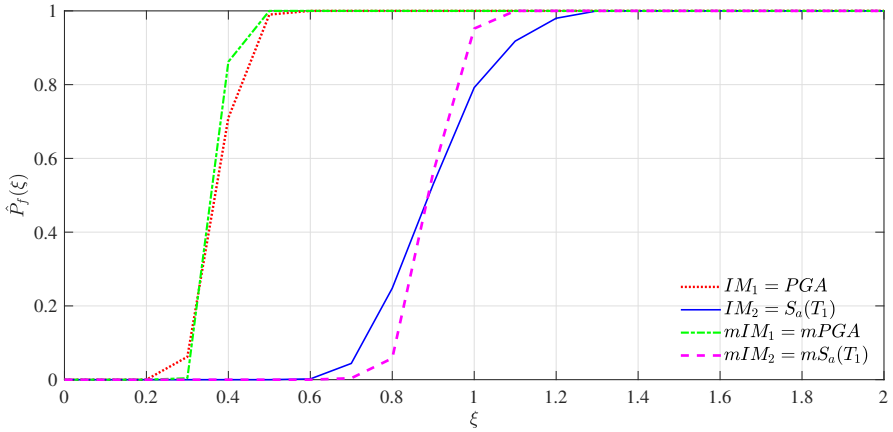

Figure 5.50: Fragilities against intensity level ξ for different definitions of IMs and its modified version $mIMs$ for three-storey plane frame at #3 storey assuming limit state $\bar{D}_d^{(3)} = 3\,cm$ - nonlinear analysis.

the nonlinear system behaviour with $n_s = 500$ samples of $A(t)$ which are scaled with IM_q and mIM_q, $q = 1, 2$, (see Section 3.6). In particular, Figure 5.48 , 5.49 and 5.50 refer to #1 storey $D_d^{(1)}$, #2 storey $D_d^{(2)}$ and #3 storey $D_d^{(3)}$, respectively. Morever, the dotted red, dash-dotted green, continuous blue and dashed magenta line regard to PGA, $mPGA$, $S_a(T_1)$ and $mS_a(T_1)$, respectively.

In any case, for both linear and nonlinear analysis, the evaluated fragilities with mIM_q provide best information on the seismic performance of the system. This is clear if they are compared with those obtained by IM_q, $q = 1, 2$. The improvement in dependence (correlation) produces a lower aleatory uncertainties in fragility analysis and this suggests that the modified intensity measure approach determine efficient IMs.

Chapter 6

Fragility analysis accuracy improvement for complex real systems

6.1 Introduction

The present chapter represents one of the main contributions for this thesis work in which the fragility analysis is developed for an complex real multi-degree of freedom structural system. A severely damaged school struck by the 2016 earthquake in Umbria, Italy is selected. This structure is equipped with a continuous monitoring system and its structural model consists in a linear/nonlinear dynamic system with a large number of degrees of freedom. Fragility analysis improvement is provided by the approach of the modified intensity measure introduced in Section 4.4 . It is demonstrated the effectiveness of this novel methodology for complex real system.

Several intensity measure definitions usually used in PBEE are investigated and the influence of them to produce fragility function are shown. For some of them, the developed fragilities are compared with those obtained from their modified intensity

measure versions.

Samples of spectra-compatible stochastic process in Subsection 2.4.1, inherent with the local seismic hazard of the building school site, are taken into account as inputs for the FE Model. Moreover, experimental data provided by the continuously monitoring system are used to calibrate a non-stationary stochastic process (see Subsection 2.4.2) able to produce samples of ground motion acceleration time series.

6.2 The school in Norcia, Italy

The Norcia building school dates back to the early 1960s, its structural system is a reinforced concrete 3D frame with a bracing system made of axial nonlinear dampers and it is founded on inverse beams. Particulars of the structure geometry is reported in Figures 6.1 - 6.2 , in which the dimensions are expressed in meters. The building has a rectangular footprint, $59.8\,m$ x $12.8\,m$ (Figure 6.1). The total height is about $16.1\,m$. In particular, the elevated structure consists of four floors, three raised storey, the underground basement and a garret (Figure 6.2).

Since 2011 through a seismic adjustment intervention the bracing dissipative system have been installed. This last, it consists by dissipative Buckling-Restrained Axial Dampers (BRADs) which are installed with metal plates connected on the reinforced concrete frame system. The installation concerns a number of 24 dissipative elements on the ground floor and 16 on the first and second floors. In particular, a total of 32 and 24 dissipative elements work in x and y direction, i.e. long and short side, respectively (Figure 6.1).

The building as a whole has good elevation regularity. However, in plan it is possible to identify only one symmetry axis in the transverse direction, i.e. y-direction (see Figure 6.1). This aspect determines a clear difference in resistance capacity in the two main directions when the structural system is subjected by horizontal actions, e.g. the

earthquake.

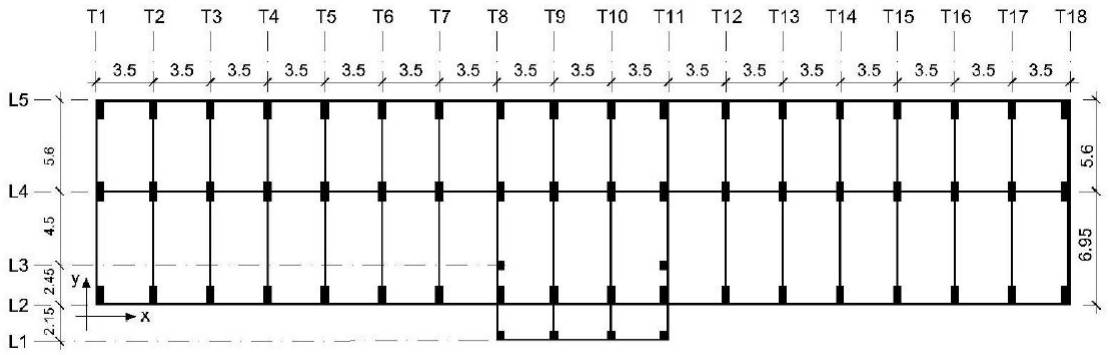

Figure 6.1: Building plan view.

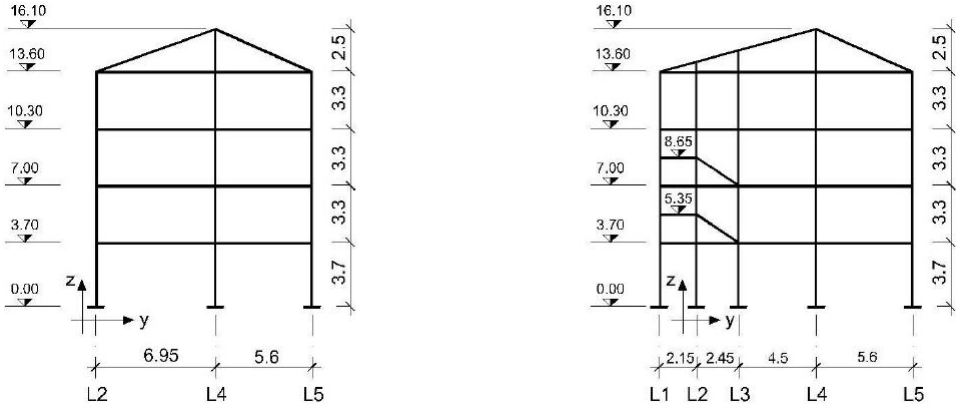

Figure 6.2: Building cross sections.

The motivation of choice this building is two fold. First, the school is continuously monitored by the Italian National Seismic Observatory using a number of accelerometers: one tri-axial accelerometer on the ground and 10 uni-axial and bi-axial accelerometers on the three upper building floors for a total of 18 synchronized time history measurements of the structural response and seismic input. Figure 6.3 shows the building continuously monitoring system scheme.

Second, the structure was severely damaged on the external cladding and on the non-structural internal walls by the 2016 seismic sequence, while the main resiting structure experiences a good behavior with irrelevant damage because it was equipped

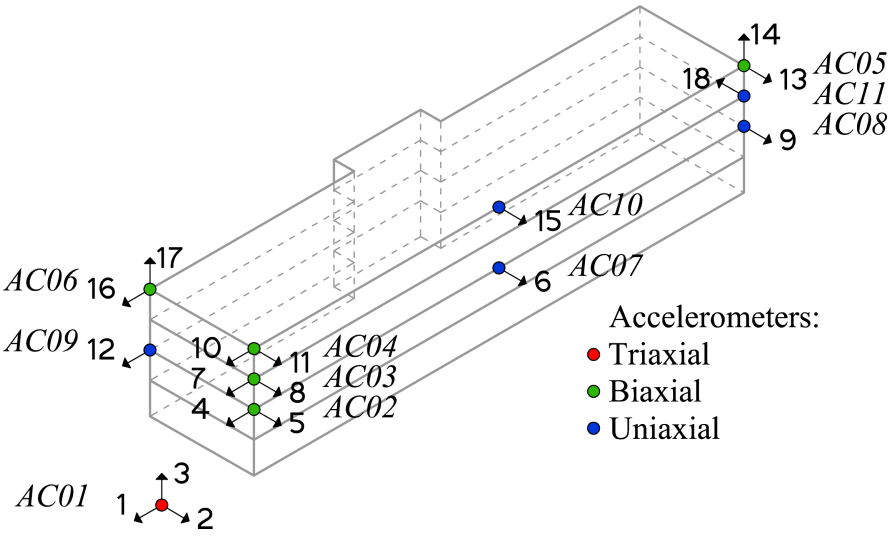

Figure 6.3: Building continuously monitoring system scheme.

with the dissipative bracing system.

This school represents a reference for a series of benchmarks studies in Italy because of the significant amount of available data before, during, and after the major seismic tremor.

6.2.1 Seismic acceleration ground motion stochastic processes

Norcia is situated in an area with high seismicity, the 2016 earthquake demonstrates the hazard to which this geographical area is exposed. Fragility analysis requires accelerograms consistent with the geological properties of a site on which a civil construction stands in order to determine the expected seismic performance.

To represent the local seismic hazard for the site of Norcia building two kind of ground acceleration stochastic processes are taken into account to developing the numerical analysis. More specifically, these two types of inputs are reported below.

Spectra-compatible stochastic process

Artificial spectrum-compatible accelerograms are normally used to describe the local seismic hazard [130–134]. This practice is widespread, especially when adequately representative natural accelerograms are not available. However, the compatibility spectrum does not have any physical sense, but only has a normative reference character, e.g. Eurocode (EC8).

In reference to the current Italian technical construction regulations (NTC 2018), seismicity is mapped as a grid on the Italian area, where for each of its node, the informations are provided to evaluate the pseudo-acceleration response spectrum $S_a(T)$. Then, the $S_a(T)$ is the reference for design and verification for civil structures.

Consider the procedure in Subsection 2.4.1 , the spectra-compatible stochastic process $A(t)$ are calibrated in order that its acceleration time series samples are consistent with the technical regulations about the Norcia school site. Figure 6.4 reports one of the $n_s = 500$ samples of the $A(t)$, i.e. $a(t)$, computed by Equation (2.76) considering a total length of $60\,s$. In the modulation function, Eq. (2.77) , t_1 and T_s have been set as 6 and 10 seconds.

The pseudo-acceleration response spectrum $S_a(T)$ (see Eq. (2.38)) by the accelerometric time history, i.e. $a(t)$ in Figure 6.4 , is shown in Figure 6.5 considering the damping ratio $\zeta = 5\%$.

The set of the $n_s = 500$ samples of $A(t)$ is defined as the spectra-compatible accelerograms since the mean spectrum estimated by them, black line in Figure 6.6 , is at least equal to ninety percent of the NTC 2018 standard reference in the period range of $0 - 2\,s$. In Figure 6.6 the blue and magenta line regard to the NTC 2018 pseudo-acceleration response spectrum for the Norcia school site and its ninety percent spectrum, respectively. The result in Figure 6.6 validates the concept of the

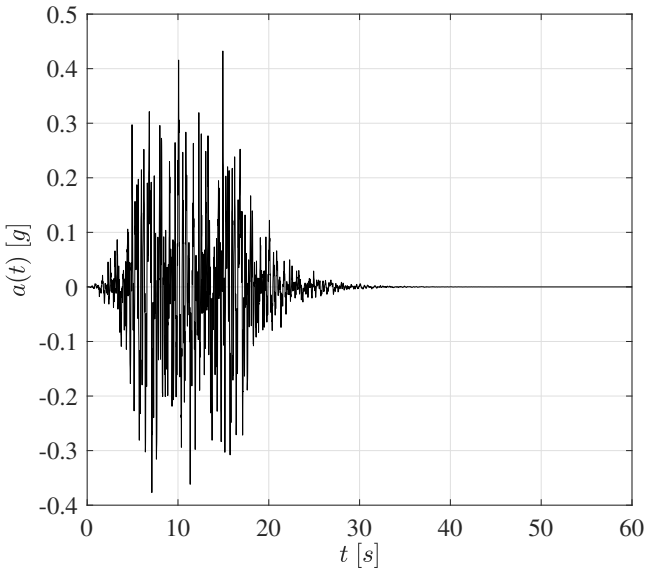

Figure 6.4: One sample of the spectra-compatible stochastic process consistent with the Norcia school site.

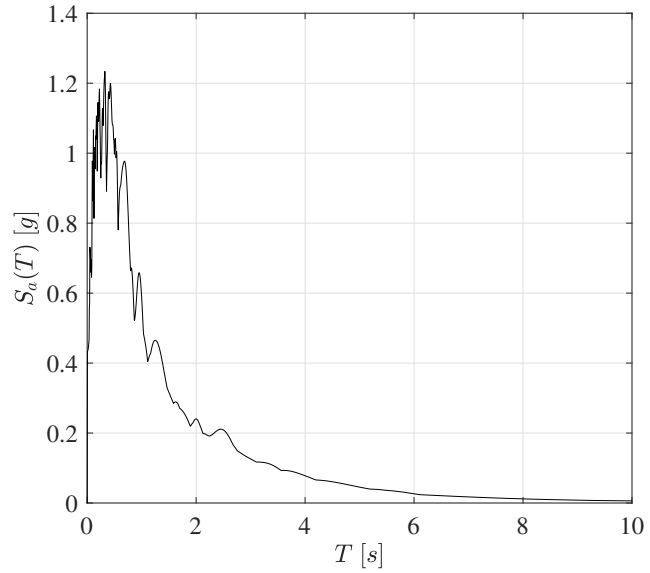

Figure 6.5: Pseudo-acceleration response spectrum by the accelerometric time history in Figure 6.4 , assuming $\zeta = 5\%$.

spectra-compatibility for the $n_s = 500$ acceleration ground motion time series of $A(t)$. Then, these accelerometric samples can be used to perform dynamic analysis describing seismic hazard for the site under consideration (i.e. Norcia school) inherent with the regulations.

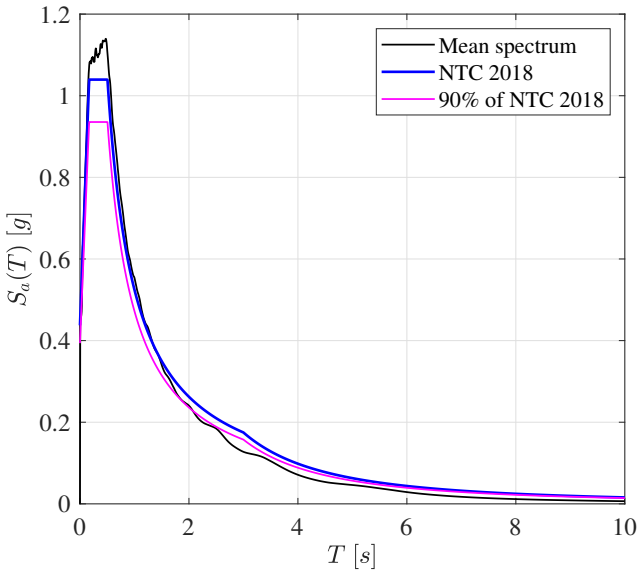

Figure 6.6: Pseudo-acceleration response spectra for $\zeta = 5\%$: mean spectrum of $n_s = 500$ samples of the spectra-compatible stochastic process; NTC 2018 reference for Norcia school site; 90% of NTC 2018 reference for Norcia school site.

Non-stationary stochastic process

A consolidated practice in seismic engineering, when experimental records of earthquakes in a specific site are available, is to use analytical models calibrated by experimental data for the simulation of artificial accelerograms [34, 135–137]. This guarantees to represent the specific characteristics of the local seismic activity.

The strong event recorded in Norcia on October 30th, 2016 by the continuous monitoring system of the school building, i.e. Figure 6.3 , is used to calibrate the stochastic non-stationary process $\boldsymbol{A}(t)$. Both, the two horizontal component of the triaxial accelerometer at the base of the Norcia school (Figure 6.3), i.e. the *AC01*-1 and *AC01*-2 channels, are taken into account in order to define the non-stationary stochastic process in x-direction and y-direction, $A_x(t)$ and $A_y(t)$, respectively. The procedure in Subsection 2.4.2 is used to calibrate $A_x(t)$ and $A_y(t)$ to define $\boldsymbol{A}(t) = \{A_x(t); A_y(t)\}$, i.e. $\boldsymbol{A}(t)$ is stochastic process with independent components, that acts in x and y global

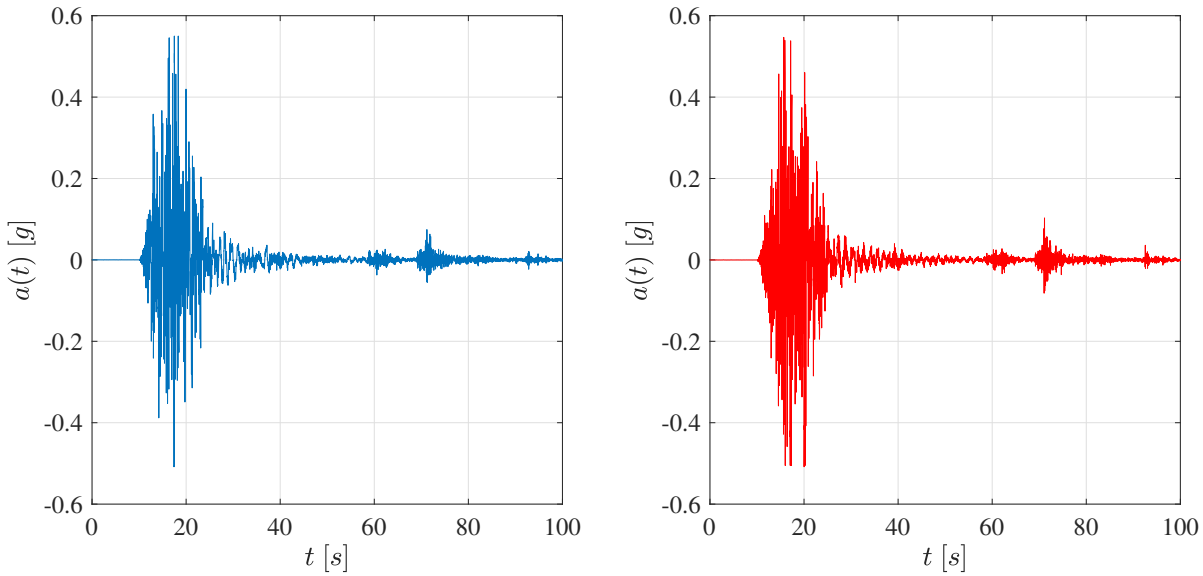

Figure 6.7: Event recorded in Norcia on October 30th, 2016 by the continuous monitoring system of the school building (Figure 6.3): x component by *AC01*-1 channel (left panel); y component by *AC01*-2 channel (right panel).

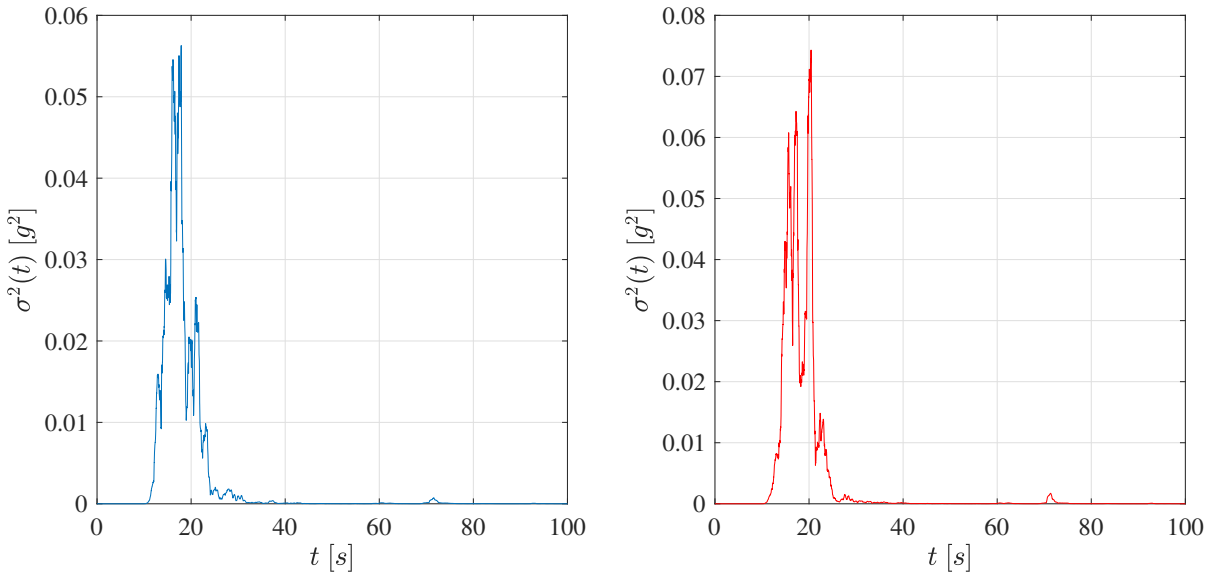

Figure 6.8: Local variance of x component in left of Figure 6.7 (left panel) and of y component in right of Figure 6.7 (right panel).

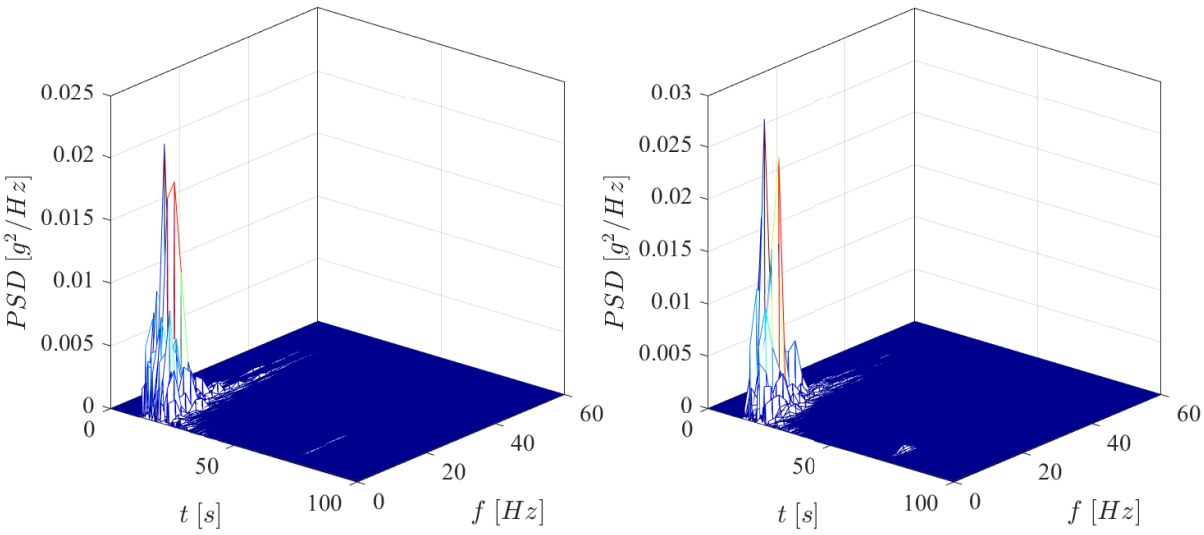

Figure 6.9: Evolutionary spectral density of x component in left of Figure 6.7 (left panel) and of y component in right of Figure 6.7 (right panel).

direction.

Figure 6.7 reports the two horizontal components of the reference experimental seismic event recorded in Norcia on October 30th, 2016 by the continuous monitoring system (Figure 6.3). In this figure, the left panel regard to the x component by *AC01*-1 channel used to calibrated the $A_x(t)$ process, while in the right panel, the y component by *AC01*-2 channel is shown and, than it is used to calibrated the $A_y(t)$ process. The calibration procedure is developed by considering the local variance of the x and y component in the left and right of the Figure 6.8, respectively. The estimated spectrogram of x and y component, i.e. evolutionary spectral density for these two components, in Figure 6.9 demonstrate a variation of the frequency content with time.

The assumed evolutionary spectral density model for $A_x(t)$ and $A_y(t)$ is shown in left and right of Figure 6.10 .

Artificial acceleration time series samples of $A_x(t)$ and $A_y(t)$ are generated by Equation (2.92) in order to describe the statistical variability of the strong event of Norcia

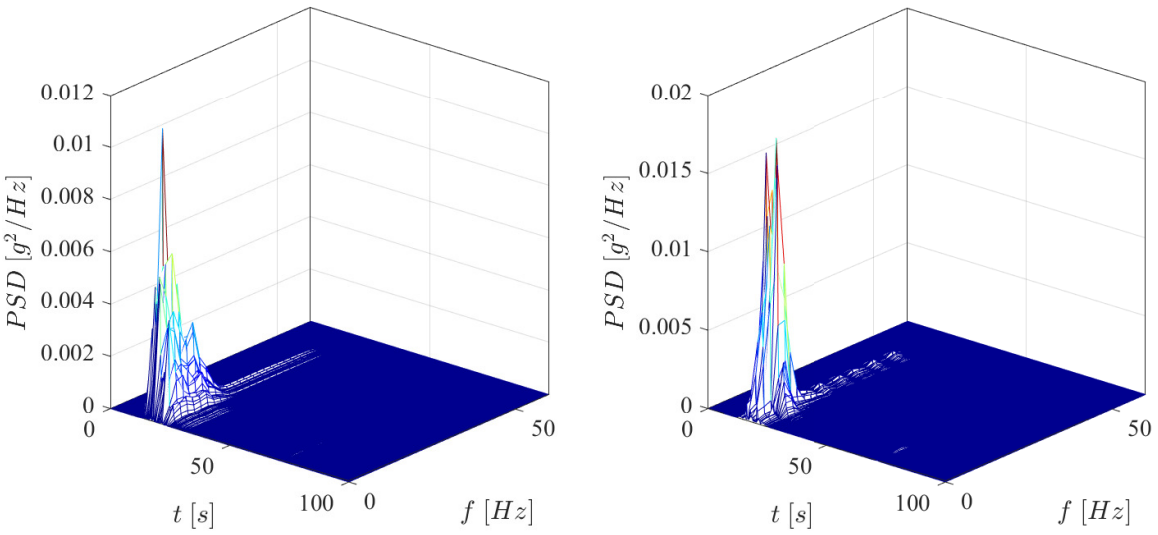

Figure 6.10: Evolutionary spectral density model for $A_x(t)$ (left) and $A_y(t)$ (right).

on October 30th, 2016. Figure 6.11 reports one of the $n_s = 500$ samples of the $A_x(t)$ and $A_y(t)$, i.e. $a_x(t)$ and $a_y(t)$, on the left and right, respectively.

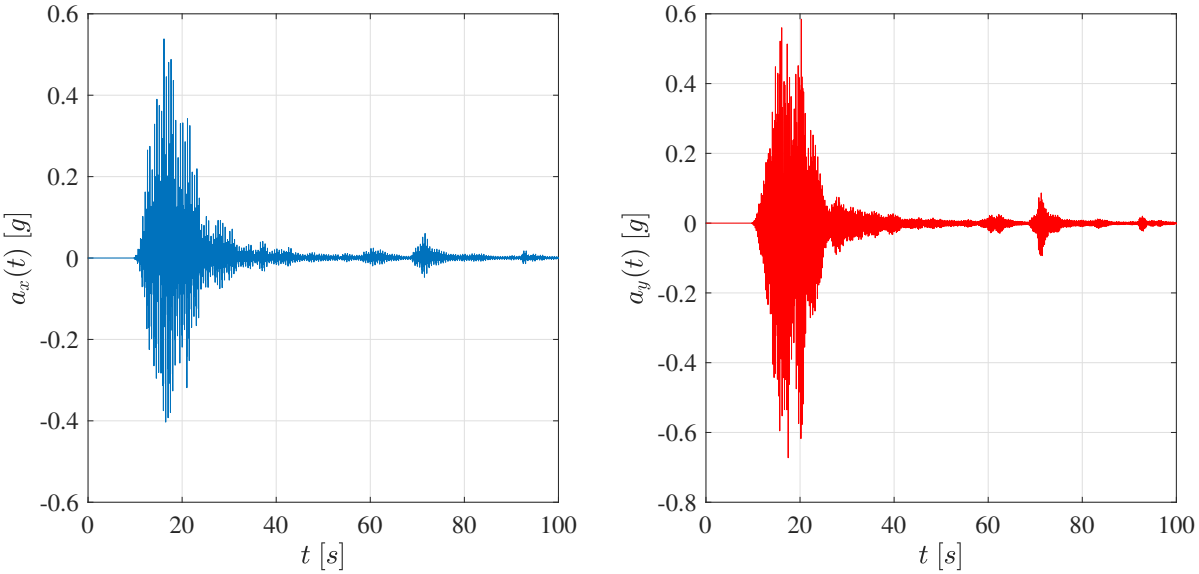

Figure 6.11: One sample of the simulated non-stationary stochastic process: $a_x(t)$ of $A_x(t)$ (left); $a_y(t)$ of $A_y(t)$ (right).

The $\boldsymbol{A}(t) = \{A_x(t); A_y(t)\}$ process is able to represent the local seismic hazard about the Norcia school site, therefore thus, it is can be used to develop dynamic

analysis in order to study the probabilistic response of this building.

6.2.2 Numerical model and dynamic analysis

Standard beam elements are used to model the reinforced concrete frame and the foundation grid (Figure 6.12). The bracing system is used in both x and y directions. Linear and nonlinear dynamic analyses are performed to obtain estimates of the structural response to virtual samples of the ground acceleration processes in Subsection 6.2.1. In particular, samples of the $A(t)$ process in Subsection 6.2.1 are used to develop unidirectional analysis according to the scheme in Figure 6.13. While, the $\boldsymbol{A}(t)$ in Subsection 6.2.1 is used for bidirectional analysis according to Figure 6.14.

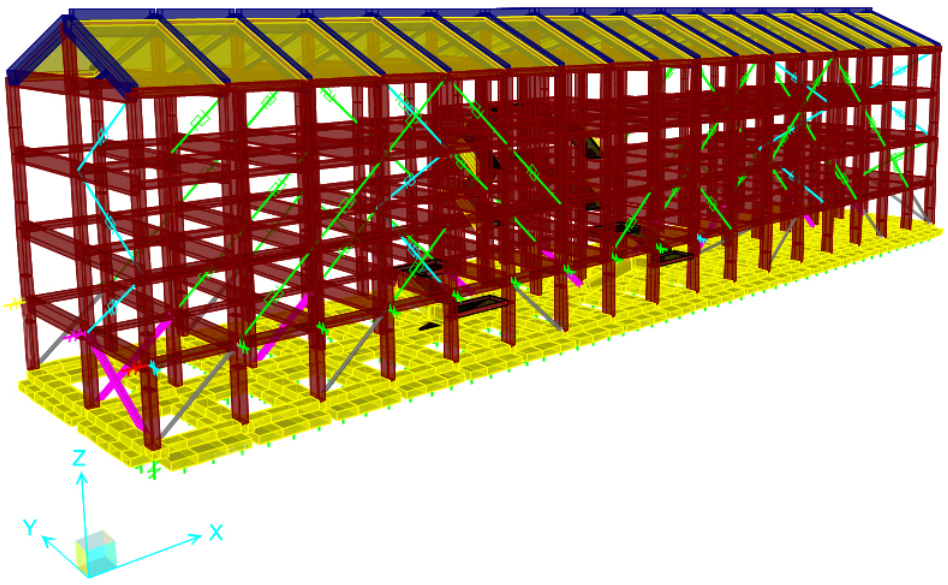

Figure 6.12: 3D numerical FE model of Norcia school building.

Standard truss elements are used for the bracing system in the linear analyses, while nonlinear link elements are used to model the dissipative BRADs, which are described by using the model in [25]. Since the model has a limited number of nonlinear elements, only given by the bracing system, the Fast Nonlinear Analysis (see Subsection 2.3.4) is efficiently used for the response evaluation. Figure 6.15 and Table 6.1 report five

significant mode shapes, natural periods and participant masses of the obtained FE model.

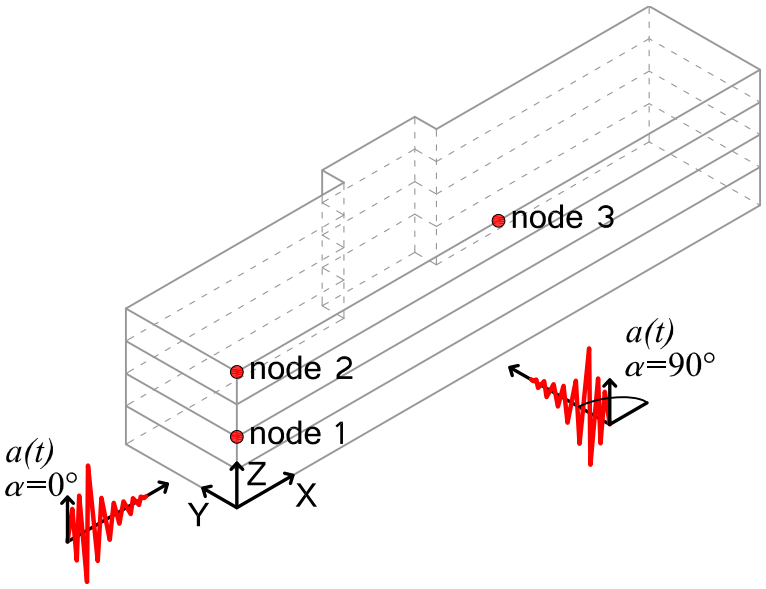

Figure 6.13: Unidirectional earthquake application and selected nodes.

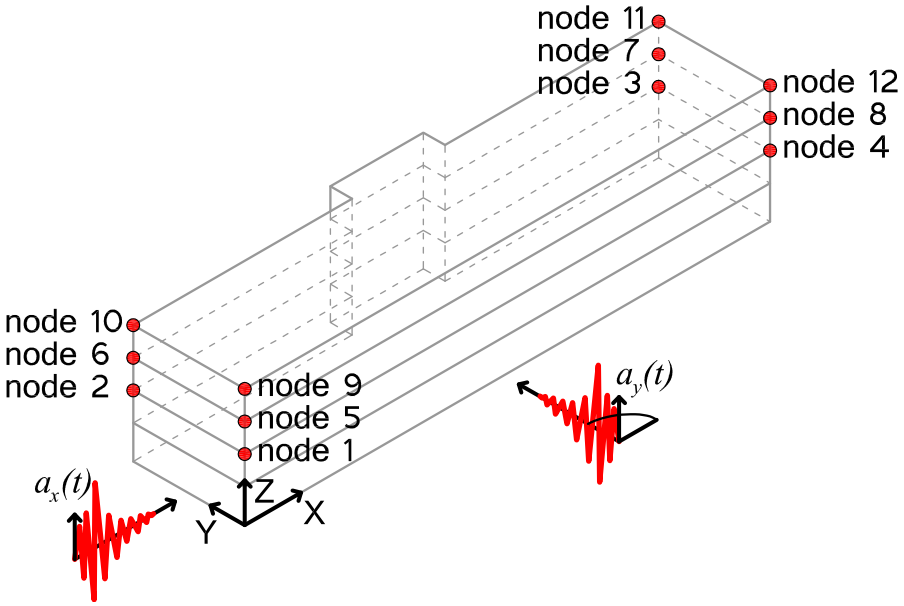

Figure 6.14: Bidirectional earthquake application and selected nodes.

A more specific representation of Equation (3.11), can be used to evaluate the

Table 6.1: FE model modal parameters of Norcia school building.

Modal shape	Period	Participant mass		
#	[s]	x	y	z
1	0.348	0.571	0.001	5.6e-7
2	0.289	0.065	0.074	3.0e-5
3	0.267	0.004	0.607	6.0e-5
4	0.119	0.091	3e-5	1.6e-8
8	0.09	1.8e-4	0.099	2.0e-6

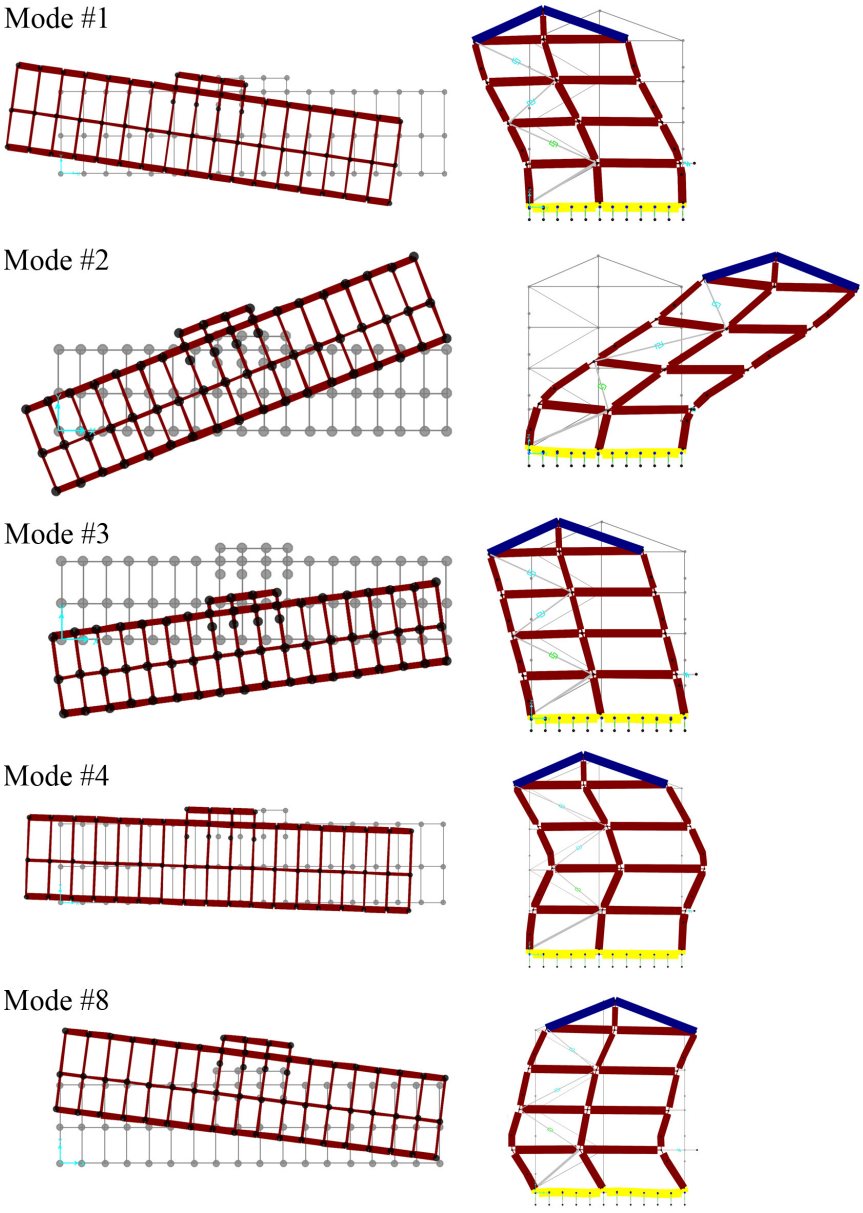

Figure 6.15: FE model mode shapes of Norcia school building.

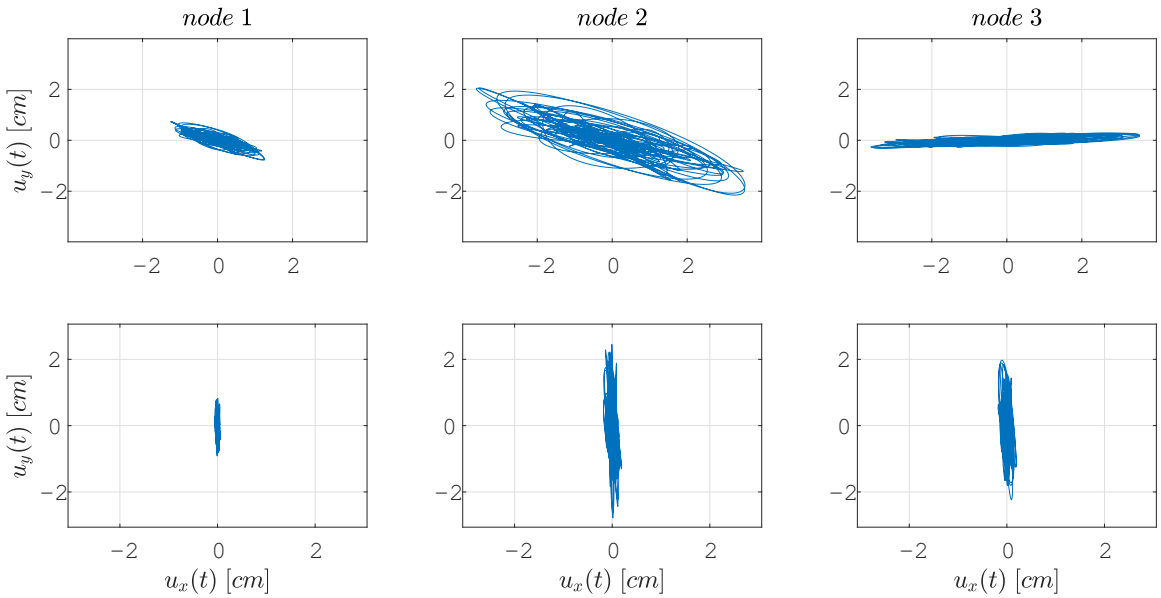

Figure 6.16: Plan displacement response time histories $u(t) = \{u_x(t); u_y(t)\}$ at nodes #1, #2, and #3 for earthquake directions x, $\alpha = 0°$, (top panels) and y, $\alpha = 90°$, (bottom panels).

system demand parameters as

$$D^{(j)} = \max_{0 \leqslant t \leqslant \tau} |h^{(j)}(\boldsymbol{X}(t))|, \quad j = 1, \ldots, m \tag{6.1}$$

where τ is the time length of the ground acceleration stochastic process, m is the total number of demand parameters of interest and $h^{(j)}(\cdot)$ is a function that mapping the response $\boldsymbol{X}(t)$ into the j-th demand parameter of interest to define:

- the maximum absolute displacement random vector $D_d = \{D_d^{(1)}, \ldots, D_d^{(m)}\}$;
- the maximum absolute acceleration random vector $D_a = \{D_a^{(1)}, \ldots, D_a^{(m)}\}$;
- the drift random vector $D_{dr} = \{D_{dr}^{(1)}, \ldots, D_{dr}^{(m)}\}$.

For nonlinear dynamic analysis, considering different input level intensity number l and the corresponding level coefficient ξ_l, i.e. scaling the input stochastic process by ξ_l, the Eq. (6.1) can used to define the demand parameter random vector

$D_r^{(l)} = \{D_r^{(1)}, \ldots, D_r^{(m)}\}$, $r = d, a, dr$, to investigate the dependence with IMs at prefixed l. In the case of apex l omission, it means that the ground acceleration stochastic process is not scaled ($l = \xi_l = 1$). This is always found for linear analysis results, but for those nonlinear too.

The demand parameters for the school structural system are estimated according to unidirectional dynamic analysis as follows:

1. $n_s = 500$ spectra-compatible samples $a(t)$ of the process $A(t)$ in Subsection 6.2.1 are applied in x or y-direction, i.e. $\alpha = 0°$ or $\alpha = 90°$, (Figure 6.13);

2. linear and nonlinear time domain numerical dynamic structural analyses are used to obtain response samples $\boldsymbol{x}(t)$ of $\boldsymbol{X}(t)$ assuming proportional damping ratio $\zeta = 5\%$;

3. displacement, D_d, and acceleration, D_a, are estimated using Equation (6.1) with $m = 3$ (Figure 6.13).

Figure 6.16 reports the plan displacements $u(t) = \{u_x(t); u_y(t)\}$ time histories of nodes #1, #2 and #3 for the same spectra-compatible acceleration sample in the building x-direction, $\alpha = 0°$, (top panels) and y-direction, $\alpha = 90°$ (bottom panels)(Figure 6.13). As expected from the results in Figure 6.15 and Table 6.1, modes #1 and #3 play the main role in the response of the selected nodes. Furthermore, it is clear that the structural centers of mass and stiffness are aligned in the building x-direction, while they are eccentric in the y-direction.

In a conceptually similar way, the demand parameters for the school structural system are estimated by bidirectional dynamic analysis as:

1. $n_s = 500$ virtual acceleration samples $a_x(t)$ and $a_y(t)$ of the process $\boldsymbol{A}(t) = \{A_x(t); A_y(t)\}$ in Subsection 6.2.1 are applied in x and y-direction (Figure 6.14);

2. linear and nonlinear time domain numerical dynamic structural analyses are used to obtain response samples $\boldsymbol{x}(t)$ of $\boldsymbol{X}(t)$ assuming proportional damping ratio $\zeta = 5\%$;

3. displacement, D_d, and acceleration, D_a, are estimated using Equation (6.1) with $m = 12$ (Figure 6.14); drift, D_{dr}, is estimated using Equation (6.1) with $m = 3$, where its components refer to the drift at each floor in elevation considering the same earthquake application scheme in Figure 6.14.

6.3 Dependence between demand parameters and intensity measures

In this Section, scatter plots and relative correlation coefficients ρ are used to give information on the dependence between demand parameters D and the IMs defined in Equations (3.12)-(3.16). Consider the spectra-compatible samples $a(t)$ of the process $A(t)$ (Subsection 6.2.1), for each of these the PGA is computed together with the pseudo-acceleration response spectra $S_a(T, \zeta)$, $\zeta = 5\%$ and I_h, to obtain samples of the random variables PGA, $S_a(T_1, \zeta_1)$, $S_a(T_3, \zeta_3)$, I_h and $S^*(T_1, \zeta_1, C, \alpha)$, with $\zeta_1 = \zeta_3 = 5\%$. The ordinates of $S_a(T, \zeta)$ are selected at first structural system period T_1, i.e. Eq. (3.13), since the fist modal shape plays a fundamental role in the structural response. This is a practice in seismic engineering, such as in [74, 95, 96]. However the third modal shape contributes greatly (Table 6.1), therefore ordinates of $S_a(T, \zeta)$ are selected also at third period T_3 (Eq. (3.14)).

Figures 6.17 - 6.24 show scatter plots of $n_s = 500$ samples of the demand parameter D and the selected IMs at node #2 in Figure 6.13 for linear and nonlinear analyses. The x-axis reports the intensity measures IM_1, IM_2, IM_3, IM_4 and IM_5 from the left

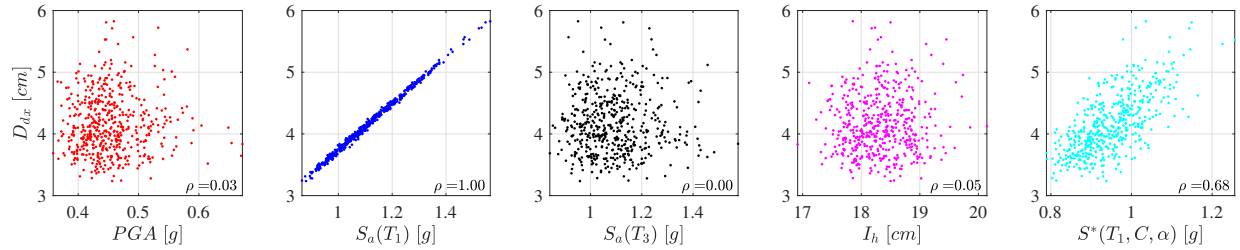

Figure 6.17: Scatter plots of $n_s = 500$ samples of (PGA, D_{dx}), $(S_a(T_1), D_{dx})$, $(S_a(T_3), D_{dx})$, (I_h, D_{dx}) and $(S^*(T_1, C, \alpha), D_{dx})$, $\alpha = 0°$, at node #2 - linear analysis.

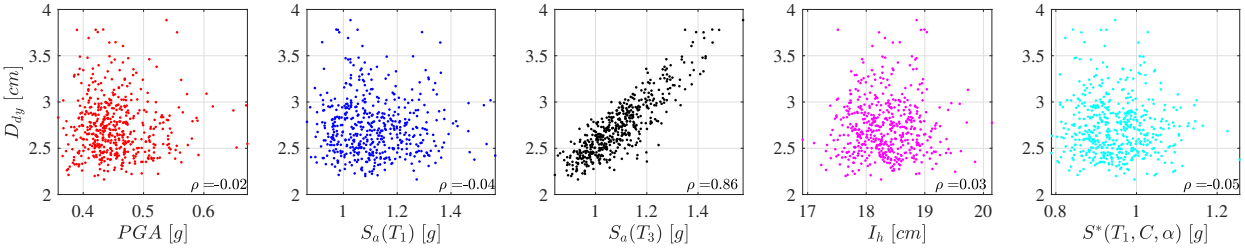

Figure 6.18: Scatter plots of $n_s = 500$ samples of (PGA, D_{dy}), $(S_a(T_1), D_{dy})$, $(S_a(T_3), D_{dy})$, (I_h, D_{dy}) and $(S^*(T_1, C, \alpha), D_{dy})$, $\alpha = 90°$, at node #2 - linear analysis.

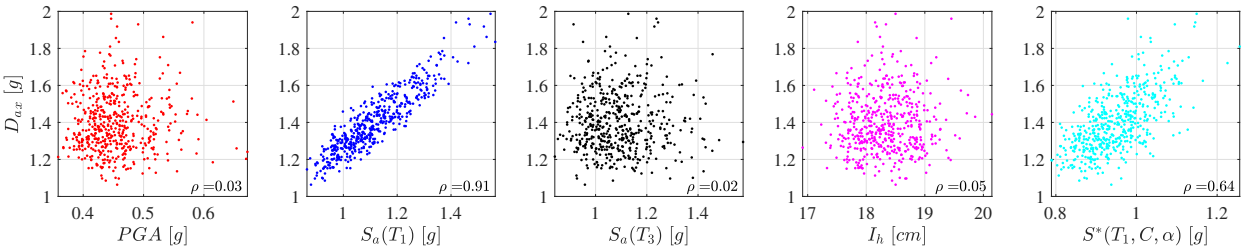

Figure 6.19: Scatter plots of $n_s = 500$ samples of (PGA, D_{ax}), $(S_a(T_1), D_{ax})$, $(S_a(T_3), D_{ax})$, (I_h, D_{ax}) and $(S^*(T_1, C, \alpha), D_{ax})$, $\alpha = 0°$, at node #2 - linear analysis.

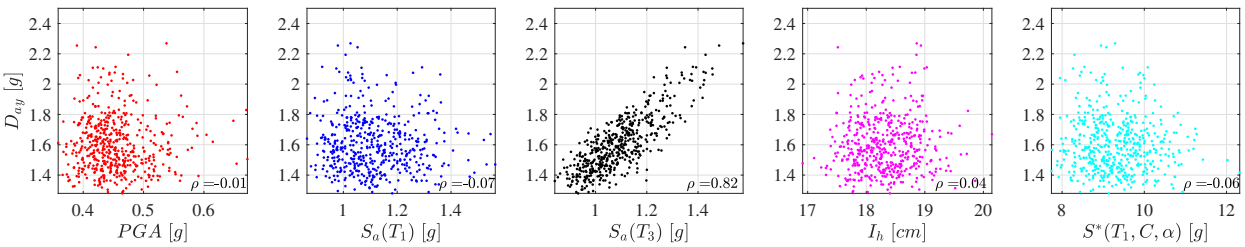

Figure 6.20: Scatter plots of $n_s = 500$ samples of (PGA, D_{ay}), $(S_a(T_1), D_{ay})$, $(S_a(T_3), D_{ay})$, (I_h, D_{ay}) and $(S^*(T_1, C, \alpha), D_{ay})$, $\alpha = 90°$, at node #2 - linear analysis.

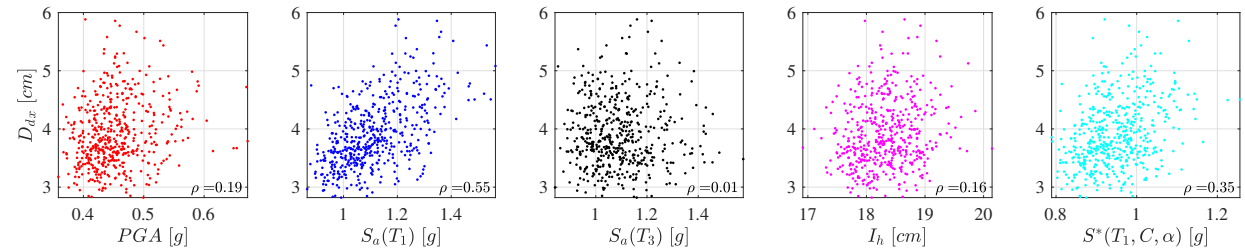

Figure 6.21: Scatter plots of $n_s = 500$ samples of (PGA, D_{dx}), $(S_a(T_1), D_{dx})$, $(S_a(T_3), D_{dx})$, (I_h, D_{dx}) and $(S^*(T_1, C, \alpha), D_{dx})$, $\alpha = 0°$, at node #2 - nonlinear analysis.

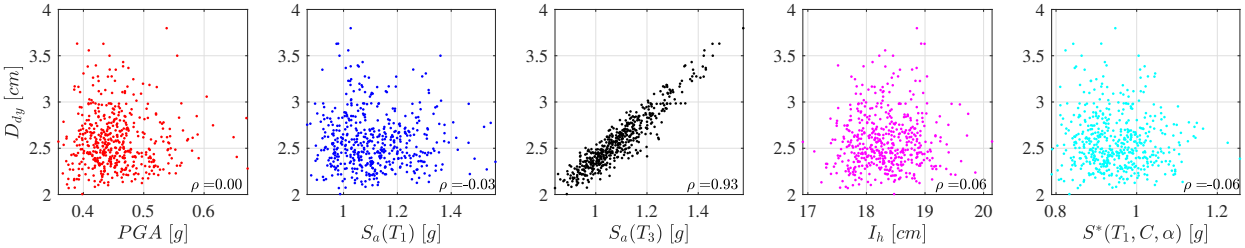

Figure 6.22: Scatter plots of $n_s = 500$ samples of (PGA, D_{dy}), $(S_a(T_1), D_{dy})$, $(S_a(T_3), D_{dy})$, (I_h, D_{dy}) and $(S^*(T_1, C, \alpha), D_{dy})$, $\alpha = 90°$, at node #2 - nonlinear analysis.

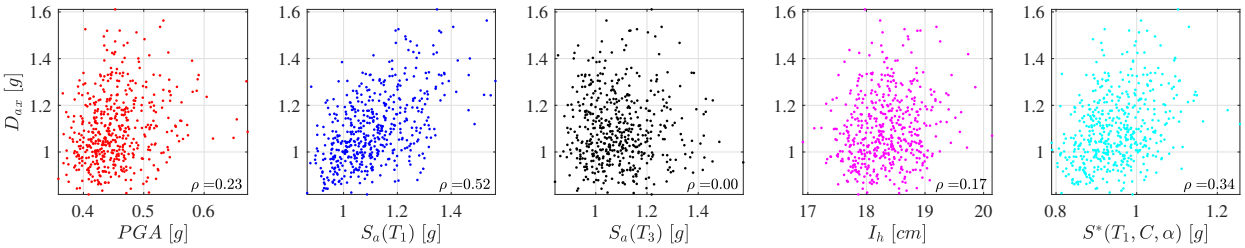

Figure 6.23: Scatter plots of $n_s = 500$ samples of (PGA, D_{ax}), $(S_a(T_1), D_{ax})$, $(S_a(T_3), D_{ax})$, (I_h, D_{ax}) and $(S^*(T_1, C, \alpha), D_{ax})$, $\alpha = 0°$, at node #2 - nonlinear analysis.

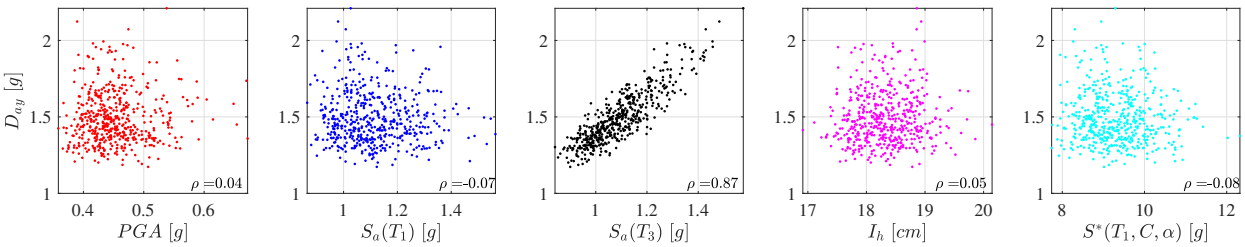

Figure 6.24: Scatter plots of $n_s = 500$ samples of (PGA, D_{ay}), $(S_a(T_1), D_{ay})$, $(S_a(T_3), D_{ay})$, (I_h, D_{ay}) and $(S^*(T_1, C, \alpha), D_{ay})$, $\alpha = 90°$, at node #2 - nonlinear analysis.

panel to the right, respectively. The y-axis reports the demand parameters D_{dx}, D_{dy}, D_{ax}, D_{ay}, i.e. maximum displacement in the x, y direction and peak acceleration in x, y direction (Figure 6.13). The estimated correlation coefficient, ρ, between the demand parameter D and intensity measure IM_i, $i = 1, \ldots, 5$ is also reported in each panel. Same typology results for node #1 and #3 (Figure 6.13), are shown in Figures A.1 - A.8 and Figures A.9 - A.16 in Appendix A, respectively.

In a conceptually similar way, by considering the non-stationary process $\boldsymbol{A}(t) = \{A_x(t); A_y(t)\}$ in Subsection 6.2.1, from the samples $a_n(t)$ of $A_n(t)$, $n = x, y$, the PGA and $S_a(T, \zeta)$, $\zeta = 5\%$, and I_h are computed. The purpose is to evaluate samples of the stochastic variables PGA_n, $S_{an}(T_1, \zeta_1)$, $S_{an}(T_3, \zeta_3)$, I_{hn} and ${S^*}_n(T_1, C, \alpha)$, $n = x, y$ and $\zeta_1 = \zeta_3 = 5\%$.

Scatter plots of $n_s = 500$ samples of D and the selected IMs at node #9 in Figure 6.14 (same location of #2 in Figure 6.13) for linear and nonlinear analysis are shown in Figures 6.25 - 6.32. In the x-axis, the intensity measures IM_{1n}, IM_{2n}, IM_{3n}, IM_{4n} and IM_{5n}, $n = x, y$, are reported from left to right panels. While, the y-axis reports the demand parameters D_{dx}, D_{dy}, D_{ax}, and D_{ay} in x and y direction (Figure 6.14). In each panel, the correlation coefficient between D and IM_{in}, $i = 1, \ldots, 5$ and $n = x, y$, are reported in right bottom. The results for other nodes (Figure 6.14) are reported in Figures B.1 - B.88 in Appendix B. While, Figures B.89 - B.100 report results about the demand parameter D_{dr} at each floor in elevation for both x- and y-direction.

The scatter plots in these figures confirm that $IM_1 = PGA/IM_{1n} = PGA_n$, $n = x, y$, commonly used in the past in PBEE, contains very little information about the ground motion and it is weakly dependent with the structural response in all cases (e.g. left panel of Figures 6.17 - 6.24/Figures 6.25 - 6.32). Furthermore, the IMs based on single/multiple ordinates of the pseudo-acceleration spectrum $S_a(T)$ are generally weak predictors of the seismic performance of MDOF linear and nonlinear structures.

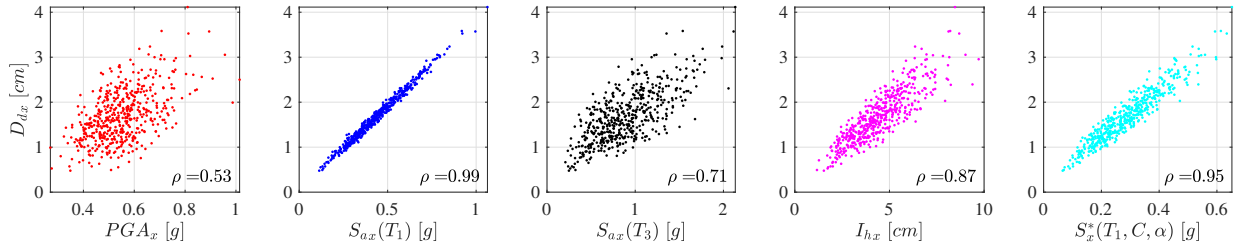

Figure 6.25: Scatter plots of $n_s = 500$ samples of (PGA_x, D_{dx}), $(S_{ax}(T_1), D_{dx})$, $(S_{ax}(T_3), D_{dx})$, (I_{hx}, D_{dx}) and $(S^*{}_x(T_1, C, \alpha), D_{dx})$ at node #9 - linear analysis.

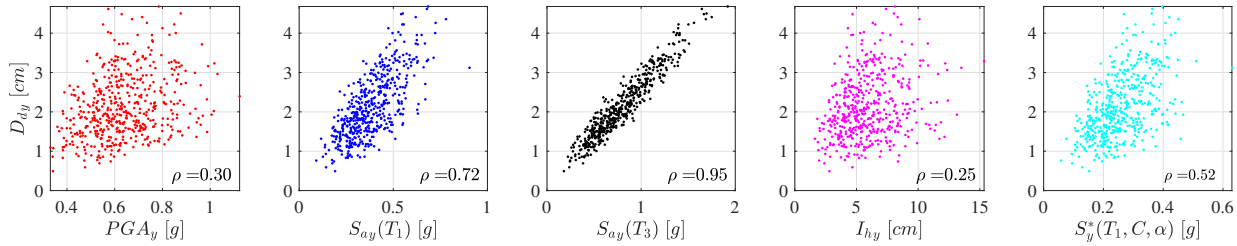

Figure 6.26: Scatter plots of $n_s = 500$ samples of $(PGA_y, D_{d)}$, $(S_{ay}(T_1), D_{dy})$, $(S_{ay}(T_3), D_{dy})$, (I_{hy}, D_{dy}) and $(S^*{}_y(T_1, C, \alpha), D_{dy})$ at node #9 - linear analysis.

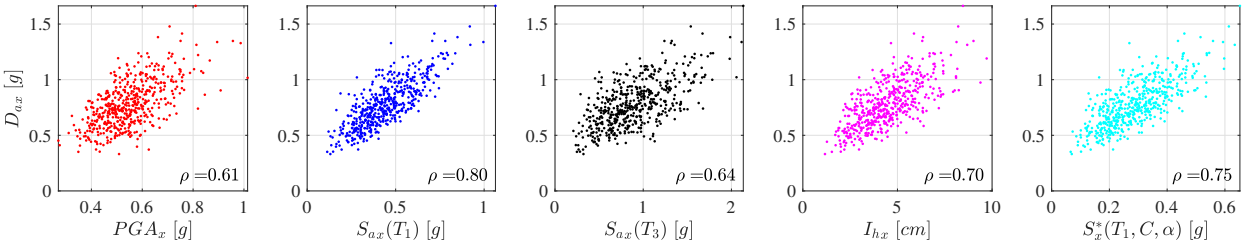

Figure 6.27: Scatter plots of $n_s = 500$ samples of (PGA_x, D_{ax}), $(S_{ax}(T_1), D_{ax})$, $(S_{ax}(T_3), D_{ax})$, (I_{hx}, D_{ax}) and $(S^*{}_x(T_1, C, \alpha), D_{ax})$ at node #9 - linear analysis.

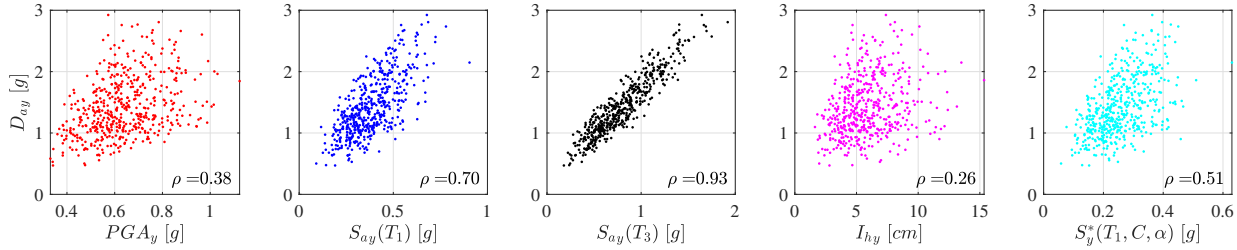

Figure 6.28: Scatter plots of $n_s = 500$ samples of (PGA_y, D_{ay}), $(S_{ay}(T_1), D_{ay})$, $(S_{ay}(T_3), D_{ay})$, (I_{hy}, D_{ay}) and $(S^*{}_y(T_1, C, \alpha), D_{ay})$ at node #9 - linear analysis.

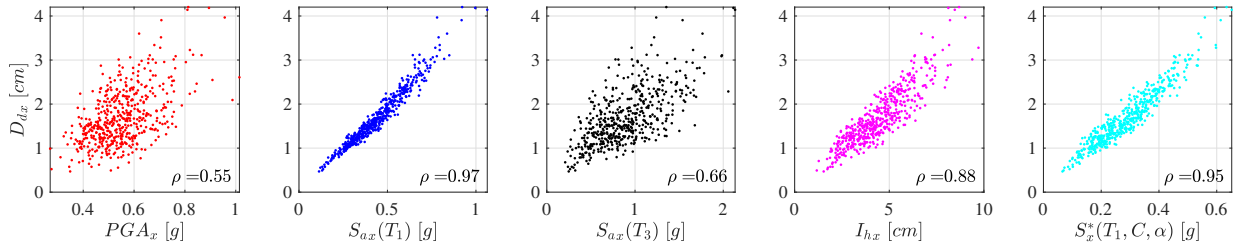

Figure 6.29: Scatter plots of $n_s = 500$ samples of (PGA_x, D_{dx}), $(S_{ax}(T_1), D_{dx})$, $(S_{ax}(T_3), D_{dx})$, (I_{hx}, D_{dx}) and $(S^*{}_x(T_1, C, \alpha), D_{dx})$ at node #9 - nonlinear analysis.

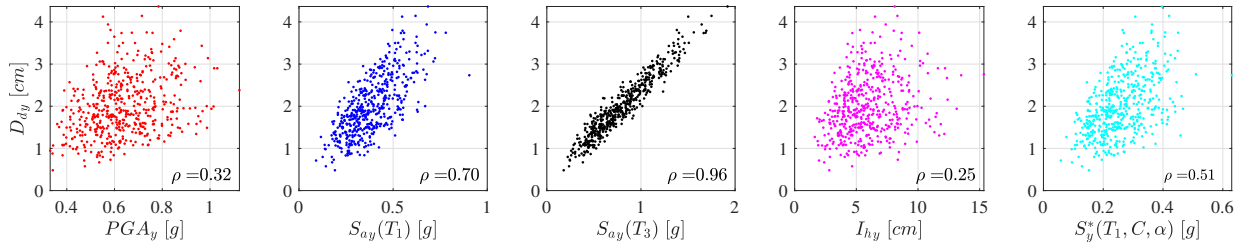

Figure 6.30: Scatter plots of $n_s = 500$ samples of $(PGA_y, D_{d)}$, $(S_{ay}(T_1), D_{dy})$, $(S_{ay}(T_3), D_{dy})$, (I_{hy}, D_{dy}) and $(S^*{}_y(T_1, C, \alpha), D_{dy})$ at node #9 - nonlinear analysis.

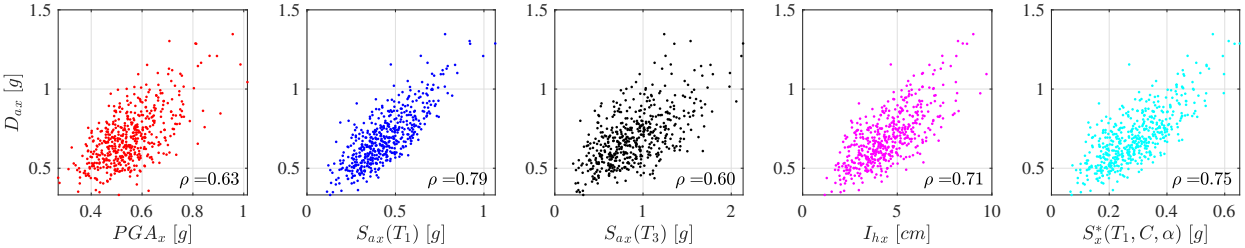

Figure 6.31: Scatter plots of $n_s = 500$ samples of (PGA_x, D_{ax}), $(S_{ax}(T_1), D_{ax})$, $(S_{ax}(T_3), D_{ax})$, (I_{hx}, D_{ax}) and $(S^*{}_x(T_1, C, \alpha), D_{ax})$ at node #9 - nonlinear analysis.

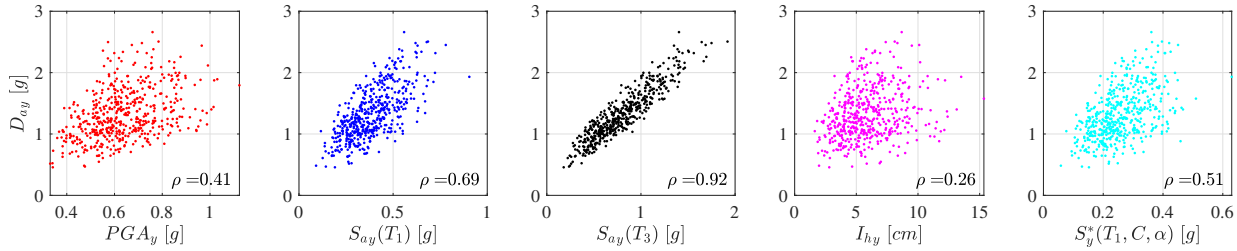

Figure 6.32: Scatter plots of $n_s = 500$ samples of (PGA_y, D_{ay}), $(S_{ay}(T_1), D_{ay})$, $(S_{ay}(T_3), D_{ay})$, (I_{hy}, D_{ay}) and $(S^*{}_y(T_1, C, \alpha), D_{ay})$ at node #9 - nonlinear analysis.

Indeed, it is clear, when considering the second panel from the left of Figures 6.17 - 6.20/Figures 6.25 - 6.28 (linear analysis), that the spectral acceleration at the first structural natural period, $IM_2 = S_a(T_1)/IM_{2n} = S_{an}(T_1)$, $n = x, y$, can be both strongly and weakly correlated with the demand parameter depending on the selected response, i.e. x-, y- displacements or accelerations, and earthquake direction. Similar findings can be observed in the system response at different node locations (see Appendix A and B). This means that the first mode spectral acceleration, can be an inaccurate index even for linear structures. The 2nd panels from the left of Figures 6.21 - 6.24 and Figures 6.29 - 6.32 show a similar trend so that $S_a(T_1)$ can be inaccurate for nonlinear MDOF, confirming what was already reported in [113].

The middle panel of Figures 6.18 and 6.20 (similarly for Figures 6.26 and 6.28) show that the spectral acceleration at the third structural natural period, $IM_3 = S_a(T_3)$ ($IM_{3y} = S_{ay}(T_3)$), can be informative of the ground motion since the selected responses seem to be dependent on this IM for the linear structural model. This result is strictly related to the system modal properties described in Table 6.1 . Figures 6.22 and 6.24 (Figures 6.30 and 6.32) also confirm for nonlinear analysis this achievement since the nonlinearity elements (BRADs) are installed more in the x direction. This causes less nonlinearity in the y direction to be activated.

Similar trends are observed for IM_4 and IM_5 (IM_{4n} and IM_{5n}, $n = x, y$) in second and first panel from right of Figures 6.17 - 6.24 (Figures 6.25 - 6.32). In general, the demand parameter D selected in these scatter plots has poor dependence on the Housner intensity, Eq. (3.15), sometimes comparable with the dependence obtained by considering IM_1 (IM_{1n}, $n = x, y$) as intensity measure. The scatter plots with IM_5 (IM_{5n}, $n = x, y$) closely follow the trends of the corresponding IM_2 (IM_{2n}, $n = x, y$). This was expected because Equation (3.16) is a function of Equation (3.13) [110]. The correlation coefficients estimated by D and IM_5 (IM_{5n}, $n = x, y$) are generally lower than those obtained with IM_2 (IM_{2n}, $n = x, y$).

In addition, it would seem that the use of non-stationary accelerograms, rather the spectra-compatible, give better results in terms of dependence between D and IM, i.e. highest value of ρ (e.g. Figures 6.17 - 6.24 and Figures 6.25 - 6.32). This aspect encourages the use of non-stationary accelerograms to develop the fragility analysis for Norcia school building in the following. In any case, for both the results of dynamic analysis by non-stationary and spectra-compatible accelerograms, it shows evident as the earthquake direction influences the dependence between D and the different IMs.

Finally, the results in Figures 6.17 - 6.32 (as in Appendix A and B) are consistent with the findings in [15]. First, for nonlinear analysis, the dependence between demand parameters and IMs decreases with the earthquake intensity. Second, when a mode j is dominant for the selected demand parameter, then the dependence between D and the spectral acceleration at the corresponding natural period $S_a(T_j)$ is stronger than dependence between D and other spectral acceleration $S_a(T_i)$, for $i \neq j$.

6.4 Dependence improvement

As discussed extensively in this research work, an improvement in dependence between the structural demand parameter D and the intensity measure IM results in an accuracy of the fragility analysis by providing a much better estimation for the structural system seismic performance. A tool that requires onerous calculation such as the construction of fragility curves must ultimately be able to produce strong and reliable results. Following this concept the modified intensity measure algorithm in Section 4.4 is applied to increasing the dependence between D and selected IMs for linear/nonlinear MDOF real complex structural system, such as the Norcia school.

The modified intensity measure methodology is applied assuming for the school

model:

- linear behaviour, demand parameter $D_{dn} = \{D_{d_n}^{(1)}, \ldots, D_{d_n}^{(12)}\}$ and $D_{drn} = \{D_{dr_n}^{(1)}, D_{dr_n}^{(2)}, D_{dr_n}^{(3)}\}$, $n = x, y$, computed by Eq. (6.1) with $m = 12$ and $m = 3$, respectively;

- nonlinear behaviour, demand parameter $D_{d_n}^{(l)} = \{D_{d_n}^{(1,l)}, \ldots, D_{d_n}^{(12,l)}\}$ and $D_{dr_n}^{(l)} = \{D_{dr_n}^{(1,l)}, D_{dr_n}^{(2,l)}, D_{dr_n}^{(3,l)}\}$, $n = x, y$ and $l = 1, 2, 3$ ($\xi_l = 1, 1.5, 2$), computed by Eq. (6.1) with $m = 12$ and $m = 3$, respectively.

The Equations (3.12) and (3.13) are selected as intensity measures being normally the most used in PBEE. Since the previous dependence study, i.e. Section 6.3, shows the high variability of the correlation between D and several IMs, and particularly the inadequacy of PGA and $S_a(T_1)$ to be an efficient IMs, the modified intensity measure approach can be a effectiveness way to solve the weak dependence problem for the linear/nonlinear MDOF complex structural system.

Let consider the following way to proceed. First, samples of the demand parameter and the selected IM are transformed into standardized versions by Equations (4.3) and (4.4), respectively. Second, the distance from perfect correlation is evaluated using Equation (4.5). Third, the n_s average distances are evaluated by Eq. (4.6) and are collected in the vector $\bar{E}$. Fourth, samples of $\bar{E}$ are used to correct the standardized samples of the selected IM, i.e. $z(im)$, in order to compute samples of the modified intensity measure mIM by Equation (4.7).

6.4.1 Linear behaviour

Figures 6.33 and 6.34 report the obtained results by linear analysis for the intensity measures $IM_{1n} = PGA_n$ and the maximum absolute displacement D_{dn}, $n = x, y$, at node #9 (Figure 6.14), i.e. $D_{dn} = D_{d_n}^{(j)}$, $j = 9$ and $n = x, y$. In particular the left panels show the scatter plots and the correlation coefficients before and after

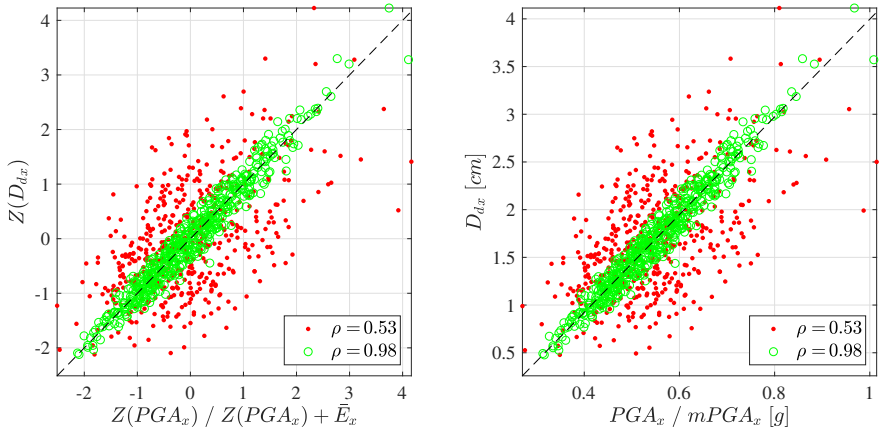

Figure 6.33: Scatter plots of $n_s = 500$ samples at node #9: $(Z(PGA_x), Z(D_{dx}))$ red dots, $(Z(PGA_x) + \bar{E}_x, Z(D_{dx}))$ green circles (left panel); (PGA_x, D_{dx}) red dots, $(mPGA_x, D_{dx})$ green circles (right panel) - linear analysis.

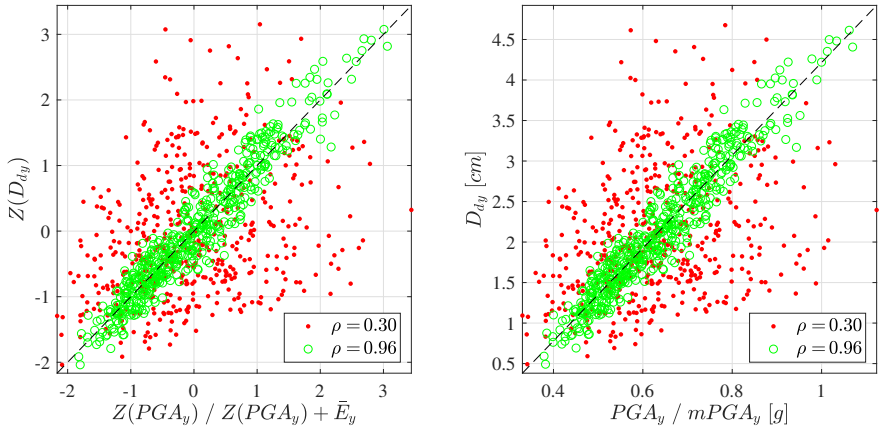

Figure 6.34: Scatter plots of $n_s = 500$ samples at node #9: $(Z(PGA_y), Z(D_{dy}))$ red dots, $(Z(PGA_y) + \bar{E}_y, Z(D_{dy}))$ green circles (left panel); (PGA_y, D_{dy}) red dots, $(mPGA_y, D_{dy})$ green circles (right panel) - linear analysis.

(red and green) the correction in the standardized space, i.e. $(Z(IM_{1n}), Z(D_{dn}))$ and $(Z(IM_{1n}) + \bar{E}_n, Z(D_{dn}))$, $n = x, y$, respectively. While, the right panels report the scatter plots (before and after the correction) linearly transformed back into their original space representation by Equation (4.7), i.e. (IM_{1n}, D_{dn}) and (mIM_{1n}, D_{dn}), $n = x, y$, respectively.

Analogous results for the other demand parameters, $D_{dn} = D_d^{(j)}_n$, $j = 4, 7, 10$ and $n = x, y$, are shown in Figures B.101 - B.106. Considering for node #9 the computed $n_s = 500$ samples of the distance from the perfect correlation (Eq. (4.5)),

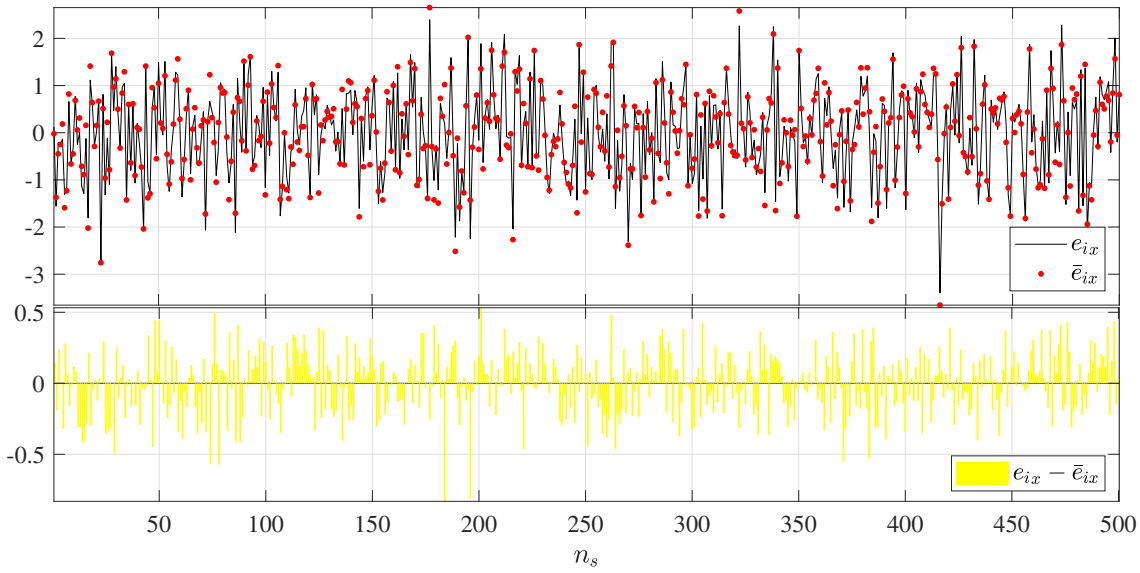

Figure 6.35: Computed distances of $n_s = 500$ samples at node #9 considering D_{dx} and PGA_x: distance from the perfect correlation e_{ix} versus average distance $\bar{e}_{ix}$, $i = 1, \ldots, n_s$ (top panel); difference $e_{ix} - \bar{e}_{ix}$, $i = 1, \ldots, n_s$ (bottom panel) - linear analysis.

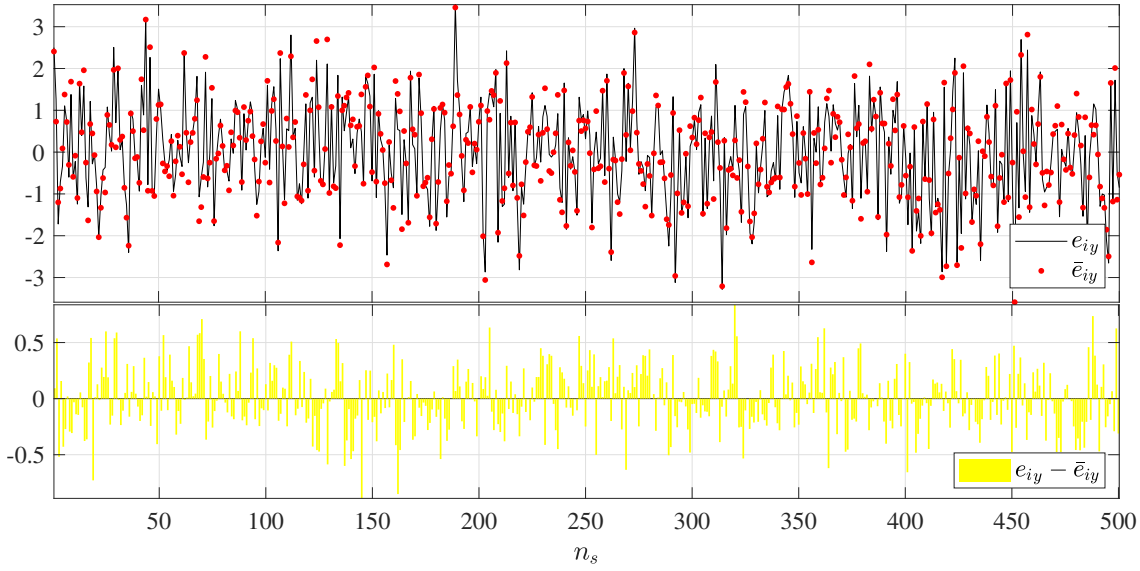

Figure 6.36: Computed distances of $n_s = 500$ samples at node #9 considering D_{dy} and PGA_y: distance from the perfect correlation e_{iy} versus average distance $\bar{e}_{iy}$, $i = 1, \ldots, n_s$ (top panel); difference $e_{iy} - \bar{e}_{iy}$, $i = 1, \ldots, n_s$ (bottom panel) - linear analysis.

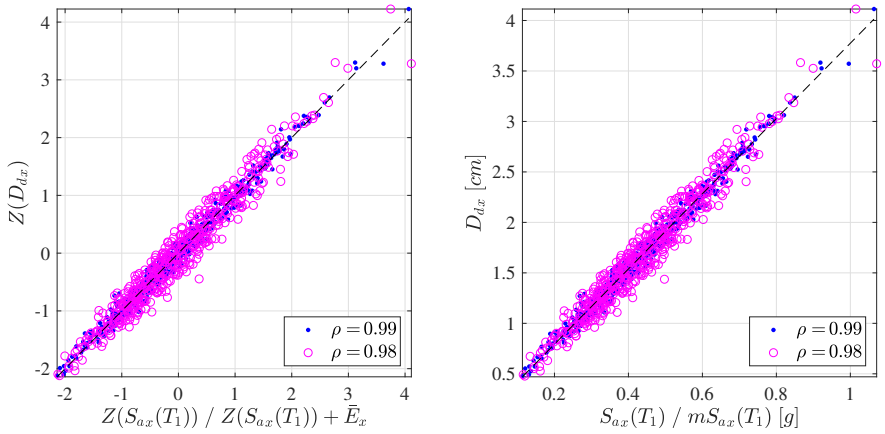

Figure 6.37: Scatter plots of $n_s = 500$ samples at node #9: $(Z(S_{ax}(T_1)), Z(D_{dx}))$ red dots, $(Z(S_{ax}(T_1)) + \bar{E}_x, Z(D_{dx}))$ green circles (left panel); $(S_{ax}(T_1), D_{dx})$ red dots, $(mS_{ax}(T_1), D_{dx})$ green circles (right panel) - linear analysis.

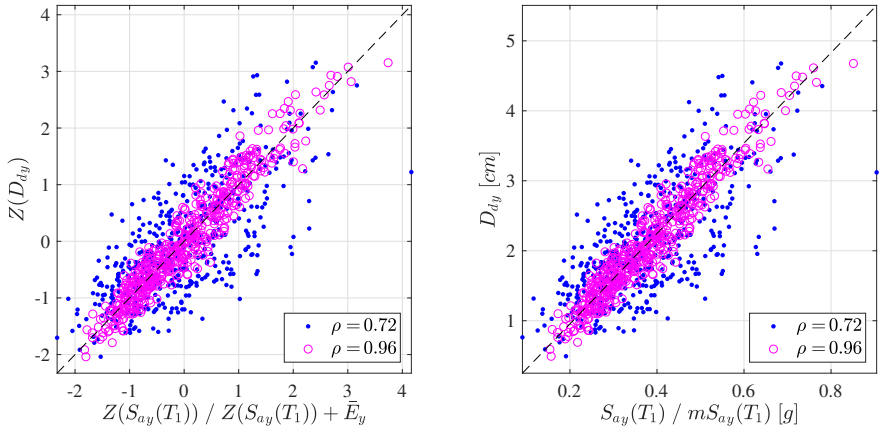

Figure 6.38: Scatter plots of $n_s = 500$ samples at node #9: $(Z(S_{ay}(T_1)), Z(D_{dy}))$ red dots, $(Z(S_{ay}(T_1)) + \bar{E}_y, Z(D_{dy}))$ green circles (left panel); $(S_{ay}(T_1), D_{dy})$ red dots, $(mS_{ay}(T_1), D_{dy})$ green circles (right panel) - linear analysis.

$e_{in} = z(d_{din}) - z(im_{1in})$, versus the average distance (Eq. (4.6)), $\bar{e}_{in}$ with $m = 12$ and $k = 1$ ($l = \xi_l = 1$, linear analysis), $i = 1, \ldots, n_s$ and $n = x, y$, in top panels of Figures 6.35 and 6.36 . The red dots, $\bar{e}_{in}$, match with good approximation to the continuous black line, e_{in}. The bottom panels report the difference $e_{in} - \bar{e}_{in}$, $i = 1, \ldots, n_s$ and $n = x, y$, in yellow. The results in Figures 6.35 and 6.36 refer to $n = x$ and $n = y$. The errors, i.e. $e_{in} - \bar{e}_{in}$ differences on the n_s samples for $n = x, y$, experience a low level and this produces higher correlation after the correction in Figures 6.33 and 6.34 (green circles).

Linear analysis results in Figures 6.37 and 6.38 refer to $IM_{2n} = S_{an}(T_1)$ and same samples of $D_{dn} = D_{d_n^{(j)}}$, $j = 9$ (node #9 in Figure 6.14) and $n = x, y$. In these figures, on the left panels, scatter plots and the correlation coefficients before and after (blue and magenta) the correction in the standardized space, i.e. $(Z(IM_{2n}), Z(D_{dn}))$ and $(Z(IM_{2n}) + \bar{E}_n, Z(D_{dn}))$, $n = x, y$, respectively, are reported. On the right panels, the scatter plots of (IM_{2n}, D_{dn}), blue dots (before correction), and (mIM_{2n}, D_{dn}), magenta circles (after correction), $n = x, y$, are shown in the original space, respectively. Figures B.107 - B.112 report the obtained results for other demand parameters of interest.

It is worth noting that, after the correlation correction $mS_{ax}(T_1)$ $(Z(S_{ax}(T_1)) + \bar{E}_x)$ determines less correlation with D_{dx} $(Z(D_{dx}))$ at node #9 (Figure 6.37). This is attributable to the fact that the best correlation that existed at the beginning of the correction by $S_{ax}(T_1)$ $(Z(S_{ax}(T_1)))$ is minimally yielded to improve that on the other considered nodes, e.g. Figure B.107. While, the $mS_{ay}(T_1)$ $(Z(S_{ay}(T_1)) + \bar{E}_y)$ always shows a marked improvement of the correlation with the demand parameters as in Figure 6.38.

The computed $n_s = 500$ samples of the distance from the perfect correlation $e_{in} = z(d_{din}) - z(im_{2in})$ versus the average distance $\bar{e}_{in}$ (Eq. (4.6) with $m = 12$ and $k = 1$), $i = 1, \ldots, n_s$ and $n = x, y$, for node #9 by linear analysis are shown in the top panels of Figures 6.39 and 6.40 . For these panels, the blue dots and the continuous black line refer to $\bar{e}_{in}$ and e_{in}, $n = x, y$, respectively. The bottom panels regard to $e_{in} - \bar{e}_{in}$ differences on the n_s samples for $n = x, y$.

Focusing attention on Figure 6.39, the blue dots do not match very well the results provided by the continuous black line since the better previous correlation by $Z(S_{ax}(T_1))$ is yielded for the improving on the other demand parameters of interest as introduced above. For Figure 6.40, there is a good correspondence between $\bar{e}_{iy}$ and e_{iy}.

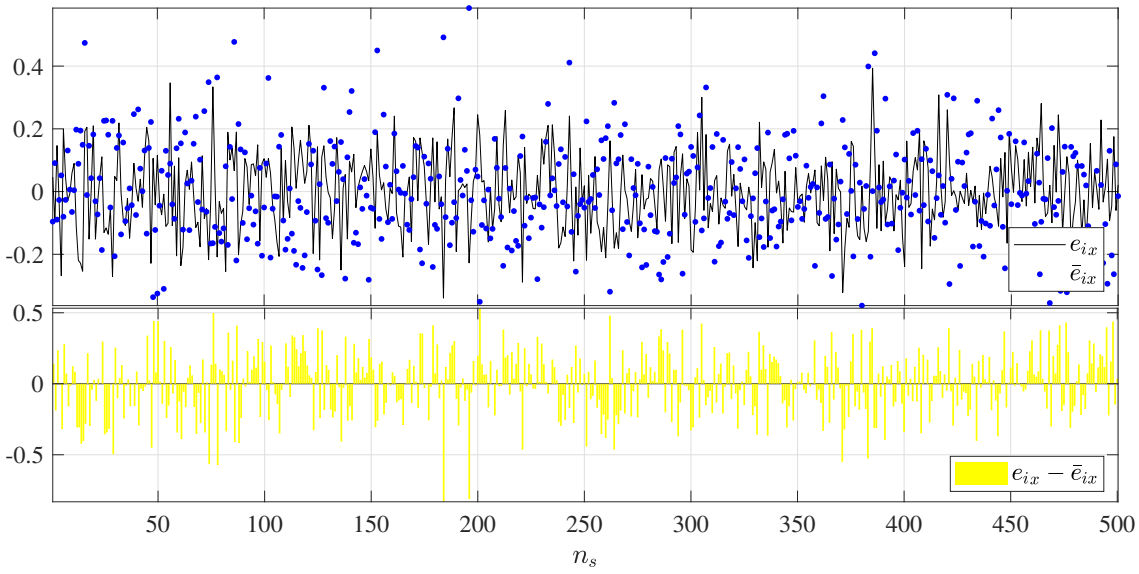

Figure 6.39: Computed distances of $n_s = 500$ samples at node #9 considering D_{dx} and $S_{ax}(T_1)$: distance from the perfect correlation e_{ix} versus average distance $\bar{e}_{ix}$, $i = 1, \ldots, n_s$ (top panel); difference $e_{ix} - \bar{e}_{ix}$, $i = 1, \ldots, n_s$ (bottom panel) - linear analysis.

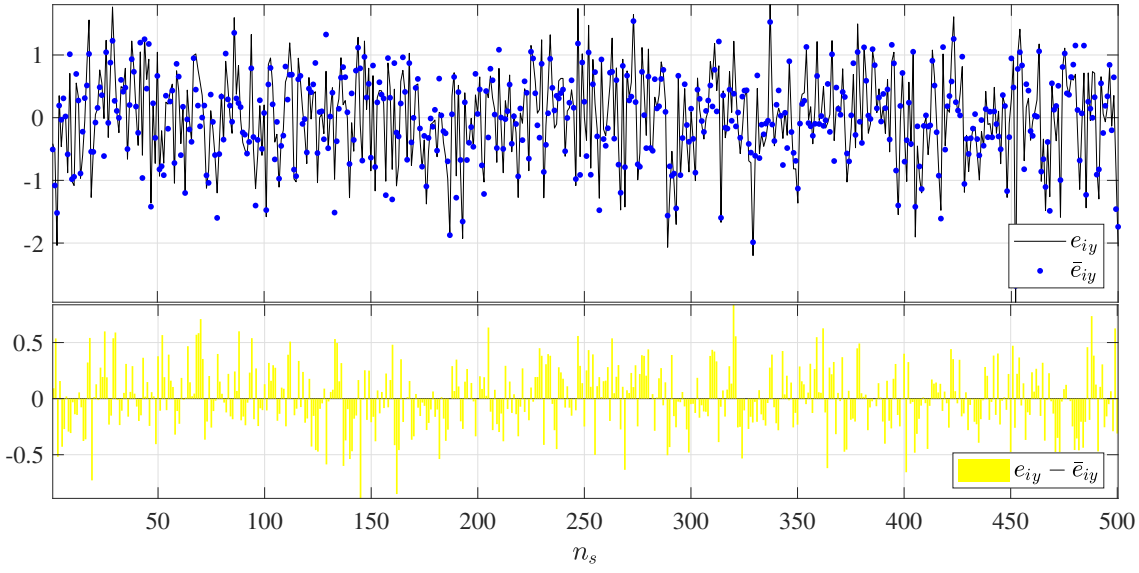

Figure 6.40: Computed distances of $n_s = 500$ samples at node #9 considering D_{dy} and $S_{ay}(T_1)$: distance from the perfect correlation e_{iy} versus average distance $\bar{e}_{iy}$, $i = 1, \ldots, n_s$ (top panel); difference $e_{iy} - \bar{e}_{iy}$, $i = 1, \ldots, n_s$ (bottom panel) - linear analysis.

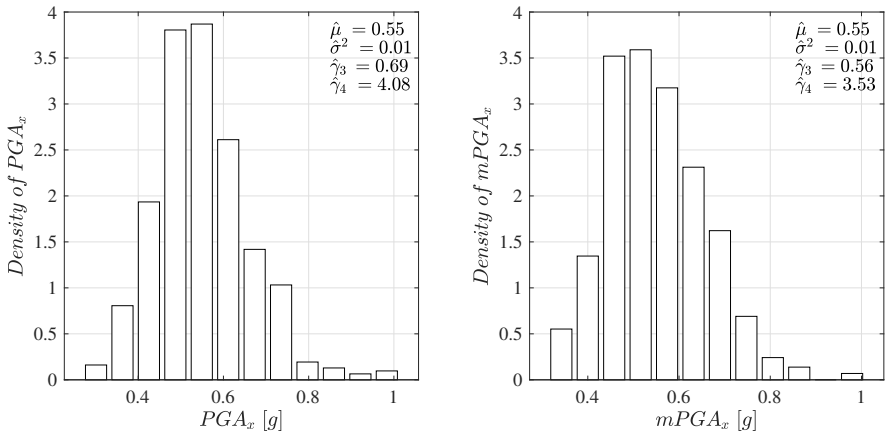

Figure 6.41: Estimated PDF for $n_s = 500$ samples of PGA_x (left panel) and $mPGA_x$ (right panel) computed with $m = 12$ and $k = 1$.

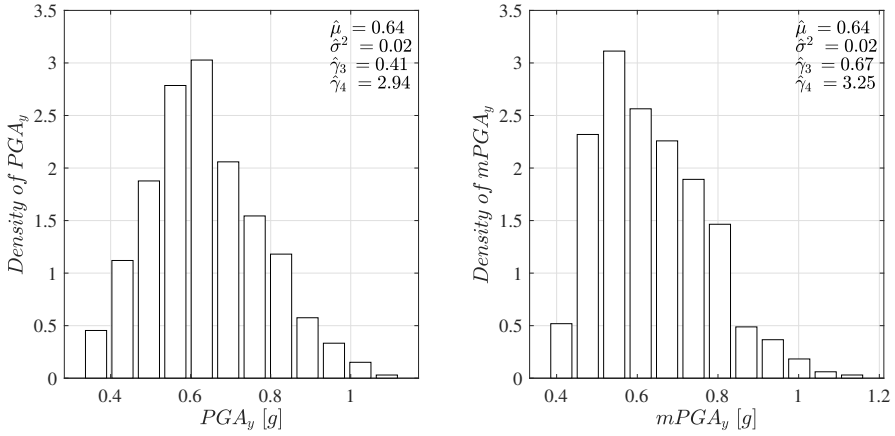

Figure 6.42: Estimated PDF for $n_s = 500$ samples of PGA_y (left panel) and $mPGA_y$ (right panel) computed with $m = 12$ and $k = 1$.

In the Figures 6.41 - 6.44 a comparison is carried out between the PDFs and first four statical moments estimated of the original intensity measures IM_{q_n}, $q = 1, 2$ and $n = x, y$, (left panels) and their modified versions mIM_{q_n} (right panels). In particular, Figures 6.41 and 6.42 refer to $PGA_x/mPGA_x$ and $PGA_y/mPGA_y$, respectively, while Figures 6.43 and 6.44 to $S_{ax}(T_1)/mS_{ax}(T_1)$ and $S_{ay}(T_1)/mS_{ay}(T_1)$, respectively. The linear transformation of which is based the modified intensity measure definition does not substantially change the original probability density function of an IM.

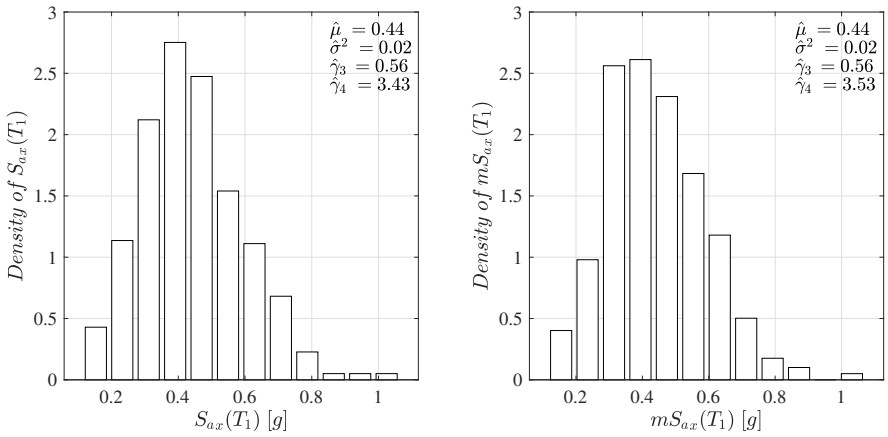

Figure 6.43: Estimated PDF for $n_s = 500$ samples of $S_{ax}(T_1)$ (left panel) and $mS_{ax}(T_1)$ (right panel) computed with $m = 12$ and $k = 1$.

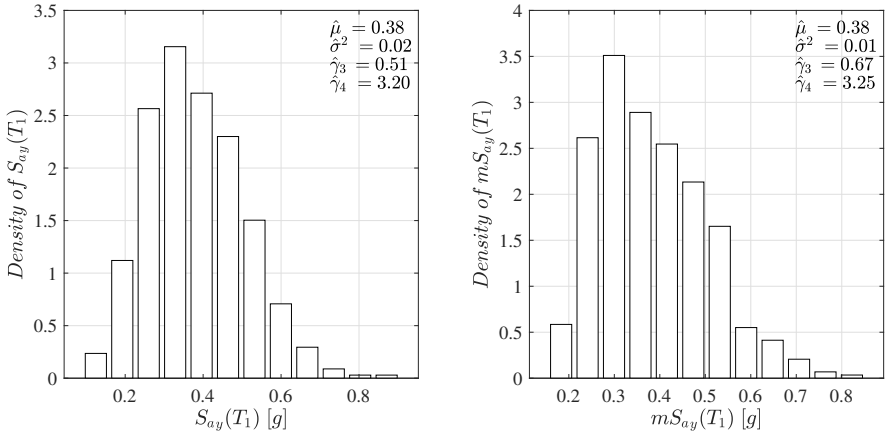

Figure 6.44: Estimated PDF for $n_s = 500$ samples of $S_{ay}(T_1)$ (left panel) and $mS_{ay}(T_1)$ (right panel) computed with $m = 12$ and $k = 1$.

All previous obtained results refer to the modified intensity measure approach in which the demand parameters of interest (Figure 6.14) are twelve, i.e. $m = 12$. Similar results are now shown for the seismic drifts $D_{drn} = \{D_{dr}{}_n^{(1)}, D_{dr}{}_n^{(2)}, D_{dr}{}_n^{(3)}\}$ $(m = 3)$ with $n = x, y$ again considering a linear behavior of the system. Scatter plots of $n_s = 500$ samples of selected intensity measures IM_{q_n} and the maximum absolute inter-storey displacement D_{drn}, $n = x, y$, at 3rd storey, i.e. $D_{drn} = D_{dr}{}_n^{(j)}$, $j = 3$ and $n = x, y$, are shown in Figures 6.45 - 6.48 . The left panels refer to the standardized space representation of the random variables in the plots, while on the right to normal

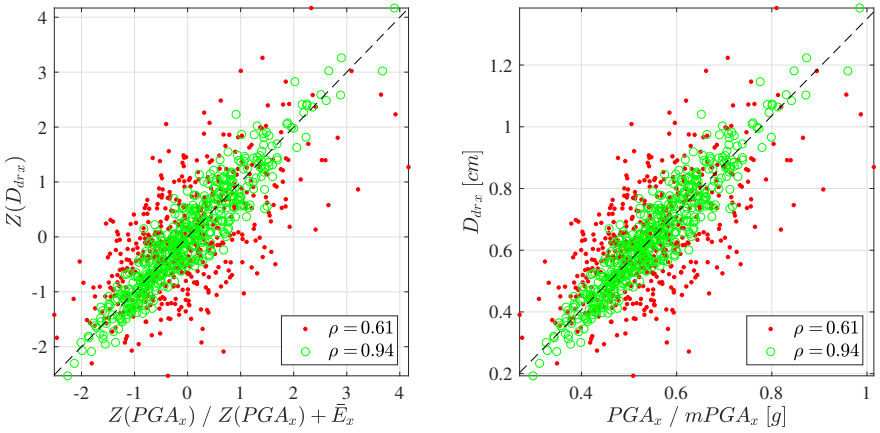

Figure 6.45: Scatter plots of $n_s = 500$ samples at 3rd storey: $(Z(PGA_x), Z(D_{drx}))$ red dots, $(Z(PGA_x) + \bar{E}_x, Z(D_{drx}))$ green circles (left panel); (PGA_x, D_{drx}) red dots, $(mPGA_x, D_{drx})$ green circles (right panel) - linear analysis.

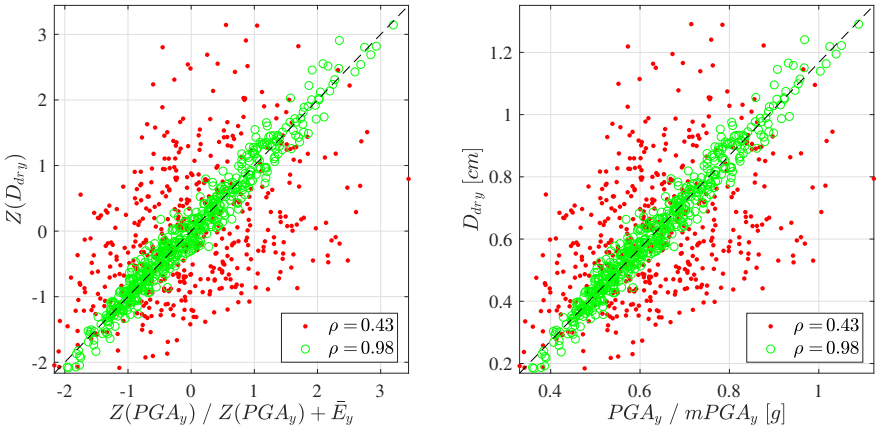

Figure 6.46: Scatter plots of $n_s = 500$ samples at 3rd storey: $(Z(PGA_y), Z(D_{dry}))$ red dots, $(Z(PGA_y) + \bar{E}_y, Z(D_{dry}))$ green circles (left panel); (PGA_y, D_{dry}) red dots, $(mPGA_y, D_{dry})$ green circles (right panel) - linear analysis.

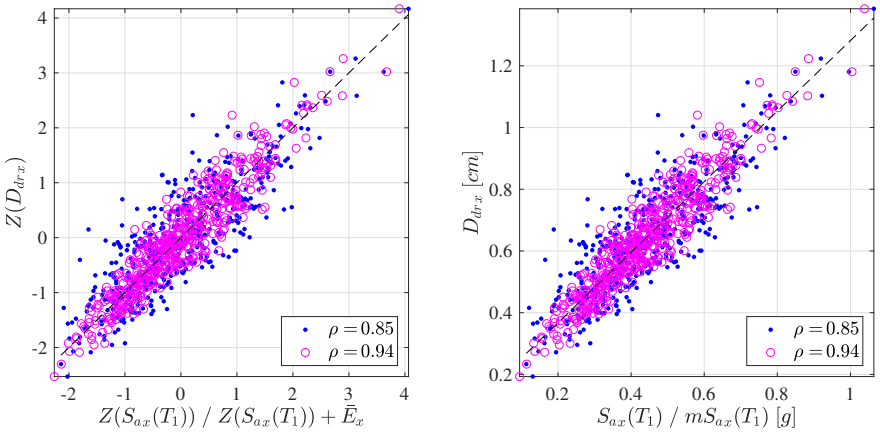

Figure 6.47: Scatter plots of $n_s = 500$ samples at 3rd storey: $(Z(S_{ax}(T_1)), Z(D_{drx}))$ blue dots, $(Z(S_{ax}(T_1)) + \bar{E}_x, Z(D_{drx}))$ magenta circles (left panel); $(S_{ax}(T_1), D_{drx})$ blue dots, $(mS_{ax}(T_1), D_{drx})$ magenta circles (right panel) - linear analysis.

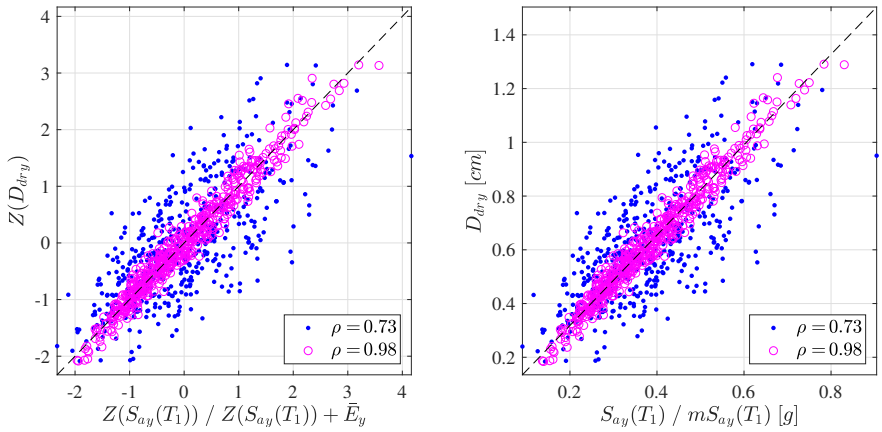

Figure 6.48: Scatter plots of $n_s = 500$ samples at 3rd storey: $(Z(S_{ay}(T_1)), Z(D_{dry}))$ blue dots, $(Z(S_{ay}(T_1)) + \bar{E}_y, Z(D_{dry}))$ magenta circles (left panel); $(S_{ay}(T_1), D_{dry})$ blue dots, $(mS_{ay}(T_1), D_{dry})$ magenta circles (right panel) - linear analysis.

space. In general, the change in color (red to green or blue to magenta) describes the situation before and after the correlation (dependence) correction. Results for the first and second storey are reported in Figures B.137 - B.142 and Figures B.139 - B.144, respectively.

The top panels of Figures 6.49 - 6.52 show the computed $n_s = 500$ samples of the distance from the perfect correlation $e_{in} = z(d_{drin}) - z(im_{q_{in}})$, $q = 1, 2$, and the average distance $\bar{e}_{in}$ by Eq. (4.6) (with $m = 3$ and $k = 1$), $i = 1, \ldots, n_s$ and $n = x, y$, for the third storey. In the bottom, the quantities $e_{in} - \bar{e}_{in}$, $i = 1, \ldots, n_s$ and $n = x, y$, are reported in yellow. In Figures 6.49 and 6.50 (Figures 6.51 and 6.52), the red (blue) dots are the distances from the perfect correlation computed by the samples of $Z(PGA_n)$ $(Z(S_{an}(T_1)))$, $n = x, y$, and the continuous black line, the respective average distances. These figures describe satisfactory results for the two considered intensity measures.

The comparison of the probability densities and first four moments estimated for the original intensity measures PGA_n and their modified versions $mPGA_n$, $n = x, y$, are shown in Figures 6.53 and 6.54. The PDFs of $S_{an}(T_1)$ and $mS_{an}(T_1)$, $n = x, y$, are reported in Figures 6.55 and 6.56.

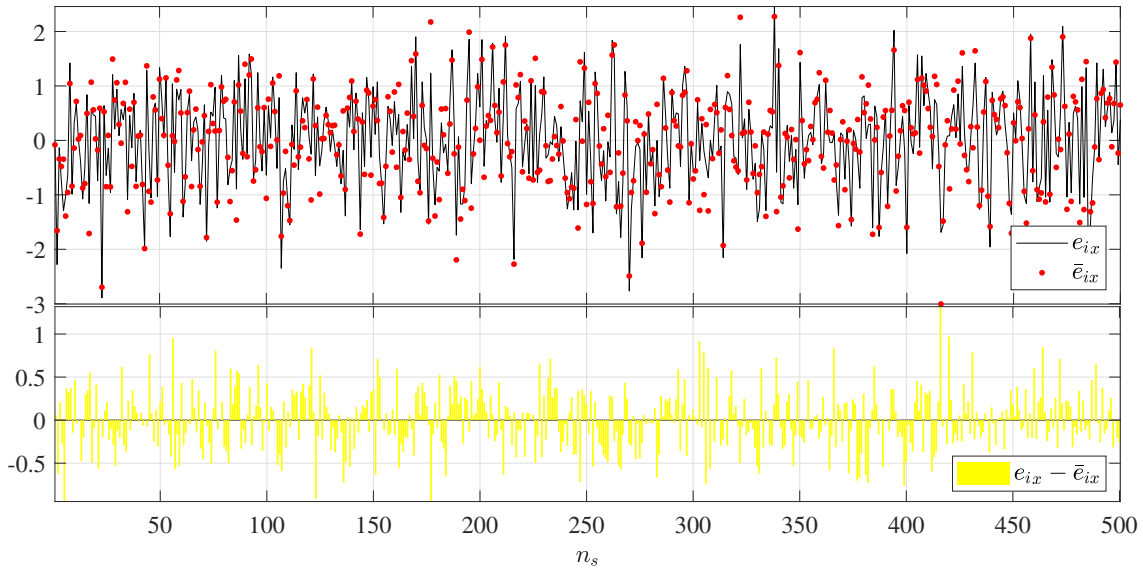

Figure 6.49: Computed distances of $n_s = 500$ samples at 3rd storey considering D_{drx} and PGA_x: distance from the perfect correlation e_{ix} versus average distance $\bar{e}_{ix}$, $i = 1, \ldots, n_s$ (top panel); difference $e_{ix} - \bar{e}_{ix}$, $i = 1, \ldots, n_s$ (bottom panel) - linear analysis.

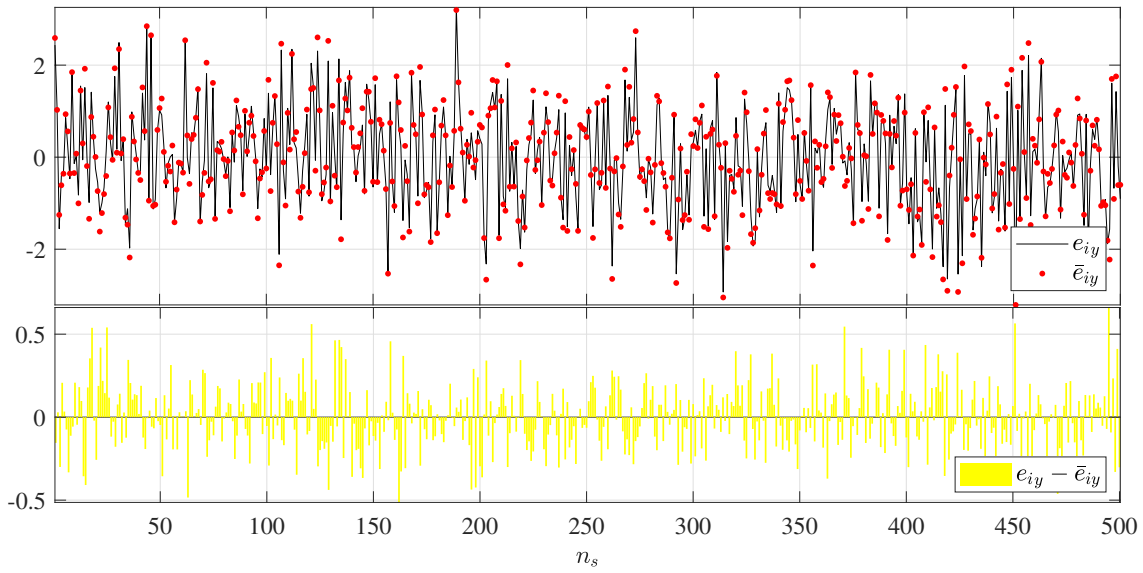

Figure 6.50: Computed distances of $n_s = 500$ samples at 3rd storey considering D_{drx} and PGA_y: distance from the perfect correlation e_{iy} versus average distance $\bar{e}_{iy}$, $i = 1, \ldots, n_s$ (top panel); difference $e_{iy} - \bar{e}_{iy}$, $i = 1, \ldots, n_s$ (bottom panel) - linear analysis.

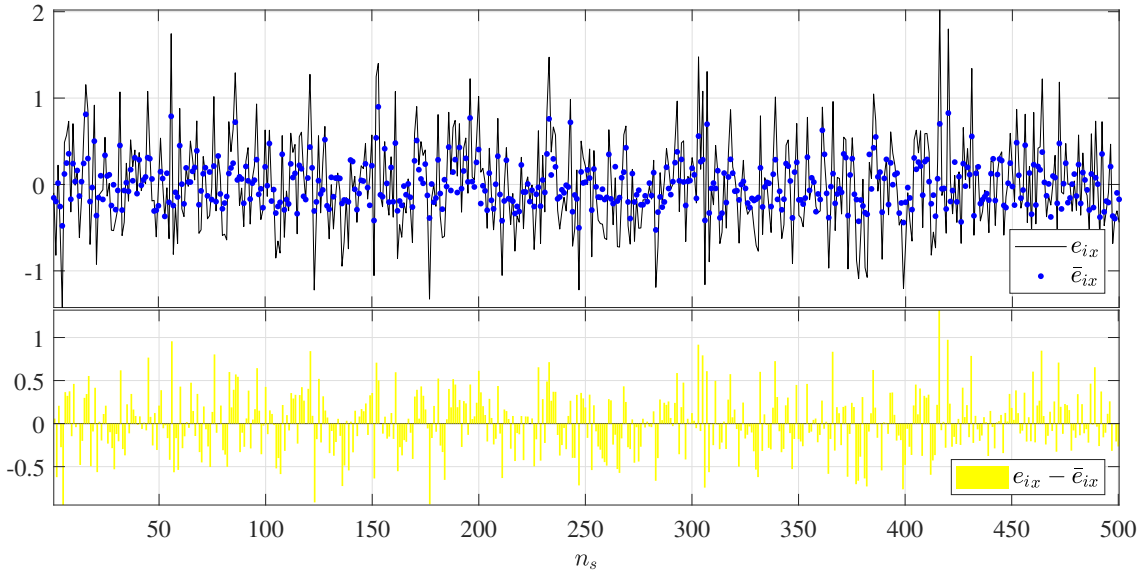

Figure 6.51: Computed distances of $n_s = 500$ samples at 3rd storey considering D_{drx} and $S_{ax}(T_1)$: distance from the perfect correlation e_{ix} versus average distance $\bar{e}_{ix}$, $i = 1, \ldots, n_s$ (top panel); difference $e_{ix} - \bar{e}_{ix}$, $i = 1, \ldots, n_s$ (bottom panel) - linear analysis.

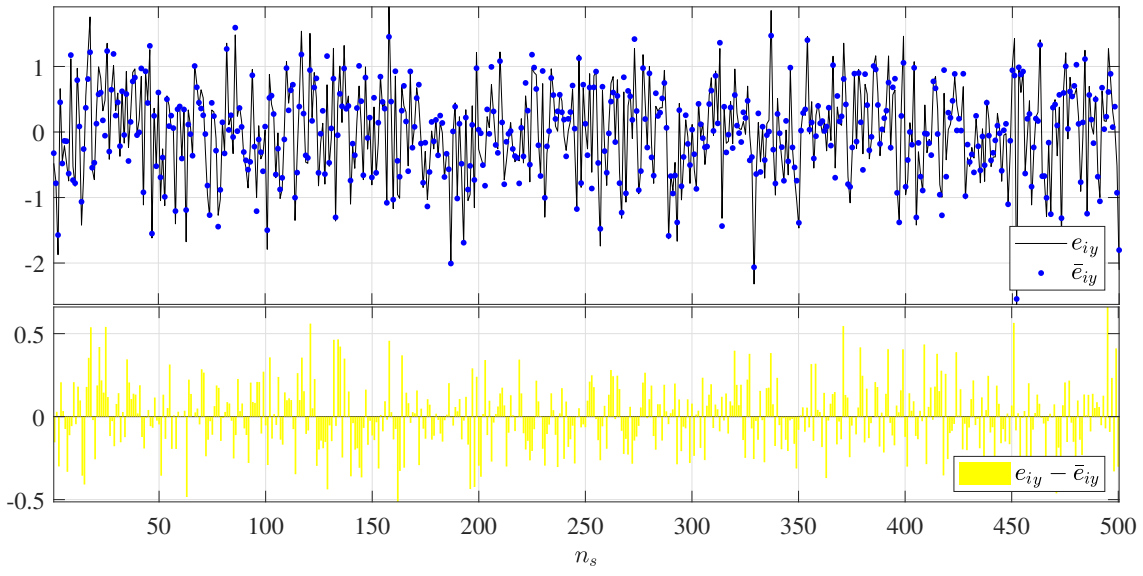

Figure 6.52: Computed distances of $n_s = 500$ samples at 3rd storey considering D_{drx} and $S_{ay}(T_1)$: distance from the perfect correlation e_{iy} versus average distance $\bar{e}_{iy}$, $i = 1, \ldots, n_s$ (top panel); difference $e_{iy} - \bar{e}_{iy}$, $i = 1, \ldots, n_s$ (bottom panel) - linear analysis.

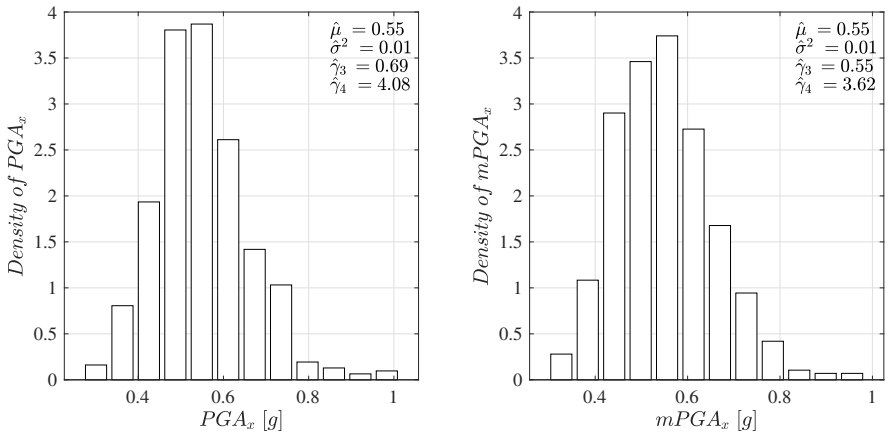

Figure 6.53: Estimated PDF for $n_s = 500$ samples of PGA_x (left panel) and $mPGA_x$ (right panel) computed with $m = 3$ and $k = 1$.

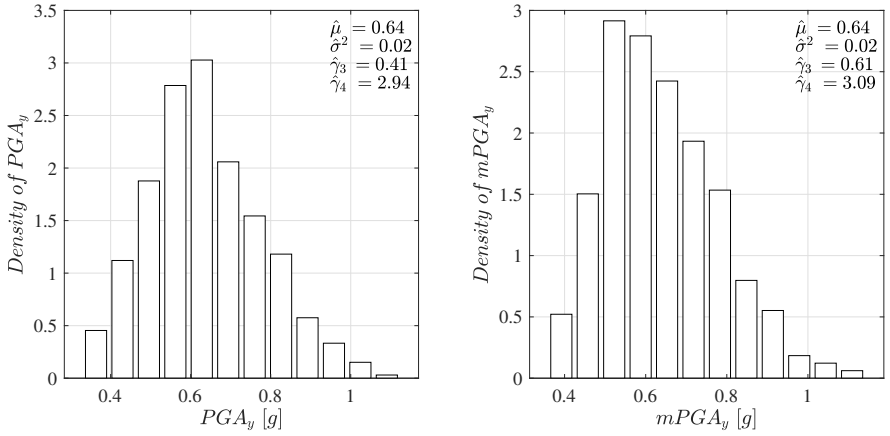

Figure 6.54: Estimated PDF for $n_s = 500$ samples of PGA_y (left panel) and $mPGA_y$ (right panel) computed with $m = 3$ and $k = 1$.

It is worth noting that, the modified intensity measures, mIM_{q_n}, $q = 1, 2$ and $n = x, y$, evaluate on three demand parameters of interest, i.e. $m = 3$, (right panels of Figures 6.53 - 6.56) tend to have a much similar PDFs to that of the original intensity measures IM_{q_n} (left on Figures 6.53 - 6.56 or Figures 6.41 - 6.44), rather than those obtained from twelve demand parameters ($m = 12$). This aspect is inherent in the definition of mIM (Eq. (4.7)).

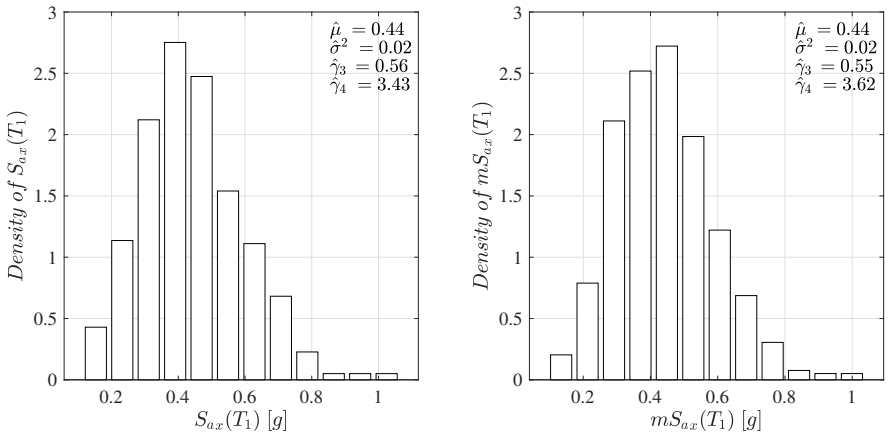

Figure 6.55: Estimated PDF for $n_s = 500$ samples of $S_{ax}(T_1)$ (left panel) and $mS_{ax}(T_1)$ (right panel) computed with $m = 3$ and $k = 1$.

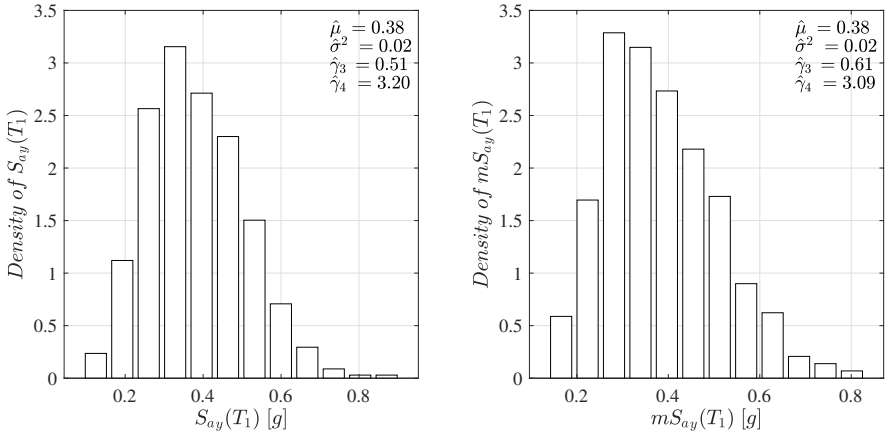

Figure 6.56: Estimated PDF for $n_s = 500$ samples of $S_{ay}(T_1)$ (left panel) and $mS_{ay}(T_1)$ (right panel) computed with $m = 3$ and $k = 1$.

6.4.2 Nonlinear behaviour

The nonlinear behaviour for the school building model are considered in this subsection. Scatter plots of $n_s = 500$ samples (before and after the correlation improvement) for IM_{q_n}, $q = 1, 2$, and the maximum absolute displacement for different level intensity input $D_{d_n}^{(l)}$, $l = 1, 2, 3$ ($\xi_l = 1, 1.5, 2$) and $n = x, y$, at node #9 (Figure 6.14), i.e. $D_{d_n}^{(l)} = D_{d_n}^{(j,l)}$ with $j = 9$, are shown in Figures 6.57 - 6.64. In these figures, from left to right panel the level intensity of input process, i.e. l and associated ξ_l, increases ($\xi_l \boldsymbol{A}(t)$). In particular, Figures 6.57 and 6.59 (Figures 6.61 and 6.63) show the disper-

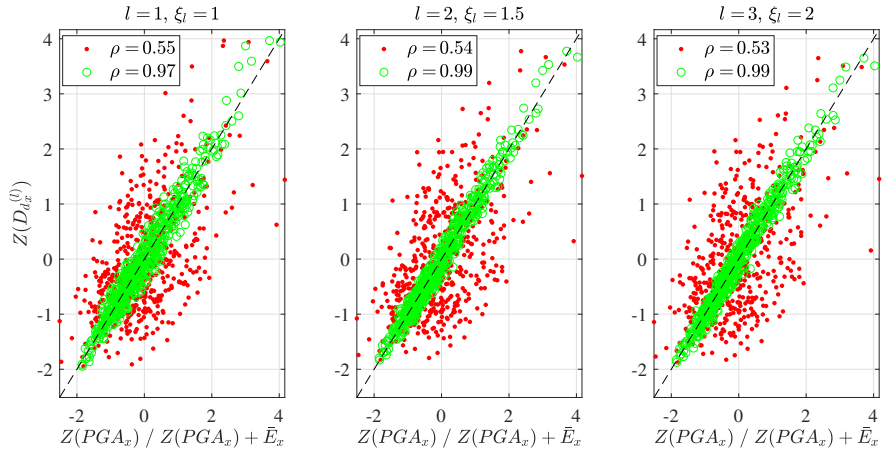

Figure 6.57: Scatter plots of $n_s = 500$ samples of $(Z(PGA_x), Z(D_{d_x}^{(l)}))$ red dots, $(Z(PGA_x) + \bar{E}_x, Z(D_{d_x}^{(l)}))$ green circles at node #9: $l = 1$ with $\xi_l = 1$ (left panel); $l = 2$ with $\xi_l = 1.5$ (center panel); $l = 3$ with $\xi_l = 2$ (right panel).

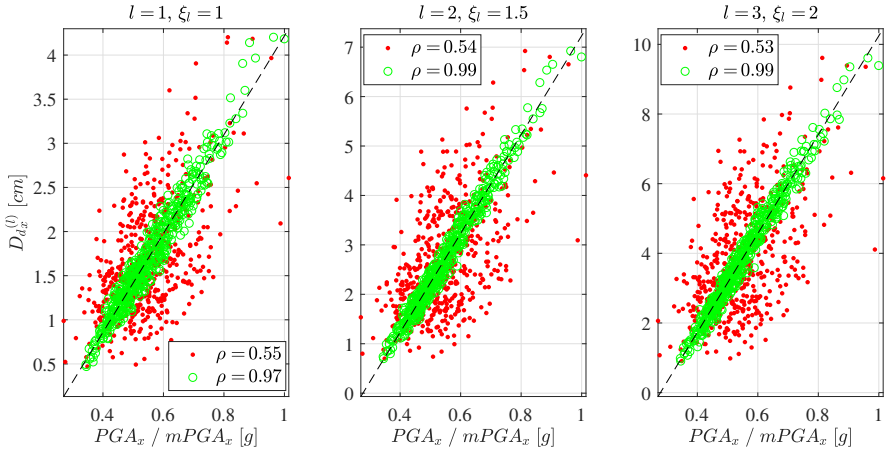

Figure 6.58: Scatter plots of $n_s = 500$ samples of $(PGA_x, D_{d_x}^{(l)})$ red dots, $(PGA_x + \bar{E}_x, D_{d_x}^{(l)})$ green circles at node #9: $l = 1$ with $\xi_l = 1$ (left panel); $l = 2$ with $\xi_l = 1.5$ (center panel); $l = 3$ with $\xi_l = 2$ (right panel).

sion of $(Z(PGA_n), Z(D_{d_n}^{(l)}))$ $((Z(S_{an}(T_1)), Z(D_{d_n}^{(l)})))$ and $(Z(PGA_n) + \bar{E}_n, Z(D_{d_n}^{(l)}))$ $((Z(S_{an}(T_1)) + \bar{E}_n, Z(D_{d_n}^{(l)})))$, while back into the normal space representation the Figures 6.58 and 6.60 (Figures 6.62 and 6.64) report the dispersion of $(PGA_n, D_{d_n}^{(l)})$ $((S_{an}(T_1), D_{d_n}^{(l)}))$ and $(mPGA_n, D_{d_n}^{(l)})$ $((mS_{an}(T_1),\ D_{d_n}^{(l)}))$, $l = 1, \ldots, 3$ and $n = x, y$. The changes in color from red to green (blue to magenta) refer to the dispersion before and after the dependence improvement. In reference to the situation before the correlation correction, i.e. red or blue dots, the dispersion increases with increasing the intensity level ξ_l.

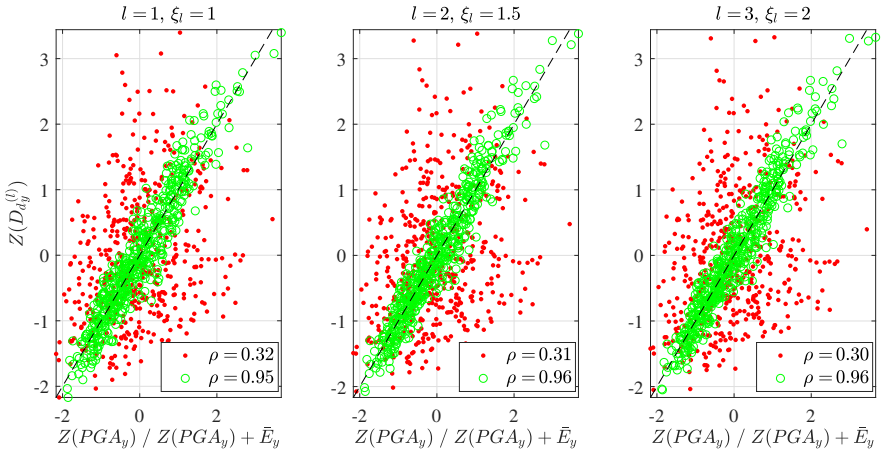

Figure 6.59: Scatter plots of $n_s = 500$ samples of $(Z(PGA_y), Z(D_{d_y}^{(l)}))$ red dots, $(Z(PGA_y)+\bar{E}_y, Z(D_{d_y}^{(l)}))$ green circles at node #9: $l = 1$ with $\xi_l = 1$ (left panel); $l = 2$ with $\xi_l = 1.5$ (center panel); $l = 3$ with $\xi_l = 2$ (right panel).

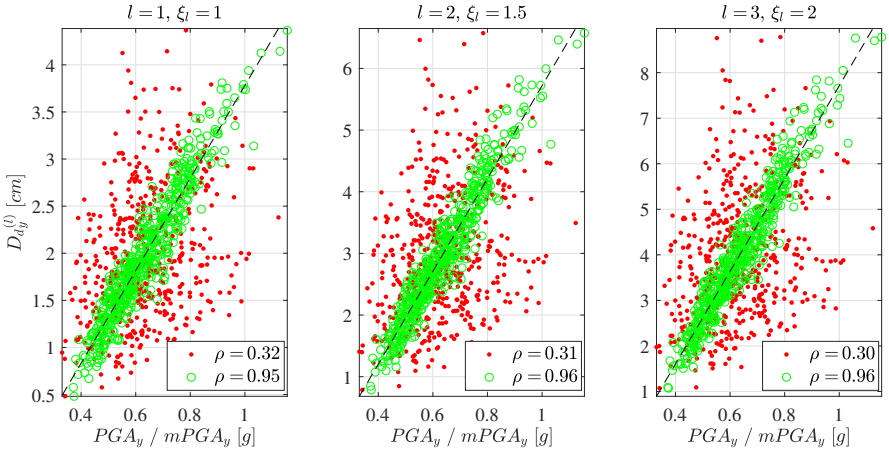

Figure 6.60: Scatter plots of $n_s = 500$ samples of $(PGA_y, D_{d_y}^{(l)})$ red dots, $(PGA_y + \bar{E}_y, D_{d_y}^{(l)})$ green circles at node #9: $l = 1$ with $\xi_l = 1$ (left panel); $l = 2$ with $\xi_l = 1.5$ (center panel); $l = 3$ with $\xi_l = 2$ (right panel).

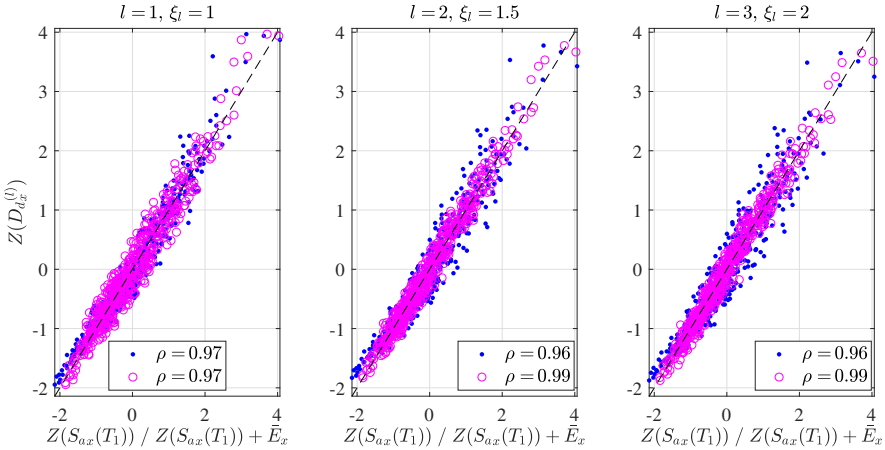

Figure 6.61: Scatter plots of $n_s = 500$ samples of $(Z(S_{ax}(T_1)), Z(D_{d_x}^{(l)}))$ blue dots, $(Z(S_{ax}(T_1)) + \bar{E}_x, Z(D_{d_x}^{(l)}))$ magenta circles at node #9: $l = 1$ with $\xi_l = 1$ (left panel); $l = 2$ with $\xi_l = 1.5$ (center panel); $l = 3$ with $\xi_l = 2$ (right panel).

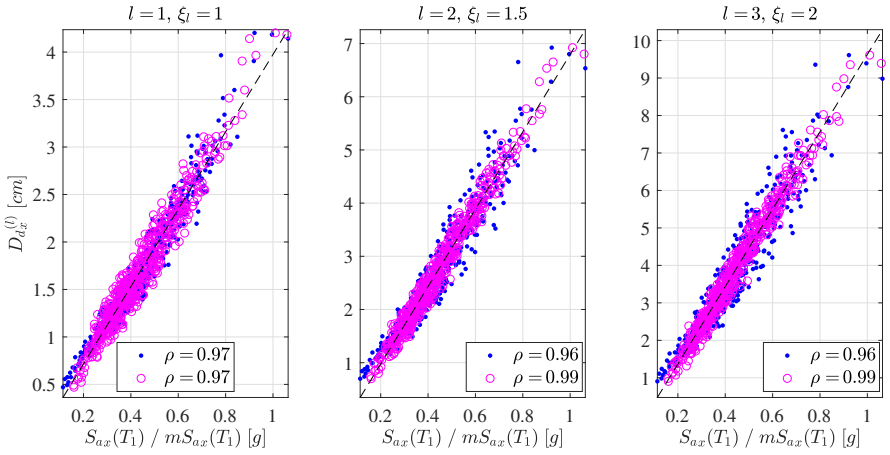

Figure 6.62: Scatter plots of $n_s = 500$ samples of $(S_{ax}(T_1), D_{dx}^{(l)})$ blue dots, $(S_{ax}(T_1)+\bar{E}_x, D_{dx}^{(l)})$ magenta circles at node #9: $l = 1$ with $\xi_l = 1$ (left panel); $l = 2$ with $\xi_l = 1.5$ (center panel); $l = 3$ with $\xi_l = 2$ (right panel).

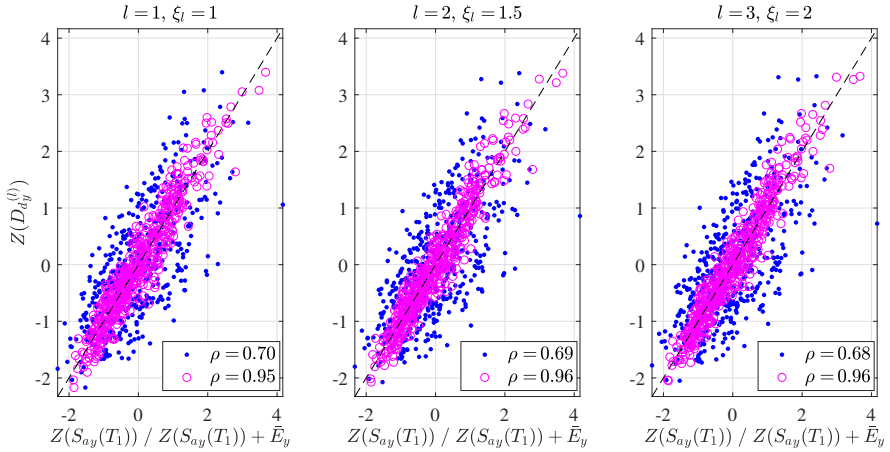

Figure 6.63: Scatter plots of $n_s = 500$ samples of $(Z(S_{ay}(T_1)), Z(D_{dy}^{(l)}))$ blue dots, $(Z(S_{ay}(T_1))+\bar{E}_y, Z(D_{dy}^{(l)}))$ magenta circles at node #9: $l = 1$ with $\xi_l = 1$ (left panel); $l = 2$ with $\xi_l = 1.5$ (center panel); $l = 3$ with $\xi_l = 2$ (right panel).

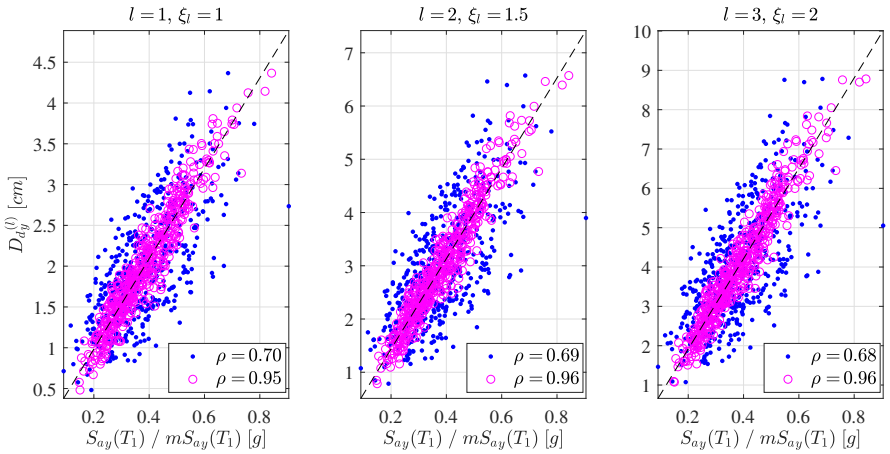

Figure 6.64: Scatter plots of $n_s = 500$ samples of $(S_{ay}(T_1), D_{dy}^{(l)})$ blue dots, $(S_{ay}(T_1)+\bar{E}_y, D_{dy}^{(l)})$ magenta circles at node #9: $l = 1$ with $\xi_l = 1$ (left panel); $l = 2$ with $\xi_l = 1.5$ (center panel); $l = 3$ with $\xi_l = 2$ (right panel).

Similar results are obtained by considering other demand parameters of interest at different level intensity, i.e. $D_{d_n}^{(l)} = D_{d_n}^{(j,l)}$, $j = 4, 7, 10$, $l = 1, 2, 3$ and $n = x, y$, they are reported in Figures B.113 - B.136.

On the top panels of Figures 6.65 - 6.76, it is possible to see the computed $n_s = 500$ samples of the distances $e_{in}^{(l)} = z(d_{d_{in}}^{(l)}) - z(im_{q_{in}})$, $q = 1, 2$ and $l = 1, 2, 3$, and the average distance $\bar{e}_{in}$ by Equation (4.6) considering $m = 12$ and $k = 3$, $i = 1, \ldots, n_s$ and $n = x, y$, for the node #9. The red (blue) dots are the average distances, $\bar{e}_{in}$, and the black line, the distances from perfect correlation computed by considering sample of $Z(D_{d_n}^{(l)})$ and $Z(PGA_n)$ ($Z(S_{an}(T_1))$), $l = 1, 2, 3$ and $n = x, y$. The bottom panels show the quantities $e_{in}^{(l)} - \bar{e}_{in}$.

In general, after the correction, the correlation coefficient ρ at the first panels from left of Figures 6.57 - 6.64 (i.e. $l = \xi_l = 1$) results lower that those in second and third panels. This is due to the fact that the correlation at $l = 1$ is sacrificed to improve the lower one at higher intensity levels ($l = 2, 3$). This aspect is further marked in the Figures 6.66 - 6.67, 6.69 - 6.70, 6.72 - 6.73, and 6.75 - 6.76, where the red or blue dots match satisfactory with the continuous black line.

Figures 6.77 and 6.78 report the probability density function and first four statical moments estimated of the original intensity measure PGA_n, $n = x, y$, (left panels) and of their modified versions $mPGA_n$ (right panels). In a respective way, the Figures 6.79 and 6.80 refer to $S_{an}(T_1)$ and $mS_{an}(T_1)$, $n = x, y$, (left and right panels).

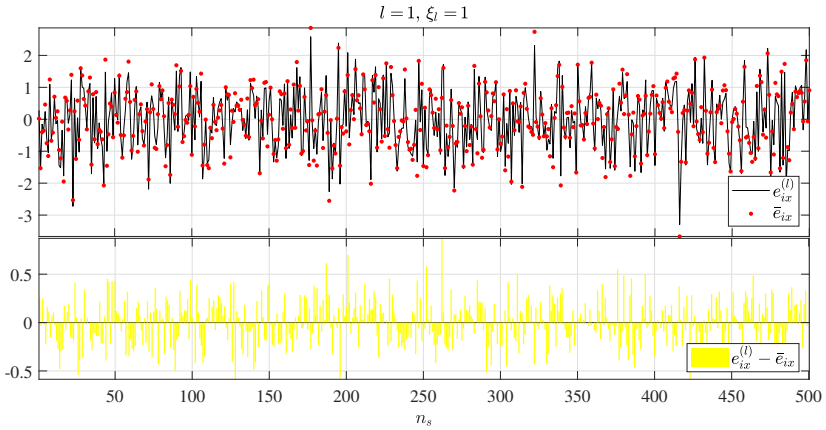

Figure 6.65: Computed distances of $n_s = 500$ samples at node #9 considering $D_{d_x}^{(l)}$, $l = 1$, and PGA_x: distance from the perfect correlation $e_{ix}^{(l)}$ versus average distance $\bar{e}_{ix}$, $l = 1$ and $i = 1, \ldots, n_s$ (top panel); difference $e_{ix}^{(l)} - \bar{e}_{ix}$, $l = 1$ and $i = 1, \ldots, n_s$ (bottom panel) - nonlinear analysis.

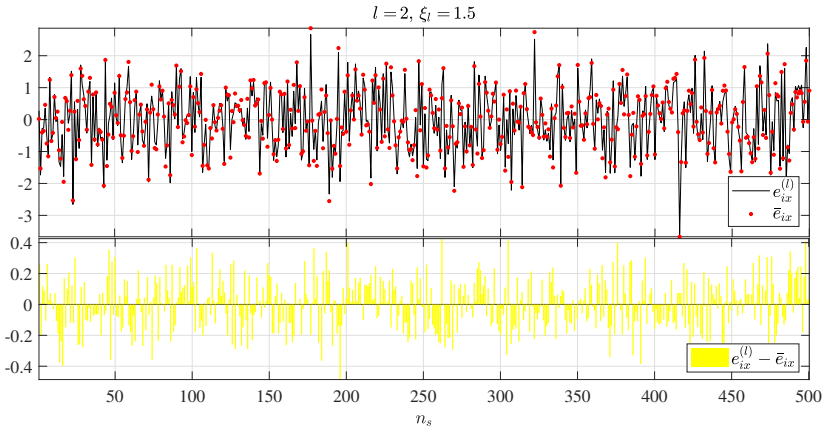

Figure 6.66: Computed distances of $n_s = 500$ samples at node #9 considering $D_{d_x}^{(l)}$, $l = 1.5$, and PGA_x: distance from the perfect correlation $e_{ix}^{(l)}$ versus average distance $\bar{e}_{ix}$, $l = 1.5$ and $i = 1, \ldots, n_s$ (top panel); difference $e_{ix}^{(l)} - \bar{e}_{ix}$, $l = 1.5$ and $i = 1, \ldots, n_s$ (bottom panel) - nonlinear analysis.

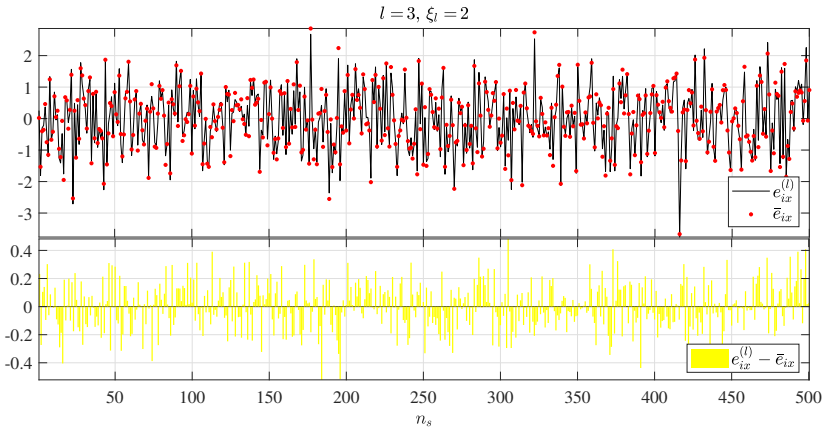

Figure 6.67: Computed distances of $n_s = 500$ samples at node #9 considering $D_{d_x}^{(l)}$, $l = 2$, and PGA_x: distance from the perfect correlation $e_{ix}^{(l)}$ versus average distance $\bar{e}_{ix}$, $l = 2$ and $i = 1, \ldots, n_s$ (top panel); difference $e_{ix}^{(l)} - \bar{e}_{ix}$, $l = 2$ and $i = 1, \ldots, n_s$ (bottom panel) - nonlinear analysis.

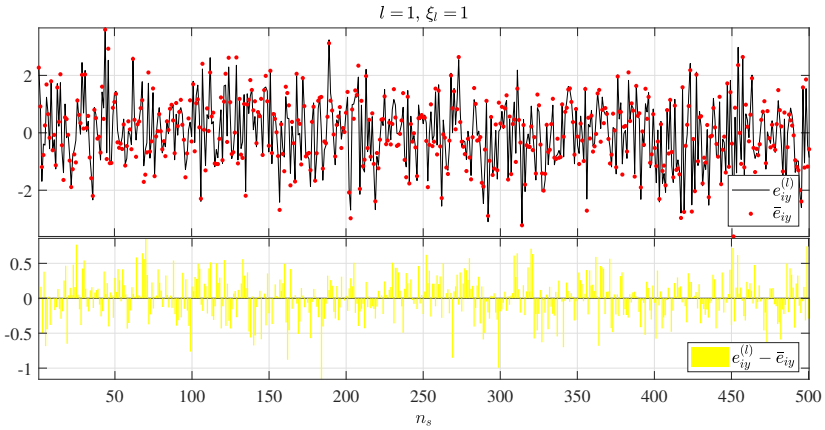

Figure 6.68: Computed distances of $n_s = 500$ samples at node #9 considering $D_{d_y}^{(l)}$, $l = 1$, and PGA_y: distance from the perfect correlation $e_{iy}^{(l)}$ versus average distance $\bar{e}_{iy}$, $l = 1$ and $i = 1, \ldots, n_s$ (top panel); difference $e_{iy}^{(l)} - \bar{e}_{iy}$, $l = 1$ and $i = 1, \ldots, n_s$ (bottom panel) - nonlinear analysis.

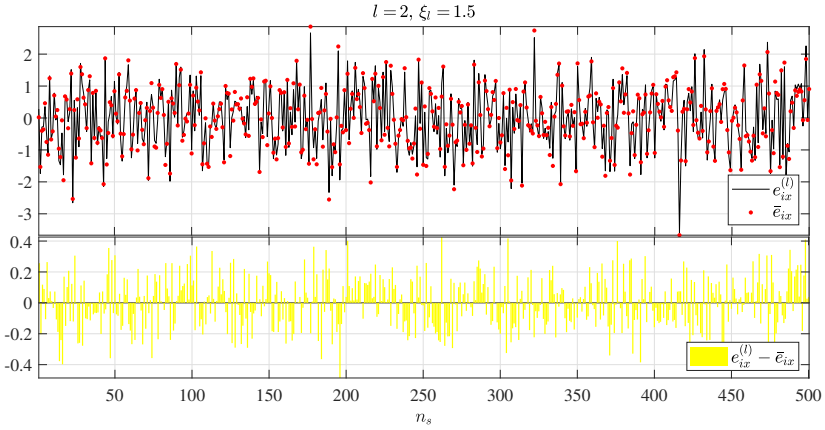

Figure 6.69: Computed distances of $n_s = 500$ samples at node #9 considering $D_{d_y}^{(l)}$, $l = 1.5$, and PGA_y: distance from the perfect correlation $e_{iy}^{(l)}$ versus average distance $\bar{e}_{iy}$, $l = 1.5$ and $i = 1, \ldots, n_s$ (top panel); difference $e_{iy}^{(l)} - \bar{e}_{iy}$, $l = 1.5$ and $i = 1, \ldots, n_s$ (bottom panel) - nonlinear analysis.

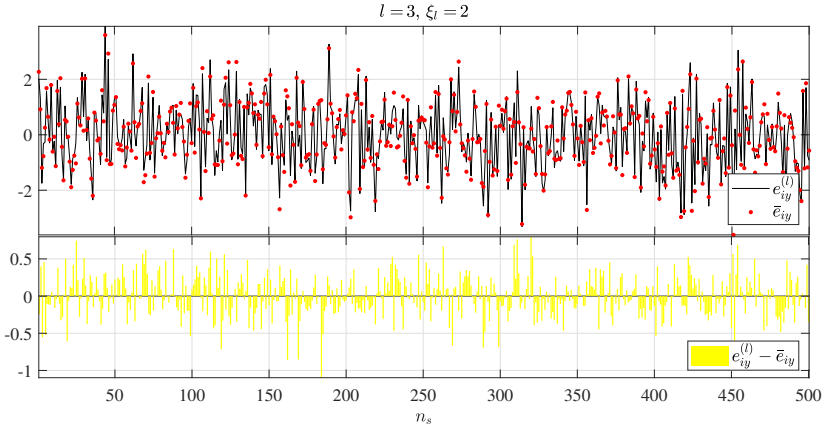

Figure 6.70: Computed distances of $n_s = 500$ samples at node #9 considering $D_{d_y}^{(l)}$, $l = 2$, and PGA_y: distance from the perfect correlation $e_{iy}^{(l)}$ versus average distance $\bar{e}_{iy}$, $l = 2$ and $i = 1, \ldots, n_s$ (top panel); difference $e_{iy}^{(l)} - \bar{e}_{iy}$, $l = 2$ and $i = 1, \ldots, n_s$ (bottom panel) - nonlinear analysis.

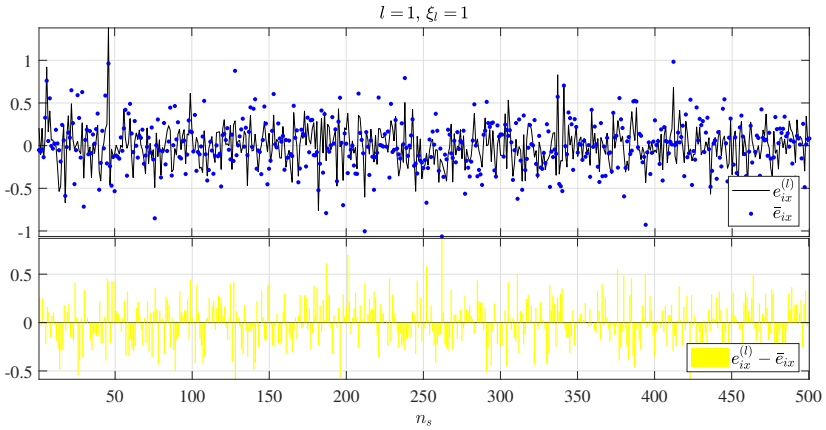

Figure 6.71: Computed distances of $n_s = 500$ samples at node #9 considering $D_{d_x}^{(l)}$, $l = 1$, and $S_{ax}(T_1)$: distance from the perfect correlation $e_{ix}^{(l)}$ versus average distance $\bar{e}_{ix}$, $l = 1$ and $i = 1, \ldots, n_s$ (top panel); difference $e_{ix}^{(l)} - \bar{e}_{ix}$, $l = 1$ and $i = 1, \ldots, n_s$ (bottom panel) - nonlinear analysis.

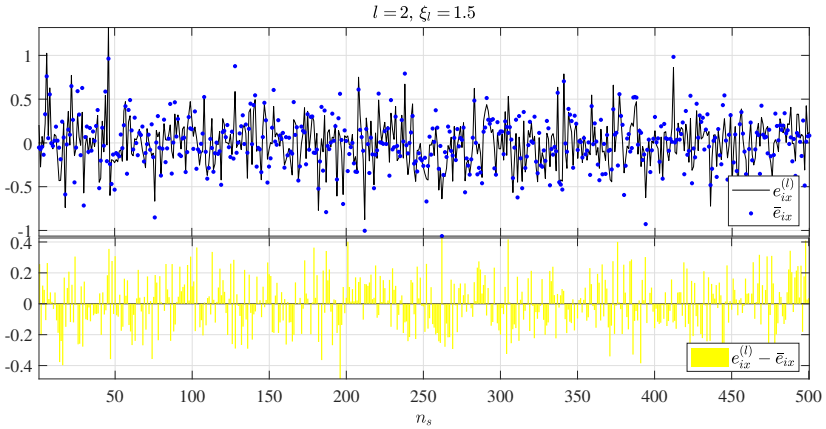

Figure 6.72: Computed distances of $n_s = 500$ samples at node #9 considering $D_{d_x}^{(l)}$, $l = 1.5$, and $S_{ax}(T_1)$: distance from the perfect correlation $e_{ix}^{(l)}$ versus average distance $\bar{e}_{ix}$, $l = 1.5$ and $i = 1, \ldots, n_s$ (top panel); difference $e_{ix}^{(l)} - \bar{e}_{ix}$, $l = 1.5$ and $i = 1, \ldots, n_s$ (bottom panel) - nonlinear analysis.

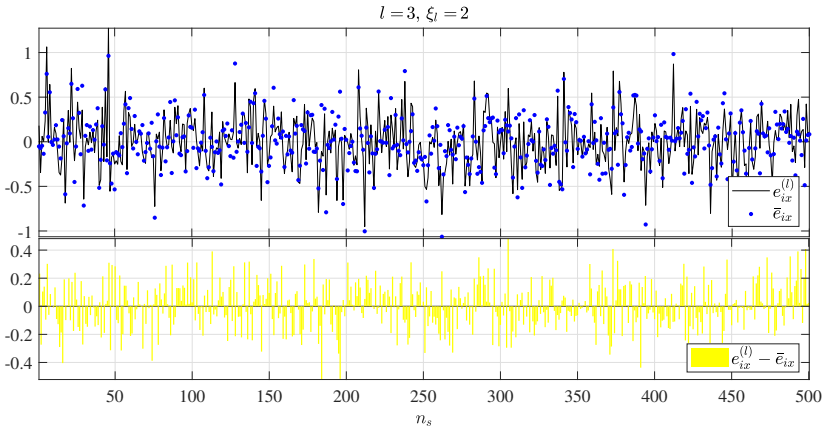

Figure 6.73: Computed distances of $n_s = 500$ samples at node #9 considering $D_{d_x}^{(l)}$, $l = 2$, and $S_{ax}(T_1)$: distance from the perfect correlation $e_{ix}^{(l)}$ versus average distance $\bar{e}_{ix}$, $l = 2$ and $i = 1, \ldots, n_s$ (top panel); difference $e_{ix}^{(l)} - \bar{e}_{ix}$, $l = 2$ and $i = 1, \ldots, n_s$ (bottom panel) - nonlinear analysis.

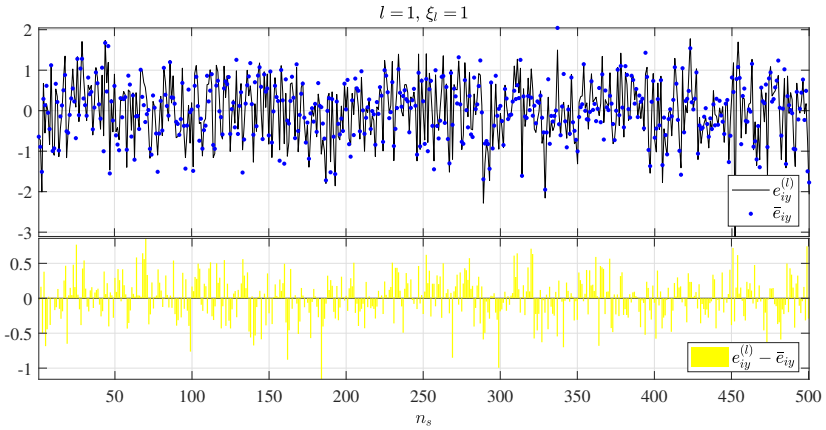

Figure 6.74: Computed distances of $n_s = 500$ samples at node #9 considering $D_{d_y}^{(l)}$, $l = 1$, and $S_{ay}(T_1)$: distance from the perfect correlation $e_{iy}^{(l)}$ versus average distance $\bar{e}_{iy}$, $l = 1$ and $i = 1, \ldots, n_s$ (top panel); difference $e_{iy}^{(l)} - \bar{e}_{iy}$, $l = 1$ and $i = 1, \ldots, n_s$ (bottom panel) - nonlinear analysis.

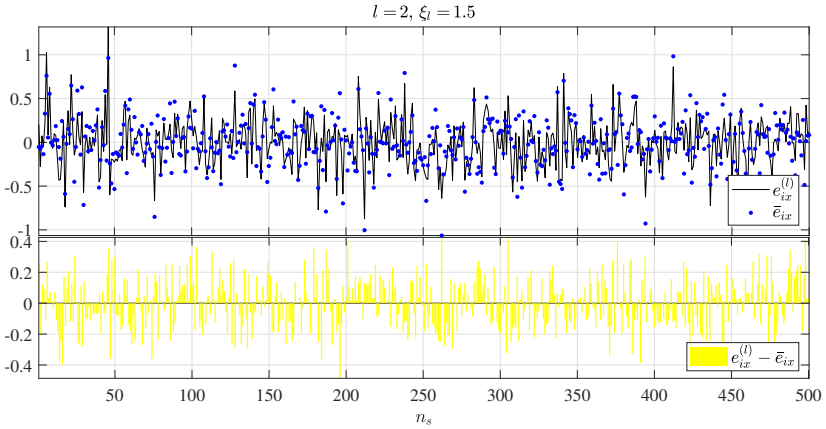

Figure 6.75: Computed distances of $n_s = 500$ samples at node #9 considering $D_{d_y}^{(l)}$, $l = 1.5$, and $S_{ay}(T_1)$: distance from the perfect correlation $e_{iy}^{(l)}$ versus average distance $\bar{e}_{iy}$, $l = 1.5$ and $i = 1, \ldots, n_s$ (top panel); difference $e_{iy}^{(l)} - \bar{e}_{iy}$, $l = 1.5$ and $i = 1, \ldots, n_s$ (bottom panel) - nonlinear analysis.

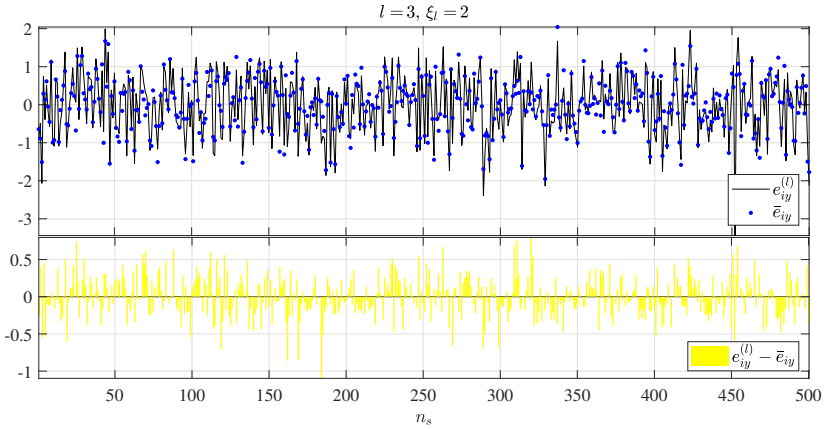

Figure 6.76: Computed distances of $n_s = 500$ samples at node #9 considering $D_{d_y}^{(l)}$, $l = 2$, and $S_{ay}(T_1)$: distance from the perfect correlation $e_{iy}^{(l)}$ versus average distance $\bar{e}_{iy}$, $l = 2$ and $i = 1, \ldots, n_s$ (top panel); difference $e_{iy}^{(l)} - \bar{e}_{iy}$, $l = 2$ and $i = 1, \ldots, n_s$ (bottom panel) - nonlinear analysis.

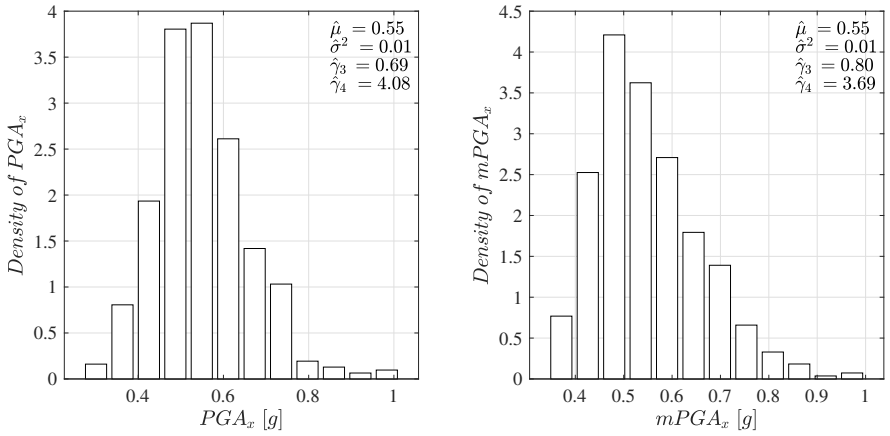

Figure 6.77: Estimated PDF for $n_s = 500$ samples of PGA_x (left panel) and $mPGA_x$ (right panel) computed with $m = 12$ and $k = 3$.

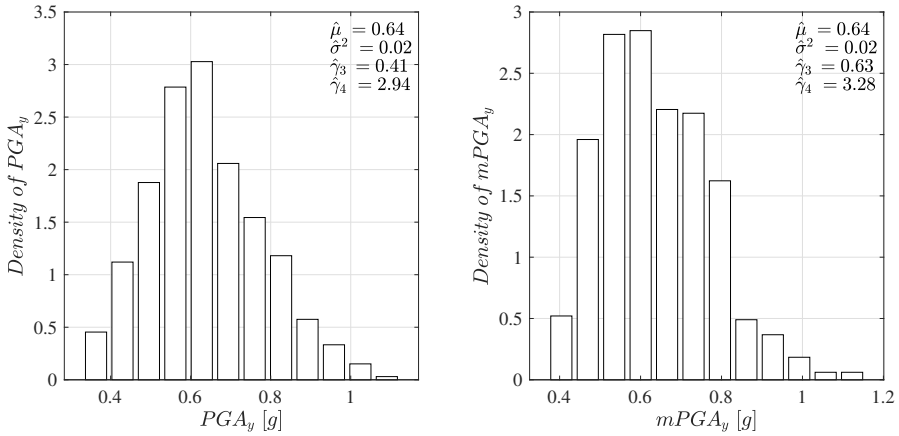

Figure 6.78: Estimated PDF for $n_s = 500$ samples of PGA_y (left panel) and $mPGA_y$ (right panel) computed with $m = 12$ and $k = 3$.

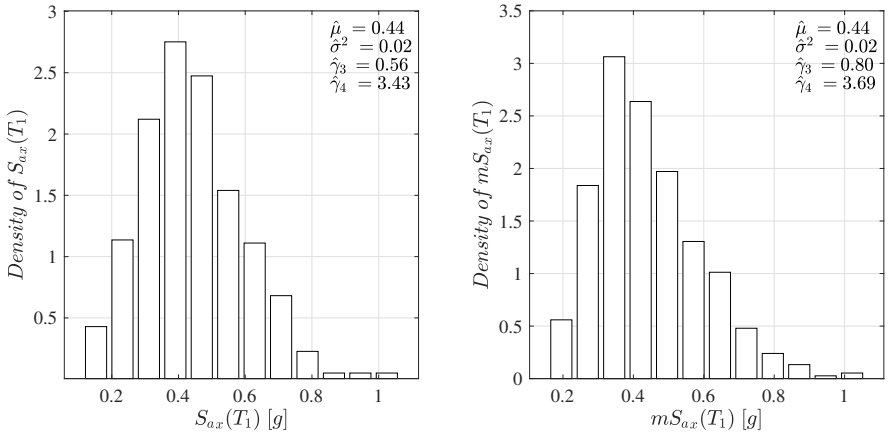

Figure 6.79: Estimated PDF for $n_s = 500$ samples of $S_{ax}(T_1)$ (left panel) and $mS_{ax}(T_1)$ (right panel) computed with $m = 12$ and $k = 3$.

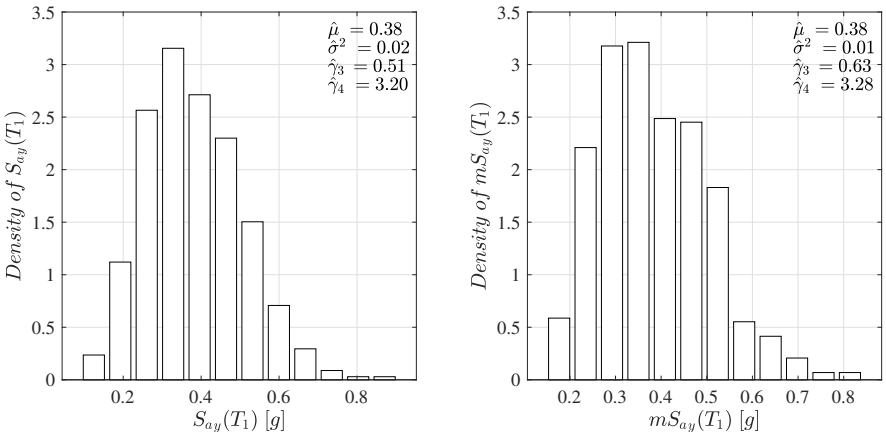

Figure 6.80: Estimated PDF for $n_s = 500$ samples of $S_{ay}(T_1)$ (left panel) and $mS_{ay}(T_1)$ (right panel) computed with $m = 12$ and $k = 3$.

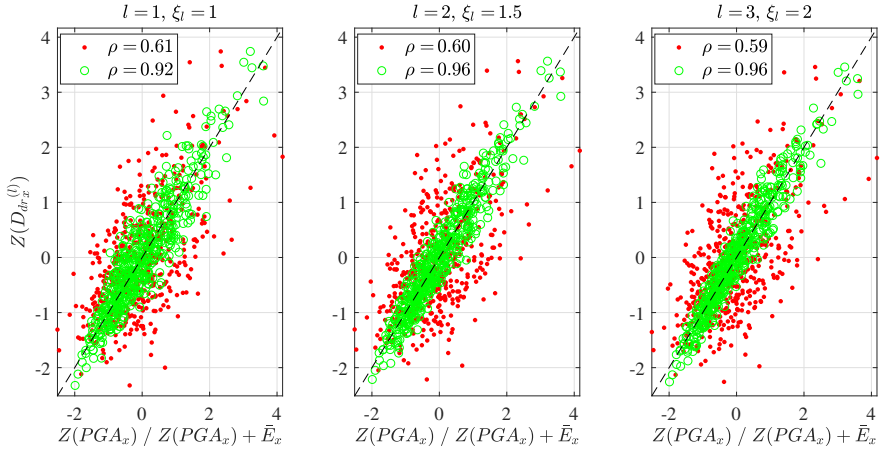

Figure 6.81: Scatter plots of $n_s = 500$ samples of $(Z(PGA_x), Z(D_{drx}^{(l)}))$ red dots, $(Z(PGA_x) + \bar{E}_x, Z(D_{drx}^{(l)}))$ green circles at 3rd storey: $l = 1$ with $\xi_l = 1$ (left panel); $l = 2$ with $\xi_l = 1.5$ (center panel); $l = 3$ with $\xi_l = 2$ (right panel) - nonlinear analysis.

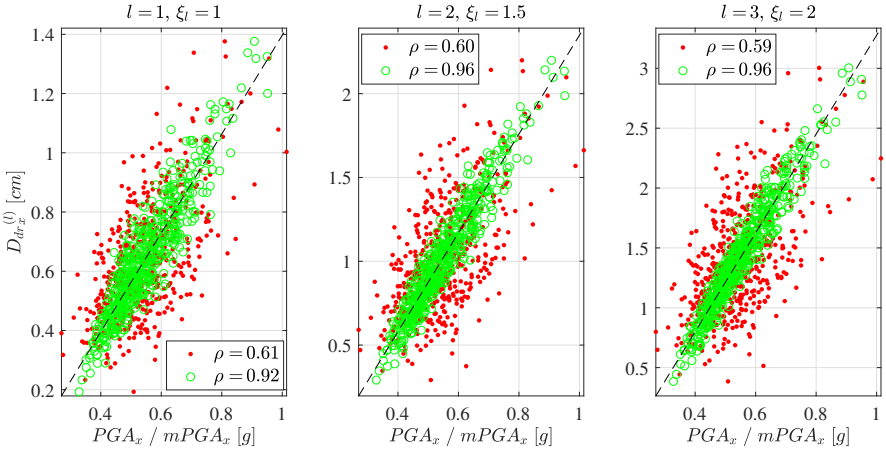

Figure 6.82: Scatter plots of $n_s = 500$ samples of $(PGA_x, D_{drx}^{(l)})$ red dots, $(PGA_x + \bar{E}_x, D_{drx}^{(l)})$ green circles at 3rd storey: $l = 1$ with $\xi_l = 1$ (left panel); $l = 2$ with $\xi_l = 1.5$ (center panel); $l = 3$ with $\xi_l = 2$ (right panel) - nonlinear analysis.

The seismic drifts for the three storey and different intensity level $D_{dr_n}^{(l)} = \{D_{dr_n}^{(1,l)}, D_{dr_n}^{(2,l)}, D_{dr_n}^{(3,l)}\}$ $(m = 3)$, $l = 1, 2, 3$ and $n = x, y$, in following are considered as the demand parameters in the modified intensity measures approach. As an example of the methodology results, Figures 6.81 - 6.88 show the scatter plots of $n_s = 500$ samples of the drift at 3rd storey for different level ξ_l, i.e. $D_{dr_n}^{(l)} = D_{dr_n}^{(3,l)}$, $l = 1, 2, 3$, and $IM_{1n} = PGA_n$ or $IM_{2n} = S_{an}(T_1)$, $n = x, y$. The Figures 6.81, 6.83, 6.85 and 6.87 report the plots in the standardized space (Equations (4.4) and (4.3), with $m = k = 3$), while Figures 6.82, 6.84, 6.86 and 6.88 in normal representation. Results regard the other storey, the first $D_{dr_n}^{(l)} = D_{dr_n}^{(1,l)}$ and the second $D_{dr_n}^{(l)} = D_{dr_n}^{(2,l)}$, $l = 1, 2, 3$, are shown in Figures B.145 - B.160.

Computed $n_s = 500$ samples by Equation (4.5) with $m = k = 3$, i.e. $e_{in}^{(l)} = z(d_{dr_{in}}^{(l)}) - z(im_{q_{in}})$, $q = 1, 2$, $n = x, y$ and $l = 1, 2, 3$, and Equation (4.6), $\bar{e}_{in}$ for the third storey seismic drift, are reported on the top panels of Figures 6.89 - 6.100. In these panels the average distances in red dots are computed from samples of $Z(PGA_n)$, $n = x, y$, instead the those in blue by samples of $Z(S_{an}(T_1))$. The black lines are $e_{in}^{(l)}$, $i = 1, \ldots, n_s$ and $l = 1, 2, 3$. For each figure, in the bottom panel, the difference $e_{in}^{(l)} - \bar{e}_{in}$ on the n_s samples are shown.

The comparison of the PDFs and first four statical moments estimated for the samples of PGA_n, $n = x, y$, and of the computed modified intensity measures $mPGA_n$ with $m = k = 3$ are reported in Figures 6.101 and 6.102, left and right panels, respectively. Instead, the left panels of Figures 6.103 and 6.104 refer to the intensity measures $S_{an}(T_1)$ and the right panels refer to their modified versions $mS_{an}(T_1)$. Once again, it is possible to see as the probability density function of an IM is not substantially different with its modified version mIM obtain by the proposed approach in Section 4.4.

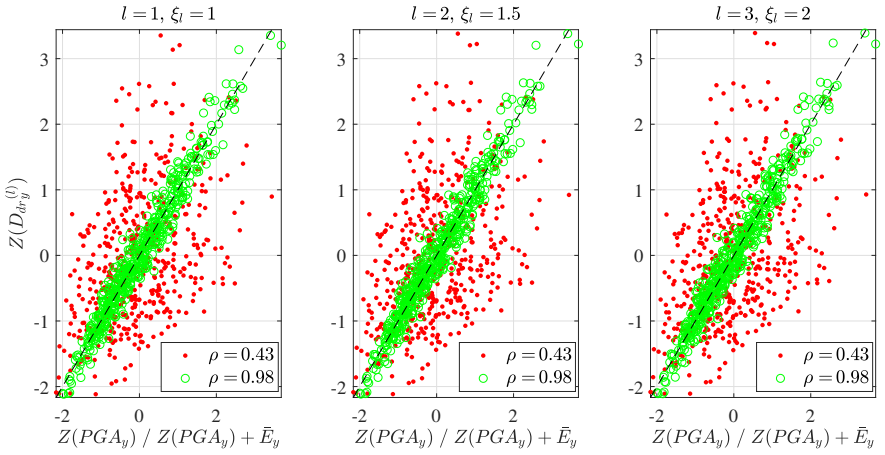

Figure 6.83: Scatter plots of $n_s = 500$ samples of $(Z(PGA_y), Z(D_{dr_y}^{(l)}))$ red dots, $(Z(PGA_y) + \bar{E}_y, Z(D_{dr_y}^{(l)}))$ green circles at 3rd storey: $l = 1$ with $\xi_l = 1$ (left panel); $l = 2$ with $\xi_l = 1.5$ (center panel); $l = 3$ with $\xi_l = 2$ (right panel) - nonlinear analysis.

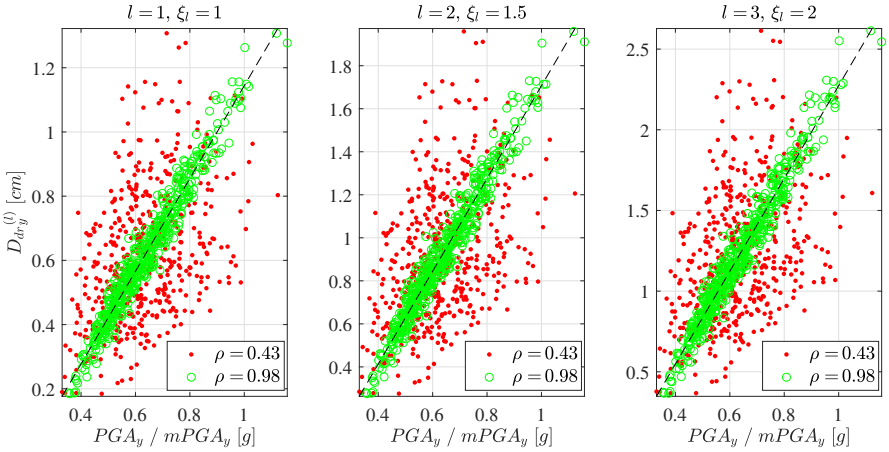

Figure 6.84: Scatter plots of $n_s = 500$ samples of $(PGA_y, D_{dr_y}^{(l)})$ red dots, $(PGA_y + \bar{E}_y, D_{dr_y}^{(l)})$ green circles at 3rd storey: $l = 1$ with $\xi_l = 1$ (left panel); $l = 2$ with $\xi_l = 1.5$ (center panel); $l = 3$ with $\xi_l = 2$ (right panel) - nonlinear analysis.

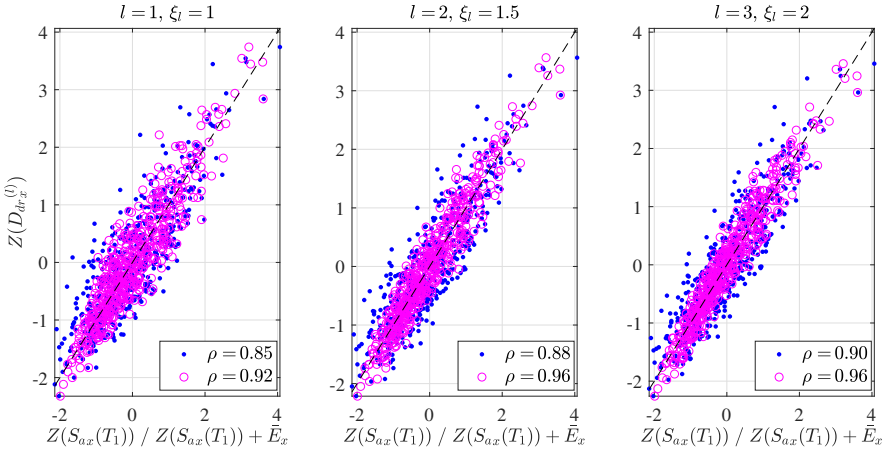

Figure 6.85: Scatter plots of $n_s = 500$ samples of $(Z(S_{ax}(T_1)), Z(D_{dr_x}^{(l)}))$ blue dots, $(Z(S_{ax}(T_1)) + \bar{E}_x, Z(D_{dr_x}^{(l)}))$ magenta circles at 3rd storey: $l = 1$ with $\xi_l = 1$ (left panel); $l = 2$ with $\xi_l = 1.5$ (center panel); $l = 3$ with $\xi_l = 2$ (right panel) - nonlinear analysis.

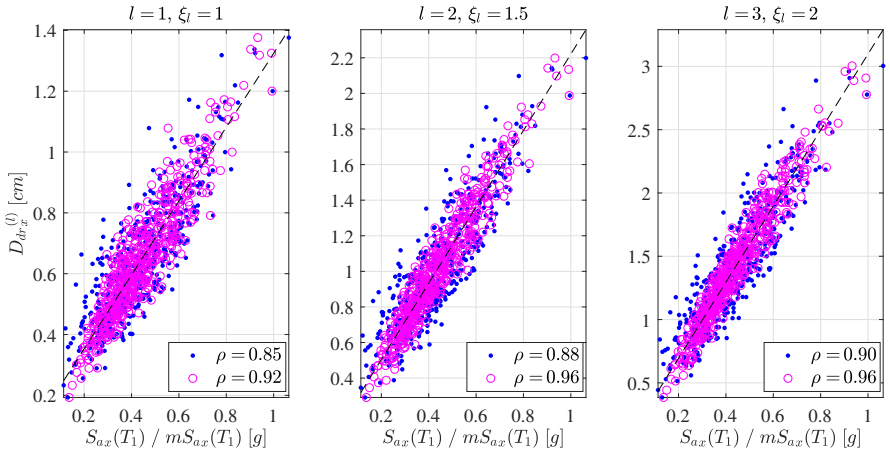

Figure 6.86: Scatter plots of $n_s = 500$ samples of $(S_{ax}(T_1), D_{dr_x}^{(l)})$ blue dots, $(S_{ax}(T_1) + \bar{E}_x, D_{dr_x}^{(l)})$ magenta circles at 3rd storey: $l = 1$ with $\xi_l = 1$ (left panel); $l = 2$ with $\xi_l = 1.5$ (center panel); $l = 3$ with $\xi_l = 2$ (right panel) - nonlinear analysis.

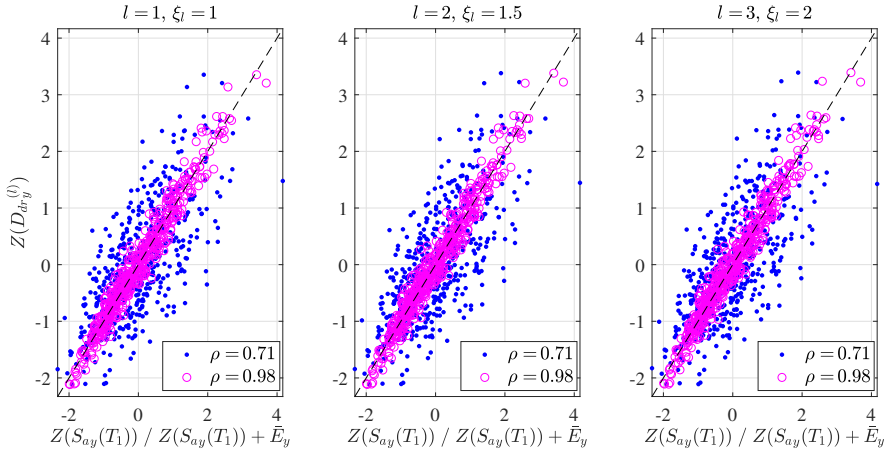

Figure 6.87: Scatter plots of $n_s = 500$ samples of $(Z(S_{ay}(T_1)), Z(D_{dr_y}^{(l)}))$ blue dots, $(Z(S_{ay}(T_1)) + \bar{E}_y, Z(D_{dr_y}^{(l)}))$ magenta circles at 3rd storey: $l = 1$ with $\xi_l = 1$ (left panel); $l = 2$ with $\xi_l = 1.5$ (center panel); $l = 3$ with $\xi_l = 2$ (right panel) - nonlinear analysis.

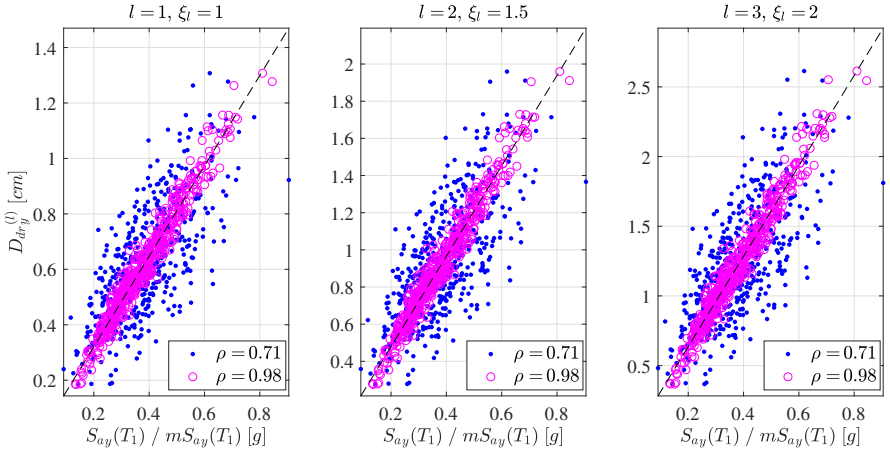

Figure 6.88: Scatter plots of $n_s = 500$ samples of $(S_{ay}(T_1), D_{dr_y}^{(l)})$ blue dots, $(S_{ay}(T_1) + \bar{E}_y, D_{dr_y}^{(l)})$ magenta circles at 3rd storey: $l = 1$ with $\xi_l = 1$ (left panel); $l = 2$ with $\xi_l = 1.5$ (center panel); $l = 3$ with $\xi_l = 2$ (right panel) - nonlinear analysis.

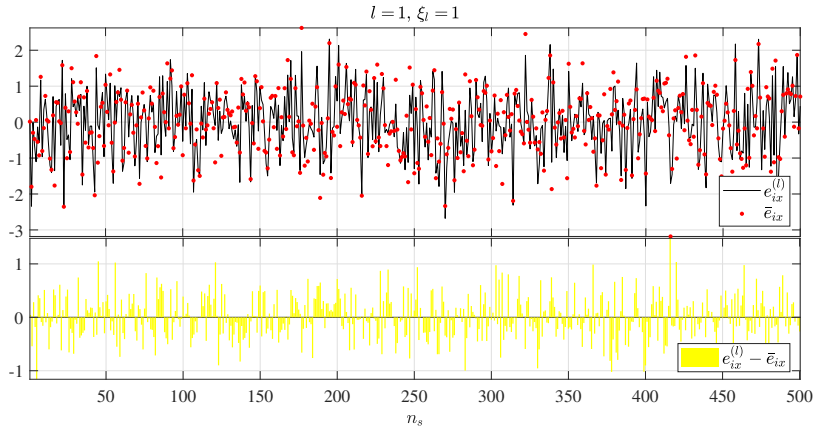

Figure 6.89: Computed distances of $n_s = 500$ samples at 3rd storey considering $D_{drx}^{(l)}$, $l = 1$, and PGA_x: distance from the perfect correlation $e_{ix}^{(l)}$ versus average distance $\bar{e}_{ix}$, $l = 1$ and $i = 1, \ldots, n_s$ (top panel); difference $e_{ix}^{(l)} - \bar{e}_{ix}$, $l = 1$ and $i = 1, \ldots, n_s$ (bottom panel) - nonlinear analysis.

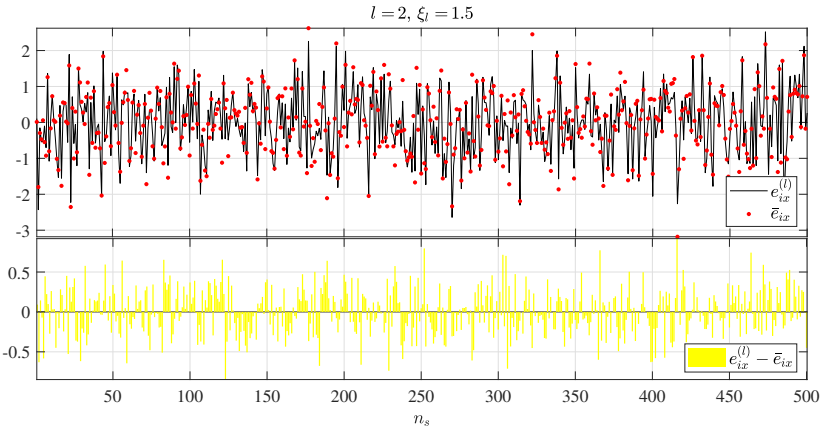

Figure 6.90: Computed distances of $n_s = 500$ samples at 3rd storey considering $D_{drx}^{(l)}$, $l = 1.5$, and PGA_x: distance from the perfect correlation $e_{ix}^{(l)}$ versus average distance $\bar{e}_{ix}$, $l = 1.5$ and $i = 1, \ldots, n_s$ (top panel); difference $e_{ix}^{(l)} - \bar{e}_{ix}$, $l = 1.5$ and $i = 1, \ldots, n_s$ (bottom panel) - nonlinear analysis.

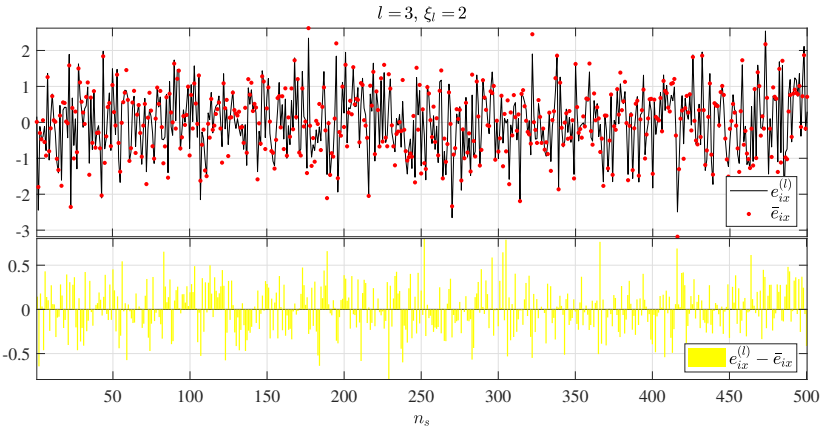

Figure 6.91: Computed distances of $n_s = 500$ samples at 3rd storey considering $D_{drx}^{(l)}$, $l = 2$, and PGA_x: distance from the perfect correlation $e_{ix}^{(l)}$ versus average distance $\bar{e}_{ix}$, $l = 2$ and $i = 1, \ldots, n_s$ (top panel); difference $e_{ix}^{(l)} - \bar{e}_{ix}$, $l = 2$ and $i = 1, \ldots, n_s$ (bottom panel) - nonlinear analysis.

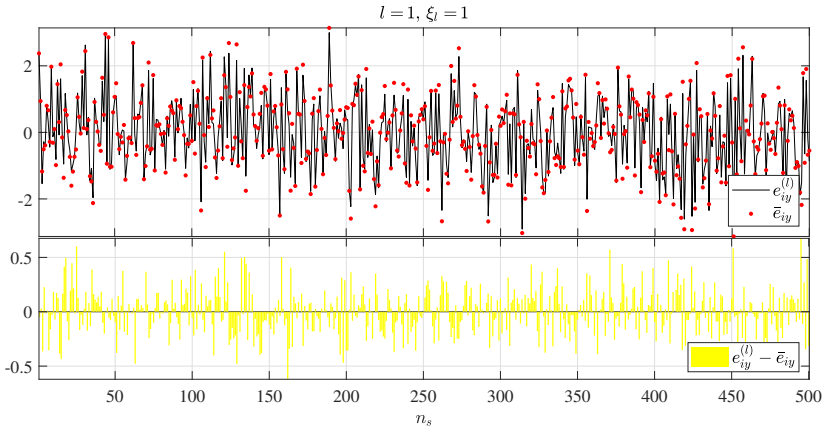

Figure 6.92: Computed distances of $n_s = 500$ samples at node #9 considering $D_{dr_y}^{(l)}$, $l = 1$, and PGA_y: distance from the perfect correlation $e_{iy}^{(l)}$ versus average distance $\bar{e}_{iy}$, $l = 1$ and $i = 1, \ldots, n_s$ (top panel); difference $e_{iy}^{(l)} - \bar{e}_{iy}$, $l = 1$ and $i = 1, \ldots, n_s$ (bottom panel) - nonlinear analysis.

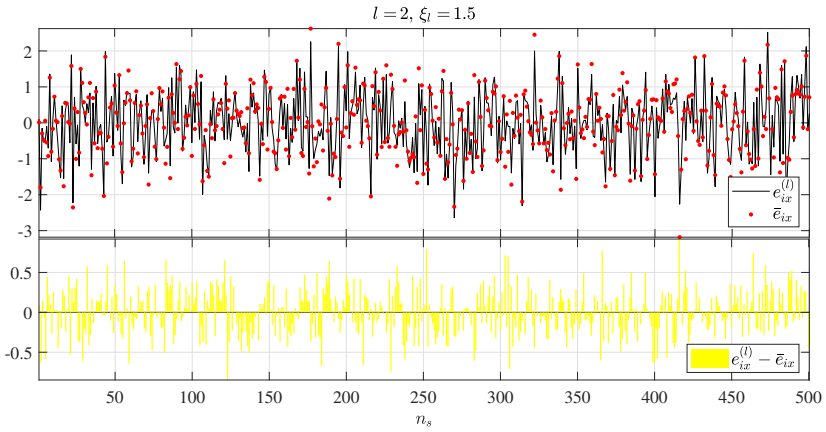

Figure 6.93: Computed distances of $n_s = 500$ samples at 3rd storey considering $D_{dr_y}^{(l)}$, $l = 1.5$, and PGA_y: distance from the perfect correlation $e_{iy}^{(l)}$ versus average distance $\bar{e}_{iy}$, $l = 1.5$ and $i = 1, \ldots, n_s$ (top panel); difference $e_{iy}^{(l)} - \bar{e}_{iy}$, $l = 1.5$ and $i = 1, \ldots, n_s$ (bottom panel) - nonlinear analysis.

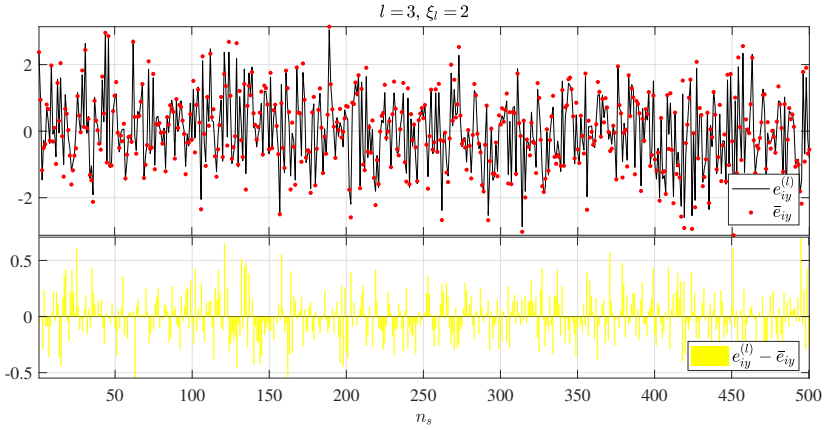

Figure 6.94: Computed distances of $n_s = 500$ samples at node #9 considering $D_{dr_y}^{(l)}$, $l = 2$, and PGA_y: distance from the perfect correlation $e_{iy}^{(l)}$ versus average distance $\bar{e}_{iy}$, $l = 2$ and $i = 1, \ldots, n_s$ (top panel); difference $e_{iy}^{(l)} - \bar{e}_{iy}$, $l = 2$ and $i = 1, \ldots, n_s$ (bottom panel) - nonlinear analysis.

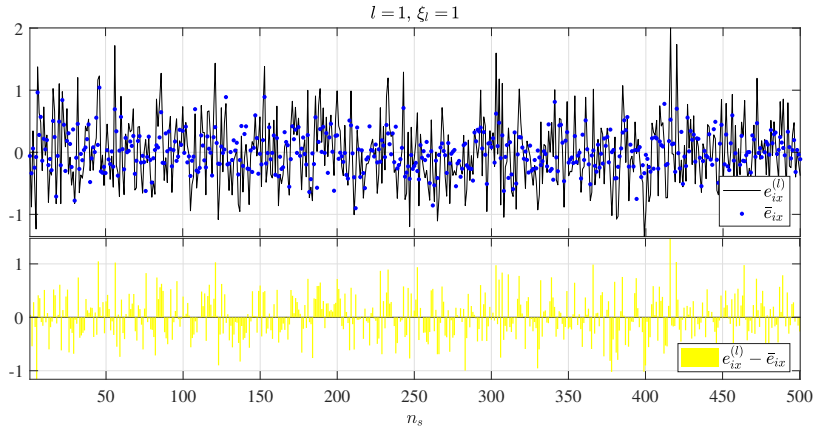

Figure 6.95: Computed distances of $n_s = 500$ samples at 3rd storey considering $D_{drx}^{(l)}$, $l = 1$, and $S_{ax}(T_1)$: distance from the perfect correlation $e_{ix}^{(l)}$ versus average distance $\bar{e}_{ix}$, $l = 1$ and $i = 1, \ldots, n_s$ (top panel); difference $e_{ix}^{(l)} - \bar{e}_{ix}$, $l = 1$ and $i = 1, \ldots, n_s$ (bottom panel) - nonlinear analysis.

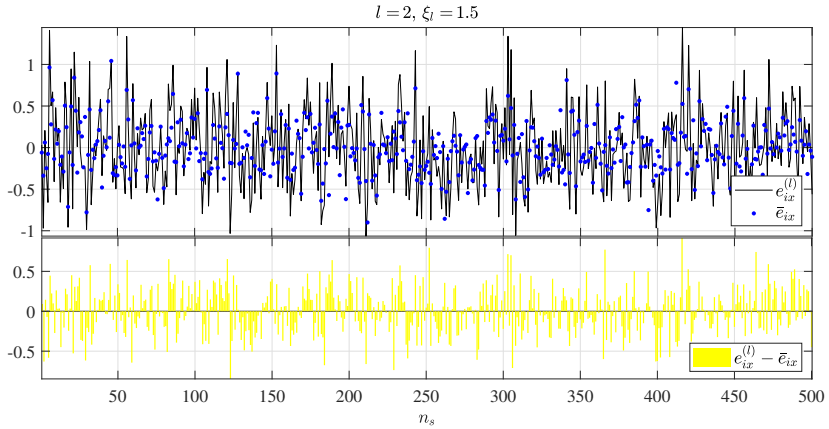

Figure 6.96: Computed distances of $n_s = 500$ samples at node #9 considering $D_{drx}^{(l)}$, $l = 1.5$, and $S_{ax}(T_1)$: distance from the perfect correlation $e_{ix}^{(l)}$ versus average distance $\bar{e}_{ix}$, $l = 1.5$ and $i = 1, \ldots, n_s$ (top panel); difference $e_{ix}^{(l)} - \bar{e}_{ix}$, $l = 1.5$ and $i = 1, \ldots, n_s$ (bottom panel) - nonlinear analysis.

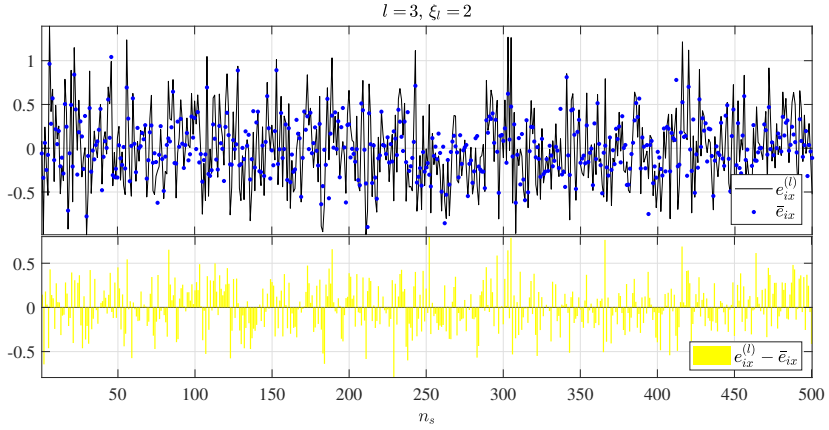

Figure 6.97: Computed distances of $n_s = 500$ samples at node #9 considering $D_{drx}^{(l)}$, $l = 2$, and $S_{ax}(T_1)$: distance from the perfect correlation $e_{ix}^{(l)}$ versus average distance $\bar{e}_{ix}$, $l = 2$ and $i = 1, \ldots, n_s$ (top panel); difference $e_{ix}^{(l)} - \bar{e}_{ix}$, $l = 2$ and $i = 1, \ldots, n_s$ (bottom panel) - nonlinear analysis.

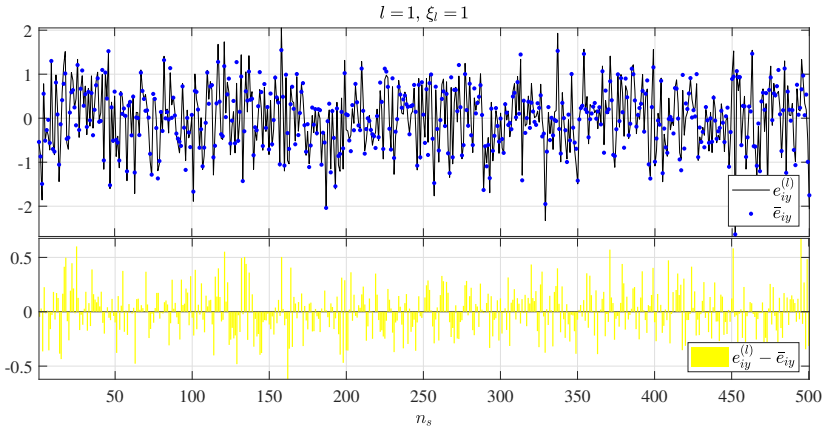

Figure 6.98: Computed distances of $n_s = 500$ samples at 3rd storey considering $D_{dry}^{(l)}$, $l = 1$, and $S_{ay}(T_1)$: distance from the perfect correlation $e_{iy}^{(l)}$ versus average distance $\bar{e}_{iy}$, $l = 1$ and $i = 1, \ldots, n_s$ (top panel); difference $e_{iy}^{(l)} - \bar{e}_{iy}$, $l = 1$ and $i = 1, \ldots, n_s$ (bottom panel) - nonlinear analysis.

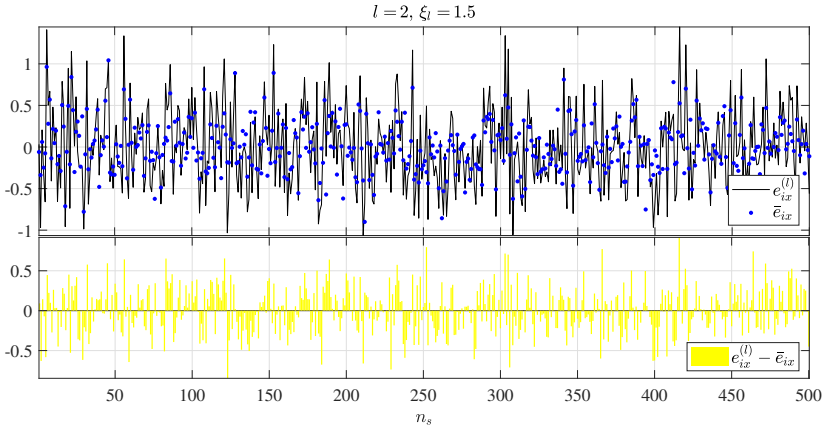

Figure 6.99: Computed distances of $n_s = 500$ samples at 3rd storey considering $D_{dry}^{(l)}$, $l = 1.5$, and $S_{ay}(T_1)$: distance from the perfect correlation $e_{iy}^{(l)}$ versus average distance $\bar{e}_{iy}$, $l = 1.5$ and $i = 1, \ldots, n_s$ (top panel); difference $e_{iy}^{(l)} - \bar{e}_{iy}$, $l = 1.5$ and $i = 1, \ldots, n_s$ (bottom panel) - nonlinear analysis.

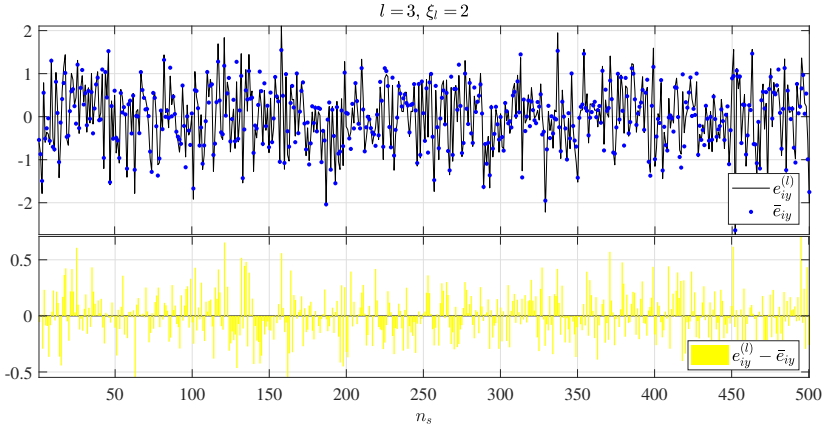

Figure 6.100: Computed distances of $n_s = 500$ samples at 3rd storey considering $D_{dry}^{(l)}$, $l = 2$, and $S_{ay}(T_1)$: distance from the perfect correlation $e_{iy}^{(l)}$ versus average distance $\bar{e}_{iy}$, $l = 2$ and $i = 1, \ldots, n_s$ (top panel); difference $e_{iy}^{(l)} - \bar{e}_{iy}$, $l = 2$ and $i = 1, \ldots, n_s$ (bottom panel) - nonlinear analysis.

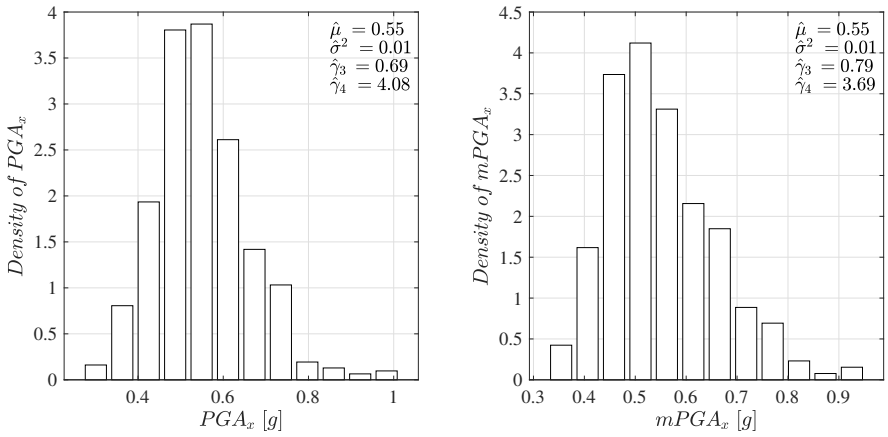

Figure 6.101: Estimated PDF for $n_s = 500$ samples of PGA_x (left panel) and $mPGA_x$ (right panel) computed with $m = 3$ and $k = 3$.

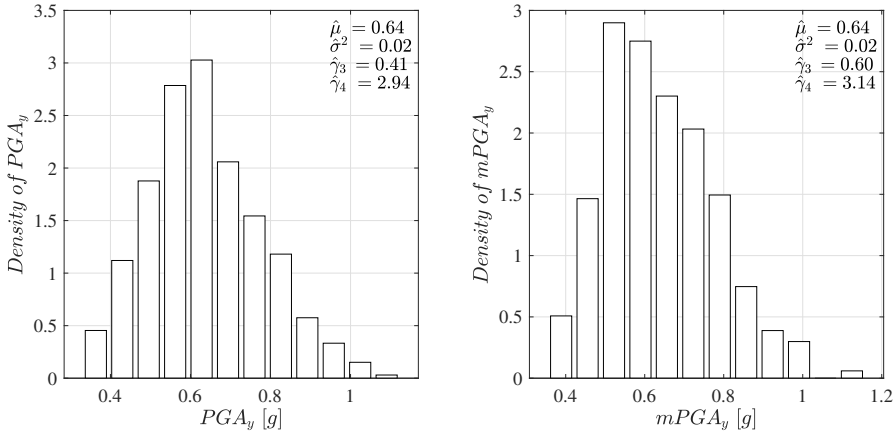

Figure 6.102: Estimated PDF for $n_s = 500$ samples of PGA_y (left panel) and $mPGA_y$ (right panel) computed with $m = 3$ and $k = 3$.

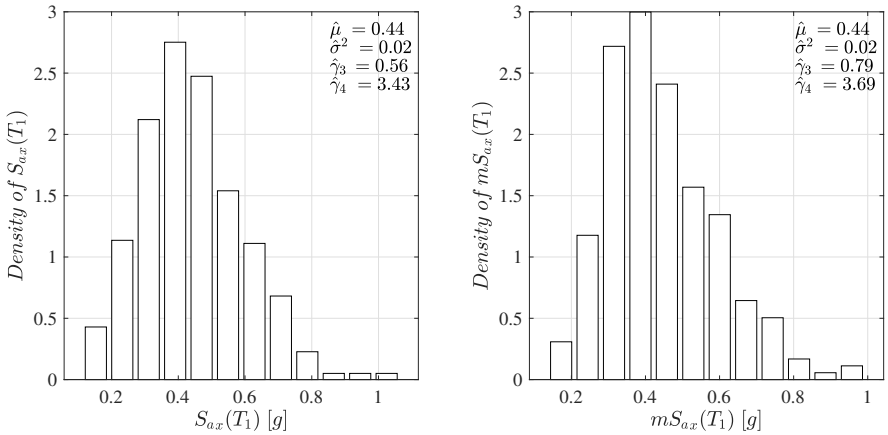

Figure 6.103: Estimated PDF for $n_s = 500$ samples of $S_{ax}(T_1)$ (left panel) and $mS_{ax}(T_1)$ (right panel) computed with $m = 3$ and $k = 3$.

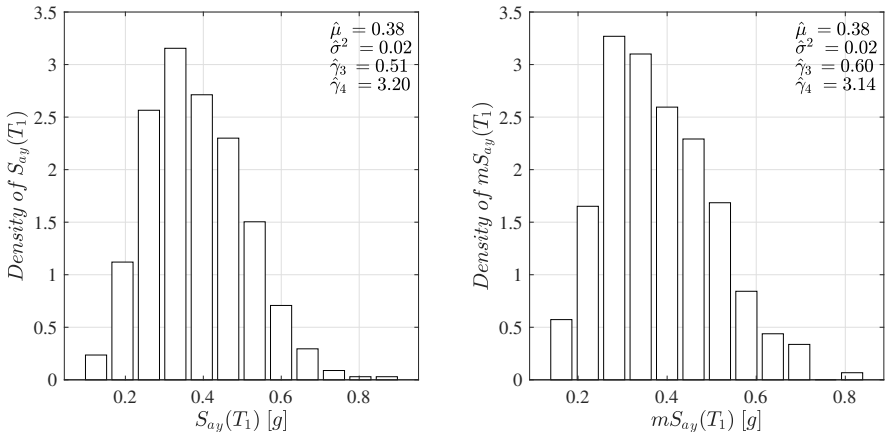

Figure 6.104: Estimated PDF for $n_s = 500$ samples of $S_{ay}(T_1)$ (left panel) and $mS_{ay}(T_1)$ (right panel) computed with $m = 3$ and $k = 3$.

6.5 Fragility analysis

This chapter is concluded with the results regarding the fragility analysis development for the model of Norcia school building. The obtained fragilities, considering linear/nonlinear model behaviour, are estimated for the chosen demand parameters and intensity measures. For same selected intensity measures, see Section 6.4, the modified version of them is defined by the introduced novel approach in Section 4.4. In following, it will be shown that the fragility analysis performed by using these modified intensity measures provide access to more accurate seismic performance informations for real complex linear/nonlinear MDOF structural system rather the those obtained by their original version (classical intensity measures).

Considering the Monte Carlo algorithm in Section 3.6, in a similar way the fragility curves are estimated thought the steps below:

1. selection of a finite set of intensity measure $\{\xi_k\}$, $k = 1, \ldots, N$;

2. consider the $n_s = 500$ independent samples $a_{xi}(t)$ and $a_{y_i}(t)$, $i = 1, \ldots, n_s$, of the non-stationary acceleration ground motion process $\boldsymbol{A}(t) = \{A_x(t); A_y(t)\}$ in

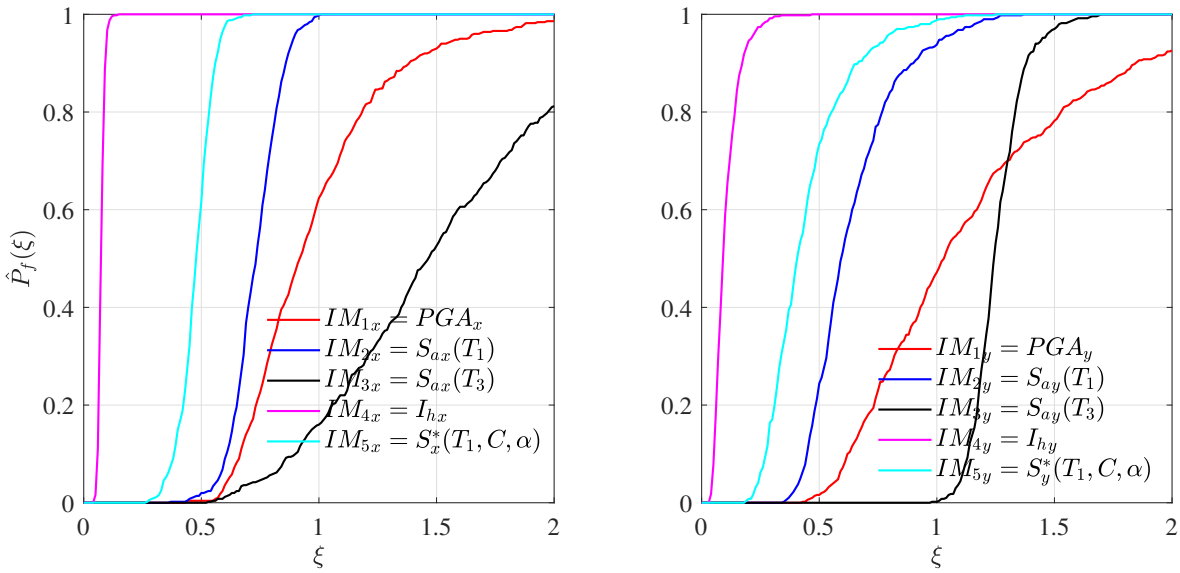

Figure 6.105: Fragilities against intensity level ξ for different definitions of IMs at node #1: demand parameter D_{dx} and limit state $\bar{D}_{dx} = 1\,cm$ (left panel); demand parameter D_{dy} and limit state $\bar{D}_{dy} = 1\,cm$ (right panel) - linear analysis.

Subsection 6.2.1;

3. for each of the values $\{\xi_k\}$ scale the n_s acceleration records, $a_{x_i}(t)$ and $a_{y_i}(t)$, in order to have the intensity level $IM_n = \xi_k$, $\xi_k > 0$ and $n = x, y$;

4. given a prefixed limit state value, samples of the demand parameter $d_{nk,i}$, $k = 1, \ldots, N$, $i = 1, \ldots, n_s$ and $n = x, y$, are computed for the Norcia school model with linear or nonlinear behaviour;

5. for each of the values $\{\xi_k\}$ estimate fragility as in Equation (3.8).

As an example of the high variability for the fragilities by different IMs, Figures 6.105 - 6.108 show the obtained curves with the intensity measures in Equations (3.12) - (3.16). These IMs are computed for both the components of $\boldsymbol{A}(t)$ with $n_s = 500$ samples, i.e. IM_{q_n}, $q = 1, \ldots, 5$ and $n = x, y$. The previous five-steps algorithm with the linear behaviour for FE model (Figure 6.12) is considered. In each of these figures, i.e. Figures 6.105 - 6.108, the left panels report the demand parameters in x-direction,

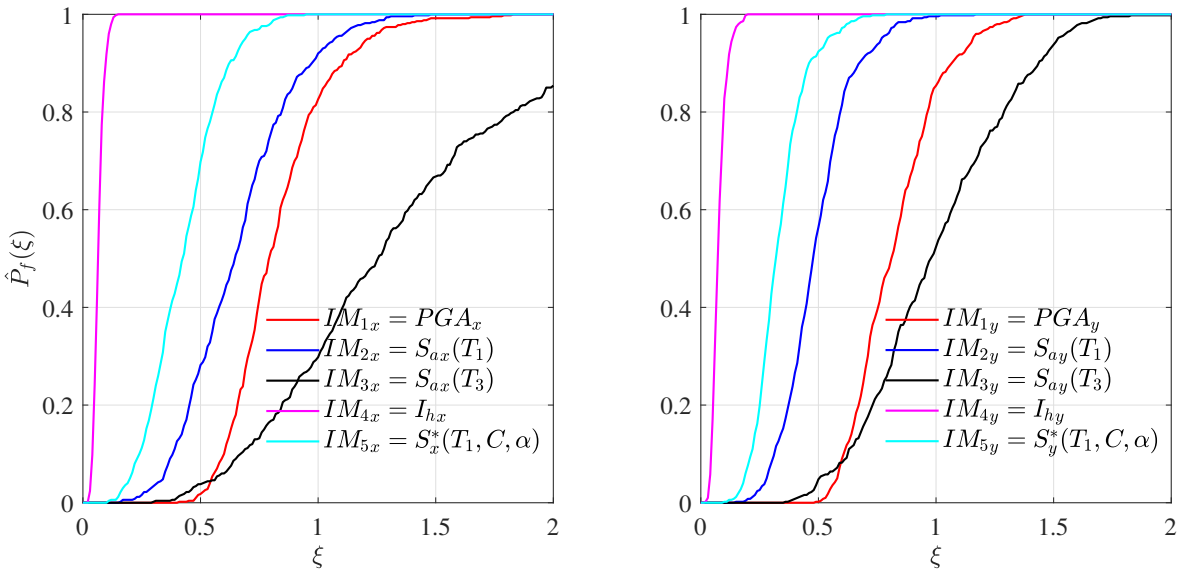

Figure 6.106: Fragilities against intensity level ξ for different definitions of IMs at node #1: demand parameter D_{ax} and limit state $\bar{D}_{ax} = 1\,g$ (left panel); demand parameter D_{ay} and limit state $\bar{D}_{ay} = 1\,g$ (right panel) - linear analysis.

while the right panels those in y-direction, for the displacement or acceleration D_{rn}, $r = d$ or $r = a$ and $n = x, y$. In particular, Figure 6.105 (Figure 6.107) shows the fragilities for the different IMs at the node #1 (#9), see Figure 6.14 , for the displacement D_{dn}, $n = x, y$, and the prefixed limit state $\bar{D}_{dn} = 1\,cm$ ($\bar{D}_{dn} = 2\,cm$). In Figure 6.106 (Figure 6.108) the curves are again shown for the node #1 (#9), but considering the acceleration D_{an}, $n = x, y$, and limit state $\bar{D}_{an} = 1\,g$. It is difficult to determine which is the best intensity measure just by considering the obtained curves in these figures. The high variability of the fragilities depends on the selected demand parameter D, the considered direction, i.e. x or y, and essentially it is summarized in the considered IM to develop the fragility analysis. The dependence study in Section 6.3 helps to understand what is the best candidate IM to provide useful informations on seismic performance.

Considering the Figures 6.25 and 6.26, the 2nd and 3rd panel from left, it is clear as the blue curve in left panel of Figure 6.107 and the black one in the right panel of same figure, are the best fragilities for D_{dx} and D_{dy}, at the node #9, respectively. This is due

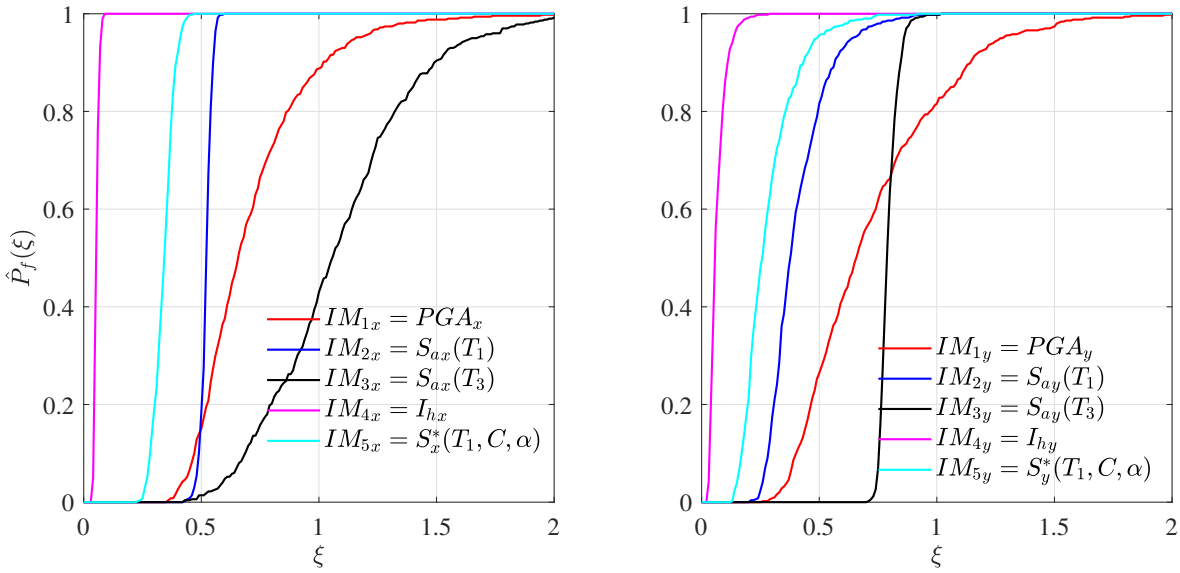

Figure 6.107: Fragilities against intensity level ξ for different definitions of IMs at node #9: demand parameter D_{dx} and limit state $\bar{D}_{dx} = 2\,cm$ (left panel); demand parameter D_{dy} and limit state $\bar{D}_{dy} = 2\,cm$ (right panel) - linear analysis.

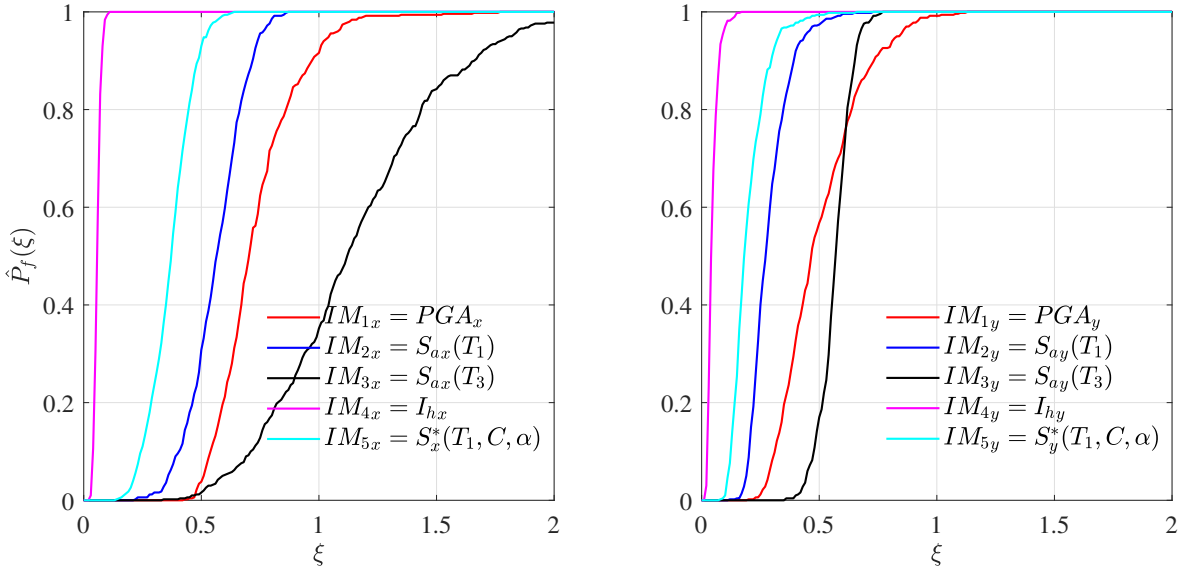

Figure 6.108: Fragilities against intensity level ξ for different definitions of IMs at node #9: demand parameter D_{ax} and limit state $\bar{D}_{ax} = 1\,g$ (left panel); demand parameter D_{ay} and limit state $\bar{D}_{ay} = 1\,g$ (right panel) - linear analysis.

to the strong dependence between D_{dx} and $IM_{2x} = S_{ax}(T_1)$ ($\rho = 0.99$), and between D_{dy} and $IM_{3y} = S_{ay}(T_3)$ ($\rho = 0.95$), respectively. However, for the same node, but for the acceleration D_{ax} and D_{ay}, the blue and black curves in left and right panel of Figure 6.108, respectively, are always the best fragilities. The correlation coefficient is diminished to 0.80 in 2nd panel form left of Figure 6.27, and to 0.93 in the middle panel of Figure 6.28 .

Same considerations can be made for D_{dn}, $n = x, y$, at node #1 (Figure 6.14) and the fragilities in Figure 6.105 to seeing the dependence with all the IM_{q_n}, $q = 1, \ldots, 5$ and $n = x, y$, in Figures B.1 and B.2. While, for the D_{ax}, the red curve on left panel of Figure 6.106 should be selected since the dependence between D_{ax} and $IM_{1x} = PGA_x$ is the highest, i.e. $\rho = 0.54$ in Figure B.3 . For the right panel of Figure 6.106, the fragility in black line continues to be best choice for the demand parameter D_{ay} (see Figure B.4).

The previous introductory examples show the difficulty to choose the best classical intensity measure appropriate for all the demand parameter of interest in the fragility analysis in order to access the truthful seismic performance for a complex MDOF structural system, such as the Norcia school. Improving the dependence between a demand parameters and selected IM can be a strategy as in Section 6.4 . In this way, the modified intensity measures are defined by considering the proposed approach in Section 4.4 .

In following, results of the fragility analysis by selected original IMs and the their modified version $mIMs$ (IM_{q_n} and mIM_{q_n}, $q = 1, 2$ and $n = x, y$) for different m number of demand parameters of interest for the Norcia model with linear/nonlinear behaviour are shown.

Figure 6.109 shows a comparison between the obtained fragilities by the IM_{q_n} and IM_{q_n}, $q = 1, 2$, $n_s = 500$ samples, by performing linear analysis for the D_{dn} and prefixed limit value $\bar{D}_{dn} = 2\,cm$ at node #9, where $n = x$ and $n = y$ for left and

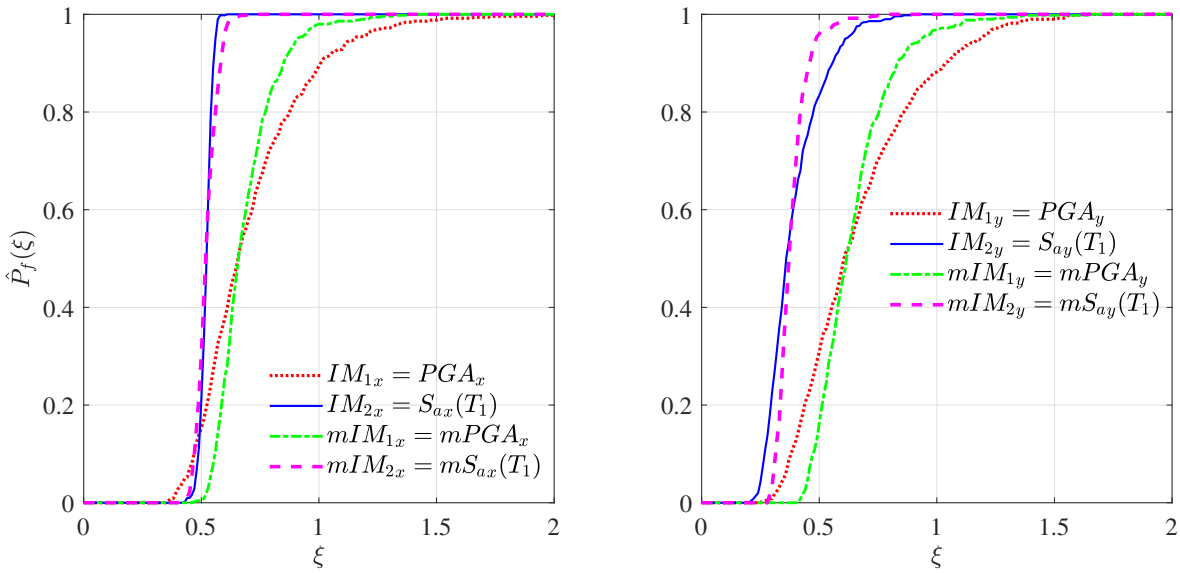

Figure 6.109: Fragilities against intensity level ξ for selected definitions of IMs and their modified versions $mIMs$ (Figures 6.41 - 6.44) at node #9: demand parameter D_{dx} and limit state $\bar{D}_{dx} = 2\,cm$ (left panel); demand parameter D_{dy} and limit state $\bar{D}_{dy} = 2\,cm$ (right panel) - linear analysis.

right panel, respectively. The dotted red and continuous blue lines refer to PGA_n and $S_{an}(T_1)$, $n = x, y$, and they are the same continuous red and blue lines of the Figure 6.107, respectively. While the those dash-dotted green and dashed magenta lines regard to modified versions $mPGA_n$ and $mS_{an}(T_1)$, $n = x, y$, which are computed with $m = 12$ demands parameters of interest and $k = 1$ number of intensity level ($l = \xi_l = 1$, linear analysis). Best seismic performance informations are provided by the curves associated to mIM_{q_n}, see the improvement correlation in Figures 6.33 - 6.34 and 6.37 - 6.38. In reality, paying attention on the results in left panel of Figure 6.109, the curve by $S_{ax}(T_1)$ describes more accurate information compared to that by $mS_{ax}(T_1)$ since the IM_{2x} provides a correlation coefficient slightly larger that by mIM_{2x} in Figure 6.37. This aspect was discussed in Section 6.3, where substantially the correlation on this node, i.e. #9, is sold to improve that on the remaining ones of interest. Same results typology of Figure 6.109 are show in Figure 6.110 and 6.111 by considering $\bar{D}_{dn} = 2.4\,cm$ and $\bar{D}_{dn} = 1\,cm$, $n = x, y$, respectively. Figures B.161 - B.169 report the fragility analysis for some investigated nodes.

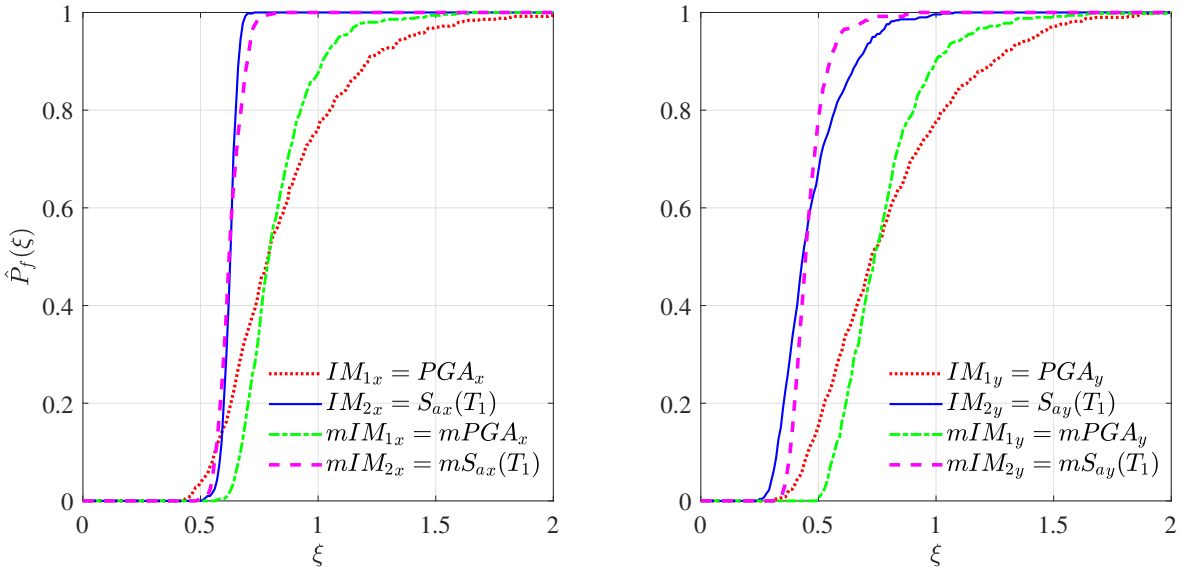

Figure 6.110: Fragilities against intensity level ξ for selected definitions of IMs and their modified versions $mIMs$ (Figures 6.41 - 6.44) at node #9: demand parameter D_{dx} and limit state $\bar{D}_{dx} = 2.4\,cm$ (left panel); demand parameter D_{dy} and limit state $\bar{D}_{dy} = 2.4\,cm$ (right panel) - linear analysis.

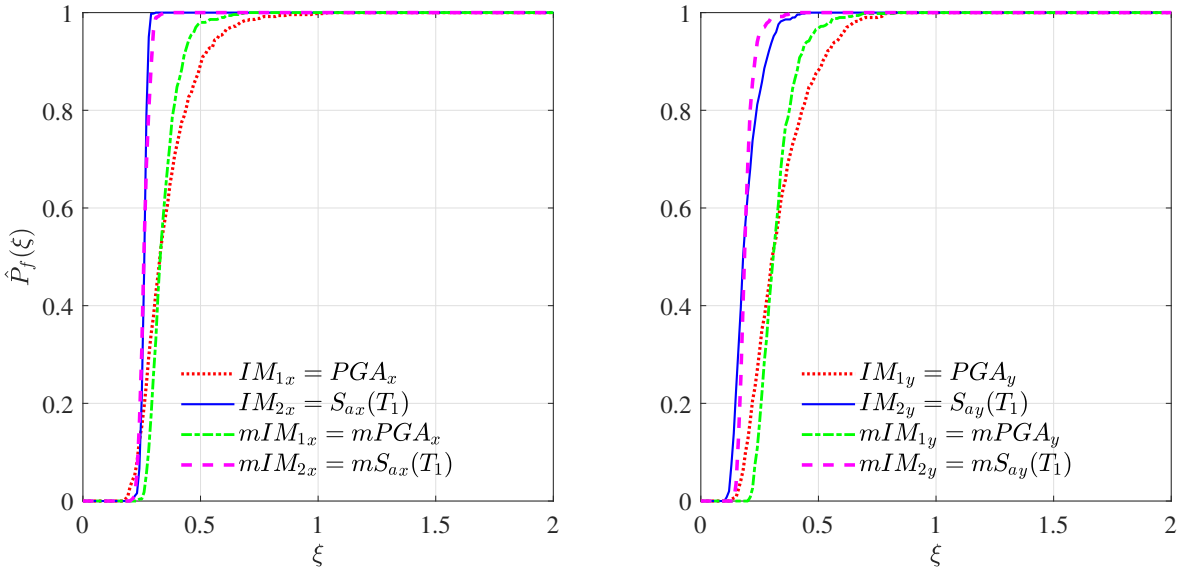

Figure 6.111: Fragilities against intensity level ξ for selected definitions of IMs and their modified versions $mIMs$ (Figures 6.41 - 6.44) at node #9: demand parameter D_{dx} and limit state $\bar{D}_{dx} = 1\,cm$ (left panel); demand parameter D_{dy} and limit state $\bar{D}_{dy} = 1\,cm$ (right panel) - linear analysis.

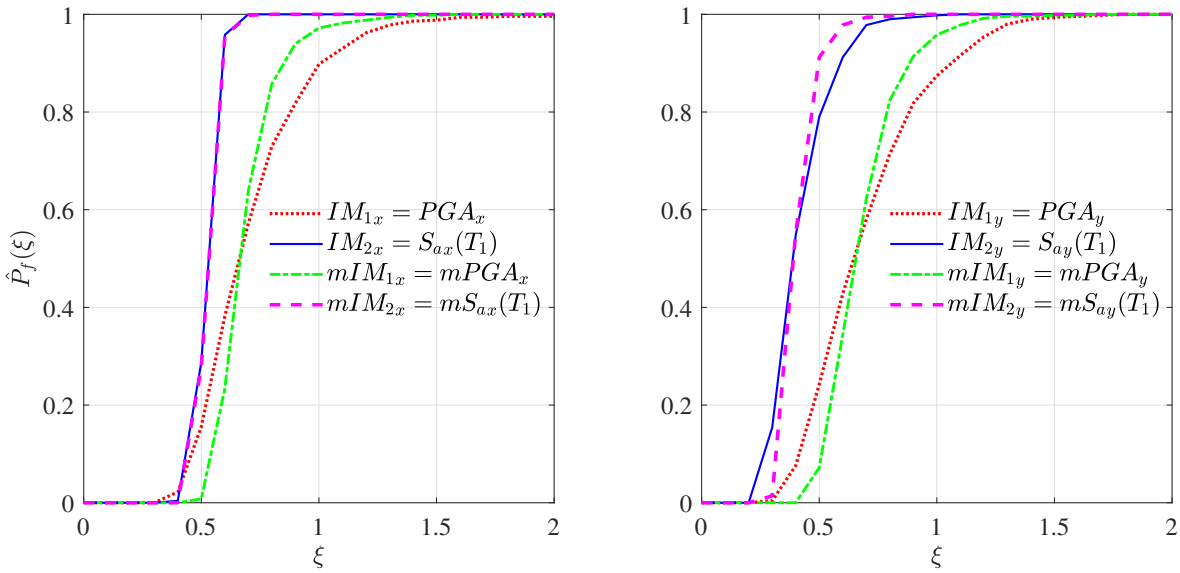

Figure 6.112: Fragilities against intensity level ξ for selected definitions of IMs and their modified versions $mIMs$ (Figures 6.77 - 6.80) at node #9: demand parameter D_{dx} and limit state $\bar{D}_{dx} = 2\,cm$ (left panel); demand parameter D_{dy} and limit state $\bar{D}_{dy} = 2\,cm$ (right panel) - nonlinear analysis.

Figures 6.112, 6.113 and 6.114 report the developed curves through nonlinear analysis ($n_s = 500$) for the displacement D_{dn}, $n = x, y$, at #9, $\bar{D}_{dn}$ are $2\,cm$, $2.4\,cm$ and $1\,cm$, respectively. In these figure, a comparison between the fragilities by the original intensity measures IM_{q_n}, $q = 1, 2$ and $n = x, y$, and the modified version mIM_{q_n} ($m = 12$ and $k = 3$), i.e. Figures 6.77 - 6.80, are shown. Best choice between these curves falls on those related to $mIMs$, the dash-dotted green and dashed magenta line, since the stochastic variables $D_{dn}|mPGA_n$ and $D_{dn}|mS_{an}(T_1)$ have a small variance. In particular, seeing Figures 6.57 - 6.64, the correlation coefficients for the different level intensity ξ_l computed by mIM_{q_n}, $q = 1, 2$ and $n = x, y$, are greater (equal in some circumstances) with those obtained by IM_{q_n}. The nonlinear fragility analysis results for some demand parameters of interest are reported in Figures B.170 - B.178.

Considering as demand parameters of the interest, the seismic drifts on the three storey in elevation ($m = 3$), Figures 6.115 and 6.116 report the fragilities estimated

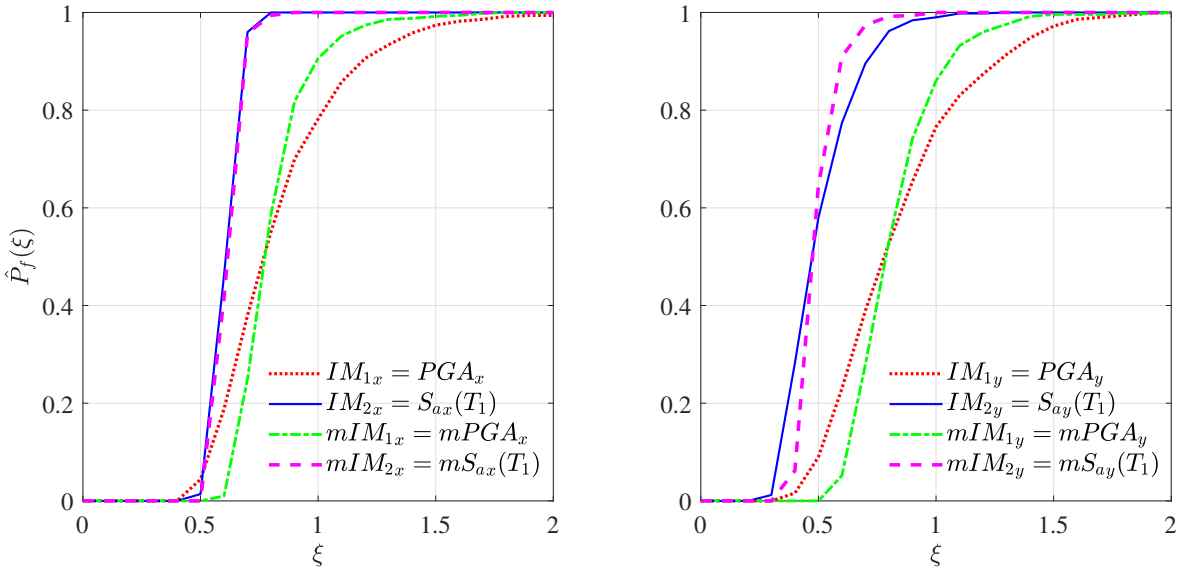

Figure 6.113: Fragilities against intensity level ξ for selected definitions of IMs and their modified versions $mIMs$ (Figures 6.77 - 6.80) at node #9: demand parameter D_{dx} and limit state $\bar{D}_{dx} = 2.4\,cm$ (left panel); demand parameter D_{dy} and limit state $\bar{D}_{dy} = 2.4\,cm$ (right panel) - nonlinear analysis.

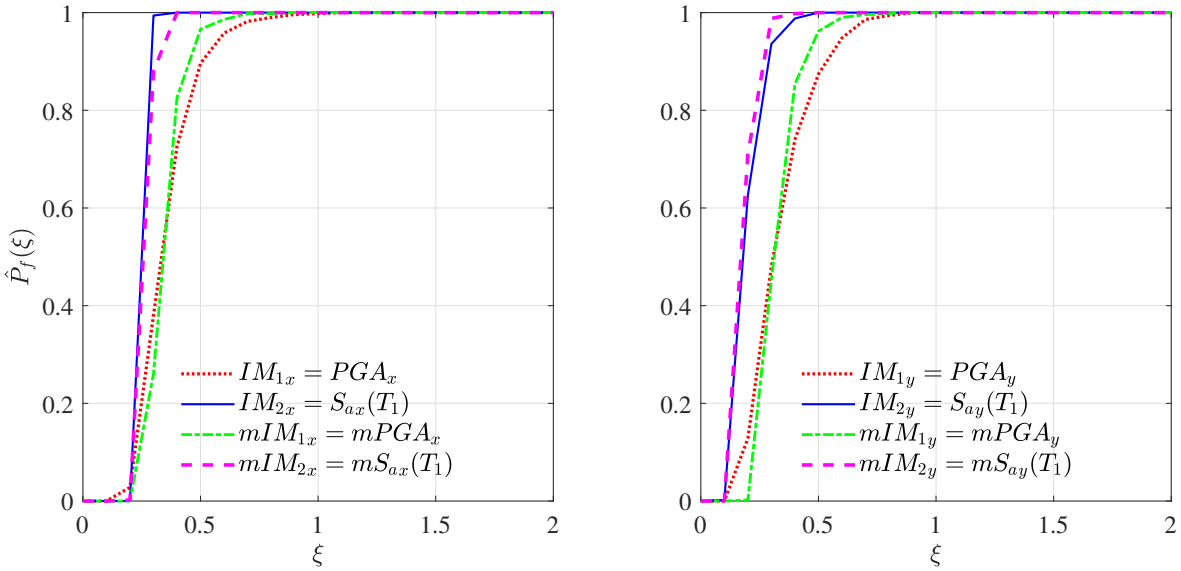

Figure 6.114: Fragilities against intensity level ξ for selected definitions of IMs and their modified versions $mIMs$ (Figures 6.77 - 6.80) at node #9: demand parameter D_{dx} and limit state $\bar{D}_{dx} = 1\,cm$ (left panel); demand parameter D_{dy} and limit state $\bar{D}_{dy} = 1\,cm$ (right panel) - nonlinear analysis.

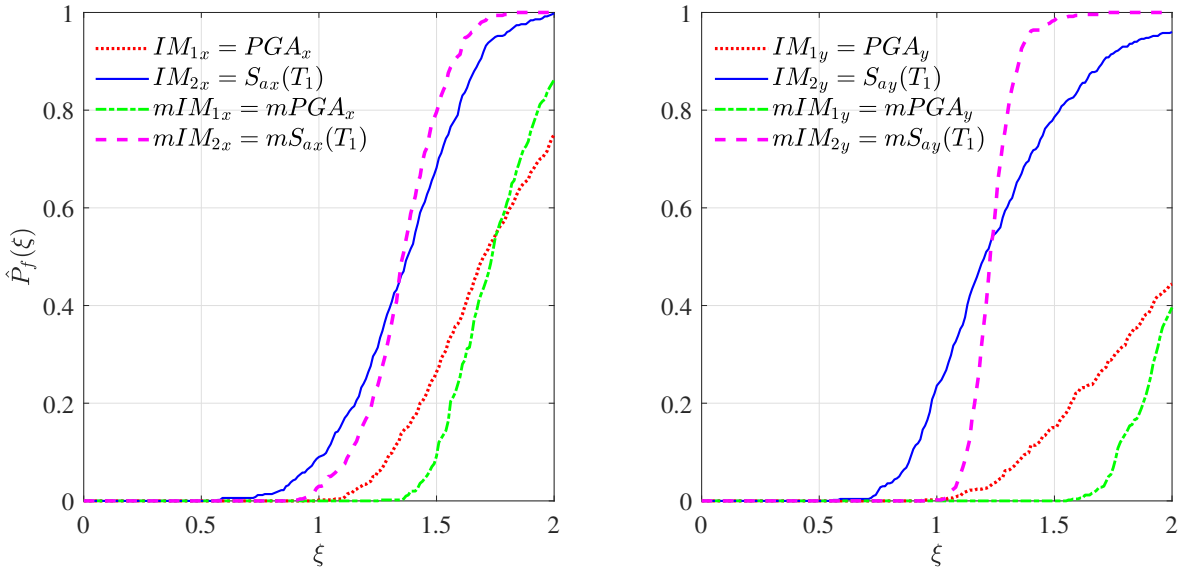

Figure 6.115: Fragilities against intensity level ξ for selected definitions of IMs and their modified versions $mIMs$ (Figures 6.53 - 6.56) at node 3rd storey: demand parameter D_{drx} and limit state $\bar{D}_{drx} = 2\,cm$ (left panel); demand parameter D_{dry} and limit state $\bar{D}_{dry} = 2\,cm$ (right panel) - linear analysis.

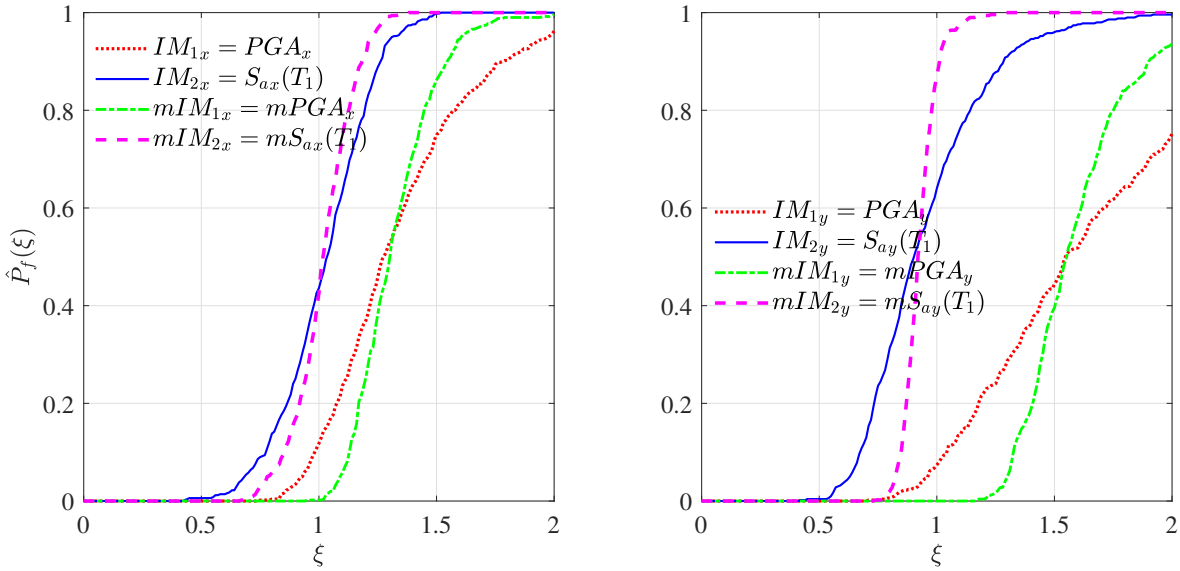

Figure 6.116: Fragilities against intensity level ξ for selected definitions of IMs and their modified versions $mIMs$ (Figures 6.53 - 6.56) at node 3rd storey: demand parameter D_{drx} and limit state $\bar{D}_{drx} = 1.5\,cm$ (left panel); demand parameter D_{dry} and limit state $\bar{D}_{dry} = 1.5\,cm$ (right panel) - linear analysis.

by scaling the $n_s = 500$ accelerograms of $\boldsymbol{A}(t)$, i.e. $a_n(t)$, $n = x, y$, by IM_{q_n} and mIM_{q_n} for the drift D_{drn} at 3rd storey, linear analysis. Left panels refer to $n = x$ and those on right to $n = y$. Limit state for Figures 6.115 and 6.116 are $\bar{D}_{drn} = 2\,cm$ and $\bar{D}_{drn} = 1.5\,cm$, $n = x, y$, respectively. The dotted red and continuous blue lines refer to PGA_n and $S_{an}(T_1)$, instead the those dash-dotted green and dashed magenta lines regard to modified versions $mPGA_n$ and $mS_{an}(T_1)$, $n = x, y$, (Figures 6.53 - 6.54 and 6.55 - 6.56). The curves computed by mIM_{q_n} provide best information on the seismic performance since the random variables $D_{drn}|mIM_{q_n}$, $n = x, y$, have small variance (see Figures 6.45 - 6.48). Fragilities for the drift at 1st and 2nd storey are reported in Figures B.179 - B.182.

Nonlinear results for same demand parameters, i.e. the drifts at three storey, are developed, and in Figures 6.117 and 6.118 are show those refer to the 3rd storey. In these figures, the drift D_{drn}, $n = x, y$, is considered on the left and right panel, respectively. The prefixed limit value in Figures 6.117 and 6.118 are $\bar{D}_{drn} = 2\,cm$ and $\bar{D}_{drn} = 1.5\,cm$, $n = x, y$. The dotted red and continuous blue curves regard to $mPGA_n$ and $mS_{an}(T_1)$, instead the dash-dotted green and dashed magenta ones to PGA_n and $S_{an}(T_1)$. Considering the dependence improvement in Figures 6.81 - 6.88, it is clear as the fragilities related to $mPGA_n$ and $mS_{an}(T_1)$, i.e. in Figures 6.117 and 6.118, provide the best information on the seismic performance. Further results are show for the first and second storey in Figures B.183 - B.186, and the same previous considerations can be made.

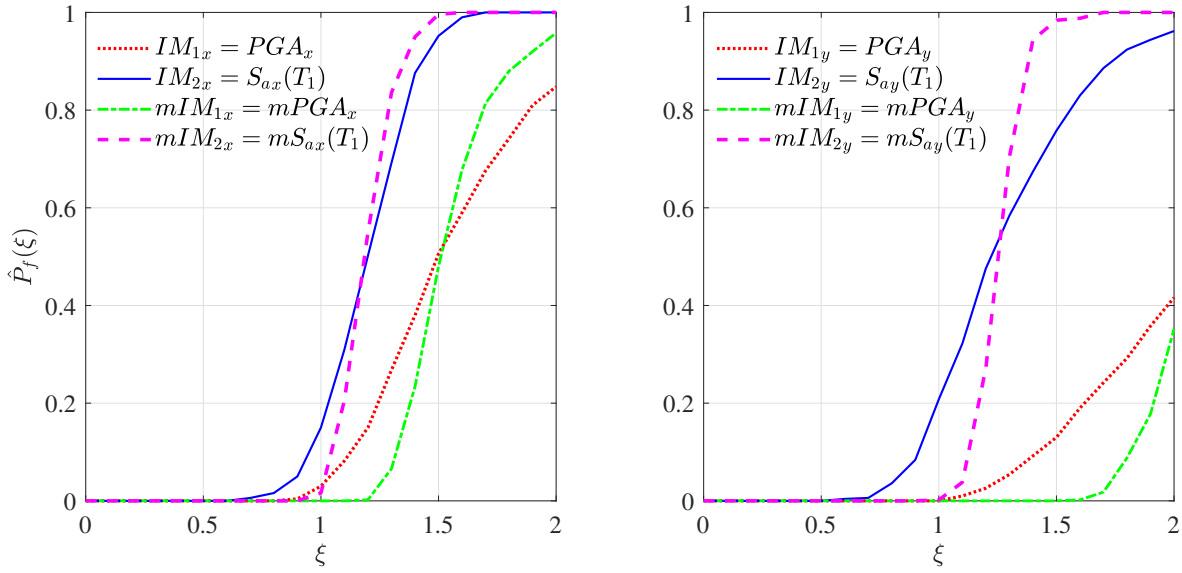

Figure 6.117: Fragilities against intensity level ξ for selected definitions of IMs and their modified versions $mIMs$ (Figures 6.101 - 6.104) at node 3rd storey: demand parameter D_{drx} and limit state $\bar{D}_{drx} = 2\,cm$ (left panel); demand parameter D_{dry} and limit state $\bar{D}_{dry} = 2\,cm$ (right panel) - nonlinear analysis.

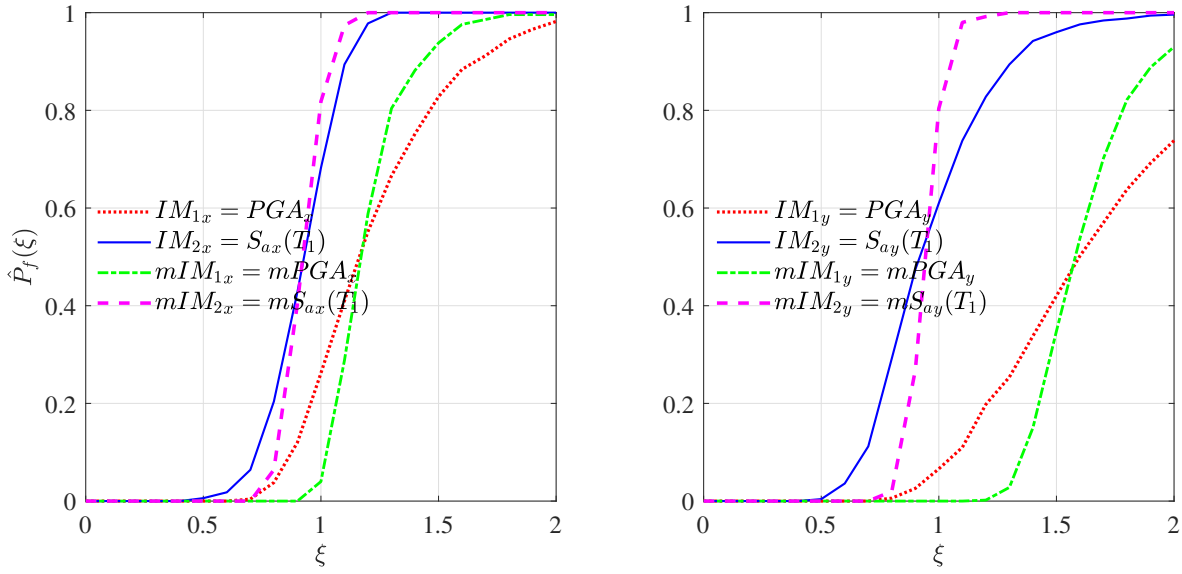

Figure 6.118: Fragilities against intensity level ξ for selected definitions of IMs and their modified versions $mIMs$ (Figures 6.101 - 6.104) at node 3rd storey: demand parameter D_{drx} and limit state $\bar{D}_{drx} = 1.5\,cm$ (left panel); demand parameter D_{dry} and limit state $\bar{D}_{dry} = 1.5\,cm$ (right panel) - nonlinear analysis.

Chapter 7

Conclusion

In Performance-Based Earthquake Engineering (PBEE) the seismic fragilities are commonly estimated by the classical approach based on scaling the seismic accelerograms with a reference intensity measure. A strong dependence is required between the demand parameter of the structural system, on which the fragility analysis is based, and the intensity measure used for scaling, in order to have accurate fragility curves. It was demonstrated that this approach provides limited if any information on the seismic performance of the structural system for weak dependence between the demand parameter and intensity measure.

The presented work in this thesis proposes a general approach to improve the accuracy in fragilities estimation when the dependence between the intensity measure IM and the structural demand parameter D is weak and the widely used method in PBEE does not give accurate results. In particular, samples of any chosen IM are linearly transformed in order to improve the correlation with a set of selected demand parameters. The new samples can be considered as realizations of a modified intensity measure mIM and used to scale the ground acceleration records to build fragility curve that give more accurate information on the structural system performance when compared with that by original IM. This method can be apply for all the intensity measure definitions reported in literature. The probability density function of the modified

intensity measure is not differ substantially with that of the original.

In order to achieve these proposes, the research work is developed by six chapters. The Chapter 1 reports a general overview on the seismic performance assessment for civil structures, the origin of Performance-Based Earthquake Engineering, and the main contributions of this thesis and the pursued strategy which is summarized in four fundamental points.

In the Chapter 2, the tools used in earthquake engineering to modelling and quantify are described. These last are necessary to apply a probabilistic treatment for the seismic performance assessment since the randomness features of the earthquake events. In particular, the probability theory and statistics, the stochastic structural dynamic, seismic acceleration ground motion stochastic processes and the Monte Carlo simulation are brief introduced.

The Chapter 3 reports a literature overview on the fundamental concepts regard to the seismic fragility analysis for the structural systems. In particular, the several contributions in this topic by scientific community are reported together to the different approaches for the derivation of the fragilities and the formulations for the approximation and estimation of these curves. Also an overview on the structural demand parameters and the intensity measures commonly used in seismic fragility analysis are reported. It is shown the Federal Emergency Management Agency (FEMA) algorithm based on the Monte Carlo for the development of the seismic fragility functions.

The Chapter 4 deals the arguments with major interest in this thesis that are focused on the role of the seismic intensity measure in fragility analysis accuracy. The issue and the problem definition of the fragility functions are discussed and the novel approach of this thesis, the modified intensity measure method, is presented. It is demonstrated, as reported in literature, that the peak ground acceleration PGA and the pseudo-acceleration response spectrum $S_a(T)$ are an inefficient and an efficient intensity measure, respectively, for a linear single degree of freedom structural system. In preliminary, effectiveness of the modified intensity measure methodology in fragility

analysis is provided for this simple linear oscillator.

The Chapter 5 reports the fragility analysis accuracy improvement for linear/nonlinear single or multiple degree of freedom analytical structural system. The Duffing oscillator, Bouc-Wen oscillator and a three-storey plane frame (with linear/nonlinear behaviour) are taken in to account. The dependence study between the system demand parameter, maximum absolute displacement, and the commonly intensity measures used in PBEE, i.e. PGA and the ordinate of $S_a(T)$ at first or fundamental system period, is developed. It is concluded that the PGA and the pseudo-acceleration response spectrum at fundamental system period $S_a(T_0)$ are an inefficient intensity measures for Duffing and Bouc-Wen oscillators both. Also the peak ground acceleration is an inefficient intensity measure for the three-storey plane frame for both linear and nonlinear behaviour. The pseudo-acceleration response spectrum at first period $S_a(T_1)$ produces low and high dispersion on the system demand parameter for linear and nonlinear behaviour, respectively. This intensity measure is efficient and inefficient, respectively. For each of these analytical systems the effectiveness of the modified intensity measure approach is demonstrated.

In the Chapter 6, the fragility analysis accuracy improvement is provided for real complex multi-degree of freedom structural system. The model of the school in Norcia, Italy is selected as the major case study for this research work. This structural model consists in a linear/nonlinear dynamic system with a large number of degrees of freedom. First of all, the seismic hazard of the site is characterized by two typology of seismic acceleration ground motion stochastic processes, and after it is shown, the dependence study for the selected demand parameters and some seismic intensity measures reported in literature. The maximum absolute displacement and acceleration at several nodes of the model, which are the interest for the fragility analysis, are considered as the demand parameters in the dependence understanding. High variability of these dependence is achieved for the real complex system. This variability depends also on the seismic direction of the analysis. It is concluded that the PGA

and $S_a(T_1)$ are inefficient intensity measures for a real complex multi-degree of freedom structural system with linear/nonlinear behaviour. The effectiveness of the modified intensity measure approach is demonstrated by considering the commonly IM definitions used in PBEE and the maximum absolute displacement/inter-storey drift for several nodes/storey of interest for the seismic performance. Moreover, the samples of distance from the perfect correlation, between a selected demand parameter and an intensity measure, is compared versus the average distances. The samples of average distance is used to define the modified intensity measure for an original IM. These kinds of comparison show encouraging results since the average distances match with a good approximation to the samples of distance from the perfect correlation.

In general, for all the case studies in this thesis the dependence between a D and the mIM version results improved, and consequentially, the obtained fragility curve have higher accuracy to access the structural seismic performance. According to the efficiency requirement, the modified intensity measure definition decreases the dispersion on a system demand parameter. For these reasons, the proposed approach that is a modified version of the current intensity measure method can be a valid methodology for seismic structural performance assessment.

Appendix A

Supplementary results of unidirectional dynamic analysis

This appendix contains further results obtained from the unidirectional dynamic analysis according to Figure 6.13. The spectra-compatible samples of the process in Subsection 6.2.1 are used to develop the linear/nonlinear analysis. Dependence study between the demand parameters and the selected intensity measures are reported.

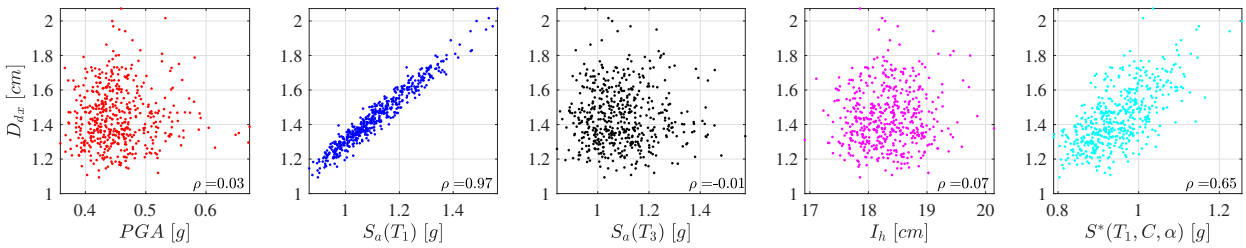

Figure A.1: Scatter plots of $n_s = 500$ samples of (PGA, D_{dx}), $(S_a(T_1), D_{dx})$, $(S_a(T_3), D_{dx})$, (I_h, D_{dx}) and $(S^*(T_1, C, \alpha), D_{dx})$, $\alpha = 0°$, at node #1 - linear analysis.

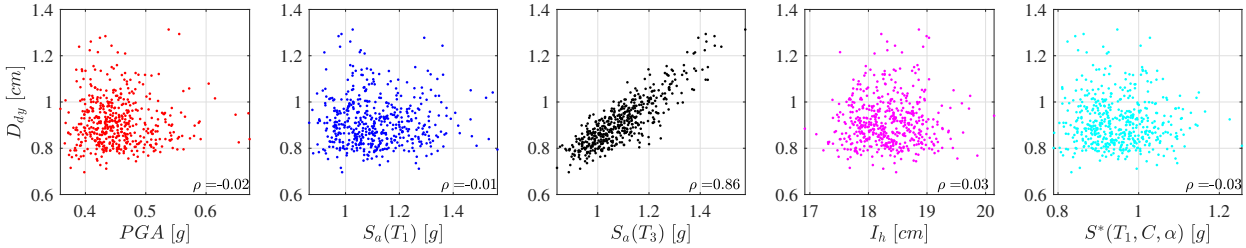

Figure A.2: Scatter plots of $n_s = 500$ samples of (PGA, D_{dy}), $(S_a(T_1), D_{dy})$, $(S_a(T_3), D_{dy})$, (I_h, D_{dy}) and $(S^*(T_1, C, \alpha), D_{dy})$, $\alpha = 90°$, at node #1 - linear analysis.

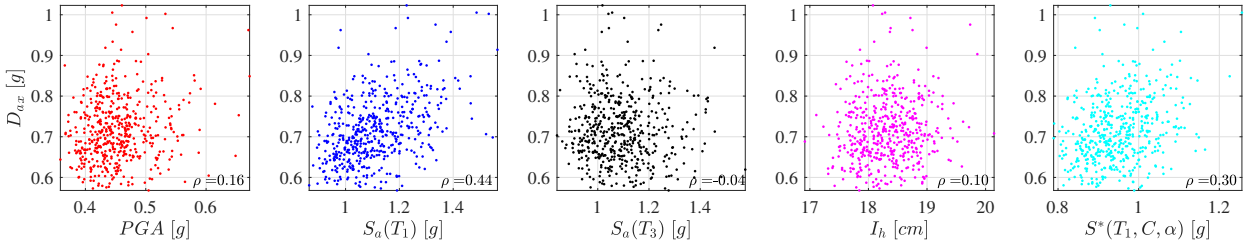

Figure A.3: Scatter plots of $n_s = 500$ samples of (PGA, D_{ax}), $(S_a(T_1), D_{ax})$, $(S_a(T_3), D_{ax})$, (I_h, D_{ax}) and $(S^*(T_1, C, \alpha), D_{ax})$, $\alpha = 0°$, at node #1 - linear analysis.

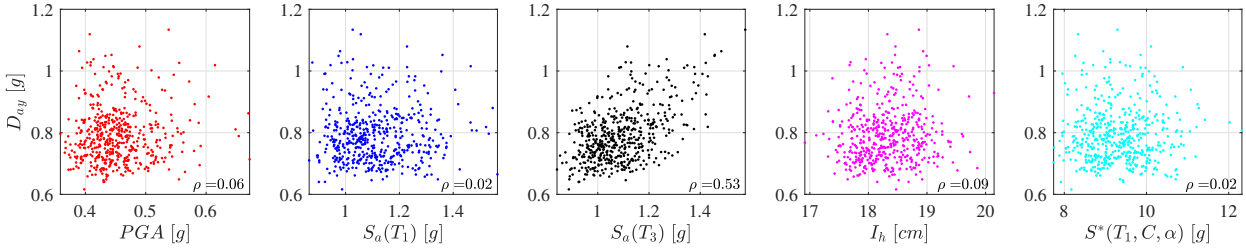

Figure A.4: Scatter plots of $n_s = 500$ samples of (PGA, D_{ay}), $(S_a(T_1), D_{ay})$, $(S_a(T_3), D_{ay})$, (I_h, D_{ay}) and $(S^*(T_1, C, \alpha), D_{ay})$, $\alpha = 90°$, at node #1 - linear analysis.

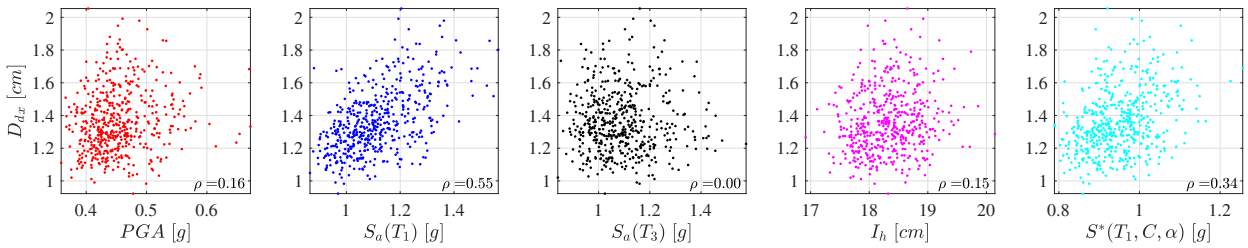

Figure A.5: Scatter plots of $n_s = 500$ samples of (PGA, D_{dx}), $(S_a(T_1), D_{dx})$, $(S_a(T_3), D_{dx})$, (I_h, D_{dx}) and $(S^*(T_1, C, \alpha), D_{dx})$, $\alpha = 0°$, at node #1 - nonlinear analysis.

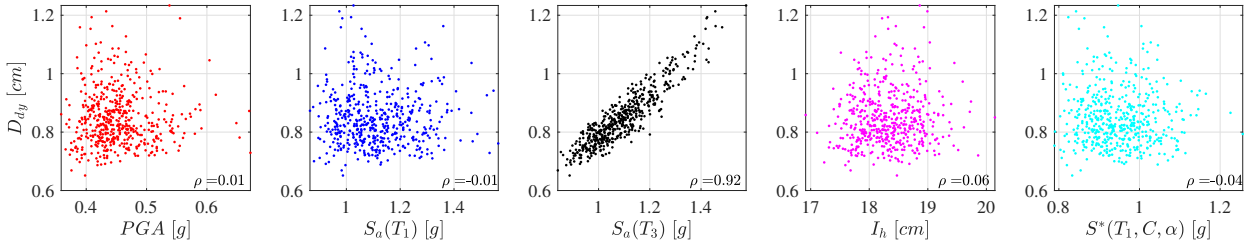

Figure A.6: Scatter plots of $n_s = 500$ samples of (PGA, D_{dy}), $(S_a(T_1), D_{dy})$, $(S_a(T_3), D_{dy})$, (I_h, D_{dy}) and $(S^*(T_1, C, \alpha), D_{dy})$, $\alpha = 90°$, at node #1 - nonlinear analysis.

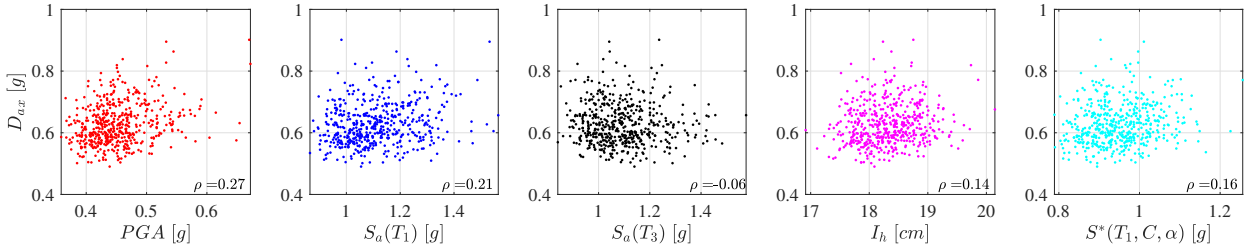

Figure A.7: Scatter plots of $n_s = 500$ samples of (PGA, D_{ax}), $(S_a(T_1), D_{ax})$, $(S_a(T_3), D_{ax})$, (I_h, D_{ax}) and $(S^*(T_1, C, \alpha), D_{ax})$, $\alpha = 0°$, at node #1 - nonlinear analysis.

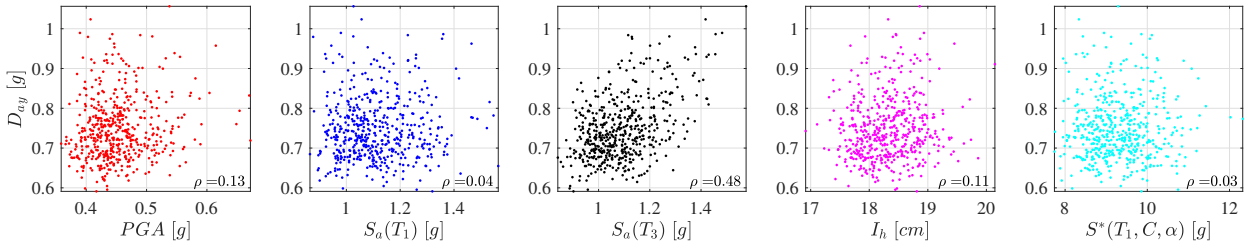

Figure A.8: Scatter plots of $n_s = 500$ samples of (PGA, D_{ay}), $(S_a(T_1), D_{ay})$, $(S_a(T_3), D_{ay})$, (I_h, D_{ay}) and $(S^*(T_1, C, \alpha), D_{ay})$, $\alpha = 90°$, at node #1 - nonlinear analysis.

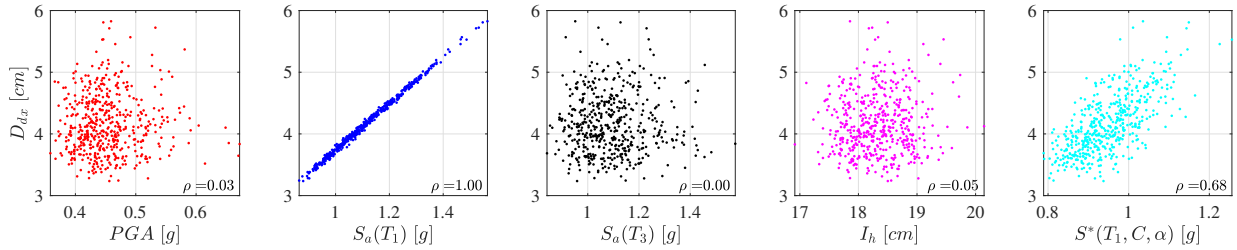

Figure A.9: Scatter plots of $n_s = 500$ samples of (PGA, D_{dx}), $(S_a(T_1), D_{dx})$, $(S_a(T_3), D_{dx})$, (I_h, D_{dx}) and $(S^*(T_1, C, \alpha), D_{dx})$, $\alpha = 0°$, at node #3 - linear analysis.

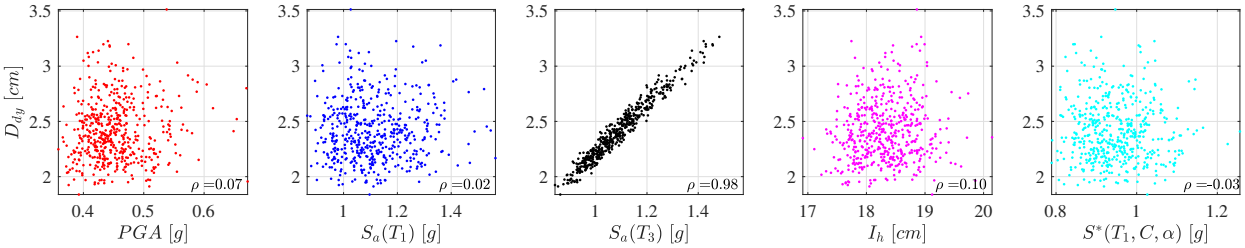

Figure A.10: Scatter plots of $n_s = 500$ samples of (PGA, D_{dy}), $(S_a(T_1), D_{dy})$, $(S_a(T_3), D_{dy})$, (I_h, D_{dy}) and $(S^*(T_1, C, \alpha), D_{dy})$, $\alpha = 90°$, at node #3 - linear analysis.

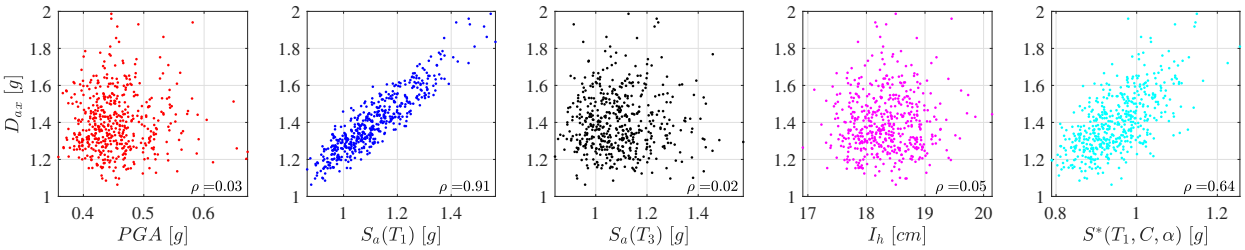

Figure A.11: Scatter plots of $n_s = 500$ samples of (PGA, D_{ax}), $(S_a(T_1), D_{ax})$, $(S_a(T_3), D_{ax})$, (I_h, D_{ax}) and $(S^*(T_1, C, \alpha), D_{ax})$, $\alpha = 0°$, at node #3 - linear analysis.

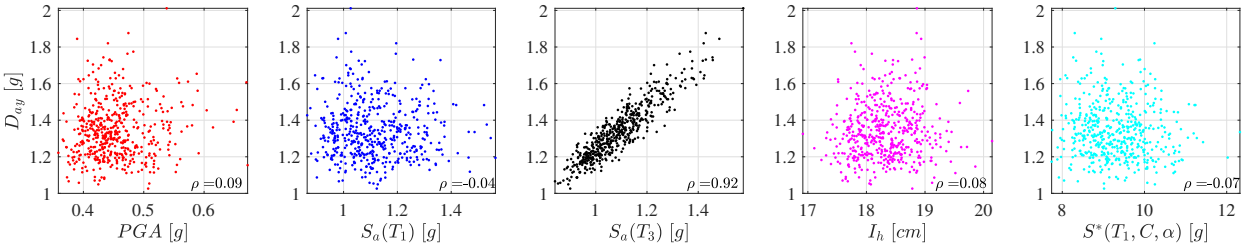

Figure A.12: Scatter plots of $n_s = 500$ samples of (PGA, D_{ay}), $(S_a(T_1), D_{ay})$, $(S_a(T_3), D_{ay})$, (I_h, D_{ay}) and $(S^*(T_1, C, \alpha), D_{ay})$, $\alpha = 90°$, at node #3 - linear analysis.

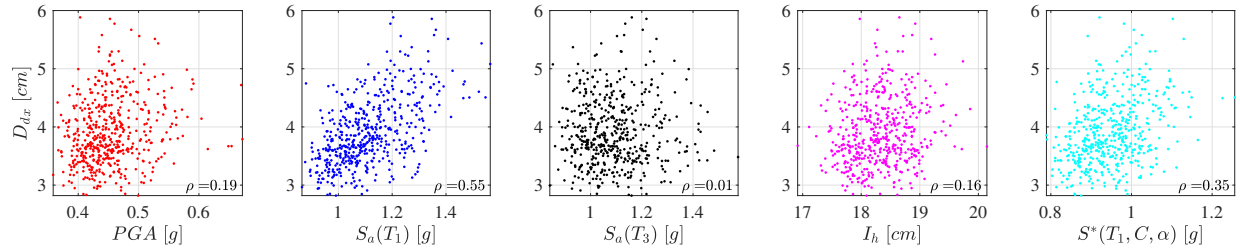

Figure A.13: Scatter plots of $n_s = 500$ samples of (PGA, D_{dx}), $(S_a(T_1), D_{dx})$, $(S_a(T_3), D_{dx})$, (I_h, D_{dx}) and $(S^*(T_1, C, \alpha), D_{dx})$, $\alpha = 0°$, at node #3 - nonlinear analysis.

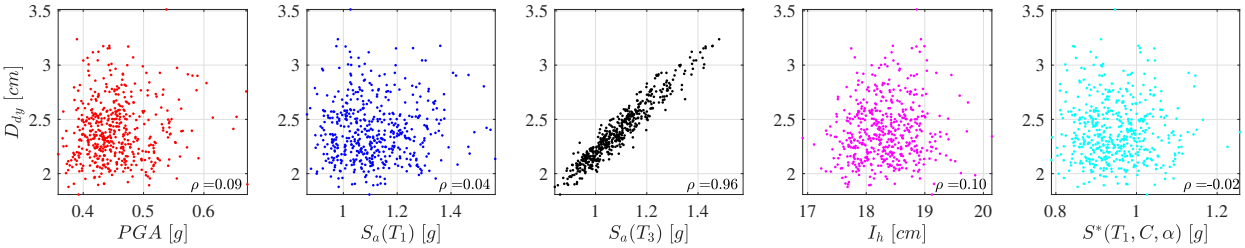

Figure A.14: Scatter plots of $n_s = 500$ samples of (PGA, D_{dy}), $(S_a(T_1), D_{dy})$, $(S_a(T_3), D_{dy})$, (I_h, D_{dy}) and $(S^*(T_1, C, \alpha), D_{dy})$, $\alpha = 90°$, at node #3 - nonlinear analysis.

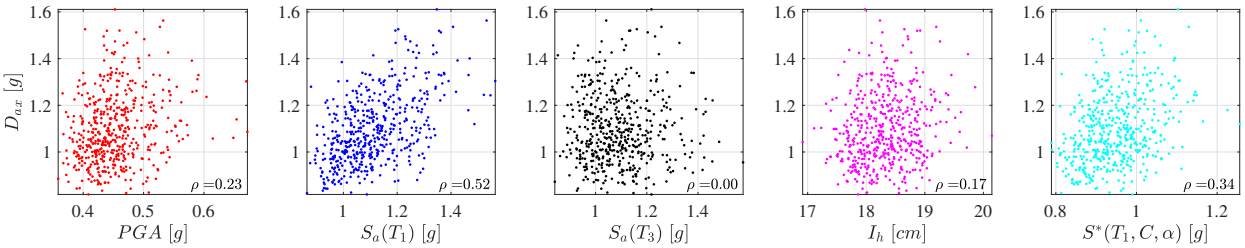

Figure A.15: Scatter plots of $n_s = 500$ samples of (PGA, D_{ax}), $(S_a(T_1), D_{ax})$, $(S_a(T_3), D_{ax})$, (I_h, D_{ax}) and $(S^*(T_1, C, \alpha), D_{ax})$, $\alpha = 0°$, at node #3 - nonlinear analysis.

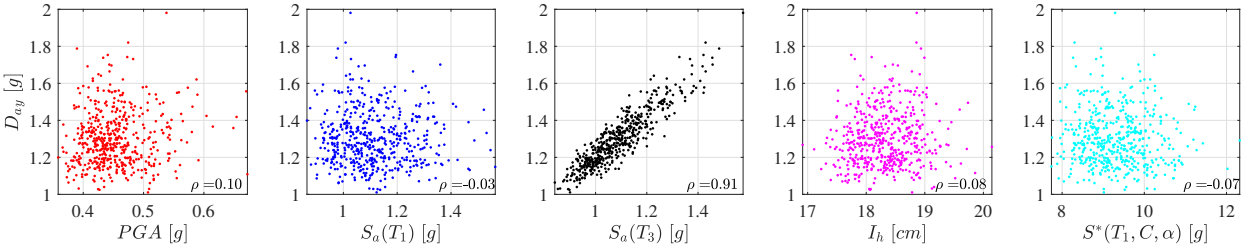

Figure A.16: Scatter plots of $n_s = 500$ samples of (PGA, D_{ay}), $(S_a(T_1), D_{ay})$, $(S_a(T_3), D_{ay})$, (I_h, D_{ay}) and $(S^*(T_1, C, \alpha), D_{ay})$, $\alpha = 90°$, at node #3 - nonlinear analysis.

Appendix B

Supplementary results of bidirectional dynamic analysis

This appendix contains further results obtained from the bidirectional dynamic analysis according to Figure 6.14. The non-stationary samples of the process in Subsection 6.2.1 are used to develop the linear/nonlinear analysis. Dependence study between the demand parameters and the selected intensity measures, the correlation improvement by procedure in Section 4.4 and all the results of the fragility analysis are reported.

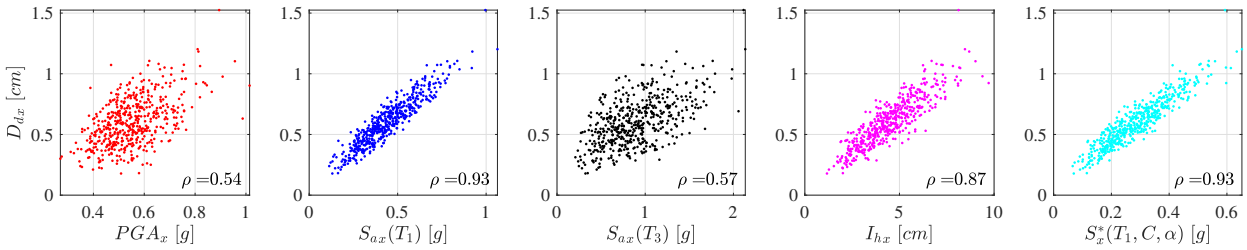

Figure B.1: Scatter plots of $n_s = 500$ samples of (PGA_x, D_{dx}), $(S_{ax}(T_1), D_{dx})$, $(S_{ax}(T_3), D_{dx})$, (I_{hx}, D_{dx}) and $(S^*{}_x(T_1, C, \alpha), D_{dx})$ at node #1 - linear analysis.

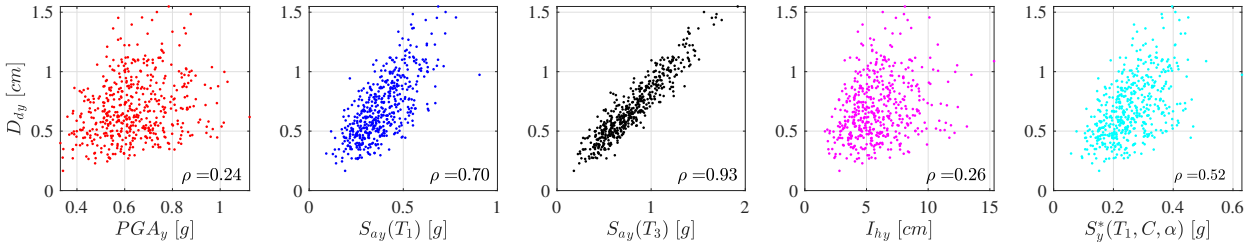

Figure B.2: Scatter plots of $n_s = 500$ samples of $(PGA_y, D_{d)}$, $(S_{ay}(T_1), D_{dy})$, $(S_{ay}(T_3), D_{dy})$, (I_{hy}, D_{dy}) and $(S^*{}_y(T_1, C, \alpha), D_{dy})$ at node #1 - linear analysis.

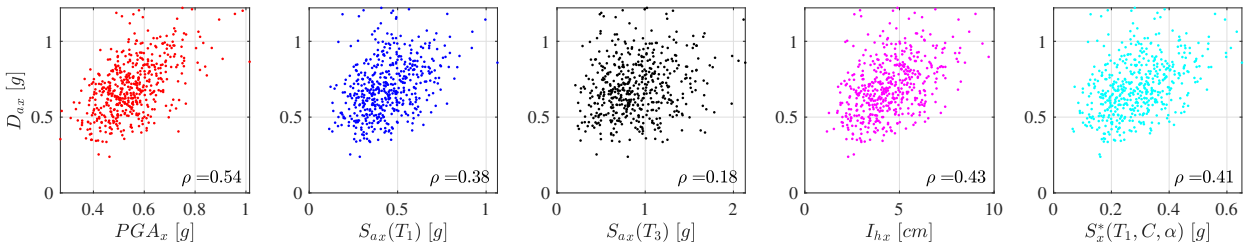

Figure B.3: Scatter plots of $n_s = 500$ samples of (PGA_x, D_{ax}), $(S_{ax}(T_1), D_{ax})$, $(S_{ax}(T_3), D_{ax})$, (I_{hx}, D_{ax}) and $(S^*{}_x(T_1, C, \alpha), D_{ax})$ at node #1 - linear analysis.

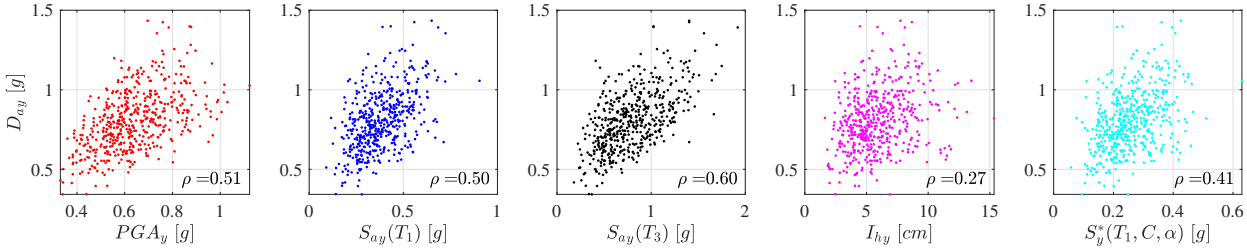

Figure B.4: Scatter plots of $n_s = 500$ samples of (PGA_y, D_{ay}), $(S_{ay}(T_1), D_{ay})$, $(S_{ay}(T_3), D_{ay})$, (I_{hy}, D_{ay}) and $(S^*{}_y(T_1, C, \alpha), D_{ay})$ at node #1 - linear analysis.

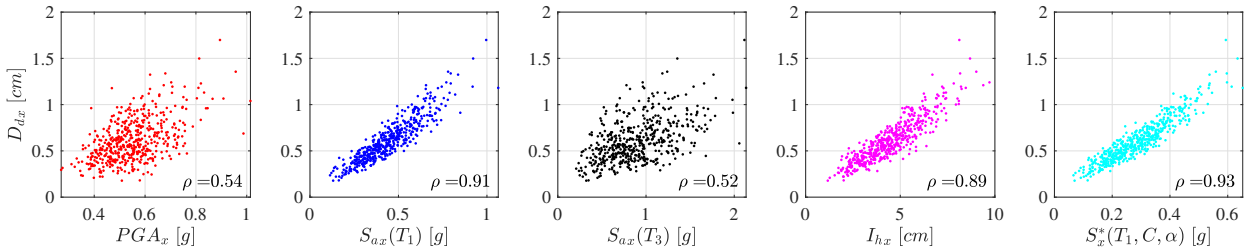

Figure B.5: Scatter plots of $n_s = 500$ samples of (PGA_x, D_{dx}), $(S_{ax}(T_1), D_{dx})$, $(S_{ax}(T_3), D_{dx})$, (I_{hx}, D_{dx}) and $(S^*{}_x(T_1, C, \alpha), D_{dx})$ at node #1 - nonlinear analysis.

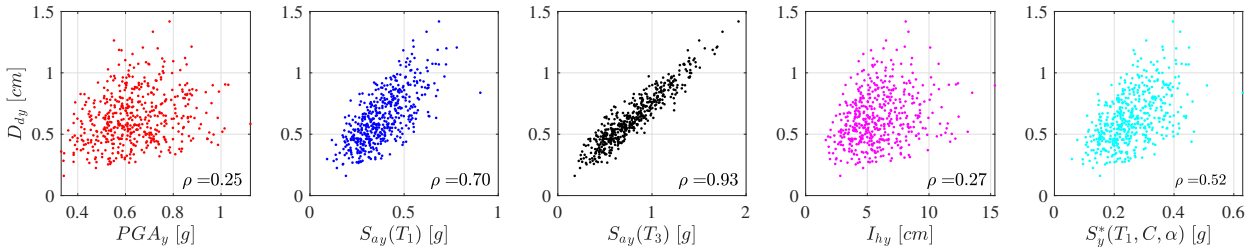

Figure B.6: Scatter plots of $n_s = 500$ samples of $(PGA_y, D_{d)}$, $(S_{ay}(T_1), D_{dy})$, $(S_{ay}(T_3), D_{dy})$, (I_{hy}, D_{dy}) and $(S^*{}_y(T_1, C, \alpha), D_{dy})$ at node #1 - nonlinear analysis.

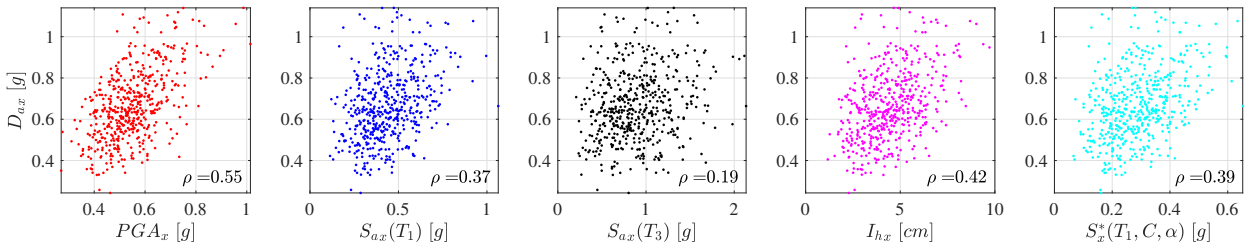

Figure B.7: Scatter plots of $n_s = 500$ samples of (PGA_x, D_{ax}), $(S_{ax}(T_1), D_{ax})$, $(S_{ax}(T_3), D_{ax})$, (I_{hx}, D_{ax}) and $(S^*{}_x(T_1, C, \alpha), D_{ax})$ at node #1 - nonlinear analysis.

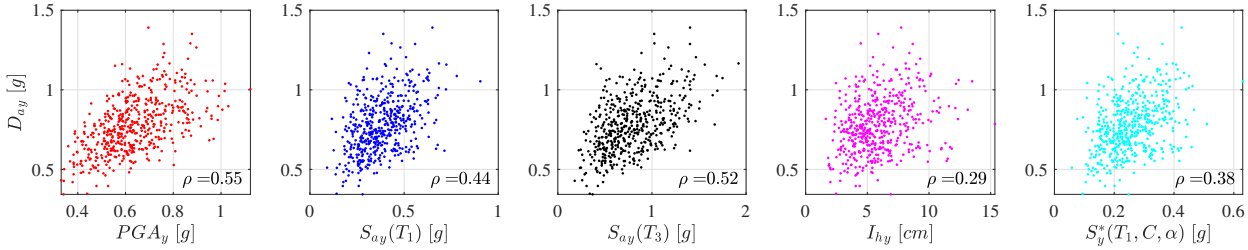

Figure B.8: Scatter plots of $n_s = 500$ samples of (PGA_y, D_{ay}), $(S_{ay}(T_1), D_{ay})$, $(S_{ay}(T_3), D_{ay})$, (I_{hy}, D_{ay}) and $(S^*{}_y(T_1, C, \alpha), D_{ay})$ at node #1 - nonlinear analysis.

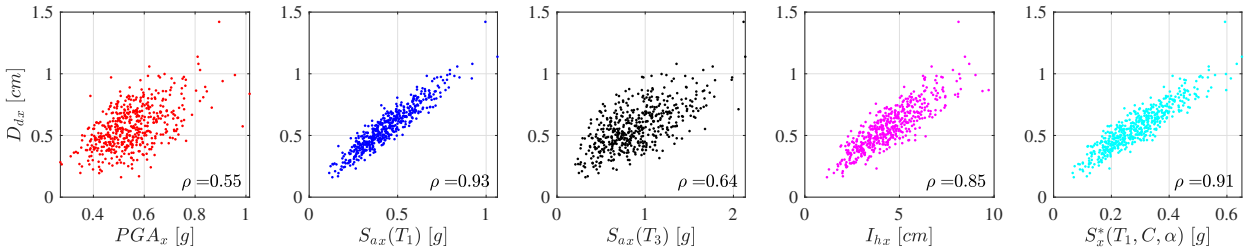

Figure B.9: Scatter plots of $n_s = 500$ samples of (PGA_x, D_{dx}), $(S_{ax}(T_1), D_{dx})$, $(S_{ax}(T_3), D_{dx})$, (I_{hx}, D_{dx}) and $(S^*{}_x(T_1, C, \alpha), D_{dx})$ at node #2 - linear analysis.

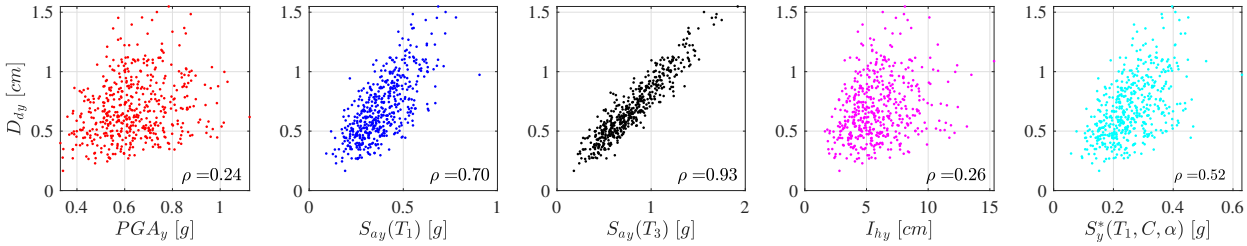

Figure B.10: Scatter plots of $n_s = 500$ samples of $(PGA_y, D_{d)}$, $(S_{ay}(T_1), D_{dy})$, $(S_{ay}(T_3), D_{dy})$, (I_{hy}, D_{dy}) and $(S^*{}_y(T_1, C, \alpha), D_{dy})$ at node #2 - linear analysis.

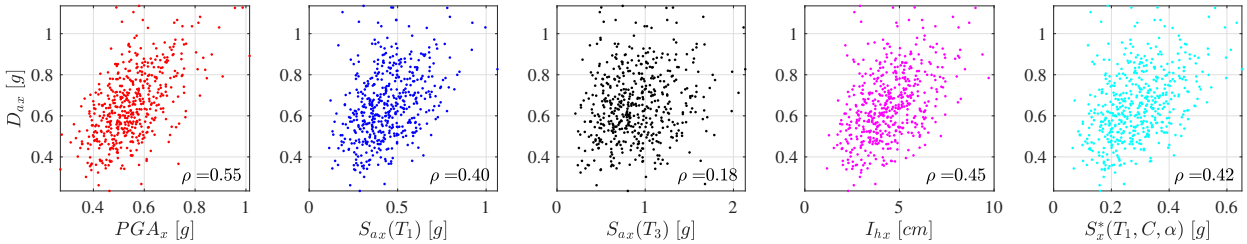

Figure B.11: Scatter plots of $n_s = 500$ samples of (PGA_x, D_{ax}), $(S_{ax}(T_1), D_{ax})$, $(S_{ax}(T_3), D_{ax})$, (I_{hx}, D_{ax}) and $(S^*{}_x(T_1, C, \alpha), D_{ax})$ at node #2 - linear analysis.

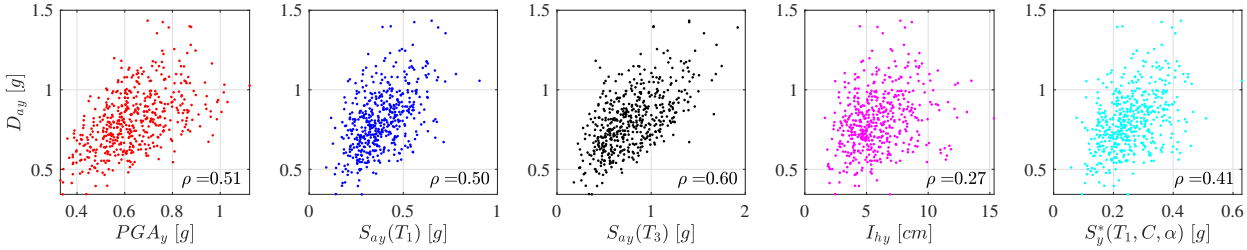

Figure B.12: Scatter plots of $n_s = 500$ samples of (PGA_y, D_{ay}), $(S_{ay}(T_1), D_{ay})$, $(S_{ay}(T_3), D_{ay})$, (I_{hy}, D_{ay}) and $(S^*{}_y(T_1, C, \alpha), D_{ay})$ at node #2 - linear analysis.

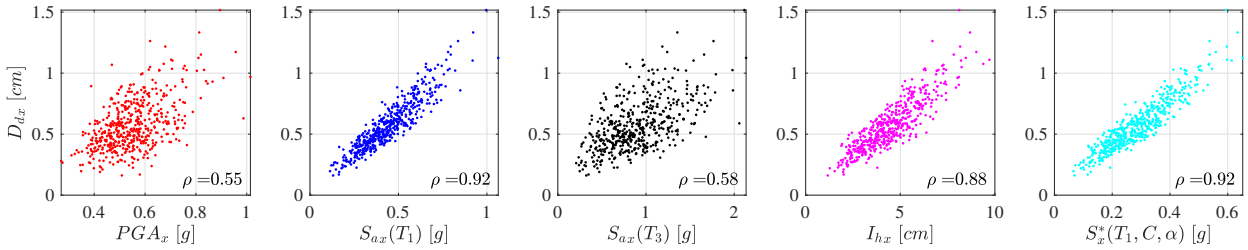

Figure B.13: Scatter plots of $n_s = 500$ samples of (PGA_x, D_{dx}), $(S_{ax}(T_1), D_{dx})$, $(S_{ax}(T_3), D_{dx})$, (I_{hx}, D_{dx}) and $(S^*{}_x(T_1, C, \alpha), D_{dx})$ at node #2 - nonlinear analysis.

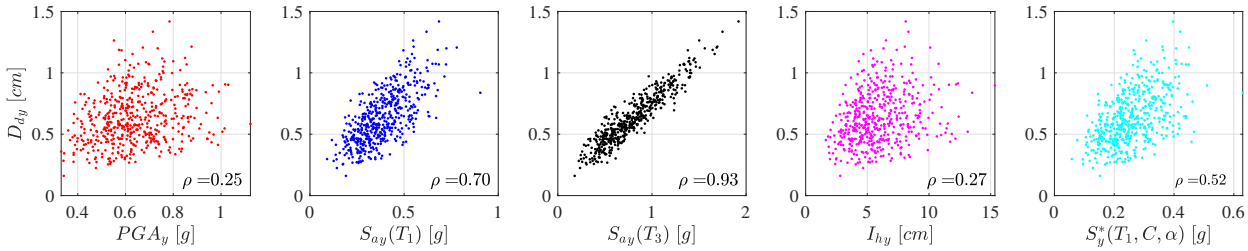

Figure B.14: Scatter plots of $n_s = 500$ samples of $(PGA_y, D_{d)}$, $(S_{ay}(T_1), D_{dy})$, $(S_{ay}(T_3), D_{dy})$, (I_{hy}, D_{dy}) and $(S^*{}_y(T_1, C, \alpha), D_{dy})$ at node #2 - nonlinear analysis.

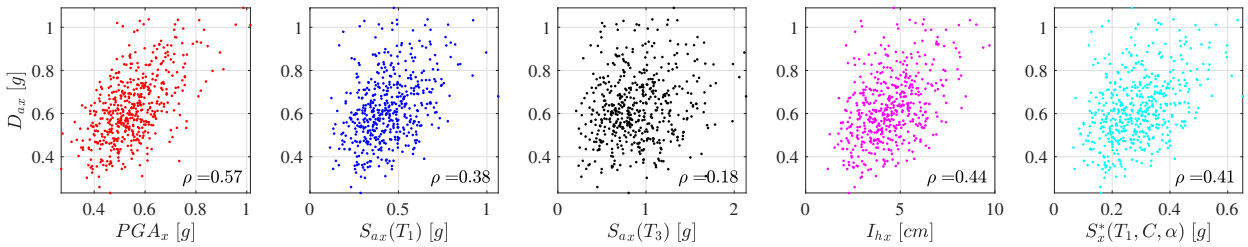

Figure B.15: Scatter plots of $n_s = 500$ samples of (PGA_x, D_{ax}), $(S_{ax}(T_1), D_{ax})$, $(S_{ax}(T_3), D_{ax})$, (I_{hx}, D_{ax}) and $(S^*{}_x(T_1, C, \alpha), D_{ax})$ at node #2 - nonlinear analysis.

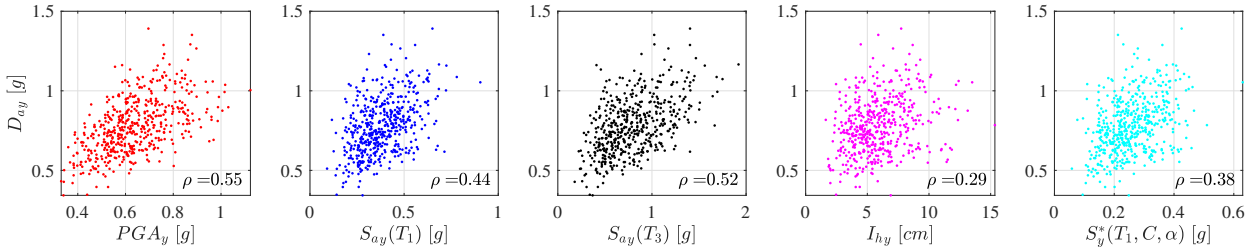

Figure B.16: Scatter plots of $n_s = 500$ samples of (PGA_y, D_{ay}), $(S_{ay}(T_1), D_{ay})$, $(S_{ay}(T_3), D_{ay})$, (I_{hy}, D_{ay}) and $(S^*{}_y(T_1, C, \alpha), D_{ay})$ at node #2 - nonlinear analysis.

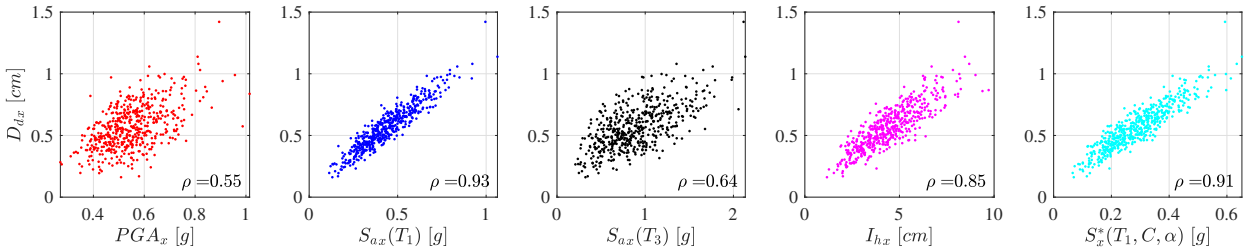

Figure B.17: Scatter plots of $n_s = 500$ samples of (PGA_x, D_{dx}), $(S_{ax}(T_1), D_{dx})$, $(S_{ax}(T_3), D_{dx})$, (I_{hx}, D_{dx}) and $(S^*{}_x(T_1, C, \alpha), D_{dx})$ at node #3 - linear analysis.

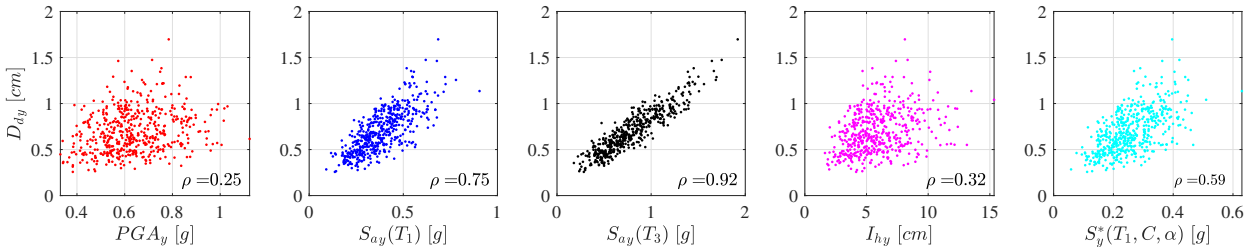

Figure B.18: Scatter plots of $n_s = 500$ samples of $(PGA_y, D_{d)}$, $(S_{ay}(T_1), D_{dy})$, $(S_{ay}(T_3), D_{dy})$, (I_{hy}, D_{dy}) and $(S^*{}_y(T_1, C, \alpha), D_{dy})$ at node #3 - linear analysis.

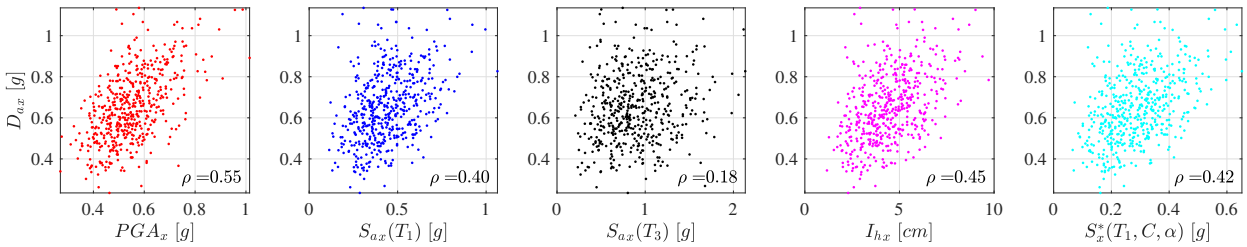

Figure B.19: Scatter plots of $n_s = 500$ samples of (PGA_x, D_{ax}), $(S_{ax}(T_1), D_{ax})$, $(S_{ax}(T_3), D_{ax})$, (I_{hx}, D_{ax}) and $(S^*{}_x(T_1, C, \alpha), D_{ax})$ at node #3 - linear analysis.

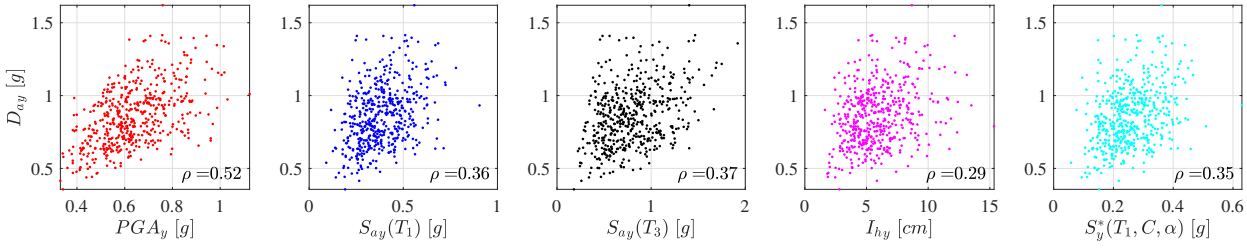

Figure B.20: Scatter plots of $n_s = 500$ samples of (PGA_y, D_{ay}), $(S_{ay}(T_1), D_{ay})$, $(S_{ay}(T_3), D_{ay})$, (I_{hy}, D_{ay}) and $(S^*{}_y(T_1, C, \alpha), D_{ay})$ at node #3 - linear analysis.

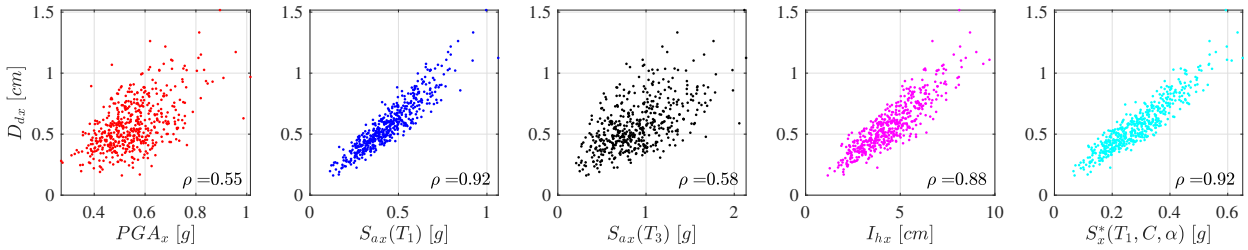

Figure B.21: Scatter plots of $n_s = 500$ samples of (PGA_x, D_{dx}), $(S_{ax}(T_1), D_{dx})$, $(S_{ax}(T_3), D_{dx})$, (I_{hx}, D_{dx}) and $(S^*{}_x(T_1, C, \alpha), D_{dx})$ at node #3 - nonlinear analysis.

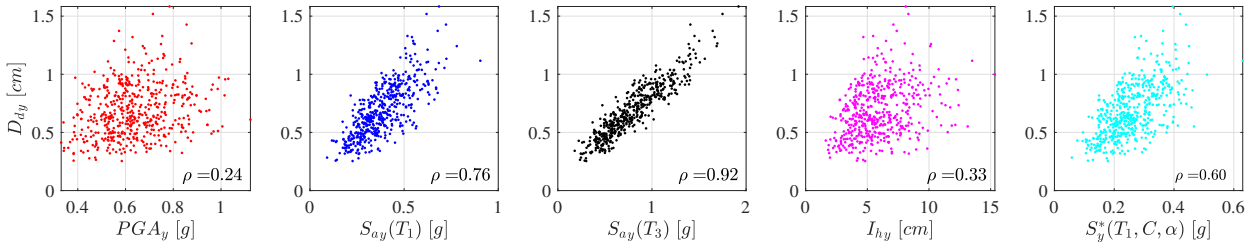

Figure B.22: Scatter plots of $n_s = 500$ samples of $(PGA_y, D_{d)}$, $(S_{ay}(T_1), D_{dy})$, $(S_{ay}(T_3), D_{dy})$, (I_{hy}, D_{dy}) and $(S^*{}_y(T_1, C, \alpha), D_{dy})$ at node #3 - nonlinear analysis.

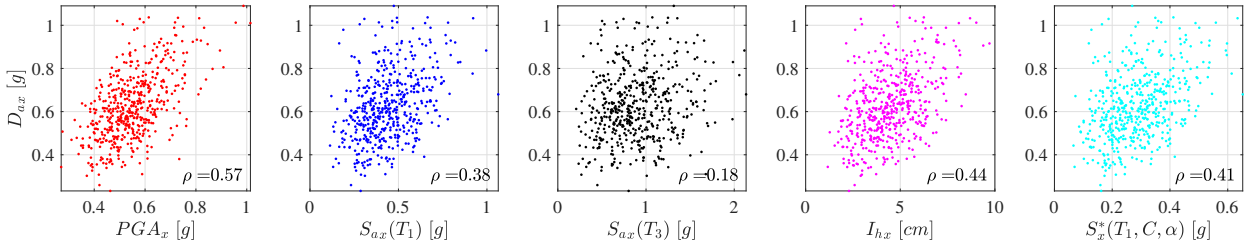

Figure B.23: Scatter plots of $n_s = 500$ samples of (PGA_x, D_{ax}), $(S_{ax}(T_1), D_{ax})$, $(S_{ax}(T_3), D_{ax})$, (I_{hx}, D_{ax}) and $(S^*{}_x(T_1, C, \alpha), D_{ax})$ at node #3 - nonlinear analysis.

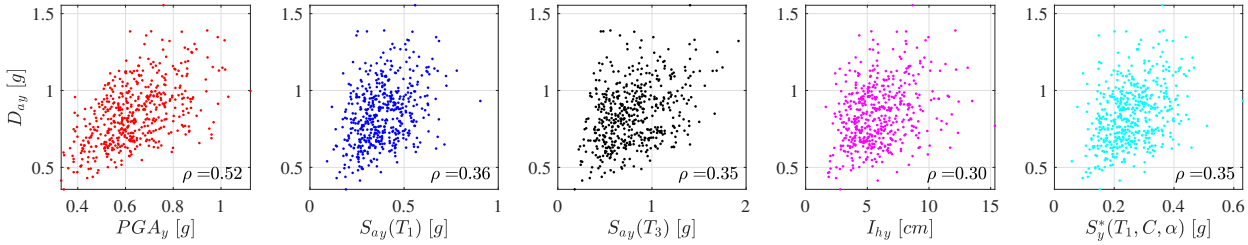

Figure B.24: Scatter plots of $n_s = 500$ samples of (PGA_y, D_{ay}), $(S_{ay}(T_1), D_{ay})$, $(S_{ay}(T_3), D_{ay})$, (I_{hy}, D_{ay}) and $(S^*{}_y(T_1, C, \alpha), D_{ay})$ at node #3 - nonlinear analysis.

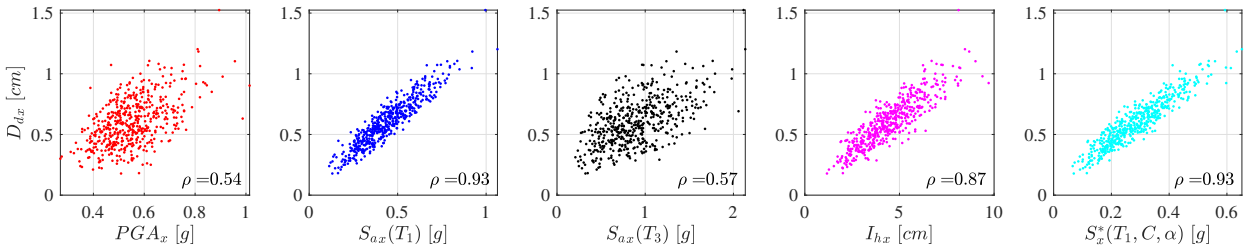

Figure B.25: Scatter plots of $n_s = 500$ samples of (PGA_x, D_{dx}), $(S_{ax}(T_1), D_{dx})$, $(S_{ax}(T_3), D_{dx})$, (I_{hx}, D_{dx}) and $(S^*{}_x(T_1, C, \alpha), D_{dx})$ at node #4 - linear analysis.

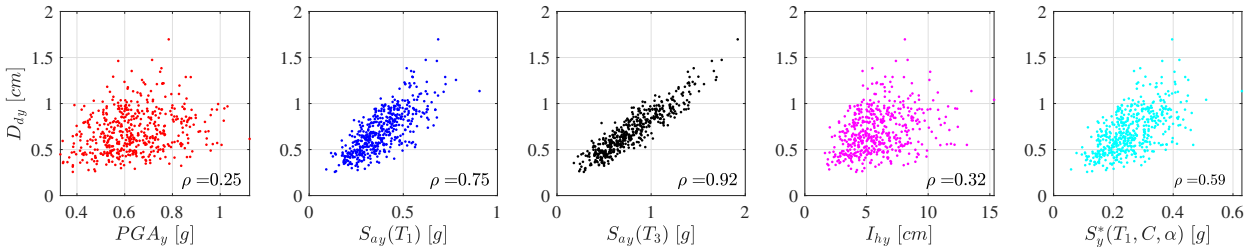

Figure B.26: Scatter plots of $n_s = 500$ samples of $(PGA_y, D_{d)}$, $(S_{ay}(T_1), D_{dy})$, $(S_{ay}(T_3), D_{dy})$, (I_{hy}, D_{dy}) and $(S^*{}_y(T_1, C, \alpha), D_{dy})$ at node #4 - linear analysis.

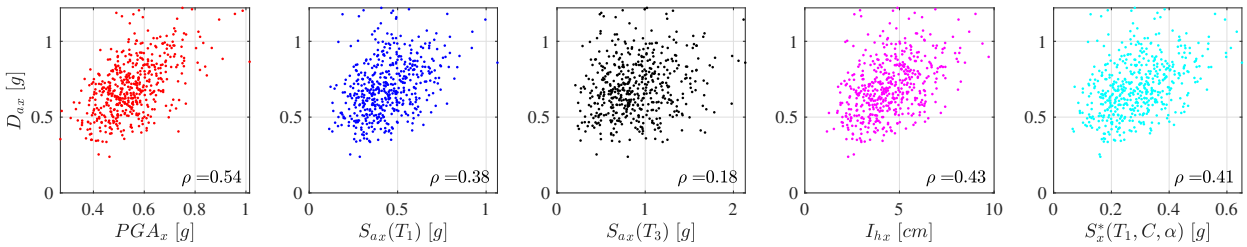

Figure B.27: Scatter plots of $n_s = 500$ samples of (PGA_x, D_{ax}), $(S_{ax}(T_1), D_{ax})$, $(S_{ax}(T_3), D_{ax})$, (I_{hx}, D_{ax}) and $(S^*{}_x(T_1, C, \alpha), D_{ax})$ at node #4 - linear analysis.

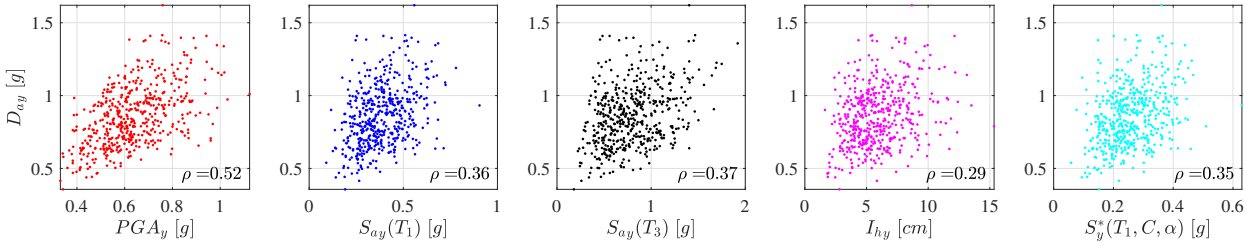

Figure B.28: Scatter plots of $n_s = 500$ samples of (PGA_y, D_{ay}), $(S_{ay}(T_1), D_{ay})$, $(S_{ay}(T_3), D_{ay})$, (I_{hy}, D_{ay}) and $(S^*{}_y(T_1, C, \alpha), D_{ay})$ at node #4 - linear analysis.

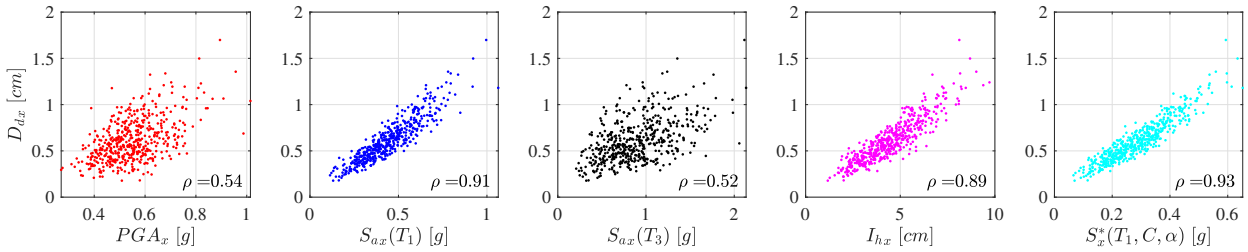

Figure B.29: Scatter plots of $n_s = 500$ samples of (PGA_x, D_{dx}), $(S_{ax}(T_1), D_{dx})$, $(S_{ax}(T_3), D_{dx})$, (I_{hx}, D_{dx}) and $(S^*{}_x(T_1, C, \alpha), D_{dx})$ at node #4 - nonlinear analysis.

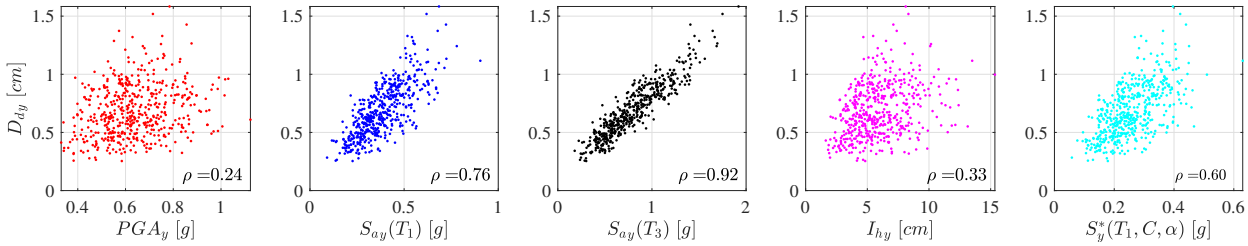

Figure B.30: Scatter plots of $n_s = 500$ samples of $(PGA_y, D_{d)}$, $(S_{ay}(T_1), D_{dy})$, $(S_{ay}(T_3), D_{dy})$, (I_{hy}, D_{dy}) and $(S^*{}_y(T_1, C, \alpha), D_{dy})$ at node #4 - nonlinear analysis.

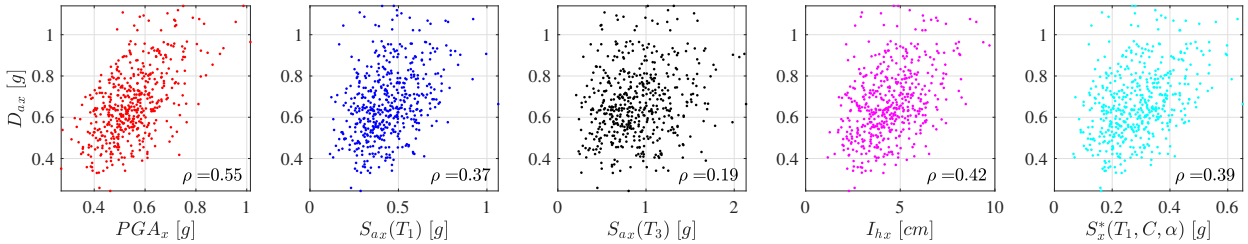

Figure B.31: Scatter plots of $n_s = 500$ samples of (PGA_x, D_{ax}), $(S_{ax}(T_1), D_{ax})$, $(S_{ax}(T_3), D_{ax})$, (I_{hx}, D_{ax}) and $(S^*{}_x(T_1, C, \alpha), D_{ax})$ at node #4 - nonlinear analysis.

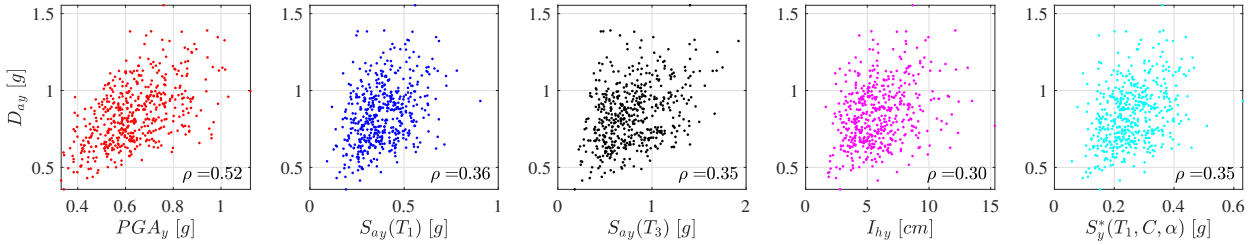

Figure B.32: Scatter plots of $n_s = 500$ samples of (PGA_y, D_{ay}), $(S_{ay}(T_1), D_{ay})$, $(S_{ay}(T_3), D_{ay})$, (I_{hy}, D_{ay}) and $(S^*{}_y(T_1, C, \alpha), D_{ay})$ at node #4 - nonlinear analysis.

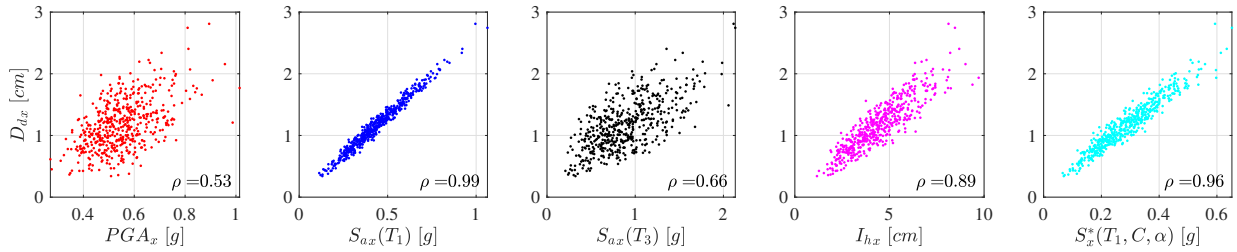

Figure B.33: Scatter plots of $n_s = 500$ samples of (PGA_x, D_{dx}), $(S_{ax}(T_1), D_{dx})$, $(S_{ax}(T_3), D_{dx})$, (I_{hx}, D_{dx}) and $(S^*{}_x(T_1, C, \alpha), D_{dx})$ at node #5 - linear analysis.

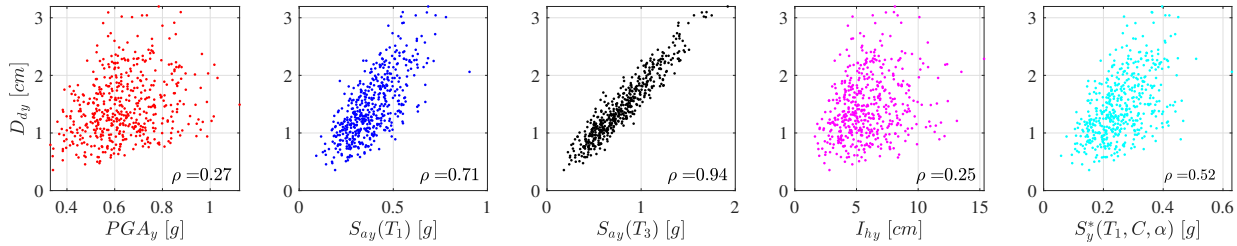

Figure B.34: Scatter plots of $n_s = 500$ samples of $(PGA_y, D_{d)}$, $(S_{ay}(T_1), D_{dy})$, $(S_{ay}(T_3), D_{dy})$, (I_{hy}, D_{dy}) and $(S^*{}_y(T_1, C, \alpha), D_{dy})$ at node #5 - linear analysis.

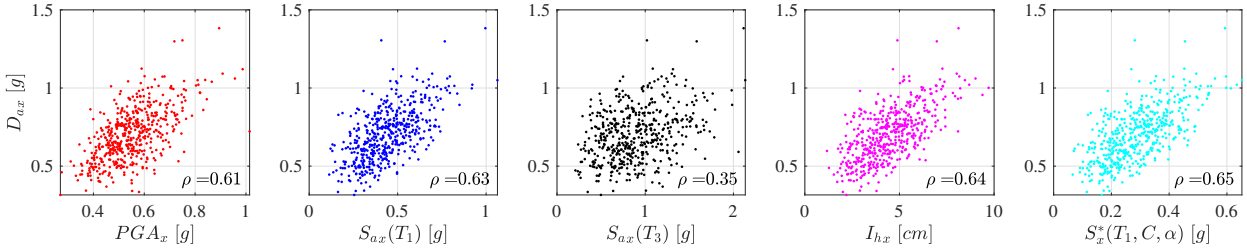

Figure B.35: Scatter plots of $n_s = 500$ samples of (PGA_x, D_{ax}), $(S_{ax}(T_1), D_{ax})$, $(S_{ax}(T_3), D_{ax})$, (I_{hx}, D_{ax}) and $(S^*{}_x(T_1, C, \alpha), D_{ax})$ at node #5 - linear analysis.

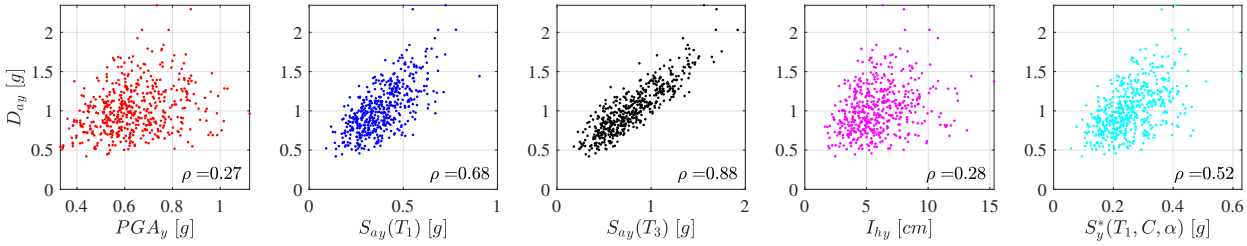

Figure B.36: Scatter plots of $n_s = 500$ samples of (PGA_y, D_{ay}), $(S_{ay}(T_1), D_{ay})$, $(S_{ay}(T_3), D_{ay})$, (I_{hy}, D_{ay}) and $(S^*{}_y(T_1, C, \alpha), D_{ay})$ at node #5 - linear analysis.

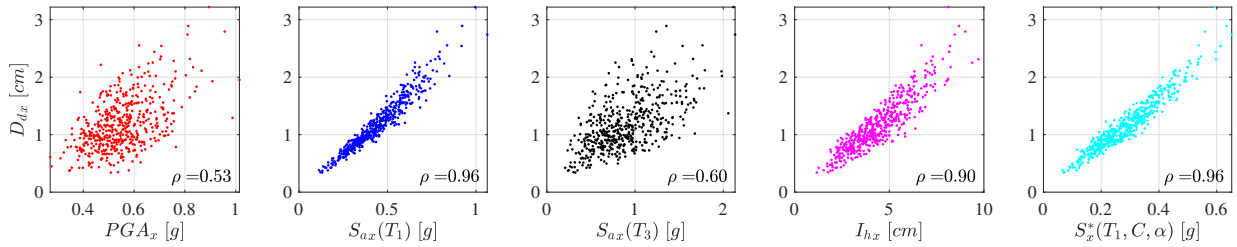

Figure B.37: Scatter plots of $n_s = 500$ samples of (PGA_x, D_{dx}), $(S_{ax}(T_1), D_{dx})$, $(S_{ax}(T_3), D_{dx})$, (I_{hx}, D_{dx}) and $(S^*{}_x(T_1, C, \alpha), D_{dx})$ at node #5 - nonlinear analysis.

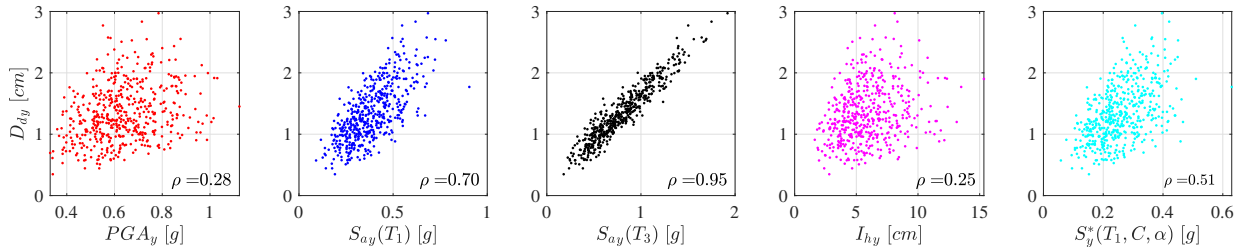

Figure B.38: Scatter plots of $n_s = 500$ samples of $(PGA_y, D_{d)}$, $(S_{ay}(T_1), D_{dy})$, $(S_{ay}(T_3), D_{dy})$, (I_{hy}, D_{dy}) and $(S^*{}_y(T_1, C, \alpha), D_{dy})$ at node #5 - nonlinear analysis.

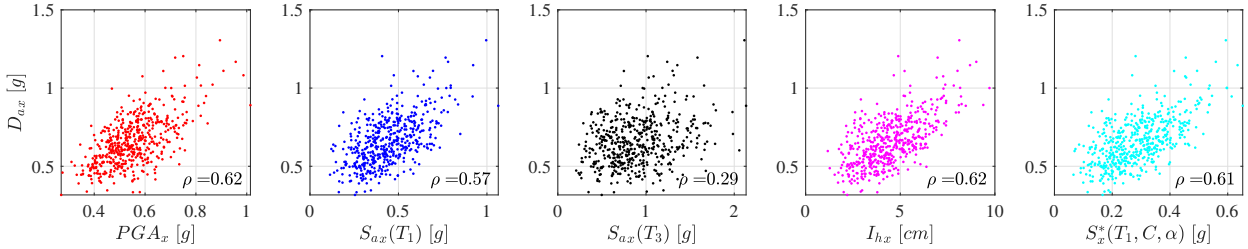

Figure B.39: Scatter plots of $n_s = 500$ samples of (PGA_x, D_{ax}), $(S_{ax}(T_1), D_{ax})$, $(S_{ax}(T_3), D_{ax})$, (I_{hx}, D_{ax}) and $(S^*{}_x(T_1, C, \alpha), D_{ax})$ at node #5 - nonlinear analysis.

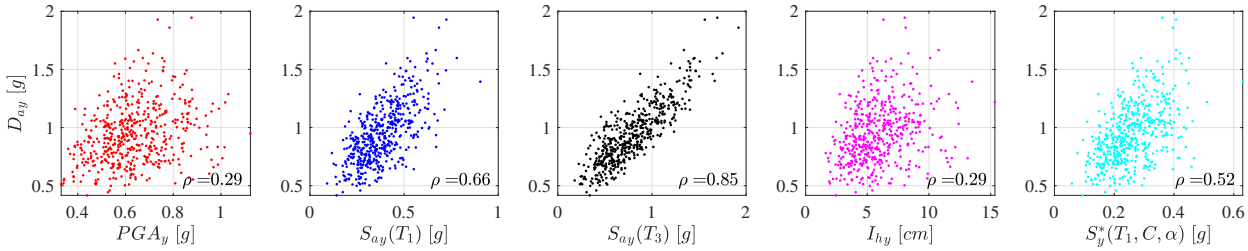

Figure B.40: Scatter plots of $n_s = 500$ samples of (PGA_y, D_{ay}), $(S_{ay}(T_1), D_{ay})$, $(S_{ay}(T_3), D_{ay})$, (I_{hy}, D_{ay}) and $(S^*{}_y(T_1, C, \alpha), D_{ay})$ at node #5 - nonlinear analysis.

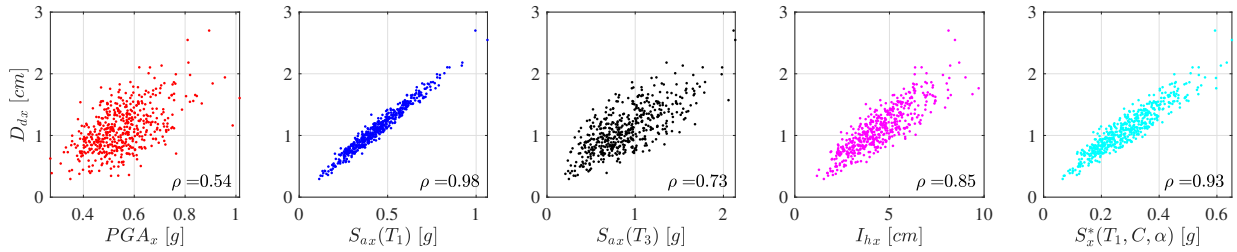

Figure B.41: Scatter plots of $n_s = 500$ samples of (PGA_x, D_{dx}), $(S_{ax}(T_1), D_{dx})$, $(S_{ax}(T_3), D_{dx})$, (I_{hx}, D_{dx}) and $(S^*{}_x(T_1, C, \alpha), D_{dx})$ at node #6 - linear analysis.

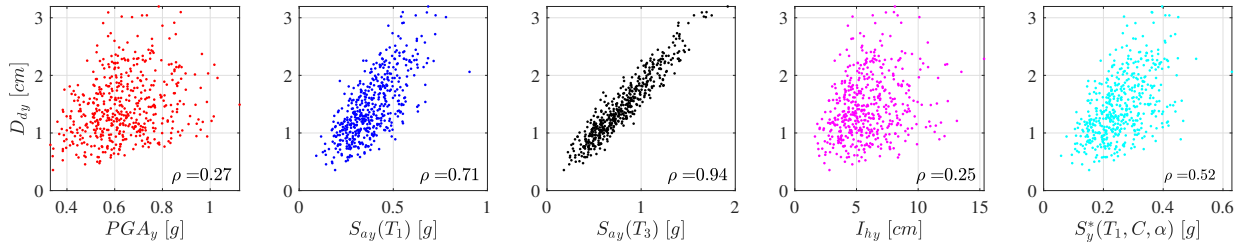

Figure B.42: Scatter plots of $n_s = 500$ samples of $(PGA_y, D_{d)}$, $(S_{ay}(T_1), D_{dy})$, $(S_{ay}(T_3), D_{dy})$, (I_{hy}, D_{dy}) and $(S^*{}_y(T_1, C, \alpha), D_{dy})$ at node #6 - linear analysis.

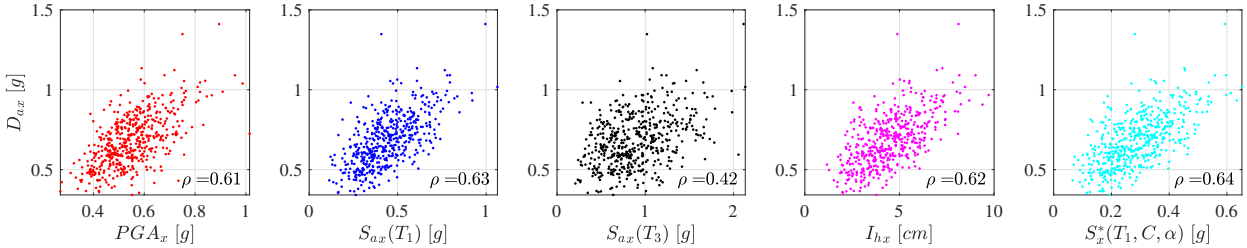

Figure B.43: Scatter plots of $n_s = 500$ samples of (PGA_x, D_{ax}), $(S_{ax}(T_1), D_{ax})$, $(S_{ax}(T_3), D_{ax})$, (I_{hx}, D_{ax}) and $(S^*{}_x(T_1, C, \alpha), D_{ax})$ at node #6 - linear analysis.

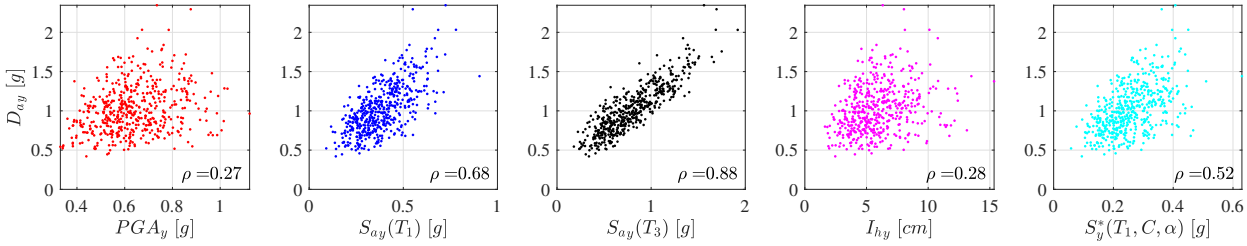

Figure B.44: Scatter plots of $n_s = 500$ samples of (PGA_y, D_{ay}), $(S_{ay}(T_1), D_{ay})$, $(S_{ay}(T_3), D_{ay})$, (I_{hy}, D_{ay}) and $(S^*{}_y(T_1, C, \alpha), D_{ay})$ at node #6 - linear analysis.

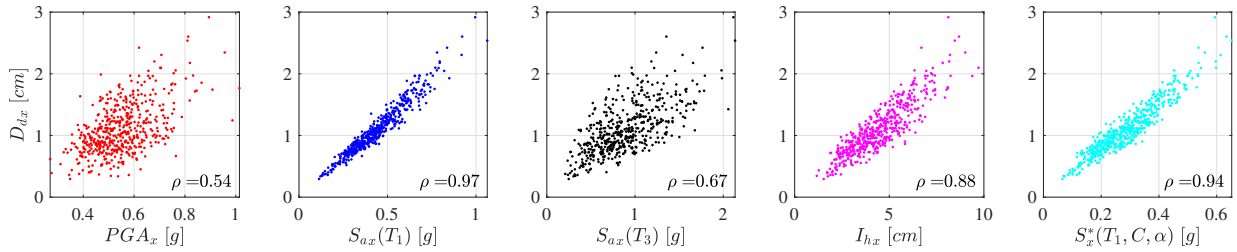

Figure B.45: Scatter plots of $n_s = 500$ samples of (PGA_x, D_{dx}), $(S_{ax}(T_1), D_{dx})$, $(S_{ax}(T_3), D_{dx})$, (I_{hx}, D_{dx}) and $(S^*{}_x(T_1, C, \alpha), D_{dx})$ at node #6 - nonlinear analysis.

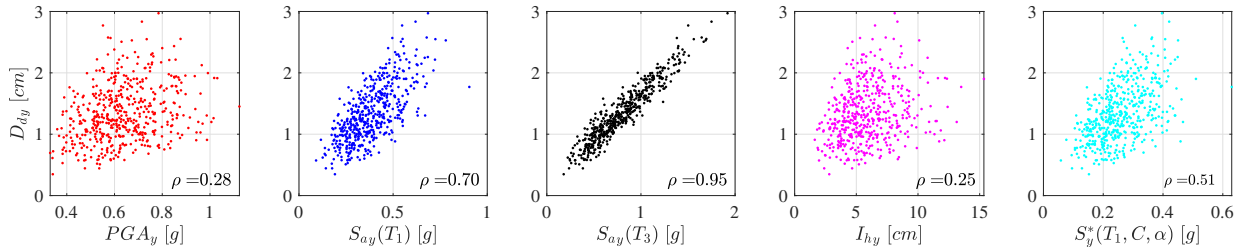

Figure B.46: Scatter plots of $n_s = 500$ samples of $(PGA_y, D_{d)}$, $(S_{ay}(T_1), D_{dy})$, $(S_{ay}(T_3), D_{dy})$, (I_{hy}, D_{dy}) and $(S^*{}_y(T_1, C, \alpha), D_{dy})$ at node #6 - nonlinear analysis.

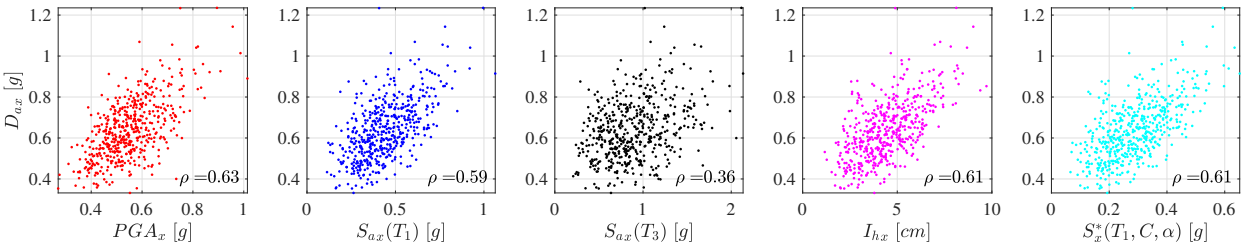

Figure B.47: Scatter plots of $n_s = 500$ samples of (PGA_x, D_{ax}), $(S_{ax}(T_1), D_{ax})$, $(S_{ax}(T_3), D_{ax})$, (I_{hx}, D_{ax}) and $(S^*{}_x(T_1, C, \alpha), D_{ax})$ at node #6 - nonlinear analysis.

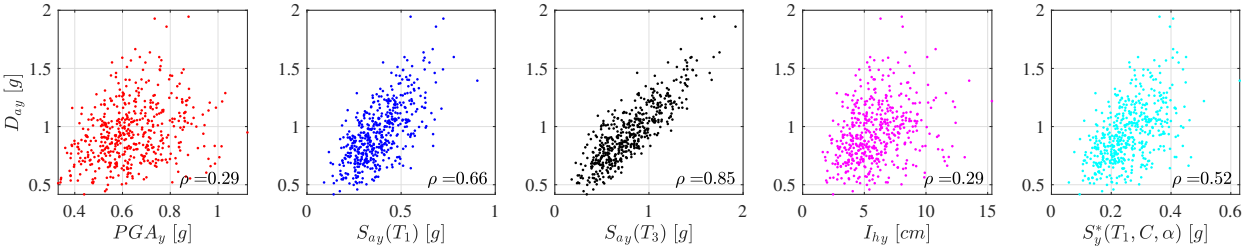

Figure B.48: Scatter plots of $n_s = 500$ samples of (PGA_y, D_{ay}), $(S_{ay}(T_1), D_{ay})$, $(S_{ay}(T_3), D_{ay})$, (I_{hy}, D_{ay}) and $(S^*{}_y(T_1, C, \alpha), D_{ay})$ at node #6 - nonlinear analysis.

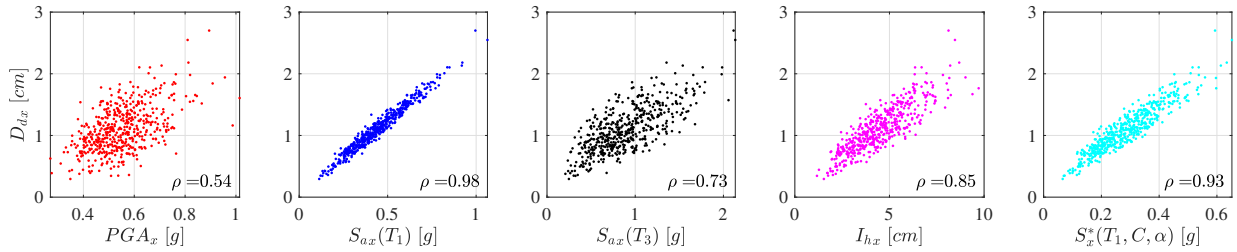

Figure B.49: Scatter plots of $n_s = 500$ samples of (PGA_x, D_{dx}), $(S_{ax}(T_1), D_{dx})$, $(S_{ax}(T_3), D_{dx})$, (I_{hx}, D_{dx}) and $(S^*{}_x(T_1, C, \alpha), D_{dx})$ at node #7 - linear analysis.

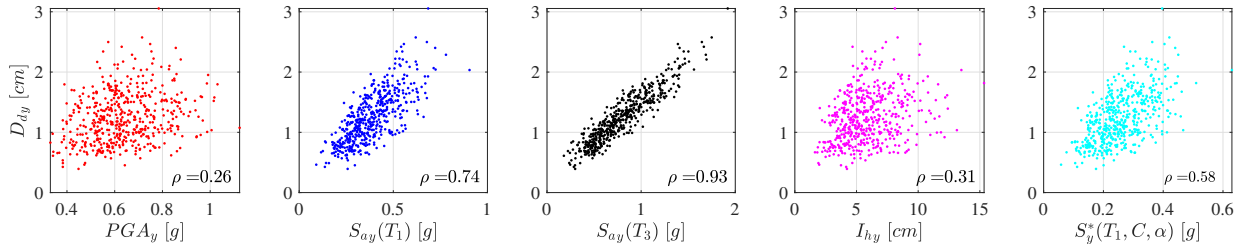

Figure B.50: Scatter plots of $n_s = 500$ samples of $(PGA_y, D_{d)}$, $(S_{ay}(T_1), D_{dy})$, $(S_{ay}(T_3), D_{dy})$, (I_{hy}, D_{dy}) and $(S^*{}_y(T_1, C, \alpha), D_{dy})$ at node #7 - linear analysis.

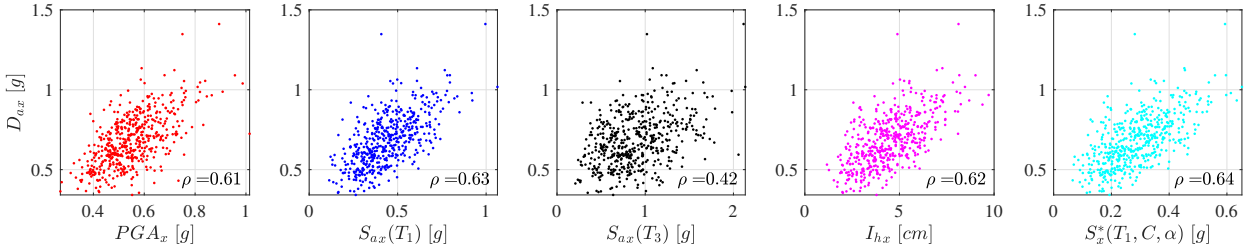

Figure B.51: Scatter plots of $n_s = 500$ samples of (PGA_x, D_{ax}), $(S_{ax}(T_1), D_{ax})$, $(S_{ax}(T_3), D_{ax})$, (I_{hx}, D_{ax}) and $(S^*{}_x(T_1, C, \alpha), D_{ax})$ at node #7 - linear analysis.

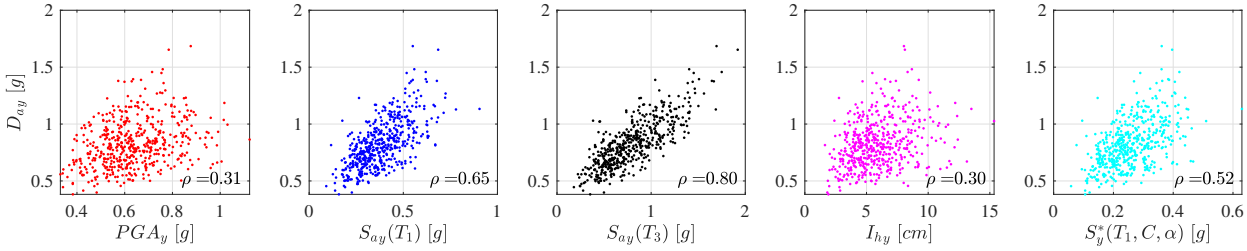

Figure B.52: Scatter plots of $n_s = 500$ samples of (PGA_y, D_{ay}), $(S_{ay}(T_1), D_{ay})$, $(S_{ay}(T_3), D_{ay})$, (I_{hy}, D_{ay}) and $(S^*{}_y(T_1, C, \alpha), D_{ay})$ at node #7 - linear analysis.

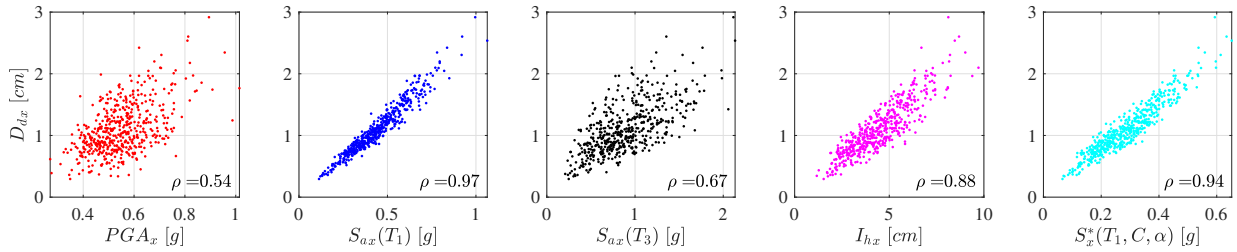

Figure B.53: Scatter plots of $n_s = 500$ samples of (PGA_x, D_{dx}), $(S_{ax}(T_1), D_{dx})$, $(S_{ax}(T_3), D_{dx})$, (I_{hx}, D_{dx}) and $(S^*{}_x(T_1, C, \alpha), D_{dx})$ at node #7 - nonlinear analysis.

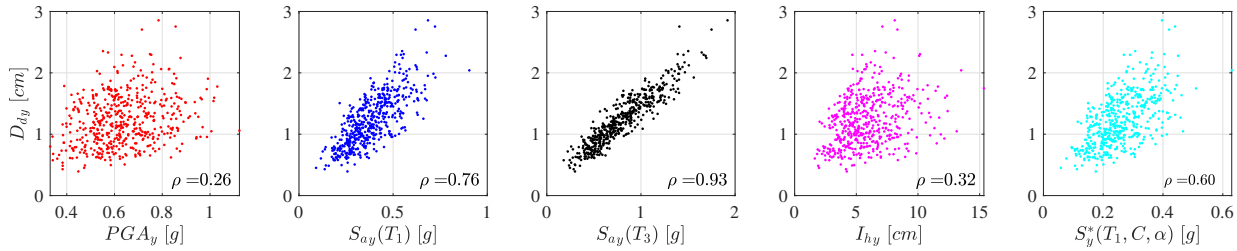

Figure B.54: Scatter plots of $n_s = 500$ samples of $(PGA_y, D_{d)}$, $(S_{ay}(T_1), D_{dy})$, $(S_{ay}(T_3), D_{dy})$, (I_{hy}, D_{dy}) and $(S^*{}_y(T_1, C, \alpha), D_{dy})$ at node #7 - nonlinear analysis.

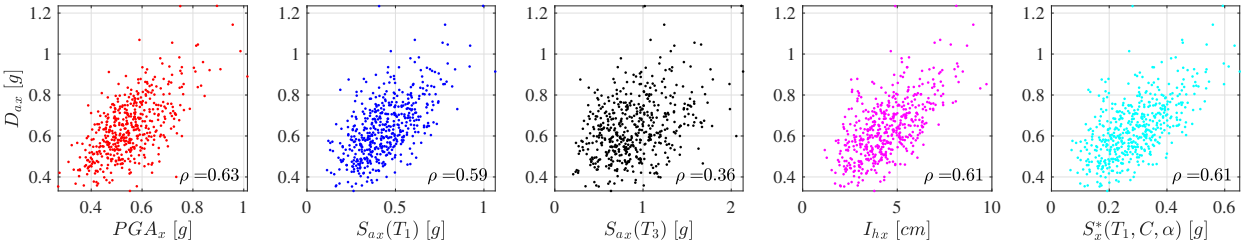

Figure B.55: Scatter plots of $n_s = 500$ samples of (PGA_x, D_{ax}), $(S_{ax}(T_1), D_{ax})$, $(S_{ax}(T_3), D_{ax})$, (I_{hx}, D_{ax}) and $(S^*{}_x(T_1, C, \alpha), D_{ax})$ at node #7 - nonlinear analysis.

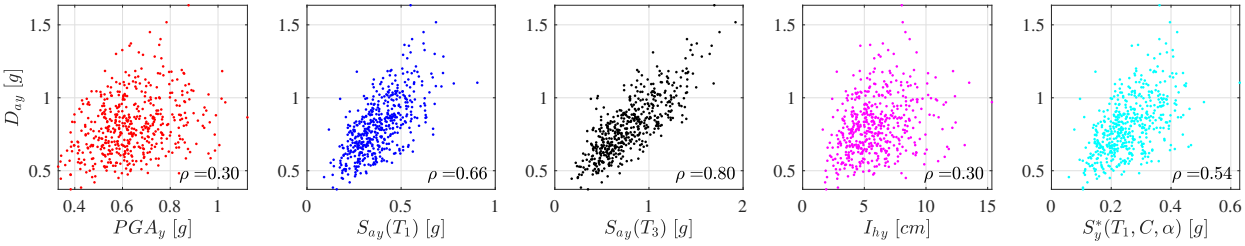

Figure B.56: Scatter plots of $n_s = 500$ samples of (PGA_y, D_{ay}), $(S_{ay}(T_1), D_{ay})$, $(S_{ay}(T_3), D_{ay})$, (I_{hy}, D_{ay}) and $(S^*{}_y(T_1, C, \alpha), D_{ay})$ at node #7 - nonlinear analysis.

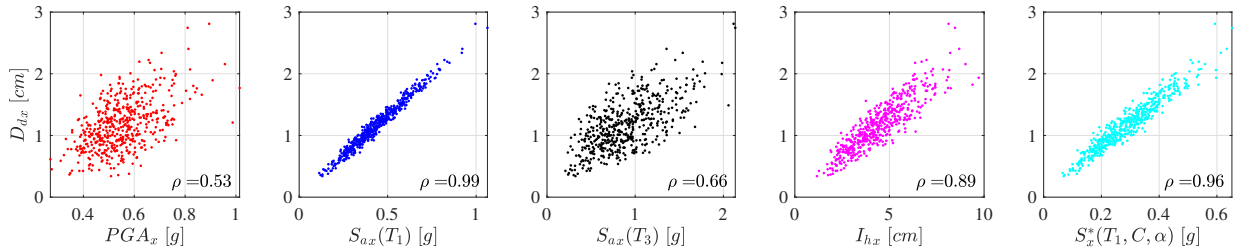

Figure B.57: Scatter plots of $n_s = 500$ samples of (PGA_x, D_{dx}), $(S_{ax}(T_1), D_{dx})$, $(S_{ax}(T_3), D_{dx})$, (I_{hx}, D_{dx}) and $(S^*{}_x(T_1, C, \alpha), D_{dx})$ at node #8 - linear analysis.

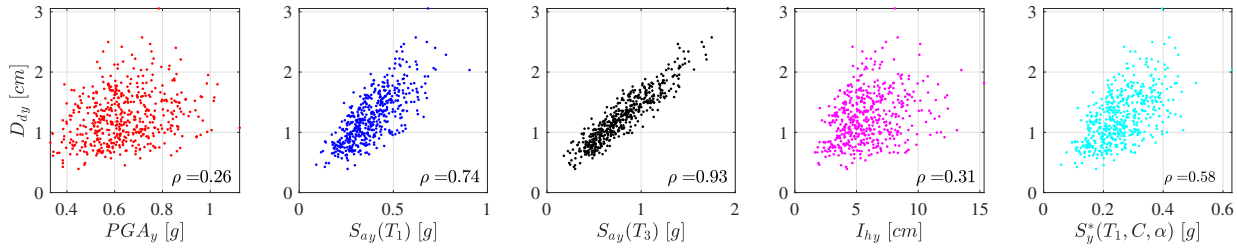

Figure B.58: Scatter plots of $n_s = 500$ samples of $(PGA_y, D_{d)}$, $(S_{ay}(T_1), D_{dy})$, $(S_{ay}(T_3), D_{dy})$, (I_{hy}, D_{dy}) and $(S^*{}_y(T_1, C, \alpha), D_{dy})$ at node #8 - linear analysis.

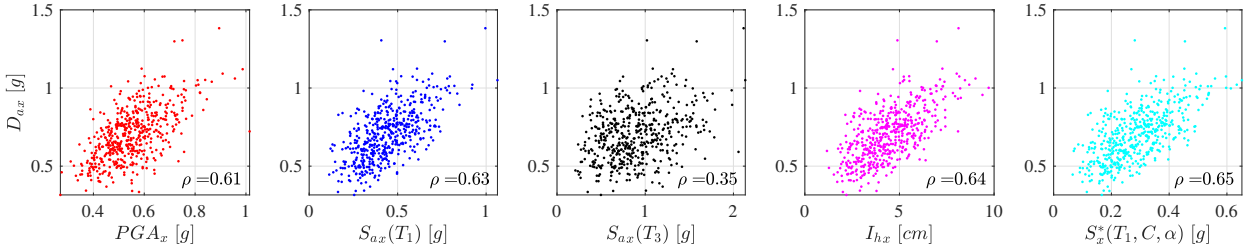

Figure B.59: Scatter plots of $n_s = 500$ samples of (PGA_x, D_{ax}), $(S_{ax}(T_1), D_{ax})$, $(S_{ax}(T_3), D_{ax})$, (I_{hx}, D_{ax}) and $(S^*{}_x(T_1, C, \alpha), D_{ax})$ at node #8 - linear analysis.

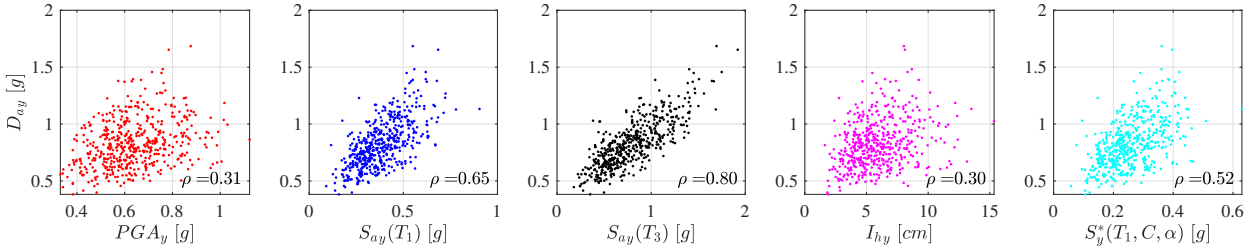

Figure B.60: Scatter plots of $n_s = 500$ samples of (PGA_y, D_{ay}), $(S_{ay}(T_1), D_{ay})$, $(S_{ay}(T_3), D_{ay})$, (I_{hy}, D_{ay}) and $(S^*{}_y(T_1, C, \alpha), D_{ay})$ at node #8 - linear analysis.

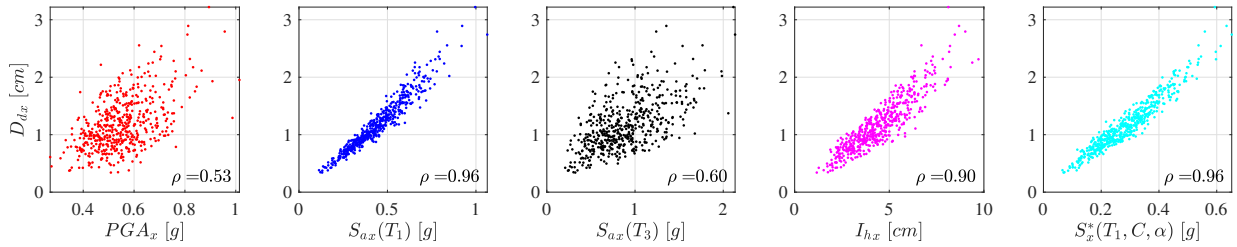

Figure B.61: Scatter plots of $n_s = 500$ samples of (PGA_x, D_{dx}), $(S_{ax}(T_1), D_{dx})$, $(S_{ax}(T_3), D_{dx})$, (I_{hx}, D_{dx}) and $(S^*{}_x(T_1, C, \alpha), D_{dx})$ at node #8 - nonlinear analysis.

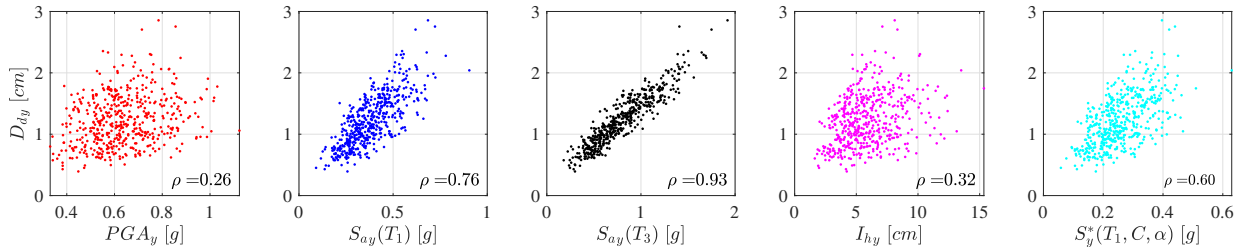

Figure B.62: Scatter plots of $n_s = 500$ samples of $(PGA_y, D_{d)}$, $(S_{ay}(T_1), D_{dy})$, $(S_{ay}(T_3), D_{dy})$, (I_{hy}, D_{dy}) and $(S^*{}_y(T_1, C, \alpha), D_{dy})$ at node #8 - nonlinear analysis.

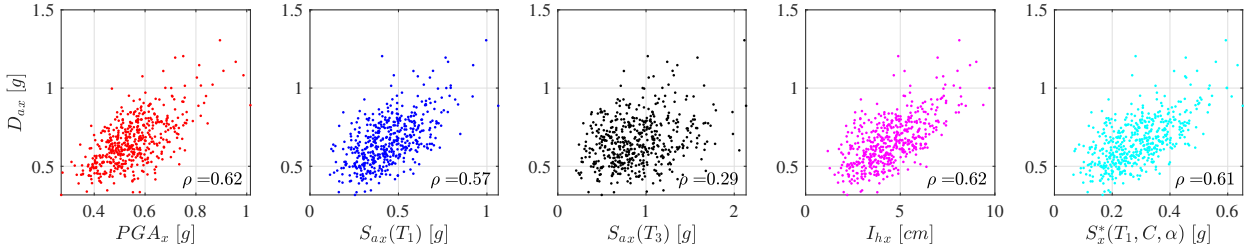

Figure B.63: Scatter plots of $n_s = 500$ samples of (PGA_x, D_{ax}), $(S_{ax}(T_1), D_{ax})$, $(S_{ax}(T_3), D_{ax})$, (I_{hx}, D_{ax}) and $(S^*{}_x(T_1, C, \alpha), D_{ax})$ at node #8 - nonlinear analysis.

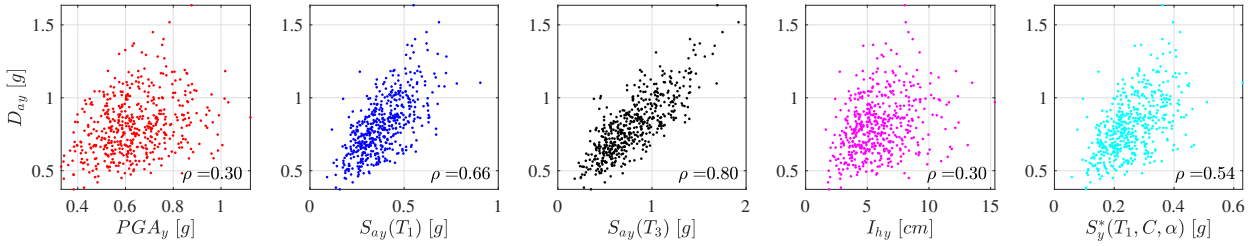

Figure B.64: Scatter plots of $n_s = 500$ samples of (PGA_y, D_{ay}), $(S_{ay}(T_1), D_{ay})$, $(S_{ay}(T_3), D_{ay})$, (I_{hy}, D_{ay}) and $(S^*{}_y(T_1, C, \alpha), D_{ay})$ at node #8 - nonlinear analysis.

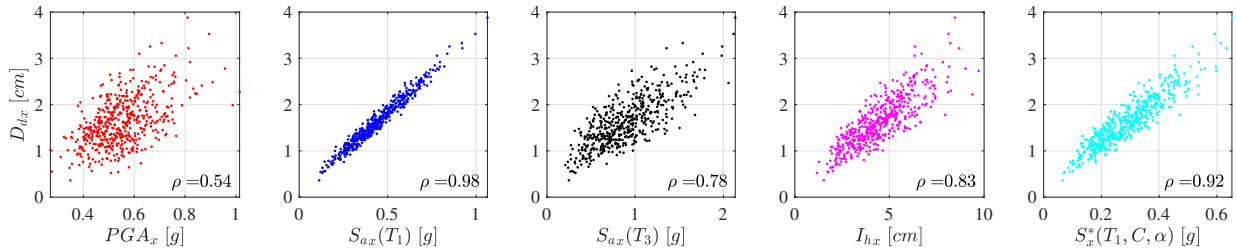

Figure B.65: Scatter plots of $n_s = 500$ samples of (PGA_x, D_{dx}), $(S_{ax}(T_1), D_{dx})$, $(S_{ax}(T_3), D_{dx})$, (I_{hx}, D_{dx}) and $(S^*{}_x(T_1, C, \alpha), D_{dx})$ at node #10 - linear analysis.

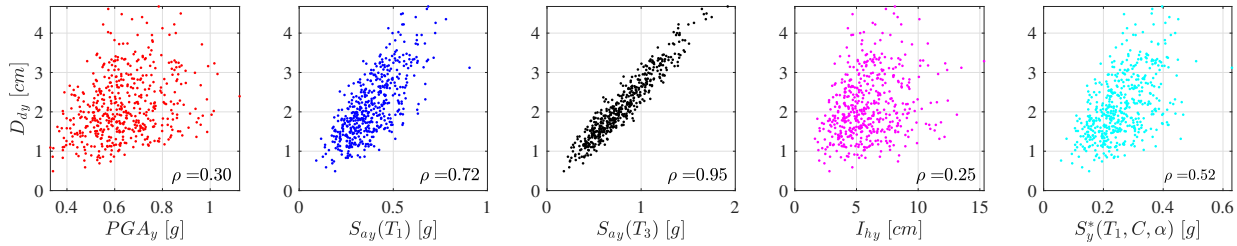

Figure B.66: Scatter plots of $n_s = 500$ samples of $(PGA_y, D_{d)}$, $(S_{ay}(T_1), D_{dy})$, $(S_{ay}(T_3), D_{dy})$, (I_{hy}, D_{dy}) and $(S^*{}_y(T_1, C, \alpha), D_{dy})$ at node #10 - linear analysis.

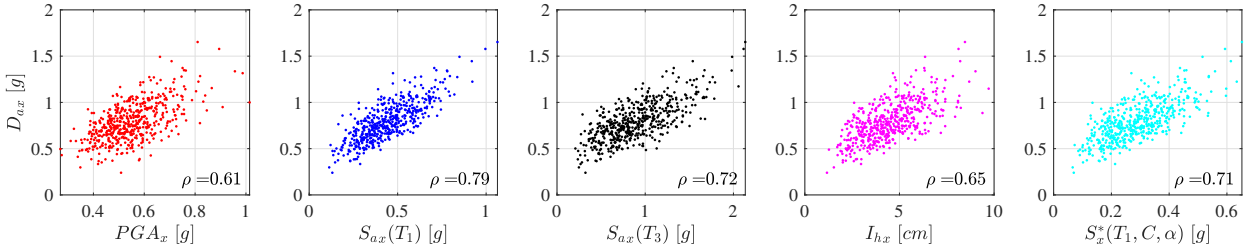

Figure B.67: Scatter plots of $n_s = 500$ samples of (PGA_x, D_{ax}), $(S_{ax}(T_1), D_{ax})$, $(S_{ax}(T_3), D_{ax})$, (I_{hx}, D_{ax}) and $(S^*{}_x(T_1, C, \alpha), D_{ax})$ at node #10 - linear analysis.

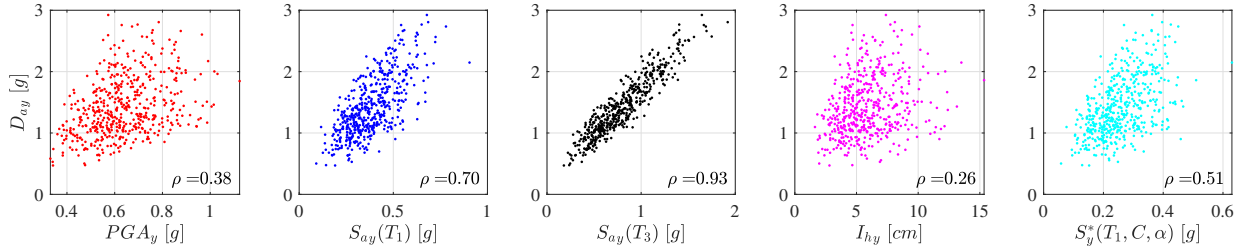

Figure B.68: Scatter plots of $n_s = 500$ samples of (PGA_y, D_{ay}), $(S_{ay}(T_1), D_{ay})$, $(S_{ay}(T_3), D_{ay})$, (I_{hy}, D_{ay}) and $(S^*{}_y(T_1, C, \alpha), D_{ay})$ at node #10 - linear analysis.

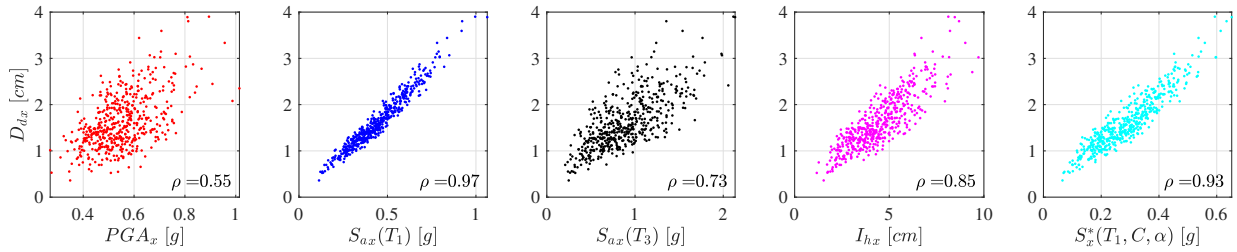

Figure B.69: Scatter plots of $n_s = 500$ samples of (PGA_x, D_{dx}), $(S_{ax}(T_1), D_{dx})$, $(S_{ax}(T_3), D_{dx})$, (I_{hx}, D_{dx}) and $(S^*{}_x(T_1, C, \alpha), D_{dx})$ at node #10 - nonlinear analysis.

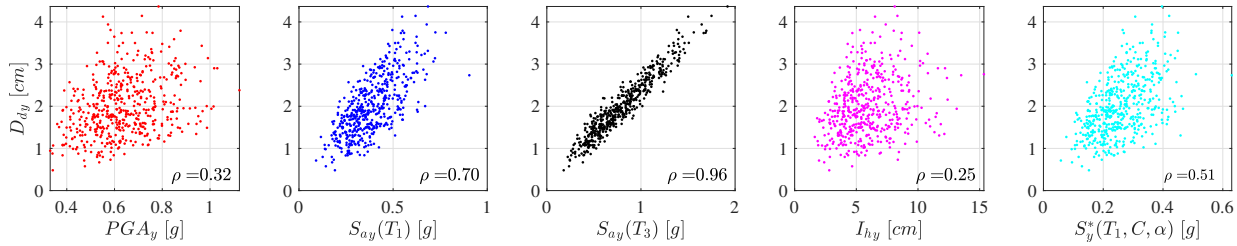

Figure B.70: Scatter plots of $n_s = 500$ samples of $(PGA_y, D_{d)}$, $(S_{ay}(T_1), D_{dy})$, $(S_{ay}(T_3), D_{dy})$, (I_{hy}, D_{dy}) and $(S^*{}_y(T_1, C, \alpha), D_{dy})$ at node #10 - nonlinear analysis.

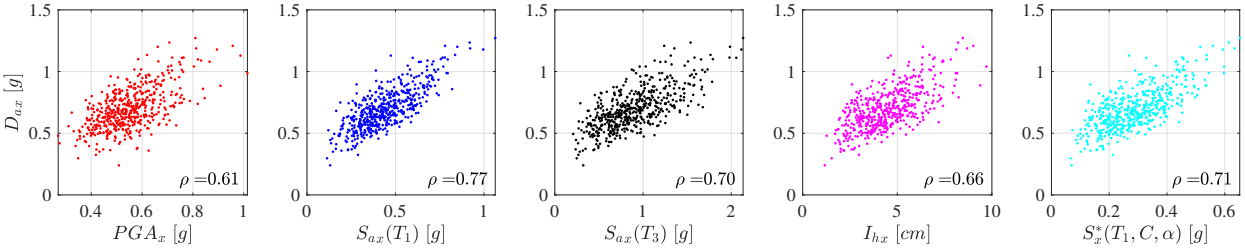

Figure B.71: Scatter plots of $n_s = 500$ samples of (PGA_x, D_{ax}), $(S_{ax}(T_1), D_{ax})$, $(S_{ax}(T_3), D_{ax})$, (I_{hx}, D_{ax}) and $(S^*{}_x(T_1, C, \alpha), D_{ax})$ at node #10 - nonlinear analysis.

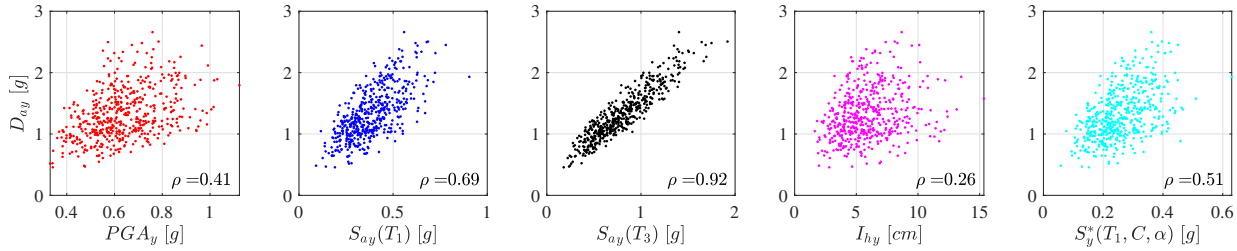

Figure B.72: Scatter plots of $n_s = 500$ samples of (PGA_y, D_{ay}), $(S_{ay}(T_1), D_{ay})$, $(S_{ay}(T_3), D_{ay})$, (I_{hy}, D_{ay}) and $(S^*{}_y(T_1, C, \alpha), D_{ay})$ at node #10 - nonlinear analysis.

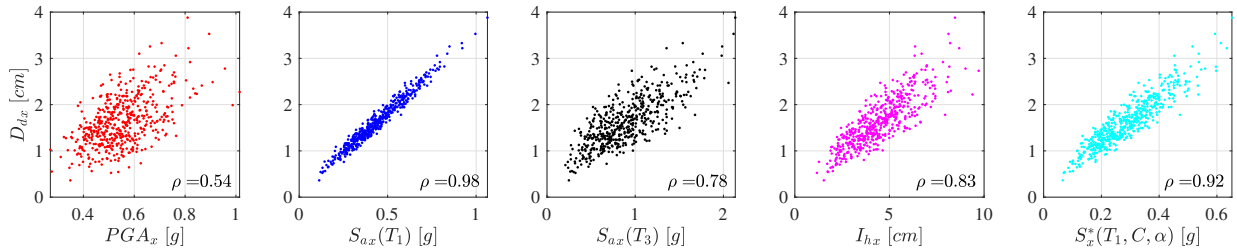

Figure B.73: Scatter plots of $n_s = 500$ samples of (PGA_x, D_{dx}), $(S_{ax}(T_1), D_{dx})$, $(S_{ax}(T_3), D_{dx})$, (I_{hx}, D_{dx}) and $(S^*{}_x(T_1, C, \alpha), D_{dx})$ at node #11 - linear analysis.

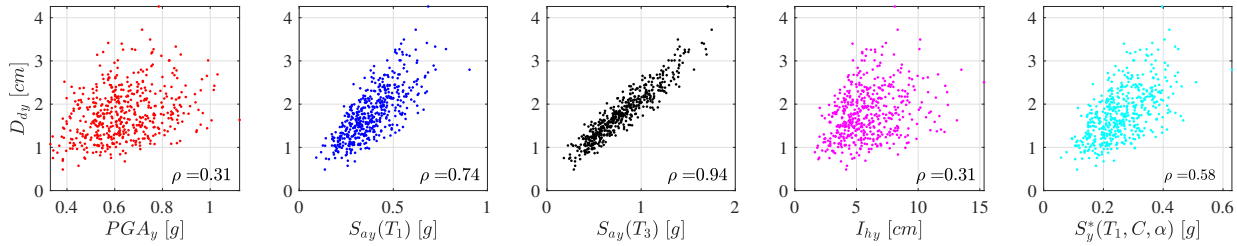

Figure B.74: Scatter plots of $n_s = 500$ samples of $(PGA_y, D_{d)}$, $(S_{ay}(T_1), D_{dy})$, $(S_{ay}(T_3), D_{dy})$, (I_{hy}, D_{dy}) and $(S^*{}_y(T_1, C, \alpha), D_{dy})$ at node #11 - linear analysis.

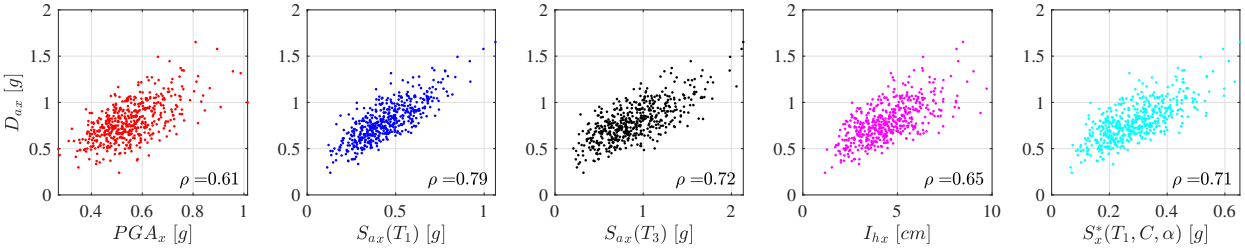

Figure B.75: Scatter plots of $n_s = 500$ samples of (PGA_x, D_{ax}), $(S_{ax}(T_1), D_{ax})$, $(S_{ax}(T_3), D_{ax})$, (I_{hx}, D_{ax}) and $(S^*{}_x(T_1, C, \alpha), D_{ax})$ at node #11 - linear analysis.

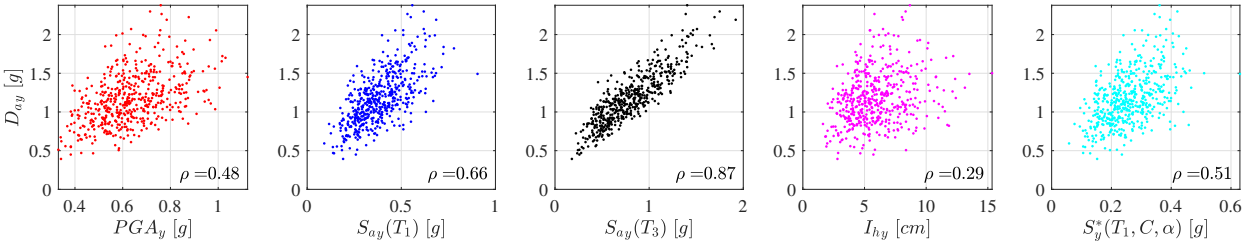

Figure B.76: Scatter plots of $n_s = 500$ samples of (PGA_y, D_{ay}), $(S_{ay}(T_1), D_{ay})$, $(S_{ay}(T_3), D_{ay})$, (I_{hy}, D_{ay}) and $(S^*{}_y(T_1, C, \alpha), D_{ay})$ at node #11 - linear analysis.

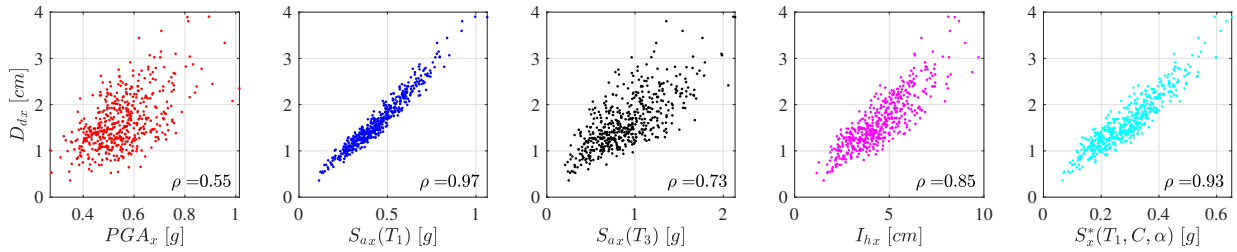

Figure B.77: Scatter plots of $n_s = 500$ samples of (PGA_x, D_{dx}), $(S_{ax}(T_1), D_{dx})$, $(S_{ax}(T_3), D_{dx})$, (I_{hx}, D_{dx}) and $(S^*{}_x(T_1, C, \alpha), D_{dx})$ at node #11 - nonlinear analysis.

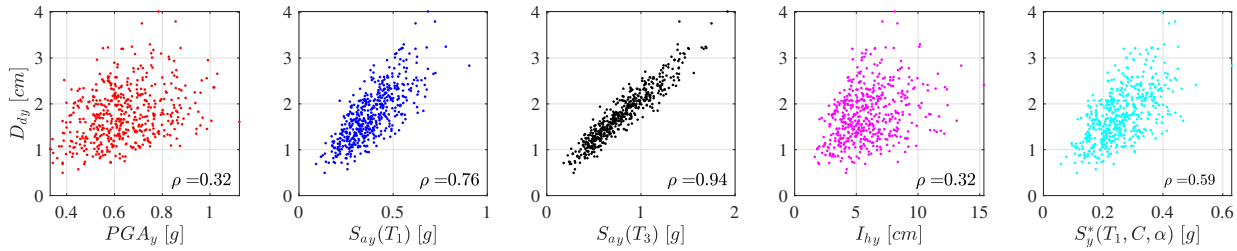

Figure B.78: Scatter plots of $n_s = 500$ samples of $(PGA_y, D_{d)}$, $(S_{ay}(T_1), D_{dy})$, $(S_{ay}(T_3), D_{dy})$, (I_{hy}, D_{dy}) and $(S^*{}_y(T_1, C, \alpha), D_{dy})$ at node #11 - nonlinear analysis.

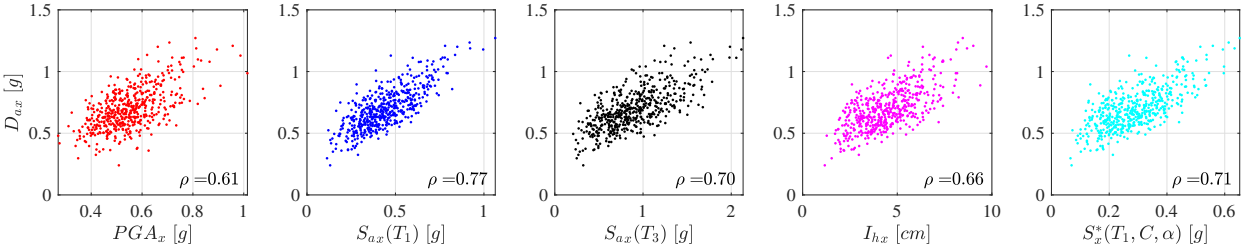

Figure B.79: Scatter plots of $n_s = 500$ samples of (PGA_x, D_{ax}), $(S_{ax}(T_1), D_{ax})$, $(S_{ax}(T_3), D_{ax})$, (I_{hx}, D_{ax}) and $(S^*{}_x(T_1, C, \alpha), D_{ax})$ at node #11 - nonlinear analysis.

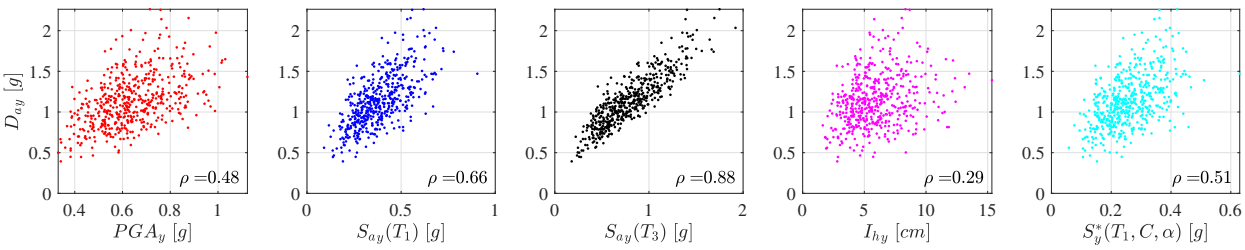

Figure B.80: Scatter plots of $n_s = 500$ samples of (PGA_y, D_{ay}), $(S_{ay}(T_1), D_{ay})$, $(S_{ay}(T_3), D_{ay})$, (I_{hy}, D_{ay}) and $(S^*{}_y(T_1, C, \alpha), D_{ay})$ at node #11 - nonlinear analysis.

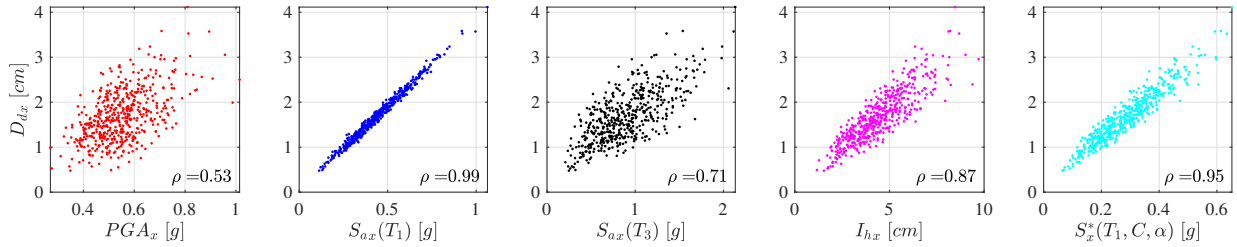

Figure B.81: Scatter plots of $n_s = 500$ samples of (PGA_x, D_{dx}), $(S_{ax}(T_1), D_{dx})$, $(S_{ax}(T_3), D_{dx})$, (I_{hx}, D_{dx}) and $(S^*{}_x(T_1, C, \alpha), D_{dx})$ at node #12 - linear analysis.

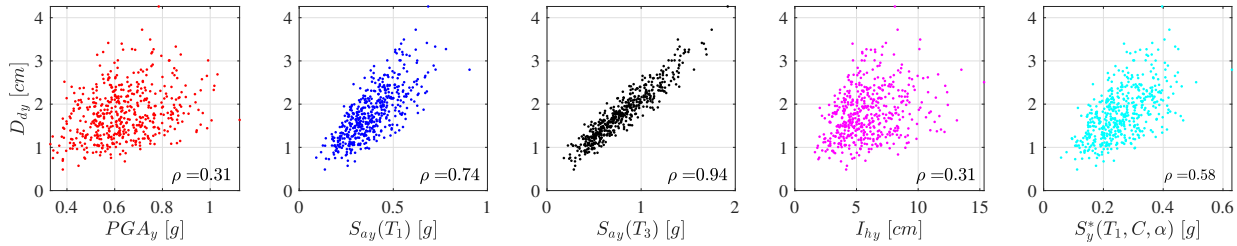

Figure B.82: Scatter plots of $n_s = 500$ samples of $(PGA_y, D_{d)}$, $(S_{ay}(T_1), D_{dy})$, $(S_{ay}(T_3), D_{dy})$, (I_{hy}, D_{dy}) and $(S^*{}_y(T_1, C, \alpha), D_{dy})$ at node #12 - linear analysis.

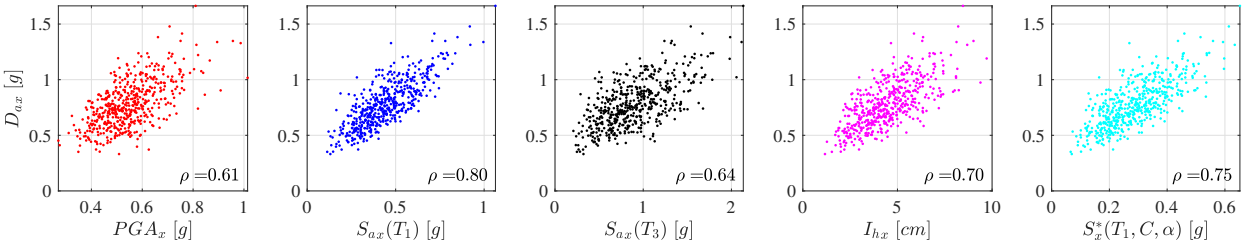

Figure B.83: Scatter plots of $n_s = 500$ samples of (PGA_x, D_{ax}), $(S_{ax}(T_1), D_{ax})$, $(S_{ax}(T_3), D_{ax})$, (I_{hx}, D_{ax}) and $(S^*{}_x(T_1, C, \alpha), D_{ax})$ at node #12 - linear analysis.

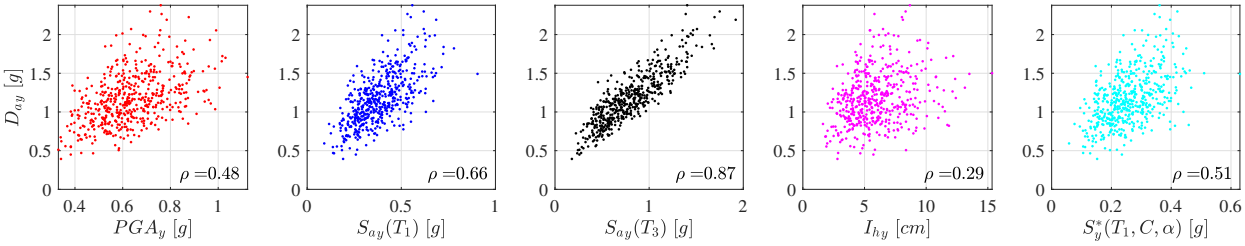

Figure B.84: Scatter plots of $n_s = 500$ samples of (PGA_y, D_{ay}), $(S_{ay}(T_1), D_{ay})$, $(S_{ay}(T_3), D_{ay})$, (I_{hy}, D_{ay}) and $(S^*{}_y(T_1, C, \alpha), D_{ay})$ at node #12 - linear analysis.

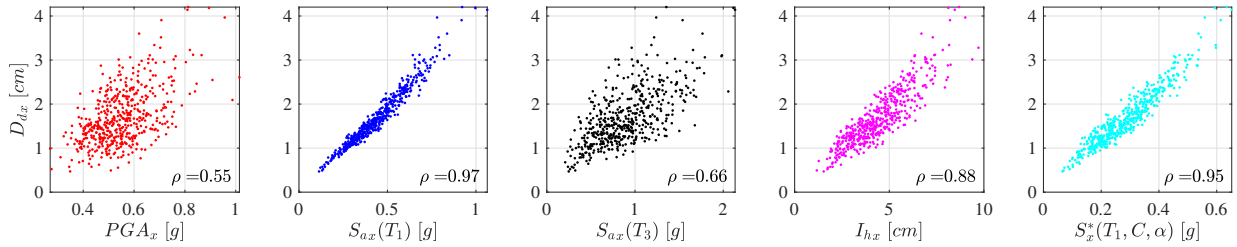

Figure B.85: Scatter plots of $n_s = 500$ samples of (PGA_x, D_{dx}), $(S_{ax}(T_1), D_{dx})$, $(S_{ax}(T_3), D_{dx})$, (I_{hx}, D_{dx}) and $(S^*{}_x(T_1, C, \alpha), D_{dx})$ at node #12 - nonlinear analysis.

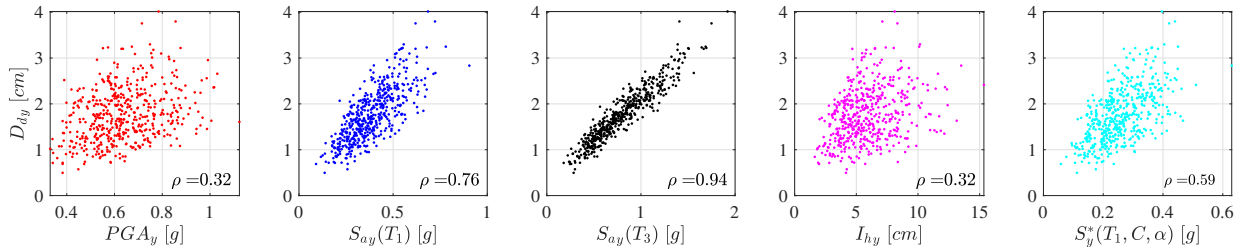

Figure B.86: Scatter plots of $n_s = 500$ samples of $(PGA_y, D_{d)}$, $(S_{ay}(T_1), D_{dy})$, $(S_{ay}(T_3), D_{dy})$, (I_{hy}, D_{dy}) and $(S^*{}_y(T_1, C, \alpha), D_{dy})$ at node #12 - nonlinear analysis.

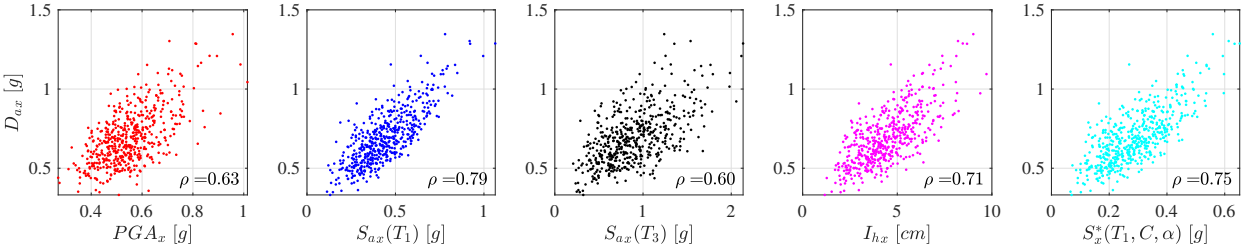

Figure B.87: Scatter plots of $n_s = 500$ samples of (PGA_x, D_{ax}), $(S_{ax}(T_1), D_{ax})$, $(S_{ax}(T_3), D_{ax})$, (I_{hx}, D_{ax}) and $(S^*{}_x(T_1, C, \alpha), D_{ax})$ at node #12 - nonlinear analysis.

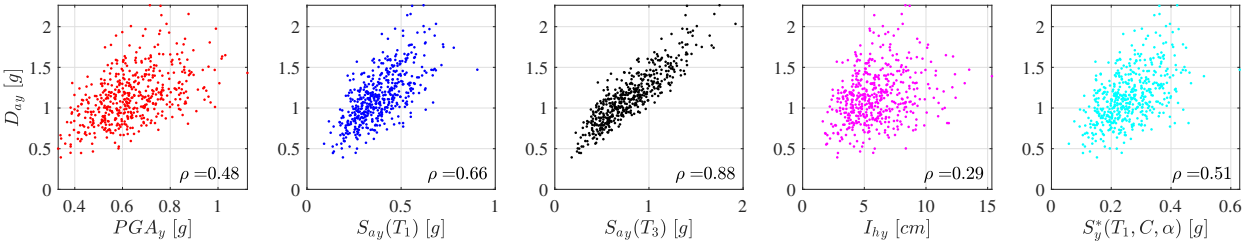

Figure B.88: Scatter plots of $n_s = 500$ samples of (PGA_y, D_{ay}), $(S_{ay}(T_1), D_{ay})$, $(S_{ay}(T_3), D_{ay})$, (I_{hy}, D_{ay}) and $(S^*{}_y(T_1, C, \alpha), D_{ay})$ at node #12 - nonlinear analysis.

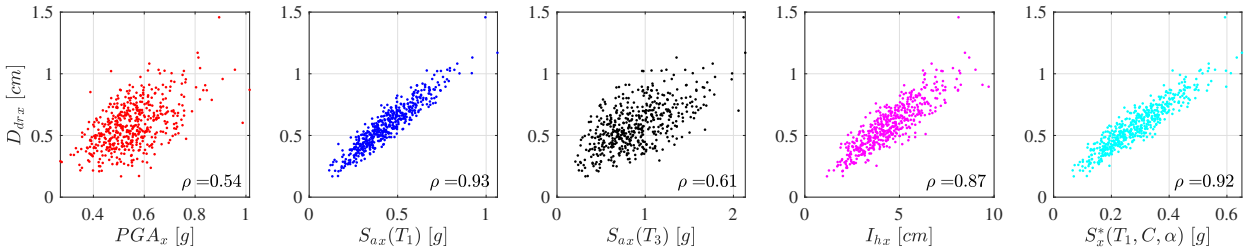

Figure B.89: Scatter plots of $n_s = 500$ samples of (PGA_x, D_{drx}), $(S_{ax}(T_1), D_{drx})$, $(S_{ax}(T_3), D_{drx})$, (I_{hx}, D_{drx}) and $(S^*{}_x(T_1, C, \alpha), D_{drx})$ at #1 storey - linear analysis.

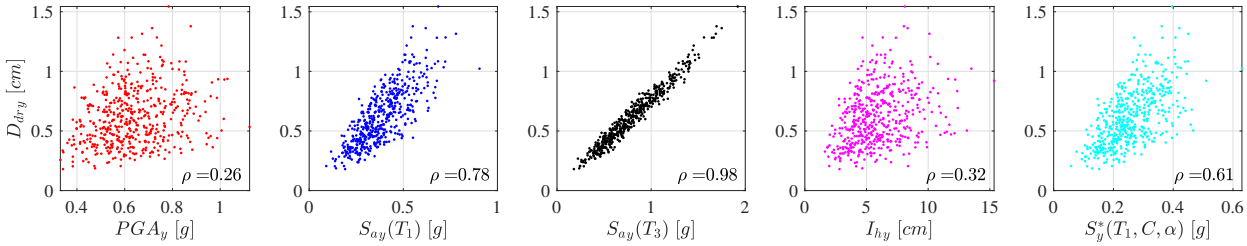

Figure B.90: Scatter plots of $n_s = 500$ samples of (PGA_y, D_{dry}), $(S_{ay}(T_1), D_{dry})$, $(S_{ay}(T_3), D_{dry})$, (I_{hy}, D_{dry}) and $(S^*{}_y(T_1, C, \alpha), D_{dry})$ at #1 storey - linear analysis.

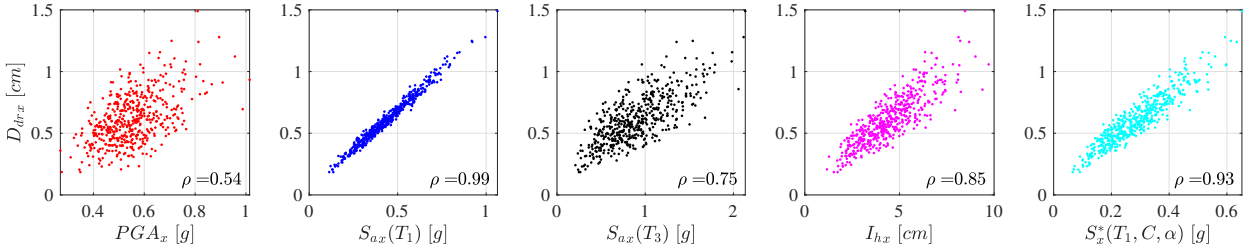

Figure B.91: Scatter plots of $n_s = 500$ samples of (PGA_x, D_{drx}), $(S_{ax}(T_1), D_{drx})$, $(S_{ax}(T_3), D_{drx})$, (I_{hx}, D_{drx}) and $(S^*{}_x(T_1, C, \alpha), D_{drx})$ at #2 storey - linear analysis.

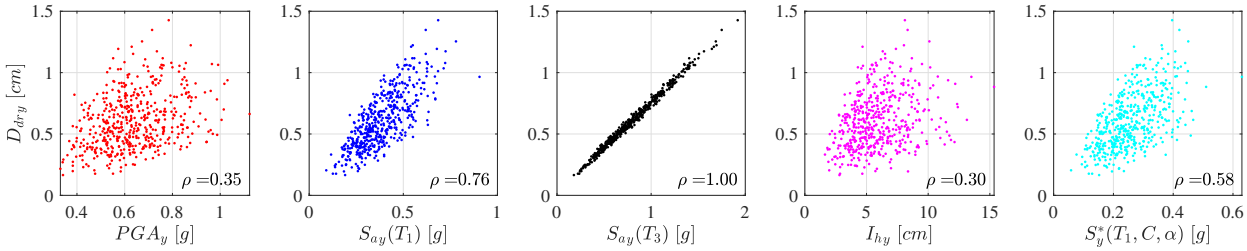

Figure B.92: Scatter plots of $n_s = 500$ samples of (PGA_y, D_{dry}), $(S_{ay}(T_1), D_{dry})$, $(S_{ay}(T_3), D_{dry})$, (I_{hy}, D_{dry}) and $(S^*{}_y(T_1, C, \alpha), D_{dry})$ at #2 storey - linear analysis.

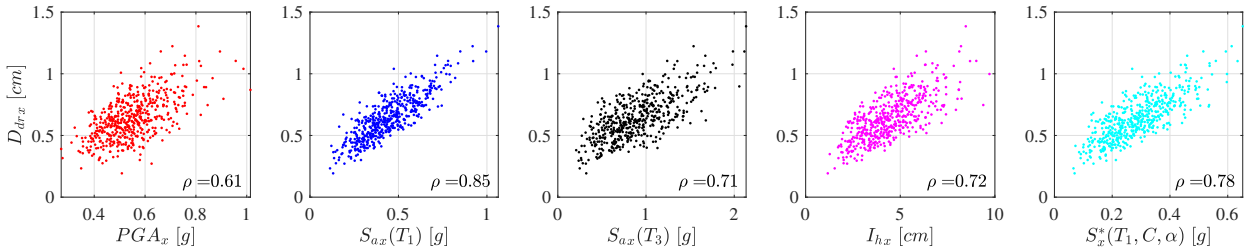

Figure B.93: Scatter plots of $n_s = 500$ samples of (PGA_x, D_{drx}), $(S_{ax}(T_1), D_{drx})$, $(S_{ax}(T_3), D_{drx})$, (I_{hx}, D_{drx}) and $(S^*{}_x(T_1, C, \alpha), D_{drx})$ at #3 storey - linear analysis.

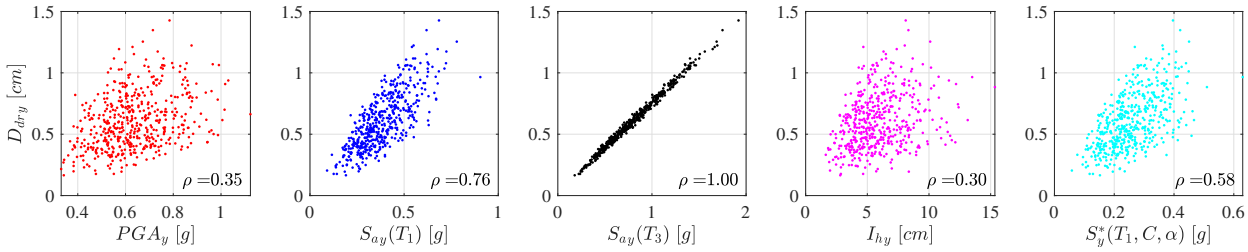

Figure B.94: Scatter plots of $n_s = 500$ samples of (PGA_y, D_{dry}), $(S_{ay}(T_1), D_{dry})$, $(S_{ay}(T_3), D_{dry})$, (I_{hy}, D_{dry}) and $(S^*{}_y(T_1, C, \alpha), D_{dry})$ at #3 storey - linear analysis.

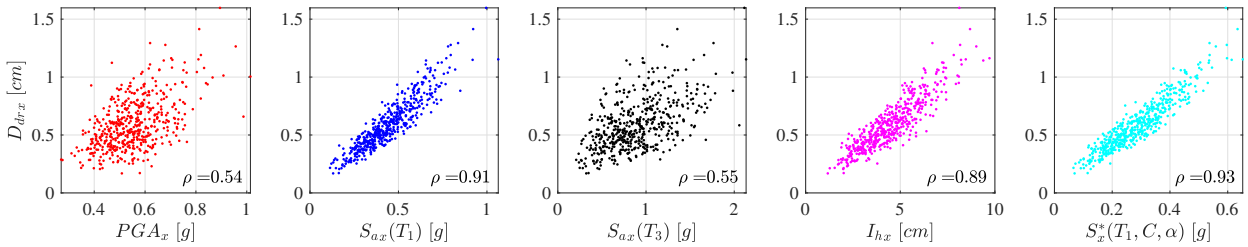

Figure B.95: Scatter plots of $n_s = 500$ samples of (PGA_x, D_{drx}), $(S_{ax}(T_1), D_{drx})$, $(S_{ax}(T_3), D_{drx})$, (I_{hx}, D_{drx}) and $(S^*{}_x(T_1, C, \alpha), D_{drx})$ at #1 storey - nonlinear analysis.

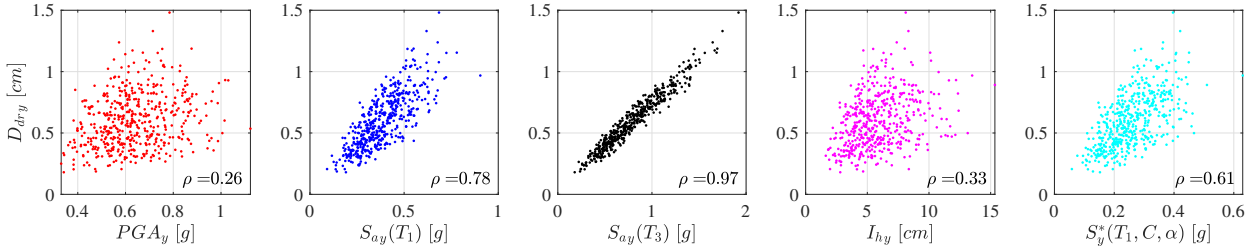

Figure B.96: Scatter plots of $n_s = 500$ samples of (PGA_y, D_{dry}), $(S_{ay}(T_1), D_{dry})$, $(S_{ay}(T_3), D_{dry})$, (I_{hy}, D_{dry}) and $(S^*{}_y(T_1, C, \alpha), D_{dry})$ at #1 storey - nonlinear analysis.

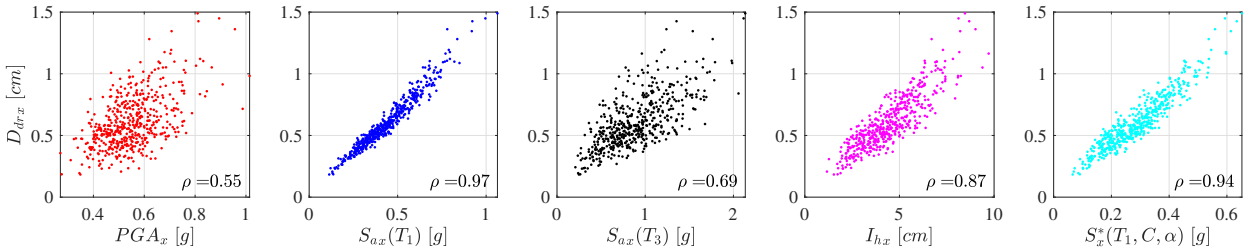

Figure B.97: Scatter plots of $n_s = 500$ samples of (PGA_x, D_{drx}), $(S_{ax}(T_1), D_{drx})$, $(S_{ax}(T_3), D_{drx})$, (I_{hx}, D_{drx}) and $(S^*{}_x(T_1, C, \alpha), D_{drx})$ at #2 storey - nonlinear analysis.

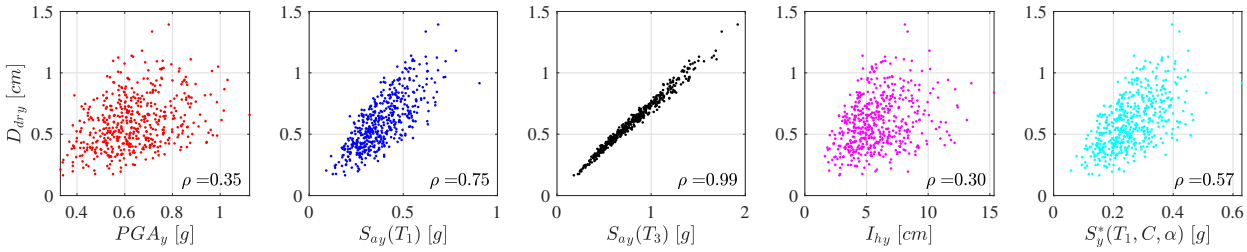

Figure B.98: Scatter plots of $n_s = 500$ samples of (PGA_y, D_{dry}), $(S_{ay}(T_1), D_{dry})$, $(S_{ay}(T_3), D_{dry})$, (I_{hy}, D_{dry}) and $(S^*{}_y(T_1, C, \alpha), D_{dry})$ at #2 storey - nonlinear analysis.

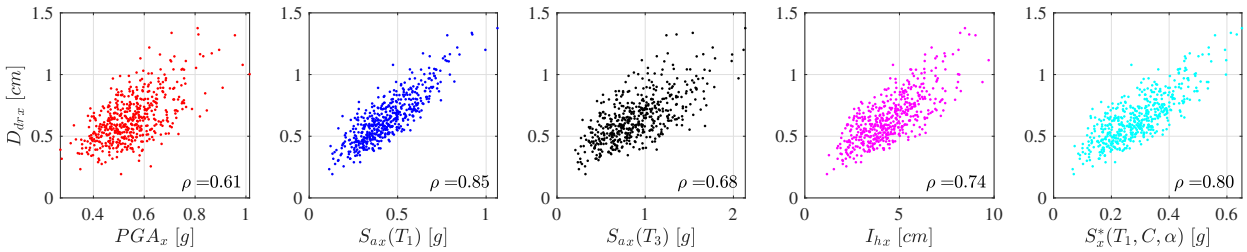

Figure B.99: Scatter plots of $n_s = 500$ samples of (PGA_x, D_{drx}), $(S_{ax}(T_1), D_{drx})$, $(S_{ax}(T_3), D_{drx})$, (I_{hx}, D_{drx}) and $(S^*{}_x(T_1, C, \alpha), D_{drx})$ at #3 storey - nonlinear analysis.

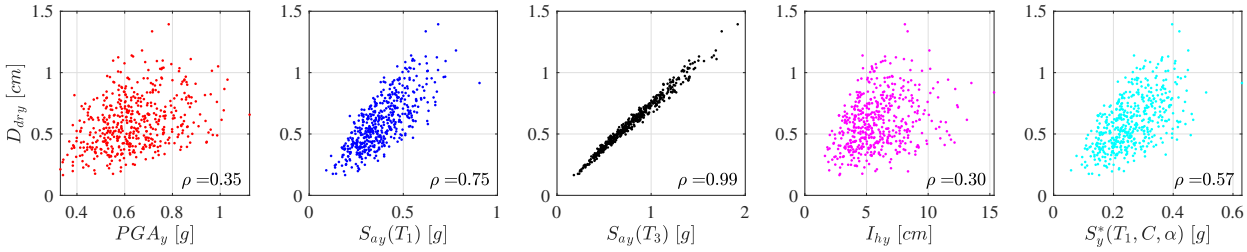

Figure B.100: Scatter plots of $n_s = 500$ samples of (PGA_y, D_{dry}), $(S_{ay}(T_1), D_{dry})$, $(S_{ay}(T_3), D_{dry})$, (I_{hy}, D_{dry}) and $(S^*{}_y(T_1, C, \alpha), D_{dry})$ at #3 storey - nonlinear analysis.

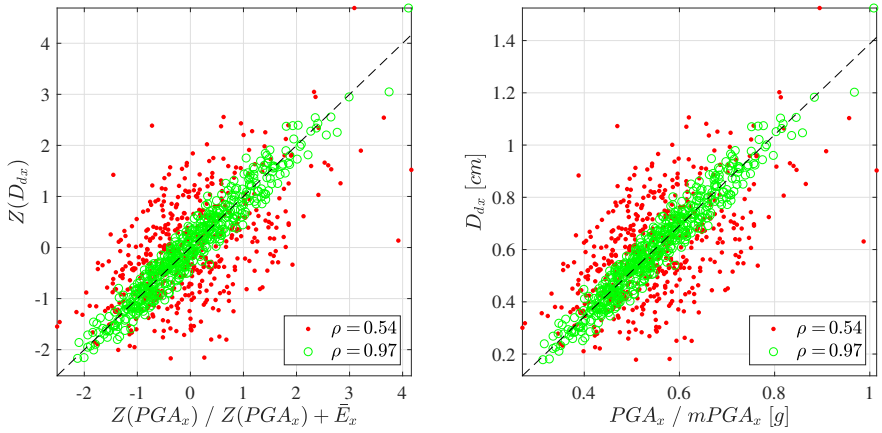

Figure B.101: Scatter plots of $n_s = 500$ samples at node #4: $(Z(PGA_x), Z(D_{dx}))$ red dots, $(Z(PGA_x) + \bar{E}_x, Z(D_{dx}))$ green circles (left panel); (PGA_x, D_{dx}) red dots, $(mPGA_x, D_{dx})$ green circles (right panel) - linear analysis.

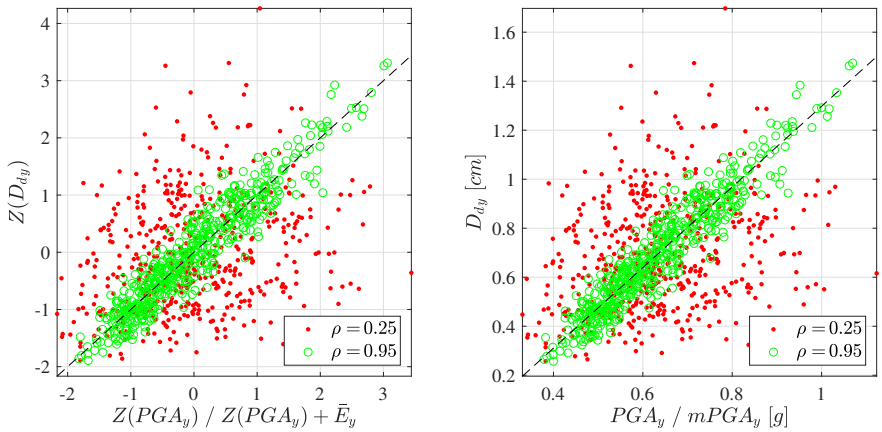

Figure B.102: Scatter plots of $n_s = 500$ samples at node #4: $(Z(PGA_y), Z(D_{dy}))$ red dots, $(Z(PGA_y) + \bar{E}_y, Z(D_{dy}))$ green circles (left panel); (PGA_y, D_{dy}) red dots, $(mPGA_y, D_{dy})$ green circles (right panel) - linear analysis.

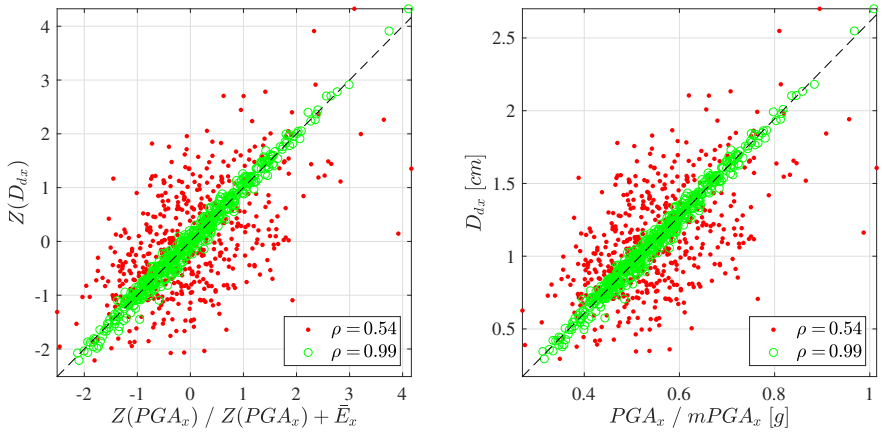

Figure B.103: Scatter plots of $n_s = 500$ samples at node #7: $(Z(PGA_x), Z(D_{dx}))$ red dots, $(Z(PGA_x) + \bar{E}_x, Z(D_{dx}))$ green circles (left panel); (PGA_x, D_{dx}) red dots, $(mPGA_x, D_{dx})$ green circles (right panel) - linear analysis.

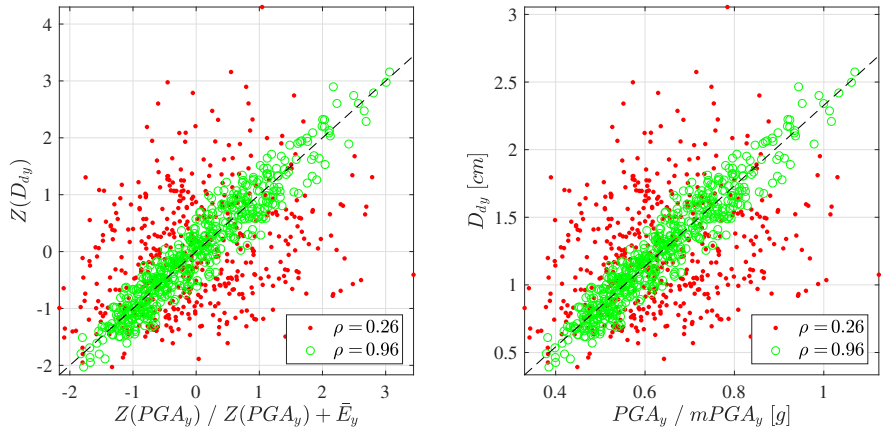

Figure B.104: Scatter plots of $n_s = 500$ samples at node #7: $(Z(PGA_y), Z(D_{dy}))$ red dots, $(Z(PGA_y) + \bar{E}_y, Z(D_{dy}))$ green circles (left panel); (PGA_y, D_{dy}) red dots, $(mPGA_y, D_{dy})$ green circles (right panel) - linear analysis.

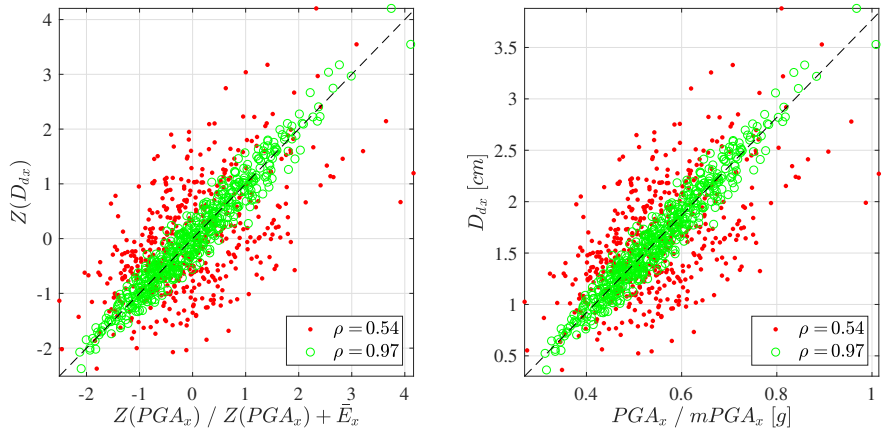

Figure B.105: Scatter plots of $n_s = 500$ samples at node #10: $(Z(PGA_x), Z(D_{dx}))$ red dots, $(Z(PGA_x) + \bar{E}_x, Z(D_{dx}))$ green circles (left panel); (PGA_x, D_{dx}) red dots, $(mPGA_x, D_{dx})$ green circles (right panel) - linear analysis.

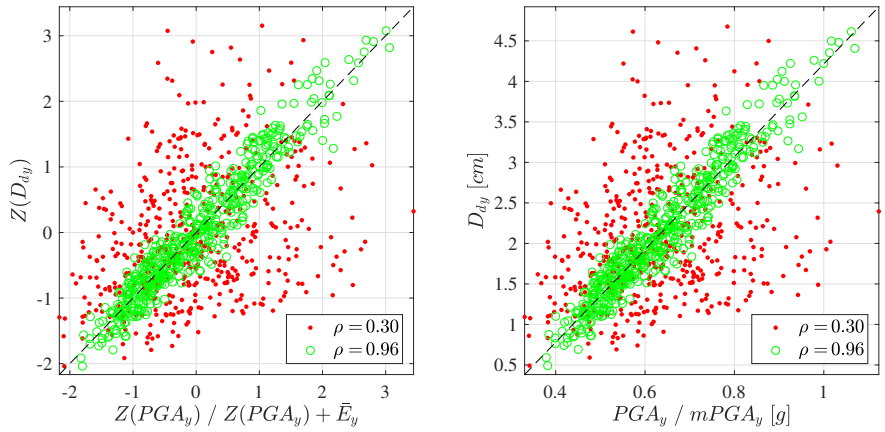

Figure B.106: Scatter plots of $n_s = 500$ samples at node #10: $(Z(PGA_y), Z(D_{dy}))$ red dots, $(Z(PGA_y) + \bar{E}_y, Z(D_{dy}))$ green circles (left panel); (PGA_y, D_{dy}) red dots, $(mPGA_y, D_{dy})$ green circles (right panel) - linear analysis.

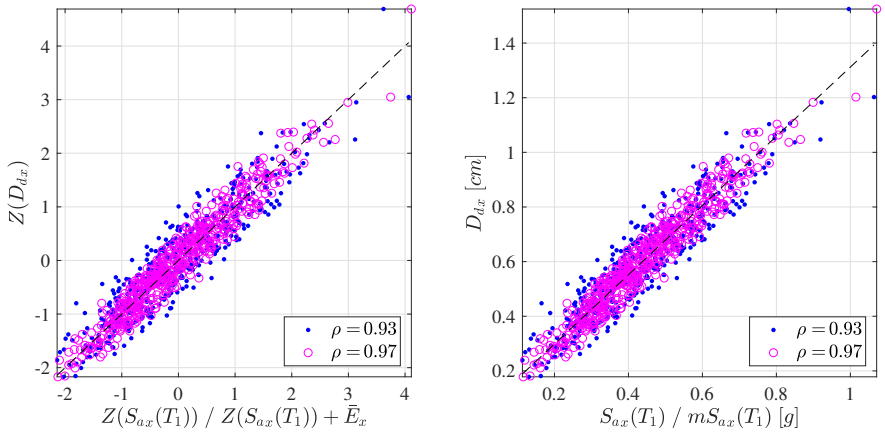

Figure B.107: Scatter plots of $n_s = 500$ samples at node #4: $(Z(S_{ax}(T_1)), Z(D_{dx}))$ red dots, $(Z(S_{ax}(T_1)) + \bar{E}_x, Z(D_{dx}))$ green circles (left panel); $(S_{ax}(T_1), D_{dx})$ red dots, $(mS_{ax}(T_1), D_{dx})$ green circles (right panel) - linear analysis.

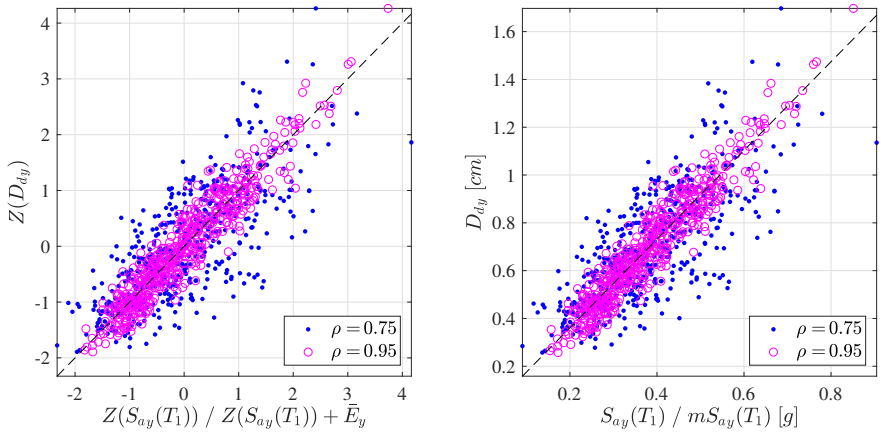

Figure B.108: Scatter plots of $n_s = 500$ samples at node #4: $(Z(S_{ay}(T_1)), Z(D_{dy}))$ red dots, $(Z(S_{ay}(T_1)) + \bar{E}_y, Z(D_{dy}))$ green circles (left panel); $(S_{ay}(T_1), D_{dy})$ red dots, $(mS_{ay}(T_1), D_{dy})$ green circles (right panel) - linear analysis.

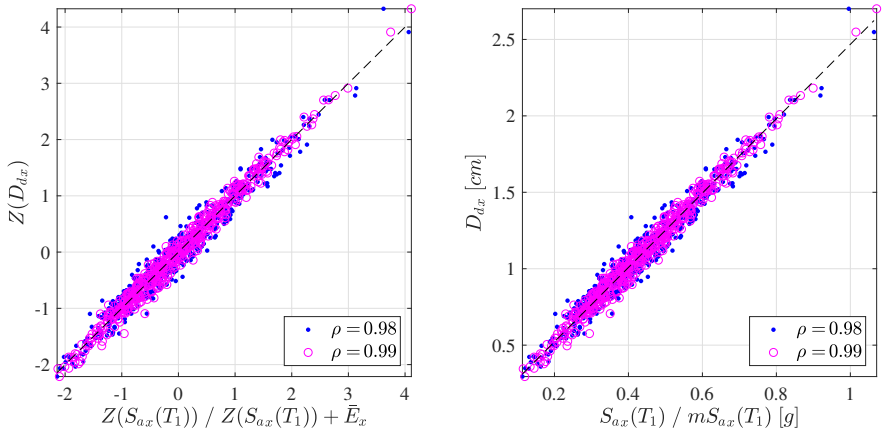

Figure B.109: Scatter plots of $n_s = 500$ samples at node #7: $(Z(S_{ax}(T_1)), Z(D_{dx}))$ red dots, $(Z(S_{ax}(T_1)) + \bar{E}_x, Z(D_{dx}))$ green circles (left panel); $(S_{ax}(T_1), D_{dx})$ red dots, $(mS_{ax}(T_1), D_{dx})$ green circles (right panel) - linear analysis.

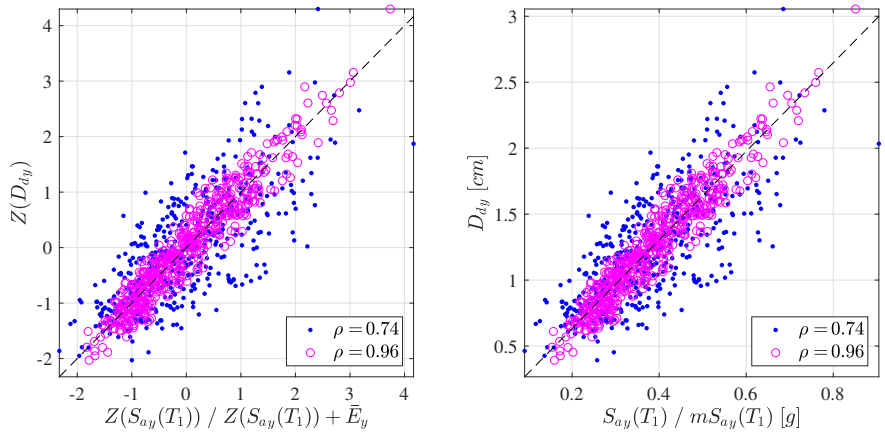

Figure B.110: Scatter plots of $n_s = 500$ samples at node #7: $(Z(S_{ay}(T_1)), Z(D_{dy}))$ red dots, $(Z(S_{ay}(T_1)) + \bar{E}_y, Z(D_{dy}))$ green circles (left panel); $(S_{ay}(T_1), D_{dy})$ red dots, $(mS_{ay}(T_1), D_{dy})$ green circles (right panel) - linear analysis.

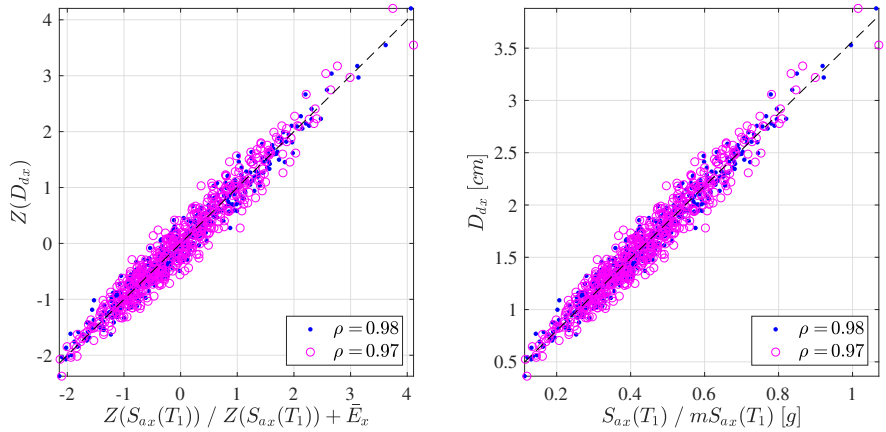

Figure B.111: Scatter plots of $n_s = 500$ samples at node #10: $(Z(S_{ax}(T_1)), Z(D_{dx}))$ red dots, $(Z(S_{ax}(T_1)) + \bar{E}_x, Z(D_{dx}))$ green circles (left panel); $(S_{ax}(T_1), D_{dx})$ red dots, $(mS_{ax}(T_1), D_{dx})$ green circles (right panel) - linear analysis.

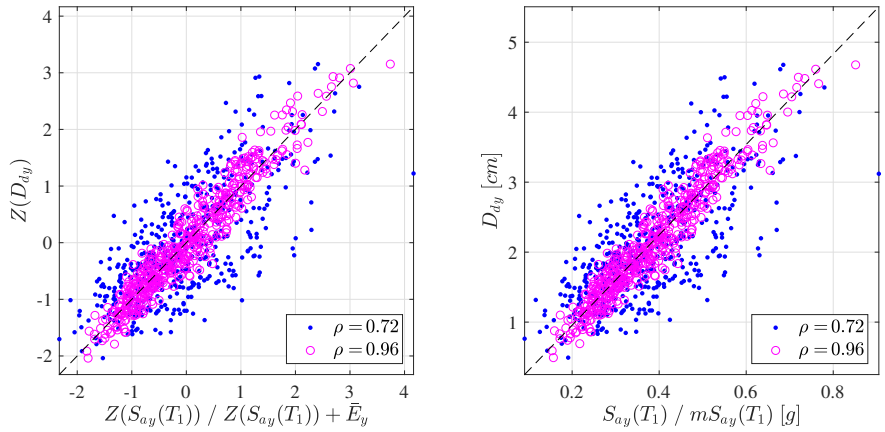

Figure B.112: Scatter plots of $n_s = 500$ samples at node #10: $(Z(S_{ay}(T_1)), Z(D_{dy}))$ red dots, $(Z(S_{ay}(T_1)) + \bar{E}_y, Z(D_{dy}))$ green circles (left panel); $(S_{ay}(T_1), D_{dy})$ red dots, $(mS_{ay}(T_1), D_{dy})$ green circles (right panel) - linear analysis.

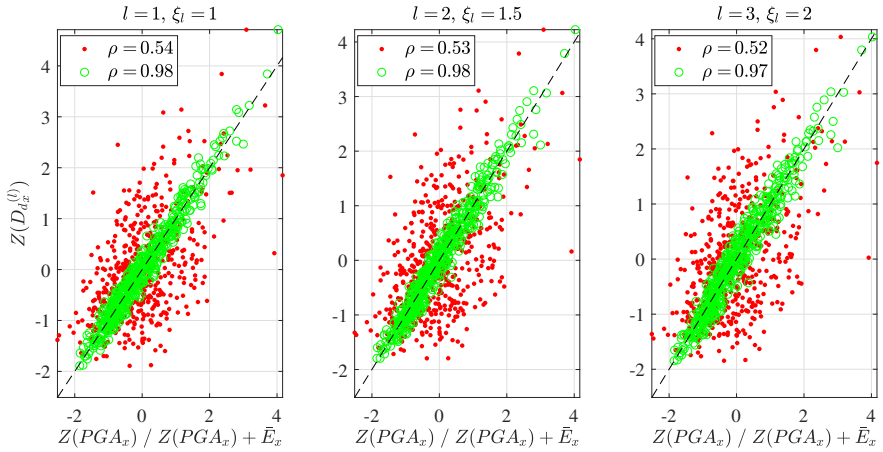

Figure B.113: Scatter plots of $n_s = 500$ samples of $(Z(PGA_x), Z(D_{d_x}^{(l)}))$ red dots, $(Z(PGA_x) + \bar{E}_x, Z(D_{d_x}^{(l)}))$ green circles at node #4: $l = 1$ with $\xi_l = 1$ (left panel); $l = 2$ with $\xi_l = 1.5$ (center panel); $l = 3$ with $\xi_l = 2$ (right panel) - nonlinear analysis.

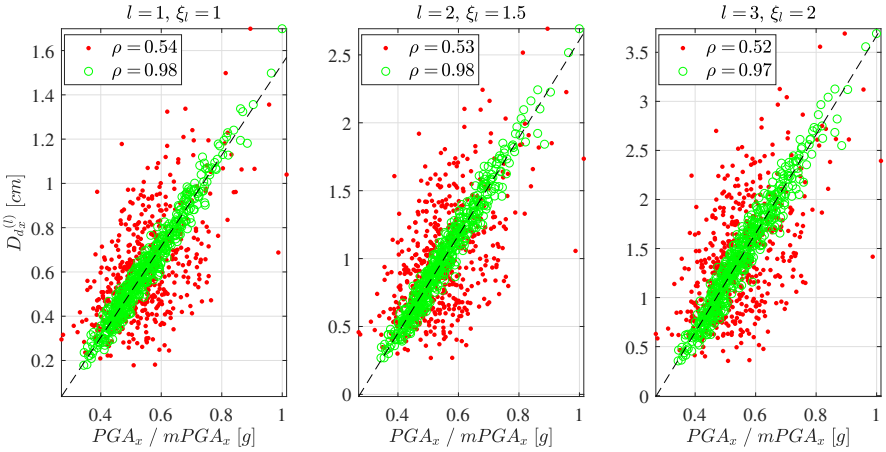

Figure B.114: Scatter plots of $n_s = 500$ samples of $(PGA_x, D_{d_x}^{(l)})$ red dots, $(PGA_x + \bar{E}_x, D_{d_x}^{(l)})$ green circles at node #4: $l = 1$ with $\xi_l = 1$ (left panel); $l = 2$ with $\xi_l = 1.5$ (center panel); $l = 3$ with $\xi_l = 2$ (right panel) - nonlinear analysis.

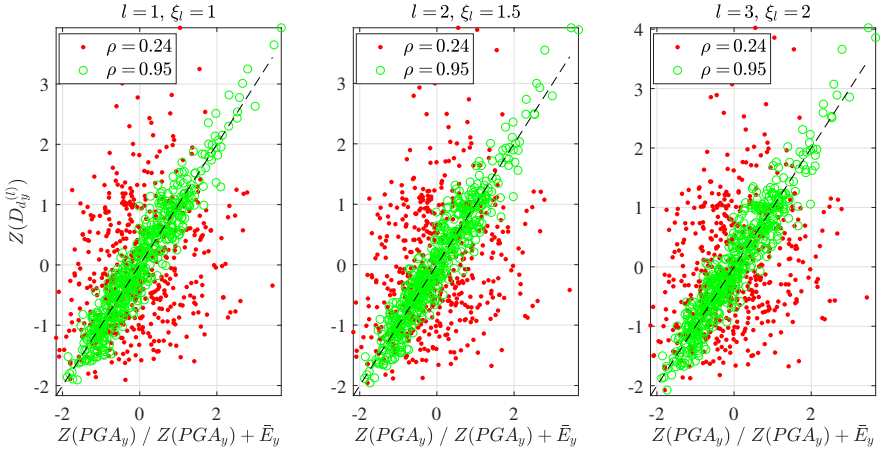

Figure B.115: Scatter plots of $n_s = 500$ samples of $(Z(PGA_y), Z(D_{d_y}^{(l)}))$ red dots, $(Z(PGA_y) + \bar{E}_y, Z(D_{d_y}^{(l)}))$ green circles at node #4: $l = 1$ with $\xi_l = 1$ (left panel); $l = 2$ with $\xi_l = 1.5$ (center panel); $l = 3$ with $\xi_l = 2$ (right panel) - nonlinear analysis.

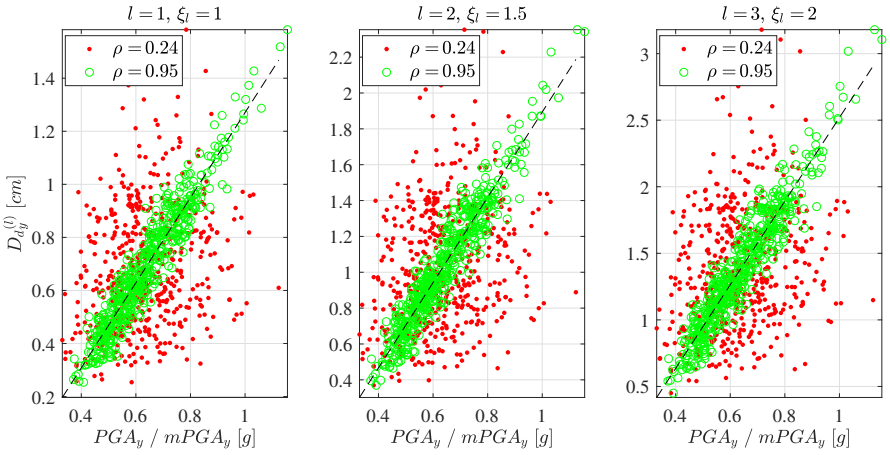

Figure B.116: Scatter plots of $n_s = 500$ samples of $(PGA_y, D_{d_y}^{(l)})$ red dots, $(PGA_y + \bar{E}_y, D_{d_y}^{(l)})$ green circles at node #4: $l = 1$ with $\xi_l = 1$ (left panel); $l = 2$ with $\xi_l = 1.5$ (center panel); $l = 3$ with $\xi_l = 2$ (right panel) - nonlinear analysis.

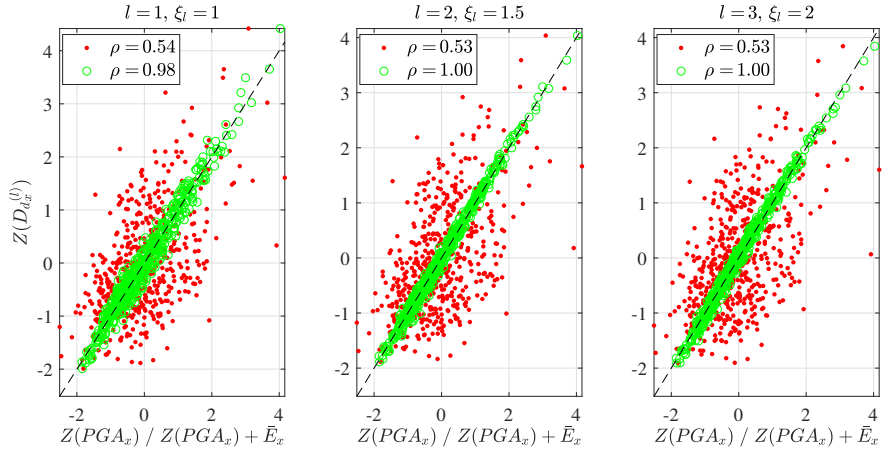

Figure B.117: Scatter plots of $n_s = 500$ samples of $(Z(PGA_x), Z(D_{d_x}^{(l)}))$ red dots, $(Z(PGA_x) + \bar{E}_x, Z(D_{d_x}^{(l)}))$ green circles at node #7: $l = 1$ with $\xi_l = 1$ (left panel); $l = 2$ with $\xi_l = 1.5$ (center panel); $l = 3$ with $\xi_l = 2$ (right panel) - nonlinear analysis.

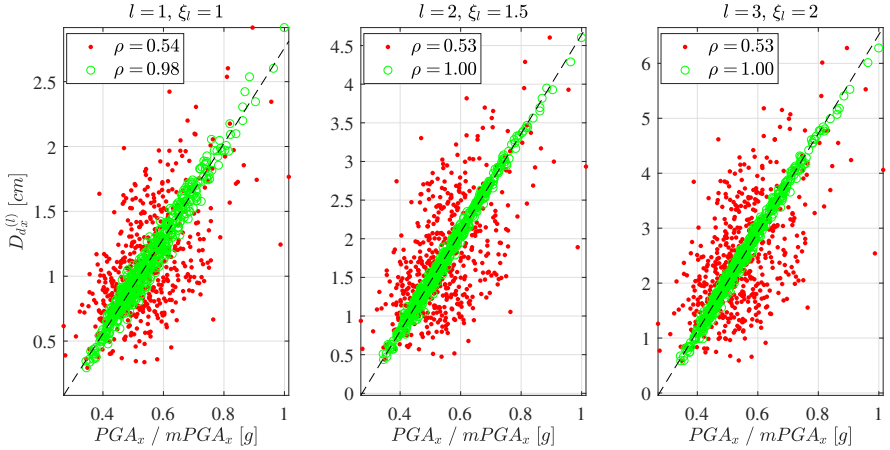

Figure B.118: Scatter plots of $n_s = 500$ samples of $(PGA_x, D_{d_x}^{(l)})$ red dots, $(PGA_x + \bar{E}_x, D_{d_x}^{(l)})$ green circles at node #7: $l = 1$ with $\xi_l = 1$ (left panel); $l = 2$ with $\xi_l = 1.5$ (center panel); $l = 3$ with $\xi_l = 2$ (right panel) - nonlinear analysis.

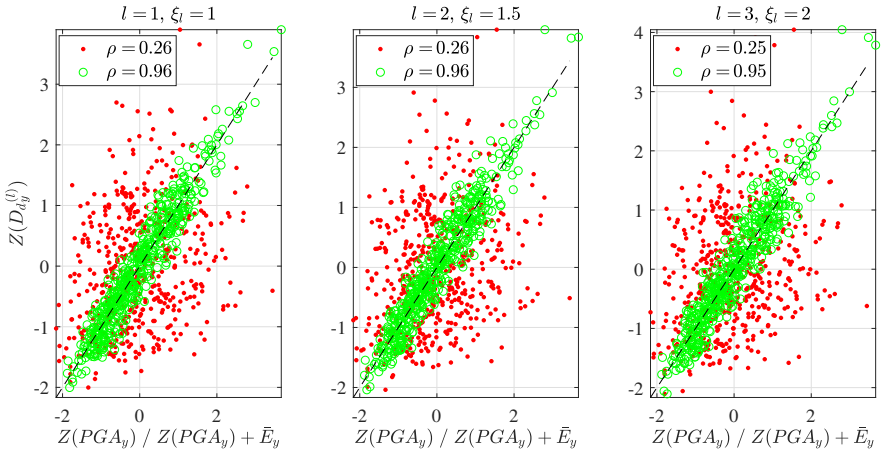

Figure B.119: Scatter plots of $n_s = 500$ samples of $(Z(PGA_y), Z(D_{d_y}^{(l)}))$ red dots, $(Z(PGA_y) + \bar{E}_y, Z(D_{d_y}^{(l)}))$ green circles at node #7: $l = 1$ with $\xi_l = 1$ (left panel); $l = 2$ with $\xi_l = 1.5$ (center panel); $l = 3$ with $\xi_l = 2$ (right panel) - nonlinear analysis.

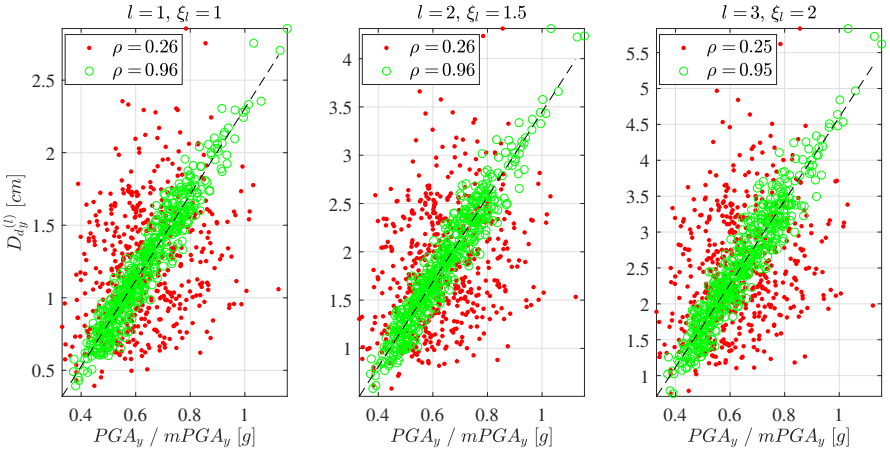

Figure B.120: Scatter plots of $n_s = 500$ samples of $(PGA_y, D_{d_y}^{(l)})$ red dots, $(PGA_y + \bar{E}_y, D_{d_y}^{(l)})$ green circles at node #7: $l = 1$ with $\xi_l = 1$ (left panel); $l = 2$ with $\xi_l = 1.5$ (center panel); $l = 3$ with $\xi_l = 2$ (right panel) - nonlinear analysis.

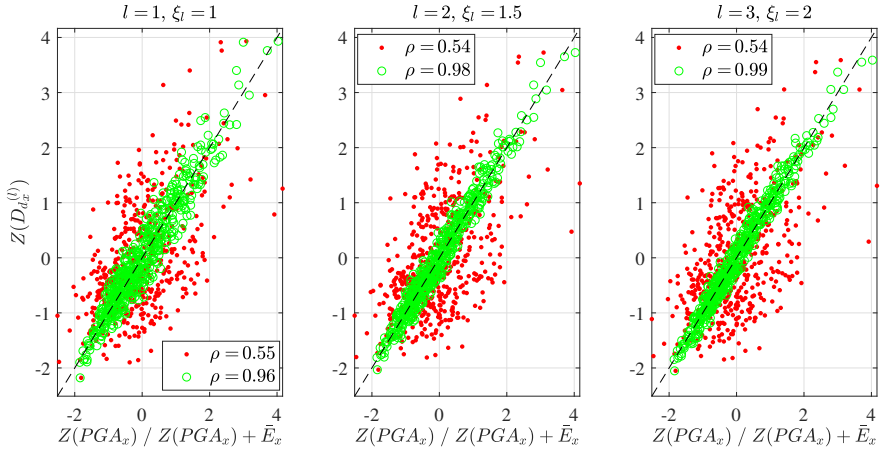

Figure B.121: Scatter plots of $n_s = 500$ samples of $(Z(PGA_x), Z(D_{d_x}^{(l)}))$ red dots, $(Z(PGA_x) + \bar{E}_x, Z(D_{d_x}^{(l)}))$ green circles at node #10: $l = 1$ with $\xi_l = 1$ (left panel); $l = 2$ with $\xi_l = 1.5$ (center panel); $l = 3$ with $\xi_l = 2$ (right panel) - nonlinear analysis.

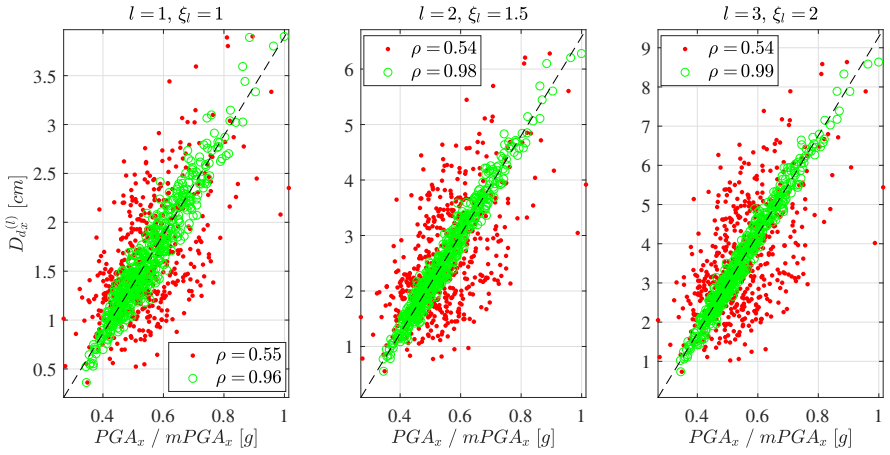

Figure B.122: Scatter plots of $n_s = 500$ samples of $(PGA_x, D_{d_x}^{(l)})$ red dots, $(PGA_x + \bar{E}_x, D_{d_x}^{(l)})$ green circles at node #10: $l = 1$ with $\xi_l = 1$ (left panel); $l = 2$ with $\xi_l = 1.5$ (center panel); $l = 3$ with $\xi_l = 2$ (right panel) - nonlinear analysis.

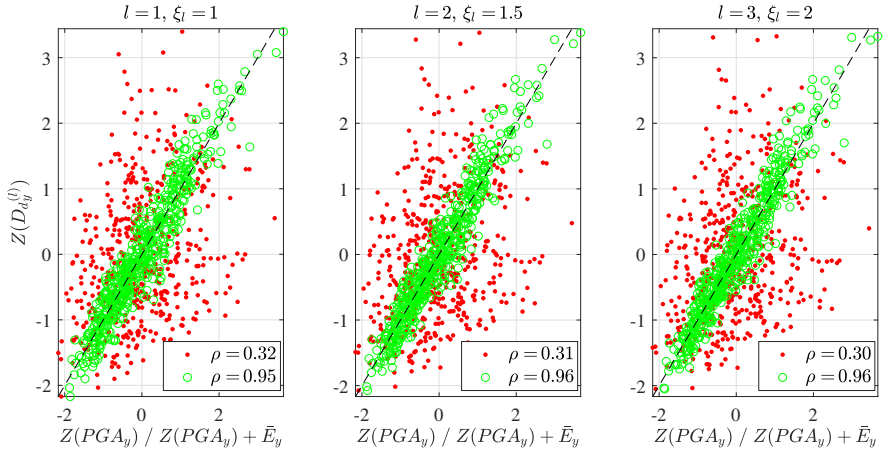

Figure B.123: Scatter plots of $n_s = 500$ samples of $(Z(PGA_y), Z(D_{d_y}^{(l)}))$ red dots, $(Z(PGA_y) + \bar{E}_y, Z(D_{d_y}^{(l)}))$ green circles at node #10: $l = 1$ with $\xi_l = 1$ (left panel); $l = 2$ with $\xi_l = 1.5$ (center panel); $l = 3$ with $\xi_l = 2$ (right panel) - nonlinear analysis.

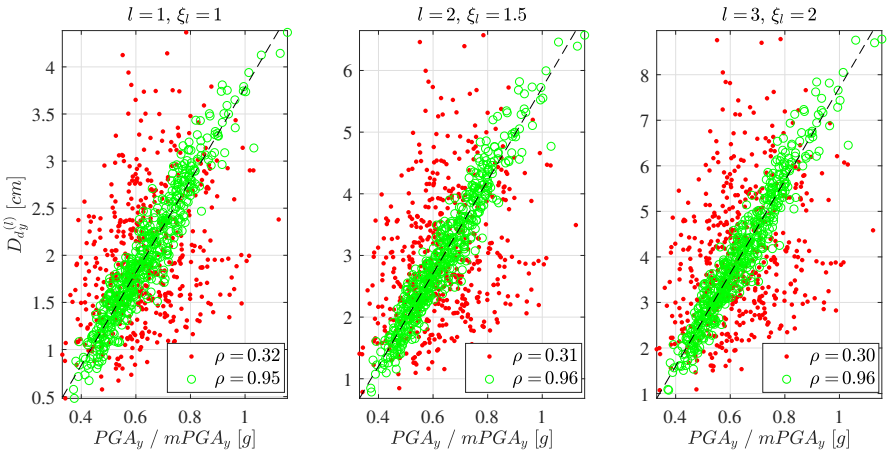

Figure B.124: Scatter plots of $n_s = 500$ samples of $(PGA_y, D_{d_y}^{(l)})$ red dots, $(PGA_y + \bar{E}_y, D_{d_y}^{(l)})$ green circles at node #10: $l = 1$ with $\xi_l = 1$ (left panel); $l = 2$ with $\xi_l = 1.5$ (center panel); $l = 3$ with $\xi_l = 2$ (right panel) - nonlinear analysis.

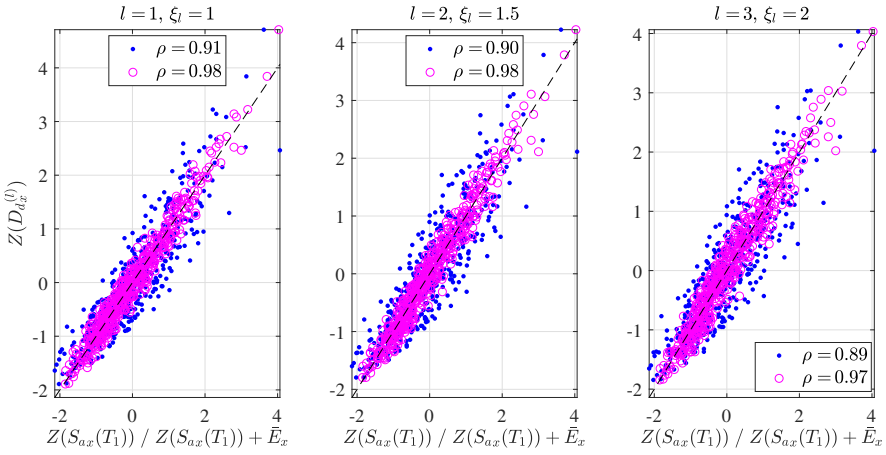

Figure B.125: Scatter plots of $n_s = 500$ samples of $(Z(S_{ax}(T_1)), Z(D_{dx}^{(l)}))$ blue dots, $(Z(S_{ax}(T_1)) + \bar{E}_x, Z(D_{dx}^{(l)}))$ magenta circles at node #4: $l = 1$ with $\xi_l = 1$ (left panel); $l = 2$ with $\xi_l = 1.5$ (center panel); $l = 3$ with $\xi_l = 2$ (right panel) - nonlinear analysis.

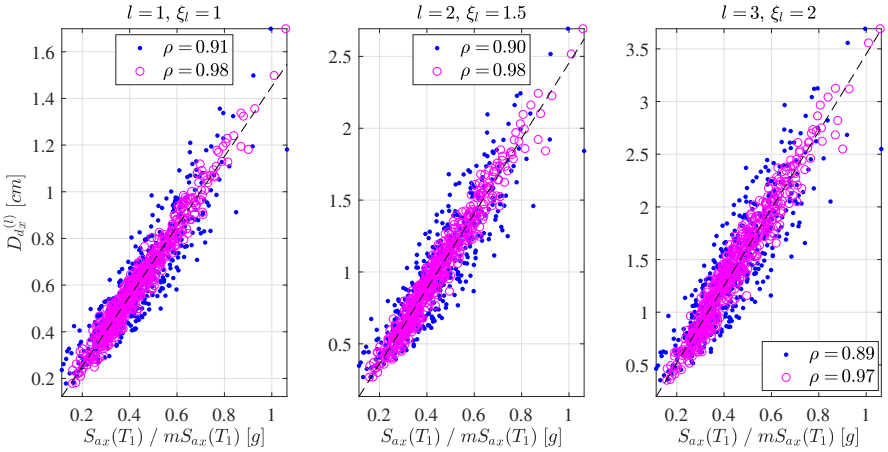

Figure B.126: Scatter plots of $n_s = 500$ samples of $(S_{ax}(T_1), D_{dx}^{(l)})$ blue dots, $(S_{ax}(T_1) + \bar{E}_x, D_{dx}^{(l)})$ magenta circles at node #4: $l = 1$ with $\xi_l = 1$ (left panel); $l = 2$ with $\xi_l = 1.5$ (center panel); $l = 3$ with $\xi_l = 2$ (right panel) - nonlinear analysis.

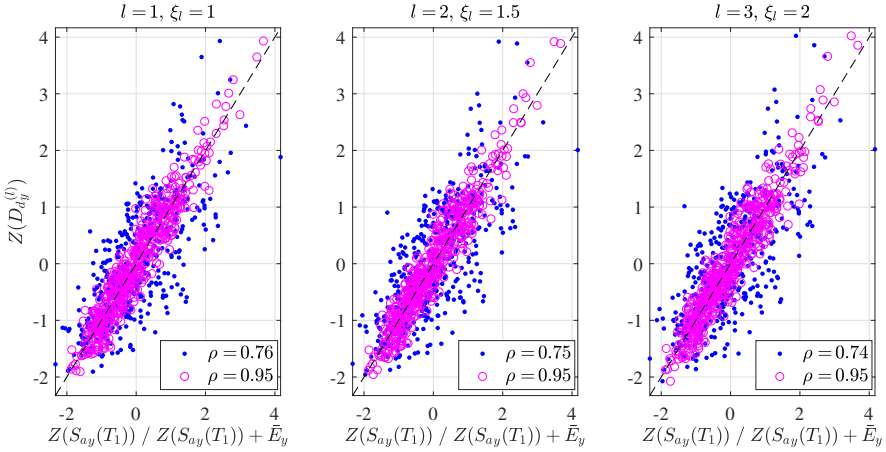

Figure B.127: Scatter plots of $n_s = 500$ samples of $(Z(S_{ay}(T_1)), Z(D_{dy}^{(l)}))$ blue dots, $(Z(S_{ay}(T_1)) + \bar{E}_y, Z(D_{dy}^{(l)}))$ magenta circles at node #4: $l = 1$ with $\xi_l = 1$ (left panel); $l = 2$ with $\xi_l = 1.5$ (center panel); $l = 3$ with $\xi_l = 2$ (right panel) - nonlinear analysis.

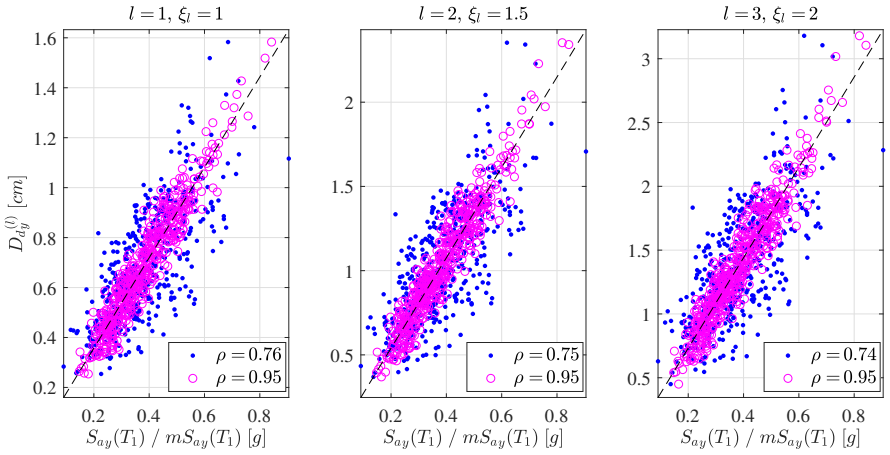

Figure B.128: Scatter plots of $n_s = 500$ samples of $(S_{ay}(T_1), D_{dy}^{(l)})$ blue dots, $(S_{ay}(T_1) + \bar{E}_y, D_{dy}^{(l)})$ magenta circles at node #4: $l = 1$ with $\xi_l = 1$ (left panel); $l = 2$ with $\xi_l = 1.5$ (center panel); $l = 3$ with $\xi_l = 2$ (right panel) - nonlinear analysis.

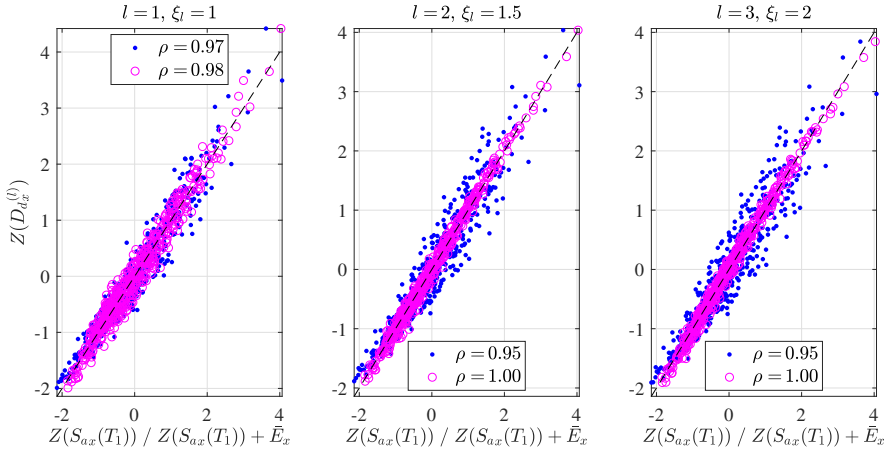

Figure B.129: Scatter plots of $n_s = 500$ samples of $(Z(S_{ax}(T_1)), Z(D_{dx}^{(l)}))$ blue dots, $(Z(S_{ax}(T_1)) + \bar{E}_x, Z(D_{dx}^{(l)}))$ magenta circles at node #7: $l = 1$ with $\xi_l = 1$ (left panel); $l = 2$ with $\xi_l = 1.5$ (center panel); $l = 3$ with $\xi_l = 2$ (right panel) - nonlinear analysis.

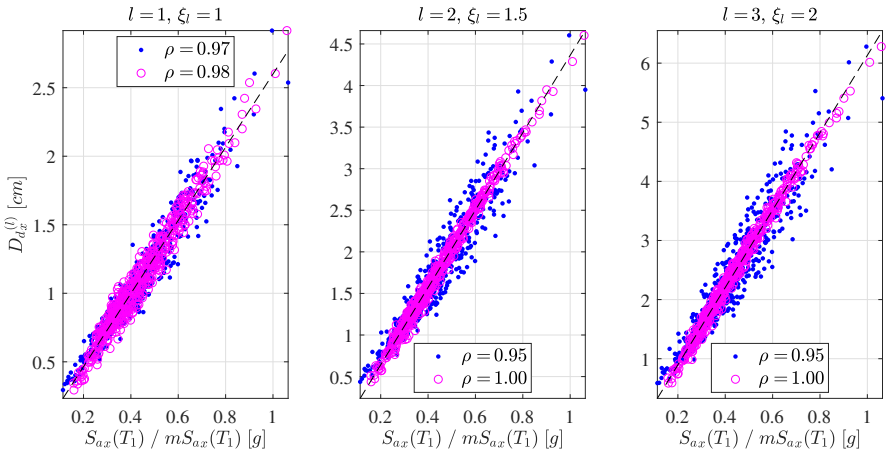

Figure B.130: Scatter plots of $n_s = 500$ samples of $(S_{ax}(T_1), D_{dx}^{(l)})$ blue dots, $(S_{ax}(T_1) + \bar{E}_x, D_{dx}^{(l)})$ magenta circles at node #7: $l = 1$ with $\xi_l = 1$ (left panel); $l = 2$ with $\xi_l = 1.5$ (center panel); $l = 3$ with $\xi_l = 2$ (right panel) - nonlinear analysis.

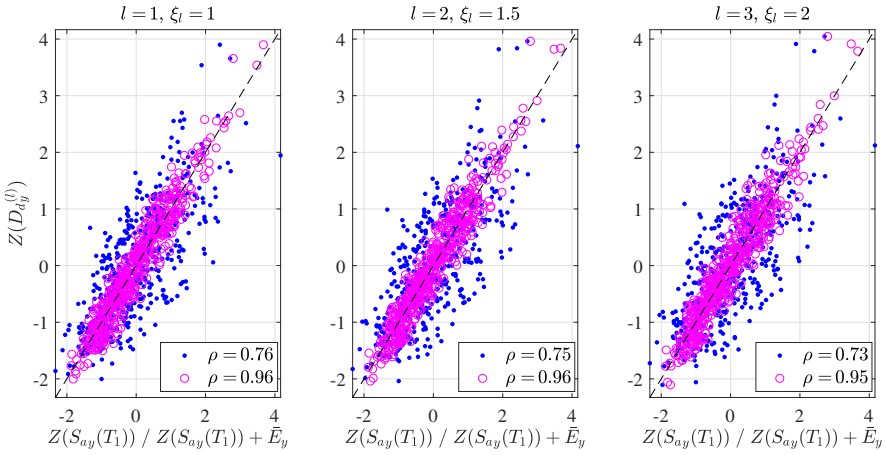

Figure B.131: Scatter plots of $n_s = 500$ samples of $(Z(S_{ay}(T_1)), Z(D_{dy}^{(l)}))$ blue dots, $(Z(S_{ay}(T_1)) + \bar{E}_y, Z(D_{dy}^{(l)}))$ magenta circles at node #7: $l = 1$ with $\xi_l = 1$ (left panel); $l = 2$ with $\xi_l = 1.5$ (center panel); $l = 3$ with $\xi_l = 2$ (right panel) - nonlinear analysis.

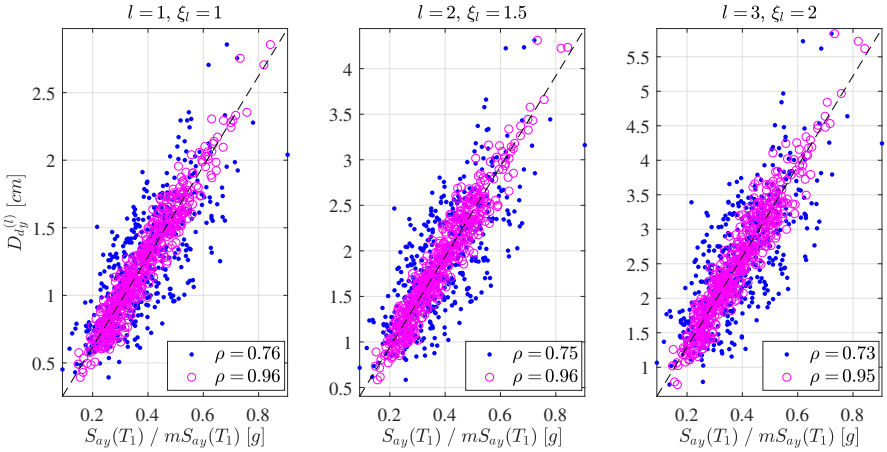

Figure B.132: Scatter plots of $n_s = 500$ samples of $(S_{ay}(T_1), D_{dy}^{(l)})$ blue dots, $(S_{ay}(T_1) + \bar{E}_y, D_{dy}^{(l)})$ magenta circles at node #7: $l = 1$ with $\xi_l = 1$ (left panel); $l = 2$ with $\xi_l = 1.5$ (center panel); $l = 3$ with $\xi_l = 2$ (right panel) - nonlinear analysis.

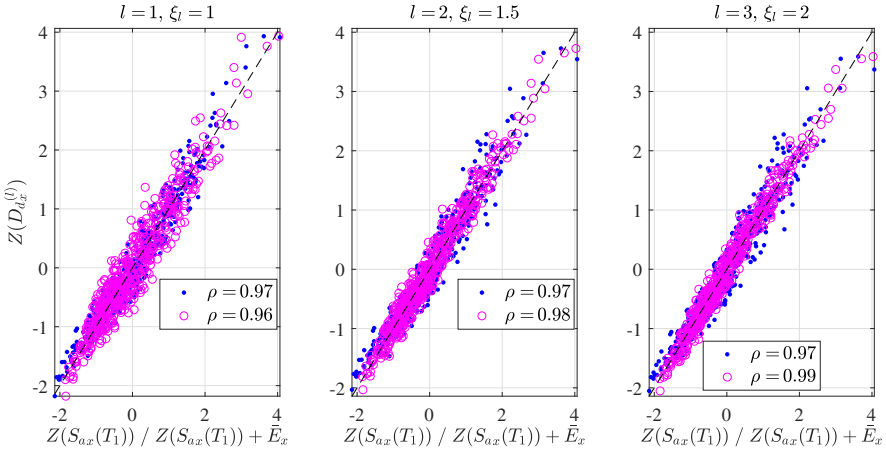

Figure B.133: Scatter plots of $n_s = 500$ samples of $(Z(S_{ax}(T_1)), Z(D_{dx}^{(l)}))$ blue dots, $(Z(S_{ax}(T_1)) + \bar{E}_x, Z(D_{dx}^{(l)}))$ magenta circles at node #10: $l = 1$ with $\xi_l = 1$ (left panel); $l = 2$ with $\xi_l = 1.5$ (center panel); $l = 3$ with $\xi_l = 2$ (right panel) - nonlinear analysis.

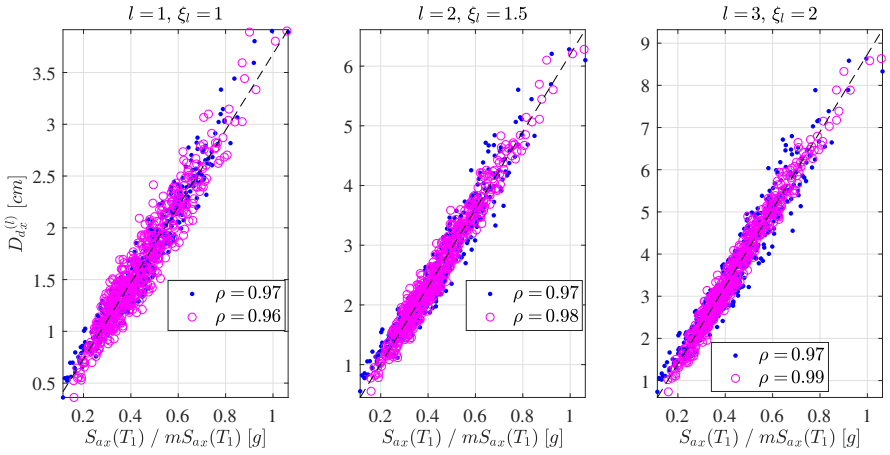

Figure B.134: Scatter plots of $n_s = 500$ samples of $(S_{ax}(T_1), D_{dx}^{(l)})$ blue dots, $(S_{ax}(T_1) + \bar{E}_x, D_{dx}^{(l)})$ magenta circles at node #10: $l = 1$ with $\xi_l = 1$ (left panel); $l = 2$ with $\xi_l = 1.5$ (center panel); $l = 3$ with $\xi_l = 2$ (right panel) - nonlinear analysis.

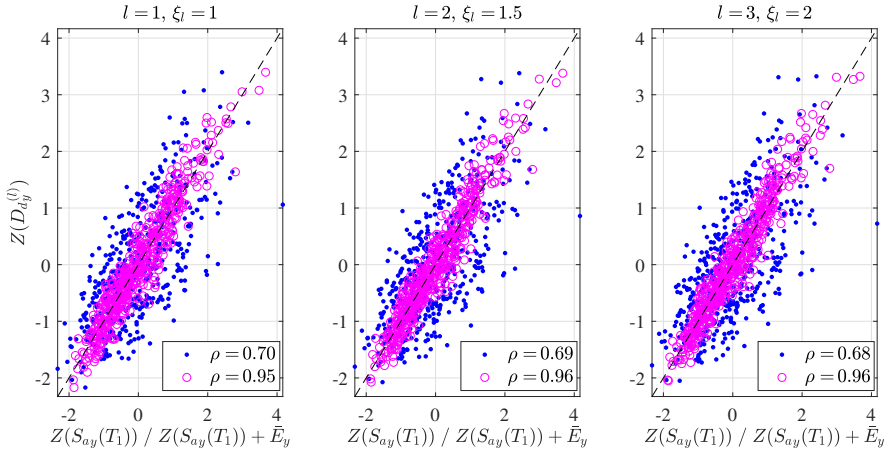

Figure B.135: Scatter plots of $n_s = 500$ samples of $(Z(S_{ay}(T_1)), Z(D_{dy}^{(l)}))$ blue dots, $(Z(S_{ay}(T_1)) + \bar{E}_y, Z(D_{dy}^{(l)}))$ magenta circles at node #10: $l = 1$ with $\xi_l = 1$ (left panel); $l = 2$ with $\xi_l = 1.5$ (center panel); $l = 3$ with $\xi_l = 2$ (right panel) - nonlinear analysis.

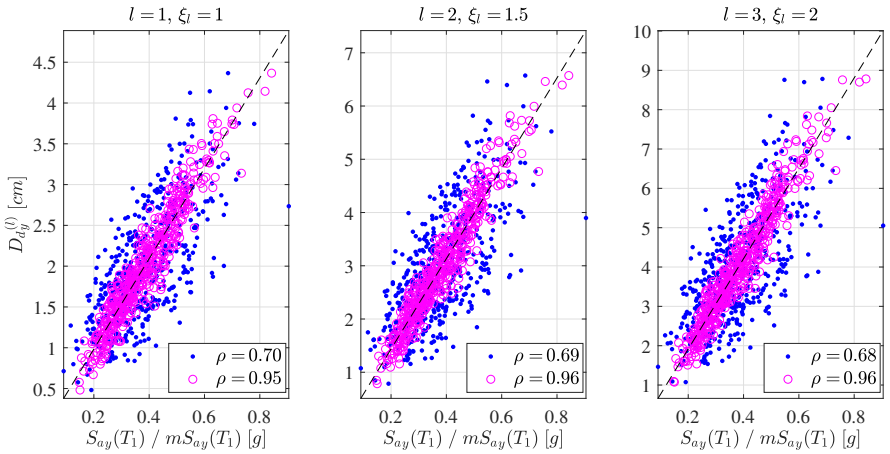

Figure B.136: Scatter plots of $n_s = 500$ samples of $(S_{ay}(T_1), D_{dy}^{(l)})$ blue dots, $(S_{ay}(T_1) + \bar{E}_y, D_{dy}^{(l)})$ magenta circles at node #10: $l = 1$ with $\xi_l = 1$ (left panel); $l = 2$ with $\xi_l = 1.5$ (center panel); $l = 3$ with $\xi_l = 2$ (right panel) - nonlinear analysis.

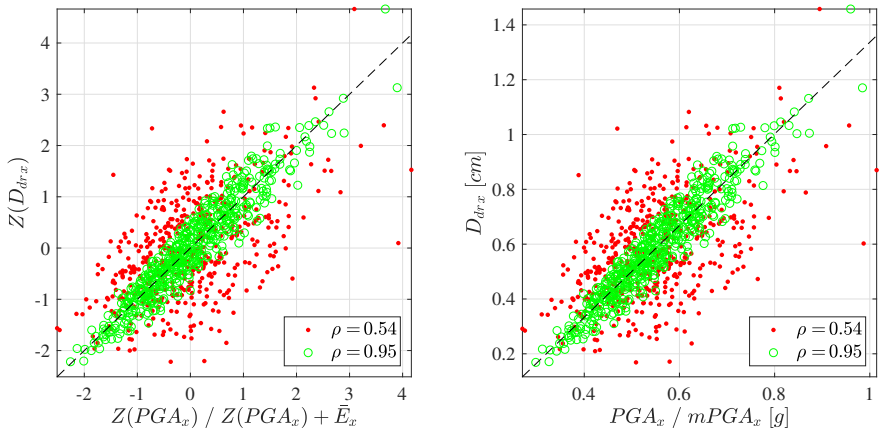

Figure B.137: Scatter plots of $n_s = 500$ samples at 1st storey: $(Z(PGA_x), Z(D_{drx}))$ red dots, $(Z(PGA_x) + \bar{E}_x, Z(D_{drx}))$ green circles (left panel); (PGA_x, D_{drx}) red dots, $(mPGA_x, D_{drx})$ green circles (right panel) - linear analysis.

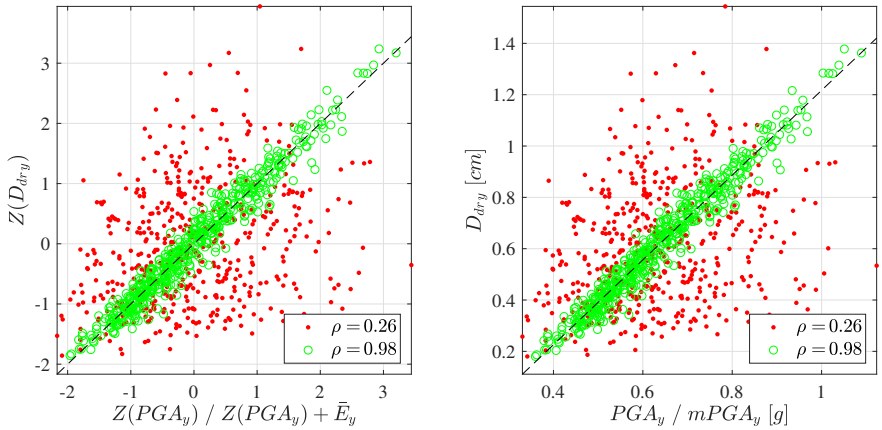

Figure B.138: Scatter plots of $n_s = 500$ samples at 1st storey: $(Z(PGA_y), Z(D_{dry}))$ red dots, $(Z(PGA_y) + \bar{E}_y, Z(D_{dry}))$ green circles (left panel); (PGA_y, D_{dry}) red dots, $(mPGA_y, D_{dry})$ green circles (right panel) - linear analysis.

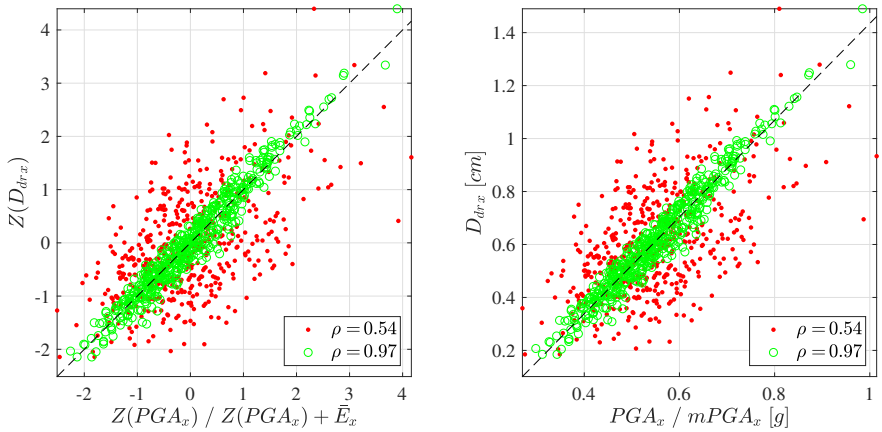

Figure B.139: Scatter plots of $n_s = 500$ samples at 2nd storey: $(Z(PGA_x), Z(D_{drx}))$ red dots, $(Z(PGA_x) + \bar{E}_x, Z(D_{drx}))$ green circles (left panel); (PGA_x, D_{drx}) red dots, $(mPGA_x, D_{drx})$ green circles (right panel) - linear analysis.

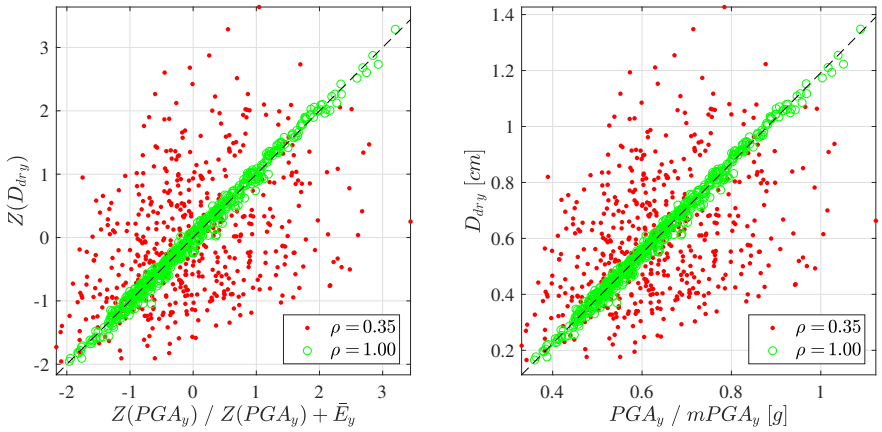

Figure B.140: Scatter plots of $n_s = 500$ samples at 2nd storey: $(Z(PGA_y), Z(D_{dry}))$ red dots, $(Z(PGA_y) + \bar{E}_y, Z(D_{dry}))$ green circles (left panel); (PGA_y, D_{dry}) red dots, $(mPGA_y, D_{dry})$ green circles (right panel) - linear analysis.

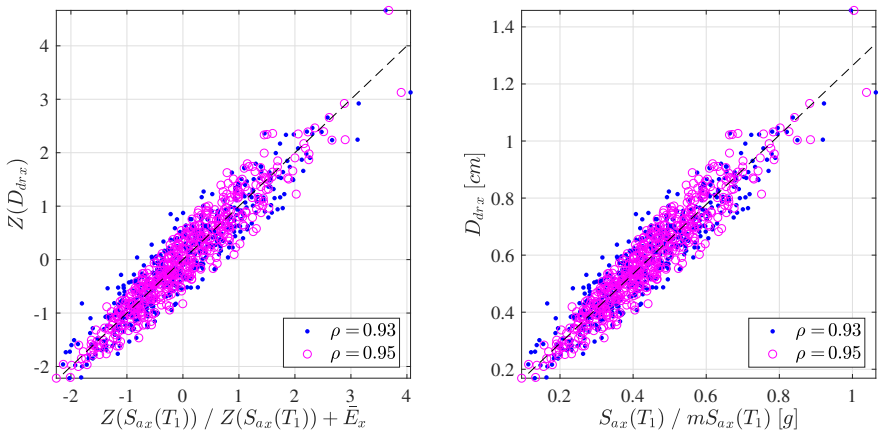

Figure B.141: Scatter plots of $n_s = 500$ samples at 1st storey: $(Z(S_{ax}(T_1)), Z(D_{drx}))$ blue dots, $(Z(S_{ax}(T_1)) + \bar{E}_x, Z(D_{drx}))$ magenta circles (left panel); $(S_{ax}(T_1), D_{drx})$ blue dots, $(mS_{ax}(T_1), D_{drx})$ magenta circles (right panel) - linear analysis.

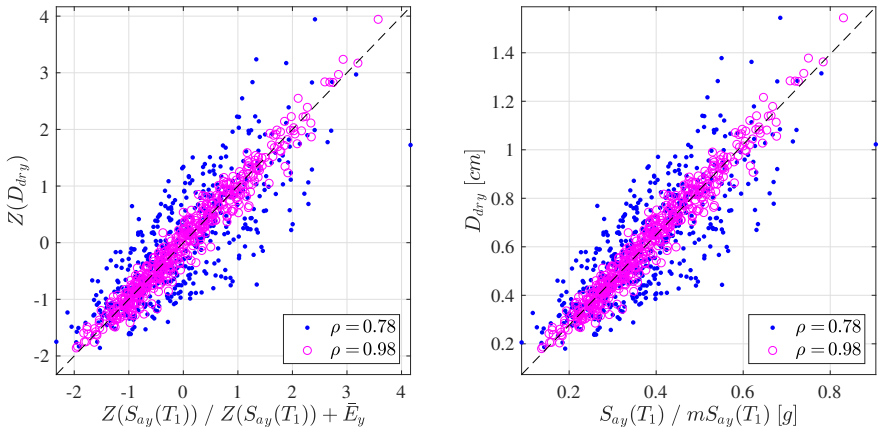

Figure B.142: Scatter plots of $n_s = 500$ samples at 1st storey: $(Z(S_{ay}(T_1)), Z(D_{dry}))$ blue dots, $(Z(S_{ay}(T_1)) + \bar{E}_y, Z(D_{dry}))$ magenta circles (left panel); $(S_{ay}(T_1), D_{dry})$ blue dots, $(mS_{ay}(T_1), D_{dry})$ magenta circles (right panel) - linear analysis.

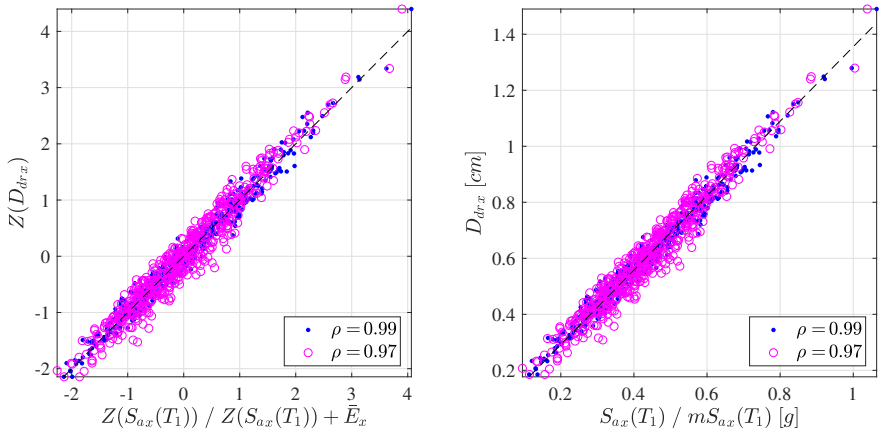

Figure B.143: Scatter plots of $n_s = 500$ samples at 2nd storey: $(Z(S_{ax}(T_1)), Z(D_{drx}))$ blue dots, $(Z(S_{ax}(T_1)) + \bar{E}_x, Z(D_{drx}))$ magenta circles (left panel); $(S_{ax}(T_1), D_{drx})$ blue dots, $(mS_{ax}(T_1), D_{drx})$ magenta circles (right panel) - linear analysis.

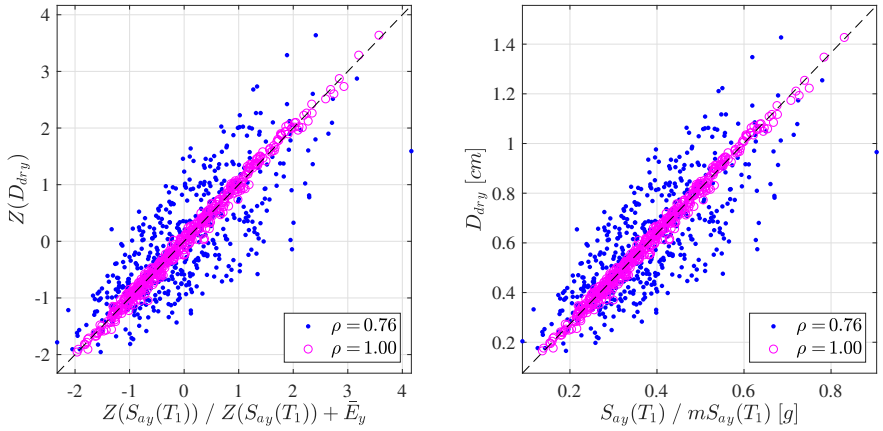

Figure B.144: Scatter plots of $n_s = 500$ samples at 2nd storey: $(Z(S_{ay}(T_1)), Z(D_{dry}))$ blue dots, $(Z(S_{ay}(T_1)) + \bar{E}_y, Z(D_{dry}))$ magenta circles (left panel); $(S_{ay}(T_1), D_{dry})$ blue dots, $(mS_{ay}(T_1), D_{dry})$ magenta circles (right panel) - linear analysis.

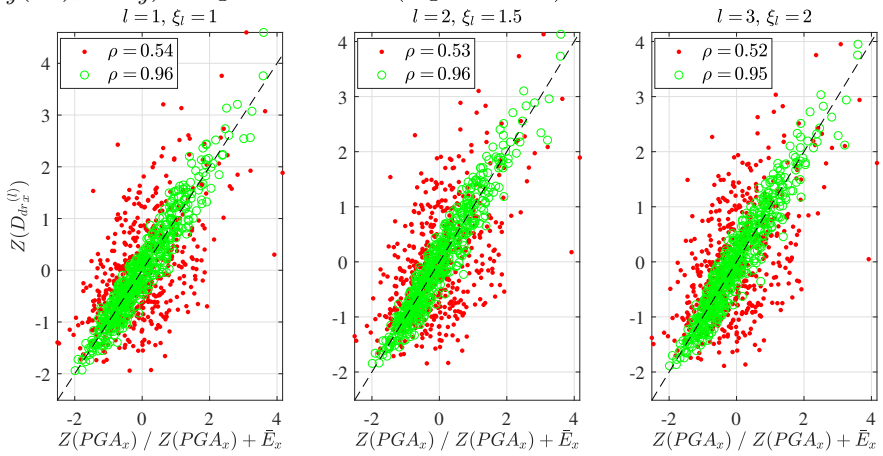

Figure B.145: Scatter plots of $n_s = 500$ samples of $(Z(PGA_x), Z(D_{drx}^{(l)}))$ red dots, $(Z(PGA_x) + \bar{E}_x, Z(D_{drx}^{(l)}))$ green circles at 1st storey: $l = 1$ with $\xi_l = 1$ (left panel); $l = 2$ with $\xi_l = 1.5$ (center panel); $l = 3$ with $\xi_l = 2$ (right panel) - nonlinear analysis.

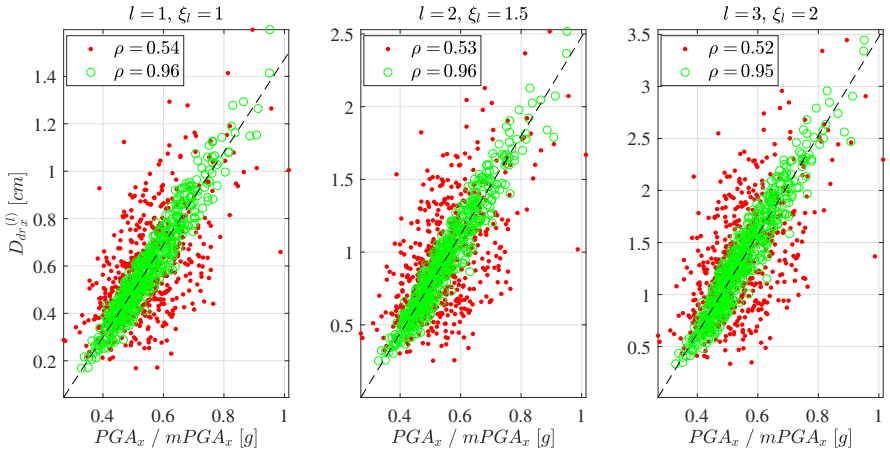

Figure B.146: Scatter plots of $n_s = 500$ samples of $(PGA_x, D_{drx}^{(l)})$ red dots, $(PGA_x + \bar{E}_x, D_{drx}^{(l)})$ green circles at 1st storey: $l = 1$ with $\xi_l = 1$ (left panel); $l = 2$ with $\xi_l = 1.5$ (center panel); $l = 3$ with $\xi_l = 2$ (right panel) - nonlinear analysis.

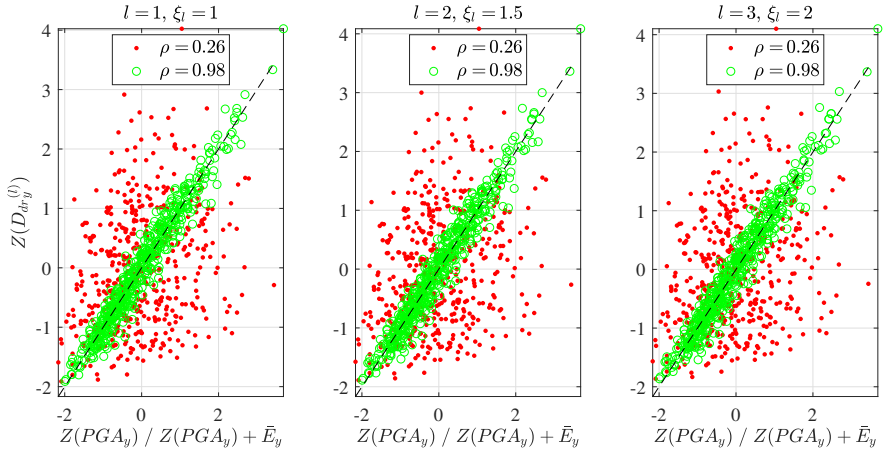

Figure B.147: Scatter plots of $n_s = 500$ samples of $(Z(PGA_y), Z(D_{dry}^{(l)}))$ red dots, $(Z(PGA_y) + \bar{E}_y, Z(D_{dry}^{(l)}))$ green circles at 1st storey: $l = 1$ with $\xi_l = 1$ (left panel); $l = 2$ with $\xi_l = 1.5$ (center panel); $l = 3$ with $\xi_l = 2$ (right panel) - nonlinear analysis.

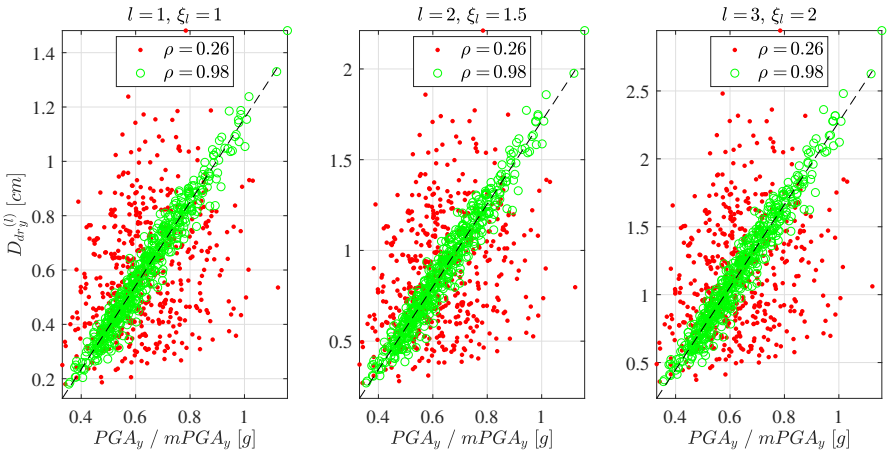

Figure B.148: Scatter plots of $n_s = 500$ samples of $(PGA_y, D_{dry}^{(l)})$ red dots, $(PGA_y + \bar{E}_y, D_{dry}^{(l)})$ green circles at 1st storey: $l = 1$ with $\xi_l = 1$ (left panel); $l = 2$ with $\xi_l = 1.5$ (center panel); $l = 3$ with $\xi_l = 2$ (right panel) - nonlinear analysis.

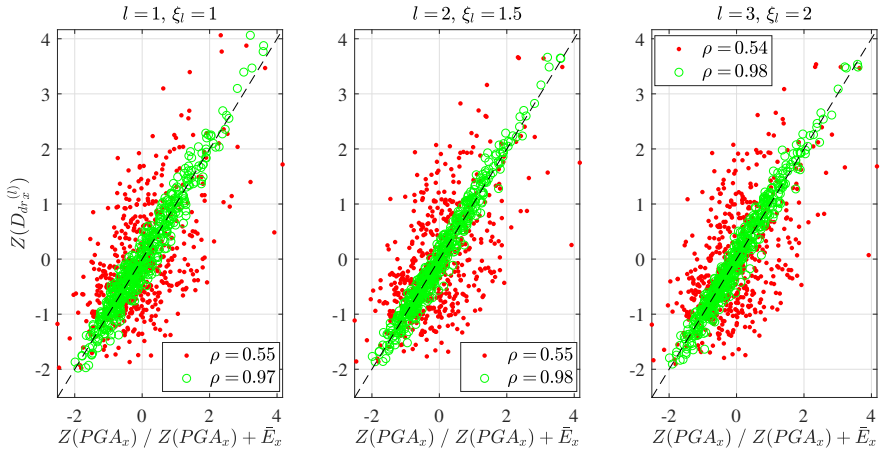

Figure B.149: Scatter plots of $n_s = 500$ samples of $(Z(PGA_x), Z(D_{drx}^{(l)}))$ red dots, $(Z(PGA_x)+\bar{E}_x, Z(D_{drx}^{(l)}))$ green circles at 2nd storey: $l=1$ with $\xi_l=1$ (left panel); $l=2$ with $\xi_l=1.5$ (center panel); $l=3$ with $\xi_l=2$ (right panel) - nonlinear analysis.

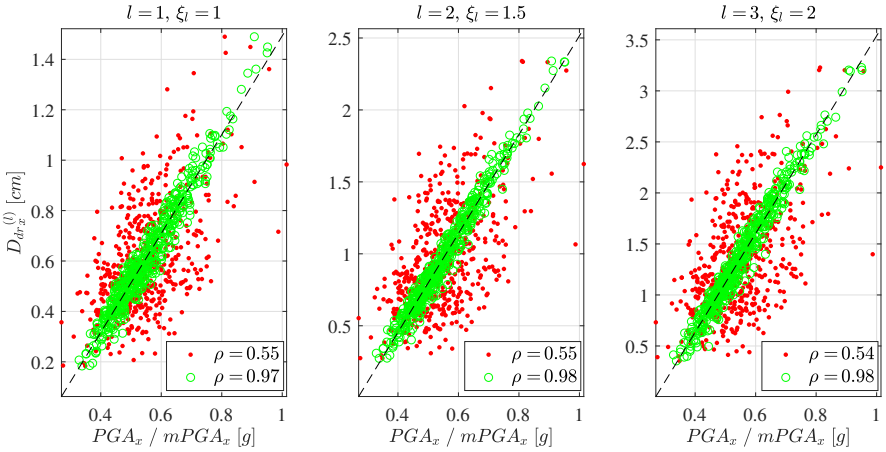

Figure B.150: Scatter plots of $n_s = 500$ samples of $(PGA_x, D_{drx}^{(l)})$ red dots, $(PGA_x+\bar{E}_x, D_{drx}^{(l)})$ green circles at 2nd storey: $l=1$ with $\xi_l=1$ (left panel); $l=2$ with $\xi_l=1.5$ (center panel); $l=3$ with $\xi_l=2$ (right panel) - nonlinear analysis.

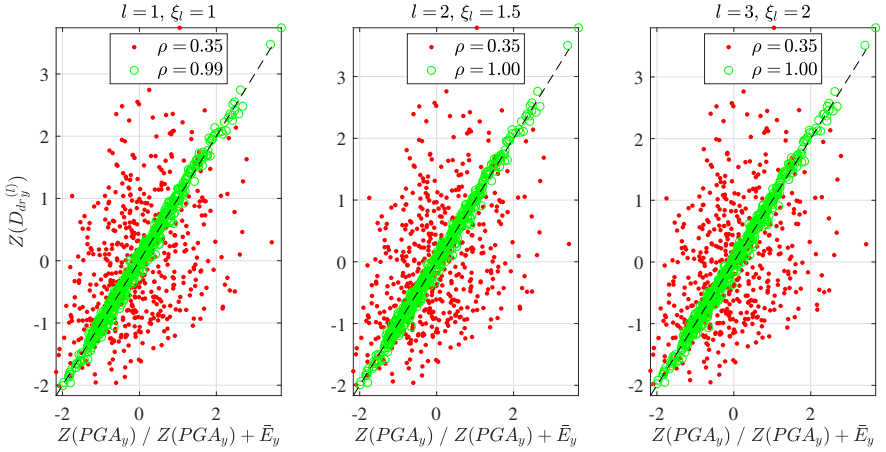

Figure B.151: Scatter plots of $n_s = 500$ samples of $(Z(PGA_y), Z(D_{dry}^{(l)}))$ red dots, $(Z(PGA_y)+\bar{E}_y, Z(D_{dry}^{(l)}))$ green circles at 2nd storey: $l=1$ with $\xi_l=1$ (left panel); $l=2$ with $\xi_l=1.5$ (center panel); $l=3$ with $\xi_l=2$ (right panel) - nonlinear analysis.

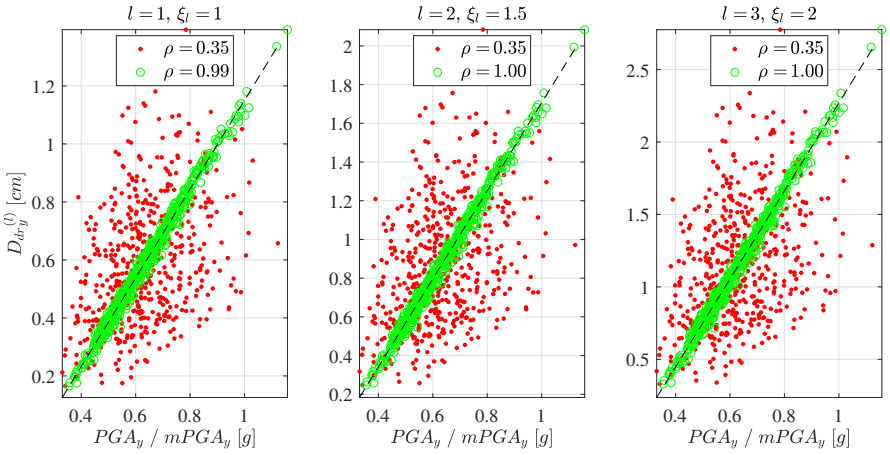

Figure B.152: Scatter plots of $n_s = 500$ samples of $(PGA_y, D_{dry}^{(l)})$ red dots, $(PGA_y + \bar{E}_y, D_{dry}^{(l)})$ green circles at 2nd storey: $l = 1$ with $\xi_l = 1$ (left panel); $l = 2$ with $\xi_l = 1.5$ (center panel); $l = 3$ with $\xi_l = 2$ (right panel) - nonlinear analysis.

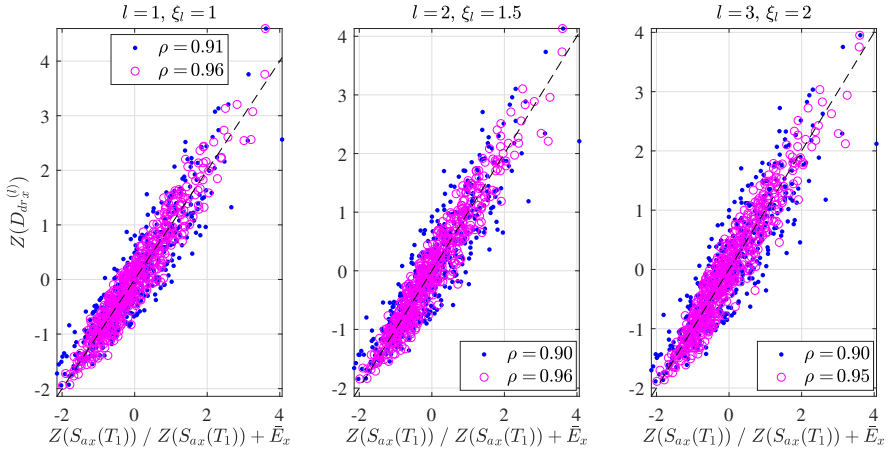

Figure B.153: Scatter plots of $n_s = 500$ samples of $(Z(S_{ax}(T_1)), Z(D_{drx}^{(l)}))$ blue dots, $(Z(S_{ax}(T_1)) + \bar{E}_x, Z(D_{drx}^{(l)}))$ magenta circles at 1st storey: $l = 1$ with $\xi_l = 1$ (left panel); $l = 2$ with $\xi_l = 1.5$ (center panel); $l = 3$ with $\xi_l = 2$ (right panel) - nonlinear analysis.

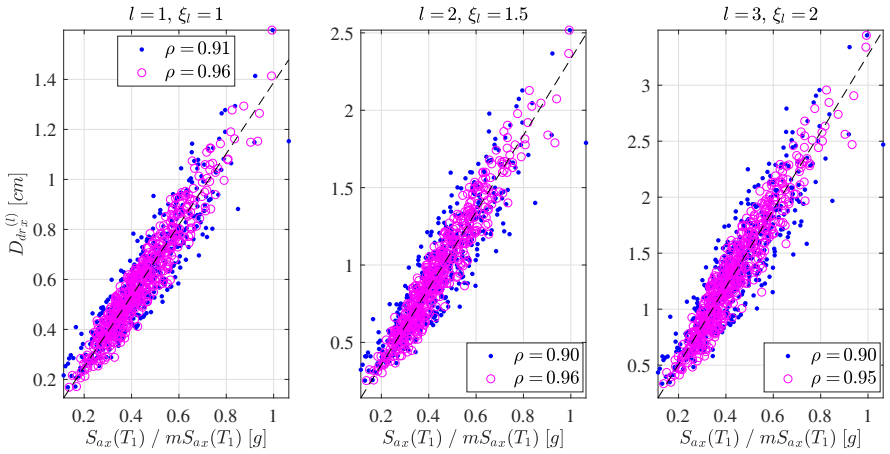

Figure B.154: Scatter plots of $n_s = 500$ samples of $(S_{ax}(T_1), D_{drx}^{(l)})$ blue dots, $(S_{ax}(T_1) + \bar{E}_x, D_{drx}^{(l)})$ magenta circles at 1st storey: $l = 1$ with $\xi_l = 1$ (left panel); $l = 2$ with $\xi_l = 1.5$ (center panel); $l = 3$ with $\xi_l = 2$ (right panel) - nonlinear analysis.

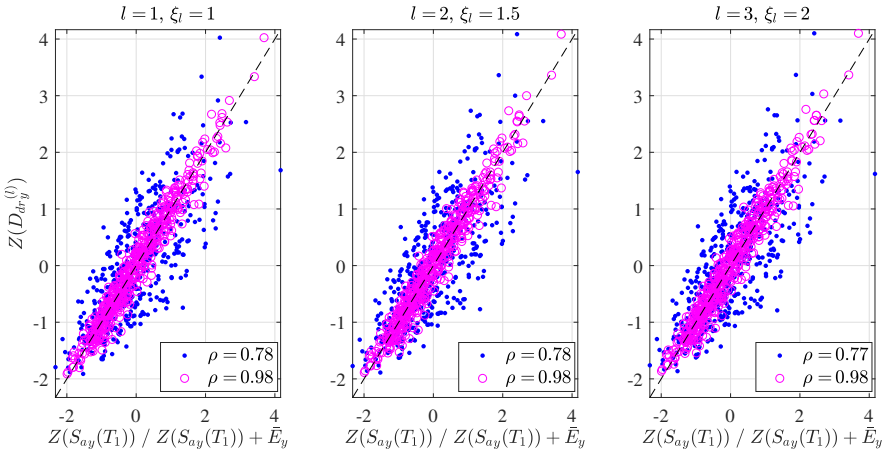

Figure B.155: Scatter plots of $n_s = 500$ samples of $(Z(S_{ay}(T_1)), Z(D_{dry}^{(l)}))$ blue dots, $(Z(S_{ay}(T_1)) + \bar{E}_y, Z(D_{dry}^{(l)}))$ magenta circles at 1st storey: $l = 1$ with $\xi_l = 1$ (left panel); $l = 2$ with $\xi_l = 1.5$ (center panel); $l = 3$ with $\xi_l = 2$ (right panel) - nonlinear analysis.

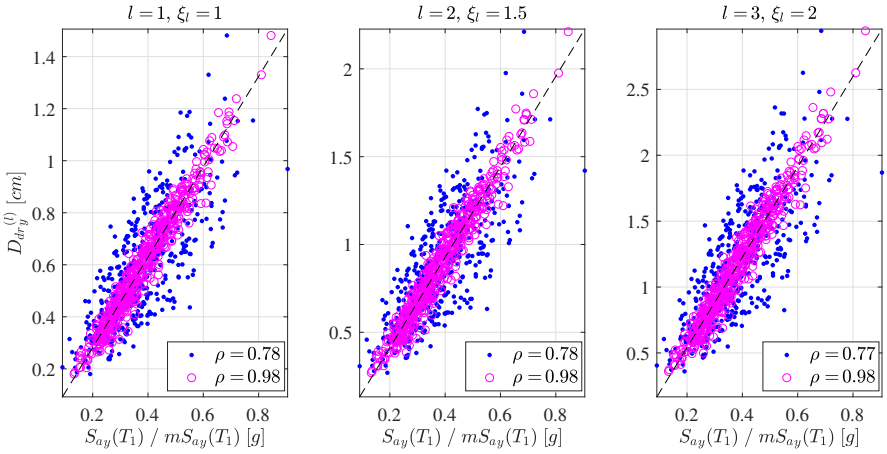

Figure B.156: Scatter plots of $n_s = 500$ samples of $(S_{ay}(T_1), D_{dry}^{(l)})$ blue dots, $(S_{ay}(T_1) + \bar{E}_y, D_{dry}^{(l)})$ magenta circles at 1st storey: $l = 1$ with $\xi_l = 1$ (left panel); $l = 2$ with $\xi_l = 1.5$ (center panel); $l = 3$ with $\xi_l = 2$ (right panel) - nonlinear analysis.

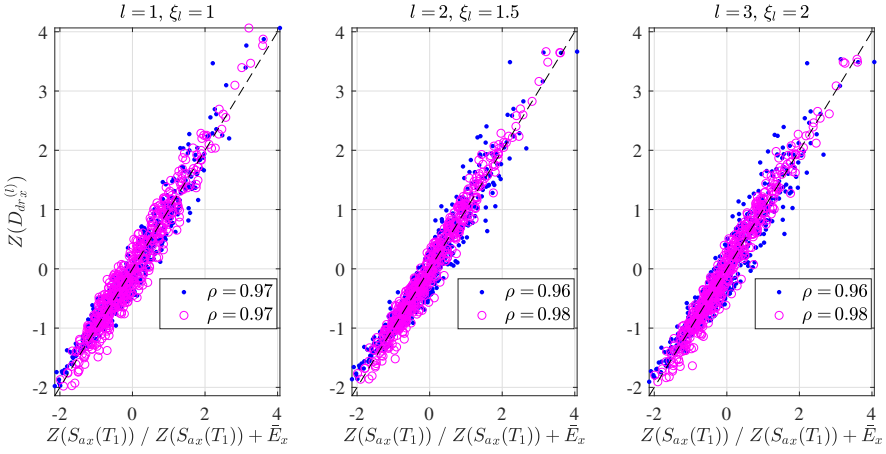

Figure B.157: Scatter plots of $n_s = 500$ samples of $(Z(S_{ax}(T_1)), Z(D_{drx}^{(l)}))$ blue dots, $(Z(S_{ax}(T_1)) + \bar{E}_x, Z(D_{drx}^{(l)}))$ magenta circles at 2nd storey: $l = 1$ with $\xi_l = 1$ (left panel); $l = 2$ with $\xi_l = 1.5$ (center panel); $l = 3$ with $\xi_l = 2$ (right panel) - nonlinear analysis.

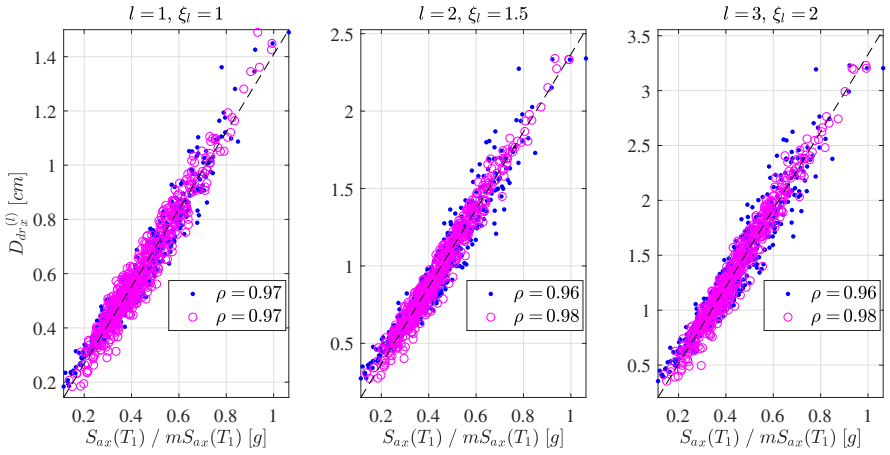

Figure B.158: Scatter plots of $n_s = 500$ samples of $(S_{ax}(T_1), D_{drx}^{(l)})$ blue dots, $(S_{ax}(T_1) + \bar{E}_x, D_{drx}^{(l)})$ magenta circles at 2nd storey: $l = 1$ with $\xi_l = 1$ (left panel); $l = 2$ with $\xi_l = 1.5$ (center panel); $l = 3$ with $\xi_l = 2$ (right panel) - nonlinear analysis.

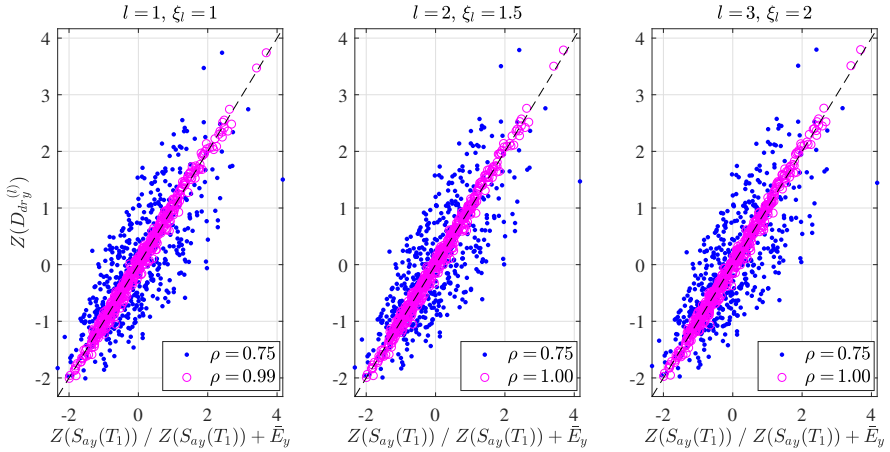

Figure B.159: Scatter plots of $n_s = 500$ samples of $(Z(S_{ay}(T_1)), Z(D_{dry}^{(l)}))$ blue dots, $(Z(S_{ay}(T_1)) + \bar{E}_y, Z(D_{dry}^{(l)}))$ magenta circles at 2nd storey: $l = 1$ with $\xi_l = 1$ (left panel); $l = 2$ with $\xi_l = 1.5$ (center panel); $l = 3$ with $\xi_l = 2$ (right panel) - nonlinear analysis.

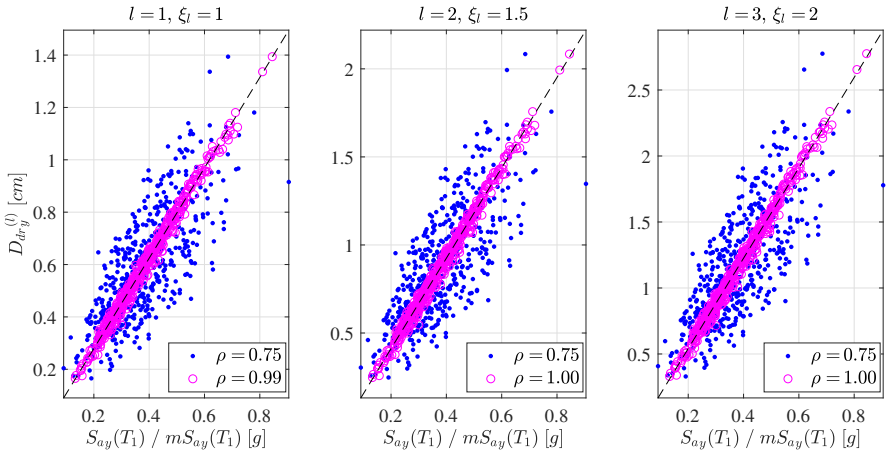

Figure B.160: Scatter plots of $n_s = 500$ samples of $(S_{ay}(T_1), D_{dry}^{(l)})$ blue dots, $(S_{ay}(T_1) + \bar{E}_y, D_{dry}^{(l)})$ magenta circles at 2nd storey: $l = 1$ with $\xi_l = 1$ (left panel); $l = 2$ with $\xi_l = 1.5$ (center panel); $l = 3$ with $\xi_l = 2$ (right panel) - nonlinear analysis.

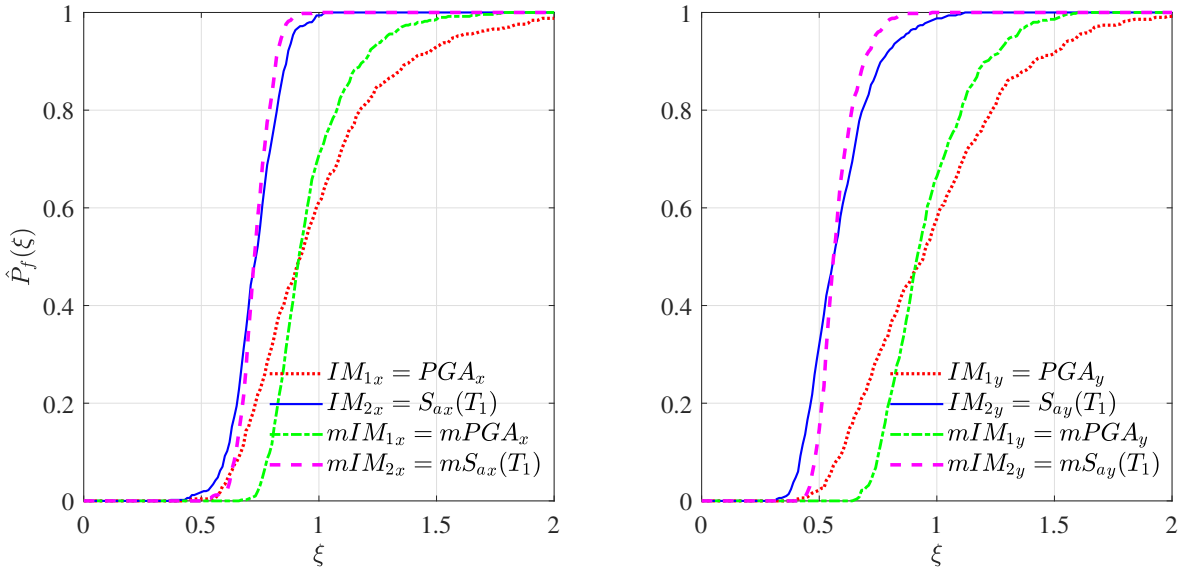

Figure B.161: Fragilities against intensity level ξ for selected definitions of IMs and their modified versions $mIMs$ (Figures 6.41 - 6.44) at node #4: demand parameter D_{dx} and limit state $\bar{D}_{dx} = 1\,cm$ (left panel); demand parameter D_{dy} and limit state $\bar{D}_{dy} = 1\,cm$ (right panel) - linear analysis.

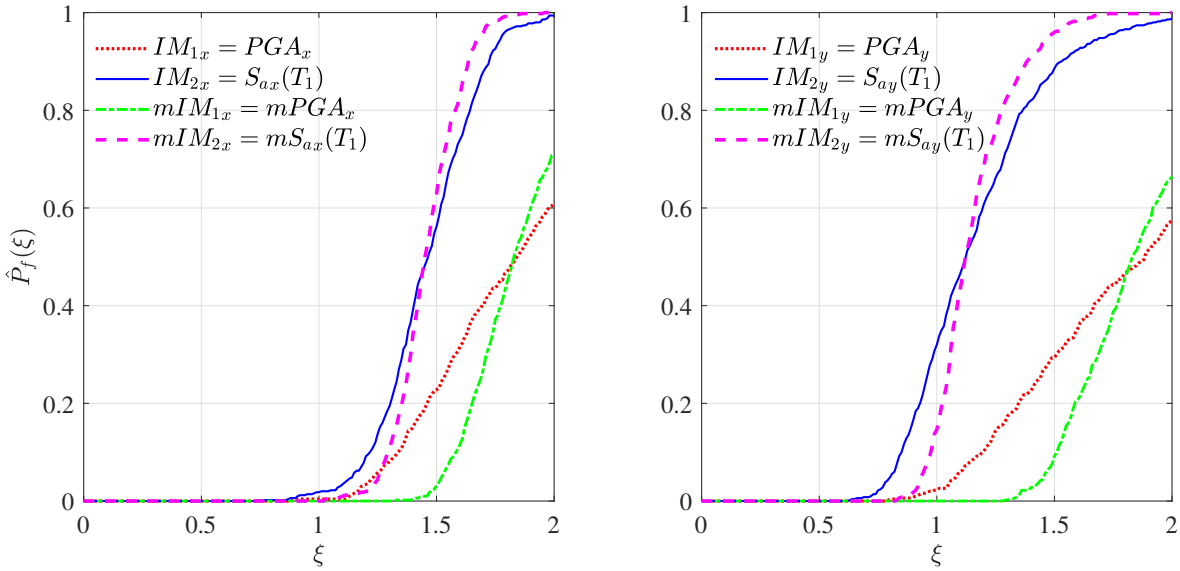

Figure B.162: Fragilities against intensity level ξ for selected definitions of IMs and their modified versions $mIMs$ (Figures 6.41 - 6.44) at node #4: demand parameter D_{dx} and limit state $\bar{D}_{dx} = 2\,cm$ (left panel); demand parameter D_{dy} and limit state $\bar{D}_{dy} = 2\,cm$ (right panel) - linear analysis.

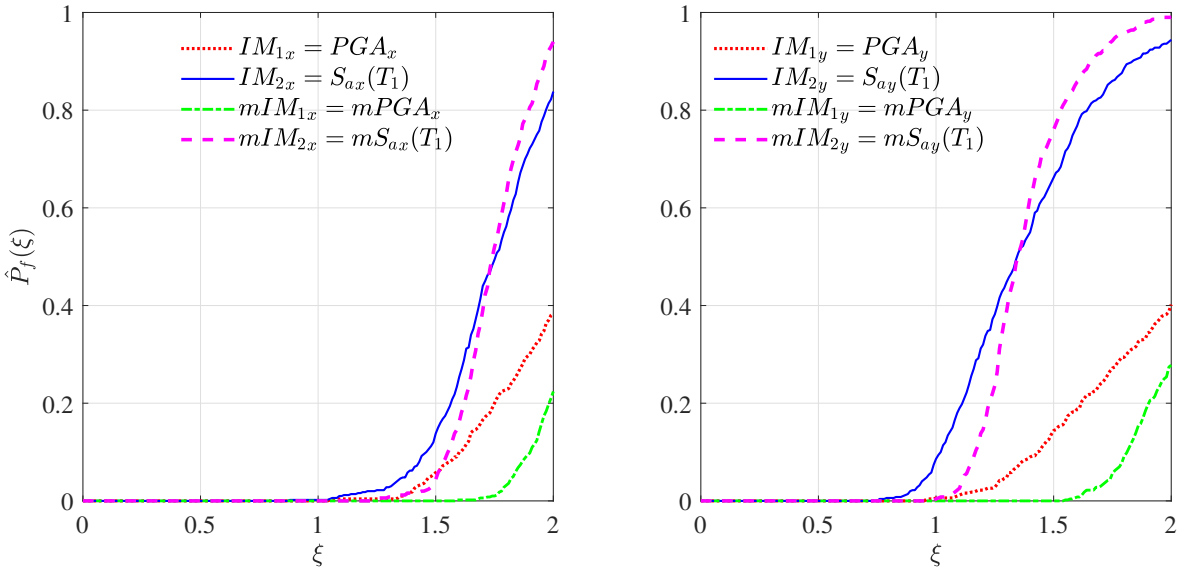

Figure B.163: Fragilities against intensity level ξ for selected definitions of IMs and their modified versions $mIMs$ (Figures 6.41 - 6.44) at node #4: demand parameter D_{dx} and limit state $\bar{D}_{dx} = 2.4\,cm$ (left panel); demand parameter D_{dy} and limit state $\bar{D}_{dy} = 2.4\,cm$ (right panel) - linear analysis.

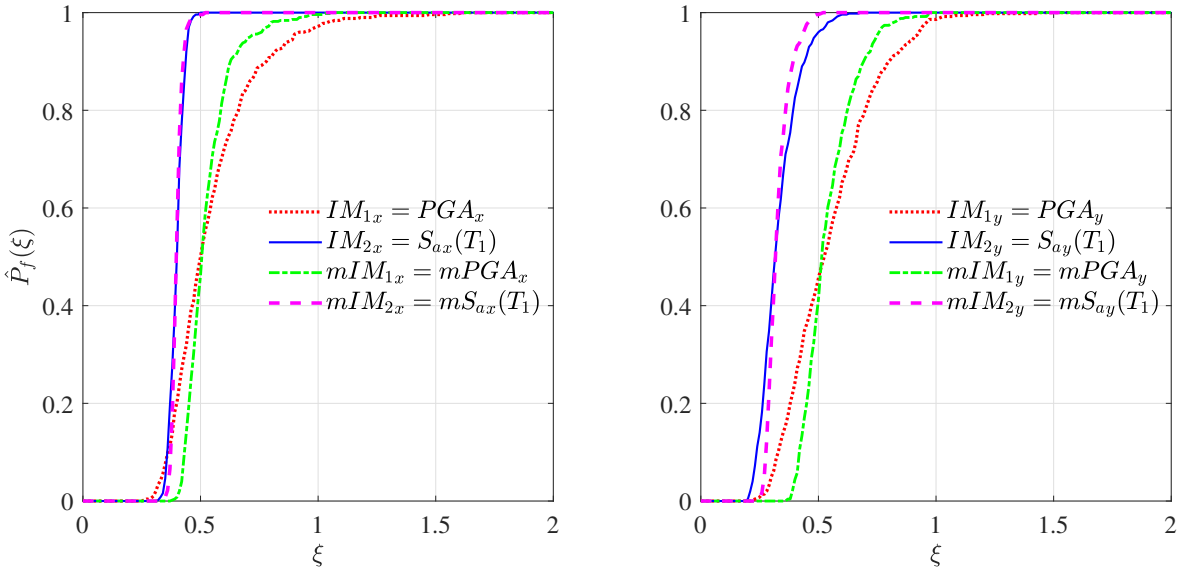

Figure B.164: Fragilities against intensity level ξ for selected definitions of IMs and their modified versions $mIMs$ (Figures 6.41 - 6.44) at node #7: demand parameter D_{dx} and limit state $\bar{D}_{dx} = 1\,cm$ (left panel); demand parameter D_{dy} and limit state $\bar{D}_{dy} = 1\,cm$ (right panel) - linear analysis.

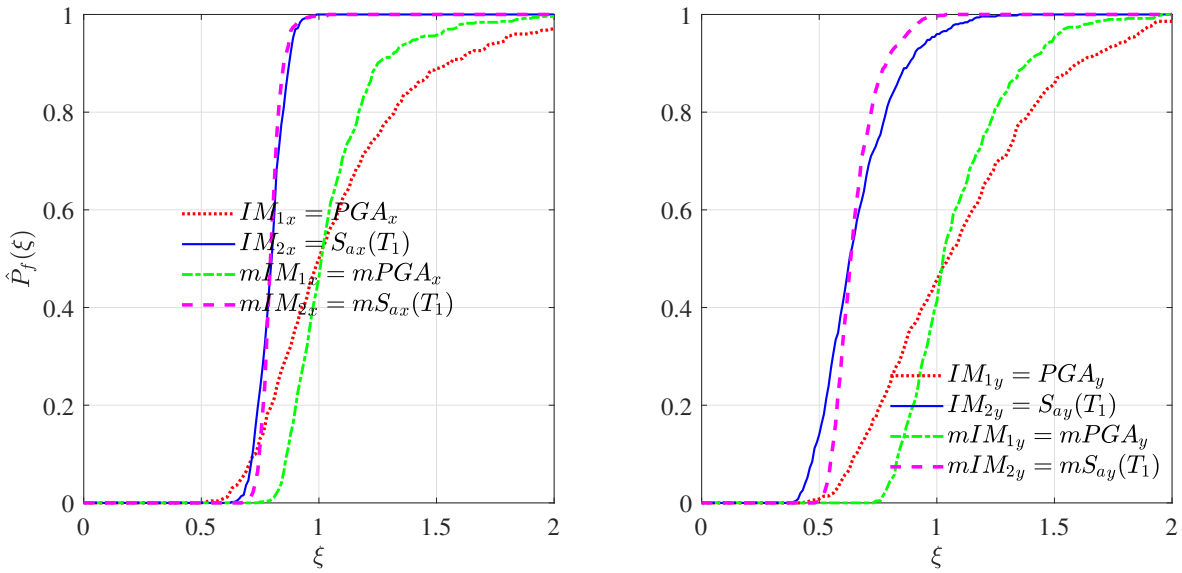

Figure B.165: Fragilities against intensity level ξ for selected definitions of IMs and their modified versions $mIMs$ (Figures 6.41 - 6.44) at node #7: demand parameter D_{dx} and limit state $\bar{D}_{dx} = 2\,cm$ (left panel); demand parameter D_{dy} and limit state $\bar{D}_{dy} = 2\,cm$ (right panel) - linear analysis.

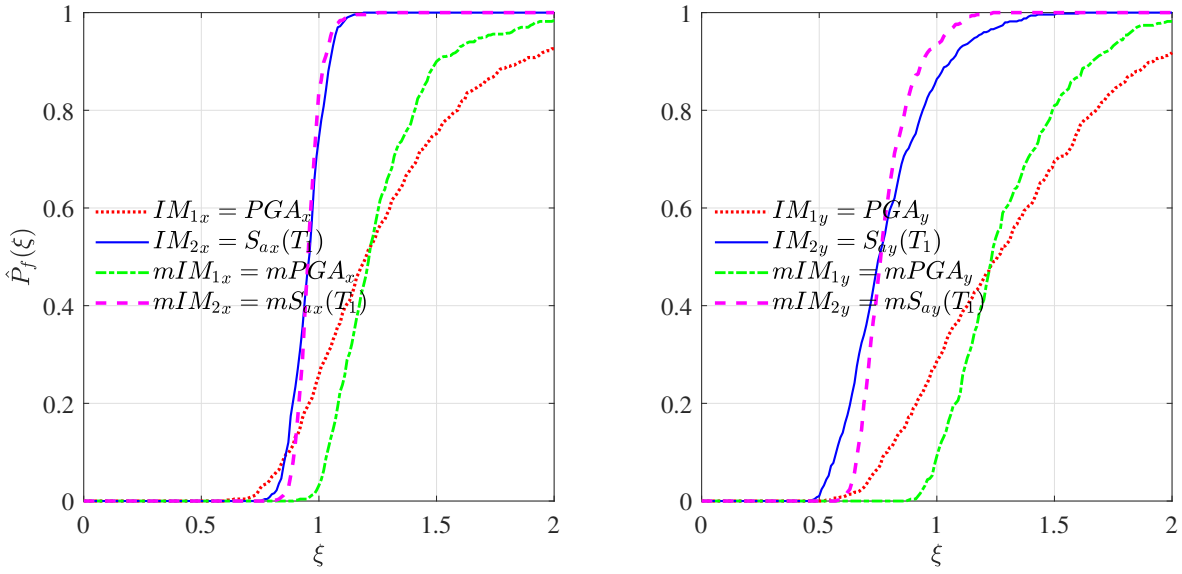

Figure B.166: Fragilities against intensity level ξ for selected definitions of IMs and their modified versions $mIMs$ (Figures 6.41 - 6.44) at node #7: demand parameter D_{dx} and limit state $\bar{D}_{dx} = 2.4\,cm$ (left panel); demand parameter D_{dy} and limit state $\bar{D}_{dy} = 2.4\,cm$ (right panel) - linear analysis.

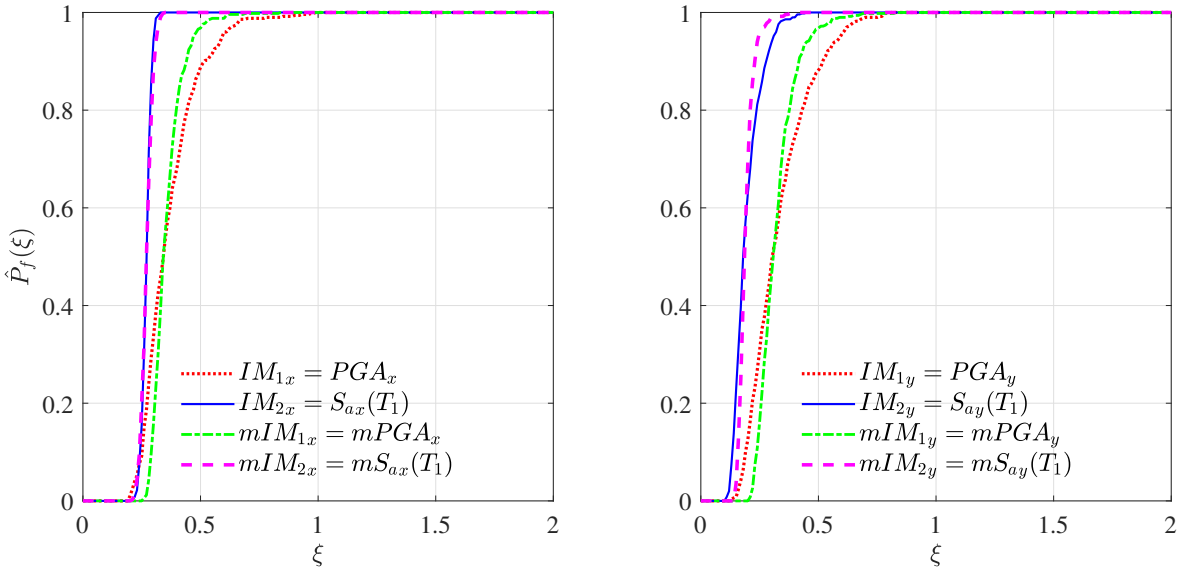

Figure B.167: Fragilities against intensity level ξ for selected definitions of IMs and their modified versions $mIMs$ (Figures 6.41 - 6.44) at node #10: demand parameter D_{dx} and limit state $\bar{D}_{dx} = 1\,cm$ (left panel); demand parameter D_{dy} and limit state $\bar{D}_{dy} = 1\,cm$ (right panel) - linear analysis.

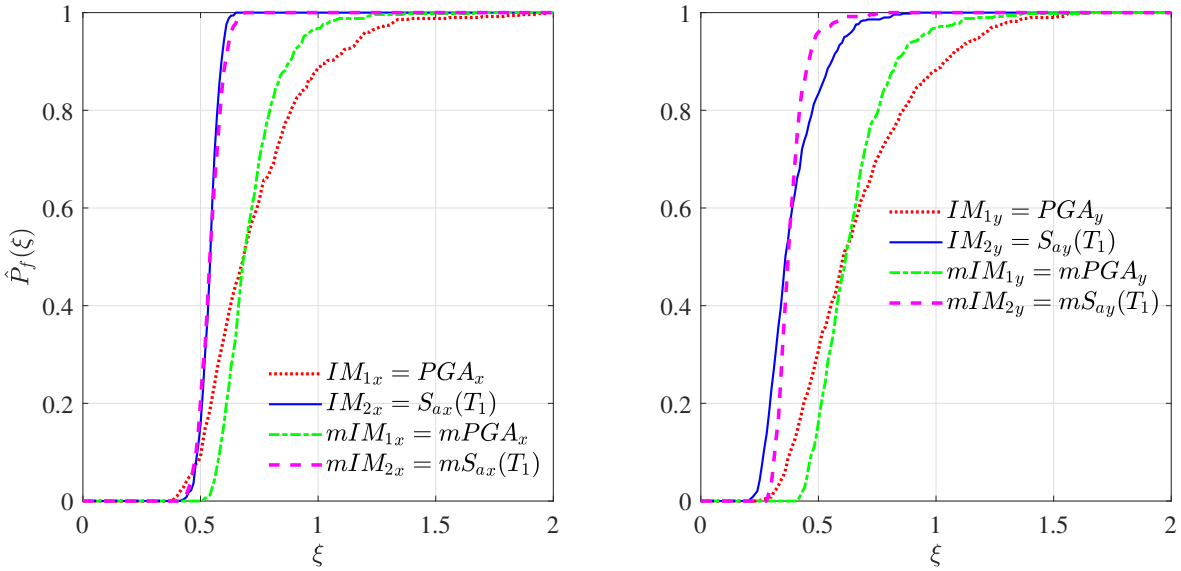

Figure B.168: Fragilities against intensity level ξ for selected definitions of IMs and their modified versions $mIMs$ (Figures 6.41 - 6.44) at node #10: demand parameter D_{dx} and limit state $\bar{D}_{dx} = 2\,cm$ (left panel); demand parameter D_{dy} and limit state $\bar{D}_{dy} = 2\,cm$ (right panel) - linear analysis.

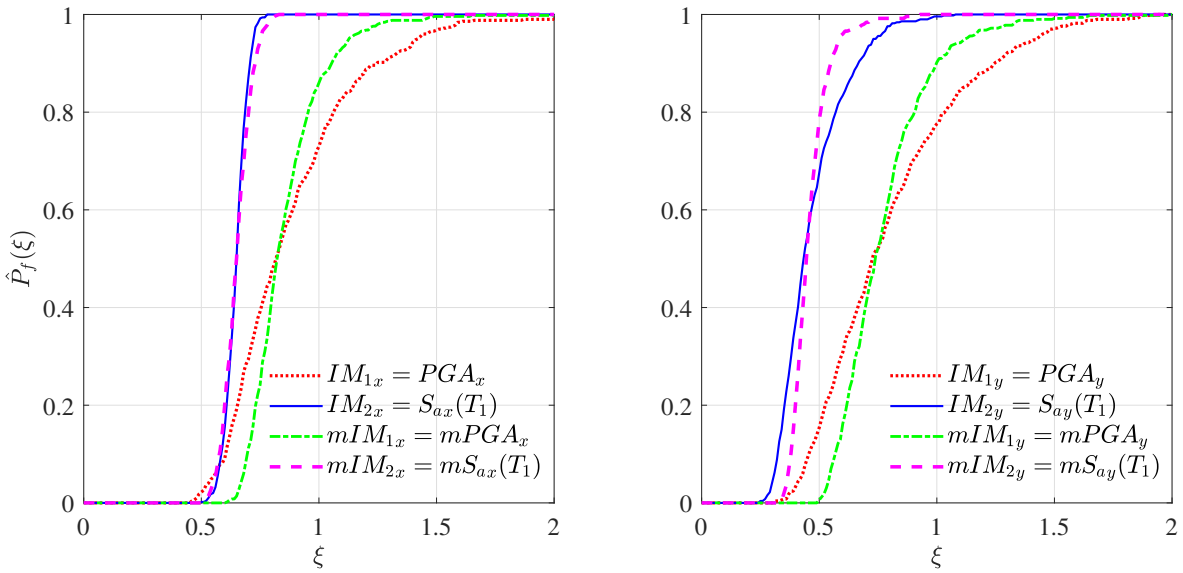

Figure B.169: Fragilities against intensity level ξ for selected definitions of IMs and their modified versions $mIMs$ (Figures 6.41 - 6.44) at node #10: demand parameter D_{dx} and limit state $\bar{D}_{dx} = 2.4\,cm$ (left panel); demand parameter D_{dy} and limit state $\bar{D}_{dy} = 2.4\,cm$ (right panel) - linear analysis.

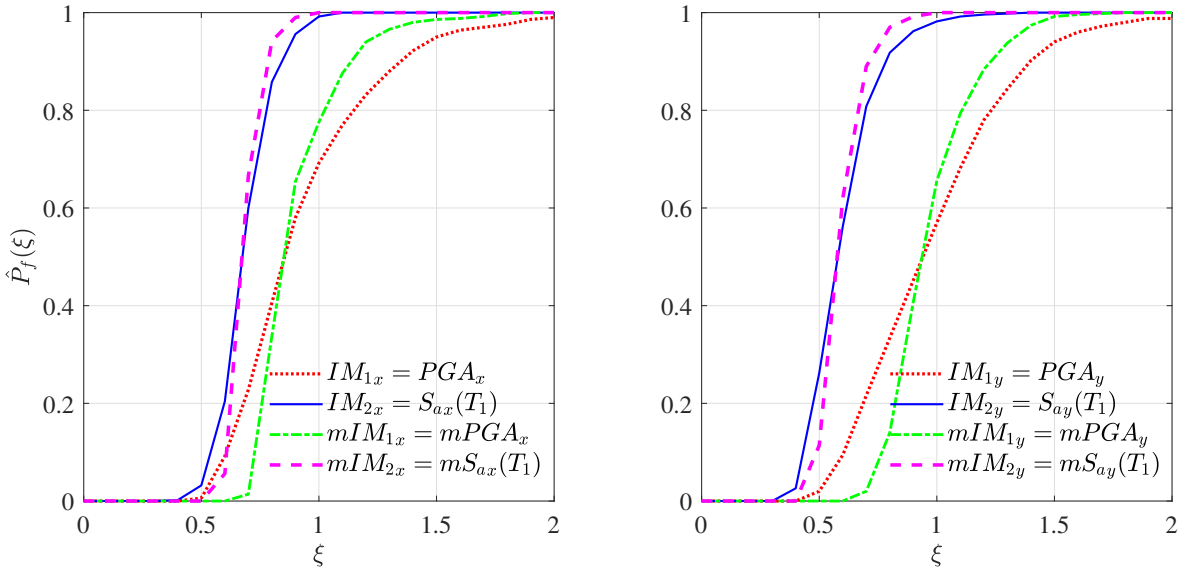

Figure B.170: Fragilities against intensity level ξ for selected definitions of IMs and their modified versions $mIMs$ (Figures 6.77 - 6.80) at node #4: demand parameter D_{dx} and limit state $\bar{D}_{dx} = 1\,cm$ (left panel); demand parameter D_{dy} and limit state $\bar{D}_{dy} = 1\,cm$ (right panel) - nonlinear analysis.

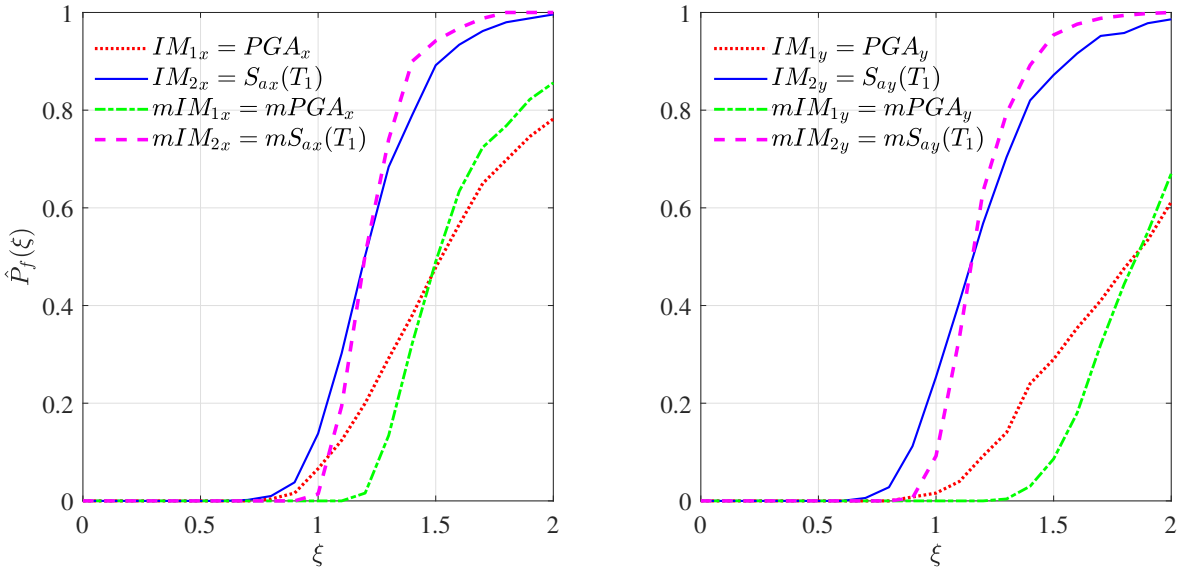

Figure B.171: Fragilities against intensity level ξ for selected definitions of IMs and their modified versions $mIMs$ (Figures 6.77 - 6.80) at node #4: demand parameter D_{dx} and limit state $\bar{D}_{dx} = 2\,cm$ (left panel); demand parameter D_{dy} and limit state $\bar{D}_{dy} = 2\,cm$ (right panel) - nonlinear analysis.

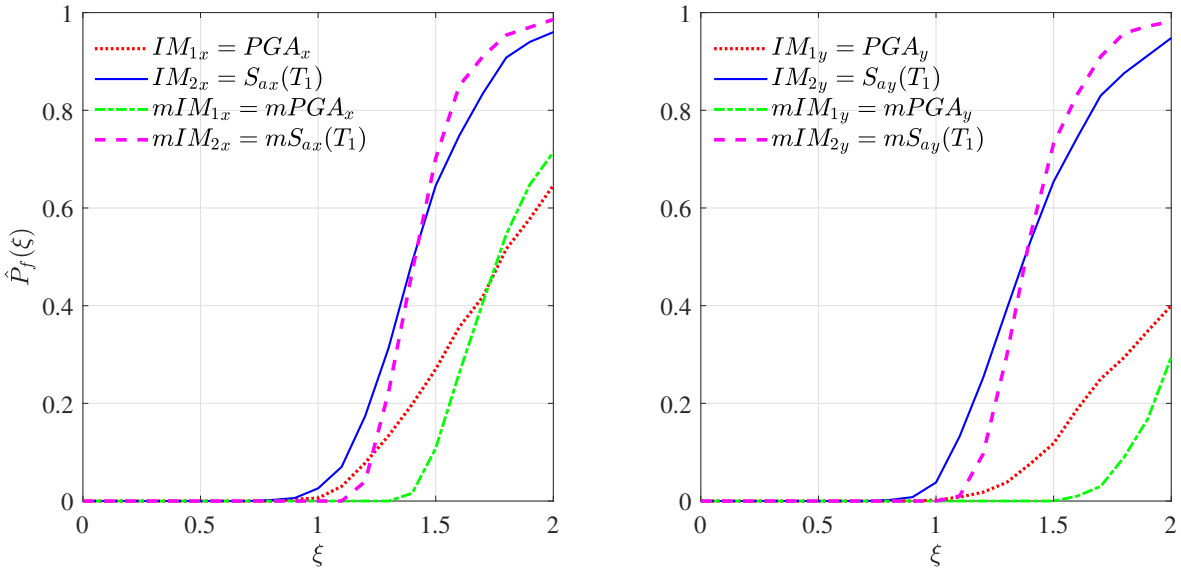

Figure B.172: Fragilities against intensity level ξ for selected definitions of IMs and their modified versions $mIMs$ (Figures 6.77 - 6.80) at node #4: demand parameter D_{dx} and limit state $\bar{D}_{dx} = 2.4\,cm$ (left panel); demand parameter D_{dy} and limit state $\bar{D}_{dy} = 2.4\,cm$ (right panel) - nonlinear analysis.

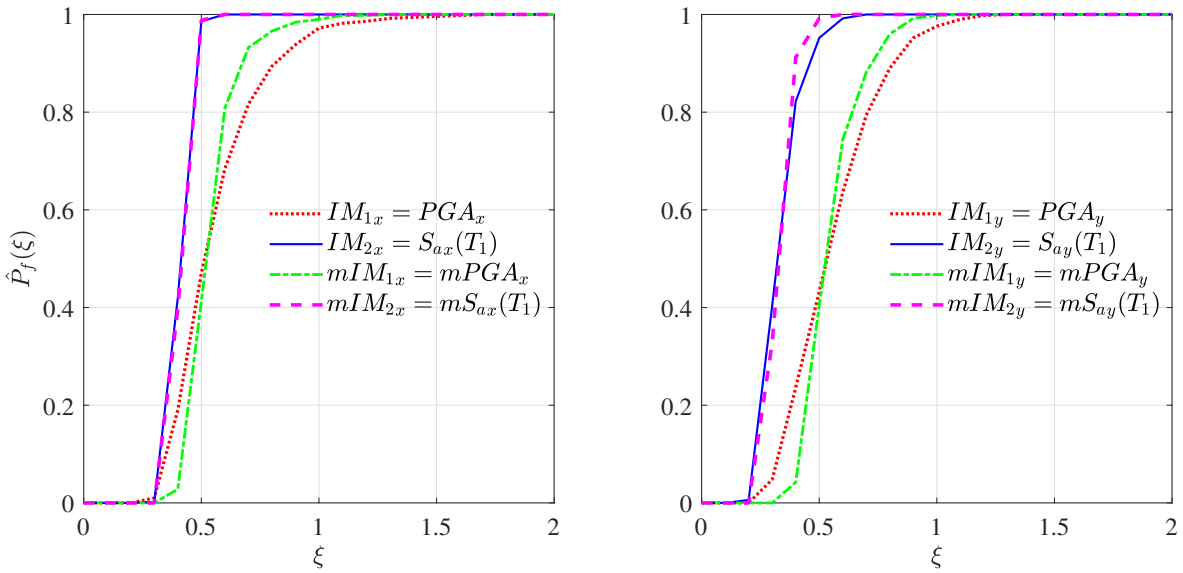

Figure B.173: Fragilities against intensity level ξ for selected definitions of IMs and their modified versions $mIMs$ (Figures 6.77 - 6.80) at node #7: demand parameter D_{dx} and limit state $\bar{D}_{dx} = 1\,cm$ (left panel); demand parameter D_{dy} and limit state $\bar{D}_{dy} = 1\,cm$ (right panel) - nonlinear analysis.

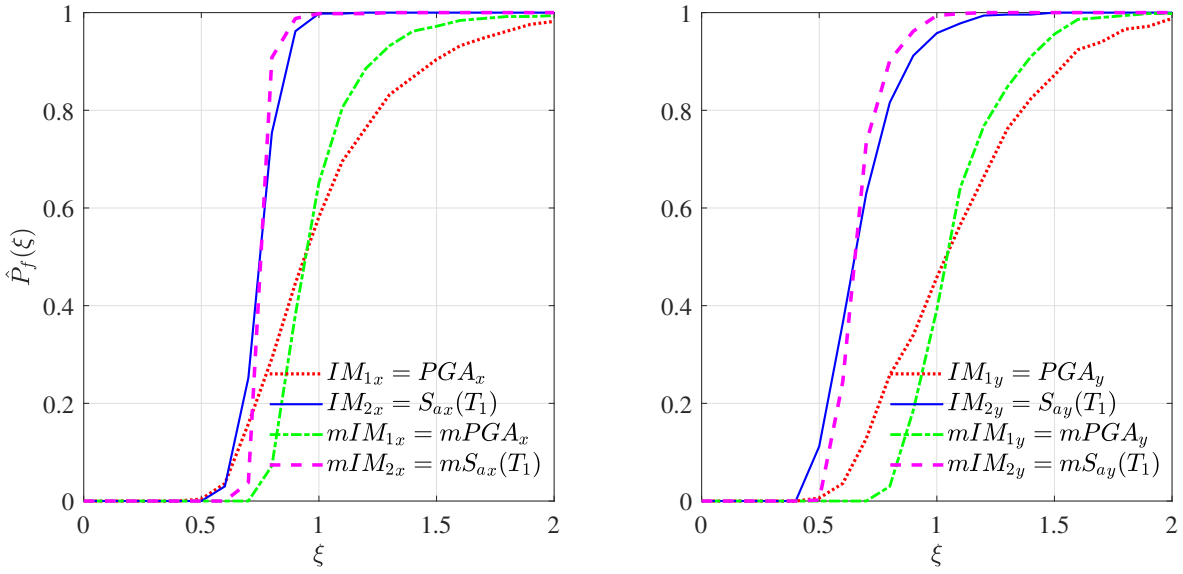

Figure B.174: Fragilities against intensity level ξ for selected definitions of IMs and their modified versions $mIMs$ (Figures 6.77 - 6.80) at node #7: demand parameter D_{dx} and limit state $\bar{D}_{dx} = 2\,cm$ (left panel); demand parameter D_{dy} and limit state $\bar{D}_{dy} = 2\,cm$ (right panel) - nonlinear analysis.

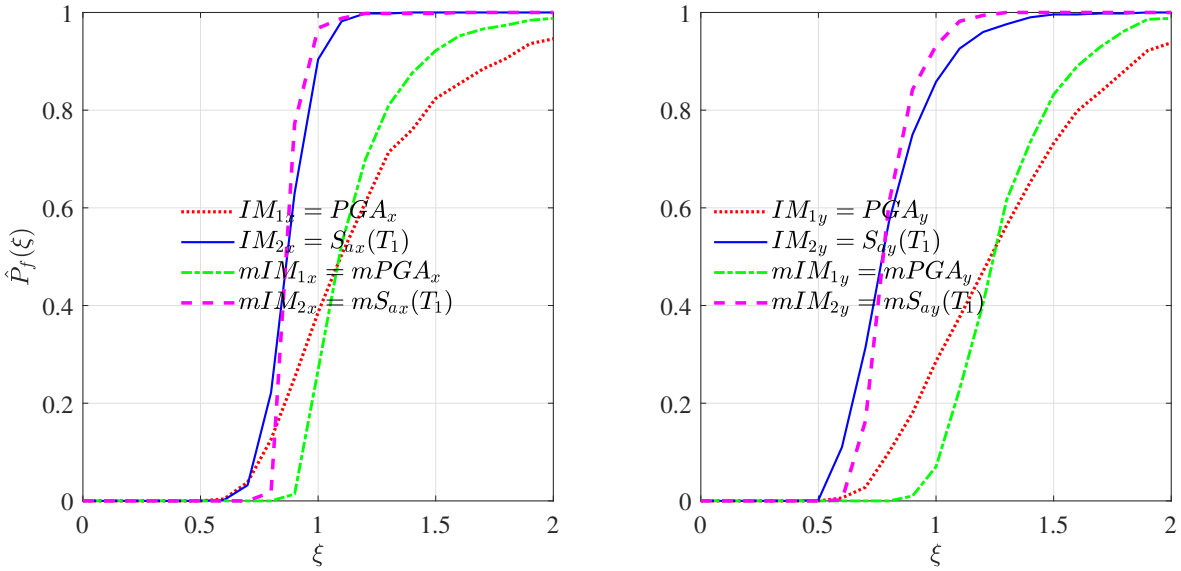

Figure B.175: Fragilities against intensity level ξ for selected definitions of IMs and their modified versions $mIMs$ (Figures 6.77 - 6.80) at node #7: demand parameter D_{dx} and limit state $\bar{D}_{dx} = 2.4\,cm$ (left panel); demand parameter D_{dy} and limit state $\bar{D}_{dy} = 2.4\,cm$ (right panel) - nonlinear analysis.

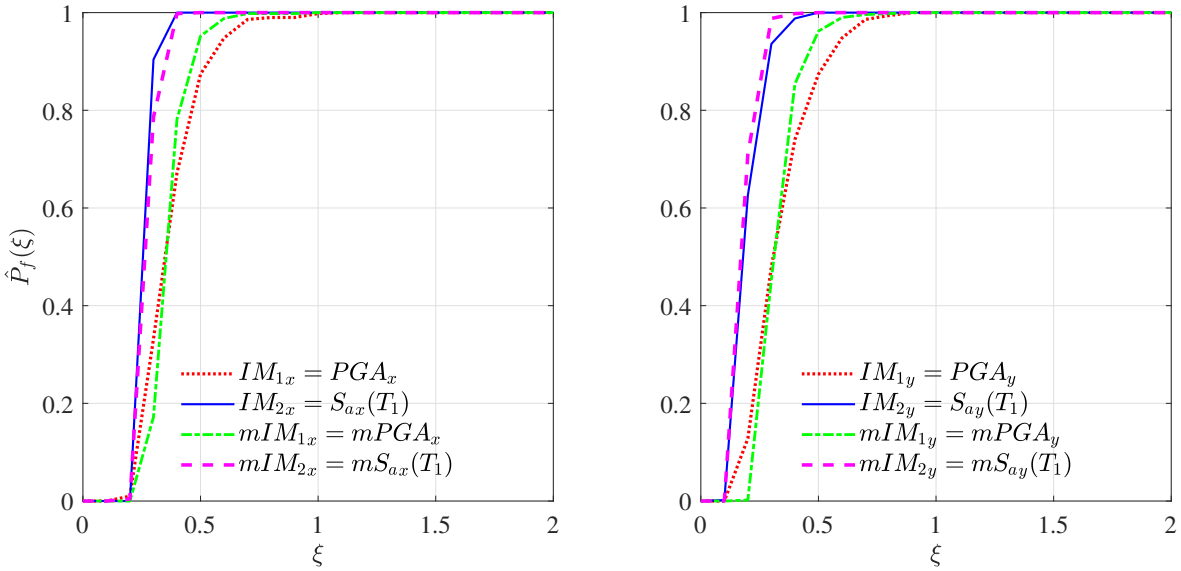

Figure B.176: Fragilities against intensity level ξ for selected definitions of IMs and their modified versions $mIMs$ (Figures 6.77 - 6.80) at node #10: demand parameter D_{dx} and limit state $\bar{D}_{dx} = 1\,cm$ (left panel); demand parameter D_{dy} and limit state $\bar{D}_{dy} = 1\,cm$ (right panel) - nonlinear analysis.

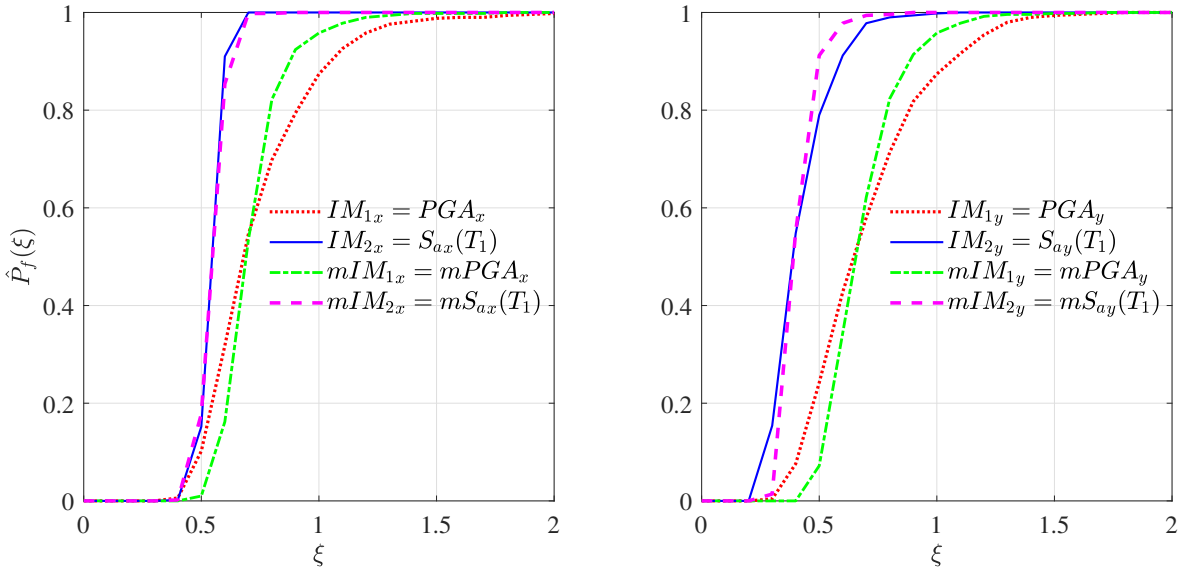

Figure B.177: Fragilities against intensity level ξ for selected definitions of IMs and their modified versions $mIMs$ (Figures 6.77 - 6.80) at node #10: demand parameter D_{dx} and limit state $\bar{D}_{dx} = 2\,cm$ (left panel); demand parameter D_{dy} and limit state $\bar{D}_{dy} = 2\,cm$ (right panel) - nonlinear analysis.

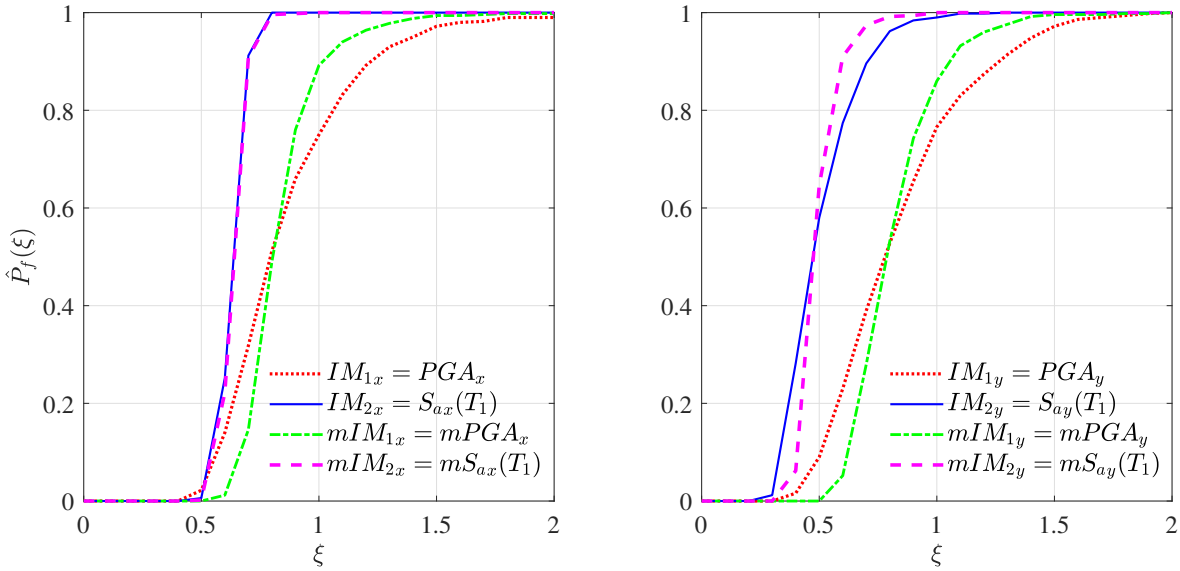

Figure B.178: Fragilities against intensity level ξ for selected definitions of IMs and their modified versions $mIMs$ (Figures 6.77 - 6.80) at node #10: demand parameter D_{dx} and limit state $\bar{D}_{dx} = 2.4\,cm$ (left panel); demand parameter D_{dy} and limit state $\bar{D}_{dy} = 2.4\,cm$ (right panel) - nonlinear analysis.

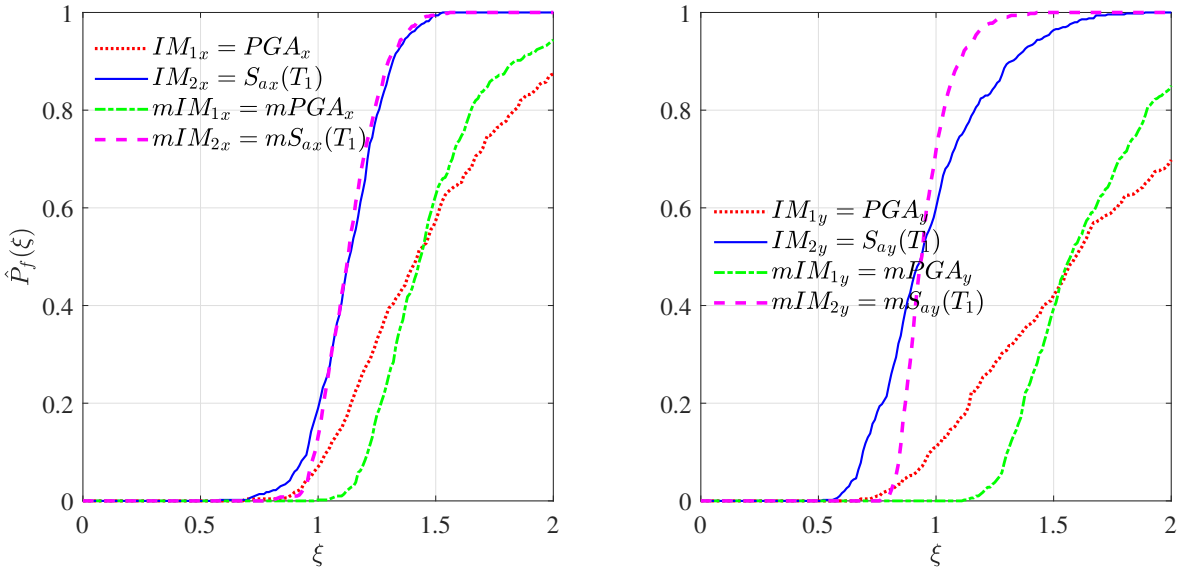

Figure B.179: Fragilities against intensity level ξ for selected definitions of IMs and their modified versions $mIMs$ (Figures 6.53 - 6.56) at node 1st storey: demand parameter D_{drx} and limit state $\bar{D}_{drx} = 1.5\,cm$ (left panel); demand parameter D_{dry} and limit state $\bar{D}_{dry} = 1.5\,cm$ (right panel) - linear analysis.

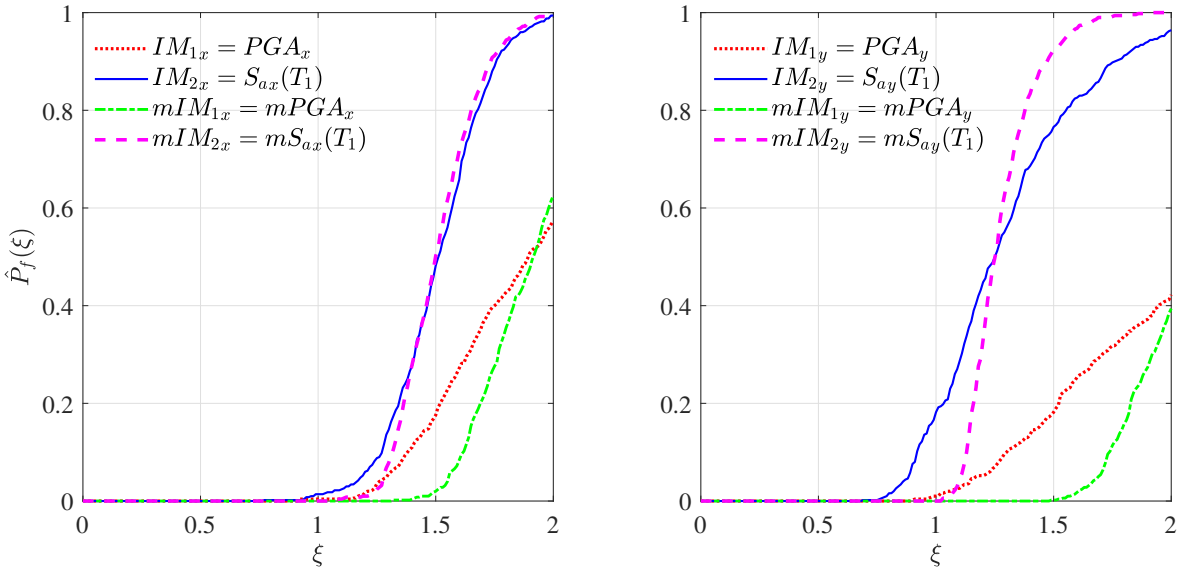

Figure B.180: Fragilities against intensity level ξ for selected definitions of IMs and their modified versions $mIMs$ (Figures 6.53 - 6.56) at node 1st storey: demand parameter D_{drx} and limit state $\bar{D}_{drx} = 2\,cm$ (left panel); demand parameter D_{dry} and limit state $\bar{D}_{dry} = 2\,cm$ (right panel) - linear analysis.

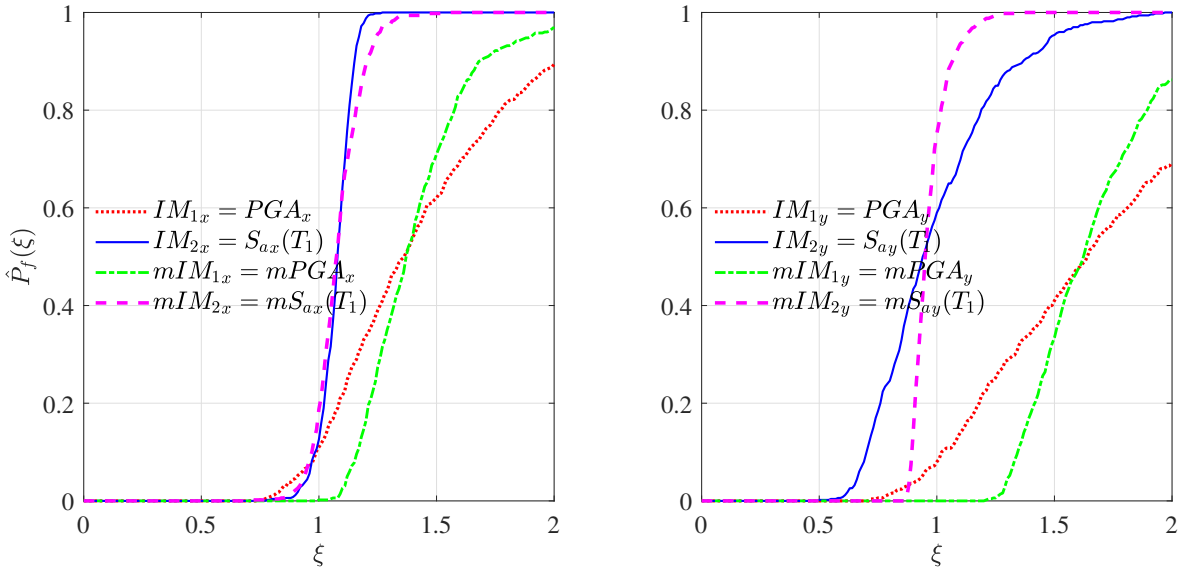

Figure B.181: Fragilities against intensity level ξ for selected definitions of IMs and their modified versions $mIMs$ (Figures 6.53 - 6.56) at node 2nd storey: demand parameter D_{drx} and limit state $\bar{D}_{drx} = 1.5\,cm$ (left panel); demand parameter D_{dry} and limit state $\bar{D}_{dry} = 1.5\,cm$ (right panel) - linear analysis.

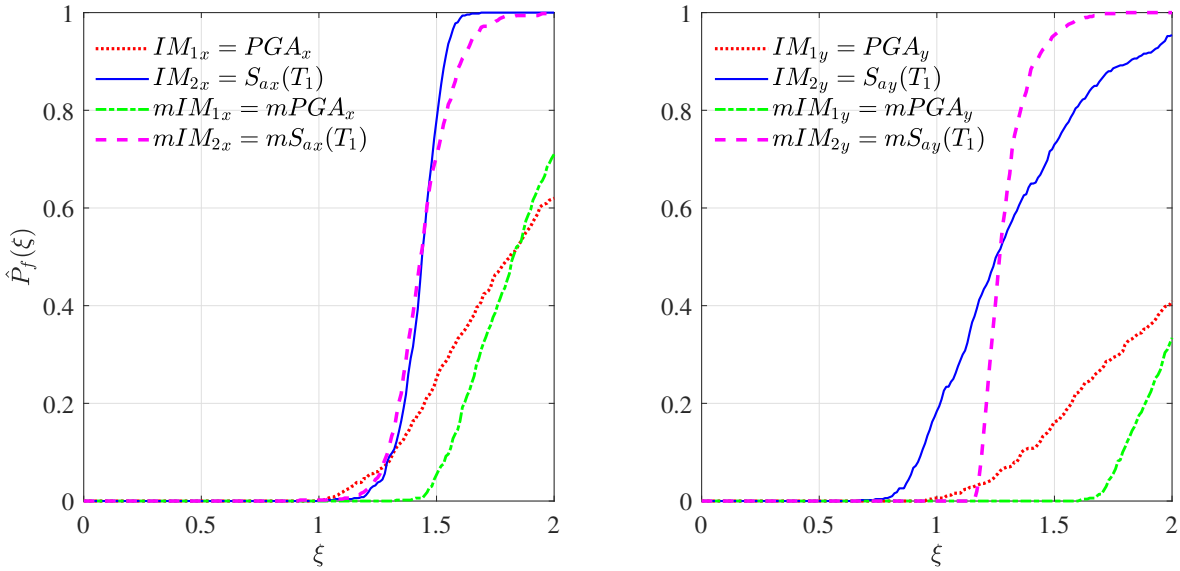

Figure B.182: Fragilities against intensity level ξ for selected definitions of IMs and their modified versions $mIMs$ (Figures 6.53 - 6.56) at node 2nd storey: demand parameter D_{drx} and limit state $\bar{D}_{drx} = 2\,cm$ (left panel); demand parameter D_{dry} and limit state $\bar{D}_{dry} = 2\,cm$ (right panel) - linear analysis.

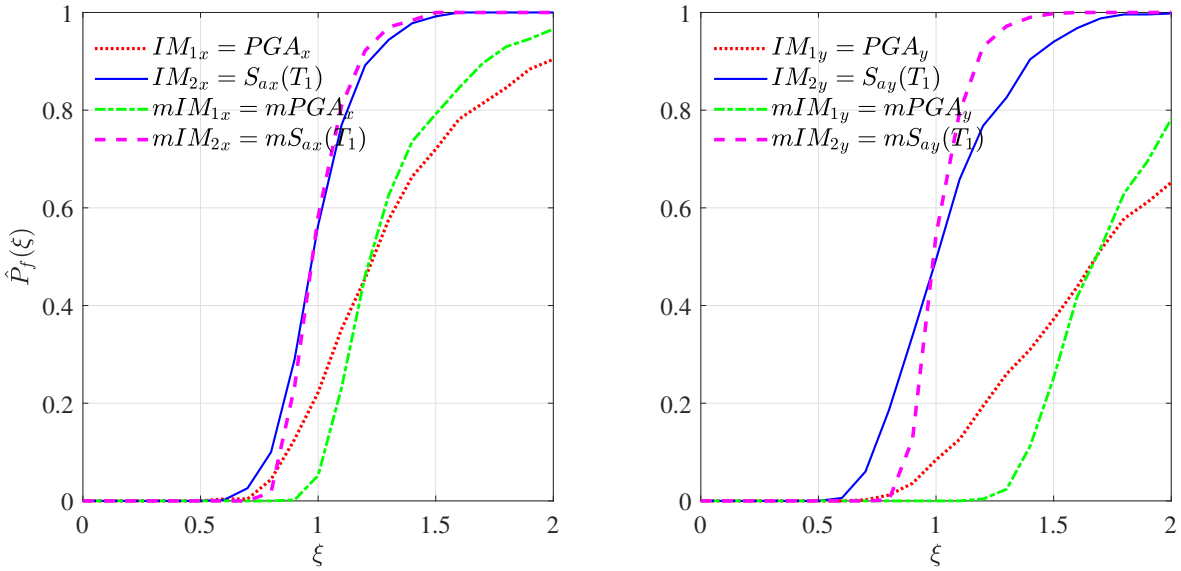

Figure B.183: Fragilities against intensity level ξ for selected definitions of IMs and their modified versions $mIMs$ (Figures 6.101 - 6.104) at node 1st storey: demand parameter D_{drx} and limit state $\bar{D}_{drx} = 1.5\,cm$ (left panel); demand parameter D_{dry} and limit state $\bar{D}_{dry} = 1.5\,cm$ (right panel) - nonlinear analysis.

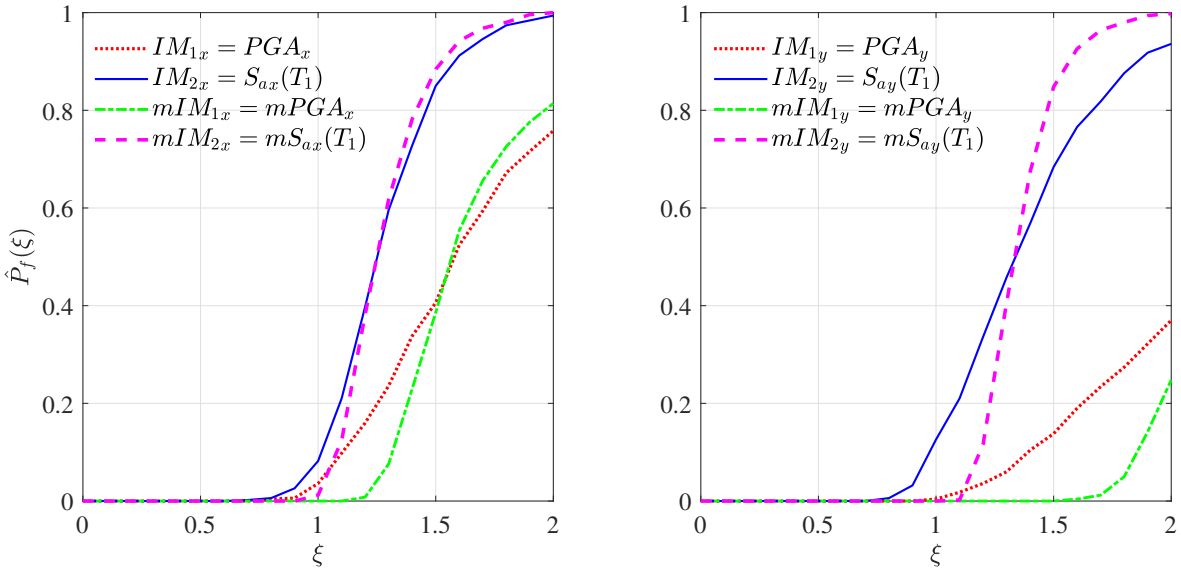

Figure B.184: Fragilities against intensity level ξ for selected definitions of IMs and their modified versions $mIMs$ (Figures 6.101 - 6.104) at node 1st storey: demand parameter D_{drx} and limit state $\bar{D}_{drx} = 2\,cm$ (left panel); demand parameter D_{dry} and limit state $\bar{D}_{dry} = 2\,cm$ (right panel) - nonlinear analysis.

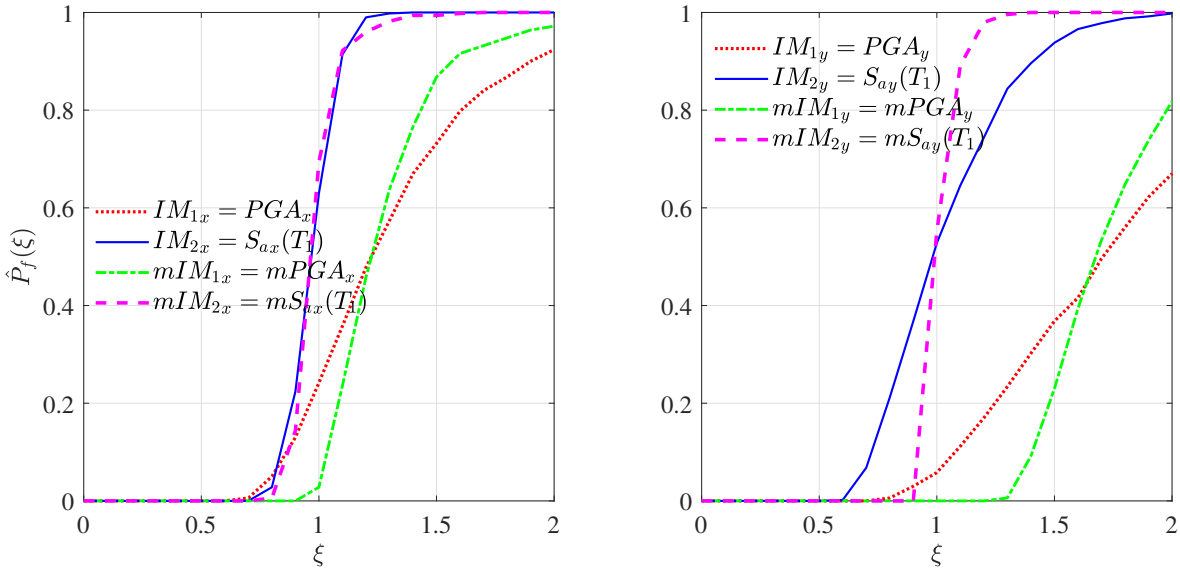

Figure B.185: Fragilities against intensity level ξ for selected definitions of IMs and their modified versions $mIMs$ (Figures 6.101 - 6.104) at node 2nd storey: demand parameter D_{drx} and limit state $\bar{D}_{drx} = 1.5\,cm$ (left panel); demand parameter D_{dry} and limit state $\bar{D}_{dry} = 1.5\,cm$ (right panel) - nonlinear analysis.

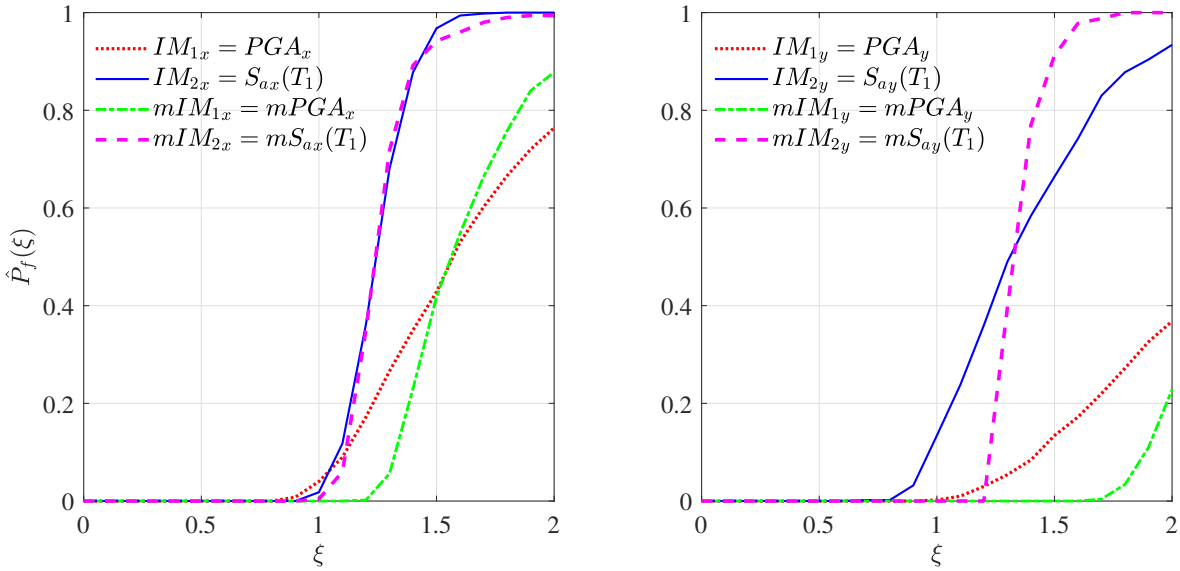

Figure B.186: Fragilities against intensity level ξ for selected definitions of IMs and their modified versions $mIMs$ (Figures 6.101 - 6.104) at node 2nd storey: demand parameter D_{drx} and limit state $\bar{D}_{drx} = 2\,cm$ (left panel); demand parameter D_{dry} and limit state $\bar{D}_{dry} = 2\,cm$ (right panel) - nonlinear analysis.

Bibliography

[1] E. Hauksson, L. M. Jones, and K. Hutton. The 1994 northridge earthquake sequence in california: Seismological and tectonic aspects. *Journal of Geophysical Research: Solid Earth*, 100(B7):12335–12355, 1995.

[2] V. V. Bertero, R. D. Borcherdt, P. W. Clark, D. S. Dreger, F. C. Filippou, D. A. Foutch, L. S. Gee, M. Higashino, S. Kono, L.-W. Lu, et al. Seismological and engineering aspects of the 1995 hyogoken-nanbu (kobe) earthquake. Technical report, Report UCB/EERC-95/10, Earthquake Engineering Research Center, University of University of California, Berkeley, 1995.

[3] SEAOC. Vision 2000, performance based seismic engineering of buildings. conceptual framework. *Structural Engineers Association of California (SEAOC), Sacramento (CA), vols I and II*, 1995.

[4] ATC. Seismic evaluation and retrofit of existing concrete buildings. *Applied Technology Council (ATC), Redwood City, CA, ATC-40*, 1996.

[5] FEMA. NEHRP guidelines for the seismic rehabilitation of buildings, FEMA -273. *Federal Emergency Management Agency (FEMA), Washnigton DC*, 1996.

[6] FEMA. Prestandard and commentary for the seismic rehabilitation of buildings, FEMA-356. *Federal Emergency Management Agency (FEMA), Washnigton DC*, 2000.

[7] ASCE. Seismic evaluation and retrofit of existing buildings, ASCE 41-13. *American Society of Civil Engineers (ASCE), Reston, Virginia, US*, 2013.

[8] J. Moehle and G. G. Deierlein. A framework methodology for performance-based earthquake engineering. In *13th world conference on earthquake engineering*, volume 679, 2004.

[9] M. Fisz. Probability theory and mathematical statistics. Technical report, 1963.

[10] FEMA. Seismic performance assessment of buildings: Vol. 1–methodology. *Applied Technology Council for the Federal Emergency Management Agency, CA, USA*, 2012.

[11] R. Kennedy, C. Cornell, R. Campbell, S. Kaplan, and H. Perla. Probabilistic seismic safety study of an existing nuclear power plant. *Nuclear Engineering and Design*, 59(2):315 – 338, 1980.

[12] R. Kennedy and M. Ravindra. Seismic fragilities for nuclear power plant risk studies. *Nuclear Engineering and Design*, 79(1):47 – 68, 1984.

[13] R. E. Melchers. *Structural reliability analysis and prediction.* Ellis Horwood, Ltd., Chichester, England, 1987.

[14] N. Luco and C. A. Cornell. Structure-specific scalar intensity measures for near-source and ordinary earthquake ground motions. *Earthquake Spectra*, 23(2):357–392, 2007.

[15] M. Grigoriu. Do seismic intensity measures (IMs) measure up? *Probabilistic Engineering Mechanics*, 46:80 – 93, 2016.

[16] A. Papoulis. *Probability, random variables, and stochastic processes.* McGraw-Hill, New York, 1965.

[17] Y.-K. Lin. *Probabilistic theory of structural dynamics.* McGraw-Hill, New York, 1976.

[18] A. K. Chopra. *Dynamic of Structures. Theory and Application to Earthquake Engineering.* 2012.

[19] N. M. Newmark. A method of computation for structural dynamics. *Journal of the engineering mechanics division*, 85(3):67–94, 1959.

[20] H. Krawinkler. *Inelastic behavior of steel beam-to-column subassemblages*, volume 71. University of California, Berkeley, 1971.

[21] S. Y. M. Ma, V. V. Bertero, and E. P. Popov. *Experimental and analytical studies on the hysteretic behavior of reinforced concrete rectangular and T-beams.* Earthquake Engineering Research Center, College of Engineering, University of California, Berkeley, 1976.

[22] G. Duffing. *Erzwungene schwingungen bei veränderlicher eigenfrequenz*, volume 7. 1918.

[23] G. Dahlquist and A. Bjorck. *Numerical Methods (transl. by N. Anderson).* Prentice-Hall, Englewood Cliffs, NJ, 1974.

[24] R. Bouc. Forced vibrations of mechanical systems with hysteresis. In *Proc. of the Fourth Conference on Nonlinear Oscillations, Prague, 1967*, 1967.

[25] Y.-K. Wen. Method for random vibration of hysteretic systems. *Journal of the engineering mechanics division*, 102(2):249–263, 1976.

[26] Y. Wen. Equivalent linearization for hysteretic systems under random excitation. 1980.

[27] T. T. Baber and Y.-K. Wen. Stochastic equivalent linearization for hysteretic,

degrading, multistory strutctures. Technical report, College of Engineering, University of Illinois at Urbana-Champaign, 1980.

[28] T. J. Hughes. *The finite element method: linear static and dynamic finite element analysis*. Courier Corporation, 2012.

[29] R. W. Clough and Y. PENZIEN. *Dynamique des structures*. 1975.

[30] E. L. Wilson. Three-dimensional static and dynamic analysis of structures. *Computers and structures*, 2002.

[31] P. Cacciola. A stochastic approach for generating spectrum compatible fully nonstationary earthquakes. *Computers & Structures*, 88(15):889 – 901, 2010.

[32] M. Shinozuka and C.-M. Jan. Digital simulation of random processes and its applications. *Journal of sound and vibration*, 25(1):111–128, 1972.

[33] E. Vanmarcke and D. Gasparini. Simulated earthquake ground motions. In *Structural mechanics in reactor technology*. 1977.

[34] M. Grigoriu, S. E. Ruiz, and E. Rosenblueth. The mexico earthquake of september 19, 1985 — nonstationary models of seismic ground acceleration. *Earthquake Spectra*, 4(3):551–568, 1988.

[35] M. Grigoriu. *Stochastic Calculus: Applications in Science and Engineering*. Springer Science & Business Media, 2002.

[36] N. M. Newmark. Design criteria for nuclear reactors subjected to earthquake hazards. *Proc. IAEA panel on aseismic design and*, 1967.

[37] C. A. Cornell. Engineering seismic risk analysis. *Bulletin of the seismological society of America*, 58(5):1583–1606, 1968.

[38] N. M. Newmark. Current trends in the seismic analysis and design of high-rise structures. pages 787–808, 1970.

[39] K. A. Porter. An overview of peer's performance-based earthquake engineering methodology. In *Proceedings of ninth international conference on applications of statistics and probability in civil engineering*, 2003.

[40] D. T. Gillespie. *Markov processes: an introduction for physical scientists*. Elsevier, 1991.

[41] J. J. Hwang H.M. Seismic fragility analysis of frame structures. *Technical Report, NCEER-88-00009 state University of New York at Buffalo*, 1988.

[42] M. Shinozuka, M. Q. Feng, J. Lee, and T. Naganuma. Statistical analysis of fragility curves. *Journal of engineering mechanics*, 126(12):1224–1231, 2000.

[43] J. Lin. Seismic fragility analysis of frame structures. *International Journal of Structural Stability and Dynamics*, 8(03):451–463, 2008.

[44] G. M. Calvi, R. Pinho, G. Magenes, J. J. Bommer, L. F. Restrepo-Vélez, and H. Crowley. Development of seismic vulnerability assessment methodologies over the past 30 years. *ISET journal of Earthquake Technology*, 43(3):75–104, 2006.

[45] K. Pitilakis, H. Crowley, and A. M. Kaynia. Syner-g: typology definition and fragility functions for physical elements at seismic risk. *Geotechnical, Geological and Earthquake Engineering*, 27, 2014.

[46] K. Porter. A beginner's guide to fragility, vulnerability, and risk. *Encyclopedia of earthquake engineering*, 2015:235–260, 2015.

[47] O. Kustu, D. D. Miller, and S. T. Brokken. Development of damage functions for high-rise building components. Technical report, URS/John A. Blume and Associates, 1982.

[48] F. Sabetta, A. Goretti, and A. Lucantoni. Empirical fragility curves from damage surveys and estimated strong ground motion. In *Proceedings of the 11th European conference on earthquake engineering, Paris, France*, pages 1–11, 1998.

[49] A. Muntasir Billah and M. Shahria Alam. Seismic fragility assessment of highway bridges: a state-of-the-art review. *Structure and Infrastructure Engineering*, 11(6):804–832, 2015.

[50] B. G. Nielson and R. DesRoches. Analytical seismic fragility curves for typical bridges in the central and southeastern united states. *Earthquake Spectra*, 23(3):615–633, 2007.

[51] M. Rota, A. Penna, and G. Magenes. A methodology for deriving analytical fragility curves for masonry buildings based on stochastic nonlinear analyses. *Engineering Structures*, 32(5):1312–1323, 2010.

[52] ATC. *Earthquake damage evaluation data for California.* Applied Technology Council (ATC), 1985.

[53] A. J. Kappos, G. Panagopoulos, C. Panagiotopoulos, and G. Penelis. A hybrid method for the vulnerability assessment of r/c and urm buildings. *Bulletin of Earthquake Engineering*, 4(4):391–413, 2006.

[54] V. Kammula, J. Erochko, O.-S. Kwon, and C. Christopoulos. Application of hybrid-simulation to fragility assessment of the telescoping self-centering energy dissipative bracing system. *Earthquake Engineering & Structural Dynamics*, 43(6):811–830, 2014.

[55] P. Gulkan and M. A. Sozen. Procedure for determining seismic vulnerability of building structures. *Structural Journal*, 96(3):336–342, 1999.

[56] M. Yücemen, G. Özcebe, and A. Pay. Prediction of potential damage due to severe earthquakes. *Structural Safety*, 26(3):349–366, 2004.

[57] T. Rossetto and A. Elnashai. Derivation of vulnerability functions for european-type rc structures based on observational data. *Engineering structures*, 25(10):1241–1263, 2003.

[58] C. A. Kircher, A. A. Nassar, O. Kustu, and W. T. Holmes. Development of building damage functions for earthquake loss estimation. *Earthquake spectra*, 13(4):663–682, 1997.

[59] S. A. Freeman. The capacity spectrum method for determining the demand displacement. In *Proceedings of the 11th European conference on earthquake engineering, Paris*, 1998.

[60] C. A. Kircher, R. K. Reitherman, R. V. Whitman, and C. Arnold. Estimation of earthquake losses to buildings. *Earthquake spectra*, 13(4):703–720, 1997.

[61] A. Singhal and A. S. Kiremidjian. Method for probabilistic evaluation of seismic structural damage. *Journal of Structural Engineering*, 122(12):1459–1467, 1996.

[62] A. Singhal and A. S. Kiremidjian. Bayesian updating of fragilities with application to rc frames. *Journal of structural Engineering*, 124(8):922–929, 1998.

[63] K. A. Porter, A. S. Kiremidjian, and J. S. LeGrue. Assembly-based vulnerability of buildings and its use in performance evaluation. *Earthquake spectra*, 17(2):291–312, 2001.

[64] C. A. Cornell, F. Jalayer, R. O. Hamburger, and D. A. Foutch. Probabilistic basis for 2000 sac federal emergency management agency steel moment frame guidelines. *Journal of structural engineering*, 128(4):526–533, 2002.

[65] P. Bazzurro and C. Cornell. Vector-valued probabilistic seismic hazard analysis (vpsha). In *Proceedings of the 7th US national conference on earthquake engineering*, pages 21–25, 2002.

[66] C. Kafali and M. Grigoriu. Seismic fragility analysis. In *9th ASCE specialty conference on probabilistic mechanics and structural reliability*, pages 1–6, 2004.

[67] C. Kafali and M. Grigoriu. Seismic fragility analysis: Application to simple linear and nonlinear systems. *Earthquake Engineering & Structural Dynamics*, 36(13):1885–1900, 2007.

[68] J. Li, B. F. Spencer Jr, and A. S. Elnashai. Bayesian updating of fragility functions using hybrid simulation. *Journal of Structural Engineering*, 139(7):1160–1171, 2013.

[69] P. Gehl, J. Douglas, and D. M. Seyedi. Influence of the number of dynamic analyses on the accuracy of structural response estimates. *Earthquake Spectra*, 31(1):97–113, 2015.

[70] M. Hariri-Ardebili and V. Saouma. Probabilistic seismic demand model and optimal intensity measure for concrete dams. *Structural Safety*, 59:67–85, 2016.

[71] E. Bojórquez, R. Chávez, A. Reyes-Salazar, S. E. Ruiz, and J. Bojórquez. A new ground motion intensity measure ib. *Soil Dynamics and Earthquake Engineering*, 99:97–107, 2017.

[72] R. Monteiro, C. Zelaschi, A. Silva, and R. Pinho. Derivation of fragility functions for seismic assessment of rc bridge portfolios using different intensity measures. *Journal of Earthquake Engineering*, 23(10):1678–1694, 2019.

[73] D.-D. Nguyen, B. Thusa, T.-S. Han, and T.-H. Lee. Identifying significant earthquake intensity measures for evaluating seismic damage and fragility of nuclear power plant structures. *Nuclear Engineering and Technology*, 52(1):192–205, 2020.

[74] G. Sevieri, A. De Falco, and G. Marmo. Shedding light on the effect of uncertainties in the seismic fragility analysis of existing concrete dams. *Infrastructures*, 5(3):22, 2020.

[75] A. B. Liel, C. B. Haselton, G. G. Deierlein, and J. W. Baker. Incorporating modeling uncertainties in the assessment of seismic collapse risk of buildings. *Structural Safety*, 31(2):197–211, 2009.

[76] B. R. Ellingwood and K. Kinali. Quantifying and communicating uncertainty in seismic risk assessment. *Structural Safety*, 31(2):179–187, 2009.

[77] K. Porter, R. Kennedy, and R. Bachman. Creating fragility functions for performance-based earthquake engineering. *Earthquake Spectra*, 23(2):471–489, 2007.

[78] I. Zentner. Numerical computation of fragility curves for npp equipment. *Nuclear Engineering and Design*, 240(6):1614–1621, 2010.

[79] I. Zentner, M. Gündel, and N. Bonfils. Fragility analysis methods: Review of existing approaches and application. *Nuclear Engineering and Design*, 323:245–258, 2017.

[80] T. Nakamura and M. Mizatani. A statistical method for fragility curve development. In *Proceedings of the 51st JSCE Annual Meeting*, volume 1, pages 938–939, 1996.

[81] K. Korkmaz. Evaluation of seismic fragility analyses. In *The 14th World Conference on Earthquake Engineering October*, pages 12–17, 2008.

[82] A. Radu and M. Grigoriu. Uncertainty in seismic intensity measures used for fragility analysis. 2017.

[83] S. Kwag, Y. Ryu, and B.-S. Ju. Efficient seismic fragility analysis for large-scale piping system utilizing bayesian approach. *Applied Sciences*, 10(4):1515, 2020.

[84] J. W. Baker and C. A. Cornell. Choice of a vector of ground motion intensity measures for seismic demand hazard analysis. In *13th World Conference on Earthquake Engineering*, number 3384, 2004.

[85] J. W. Baker and C. A. Cornell. A vector-valued ground motion intensity measure consisting of spectral acceleration and epsilon. *Earthquake engineering and structural dynamics*, 34:1193–1217, 2005.

[86] L. Elefante, F. Jalayer, I. Iervolino, and G. Manfredi. Disaggregation-based response weighting scheme for seismic risk assessment of structures. *Soil Dynamics and Earthquake Engineering*, 30(12):1513–1527, 2010.

[87] J. W. Baker and C. A. Cornell. Vector-valued intensity measures incorporating spectral shape for prediction of structural response. *Journal of Earthquake Engineering*, 12(4):534–554, 2008.

[88] J. W. Baker and C. A. Cornell. Vector-valued intensity measures for pulse-like near-fault ground motions. *Engineering structures*, 30(4):1048–1057, 2008.

[89] J. Berkson. Application of the logistic function to bio-assay. *Journal of the American Statistical Association*, 39(227):357–365, 1944.

[90] J. W. Baker. Efficient analytical fragility function fitting using dynamic structural analysis. *Earthquake Spectra*, 31(1):579–599, 2015.

[91] J. Neter, M. H. Kutner, C. J. Nachtsheim, and W. Wasserman. *Applied linear statistical models*, volume 4. Irwin Chicago, 1996.

[92] A. Benavent-Climent, L. Pujades, and F. López-Almansa. Design energy input spectra for moderate-seismicity regions. *Earthquake engineering & structural dynamics*, 31(5):1151–1172, 2002.

[93] F. López-Almansa, A. U. Yazgan, and A. Benavent-Climent. Design energy input spectra for high seismicity regions based on turkish registers. *Bulletin of Earthquake Engineering*, 11(4):885–912, 2013.

[94] P. Giovenale, C. A. Cornell, and L. Esteva. Comparing the adequacy of alternative ground motion intensity measures for the estimation of structural responses. *Earthquake engineering & structural dynamics*, 33(8):951–979, 2004.

[95] J. M. O'connor and B. R. Ellingwood. Site-dependent models of earthquake ground motion. *Earthquake Engineering & Structural Dynamics*, 21(7):573–589, 1992.

[96] D. Lopez Garcia and T. T. Soong. Sliding fragility of block-type non-structural components. part 1: Unrestrained components. *Earthquake Engineering & Structural Dynamics*, 32(1):111–129, 2003.

[97] N. S. Kwong, A. K. Chopra, and R. K. McGuire. A framework for the evaluation of ground motion selection and modification procedures. *Earthquake Engineering & Structural Dynamics*, 44(5):795–815, 2014.

[98] H. Ebrahimian, F. Jalayer, A. Lucchini, F. Mollaioli, and G. Manfredi. Preliminary ranking of alternative scalar and vector intensity measures of ground shaking. *Bulletin of Earthquake Engineering*, 13(10):2805–2840, 2015.

[99] N. S. Kwong, A. K. Chopra, and R. K. McGuire. Evaluation of ground motion selection and modification procedures using synthetic ground motions. *Earthquake Engineering & Structural Dynamics*, 44(11):1841–1861, 2015.

[100] N. S. Kwong, A. K. Chopra, and R. K. McGuire. A ground motion selection procedure for enforcing hazard consistency and estimating seismic demand hazard curves. *Earthquake Engineering & Structural Dynamics*, 44(14):2467–2487, 2015.

[101] A. Arias. Measure of earthquake intensity. Technical report, Massachusetts Inst. of Tech., Cambridge. Univ. of Chile, Santiago de Chile, 1970.

[102] A. EPRI. criterion for determining exceedance of the operating basis earthquake. rapport np-5930 2848-16. *Electric Power Research Institute, USA*, 1988.

[103] R. Riddell and J. E. Garcia. Hysteretic energy spectrum and damage control. *Earthquake Engineering & Structural Dynamics*, 30(12):1791–1816, 2001.

[104] Y.-J. Park, A. H.-S. Ang, and Y. K. Wen. Seismic damage analysis of reinforced concrete buildings. *Journal of Structural Engineering*, 111(4):740–757, 1985.

[105] P. Fajfar, T. Vidic, and M. Fischinger. A measure of earthquake motion capacity to damage medium-period structures. *Soil Dynamics and Earthquake Engineering*, 9(5):236–242, 1990.

[106] K. Mackie and B. Stojadinović. *Seismic demands for performance-based design of bridges*. Pacific Earthquake Engineering Research Center Berkeley, 2003.

[107] J. C. Anderson and V. V. Bertero. Uncertainties in establishing design earthquakes. *Journal of Structural Engineering*, 113(8):1709–1724, 1987.

[108] C.-M. Uang and V. V. Bertero. Evaluation of seismic energy in structures. *Earthquake Engineering & Structural Dynamics*, 19(1):77–90, 1990.

[109] G. W. Housner. Spectrum intensities of strong-motion earthquakes. In *Proc. Symposium on Earthquake and Blast Effects on Structures*, pages 20–36, 1952.

[110] P. P. Cordova, G. G. Deierlein, S. S. Mehanny, and C. A. Cornell. Development of a two-parameter seismic intensity measure and probabilistic assessment procedure. In *The second US-Japan workshop on performance-based earthquake engineering methodology for reinforced concrete building structures*, pages 187–206, 2000.

[111] M. Bianchini, P. Diotallevi, and J. Baker. Prediction of inelastic structural response using an average of spectral accelerations. In *10th international conference on structural safety and reliability (ICOSSAR09)*, volume 1317, 2009.

[112] L. Lin, N. Naumoski, M. Saatcioglu, and S. Foo. Improved intensity measures for probabilistic seismic demand analysis. part 1: development of improved intensity measures. *Canadian Journal of Civil Engineering*, 38(1):79–88, 2011.

[113] J. W. Baker and C. Allin Cornell. A vector-valued ground motion intensity measure consisting of spectral acceleration and epsilon. *Earthquake Engineering & Structural Dynamics*, 34(10):1193–1217, 2005.

[114] N. Shome, C. A. Cornell, P. Bazzurro, and J. E. Carballo. Earthquakes, records, and nonlinear responses. *Earthquake Spectra*, 14(3):469–500, 1998.

[115] N. Shome. *Probabilistic seismic demand analysis of nonlinear structures*. 1999.

[116] Y. Mori, T. Yamanaka, N. Luco, M. Nakashima, and C. A. Cornell. Predictors of seismic demand of smrf buildings considering post-elastic mode shape. In *13th World Conference on Earthquake Engineering, Vancouver, Canada*, volume 15, 2004.

[117] S. Akkar and Ö. Özen. Effect of peak ground velocity on deformation demands for sdof systems. *Earthquake engineering & structural dynamics*, 34(13):1551–1571, 2005.

[118] A. Yakut and H. Yılmaz. Correlation of deformation demands with ground motion intensity. *Journal of structural Engineering*, 134(12):1818–1828, 2008.

[119] N. Jayaram, F. Mollaioli, P. Bazzurro, A. De Sortis, and S. Bruno. Prediction of structural response of reinforced concrete frames subjected to earthquake ground motions. In *9th US National and 10th Canadian Conference on Earthquake Engineering*, pages 428–437, 2010.

[120] F. Mollaioli, S. Bruno, L. Decanini, and R. Saragoni. Correlations between energy and displacement demands for performance-based seismic engineering. *Pure and Applied Geophysics*, 168(1-2):237–259, 2011.

[121] N. Luco, L. Manuel, S. Baldava, and P. Bazzurro. Correlation of damage of steel moment-resisting frames to a vector-valued set of ground motion parameters. In *Proceedings of the 9th International Conference on Structural Safety and Reliability (ICOSSAR05)*, pages 2719–2726, 2005.

[122] D. Vamvatsikos and C. A. Cornell. Developing efficient scalar and vector intensity measures for ida capacity estimation by incorporating elastic spectral shape information. *Earthquake engineering & structural dynamics*, 34(13):1573–1600, 2005.

[123] J. W. Baker. Conditional mean spectrum: Tool for ground-motion selection. *Journal of Structural Engineering*, 137(3):322–331, 2011.

[124] M. Kohrangi, P. Bazzurro, and D. Vamvatsikos. Vector and scalar ims in structural response estimation, part i: Hazard analysis. *Earthquake Spectra*, 32(3):1507–1524, 2016.

[125] M. Kohrangi, P. Bazzurro, and D. Vamvatsikos. Vector and scalar ims in structural response estimation, part ii: building demand assessment. *Earthquake Spectra*, 32(3):1525–1543, 2016.

[126] H. Jamshidiha, M. Yakhchalian, and B. Mohebi. Advanced scalar intensity measures for collapse capacity prediction of steel moment resisting frames with fluid viscous dampers. *Soil Dynamics and Earthquake Engineering*, 109:102–118, 2018.

[127] D.-H. Choi and S.-H. Lee. Multi-damping earthquake design spectra-compatible motion histories. *Nuclear engineering and design*, 226(3):221–230, 2003.

[128] Y.-N. Huang, A. S. Whittaker, R. P. Kennedy, and R. L. Mayes. *Assessment of base-isolated nuclear structures for design and beyond-design basis earthquake shaking*, volume 90008. MCEER, 2009.

[129] A. Sharma, R. Tripathi, and G. Bhat. Comparative performance evaluation of rc frame structures using direct displacement-based design method and force-based design method. *Asian Journal of Civil Engineering*, 21(3):381–394, 2020.

[130] G. Atkinson, N. Allotey, A. Saudy, and M. Elgohary. Spectra-compatible time histories for the acr npp in eastern north america. 2009.

[131] Y. Zhang and F. Zhao. Artificial ground motion compatible with specified peak ground displacement and target multi-damping response spectra. *Nuclear engineering and design*, 240(10):2571–2578, 2010.

[132] S.-H. Ni, W.-C. Xie, and M. Pandey. Application of hilbert-huang transform in generating spectrum-compatible earthquake time histories. *International Scholarly Research Notices*, 2011, 2011.

[133] K. A. Bani-Hani and A. I. Malkawi. A multi-step approach to generate response-spectrum-compatible artificial earthquake accelerograms. *Soil Dynamics and Earthquake Engineering*, 97:117–132, 2017.

[134] B. Li, Y. Lu, M. D. Pandey, G. Ma, Y. Liu, Z. Mei, and L. Shen. Evaluation of amplitude-scaled and spectrum-matched motions to estimate ground-motion amplification factors. *Bulletin of Earthquake Engineering*, pages 1–21, 2020.

[135] R. Narayana Iyengar and K. Sundara Raja Iyengar. A nonstationary random process model for earthquake accelerograms. *Bulletin of the Seismological Society of America*, 59(3):1163–1188, 1969.

[136] J. Conte and B. Peng. Fully nonstationary analytical earthquake ground-motion model. *Journal of Engineering Mechanics*, 123(1):15–24, 1997.

[137] F. Rofooei, A. Mobarake, and G. Ahmadi. Generation of artificial earthquake records with a nonstationary kanai–tajimi model. *Engineering Structures*, 23(7):827–837, 2001.